THE SCANNING PROBE MICROSCOPY STUDY OF THIN POLYMER FILMS.

A thesis submitted in partial fulfilment of the requirements for the Degree of Doctor of Philosophy of De Montfort University.

By

HAMISH ROBERT HARRON

AUGUST 1995

DECLARATION

The work described in this thesis was carried out, unless otherwise stated, by the author and in the Department of Applied Physics at De Montfort University, Leicester. The programme was supervised by Dr.R.G.Pritchard, Dr.R.E.Thurstans and Dr.H.S.Derbyshire of the Department of Applied Physics.

ACKNOWLEDGEMENTS

I would like to express my thanks to the following people:

Bob Pritchard for his guidance, encouragement, confidence and organisation as supervisor for this work.

Barry Cope of the Department of Chemistry for his guidance and confidence especially in the field of polymer and polycarbonate chemistry.

Bob Thurstans and Hazel Derbyshire for their guidance and encouragement as additional supervisors for this work. Jie Shen whose knowledge of SPM and skills in developing the departmental STM were invaluable to me.

The Governors of De Montfort University for providing the laboratory resources and facilities required for the completion of the project. SERC and BNFL for financial support.

Walter Weaver and Dave Goddard of BNFL for their help throughout the project and in addition their help during SPM work with the Nanoscope III and Tapping Mode work and at various conferences.

Norman Bevan, Dave Bazeley, Les Gregson and Tony Woodford for technical assistance. Pete, Ed, Pavel and Vojta who, as fellow research students provided both scientific and non-scientific support and encouragement.

There are so many other people who contributed in so many different but equally significant ways that it is not possible within the confines of this page to thank them all individually by name. However I would like to thank my wife Helen, to whom this work is dedicated, for being considerate, tolerant, helpful and supportive throughout my studies.

ABSTRACT

Scanning Tunnelling Microscopy and Atomic Force Microscopy were used systematically to investigate the morphology, uniformity, coverage and structure of the thin films of several commercially important insulating polymers. Despite the poorly conducting nature of the polymer sample, detailed and convincing images of this class of materials were achieved by STM without the need to coat the samples with a conductive layer. The polymer regions of the sample were further investigated by the use of surface profiling with 'line scans'. The fluctuations of the amplitude therein enabled important film characteristics to be assessed.

An environmental stage was designed for the STM to enable the effect of various vapour-sample interactions to be observed during the imaging process. Using the data from the environmental stage in addition to the surface profiling with line scans, an insight into the conduction mechanism and image interpretation was gained. Results suggest that the water content of the sample and its immediate surroundings is an important factor in achieving reliable STM images in air.

The initial study culminated with the observation by STM alone of the plasticizer induced crystallization of uncoated PC thin films. The 'amorphous' PC films were observed before crystallization and small ordered regions in roughly the same proportion as that predicted by diffraction studies[Prietschk, 1959 & Schnell, 1964] were imaged. This has never been observed by a microscopy technique. Furthermore, images of the crystalline film contained elongated units that were attributed to the lamellae formations that form the basic building blocks of polymer spherulites.

The study continued with the AFM imaging of the growth of crystalline entities in a PC film, without the need for harsh sample treatment or metal coating. A method of casting and crystallizing the films was developed such that the growth was predominantly in two dimensions and consequently

ideal for observation by AFM. Different stages of crystalline growth were observed, starting with pre-spherulitic material and finishing with fully developed spherulites; a process giving a broad insight into the crystallization process at a resolution unobtainable by most other microscopy techniques.

The kinetics of growth of the spherulites within the two dimensional film can be gained from the Avrami exponent 'n'. The results presented here show that SPM can be used not only to provide a value of n (from uncoated samples), but in doing so provide very high resolution images of the film at key stages of development. In addition the size of the spherulites was controlled by the 'seeding' of the film by a suitable nucleating agent. The analysis indicates that the predominant nucleation process occurs at heterogeneities and not homogeneities in the film.

Futher to the size and growth rate of the spherulites, Daniewska et al[1986] suggested (although were unable to substantiate) that the structure of the spherulites fibrils was influenced by the chemical nature of the solvent. Results reported here confirm that the fibril structure and spherulite size was significantly affected by the chemical nature of the plasticizing solvent. Detailed observations of the spherulites are included herein.

A tapping mode AFM was used in conjunction with the usual contact mode AFM to image the fine spherulitic lamellae structure. It was found that the AFM operated in the tapping mode was less destructive than when operated in the contact mode and gave higher resolution images of the lamellae structure. The lamellae were found to be structurally very similar to the features observed in the study using STM indicating that under certain circumstances, the STM was less destructive over the 'insulating' polymer than the contact mode AFM.

CONTENTS

CHAPTER 1

INTRODUCTION

1.0 INTRODUCTION

1.1 SPM

The group of microscopes known collectively as the Scanning Probe Microscopes (SPM) emerged from the Nobel Prize winning invention of the Scanning Tunnelling Microscope(STM) by Binnig & Rohrer in 1981. The importance of the STM in surface science is readily accepted with routine atomic resolution obtainable on many different, although mainly conducting material surfaces. The SPM family expanded with the development of the Atomic Force Microscope (AFM)[Binnig, Quate & Gerber, 1986; Binnig, 1987; Heinzelmann, 1987] which was equally suited to imaging non-conducting sample surfaces in addition to those imageable by STM. The number of different probe microscopes is growing fast and now contains many new and scientifically significant probe microscopes. Examples include the Magnetic Force Microscope or MFM[Allenspach et al, 1987] and the Scanning Near-field Optical Microscope or SNOM[Fischer, 1990]. The variety and diversity of microscopes under the heading SPM has facilitated the imaging of almost every type of material and property of interest to surface science.

The group may be summarized as a set of microscopy techniques providing very high (even sub-atomic) resolution. This is achieved by scanning a probe and electronically building an image of the surface in terms of the interaction between probe and sample. The type of interaction defines the microscope for example the AFM acquires images by measuring the force between the sample and scanning tip as a function of position whereas the STM measures the tunnelling current between tip and sample.

The emphasis in this thesis is on atomic force and scanning tunnelling microscope studies of thin polymer films. These two types of SPM microscope present an invaluable set of instruments in the field of surface science because they have great resolving power and can image many different samples. Under standard laboratory conditions, atomic resolution of conducting materials (STM and AFM) and nanometre resolution in organic material (usually measured by AFM) is regularly achieved allowing detailed

studies of surface structure. Moreover unlike electron microscopy, the tunnelling and force microscopes can image samples in their natural environment without the need for harsh vacuum conditions. The employment of the SPM techniques under ambient conditions is especially useful where hydrated or other liquid based specimens, both biological and polymeric are studied. The techniques also present the added advantages of (in some cases) imaging very thin polymeric samples without the necessity of sample replication or conductive coating.

The benefit SPM brings to this study of polymeric thin films are many and will be discussed in detail in the following chapters of this thesis. However other techniques such as Scanning Electron Microscopy and Optical Microscopy are also employed. These latter techniques are not discussed in depth here, but allow vital complementary data on the films, which aid image interpretation of the SPM images.

1.2 THE SCANNING TUNNELLING MICROSCOPE

The STM is quite different from conventional microscopes in that the imaging process does not rely on optical or electromagnetic focusing, but on the quantum tunnelling of electrons from a moving probe to the specimen. The STM uses an excellent design of instrumentation that includes vibrational isolation (attenuation of the amplitude of noise vibrations from micron to sub-nanometre) and precise three dimensional mechanical movement (usually achieved by a piezoelectric device). The STM tip is accurately scanned across the sample surface with a separation suitably small (≈0.5nm) for an appreciable tunnel current to be measured. In general for ideal samples, the tunnel current (at a given tip-sample separation) fluctuates periodically with the corrugations of the surface. By recording the tunnel current as a function of position, a basic STM image of the surface detail can be achieved.

The rapid acceptance of STM as a technique of major importance in surface science was a result of the excellent high quality three dimensional representations of some conducting and semi-conducting materials. For the

first time, unambiguous images of the reconstructed Si(111) surface were obtained showing the now famous 7x7 reconstruction [Binnig et al, 1982]. Other successes followed and groups were able to image adsorbates like long chain alkanes [Eng et al, 1992] for example n-$C_{32}H_{66}$ [McGonigal et al, 1990] and even biomolecules such as nucleic acids [Allen et al, 1991, 1992; Bloomfield & Arscott, 1991], DNA [Allen et al, 1991, 1992; Bai et al, 1993; Cricenti et al, 1992]].

1.2.1 Tunnelling Mechanism.

The STM probe is usually a wire made from a transition metal or alloy (W or Pt-Ir), sharpened by grinding or electrochemical etching into a very sharp point or tip. The tip is moved using a combination of mechanical and piezoceramic control until a gap of 0.5-1.0nm between the tip and conducting sample is achieved. At this separation the electron wavefunctions around the tip overlap with those of the sample. A small external bias applied (approximately a volt), causes a nanoampere tunnel current to flow between the tip and sample (see figure 1.1). In a treatment by Tersoff & Hamman[1983], the tip is described as probing the local density of states at a short distance 'R+s' from the sample under study (R is the approximate radius of the tip and 's' represents the separation between the tip and sample). The tunnel current depends exponentially on the separation distance 's' in the following form:

$$I_t \alpha \exp^{-2ks}$$

Where k is the decay constant which is related to the mean barrier height. The STM is highly sensitive to the gap size. Under ideal conditions the change in tunnel current caused by the periodic variation in the tip sample separation due to the corrugations in the atomic surface can be measured easily.

Because it is the electronic wavefunction overlap that is responsible for the imaging mechanism for the STM, it can be shown that [Tersoff &

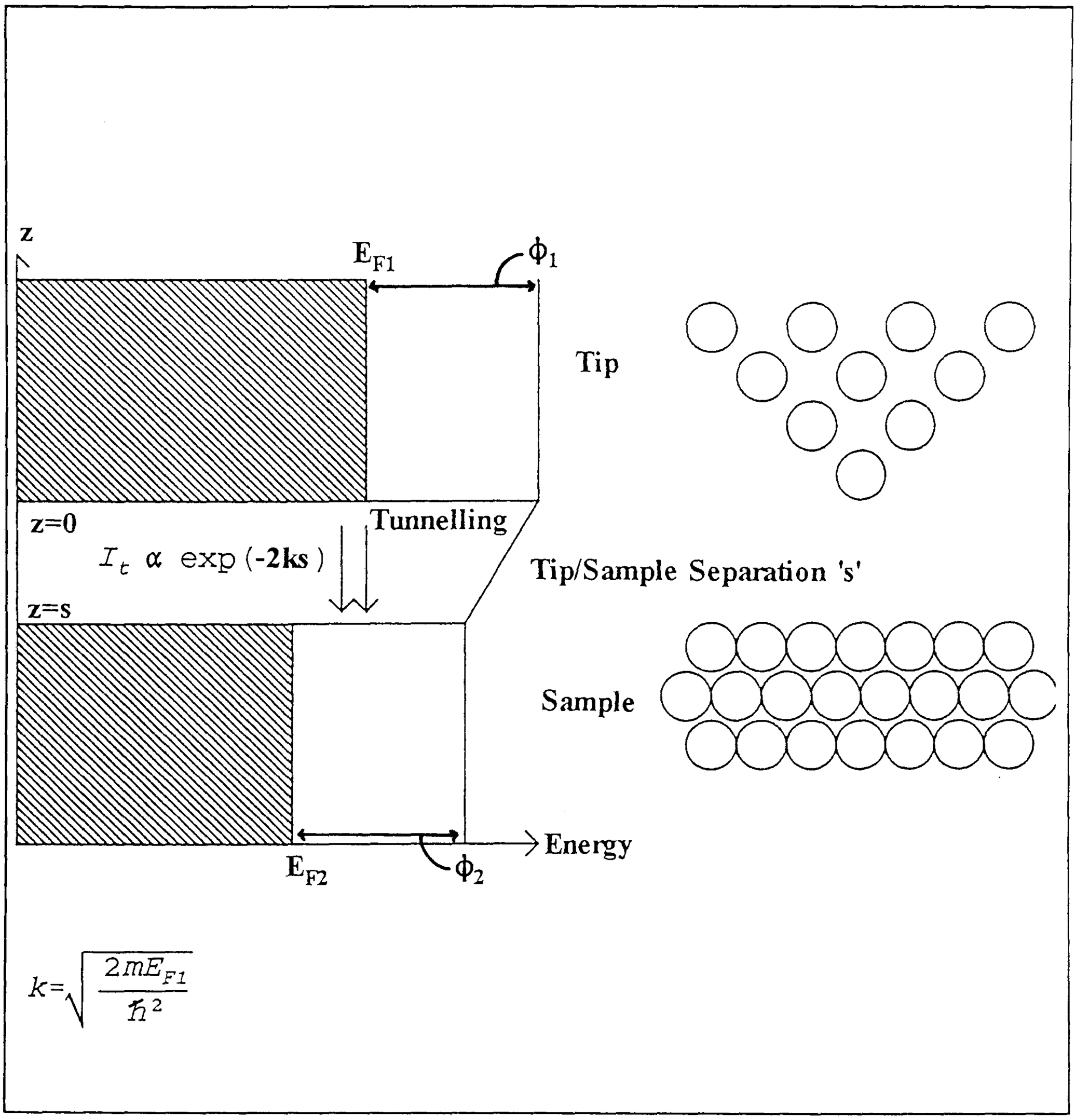

Figure 1.1: The STM tip is moved to within (0.5-1.0)nm of the sample surface. At this separation(s) and with a small bias applied (V), a tiny tunnel current (I_t) flows from the tip to the sample.

Hamman, 1983] the tip actually measures the local density of states or LDOS at the Fermi level (i.e. the electron density). In metals, the charge density distribution across the surface is spatially very similar to the atomic corrugations, in which case the STM image accurately portrays the atomic topography. However for other samples including semiconductors, the charge density distribution is not so intimately linked with the physical surface. For other samples, that include polymers, the 'electronic surface' and the physical surface can be very different leading to problems with image interpretation.

General Operation

The STM probe is scanned across the sample using for example, a piezoceramic device. The tunnel current measured is amplified and then recorded by computer. This value is then used as the input for a feedback loop which controls the scanning process (figure 1.2). By obtaining measurements as a function of scan position, a three dimensional map of the surface may be constructed in either of two modes (figure 1.3).

In the constant current mode (figure 1.3a), the local gap width is kept constant. The feedback loop responds very quickly to restore a preset value of the tunnel current. This is achieved by moving the tip closer to or further from the sample to account for changes in the local electronic surface. The image is constructed by recording the feedback signal (to the scanning device) as a function of position.

In the constant height mode (figure 1.3b), the tip is scanned with the feedback loop responding insignificantly to local variations in the surface morphology (and hence gap width). Thus whilst the tip moves very little perpendicularly to the sample, the tunnel current fluctuates exponentially as the gap width changes over the surface features. The tunnel current is recorded as a function of position enabling the image to be constructed.

1.2.2 The Study of Polymers by STM

The tunnelling process requires a conducting tip and sample and early work

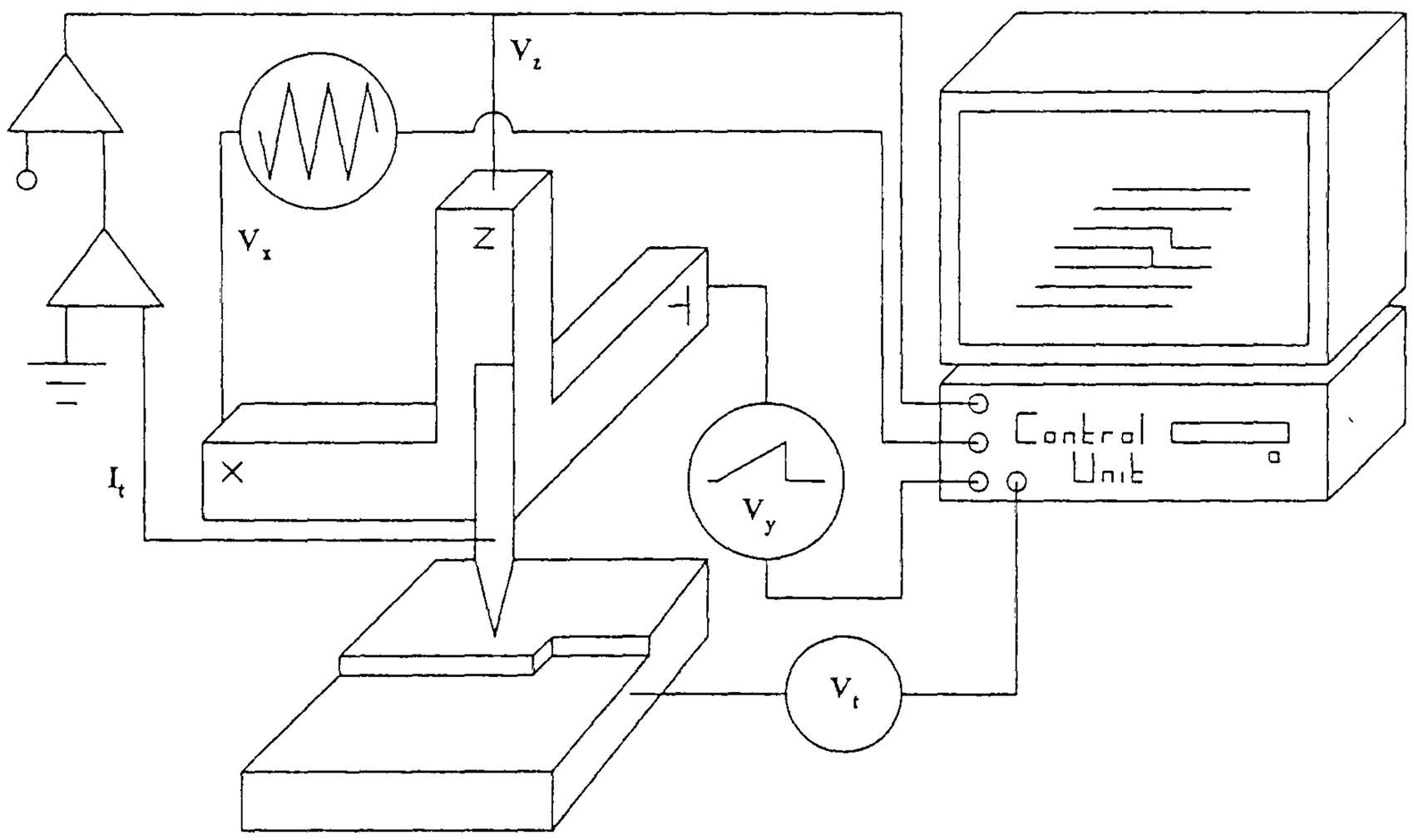

V_z= z-Voltage
V_x= x-Voltage
V_y= y-Voltage
V_t= Bias between tip and sample (Typically 80mV-550mV)
I_t= Tunnelling Current (Typically 0.050nA-1.500nA)

Figure 1.2: The tunnel current is measured as the tip is advanced towards the surface. Once a preset value is reached, the tip is scanned in two dimensions(x,y) by the piezoceramic device. The tunnel current is recorded as a function of position by the control unit and an image of the surface is constructed.

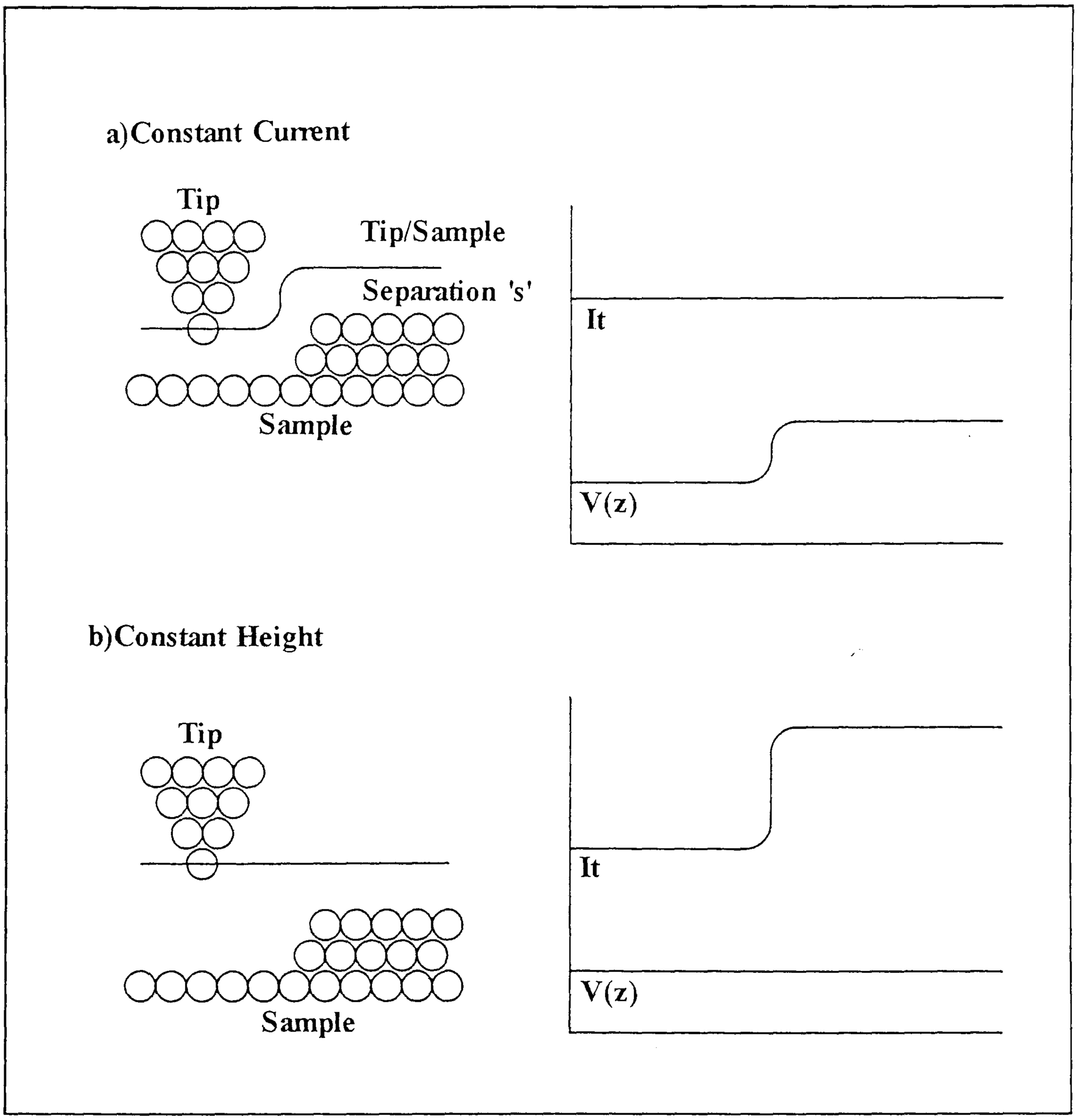

Figure 1.3: There are two modes of operation for the STM. a) During the constant current mode, the pre-set tunnel current is maintained by constant monitoring by the feedback loop. The voltage on the piezo (Vz), required to maintain the current is plotted as a function of position. b) During the constant height mode, Vz is disabled and the feedback loop measures only the variation in the tunnel current caused by the features on the surface.

with STM concentrated on metals and semiconductors. In the mid 1980's it was found that thin layers of materials regarded as insulators in the bulk state were also imaged by the STM in certain situations.

The STM can image a very wide range of organic material. Simple small molecules such as decanol [McGonigal, 1992], benzene [Fisher, 1993] can be observed as can large, complex molecules like copper phthalocyanine [Gimszewski, 1987] and high molecular weight polymers. Examples of the latter include polymethylmethacrylate[Shen, 1991], PODA [Albrecht, 1988], polystyrene[Jandt, 1992], polyethylene[Piner et al, 1990; Reneker, 1990] and paraffin wax [Travaglini, 1988].

The STM images of organic samples are difficult to interpret because of the lack in conductivity of the samples. However the best results are generally obtained when the substrate is very flat, featureless and the polymer film is very thin. The image comprises of features ranging from noisy amorphous patches to neatly aligned chains, all of which may be measured and attributed to the polymer. The extent of the polymer coverage, the state of crystallinity, the approximate thickness of the films and to some extent, the dimensions of the polymer chains can all be established.

Imaging Mechanisms Associated with Polymers

The imaging mechanisms that allow the STM to function at such high magnification are reasonably well understood for metals and semiconductors. The situation for biological and organic films is however more problematic at the present time. The STM probe (the tip) must be very close to the surface for tunnelling to occur, typically less than 1nm. However polymer films thicker than this tunnelling gap have been imaged [Travaglini, 1988; Blackford, 1991]. The observed conductivity in these cases is too high to explain by vacuum tunnelling alone and alternative mechanisms have been proposed [Garcia, 1990; Joachim & Sautet, 1990; Lindsay and Sankey, 1992]. These are discussed in more detail in chapter 2.

The difficult interpretation of STM images of polymeric materials arises as a direct result of the poorly understood conduction mechanism involved

during image acquisition. Despite this situation many convincing and useful images of polymers have been obtained, providing detailed topographical data.

Image interpretation difficulties are particularly marked if the conduction mechanism changes during an individual scan. To illustrate this, during the imaging of a gold substrate only partially coated with a polymer, the tip moves from an area of polymer to an area of bare conducting gold substrate. A complicated, possibly variable conduction mechanism is replaced by conventional barrier tunnelling. In this case great care is needed to avoid over-naive interpretation involving differentiation for example of different surface regions by their false colour alone.

To enable images to be more successfully interpreted an analysis may be made of the changes in the short term fluctuations in individual line scans taken across both polymer and substrate. As the tip moves from a polymer area where such fluctuations are often relatively large to the gold substrate area where they are small, the location of polymer (or contaminant) regions may be ascertained.

Summary

The study of thin polymer films by STM is an important research area for two reasons: Firstly, film structure, uniformity and coverage are technologically important in areas such as device fabrication, adhesion and lubrication processes and can be ascertained by STM provided the images are carefully interpreted. Secondly, the conduction mechanisms that enable images of 'insulating' polymers to be obtained by STM are not well understood. However the images contain electronic data on the polymer and may offer potentially significant insight into polymer conductivity on the microscopic level. The properties including electrical data of the thin films of polymers are vital in modern micro-components. Before this point is reached, however, further insight into the imaging mechanism is vital if organic STM is to advance.

1.3 THE ATOMIC FORCE MICROSCOPE

The atomic force microscope or AFM was developed in the mid nineteen eighties[Binnig, Quate & Gerber, 1986] and utilized the recently developed vibrational isolation, piezoceramic positioning and computerized control technology so crucial to the success of the STM some three years before. An AFM tip is different from the STM tip in that it is situated at the end of a very flexible cantilever. As the tip is lowered towards the sample, a variety of force regimes are encountered (figure 1.4). The interaction between the tip and sample can be repulsive or attractive but the net effect is to cause a deflection in the cantilever which is accurately monitored as a function of position.

In the absence of charged regions which give rise to large coulombic forces, the short range forces that are experienced when the tip and sample are very close (s<0.3nm) decay quickly as the gap width increases. However at this separation and if the tip is sufficiently small and rigid with the system isolated from vibration, fine surface detail (and even atomic corrugations) can cause a deflection in the cantilever as the tip traverses the surface.

AFM Operational Modes

The tip and cantilever are scanned across the sample surface by a piezoceramic tube and the cantilever displacement (caused by the force interaction between tip and sample) is measured by a displacement sensor (figure 1.5). The signal from this sensor forms the input of a feedback loop in the same way as the tunnel current formed the input for the STM feedback loop.

The AFM may be used in a variety of modes that depend on the force measured. The 'contact mode' is commonly associated with the repulsive interaction between the tip and sample atoms. This occurs when the gap width is effectively zero. The 'non-contact mode' is used when the tip is further from the sample and predominantly attractive forces are experienced.

Other modes of operation include the constant force operation, constant

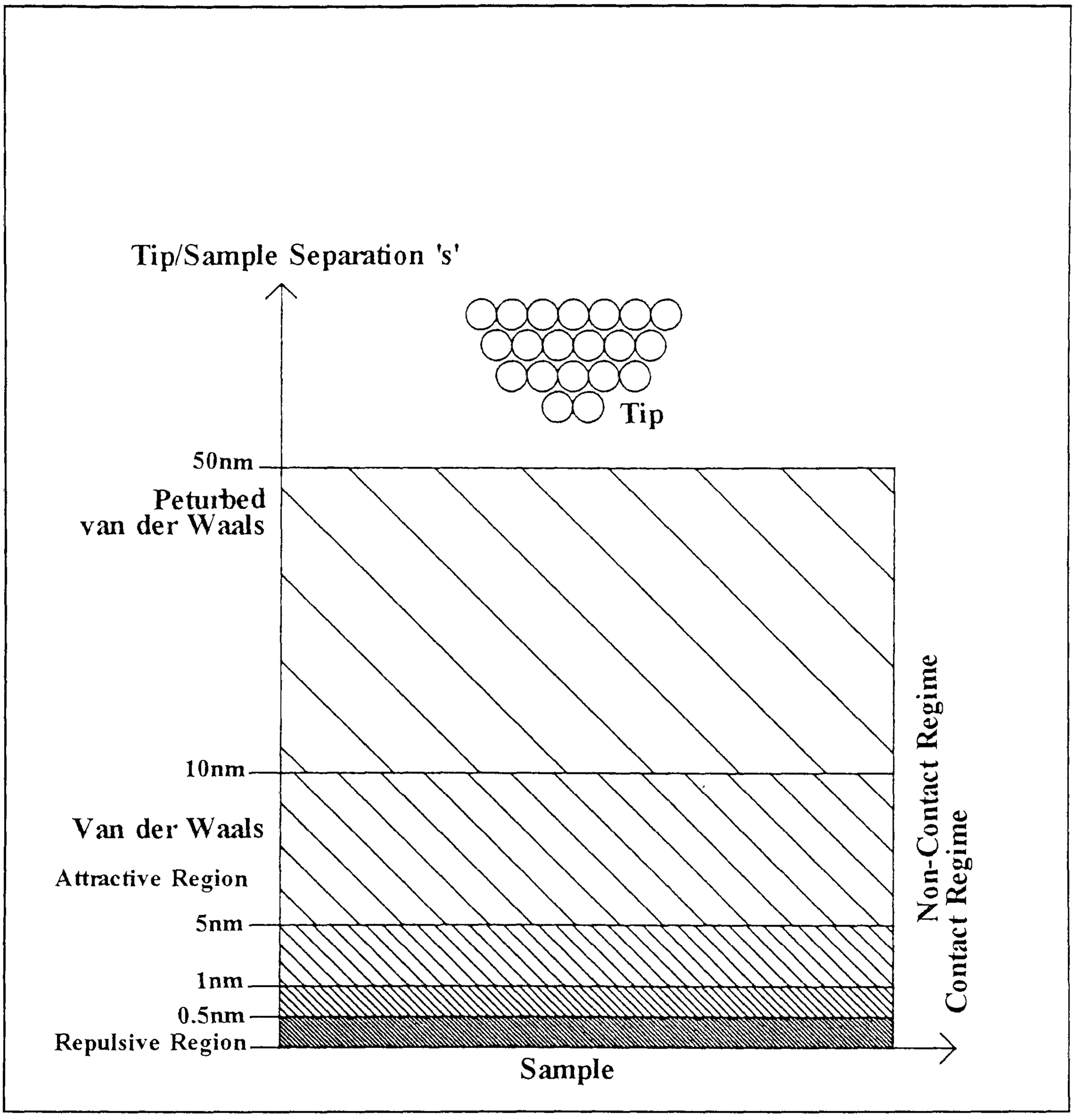

Figure 1.4: The AFM tip encounters different force regimes as it is moved towards the sample. Furthest away are the van der Waals forces and are fairly weak. Very close to the sample strong repulsive forces are encountered and it is here that the majority of AFM work is done.

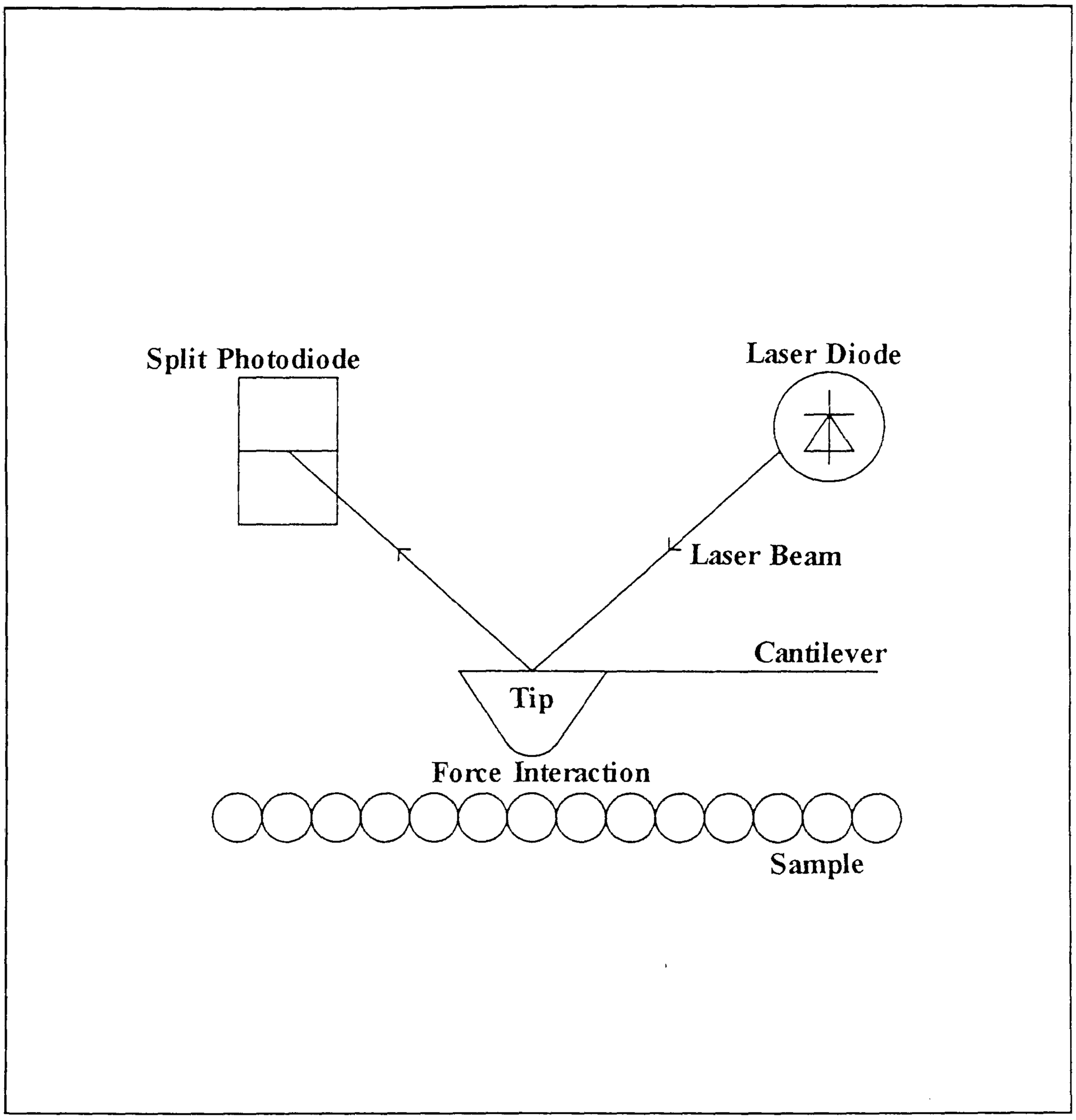

Figure 1.5: The AFM tip is mounted on a flexible cantilever. Any force interaction between the tip and sample results in the deflection of the cantilever. The deflection is measured by the movement in a split photodiode of a small laser beam.

height operation and the tapping mode of operation (see figure 1.6). These modes can be used in both the contact and non-contact regimes.

The constant force operation requires the signal to be reduced to a pre-set value at each position during the scan. This is achieved by raising or lowering the tip relative to the sample by a movement in the piezoceramic tube, the magnitude of which, is proportional to the error signal (the difference between the measured and pre-set signal). To construct an image of the sample, the error signal is recorded as a function of position. In this mode, the tip follows a contour of constant interactive force, if there is a pit in the surface, the tip must enter to re-establish the pre-set displacement and so on.

The second mode of operation is analogous to the constant height mode in STM. In this case the AFM feedback loop is disabled as soon as an interaction with the sample is measured. This prevents the piezoceramic from moving the tip in a direction perpendicular to the sample (hence constant height). The tip is scanned across the sample and the displacement in the cantilever is recorded as a function of position. The image is thus constructed from the force at any given position where the force may be repulsive or attractive. The tip, when scanned in this mode is likely to register zero displacement if the sample contains very deep pits or at the other extreme, may damage the cantilever at a sharp incline or in the presence of relatively rough features. In general this mode is used for very flat samples.

The tapping mode of operation [Goddard et al, 1993] is a recent development from the constant force mode and is commercially available from Digital Instruments, USA. In this mode (see figure 1.7), the tip is raised from the sample after every measurement of cantilever displacement and the scanning takes place remote from the sample. It has been suggested [Meyers et al, 1992] that continual contact during scanning results in significant sample damage. By removing the tip during scanning, delicate samples may remain intact and scan induced features eliminated.

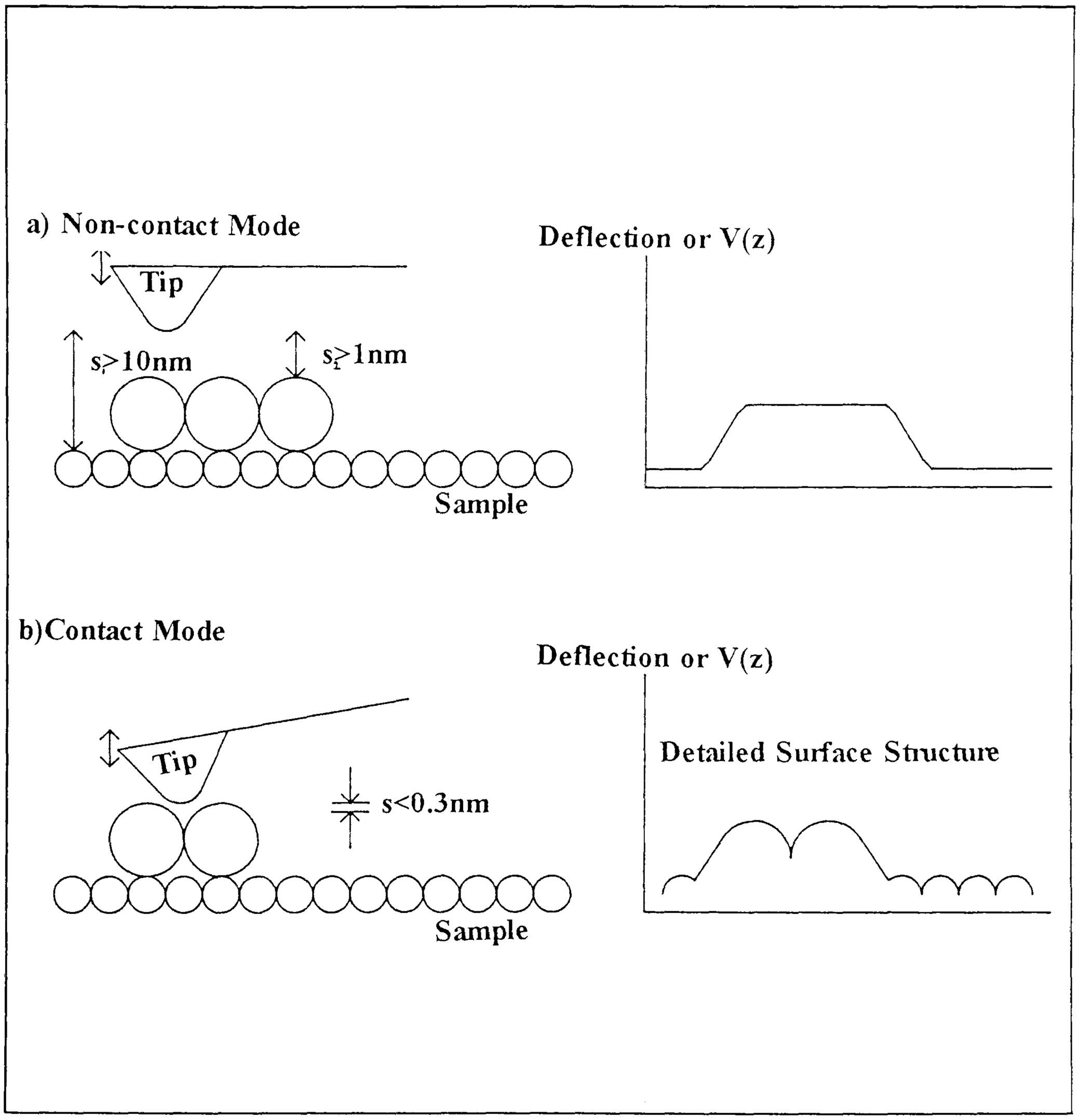

Figure 1.6: There are two general modes of operation for the AFM. a) The non-contact mode, where the tip and sample are too far apart for repulsive interactions to take place. b) The contact mode of operation requires the tip and sample to be 'in-contact'. The best images are produced in this latter mode, however significant sample damage may also occur especially if the sample is very delicate.

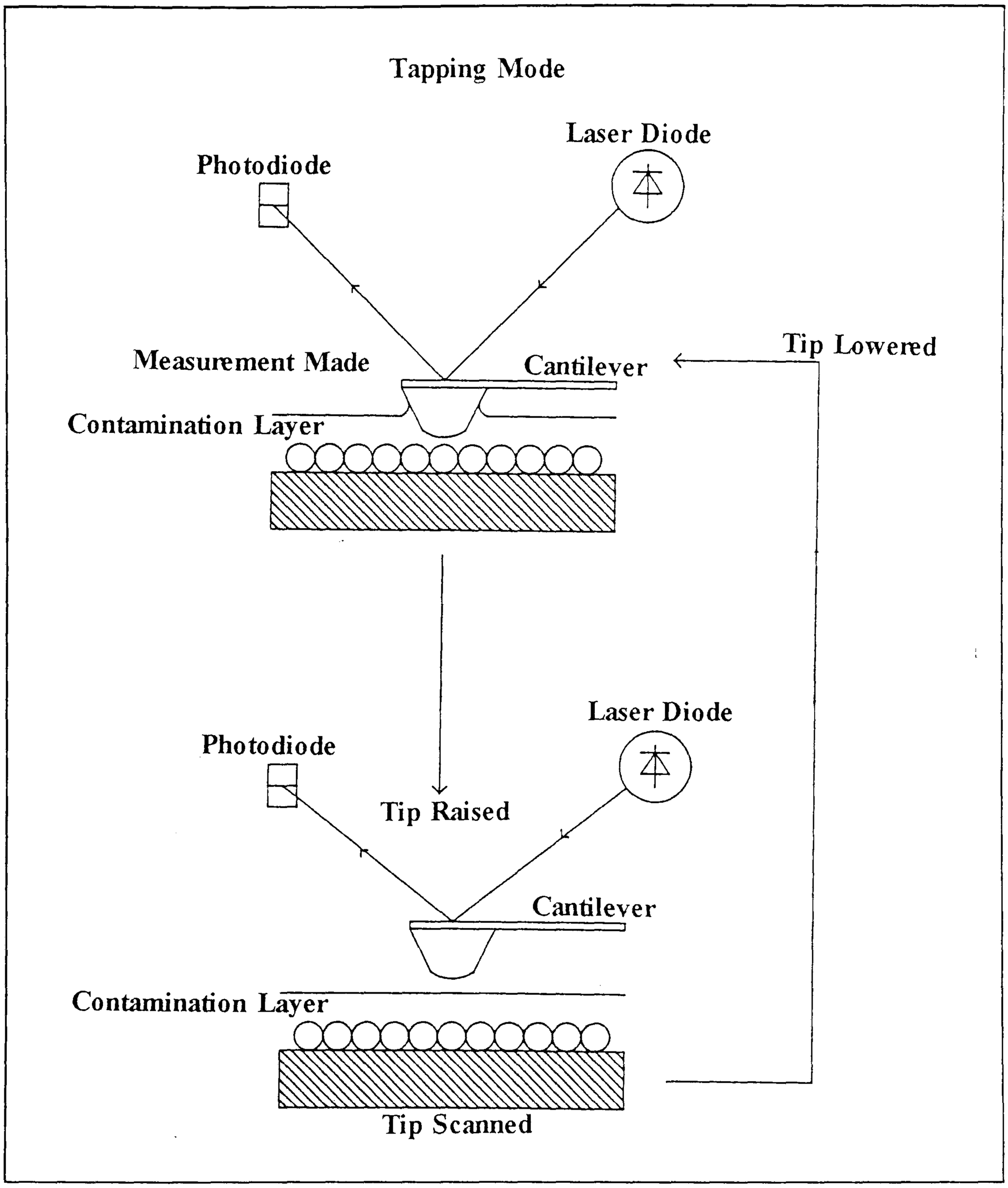

Figure 1.7: The Tapping Mode AFM is used to avoid scanning through a contaminating layer. The tip is raised clear of the sample between every measurement and scanned only in the raised position.

1.3.1 Polymers Imaged by AFM

The AFM has been used to image successfully a variety of samples including inorganic, metallic, organic or biological materials. The tip-sample interaction (and hence the imaging mechanism) is independent of conductivity and therefore samples considered too insulating for STM work can be imaged. Recent reviews by Binnig[1992], Haggerty & Lenhoff[1993], Blackford et al[1991] & Heinzelmann et al[1990] highlight the range of materials studied.

In view of current work being undertaken, it may be assumed that for insulating polymer studies, the AFM has superseded the STM as the most extensively used probe microscope. Some examples of excellent papers in the field of AFM and polymers may be found by Eng et al[1992], Hamada & Kaneko[1992], Jandt et al[1992], Leggett et al[1993], Magonov & Cantow[1990, 1991, 1992], McMaster & Morris[1993], Schonherr et al[1993], Snetivy et al[1992] Stocker et al[1992] and Zajac et al[1992]. The increase in usage of the AFM over STM in this context is mainly due to the less ambiguous mechanism responsible for image formation in AFM, and consequently the image interpretation for many polymeric samples is much easier than the STM image of the same sample.

However the interaction of the AFM tip with the sample (see chapter 3) can be extensive and damage the sample considerably, limiting resolution on delicate samples like polymers to that of the nanometre level.

1.4 AIMS OF THIS THESIS

1.4.1 THE SPM STUDY OF THIN POLYMER FILMS

This project aimed systematically to investigate the morphology, uniformity, coverage and structure of the thin films of typical insulating polymers by STM and AFM. The image interpretation of the STM images is investigated and resulting structural features discussed. The study continues, using both

STM and AFM as complimentary techniques to resolve, elucidate and confirm complex structural entities within polymer films especially during environmental changes. The study concludes with the observation of the growth of crystalline entities in a polycarbonate film without heat treating or the coating of the sample.

The study was performed in two stages, both are introduced below.

1.4.2 STAGE 1: Determination of polymer morphology

Firstly the STM was used to image substrates formed under a variety of different conditions. An assessment of suitable substrates was made with respect to polymer film deposition. A study of the substrate defects revealed how polymer image interpretation could be frustrated by substrate features (a factor that has been discussed recently in the literature).

This stage then progresses to show how line scans taken across both polymer and bare substrate were able to aid image interpretation. This is achieved by locating the different surface materials and scanning over both polymer and bare-substrate together. Numerous line scans were taken across the image and their fluctuations along with other subtle variations revealed the location and morphological components of the polymer film. The results were used to determine the polymer film topography i.e. uniformity, coverage and structure for three solution cast polymers films.

The polymers studied were poly(vinyl pyrrolidone) or PVP, poly(methyl methacrylate) or PMMA and polycarbonate or PC. These polymers were chosen because they were each expected to show different behaviour on the given substrate. This behaviour may follow predictable patterns. The differences in the film forming abilities consequently enabled the image interpretation methods, including the line scan profiling, to be tested.

The three polymers, PMMA, PVP and PC were insulating materials(in the bulk) of high molecular weight and purity. The first, PMMA was non polar (chloroform) soluble and the second, PVP was polar (water) soluble. Both were expected to be amorphous. The third polymer PC, was expected to show some degree of ordering under certain film casting conditions. The

three films were cast from solution on both hydrophobic gold and graphite (HOPG) substrates and the ensuing films observed by STM and AFM.

The internal structure of the polymer films was studied by STM. Possible polymer chain conformation and folding therein was discussed and a comparison made with AFM images and those features caused by the interference of the scanning process. The methods of film deposition were addressed, the solvent type and polarity investigated, and the ambient film casting conditions necessary to improve STM images were also studied.

The effect of the environment surrounding a polymer film has been shown to be crucial in image formation. In particular the presence of moisture and plasticizing molecules on the surface or within the bulk of the polymer influences the structure and conductivity enormously[Seanor, 1986].

Both PMMA and PVP were studied under the influence of a changing humidity during imaging. For PVP which is a highly hygroscopic polymer, water vapour acts as a plasticizer and will effect the polymer structure as well as the conductivity. For PMMA, the effect of the water molecules may not affect the morphology *per se*, but may act to enhance the conductivity of the sample (as discussed in more detail in chapter 2).

For PC, a suitable plasticizing vapour was used to promote crystallinity and this topic is expanded in the next stage. The effect of the plasticizer on the STM image formation of PC was investigated. The resulting structural changes in very thin PC films was extensively studied and the ensuing features related to basic crystalline ordering.

1.4.3 STAGE 2: The emergence of crystalline entities from the polymer film.

Polycarbonate, a technologically important polymer, is known to crystallize under the action of a plasticizing vapour. This process, in thin films of the polymer may lead to a considerable loss in mechanical strength and other important properties. The crystallization process allows the emergence of polymer crystallites from the amorphous film to be observed and charted.

The growth of polymer crystallites is still not well understood and more conventional microscopic work such as scanning electron microscopy(SEM) may be hampered by sample preparation techniques including metal coating. However AFM in this context, requires simple sample preparation and the growing crystalline entities may be observed *in-situ* at key stages of development.

This stage of the work shows how appropriate treatment of polycarbonate thin films, in a controlled and reproducible manner results in crystalline development. The stage continues by explaining how appropriate plasticizer treatment/evaporation results in a step by step growth cycle and how it was used to halt the characteristic development of the polymer crystallites. The AFM was used to image the polymer films during the cycle and important aspects of the growth mechanism observed. Important stages of crystalline development were observed. These included the formation of fibrils, containing folded chain lamellae previously imaged in stage 1.

Crystalline growth is initiated at a nucleation site, (the nature of the site is investigated in the further work study below) and twisting and branching of the fibrils as they assimilate of the amorphous film was observed.

The initial formation is that of a 'sheaf'-like entity; however this is superseded by the disc-like growth associated with spherulitic growth. Finally the film was observed at the end of the crystallization process where all the amorphous polymer has been converted into the spherulitic material. The spherulites impinge on each other and development ceases leaving a boundary mid-way between nucleation sites. The boundaries between neighbouring crystalline entities were observed for any continuity in material across the boundary.

A low voltage SEM was also used to observe the crystallizing polycarbonate film and the results compared directly with those from AFM.

1.4.4 Further and Future Work

In the two main stages of the results, the successful imaging of polycarbonate spherulites was achieved, providing detailed morphological and kinetic data

by the STM, and AFM. In this section the nucleation mechanism for the PC spherulites was investigated. The study developed the standard film casting techniques used for AFM work to include the deliberate seeding of nucleation sites. The time dependent nature of the nucleation was also investigated and it was shown that the dominant process for initial crystalline formation was due to the presence of heterogenieties in the film.

The effect on film morphology of a change in the chemical nature of the plasticizer was investigated. The study showed clearly that the spherulite structure and size is related to the solvent activity (a term that will be defined) used to induce their formation. Growth rates for the entities were calculated for each of the solvents and differences observed again related to the solvent activity. Finally a model developed after Avrami (in Chapter 4) predicted the growth mechanism for spherulites in general and this analysis was applied to the results. By plotting the data in an appropriate manner it was possible to show that the AFM technique was valid for use as a kinetic tool.

CHAPTER 2

STM THEORY AND POLYMER IMAGING

2.0 STM THEORY AND POLYMER IMAGING

2.1 INTRODUCTION

The success of the STM as a microscope for surface studies stems from the ultra-high resolution imaging of a variety of samples. There is a fundamental difference in imaging mechanism between conventional microscopies for example SEM, and STM. Whereas the former rely on optical or electromagnetic focusing, the STM relies on the quantum mechanical effect of tunnelling.

This chapter introduces a simple one dimensional model of the STM system which is used to describe the transmission of electrons between the tip and sample, through a gap that separates the two. The electronic and physical shape of the gap (which for the electron represents a classically forbidden region or barrier), is shown to be critically related to the magnitude of the small tunnelling current measured by the STM. Modifying the simple model to take into account the finite size and shape of the tip [Tersoff & Hamman; 1983] results in an approximation for the high spatial(x,y) and vertical(z) resolution of the STM with respect to the sample's electronic surface or local density of states (LDOS) near the Fermi level.

The initial model of the STM system described above reveals the salient features of the STM technique as applied to metals. In this situation the details of the geometric arrangement of atoms on the surface are reflected in the spatial distribution of the electronic states (LDOS), measured by the STM [Feenstra, 1990].

However, if the sample is non-conducting in parts or if the electronic states of the surface do not follow the atomic or molecular corrugations (for example in some polymers) image interpretation becomes very difficult. To complicate the image formation further, the imaging mechanism is found to be very different from that outlined in the model above and the tunnelling current(in the sense envisaged by Tersoff & Hamman) may contribute in only a limited way to the general conduction (imaging) mechanism.

It is to the more general conduction process that the latter part of this

chapter is dedicated showing how the current research into conductivity within polymers and the subsequent imaging by STM becomes relevant in the context of this thesis.

2.2 BASIC IMAGING.

Barrier Penetration

Electron tunnelling is essentially the electron penetration into a classically forbidden area (see figure 2.1). Consider an electron (energy E_z) incident on a potential step (height V_0). In classical terms, if the energy of the particle is less than the potential energy of the step (i.e. $E_z<V_0$), the electron is reflected. For transmission to occur and for the electron to be at any position greater then z=0, it would have to possess a negative kinetic energy.

However in quantum mechanical terms, the electron may be described in terms of a wavefunction. By solving the time independent Schroedinger equations for both negative and positive z, the wavefunction to the left of the step is found to vary sinusoidally and that to the right of the step decay exponentially (with increasing z). This result is profound as it demonstrates that as there is a non-zero probability density within the step, there must be a probability of the electron existing inside the step.

If the potential step described above is terminated at z=s, a barrier is formed of width 's' and the wavefunction of the tunnelling electron may be calculated on the far side of the barrier. By comparing the $|\psi|^2$(attributed to the wavefunction) either side of the barrier, a transmission coefficient may be calculated which can be loosely described as the 'degree of tunnelling'. In the next section, this very simple model is adapted to the STM system, the barrier represents the gap between the tip and sample and the 'degree of tunnelling' related to the actual tunnel current measured.

The simple STM model.

In a metal-vacuum system (and at zero Kelvin), all the electrons are confined

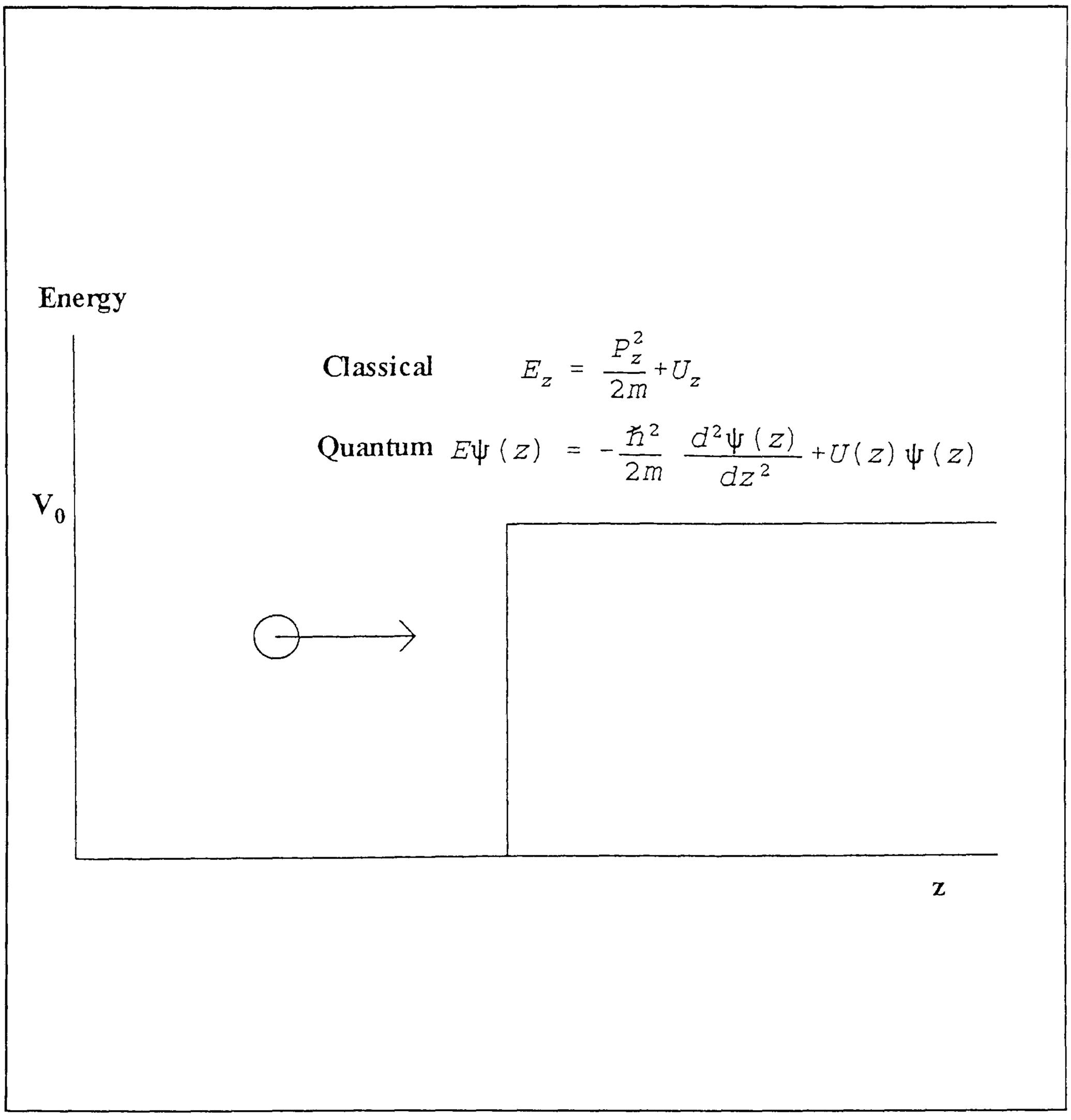

Figure 2.1: An electron with energy E_z incident on a potential step (height V_0) will bounce back according to classical theory. However, if the electron is described in terms of a wavefunction, it may penetrate the step.

to the metal and exist in energy levels which are filled up to the Fermi level or E_F (see figure 2.2a). The electrons may escape from the surface of the metal and into the vacuum but to do so they must acquire sufficient energy equivalent to the workfunction of the metal (ϕ). If two metallic regions are joined together by an external circuit (without an applied bias and shown in figure 2.2b), they may be considered to be in thermodynamic equilibrium. In this situation they share a common Fermi level and are separated by an energy barrier with a shape dependent on the workfunctions of the materials used. Finally, if a potential difference (V) is applied, the Fermi level shifts apart by an amount eV in joules (see figure 2.2c). Tunnelling may now occur between the occupied states of the material with higher Fermi level to those unoccupied states on the other side of the barrier which exist at an energy range E_F to E_F-eV.

The STM system comprises of a tip and sample separated by a small gap (see figure 2.3) of width 's'. The tip and sample are in this instance assumed to be two planar electrodes. A small bias is placed across the gap or potential barrier through which the tunnelling electrons will pass. The electron wavefunction incident on the left hand side of the barrier decays into the barrier. Solving the time independent Schrodinger equation below, enables the electron wavefunctions in each of the regions (tip, gap and substrate) to be derived assuming that at the boundaries, both the wavefunctions and their spatial derivatives are continuous.

$$E\psi(z) = -\frac{\hbar^2}{2m}\frac{d^2}{dz^2}\psi(z) + V(z)\psi(z)$$

In the classically allowed regions (in the tip and sample) the solutions have the form:

$$\psi(z)_{tip} = Ae^{ikz} + Be^{-ikz}$$

$$\psi(z)_{sample} = Fe^{ikz}$$

And in the classically forbidden region i.e. in the potential barrier or gap, the

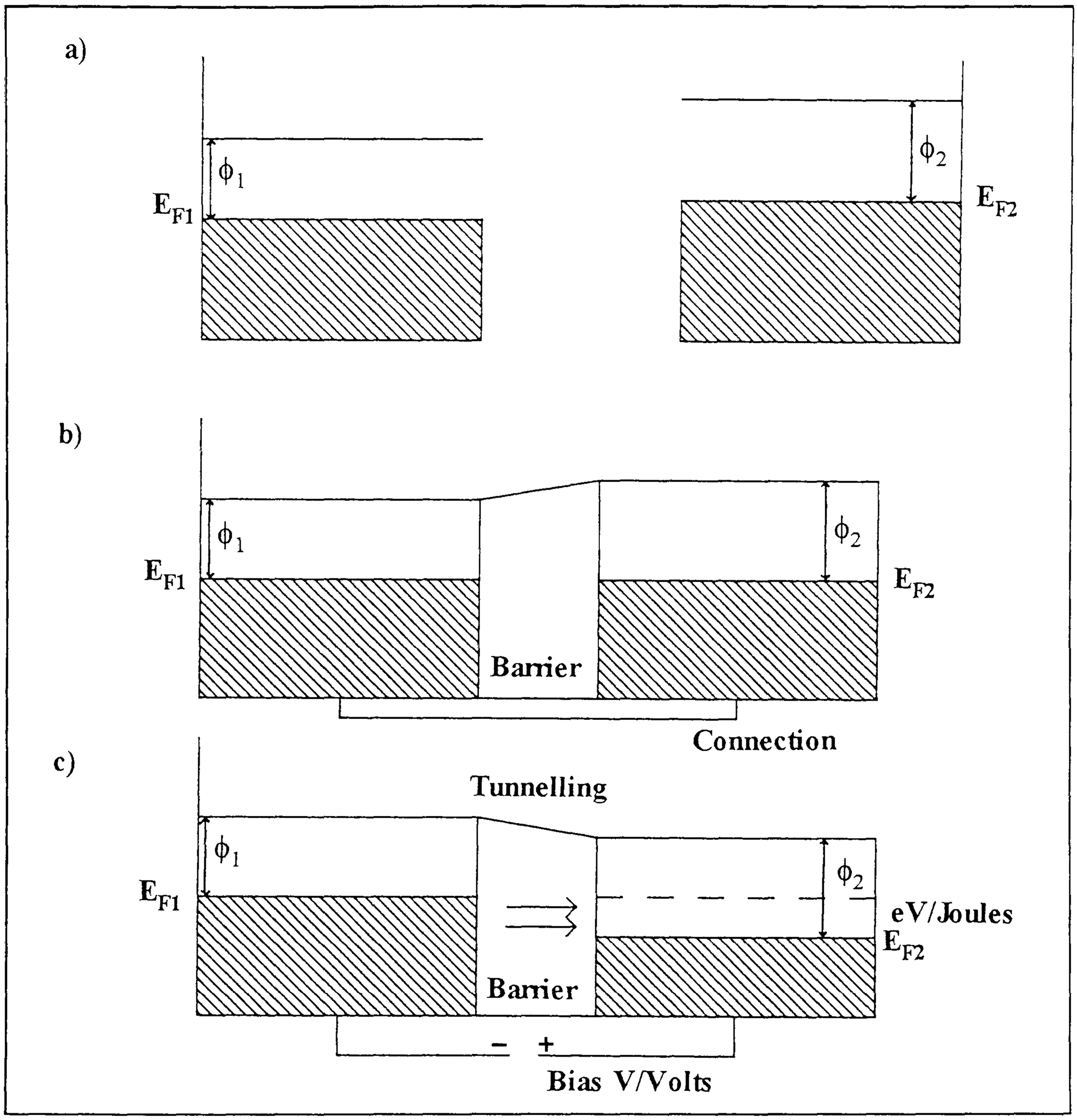

Figure 2.2: (a) In a metal-vacuum system, (at 0K) all of the electrons are confined to the metal and exist in energy levels which are filled up to the Fermi level. (b) If two metals are joined by an external circuit (with no applied bias), they share a common Fermi level. (c) If an external bias (V/Volts) is applied between the two metals, the Fermi levels shift apart by an amount eV/joules.

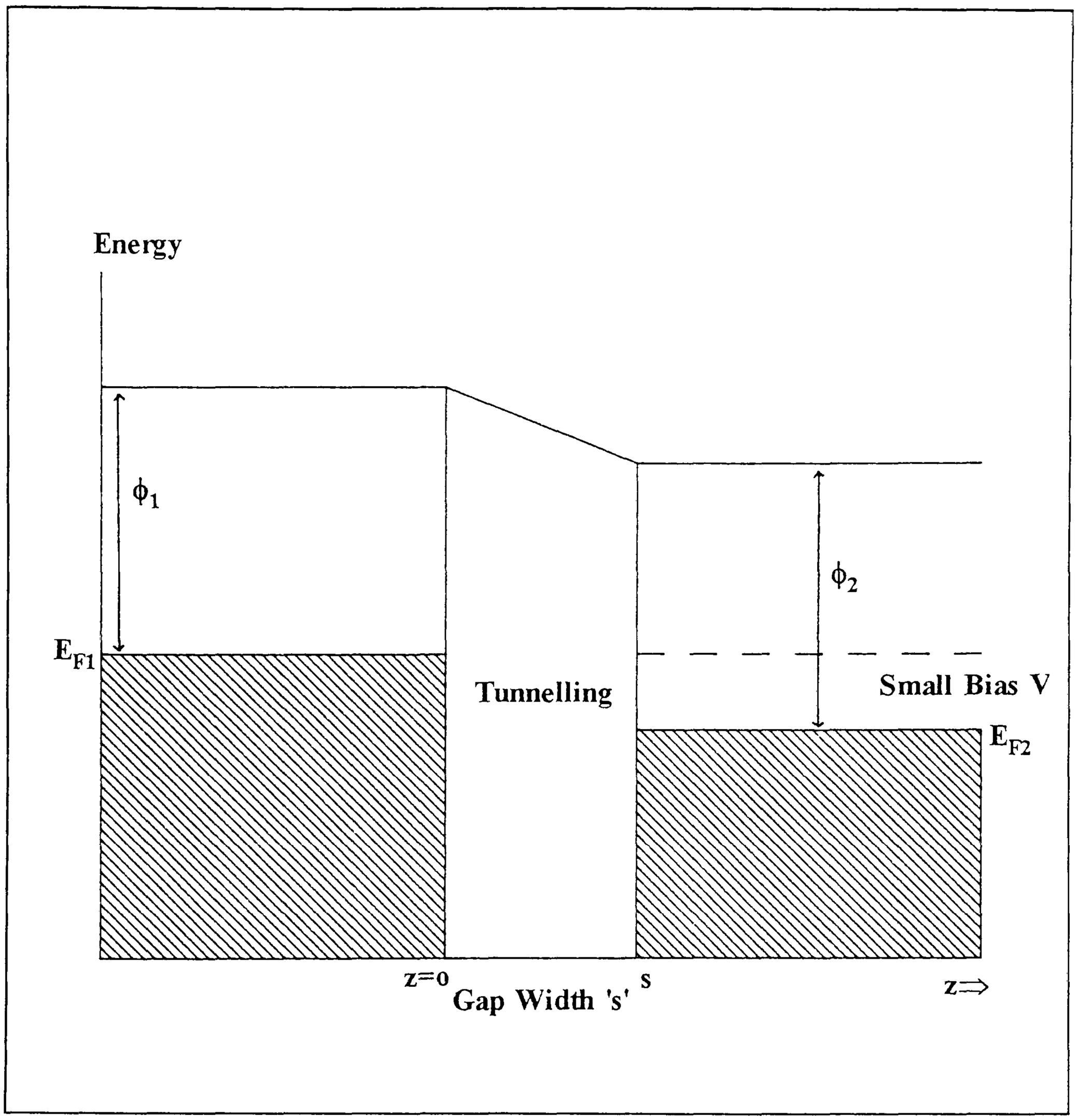

Figure 2.3: The simple model of the STM system comprises of two planar electrodes (representing the tip and sample) with local barrier heights or workfunctions of ϕ_1 and ϕ_2 respectively, separated by a potential barrier (representing the small tip-sample gap) width 's'. A small bias (V) is applied splitting the Fermi level of the tip and sample.

solution has the form:

$$\psi(z)_{barrier} = Ce^{-qz} + De^{qz}$$

Where k is:

$$k=\sqrt{\frac{2mE_z}{\hbar^2}}$$

Where q is given by:

$$q = \sqrt{\frac{2m(V_o-E_z)}{\hbar^2}}$$

The approximate forms of the wavefunctions are given in figure 2.4 and by comparing the wavefunctions on either side of the potential barrier (in the positive z direction, representing the 'tunnelling' direction) it is possible to calculate the transmission probability through the barrier as:

$$\left|\frac{F}{A}\right|^2 \approx \frac{4k^2}{k^2 + q^2} \cdot e^{-2qs}$$

Where substituting the for q and k gives an expression for the tunnelling or transmission probability $P(E_z)$:

$$P(E_z) = \frac{4E_z}{\phi+E_{F1}} \exp\left[\frac{-2s}{h}\sqrt{2m(\phi+E_{F1}-E_z)}\right]$$

The resulting wavefunction decays exponentially in the barrier. Under small bias and low temperature, the current density (j) can be expressed in terms of the transmission probability and the number of electrons (per unit volume) in the following form:

$$j = e\int v(z)\, nP(E_z)\, dv(z)$$

By substituting for $P(E_z)$ and integrating over the E_z energy regions of

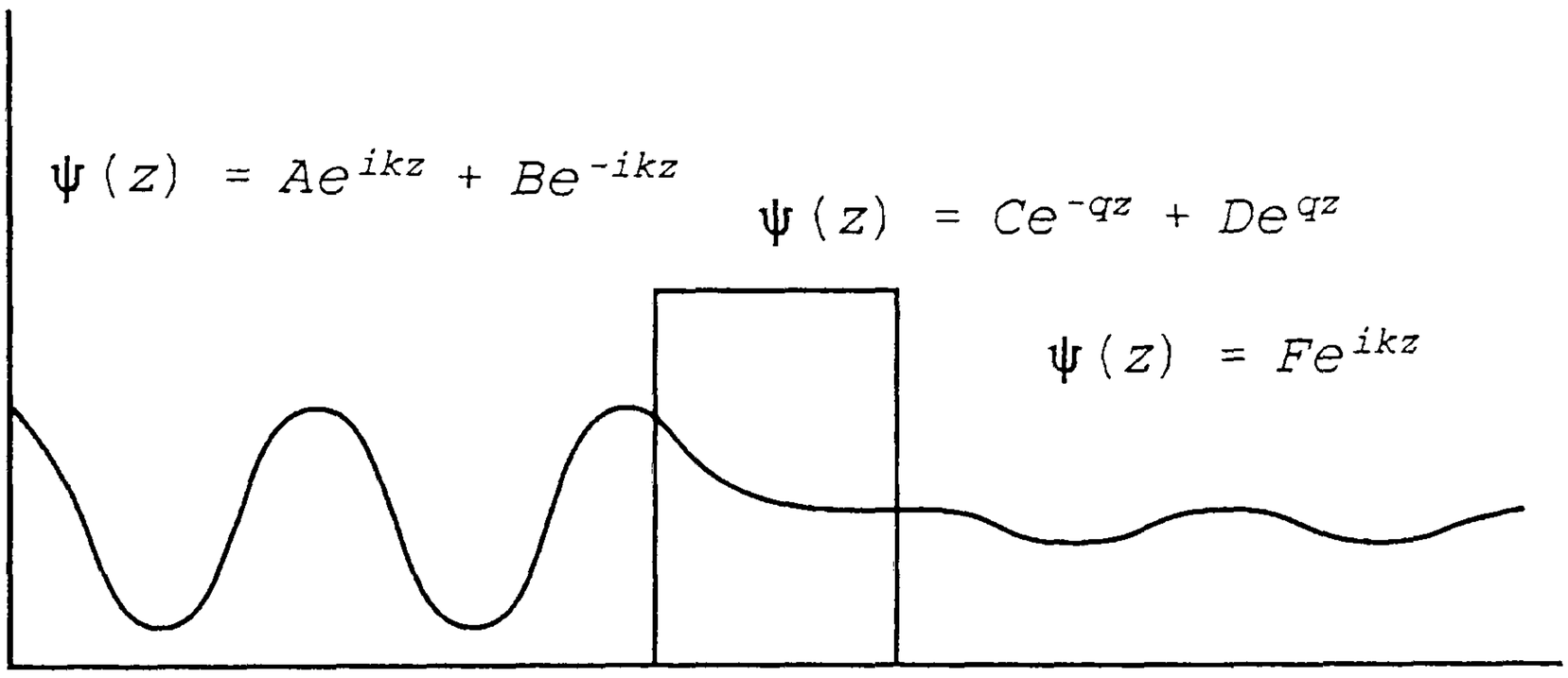

Where $k = \sqrt{\frac{2mE}{\hbar^2}}$ $q = \sqrt{\frac{2m(V_0 - E)}{\hbar^2}}$

Transmission Probability is given by:

$$\left|\frac{F}{A}\right|^2 \approx \frac{4k^2}{k^2 + q^2} e^{-2qs}$$

Where qs>>1

Figure 2.4: A sinusoidal wavefunction within the tip decays exponentially through the barrier and emerges once again as a sinusoidal function. The transmission of the electron through the barrier can be calculated by comparing the incident and the transmitted wavefunction.

$0<E_z<(E_{F1}-eV)$ and $(E_{F1}-eV)<E_z<E_{F1}$ it can be shown [Chen, 1992; Feenstra, 1990] that the current density is related to the bias applied, barrier width and workfunction in the following form:

$$j = \frac{3}{2}\sqrt{2m}\left(\frac{e}{\hbar}\right)^2 \frac{\sqrt{\Phi}}{s} . V . \exp . \left(-\frac{2s}{\hbar}\sqrt{2m\Phi}\right)$$

Where $\Phi=(\phi_1 + \phi_2)/2$, is the effective barrier height and is the mean of the workfunctions of both surfaces. Hence current density is linearly related to the applied bias and exponentially related to the barrier width and the square root of the effective barrier height.

The extreme sensitivity of the STM to height variations can be demonstrated. If the average barrier height is 4.5eV then k is calculated as $0.1nm^{-1}$. This result demonstrates that a 0.1nm increase in the separation gives a ten fold decrease in tunnel current. This extreme sensitivity results in a measurable range spanning the dimensions of atomic corrugations and it is this which makes such high vertical resolution in the STM possible.

Modified Barrier Shape

Although for the average tunnelling characteristics of the planar electrodes the term workfunction and barrier height are similar, it is important to note that the former as defined in surface science is a property associated with a (well defined) surface as a whole [Forbes, 1990]. In practice, the STM tip probes a highly localized part of the surface and the shape of the local barrier presented to the tunnelling electrons is not simple. The shape is dependent on the bias applied, the image forces created in the electrodes by the tunnelling electrons and the local electronic structure within that area[Chen, 1993].

The concept of image force was forwarded by field emission workers most notably Nordheim [Fowler & Nordheim, 1928]. An electron within the barrier (of width 's') imparts a positive charge in the metal surface which then attracts the electron with a Coulombic force of (see top of p32):

$$F \alpha -\frac{e^2}{(2d)^2}$$

Where 'd' is the distance of the electron away from the electrode surface.

There are charges induced in both electrodes and to calculate the total image force it becomes necessary to take into account the effect they all have on the electron (see figure 2.5a). The force is now modified to give:

$$F \alpha -\frac{e^2}{(2d)^2} + \sum_{n=0}^{\infty} \left(\frac{e^2}{4(ns-d)^2} - \frac{e^2}{4(ns+d)^2}\right)$$

And the force can be integrated to give the potential after Simmons[1969]:

$$U \alpha -\frac{e^2}{4d} - \frac{e^2}{2}\sum_{n=0}^{\infty} \left(\frac{ns}{n^2s^2-d^2} - \frac{1}{ns}\right)$$

The function is calculated for only one of the electrodes (in this case the left hand side from figure 2.5b) where d was assumed to be very much smaller than the gap width. In can be shown that the function applies equally for the right hand side of the potential barrier. The result of the image potential is to modify the effective barrier shape (see figure 2.5c).

Tunnelling Probability Through a Modified Barrier

The shape of the barrier is more complex than was at first assumed, taking into account image forces and local surface structure it is found that in general the barrier shape is usually a function of z. The solving of the Schrodinger Equation and calculating the tunnelling probability becomes very difficult. To aid the computation, the Wentzel-Kramers-Brillouin (WKB) approximation is used.

For an arbitrary shaped potential barrier, the WKB [Duke 1969] approach considers the two classical turning points S_1 and S_2 (see figure 2.6) where the modified $P(E_z)$ is given by:

$$P(E_z) = \exp(-2J(E_z))$$

and where $J(E_z)$ is given by (see top of p33):

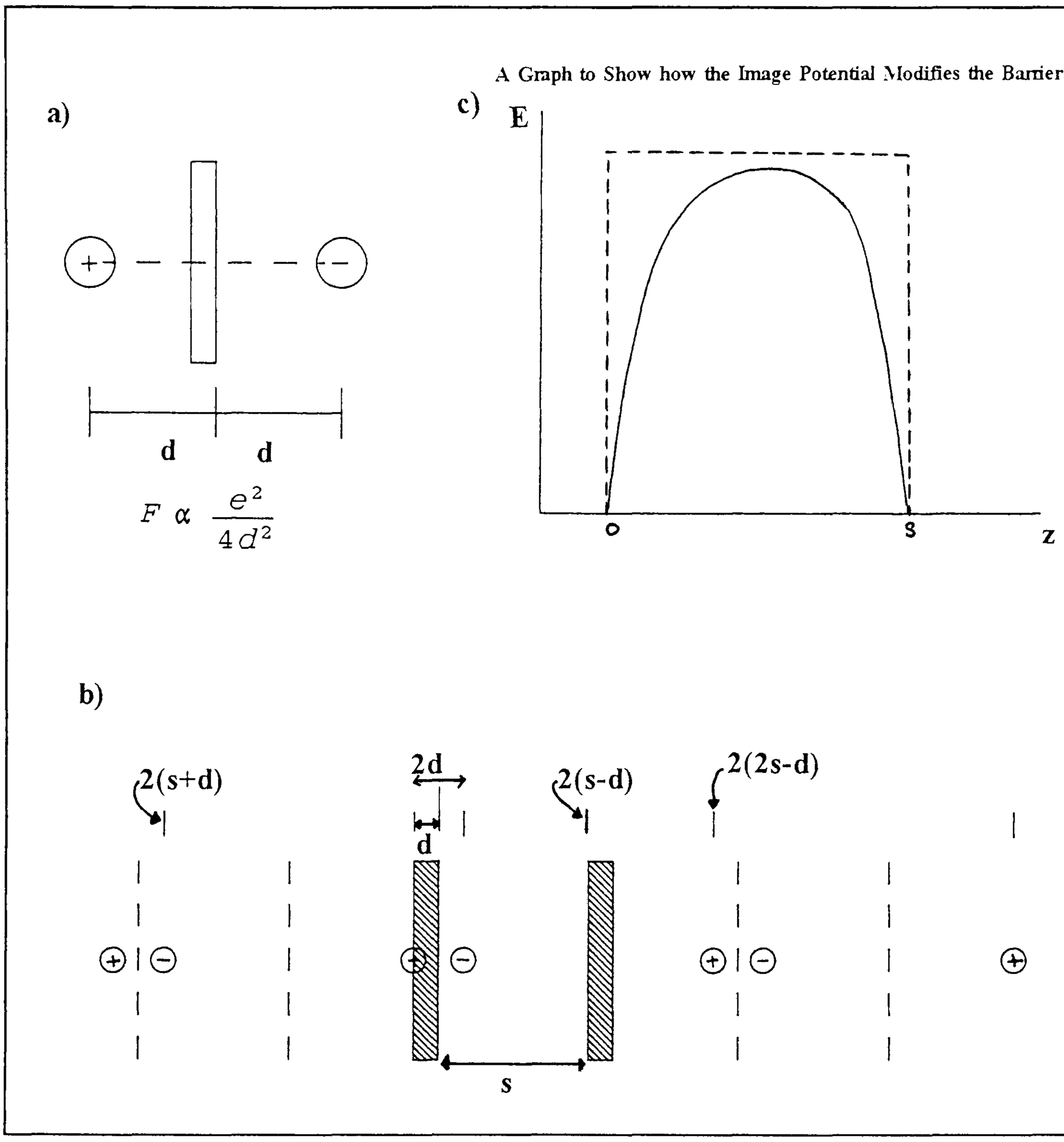

Figure 2.5: The concept of image force was forwarded by Fowler & Nordheim [1928]. (a) An electron distance 'd' from the electrode, but inside the barrier, imparts a positive charge in the metal surface which then attracts the electron with a coulombic force which is inversely proportional to d^2. (b) The positive charge and the electron induce 'image' charges in the opposite electrode and so on. (c) The net effect of the image charges on the path of the electron through the barrier is to modify the barrier shape thus influencing any tunnelling current passing through it.

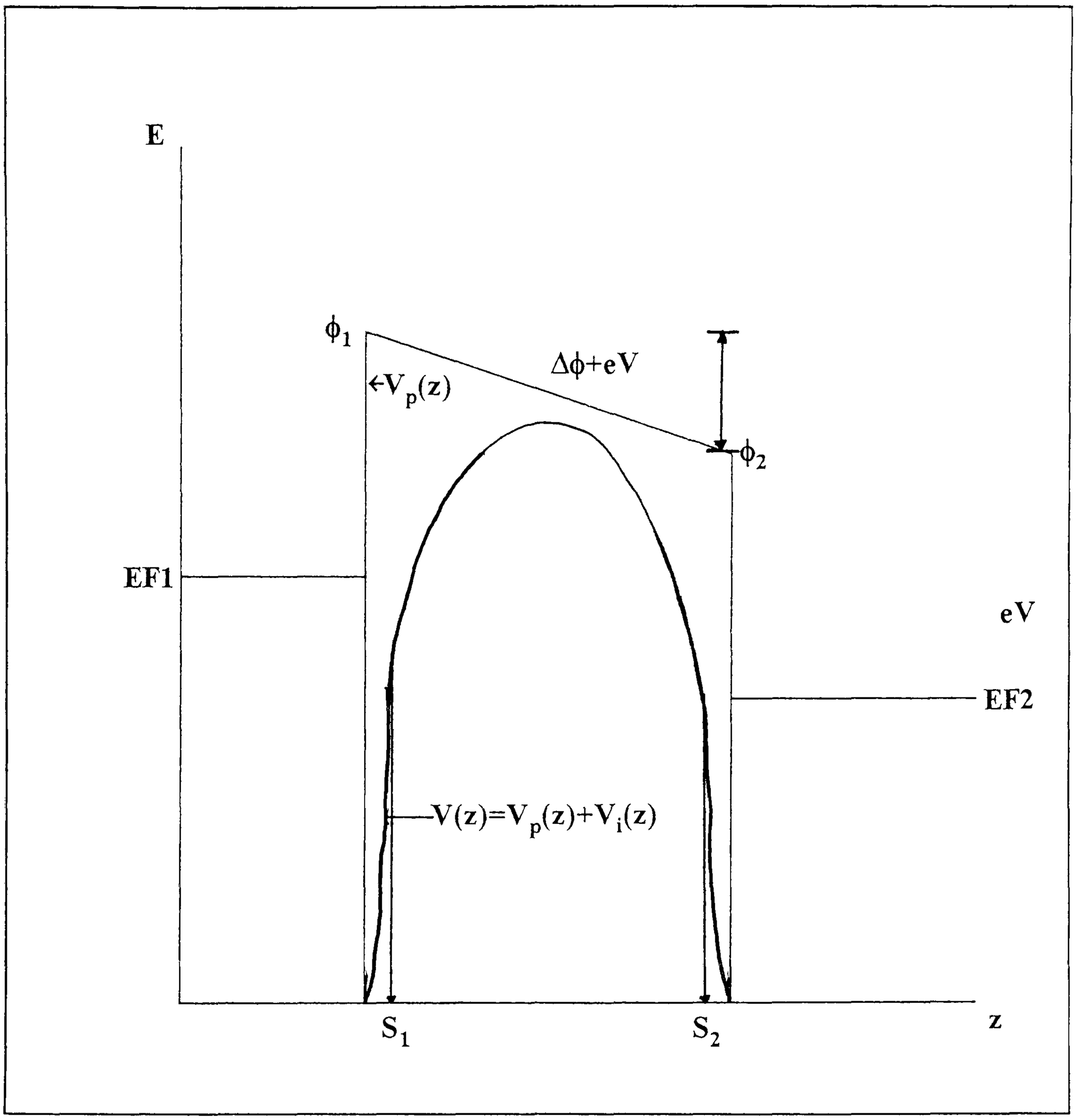

Figure 2.6: The WKB approximation allows the transmission of the electron through an arbitrarily shaped barrier to be calculated, provided there are two classical turning points S_1 and S_2.

$$J(E_z) = \int_{S_1(E_z)}^{S_2(E_z)} \frac{1}{\hbar}\sqrt{2m(V(z)-E_z)}\,dz$$

Hence for a known V(z), $J(E_z)$ can be calculated exactly in some cases, for example in the trapezoidal barrier, where V(z) is related to the left (tip) electrode Fermi level, the bias (V) and the local effective barrier heights of the tip and sample (ϕ_1 and ϕ_2 respectively) in the form:

$$V(z) = (E_{F1}+\phi_1) - (\phi_1-\phi_2+eV)\frac{z}{s}$$

If one assumes that if $(\Delta\phi+eV) << (E_{F1}+\phi_1-eV)$ where $\Delta\phi = \phi_1 - \phi_2$, then $J(E_z)$ may be calculated as:

$$J(E_z) = \frac{1}{\hbar}\sqrt{2m}\; s\left(\sqrt{E_{F1}+\phi_1-E_z} - \frac{\Delta\phi+eV}{4\sqrt{E_{F1}+\phi_1-E_z}}\right)$$

The result of this treatment is that if $\Delta\phi+eV>0$ i.e. the potential reduces in the tunnelling direction, then the probability of tunnelling increases. On the other hand if $\Delta\phi+eV<0$ then the probability of tunnelling diminishes.

In the method described above, the tip, barrier and sample were considered to be a complete quantum system. The Schrodinger Equation was solved simultaneously in these regions to enable the wavefunction of the transmitted electron and hence the tunnelling probability to be calculated. Unfortunately this approach is fraught with difficulties due mainly to the poorly defined barrier shape. However a different approach developed by Bardeen[1961] and applied to STM by Tersoff and Hamman [1983] was found to be more productive and even enabled the lateral resolution of the STM system to be established.

Transfer Hamiltonian Approach (After Tersoff and Hamman)

In the Bardeen approach, the tip and sample are considered separately at first. For each of the electrodes the surface wavefunctions are determined,

decaying into the barrier. The first step (shown in figure 2.7) shows the wavefunction for both the tip and sample (ψ_t is the tip wavefunction and ψ_s is the sample wavefunction) decaying exponentially as expected into the barrier.

The tip and sample, with their respective wavefunction description of the electrons within the barrier, are then 'combined' with a suitable potential barrier of width commensurate with the tip-sample gap. In this case the barrier now contains wavefunctions decaying from both the left and the right hand sides (see figure 2.8). The tip and sample wavefunctions are only weakly coupled within the barrier and are combined using a first order time dependent perturbation technique involving the matrix element M_{st}. The matrix element is a description of the transition between the tip and sample states and is related to the wavefunctions of the tip and sample by the equation:

$$M_{st} = \frac{\hbar^2}{2m}\int (\psi_s^* \nabla\psi_t - \psi_t \nabla\psi_s^*) \cdot dz$$

The electron progress from tip states to sample states occurs with a transition probability P(T) between the tip and sample states given by Fermi's Golden Rule.

$$P(T) = \frac{2\pi}{\hbar}\int |M_{st}|^2 \rho(E) \; dE$$

Where $\rho(E)$ describes both the occupied tip states and the unoccupied sample states (noting that the tunnelling proceeds from the former to the latter):

$$\rho(E) = f(E_{tip}) \cdot [1 - f(E_{sample} + eV)] \, \delta(E_{sample} - E_{tip})$$

and F(E), the Fermi Disdribution is :

$$f(E) = (1 + e^{(E-E_F)/kT})^{-1}$$

The current may now be calculated as a function of the transition rate between electrode states. Bardeen showed that the matrix element was related to the magnitude of the tip and sample wavefunctions (at any surface within the electrode) and the tip area, then by invoking Fermis Golden Rule, which

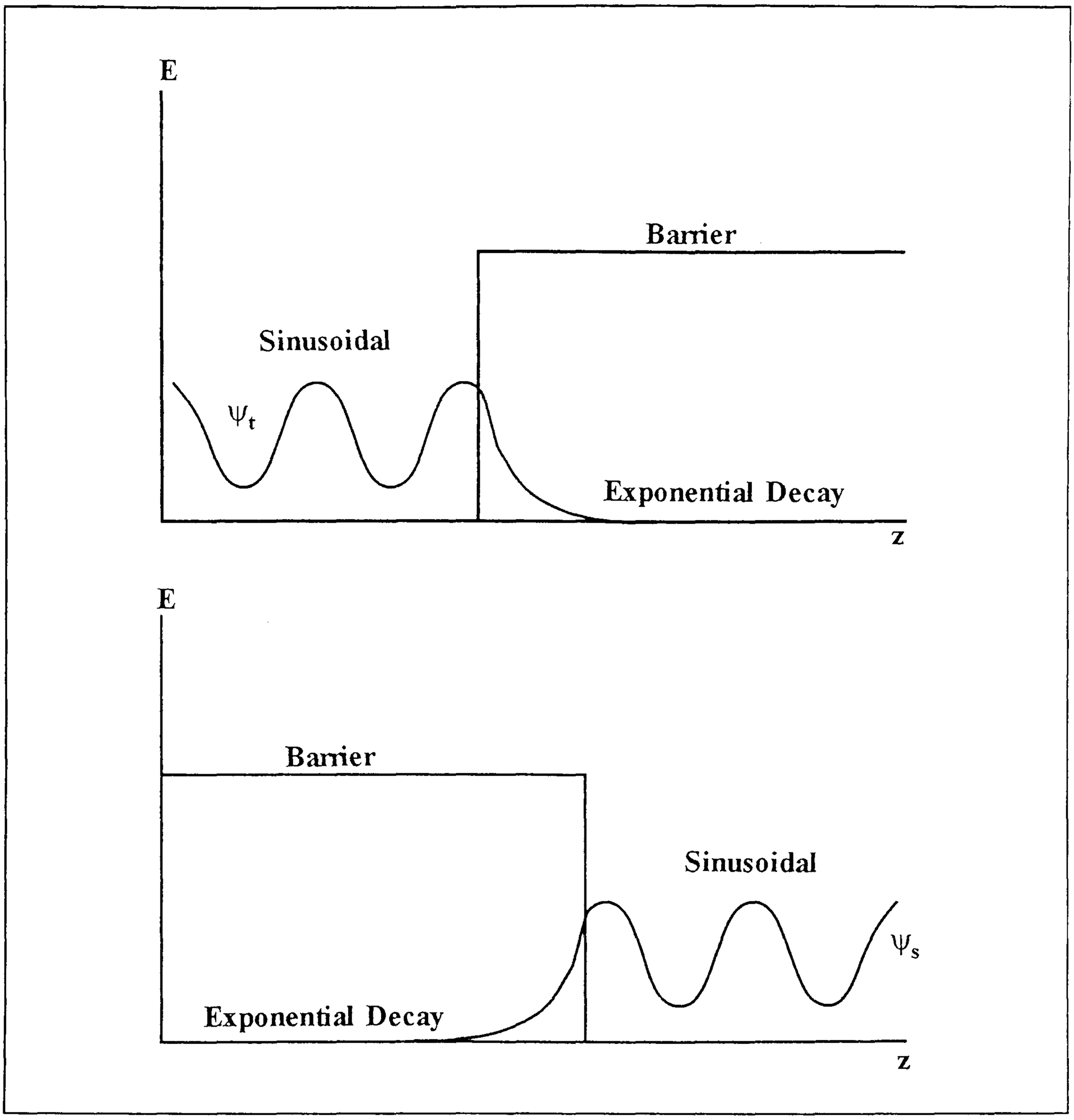

Figure 2.7: The first stage in the Bardeen approach to tunnelling through a barrier involves splitting the system into tip-barrier and sample-barrier mini-systems. The wavefunctions for the tip and sample states (i.e. in each of the mini-systems) are found including the decaying functions of the states within the barrier.

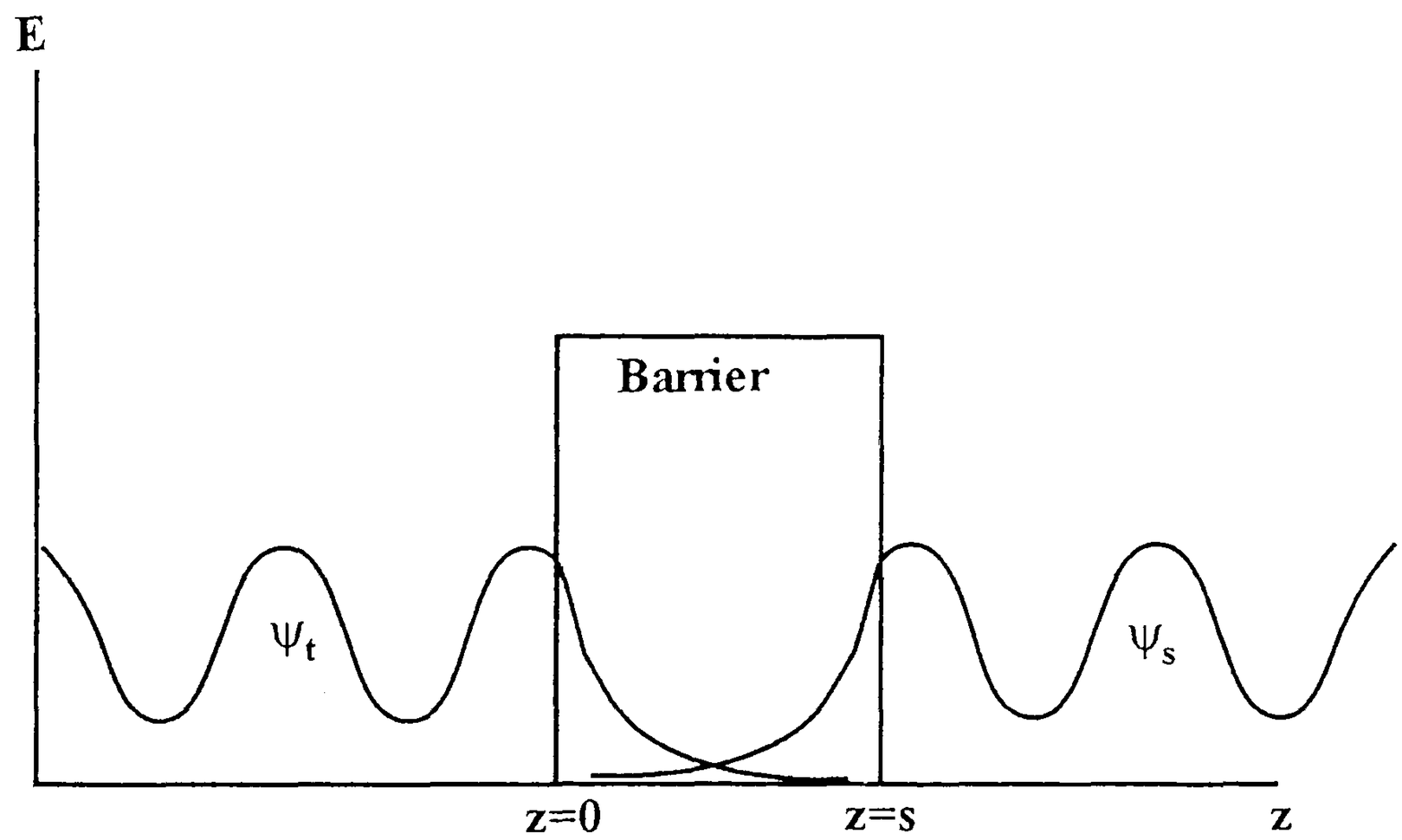

Figure 2.8: The next stage of the Bardeen approach involves the reconstruction of the tip-barrier-sample system. The transition of electrons within the barrier from the tip to sample states (which are only weakly coupled) can be calculated from the tunnelling matrix element and first order perturbation theory. The transition probability from which the tunnelling current can be derived, is given by the square of the matrix element (Fermi's Golden Rule).

relates the transition probability to the square of the matrix element:

$$I \alpha |\psi_s^0|^2 |\psi_t^0|^2 e^{-2qs}$$

Where the sample wavefunction is:

$$\psi_s = \psi_s^o . \exp(-kz)$$

And the tip wavefunction is given by:

$$\psi_t = \psi_t^o . \exp(-k(s-z))$$

The tunnel current is (as expected) exponentially related to the barrier width and square root of its height.

Tersoff and Hamman extended this theory and assumed tunnelling was from a tip radius R, where $\mathbf{r}_o$ was the central position of the tip (see figure 2.9). The tip in this case was substituted by an s-wave spherical potential well (until now the tip was assumed to be a square potential well). For a low temperature and small bias, they showed that the current may be expressed as:

$$I \alpha D_t(E_F) \rho(r_0, E_F)$$

Where:

$$\rho(r_o, E_F) \equiv \sum_{E_f - eV}^{E_F} |\psi_s(r_o)|^2 \delta(E_s - E_F)$$

The results of this treatment are critical to understanding of STM images. The tunnel current actually measured by the STM comes from those states at or around the Fermi level in the sample measured at the centre of curvature of the tip. The Tersoff & Hamman model is very useful as it demonstrates that the STM image is constructed from the sample electronic structure alone.

STM Resolution

As encountered above, the STM measures the local charge density at the

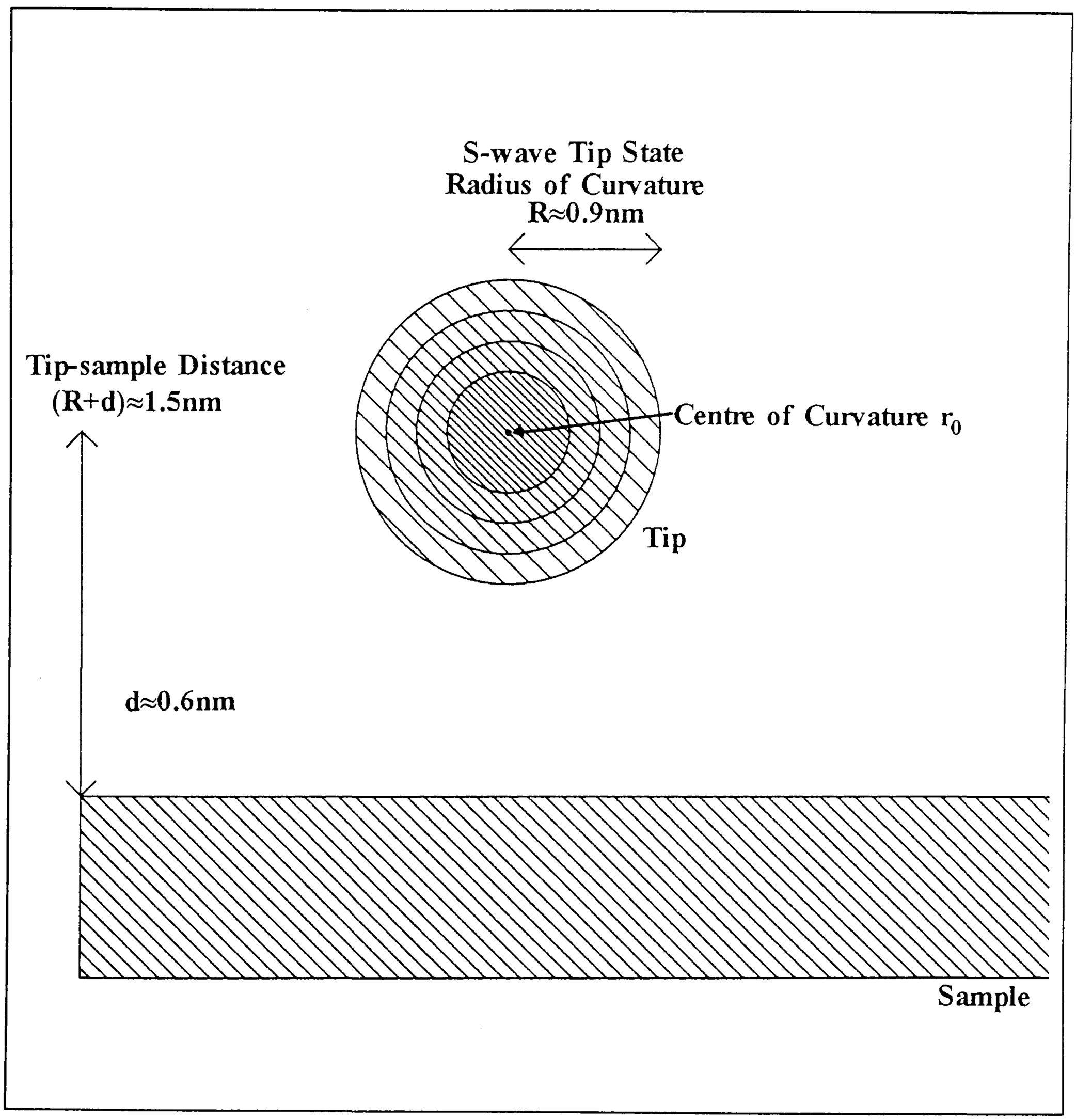

Figure 2.9: The Tersoff & Hamman approach[1983] modifies the STM model by replacing the square tip potential (until this point the tip was assumed to be a planar electrode) by an s-wave, spherical potential well. The tip (radius R) surface is a distance 'd' from the sample surface and has a centre of curvature of $\mathbf{r}_0$ (the tip hatchings in this figure are not significant).

centre of the scanning tip. In metals, the charge density distribution across the surface is spatially very similar to the atomic corrugations. In this case the STM image (of the local density of states) accurately portrays the atomic topography. The vertical resolution (in the z-direction, i.e. perpendicular to the sample plane) of the STM arises due to the exponential decay of the wavefunction overlap with increasing tip-sample separation. However the lateral resolution is not so easy to gauge.

Further insight into the lateral resolution of the STM may be gained from the Tersoff & Hamman approach. A rough approximation of lateral resolution from the spherical s-wave tip model in this case gives:

$$Resolution_{lat} \approx \sqrt{\left(\frac{2(R+d)}{k}\right)}$$

If $2k^{-1} \approx 0.16$nm and $R+d \approx 1.5$nm, the lateral resolution is about 0.5nm [Tersoff &Hamman, 1983]. This figure seemed reasonable given that Tersoff & Hamman successfully resolved the 0.8nm atomic periodicity of gold(110). It was also noted by these workers that the atomic corrugations of the lattice became less pronounced for some materials as the tip-sample separation increased (i.e. corrugation amplitude decreases as a function of d). This is shown schematically in figure 2.10. If the lattice contains a complex atomic corrugation, it is reasonable to expect the complexity to 'iron out' or diminish with increasing d. For good resolution to be achieved, it is therefore important to image the sample with as small a 'd' as possible.

2.3 IMAGING ORGANIC MATERIAL.

Organic imaging:

The successful imaging of a polymer or other organic substance physisorbed or even chemisorbed on the surface of the substrate has been demonstrated by many studies [e.g. Travaglini et al, 1990; Blackford et al, 1991; Haggerty & Lenhoff, 1992]. Results suggest that in some cases resolution approaching

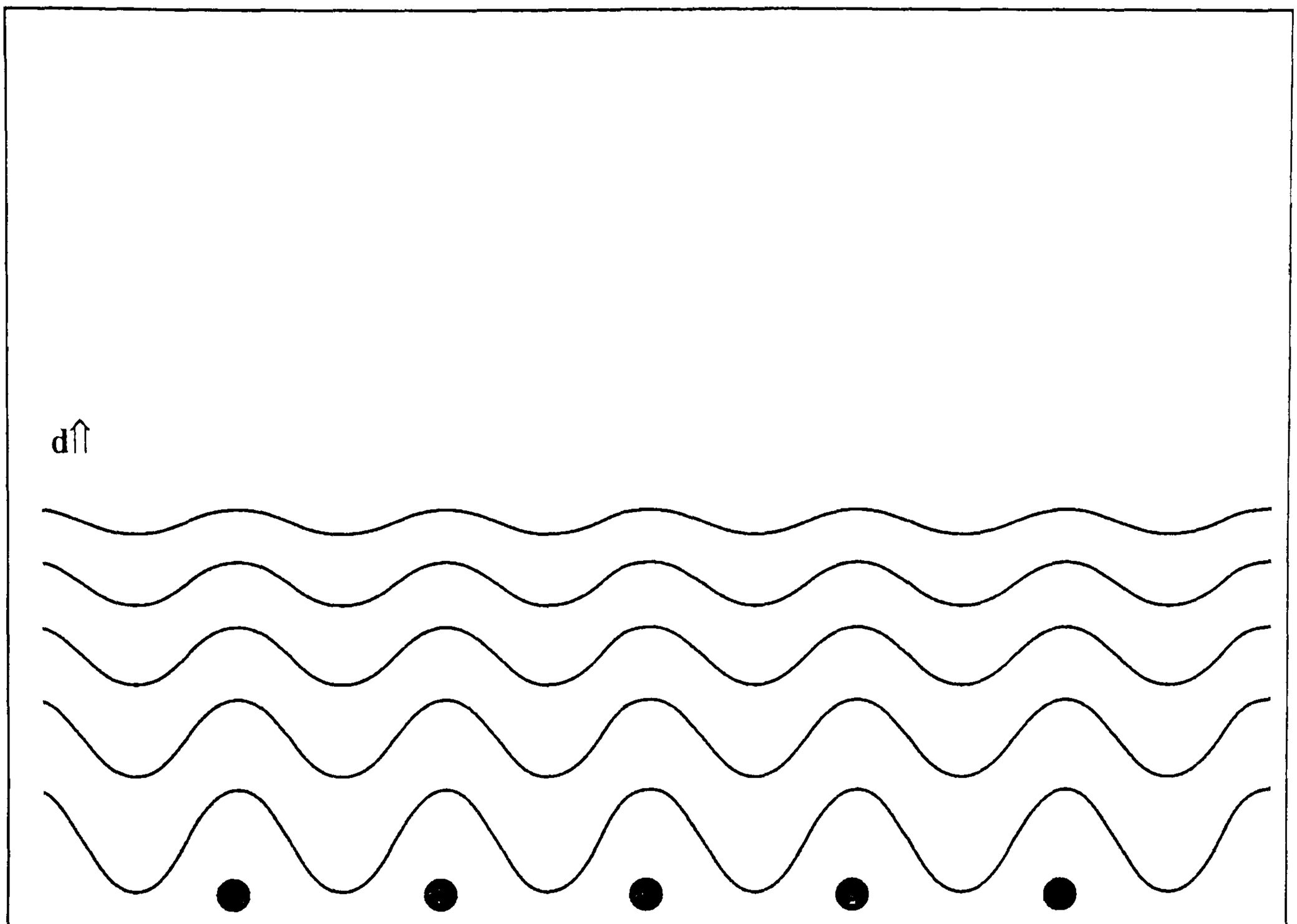

Figure 2.10: The spatial fluctuations of the LDOS match the simple surface atomic arrangement when 'd' is very small. In this ideal situation the STM image would contain a maximum level of atomic detail and any complexity in the lattice can be resolved easily. However as 'd' increases, the 'atomic-corrugations' decrease rapidly and fine structure is lost from the STM image.

that of metals (sub nanometre) can be achieved even with relatively thick samples without a metallic coating. The success of organic imaging is however surprising because these samples are in general considered to be insulators in the bulk. Furthermore, the tunnelling current calculated from the vacuum studies above (re: Tersoff & Hamman) between the tip and substrate is often very much smaller than the current actually measured.

The current detected by the STM and associated with the imaging of conventionally conducting materials is related to the overlap in electron wavefunctions of the tip and substrate. In the presence of a surface organic or polymer sample, the gap size can be as large as several nanometres. This latter sample may be considered 'thick' in this context i.e. thick enough to prevent the tip and substrate wavefunctions from overlapping significantly. Calculations of the decay constant give a value of approximately $0.1nm^{-1}$ (with respect to the barrier width). An increase of nanometres in the gap size results in a highly diminished tunnel current, to the point where it is too small to measure.

However a nanoampere current is measured by the STM system and in this case the sample must actively participate in an electronic manner towards the formation of the image. For a highly insulating class of materials, this 'active' behaviour is very difficult to explain.

This section is divided into two parts. Firstly 'thin' samples of organic material are discussed and are classed as those samples that are thinner than the gap between tip and substrate. Secondly the 'thick' samples which are defined as those that are wider than the normal gap and form the majority of samples imaged in this thesis.

Thin (t<1nm) Organic Material.

Films are considered thin in this context if they can fit into the tunnelling gap (at its widest this is about 1nm) between the tip and sample. Films of this dimension are treated by many workers as a contaminants physisorbed to the substrate[McGonigal et al, 1992]. The physisorbed material modifies the electronic surface of the substrate, changing the local effective barrier height

(Φ) for the tunnelling electrons[Blackford et al, 1991]. It is the change in the local density of states (LDOS) of the substrate with the sample in place that is imaged by the STM (see figure 2.11).

The magnitude of the change in the LDOS is not easily calculated but is influenced by the strength of interaction between the organic adsorbate and the substrate. If there is a strong interaction between the organic and the substrate or if the bias used is large[McGonigal et al, 1992], the change in the LDOS is significant at the contact points. Thus the dominant feature (as distinct from the surrounding substrate) of the image is likely to be the point on the substrate which is in contact with the adsorbate. Conversely, if the interaction is weak or the bias is low, the adsorbate will not influence the electronic structure of the substrate and the image will be dominated by the substrate and not by the adsorbate[Miles, 1991; McGonigal, 1992; Rabe, 1992; Eng et al, 1992].

Thus when the STM is operated in the constant current mode, a change in the local effective barrier height (Φ) will affect the current which in turn forces the tip closer to, or further from the surface. The polymer is then considered imageable because the substrate immediately below it appears distinct from the surrounding substrate.

Introduction to Thick Polymer Imaging By STM

Thick layers of polymer which are in this context unable to fit into the tip-substrate gap are considered to be greater than 2nm thick. In the bulk polymers in general are poor conductors of electricity (typical conductivity (σ) values lie in the range $(10^{-14}$ to $10^{-16})$ $\Omega^{-1}m^{-1}$) and would not necessarily be expected to contribute to the conduction process between the tip and substrate.

There are exceptions to this accepted view of polymers; some recently designed polymers have conductivity values some twenty orders of magnitude greater than those mentioned above, indeed some polymers e.g. TTF/TCNQ (with a value of σ reaching 10^4 $\Omega^{-1}m^{-1}$) have conductivity values

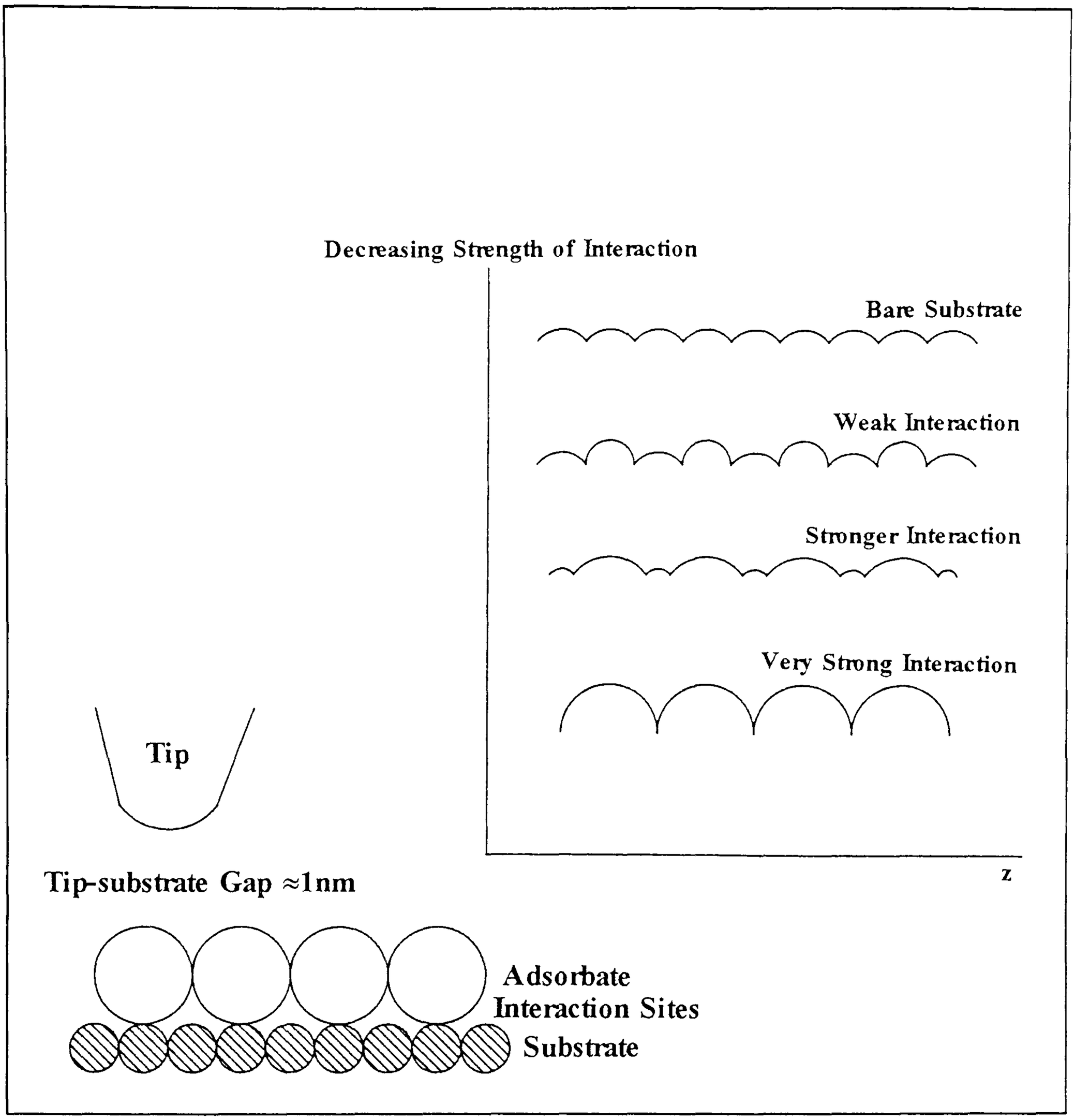

Figure 2.11: A very thin polymeric sample which may fit inside the gap, can be imaged successfully by the STM. The polymer-substrate interaction can render the substrate that is in-contact with the polymer electronically different from the surrounding substrate. If the interaction between polymer and substrate is strong, the image is dominated by the polymer. If the interaction is weak, the substrate dominates the image.

more associated with that of metals. The conducting polymers have been imaged successfully by the STM [Maganov & Cantow, 1990; Porter et al, 1990, 1993; Yang et al, 1990, 1992].

In general however, polymers are considered to be insulating and those used in this thesis (PVP, PMMA and PC) are no exception to this view. It should be noted that 'insulating' in this context is a bulk property and may be significantly different from the situation for very thin films of the same material.

Band Structure of Polymers

The energy band structure of materials, in particular that used to explain the conductivity of metals and semiconductors may be used to visualize the problems associated with polymer conductivity.

For well ordered, covalently or ionically bonded materials exhibiting lattice structures and strong interactions between neighbouring atoms, the band structure is dominated by broad energy bands (see figure 2.12a) and high charge-carrier mobility is expected.

However polymers are often disordered with weak interaction between any conducting components that may be present, which results in a very narrow band structure in which the associated carrier mobility is low. The band structure for polymers is also punctuated with localized states (discussed below) which arise as a result of the disorder and may act to trap charge-carriers (2.12b).

Conductivity

For any material the electrical conductivity may be considered as the sum of the products of the individual charges (q) with their mobility(μ) and density(n) such that:

$$\sigma = \sum_i q_i n_i \mu_i$$

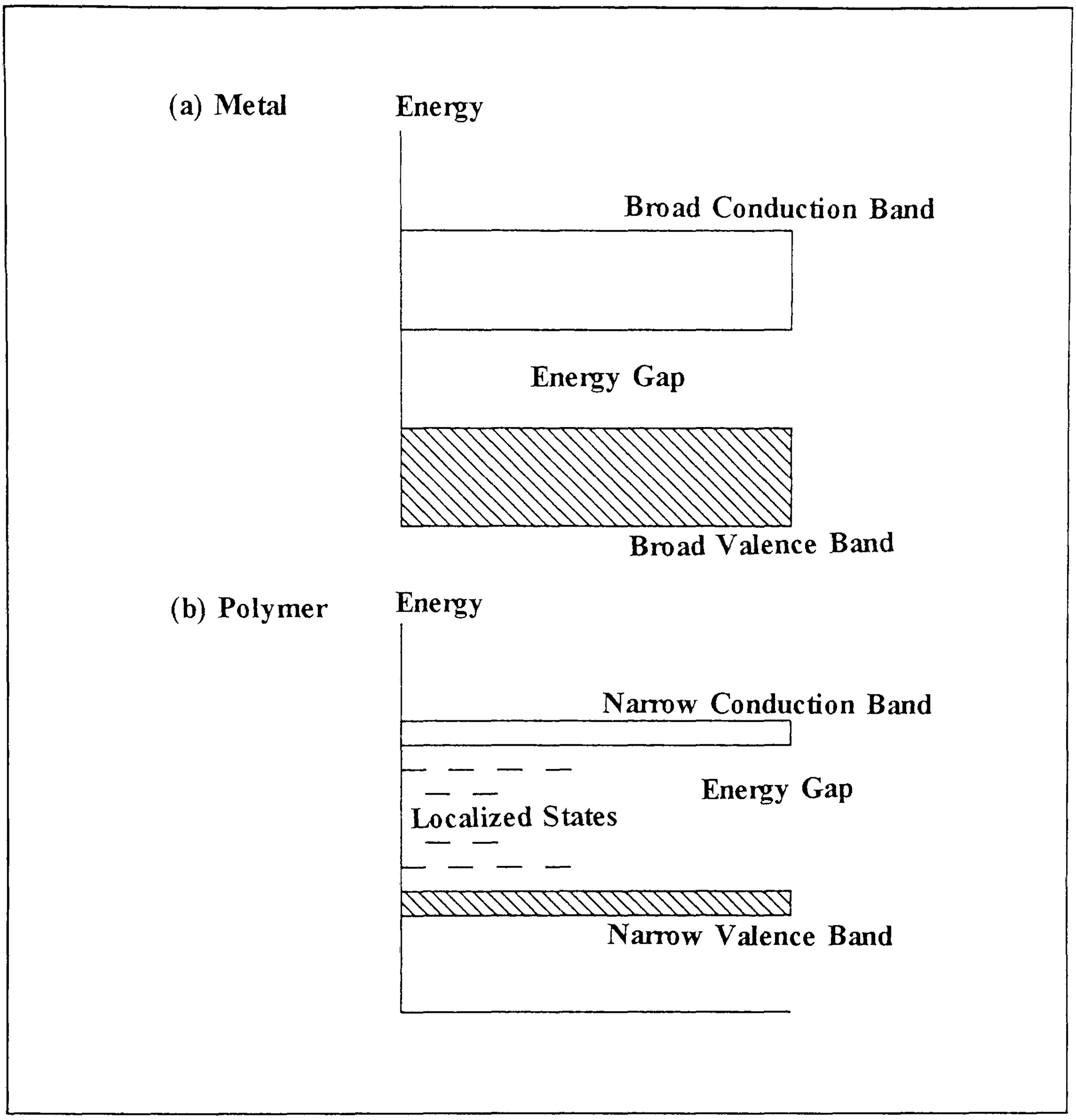

Figure 2.12: (a) The band structure of metals and other well ordered materials with strong interactions between all neighbouring atoms is dominated by broad energy bands. (b) Polymers are generally not well ordered nor do the constituaent chains interact with each other. The electronic band structure of this class of materials is dominated by narrow bands and localized states.

It may be assumed that in metals, the charge carriers are free to move throughout the matrix, but in polymers the terms $n_i\mu_i$ may be dependent on bias(V), temperature (T), mobility (μ), environment and structure (S). Mobility, is also position (z) dependent, so:

$$\sigma = \sum_i q_i n_i(V, S, T)\, \mu_i(V, S, T, z)$$

This situation applies initially, to ordered polymer entities such as polymer single crystals. However it may also act as a starting point when considering the conductivity of other polymer films.

Any factor that affects S, T and V will influence the conductivity. Although T and V may be controllable to some extent, S is dependent on either the environment around the polymer or on its structure and this may prove very difficult to assess for amorphous materials.

Structural Effect on Conductivity and Localized States.

The effect of structural changes on conductivity, in particular crystalline regions is in some circumstances, to decrease the conductivity by presenting charge-carrier traps to any mobile conducting species. It has been found that a change in conductivity in amorphous polymers can, to some extent be attributed to a range of structural changes covering everything from side-chain movement to motion of the entire chain. A change in conductivity in semi-crystalline polymers may be caused by changes in crystalline structure particularly if there is an amorphous-crystalline boundary. The change in conductivity observed has been associated with charge-carrier trapping sites and these have been more intimately associated with polymer structure by Seanor[1986] in the following list:

a) surface states induced by strain or chemical reactions.
b) surface dipole states.
c) bulk dipole states.
d) bulk molecular ion states.

Continued...

e) impurities.

f) chain ends.

g) chain branches.

h) chain folds.

i) changes in tacticity or stereochemistry.

j) crystalline-amorphous boundaries.

k) broken bonds.

l) polaron states(regions of polarized polymer).

m) local density fluctuations.

All of these factors result in an increase in the number of localization states whose energy states lie in the forbidden energy gap and can trap charge carriers during a conduction process.

Charge Carriers

The charge-carriers involved in polymer conduction are not readily identified. In some polymers charge-carriers can be generated intrinsically where their production is governed by the Boltzmann Distribution Function; The conductivity is then found to be exponentially proportional to temperature (in a way similar to that found in semiconductors).

However, the level of dopants, ionizing agents and other external species may also change the conductivity of the polymer by supplying extrinsic carriers. The deliberate doping by electron acceptors and/or donors of the polymer matrix can significantly increase the polymer conductivity.

Finally charge carriers that contribute towards the conductivity of the polymer can arise from an electrochemical current within the polymer. These charge carriers arise from 'chemical' or redox reactions occurring very close to a conducting substrate[Kwak and Bard, 1989]. The large effective mass of the charge carriers in such narrow polymer energy bands with consequently low carrier mobility means that the time spent by a such a species on a particular molecule may be significant (compared to the pico-second relaxation times) increasing the chances of an oxidation-reduction reaction,

the ionic products of which become the new charge carriers.

If this latter method of carrier generation is present, it is expected from chemical studies [Israelachvilli, 1985] that the current measured by the STM would be linearly related to the tip-sample separation.

Electrode Effects in STM

The electrodes in the STM system are comprised of a scanning tip and a substrate coated to some degree with the polymer. The effect of charge injection from the electrodes into the polymer, especially under the very high local field encountered in STM, must be taken into account when discussing conductivity.

The electrons may travel freely throughout the bulk of the electrode and the surface of the metal presents a classically forbidden boundary beyond which the electron must gain energy equivalent to the local barrier height to progress or else tunnelling must occur. The presence of an electrode in contact with a very thin polymer film may modify the band structure of the polymer (see figure 2.13). The degree of modification depends on the energy levels in the dielectric and may be sufficient to allow the electrons from the electrodes to tunnel into localized states and sites in the forbidden gap.

This process is thermally activated and the conductance of the film is further enhanced by the application of an applied field which may be large ($\approx 10^{8} Vm^{-1}$) in STM studies. The field serves to modify the local effective barrier to the tunnelling electrons in a way that facilitates transmission. Frenkl[1938] developed a relationship between conductivity and an applied electric field. Lindsay & Sankey[1992] calculated that in the context of the STM system and given the large electric fields involved, that the conductivity of the polymer could increase by up to six orders of magnitude.

Environmental Effect On Imaging

A gas or vapour (mainly water) that surrounds the polymer, in most STM experiments carried out in ambient conditions can serve as an electron donor

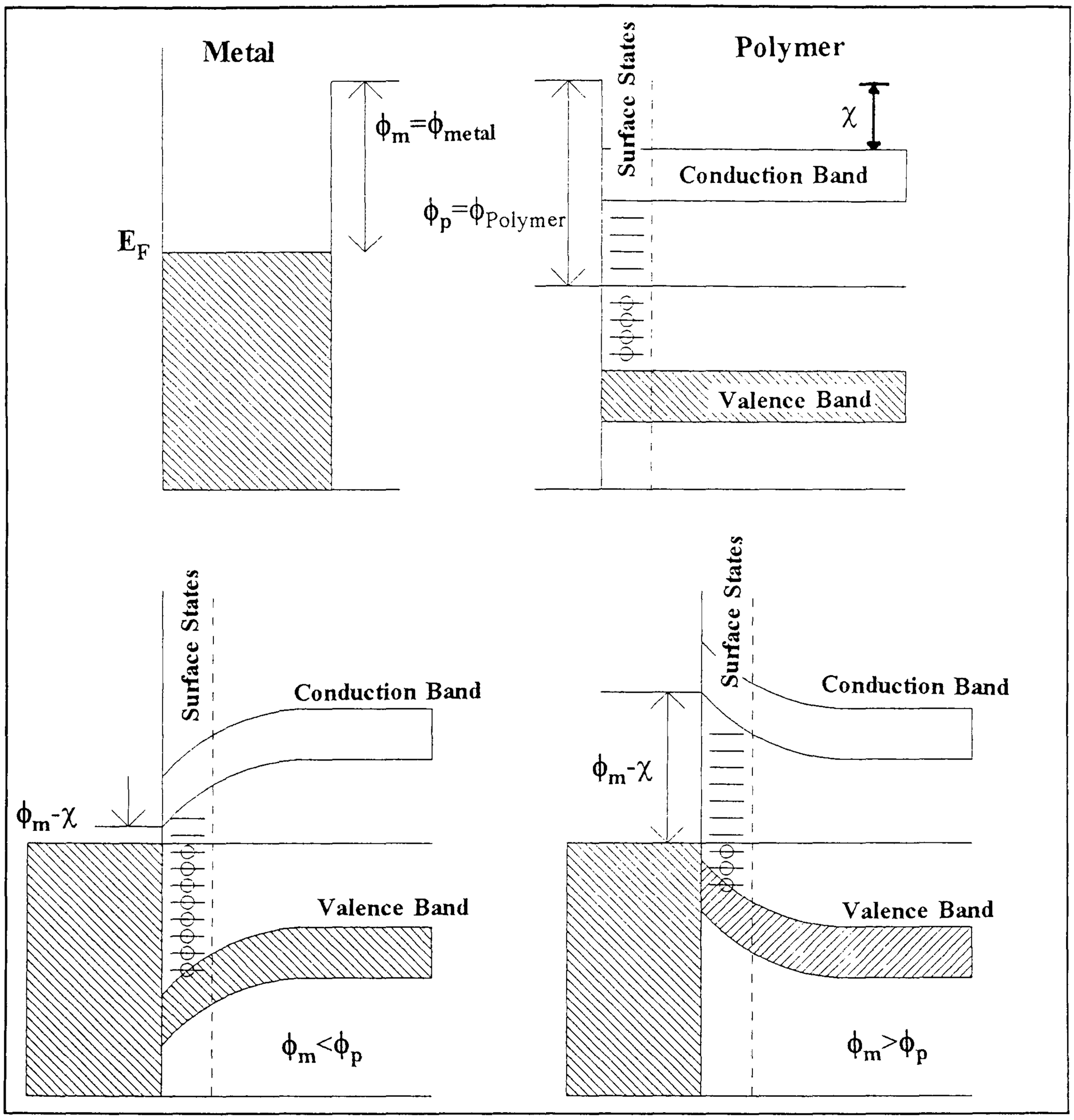

Figure 2.13: The electrode (tip or substrate) next to the polymer within a high electric field can bend the band structure of the polymer significantly. Electrons from the sample may tunnel straight in to localized polymer states or even the conduction band of the polymer.

or acceptor to the polymer, changing its conductivity. Some gases or vapours may diffuse into the polymer changing the structure (the effect on conductivity of some structural changes is discussed above) for example a plasticizing agent or even some residual un-evaporated solvent may act in this way.

Within the STM system, especially for those studies (including this one) carried out in air, water contamination from the local environment is inevitable, indeed some polymers (including PVP) actively absorb atmospheric water and others retain water even at very low values of relative humidity. The effect of water on the STM imaging is unquestionable, some studies that show very thick (100nm) organic imaging in air [Michel et al, 1989], could not be repeated in a moisture free vacuum [Blackford et al, 1991]. Other studies by Hu et al[1992] and Keller et al[1992] report samples of insulating SiO_2 and bio-organics respectively that were only imageable under high humidity conditions. The effect of water on imaging of organics was also investigated by Leggett et al[1993] where chemically bonded bio-organics on the substrate were imaged as a function of hydration.

The effect of water on the sample conductivity may be three-fold. Firstly there can be a structural effect where water may act to swell the polymer or act as a plasticizer. The resulting structural change can influence the number of localized states or charge-carrier traps.

Secondly, there can be charge transport through the water by ionic means. For example Lewis and Toomer[1981] found that the conductivity of their insulating bio-organic sample was exponentially related to the relative humidity of the sample environment. A similar 'ionic transport' mechanism may result in the charge being transported across the surface of the material by way of a 'conducting' water layer. The presence of this thin layer can act like a metallic coat and account for the imaging of samples where absorbed water is unlikely to exist such as in paraffin [Michel et al, 1989], and SiO_2 [Hu et al, 1992].

Thirdly, if there is a column of water bridging the tip sample gap then large capillary forces are expected to exist within the liquid. The force has been calculated by Woodward et al[1992] to be approximately 20nN at a

relative humidity of 30%-45% and a tip-sample separation of 1.2-1.5nm. However, the scanning tip may exert (by way of the water bridge) sufficient force to allow deformation in the sample, enabling a conduction process proposed by Lindsay and Sankay [1992] and discussed in the next section to occur.

Imaging Mechanisms

So far in this section, a general picture of the conductivity of polymers has been discussed and is broadly applicable to both thin and thick films alike. However detailed calculations are required to explain the current observed in studies by the STM and the three suggested mechanisms are outlined below following Garcia R. & Garcia N. [1990], Joachim & Sautet [1990] and Lindsay & Sankey [1992].

Garcia R. & Garcia N.[1990]

Garcia & Garcia [1990] calculated the conductance of organic samples (polypeptide chains were chosen for the calculation) through a disordered linear chain model. The model was constructed on two assumptions, the first of which was that when an organic is placed in contact with the substrate in a high external field, carrier injection from the electrodes induce changes in the band structure of that material causing energy relaxation in the sample. The second assumption was that the organic can be considered to be a disordered system both in terms of a spatial disorder (due to the difference in position of the atoms along the molecule) and of a strength disorder which arises because there are different atomic species in the molecular chain.

The polypeptide chains of approximately 5nm lengths were then assumed to be electronically remote from each other and the transmission probability for an electron tunnelling from one end of the molecule to the other was calculated numerically from the time independent Schroedinger equation. It was found that the transmission probability (at the Fermi level, E_F) increased in proportion to the degree of strength disorder within the chain

and in some cases was as high as $T(E_F)\approx10^{-5}$ (see figure 2.14). This figure is much higher than the value expected for vacuum tunnelling across a 5nm gap and may in part contribute to the nanoampere current observed. Garcia & Garcia also note pronounced fluctuations (of over three orders of magnitude) in the transmission probability between neighbouring chains with slight structural differences (in addition to fluctuation observed over a single point, as a function of energy as shown in figure 2.14). In the context of an STM image of the sample, neighbouring chains differing only slightly in structure would present very different conductive channels for tunnelling electrons and may result in sudden loss in contrast in the images.

To summarize the study, the presence of different atom type centres along the chain results in heightened strength disorder. This facilitates delocalization and strong relaxation shifts the electronic energy levels towards the centre of the band gap. The Fermi levels of both tip and substrate lie close to the relaxed states and significant conduction may result.

Other STM workers including McGonigal et al[1992], Youngquist et al[1991] and Eng et al[1992] all mention the possibility that absorption onto the surface may result in a shift in energy of the molecular orbitals to a level rendering the polymer susceptible to conduction.

Joachim & Sautet [1990]

Another approach explaining the increased conductivity within organic materials is presented in this case by Joachim, & Sautet [1990]. The approach started with the observation that the bulk band structure of a thin alkane film could not adequately describe the observed electronic properties. Instead as the film becomes thinner, transmission probability increases in the vicinity of the bulk energy gap. Work by Schnupp[1967] suggested that conductance through the polymer, between tip and substrate, at the Fermi level, would increase even though there were no molecular states in resonance with the electrodes at that energy.

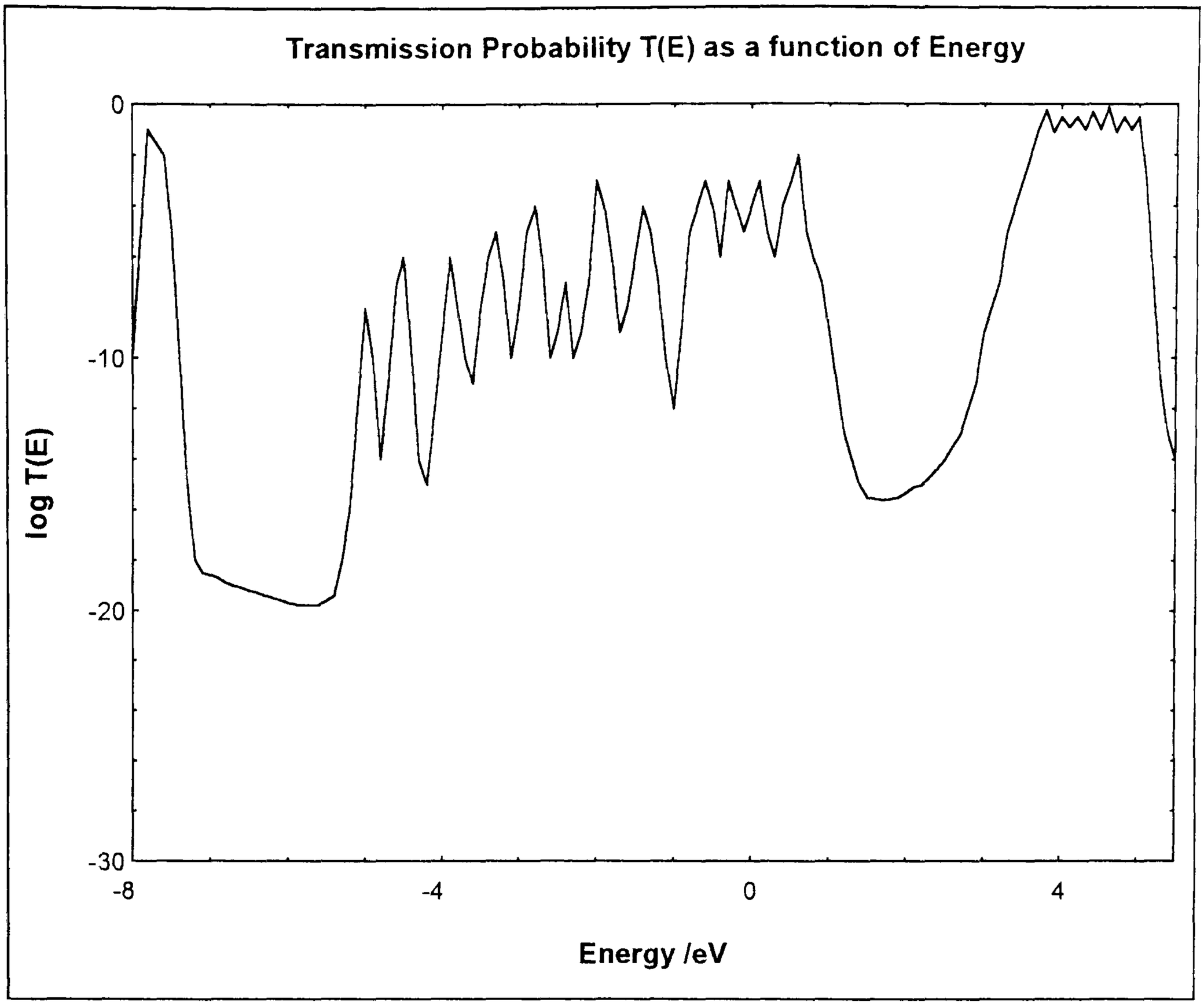

Figure 2.14: Garcia & Garcia [1990] calculate the transmission of electrons through an organic molecule. The transmission is much higher than would be expected from vacuum tunnelling alone and depends on the structural and spatial conformations of the molecules.

Joachim and Sautet considered an alkane sandwiched between two gold electrodes where the carbon backbone lay perpendicular to the substrate. The alkane is thick enough to exclude conductivity due to through space tunnelling current (i.e. overlap of tip and substrate wavefunctions). The transmission from the substrate, through the molecular sites within the physisorbed alkane and into the tip were then calculated as a function of, for example the coupling strength between the molecule and the electrodes.

The calculation of the transmission probability involved ESQC (Elastic Scattering Quantum Chemistry) and EHMO (Extended Huckel Molecular Orbital) theory. It was found that coupling between the alkane molecular orbitals and the gold created a resonance where almost unity transmission probability exists (see figure 2.15). However the peak occurs at an energy away from the Fermi level of the gold and the 'tail' of the resonant state may have only a small transmission probability of approximately 10^{-6} at this level. However the small transmission probability is still large enough to explain the nanoAmpere currents found in STM.

Lindsay & Sankey

A similar approach to Joachim and Sautet was introduced by Lindsay & Sankey [1992]. They considered a single resonant state occurring in an organic molecule sandwiched between the tip and substrate (electrodes), where the resonance is coupled to the electrodes by two hopping matrix elements. One of the matrix elements describes the coupling between the tip and the closest atoms in the molecule to the tip (τ_t) and the other, the coupling between the substrate and the corresponding closest atoms in the molecule(τ_s). The transmission probability of a resonant electron was calculated by perturbation theory as a function of the coupling between the molecule and electrode (i.e. matrix elements τ_t and τ_s). Figure 2.16 shows the results of the calculation performed by Lindsay & Sankey.

They showed that the unity transmission was possible when $\tau_t = \tau_s$, far exceeding the transmission across the tunnel gap alone. The calculations also

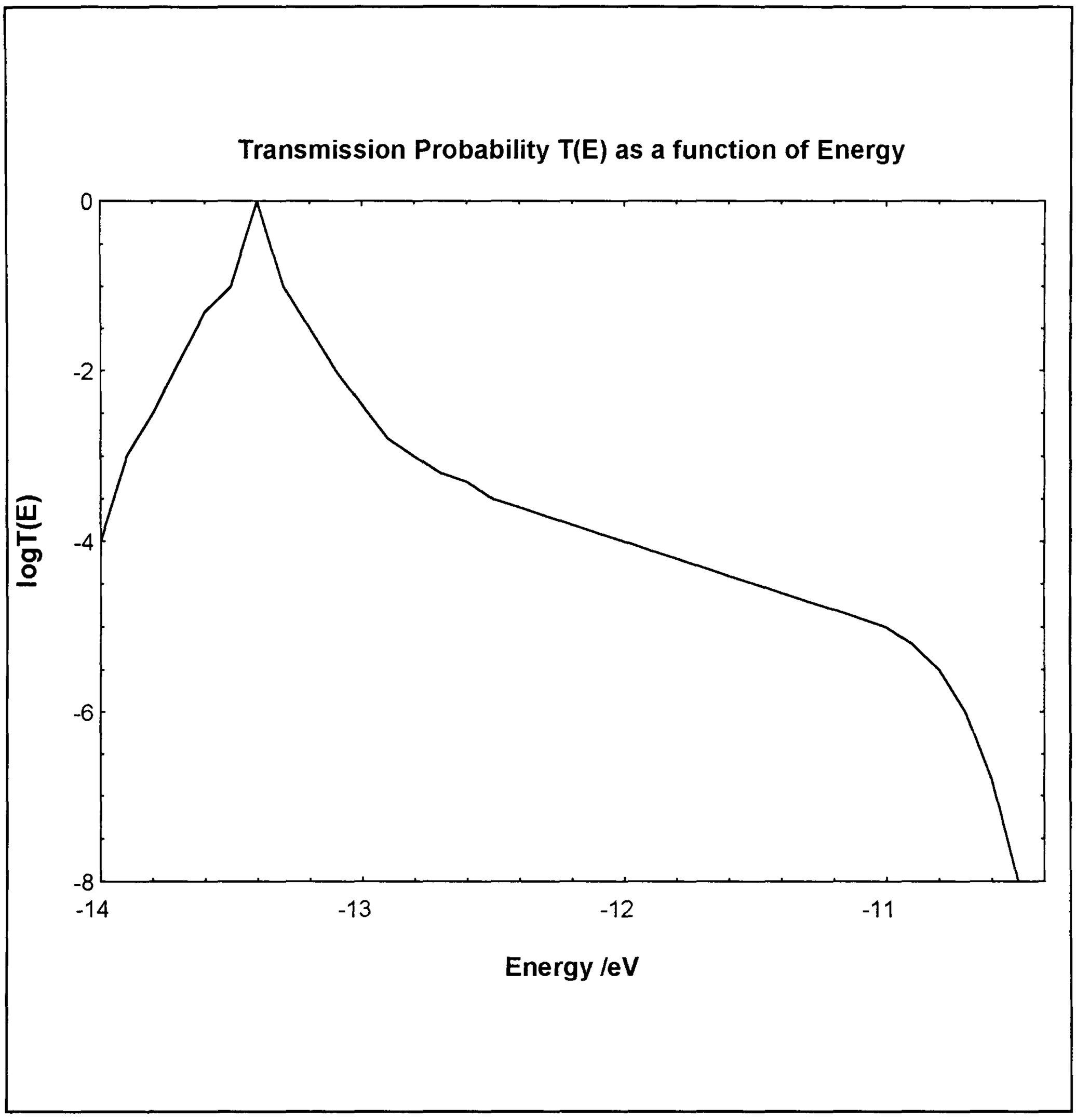

Figure 2.15: Joachim & Sautet[1990] calculated the transmission probability of an organic material sandwhiched between two electrodes. The result was a resonance curve which peaked away from the Fermi level of the electrodes but the tail of which was still significant at this energy. The transmission of electrons through the complete system (constituting the tunnel current) was found to be much larger than that due to vacuum tunnelling alone.

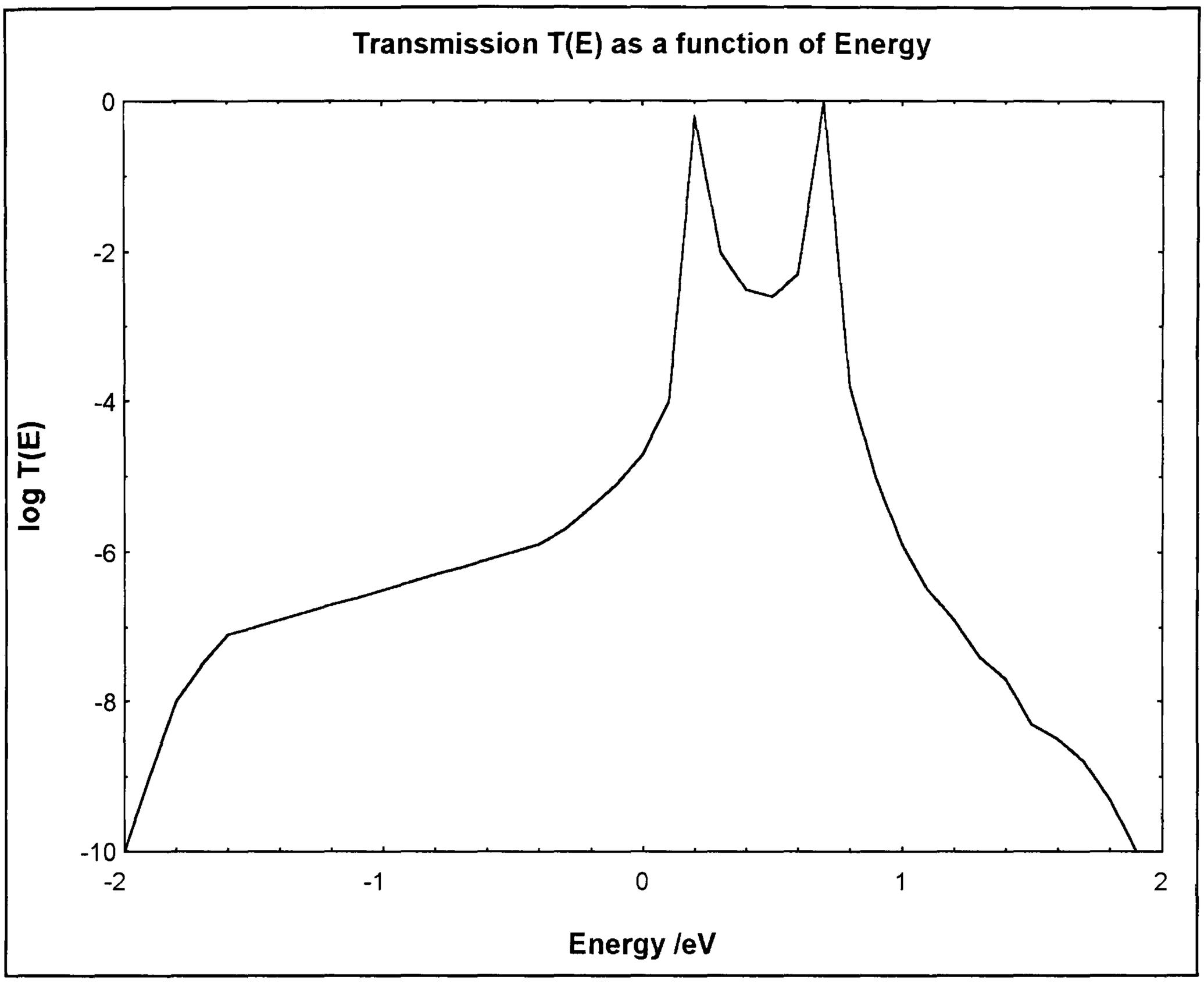

Figure 2.16: Lindsay & Sankey[1992] calculated the resonance curve for the transmission of electrons through a hypothetical model organic material. Their results suggest that the peak in transmission could approach unity although the energy position of the peak would be remote from the Fermi level of the tip and substrate. However they proposed that compression of the organic material under the STM tip may induce a phonon-electron interaction, significant enough to shift the peak to the Fermi level of the electrodes. The ramifications of such a proposal are that the organic may become as good a conductor as the electrodes themselves.

suggest that the enhanced transmission was independent of the size of either τ_t or τ_s, although in practice, as τ_t or τ_s become smaller, they take longer to evolve and transmission is inhibited by charging and incoherence effects.

The conditions for unity transmission occurring at an energy suitable for STM studies (i.e. near the Fermi level of the tip and substrate) are not generally satisfied. Lindsay & Sankey however, propose that distortions within the organic, caused by the force of the tip during operation, induce phonons that interact with the electrons and shift the resonance to a more suitable level. The phonon-electron interaction is envisaged on the macroscopic level as the increase in density of the polymer and any constituent dipolar states (due to the tip 'pressure'). The increase in these latter states enhances the dielectric effects within the material and shifts the polymer energy levels by about an electron volt [Lindsay & Sankey, 1990]. The movement of the transmission peaks due to the organic distortion results in a rapid increase in conduction. The organic material ultimately becomes a better conductor than the metal electrodes [Ehara, 1992]. The mechanism observed in this study also suggests that enhanced transmission within organic materials may be valid for a range of sample thicknesses with an upper limit of about 10nm.

2.4 CONCLUSION

Without an organic sample, the tunnel current is exponentially related to the barrier thickness and local effective barrier height. The presence of a very thin ($t<2nm$) layer of organic material can be imaged as part of the substrate because the bond it makes with the substrate modifies the local effective barrier height to the tunnelling electrons and hence to the tunnel current.

A thicker ($2nm<t<10nm$) layer of polymer may be imaged because confining it to an electrode, inducing a large electric field across a relatively thin film causes limited conduction to occur. The exact process of conduction is not well understood but the transition of electrons between localized states in the

organic and the electrode Fermi level increase the chances of conduction [Frenkl, 1938]. Resonance of the states in the polymer with the electrode energy levels was demonstrated by [Garcia & Garcia, 1990] who considered the tip-sample-substrate to be a complete quantum system. Their calculations suggest that transmission of electrons through the system (completing the circuit) during resonance enhances conductivity.

However the resonance often peaks at an energy level inappropriate for significant tunnelling to occur i.e. away from the Fermi level of the electrodes. Joachim & Sautet[1990] calculate that the 'tail' of the resonance peak permits sufficient tunnelling to be measured by the STM. Lindsay & Sankey[1992] suggest that the peak can be shifted towards the Fermi level of the electrodes (thereby increasing conductivity) if a phonon-electron interaction takes place. The interaction can arise as a result of the deformation of the polymer caused by the scanning tip coming into direct contact with the polymer or by the force exerted by a covering layer of water under the motion of the tip.

The presence of the localized states and tunnelling pathways depends on the polymer morphology and hence any conduction mechanism where the carriers are transported 'through' the polymer, may be highly structure dependent. The structure is also affected by environmental factors such as the presence of solvents, plasticizers and water, as well as by the substrate and film casting technique. Thus the conductivity may vary in a polymer sample because of many factors (see figure 2.17), the dominance of one over another is not clear but by good sample preparation and environmental monitoring, the conductivity may vary in a way that represents the morphology of the polymer surface. The STM will thus image the polymer in a reliable and informative way.

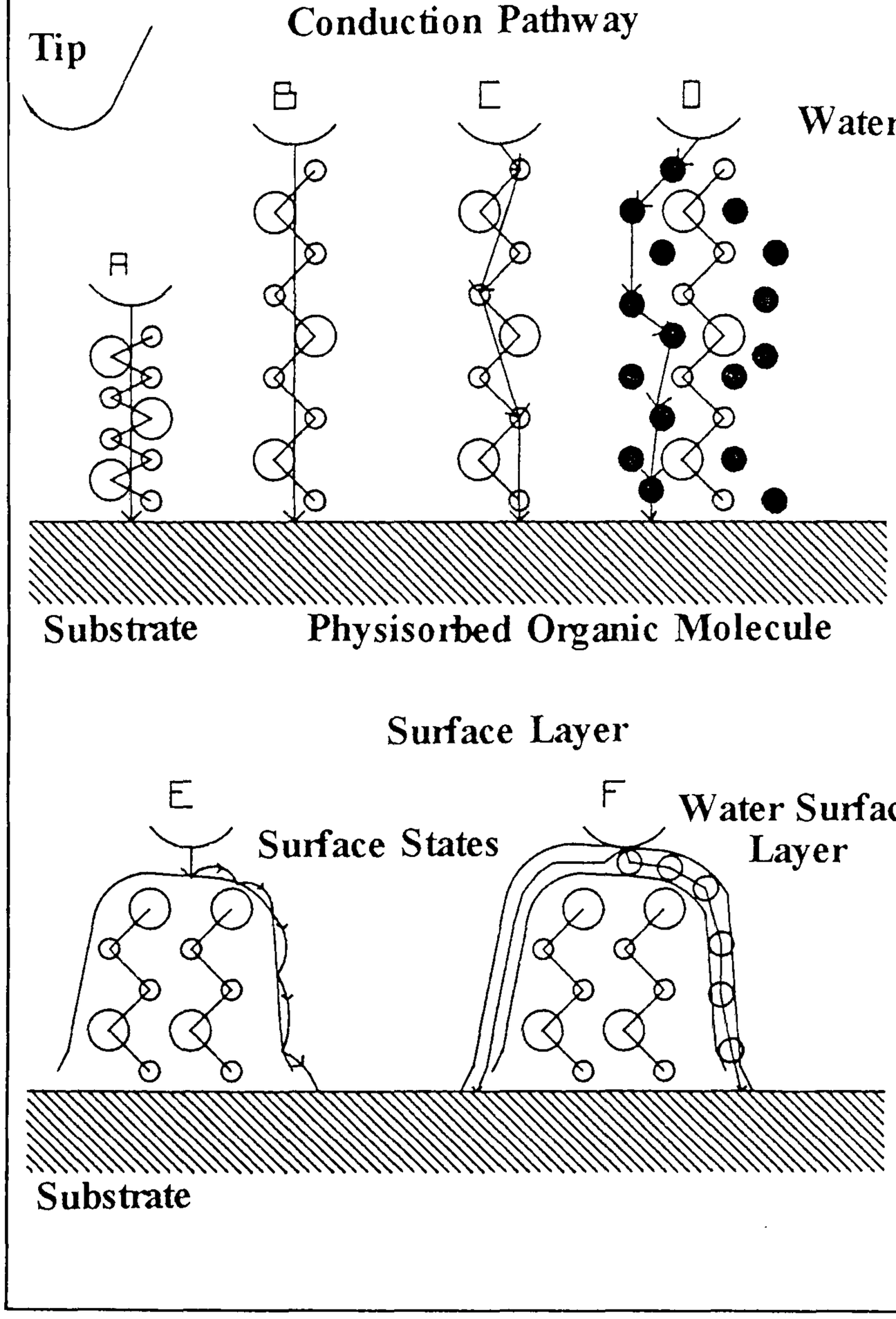

A Compression of polymer by tip to shift peak transmission towards tip/substrate Fermi level Lindsay & Sankey[1992].

B Transmission through resonant or non resonant organic molecule, Garcia & Garcia[1990], Joachim & Sautet[1990].

C Charge hopping through localized states within the polymer, Frenkel[1938].

D Conduction through film by ionic transport through water, Lewis & Toomer[1981].

E Charge hopping along surface states, Seanor [1986].

F (a) Charge transport across the surface by a conductive medium, Blackford et al [1991].
(b) Charge transport across the surface by a water medium, Hu et al [1992]

Figure 2.17: The polymer in the bulk does not normally conduct electricity. If the film is thin enough, the interaction with the substrate alone can be imaged by the STM regardless of conductivity. However thick samples can only be imaged if they can contribute to the conduction process. This may be achieved in a variety of ways set out in the diagram above and the domination of one mechanism over another has yet to be shown. It is likely however that a combination of mechanisms is present during the imaging of any one sample.

CHAPTER 3

THEORY OF AFM OPERATION

3.0 THEORY OF AFM OPERATION

3.1 INTRODUCTION

The atomic force microscope or AFM was introduced in 1986[Binnig, Quate & Gerber, 1986] as a derivation from the STM and has subsequently become one of the most important quantitative surface force probes. Other techniques that may be associated with the AFM are the stylus profilometer, the nanoindenter (hardness tester) and the surface force apparatus [Burnham et al, 1991]. Together these techniques specialize in the accurate measurement of surface forces that include for example van der Waals, magnetic or adhesive, capillary and frictional forces.

The AFM has the added advantage over the other force measuring techniques that include superior force resolution and vertical and horizontal resolutions. When coupled with the high precision micropositioning associated with the probe microscopies, the AFM can generate exceptional high resolution images of a wide range of materials.

It is the potential of the AFM as an imaging device that is of prime importance to this thesis. Unlike the situation with other imaging techniques such as the electron microscope and the STM, there is no specific requirement for the sample to be conducting. Thus bare polymeric samples that are too thick to be imaged by the STM and too 'insulating' to be imaged by the electron microscope in some cases can be imaged successfully by the AFM.

The AFM imaging relies on the force interaction of a fine tip with the surface of a sample. The image is formed as the tip is scanned across the surface and a plot of force interaction versus tip position is made. To achieve a measurable force, the AFM tip which is fixed to the back of a flexible cantilever (the displacement of which is continually monitored) is moved towards the sample until the two are very close together (see figure 3.1).

In general as the tip is lowered on to the sample, the first types of forces that are encountered are the long range van der Waals forces which are generally attractive. The tip may be stopped at this point and a non-contact

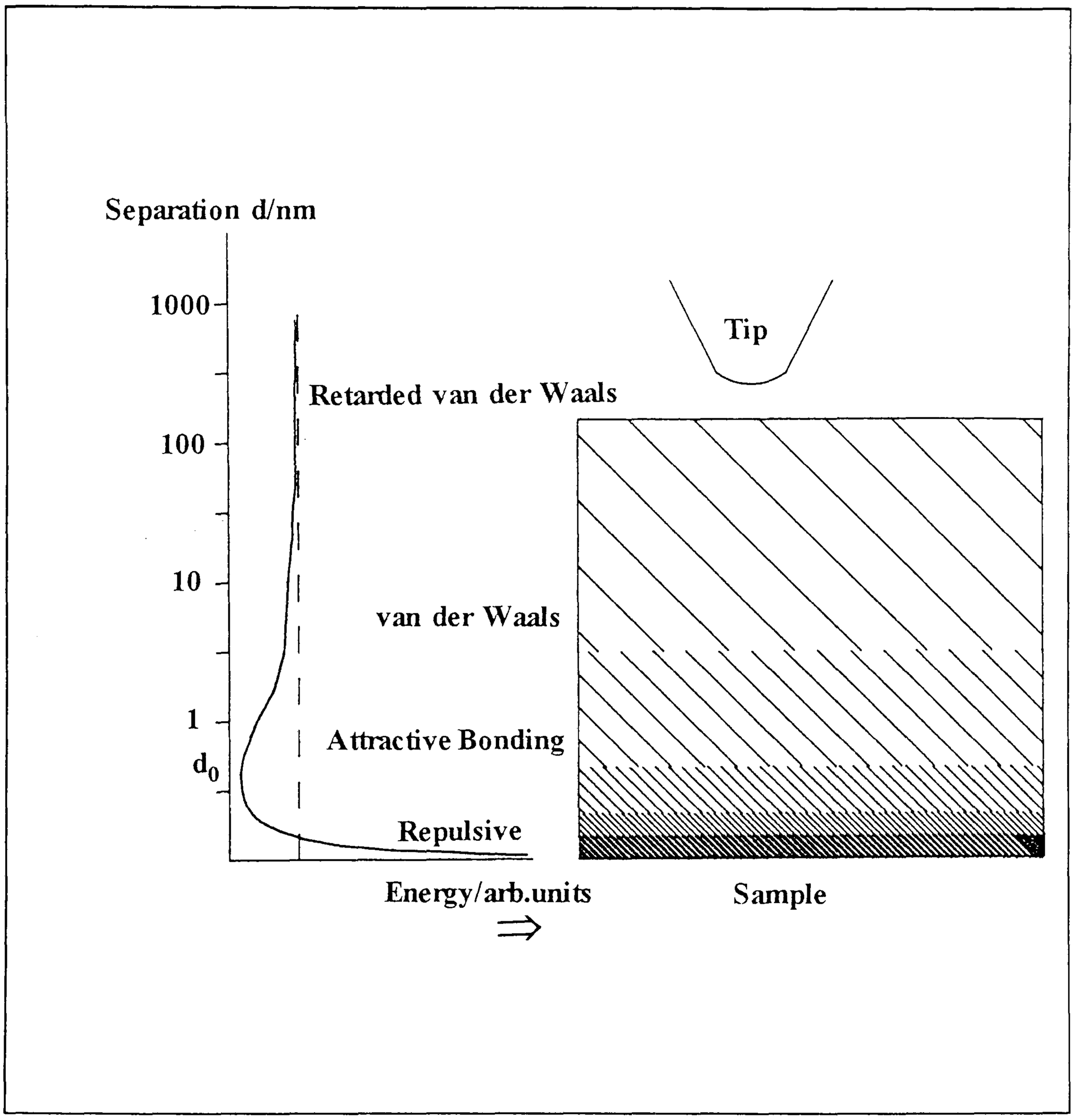

Figure 3.1: To achieve a measurable force the tip is gradually lowered until at first attractive van der Waals forces and then eventually repulsive forces are measured. The tip sample separation is several nanometres in the non-contact mode but less than a nanometre in the contact mode.

image of the long range forces acquired. Alternatively the tip may be further lowered until a repulsive force dominates. In this regime a 'contact' image of the short range repulsive forces of the surface is acquired.

The contact mode is most often used and for the sake of image interpretation it is assumed that the spatial position of the repulsive forces measured by the AFM follow the topographic contours of the sample in an accurate fashion. The image obtained in general (and on a relatively large scale) accurately reflects surface topography. In some cases atomic resolution has been reported especially on layered materials such as graphite in the form of HOPG[Binnig et al, 1987], mica and MoS_2[Albrecht & Quate, 1987]. These groups suggested that successful imaging of atomic corrugations was primarily due to the presence of a very sharp tip or lone atom remaining relatively stable and rigid during the imaging process. This single atom model was successful and unquestioned because, like the Tersoff and Hamman [1985] model of the STM it could account for the very high resolution of the AFM.

However within the last few years workers have questioned the single atom model because it cannot explain the very large corrugations within the layered materials, the difficulty in imaging (at an atomic level) other non-layered samples and also the tip/sample survival at the very large local pressures and large contact areas (calculated by Derjaguin et al[1975]) experienced within AFM. Further ideas have been developed that take into account both the extensive tip-sample contact (which can involve many atoms) and the undisputable high resolution images obtained. Fine examples of such treatments are discussed below and further details may be found in, for example Burnham, Colton and Pollock[1991, 1993], Pethica and Sutton[1990], Heinzelmann et al [1990] and others.

This chapter aims to explain the force experienced by the tip and the simple AFM model used. The single atom model of the tip is then discussed with reference to image interpretation. Finally a description of some of the latest ideas concerning AFM imaging are presented which include the effect of contamination layers on the force contribution and large contact area imaging.

3.2 MICROSCOPIC INTERACTIONS

A discussion of the forces involved between the tip and sample may be gleaned from the interaction on the microscopic level between two atoms representing the apex atom in a rigid tip and the closest atom on the sample surface. When the two atoms approach there are a variety of forces experienced (all of which may, to some degree be measured by the AFM). The interactions and their significance to the AFM system as a function of distance may be broadly categorized as follows:

Large tip-sample distance (d>10nm):

Assuming an absence of contamination layers, at this separation there is essentially no mutual interaction between the tip and sample. However in the presence of charged species, for example ions, polarons(charged regions within the polymer matrix) and dipoles, a Coulombic or electrostatic force may exist. The magnitude of the force (F) between two isolated point charges $q_1$and q_2 is inversely proportional to the square of their separation (d) in the form:

$$F = \frac{1}{4\pi\epsilon_0}\frac{q_1 \cdot q_2}{d^2}$$

When a build up of charge occurs (especially during the scanning motion of the tip over highly insulating sample), the electrostatic force can be very much larger than any other force present and in some circumstances the tip and cantilever can be pulled on to the sample surface ruining the image completely. To combat this problem manufacturers often coat the silicon nitride AFM tips with a metallic conductive layer; this helps to conduct the build up of charges to earth.

Intermediate Tip-sample Distances (1nm<d<10nm):

At this smaller separation, the force regime is dominated by the Lifshitz-van der Waals or LdvW forces (see figure 3.2). This force is very much weaker than the traditional bond types for example ionic, covalent and metallic bonding forces. LdvW forces arise from induction forces (dipole to induced dipole interaction), orientation forces (interaction between orientated permanent dipoles) and dispersion forces.

The dispersion forces act between all atoms and molecules. They are caused by the periodic variation in the electron density (due to zero-point motion) within the surface of the atom. A transient dipole is created which in turn induces a secondary transient dipole in other atoms. The variation in electron density within the affected two atoms is in phase and an attractive force is experienced between them. Dispersion forces can be used to explain many of the adhesion problems found in the SPM system. For example they are directly responsible for binding the polymer film to the substrate.

However in direct relation to the forces experienced between the tip and sample, the general form of LdvW forces given an instantaneous dipole moment ($\boldsymbol{\mu}_1$) in the tip or sample which induces a second dipole ($\boldsymbol{\mu}_2$) in the other is:

$$U \approx -\frac{\boldsymbol{\mu}_1 \cdot \boldsymbol{\mu}_2}{d^3}$$

Where an attractive interaction energy U, exists which is proportional to the product of the dipoles and inversely proportional to the cube of their separation. However μ_2 is approximately proportional to $-\mu_1/d^3$ and substituting for μ_2 gives:

$$U \approx -\frac{\alpha \boldsymbol{\mu}_1^2}{d^6}$$

The LvdW interaction that exists between the tip and sample is in general inversely proportional to the sixth power (d^6) of their separation.

This approach is viable for short ranges less than 10nm; however for

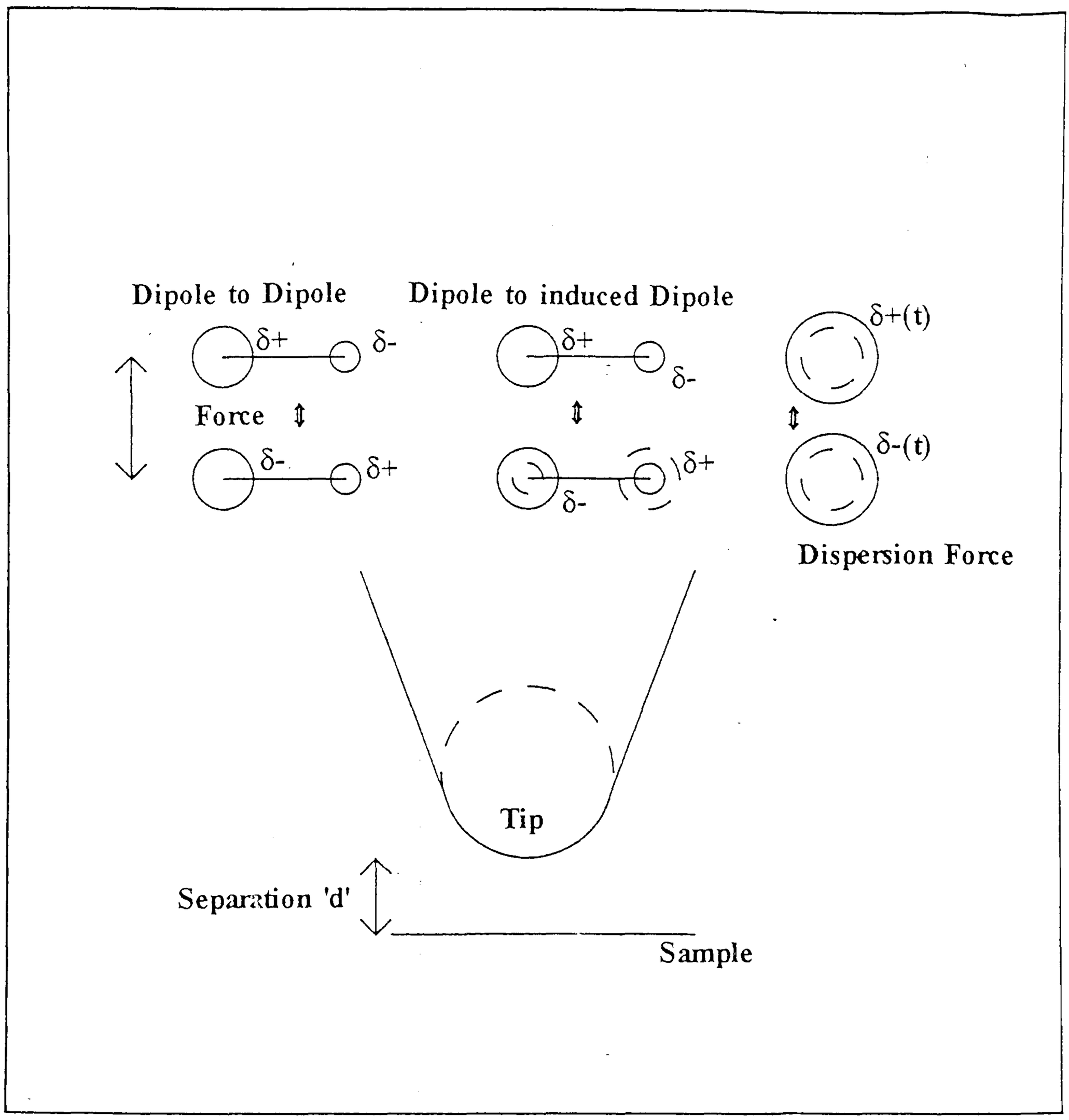

Figure 3.2: When the tip-sample separation (d) is in the range 1nm<d<10nm, the Lifshitz-van der Waals forces dominate. They arise from induction forces (dipole to induced dipole interaction), orientation forces (interaction between orientated dipoles) and dispersion or London forces.

larger separations the propagation time of the EM field in the medium between the induced dipoles may become comparable with the inverse of frequency of the dipole variation. In this case the dipoles lose some of their attraction and a retarded-dispersion which diminishes proportionally to the seventh power of the tip-sample separation exists[Lee 1991].

Hydrogen bonding is very important to SPM work carried out under ambient conditions because the ever-present water vapour results in contamination of every surface and all the samples studied. Although the bond description is essentially that of a dipole-dipole interaction as described above, it is important to note the increased strength of the interaction. On account of its very small size when bonded in a molecule the hydrogen end of the molecule becomes positively polarized and with no further electrons orbiting the nucleus the residual positive charge is unscreened. The effect is to produce a highly polarized molecule. Other neighbouring molecules, similarly polarized, orientate to achieve maximum opposite dipole attraction. The electrostatic bond between dipoles is very much stronger than other dipole forces discussed above.

Short Tip-sample distances (0.3nm<d<1nm):

At this separation, the atomic orbitals of the atoms in the tip and sample begin to interact. The overlap of the atomic orbitals may result in the formation of an intermediate bonding state. The outer orbitals in some circumstances (i.e. those with suitable quantum numbers) adopt a new configuration which effectively lowers the energy of the system and a basic Covalent Bond is formed. In the AFM system if this happens, the tip and sample may become chemically bonded with each other (this phenomena may account for the considerable hysteresis within the force-vs-separation characteristics).

If on the other hand, with the mingling of orbitals, an electron is permanently transferred from one atom to the other, an Ionic Bond is formed. In this case there is no covalent sharing of electrons and lowering of energy by the creation of a new electronic orbital structure. Instead the energy of the

system is lowered because the attractive electrostatic force between the newly created ions exceeds the ionization energy required to 'poach' the electron. This type of bond is highly unlikely because the materials chosen for the tip and sample are done so because they are particularly inert.

The overlap of atomic orbitals may not result in a lowering of the energy of the system. For example if the quantum numbers of the electrons are identical then Pauli Exclusion prevents them from occupying the same state. The intermediate bonding state raises the energy of the system as new higher energy orbitals are utilized and to do this external work must be introduced. The effect of the incompatibility of the outer orbitals results in a repulsive force between the tip and the sample.

As the tip and sample get closer together, the advantages of the attractive bonding interactions (covalent and ionic) becomes tempered by the repulsive forces experienced as more inner orbitals try to overlap. The force then moves from an attractive to a repulsive regime with a characteristic energy minimum at a point representing the stable interatomic tip-sample separation (see figure 3.3).

Very Short Tip-sample Distances (d<0.3nm)

At the very short tip-sample distances the repulsive forces dominate. These forces have been introduced above and arise as the overlap of atomic orbitals require the formation of higher energy states. The Pauli Exclusion Principle prevents electrons with the same quantum numbers from occupying the same state and a repulsion from further incursion is experienced. Experimental results suggest a rapidly increasing force with a decreasing tip-sample distance where the repulsive force is approximately inversely proportional to the twelfth power of separation. Any further movement of the tip towards the sample results in deformation of either tip or sample or even both.

Most of AFM studies to date utilize this repulsive regime. The mode of operation is the 'contact' mode. It is within this region that the tip-sample interactions become very difficult to assess and workers suggest that significant tip-sample deformation occurs, preventing true topographic

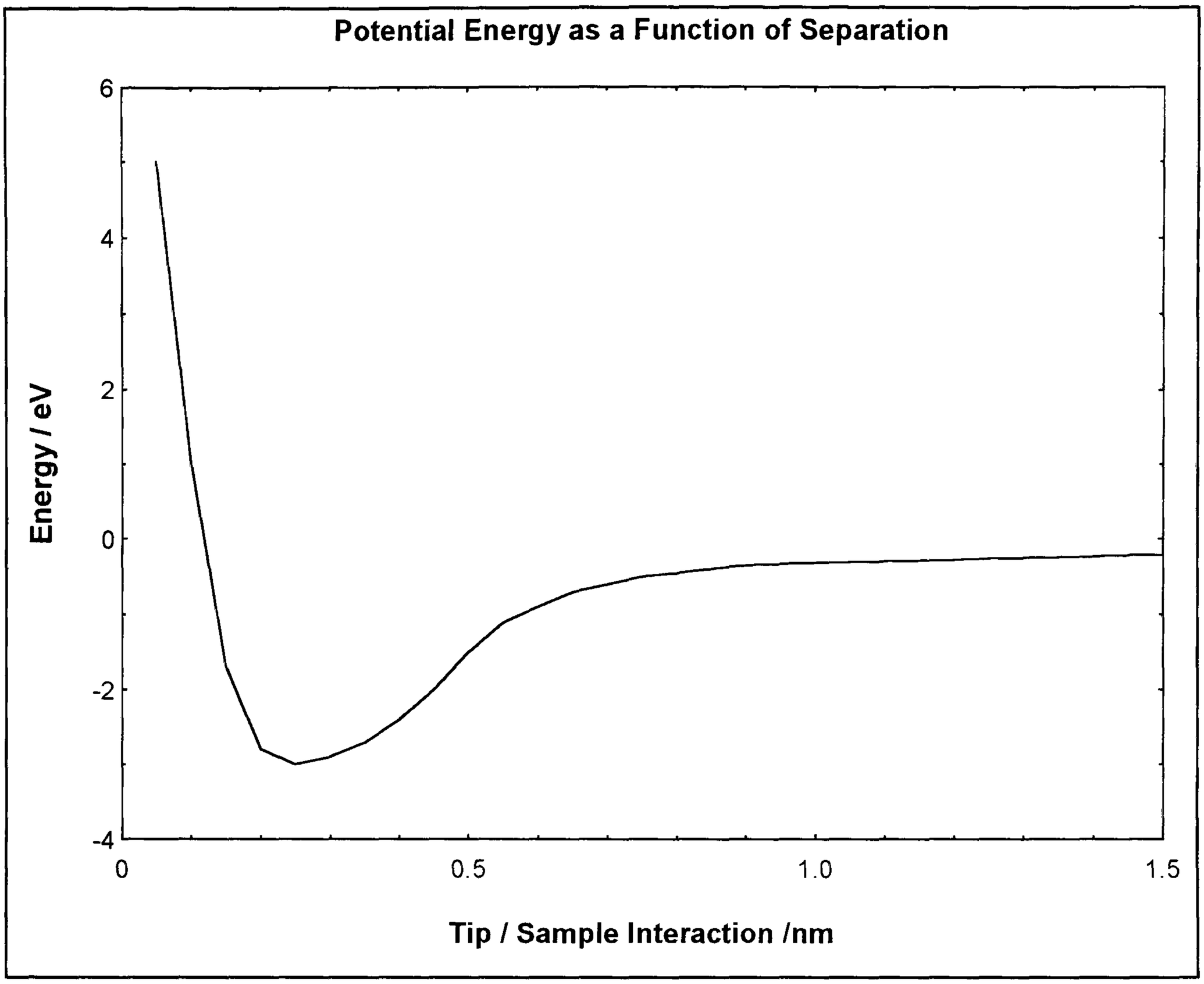

Figure 3.3: At short tip-sample separations i.e. 0.1nm<d<1nm, strong attractive forces are present as are the repulsive forces attributed to the encroaching filled atomic orbitals. There is an energy minimum where the net attractive forces are greatest and this occurs at d_0, the equilibrium position. In a lattice, this position represents the typical lattice spacing.

reconstructions of the surface by the AFM. The topic of image interpretation will be further examined in a later section of this chapter.

Summary of Forces and Bonding

Very close range interactions are dominated by repulsive forces. As the tip-sample distance increases, attractive forces that include those associated with covalent, ionic and hydrogen bonding begin to dominate over the repulsive force. However these repulsive forces diminish quickly as the distance is increased and at $d=\sigma$ the energy is zero and reaches a minimum at a point ($d=d_0$). As the gap increases, the attractive forces between atoms separated by a nanometre or more, are mainly due to Lifshitz-van der Waals forces. The Lennard Jones potential is used to describe the total interaction between the tip and sample. It contains terms representing both the attractive LvdW forces ($U\alpha\ 1/d^6$) and the repulsive short range forces ($U\alpha\ 1/d^{12}$):

$$U(d) = 4U(d_0)\left[\left(\frac{\sigma}{d}\right)^{12} - \left(\frac{\sigma}{d}\right)^{6}\right]$$

Atomic Resolution

The earliest workers with AFM who include Binnig, Quate & Gerber [1986] calculated the feasibility of the AFM obtaining atomic resolution by using cantilevers with sufficiently low spring constant ($k\approx0.016$ N/m) under the action of the interaction forces (when the tip/sample were in contact they calculated as typically 10^{-9}N). The workers concluded that the atomic corrugations were detectable given the single atom apex of a rigid tip coupled with the flexible cantilever.

The situation as regards the actual AFM imaging of the surface is more complex. It is the macroscopic treatment of the tip and sample that reveals the problems associated with true atomic resolution.

3.3 MACROSCOPIC TREATMENT OF THE IDEAL AFM

The force regimes experienced by the tip (which is represented by a rigid, very fine, atomically sharp tip) as it is moved towards an atom in the sample surface has been discussed on the atomic microscopic level. In this section the tip and sample are considered to be formed from many atoms. The force interaction between the tip and sample is discussed and is essentially a sumation of all the individual forces between each of the component atoms within the system. The treatment may be considered to be one concerning the macroscopic effect of the tip (as a whole) on the sample. The tip and sample are still represented by solid and rigid bodies which may be regarded as an over simplification of the system as a whole.

When considering the macroscopic effect of one body on another (in this case the tip and sample), it is not sufficient solely to consider the forces between one or two atoms at the extremities of the probe and sample. To establish a true picture of the forces involved it is necessary to perform a summation of all the atomic level forces, especially the LvdWs forces discussed above, over the macroscopic geometries involved.

Non-contact AFM

The non-contact mode of operation is more easily treated than the contact mode because there is little in the way of tip or sample deformation. Unfortunately when using the AFM in this (non-contact) mode, although the image interpretation is simple, the atomic corrugations and fine detail of the surface are attenuated beyond measure.

In a treatment forwarded by Hamaker[1937] a simplified model of the tip and sample are considered (see figure 3.4). The tip and the sample are assumed to be two parallel plates separated by a small gap. The energy of the interaction, as a function of separation, d is given by:

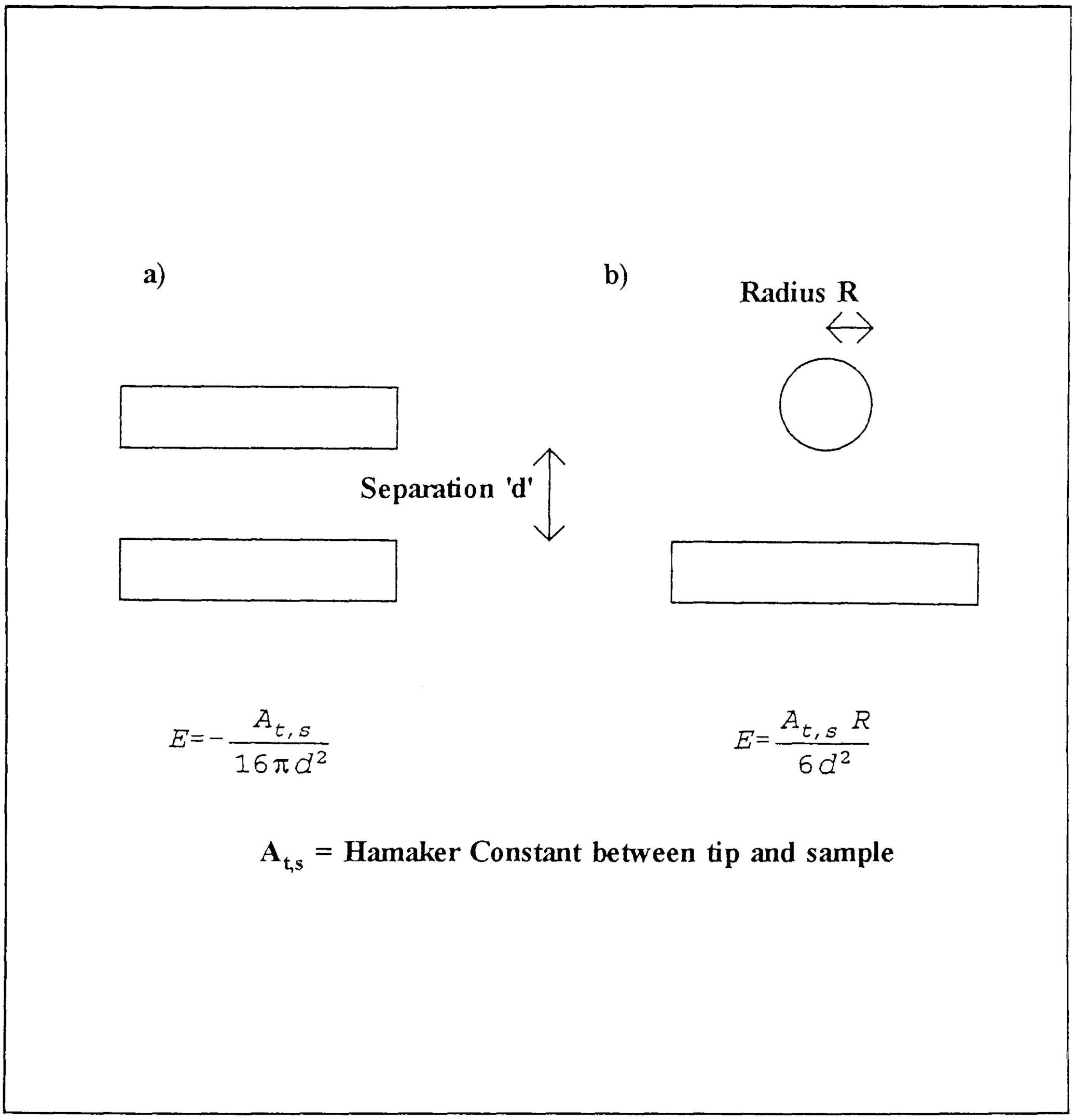

Figure 3.4: The contribution from the individual atoms/dipoles towards a generally attractive force can be calculated as a function of tip/sample geometries. In this case the tip and sample are represented by a) two plates b) a sphere and a plate.

$$E = -\frac{A_{tip,sample}}{16\pi d^2}$$

Where $A_{tip,\ sample}$ is the Hamaker constant between tip and sample and is comprised of terms representing the LvdW forces discussed above (section 3.1).

A more sophisticated approach offered by Dzyaloshinskii et al[1961], defines the Hamaker constant in terms of the electromagnetic radiation field component (with average angular frequency ω) of the Lifshitz-van Waals forces such that:

$$A_{t,s} = \frac{3h\omega}{8\pi^2}$$

By including the Hamaker constant and replacing the parallel plate geometry with a more accurate portrayal of the tip(sphere) and sample(plate), the force between the two as calculated by Tabor[1977] becomes:

$$Force_{tip,sample} = \frac{A_{tip,sample}R}{6d^2} = \frac{h\omega R}{16\pi^2 d^2}$$

The two treatments seem similar and both give an inverse square relationship between force and separation (d). However, the electromagnetic field approach by Dzyaloshinskii, allows the Hamaker constant to be either positive or negative, resulting in either an attractive or repulsive force between the tip and sample respectively. The attractive force regime occurs between similar materials and may result in movement of the tip towards the sample during AFM operation. However, dissimilar materials may result in a repulsive force, pushing the AFM tip away from the sample.

Using the same approach, Sarid [1991] calculated the force between a sphere and a plate in two different circumstances (see figure 3.5 and table 3.1 below). In one case, where the tip radius is small compared with the separation d, the force is negligible. However (case 2) if the tip radius is large and the gap separating the tip from the sample is small (this situation most closely resembles the AFM system), the force is considerable.

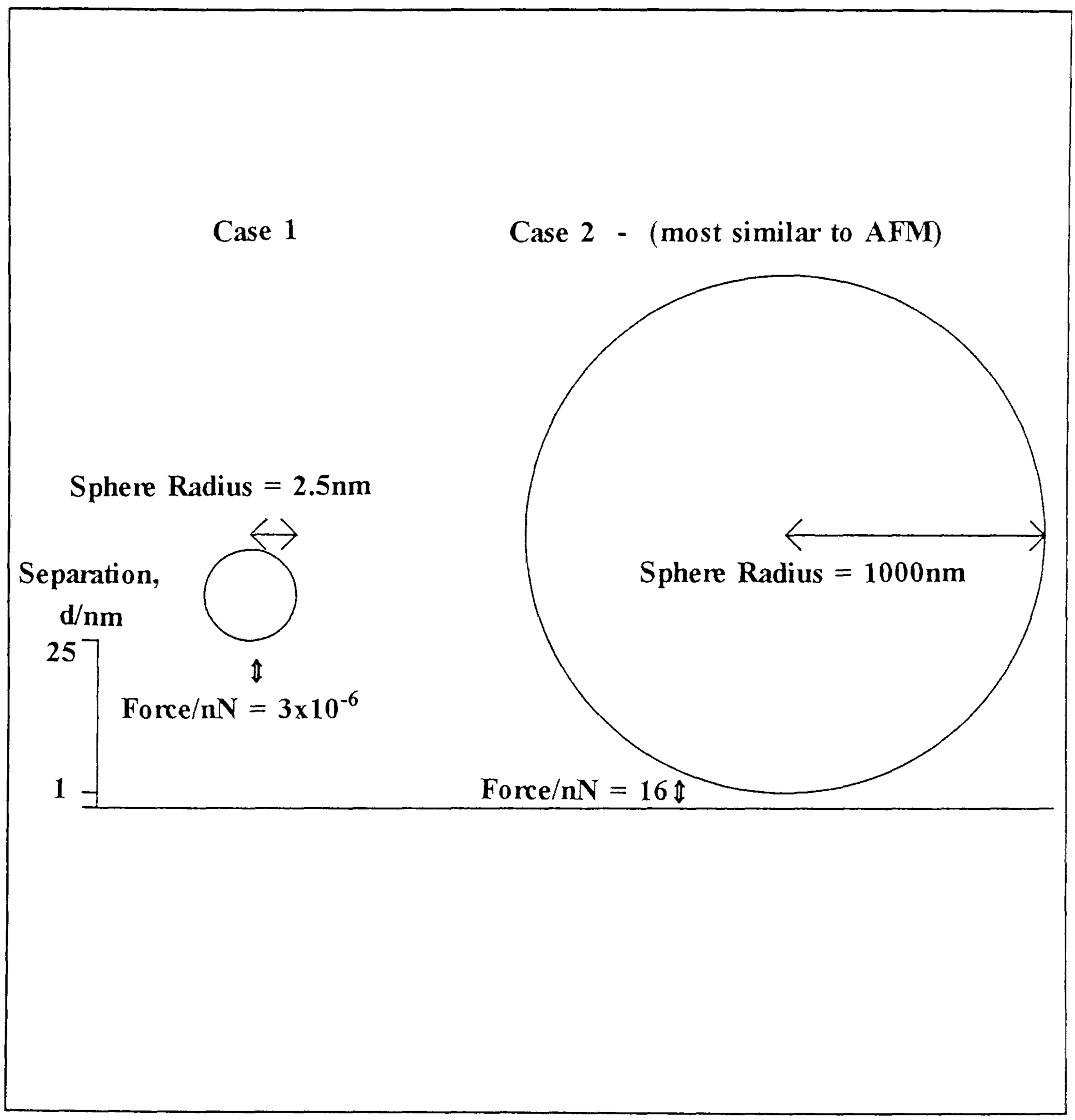

Figure 3.5: Sarid[1991] calculated the force between a sphere and a plate for a)sphere with small radius and large separation b)sphere with large radius and small separation. The latter most closely resembles the AFM situation and the force involved is considerable.

	Sphere Radius /nm	Separation/nm	Force* /nN	Cantilever Deflection† /nm
Case 1	2.5	25	$3x10^{-6}$	$3x10^{-5}$
Case 2	1000	1	16	160

Table 3.1

*With a Hamaker constant of $1x10^{-19}$ J.

† With a cantilever spring constant of 0.1N/m.

In general, in the non-contact mode of operation, the tip experiences an attractive force which is proportional to the inverse square of the distance between itself and the sample surface.

Contact Mode AFM

Until this point the macroscopic interactions discussed have been concerned with a rigid tip and sample, operating in the non-contact regime. Although this mode of operation is useful (image interpretation is much easier) especially over very delicate samples, this is at the expense of atomic resolution and fine surface detail. The contact mode does not suffer these losses and although the images may be difficult to explain in some circumstances, the benefit of substantially increased resolution cannot be ignored.

The fundamental problem with the contact mode is one of tip-sample deformation. This was not addressed by the earliest workers and the physics of the interaction is still not fully understood. However the scale of the problems and the ramifications as regards the achieving of atomic resolution can be assessed.

Classical Adhesion Models

The concept of surface energy(γ) gives an important guide to the problems associated with the tip and sample contact in contact mode AFM work. It quantifies the close contact, adhesion or tackiness arising between the tip and the sample as a result of the LvdW forces. A brief treatment by Gutowski[1991] defines surface energy as the energy required to separate two bodies (including the tip and substrate), once adhered to each other by LvdW forces alone and is given by:

$$\gamma = \frac{A_{tip,sample}}{24\pi d_o^2}$$

Where $A_{tip,sample}$ is the Hamaker constant between the tip and sample and

contains the terms associated with the LvdW forces. 'd_o' is the interatomic separation and is equivalent to the equilibrium separation at the position of the energy minima where the attractive forces are greatest.

By combining this result with the force between a plate and a sphere (the tip-sample model), the force required to separate the two, once in contact, is given by:

$$Force = 4\pi d\gamma\cos\theta$$

Where θ is the contact angle and γ, the surface energy. Experimental results suggest that in a liquid or a humid environment, the surface energy is much higher than the surface energy in the dry environment (i.e.$\gamma_{liquid} >> \gamma_{dry}$). If the tip and sample have trapped a layer of liquid between them, the adhesion force is much higher and much more energy is required to separate them. As a result, scanning in this highly tacky mode may result in considerable sample damage.

Without the presence of water, the tip when in contact with the sample will deform the sample and may remain adhered to it. A description of this situation is given by Timoshenko & Goodier[1970] who modified the lever and tip spring constant to include the deformation of the sample. The combined system exhibits some peculiarities for example, as the tip (assumed to be either a flat ended cylinder or a paraboloid [Cohen et al, 1989]) approaches the sample, the effective spring constant vanishes. The physical result of this is that the LvdW forces cause a jump or pulling of the tip towards the sample surface (see figure 3.6). The resulting contact area between the deformed surface and tip (again modelled as a sphere, radius R and plate) was calculated by Derjaguin et al[1975], the radius of contact r_c being given by:

$$r_c = (4\pi\frac{R^2}{k}\sqrt{\gamma_t\gamma_s})^{1/3}$$

Where k is the tip-lever spring constant and γ_t and γ_s are the surface energies of the tip and sample respectively. Burnham et al[1991] calculate an

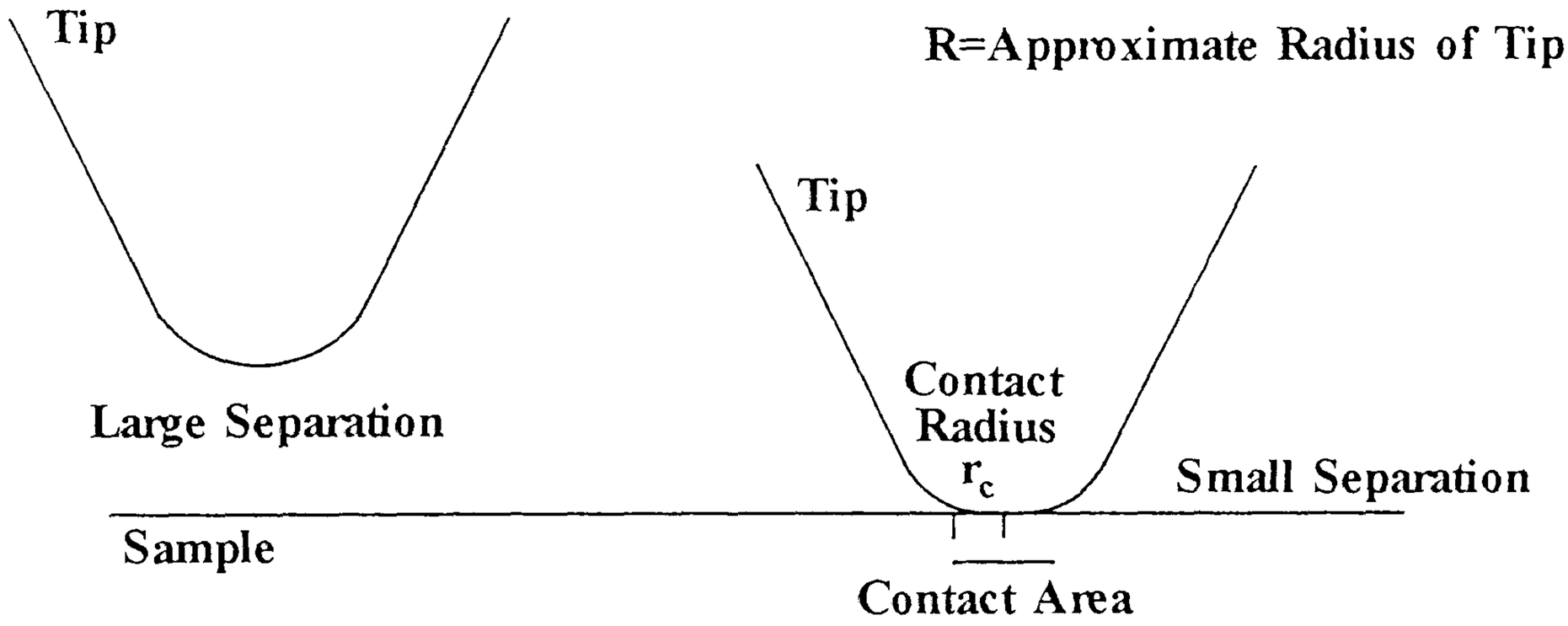

$$r_c = (4\pi \frac{R^2}{k} \sqrt{(\gamma_t \gamma_s)})^{1/3}$$

γ_t and γ_s= surface energies of tip and sample

Figure 3.6: The large LvdW forces cause the tip to jump to the sample surface and adhere with a radius of contact (as the tip and sample deform slightly) of r_c. After Derjaguin[1970].

approximate figure for the contact radius at 1nm (given a very small tip radius of 10nm). A simple calculation based on a lattice spacing of 0.25nm shows that the contact area contains at least 50 atoms, in contradiction to the single atom assumed to be present in earlier models.

Contamination Layers and Water Vapour

Typical laboratory imaging conditions are such that contaminating layers and water vapour are ever present near or on the sample. At a non-zero relative humidity, the sample surface is inevitably coated in a layer of water. Some samples, including freshly cleaved mica actively adsorb water and this can pose severe problems to the scanning tip. If the water layer is sufficiently thick (and this need only be greater than a monolayer coverage) then a water bridge connecting the tip to the sample can form (see figure 3.7).

A simple calculation by Woodward et al[1992] considered the van der Waals forces and the capillary or Laplace pressure of the water bridge, between the tip and sample. Their calculations assumed the tip-sample distance to be 1.2nm (non-contact mode) and relative humidity to be 45%. The force calculated was 23nN. This is some twenty or thirty times as large as the corresponding LvdW force contribution at this separation.

A similar calculation of the tip in the contact mode by Burnham et al [1991] under the same humidity as Woodward et al, gives the force (in the contact mode) at 90nN compared to the maximum vdW force at this separation of 60nN.

Molecular Dynamics Calculations

Further accounts of the tip and sample deformation and of the contact area are given by Landman et al [1990]. This group used the embedded atom model (EAM) developed by Daw and Baskes[1984] to model the approach of a nickel tip towards a gold sample. The EAM model allowed Landman et al to calculate the energy of each of the 450 surface (gold) atoms and of those atoms in a further ten other sub-surface layers. The energy of every nickel tip

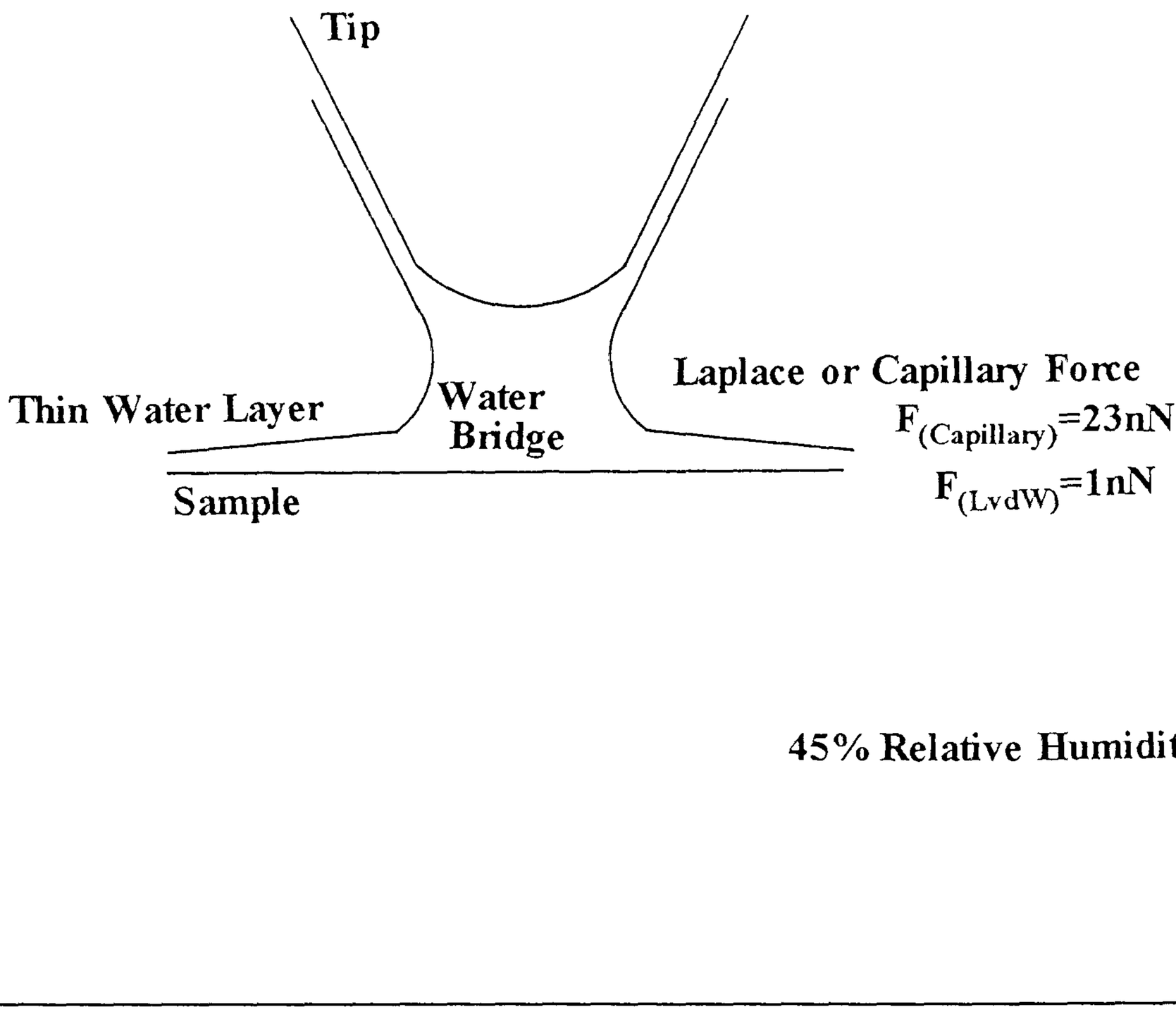

Figure 3.7: Under ambient conditions and a relative humidity of 45%, the capillary or Laplace force within the bridge of water spanning the gap between tip and sample is larger than any other force present Woodward[1992].

atom (of which there were 1400) was then calculated. The tip was also modelled as having a flat end consisting of 72 atoms.

The results of the tip-sample interaction was that at a tip-sample separation of 0.42nm, the tip suddenly jumped to the energy minima position of 0.21nm. Further movement of the tip towards the sample (in a typical contact mode operation) resulted in elastic deformation of the tip and sample. The adhesion between the two is maintained even when the tip is 'withdrawn' from the sample in fact the tip was found to become coated with the surface gold atoms and a connective neck of material was formed between tip and sample (see figure 3.8).

Imaging Mechanisms

The difficulty in understanding the imaging mechanism for the contact mode AFM may now be ascertained. The concept of surface energy and of the LvdW forces that accompany the macroscopic geometries of the tip and sample have been discussed. In short there is no such thing as a single atom tip tracing the topographic contours of the sample surface. In reality as the tip approaches the sample, whether there is a contaminating layer or not (although the presence of water may increase the tip-sample forces by an order of magnitude [Woodward[1992]), the tip will jump closer to the sample. The contact point is actually an area which for some materials can include tens or even hundreds of atoms. Even for the hardest materials like diamond, the local tip pressure is sufficient to deform the sample giving a contact area containing many atoms (Burnham et al 1991). To exacerbate the problem, on attempting to remove the tip from the surface, permanent damage to the sample can be the result (Landman et al 1990).

The question of the actual imaging mechanism thus returns. If, during the contact mode of operation, the contact area is far greater than the single atom, how is atomic resolution and fine surface detail achieved?

The main thrust of work aimed at resolving this problem concerns layered materials. It is well known that 'atomic' resolution of HOPG, MoS_2 and mica is possible. The results give a periodic morphology with a lattice

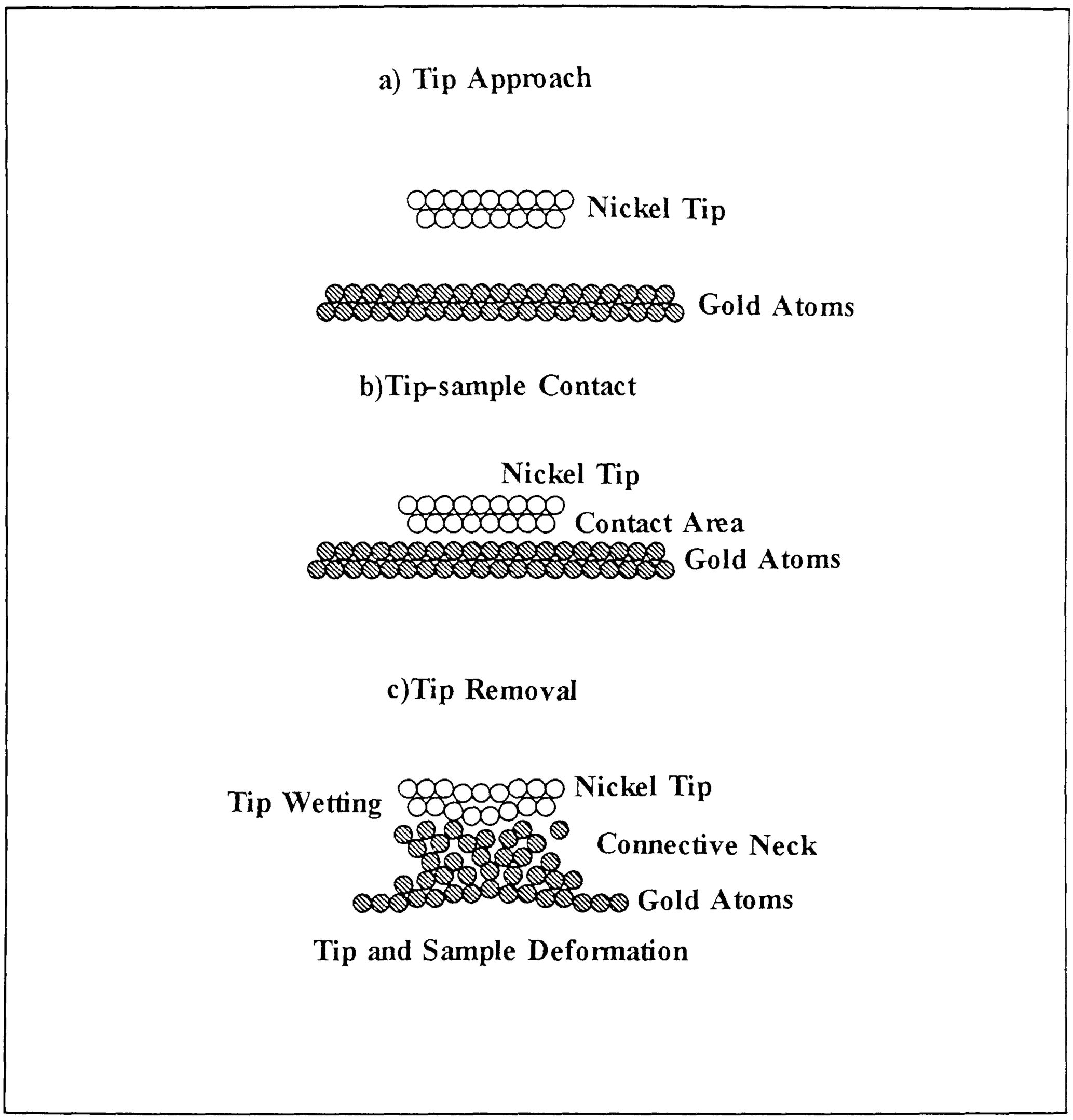

Figure 3.8: Calculations by Landman et al [1989] using molecular dynamics simulations suggest that for a nickel tip and a gold substrate, the contact area is large and on removal of the tip, permanent damage is sustained with a connective neck of gold atoms wetting the tip.

spacing consistent with the material as obtained by many other (for example diffraction) techniques. The images were assumed to represent the true morphology of the sample surface. However the large contact area makes the single atom imaging very unlikely and an alternative image acquisition mechanism is needed. The following mechanisms by Abraham & Batra [1989], Pethica[1985] and Landman et al [1989] were formulated and in part explain why 'atomic' resolution is observed.

Sliding Molecular Planes

Abraham & Batra [1989] used the Stillinger-Weber[1985] or SW model and a vdW potential on which to base molecular simulations of the AFM imaging of graphite (HOPG). The SW model was used to imitate the intra-plane covalent bonds of the graphite and the vdW potential was used to model the inter-plane bonding. The tip consisted of either a single carbon atom apex or flake of graphite.

Experimental results were unexpected in that only every other atom in the lattice was imaged. The single atom tip produced the best reconstruction of the theoretical (or actual) graphite lattice but did not predict the experimental results. The best reproduction of the experimental results was achieved with the model that consisted of the graphite flake (containing 50 atoms). Abraham & Batra suggested that a misregistry of the flake and the sample lattices gave rise to the unusual periodicity observed (see figure 3.9a).

Pethica [1986] suggested that the atomic resolution obtained with HOPG was due to one layer or a flake of HOPG being dragged across the surface of the other (see figure 3.9b). When the two layers are in their usual positions (a slight energy minima) the force differs from when one layer is in an interstitial position with respect to the other (a higher energy position). The spatial variation of the force matches the periodicity of the lattice and hence apparent atomic resolution is achieved.

This model also explains why 'atomic' resolution of HOPG is achievable using a very blunt pencil lead as the tip. There is no hope of achieving a

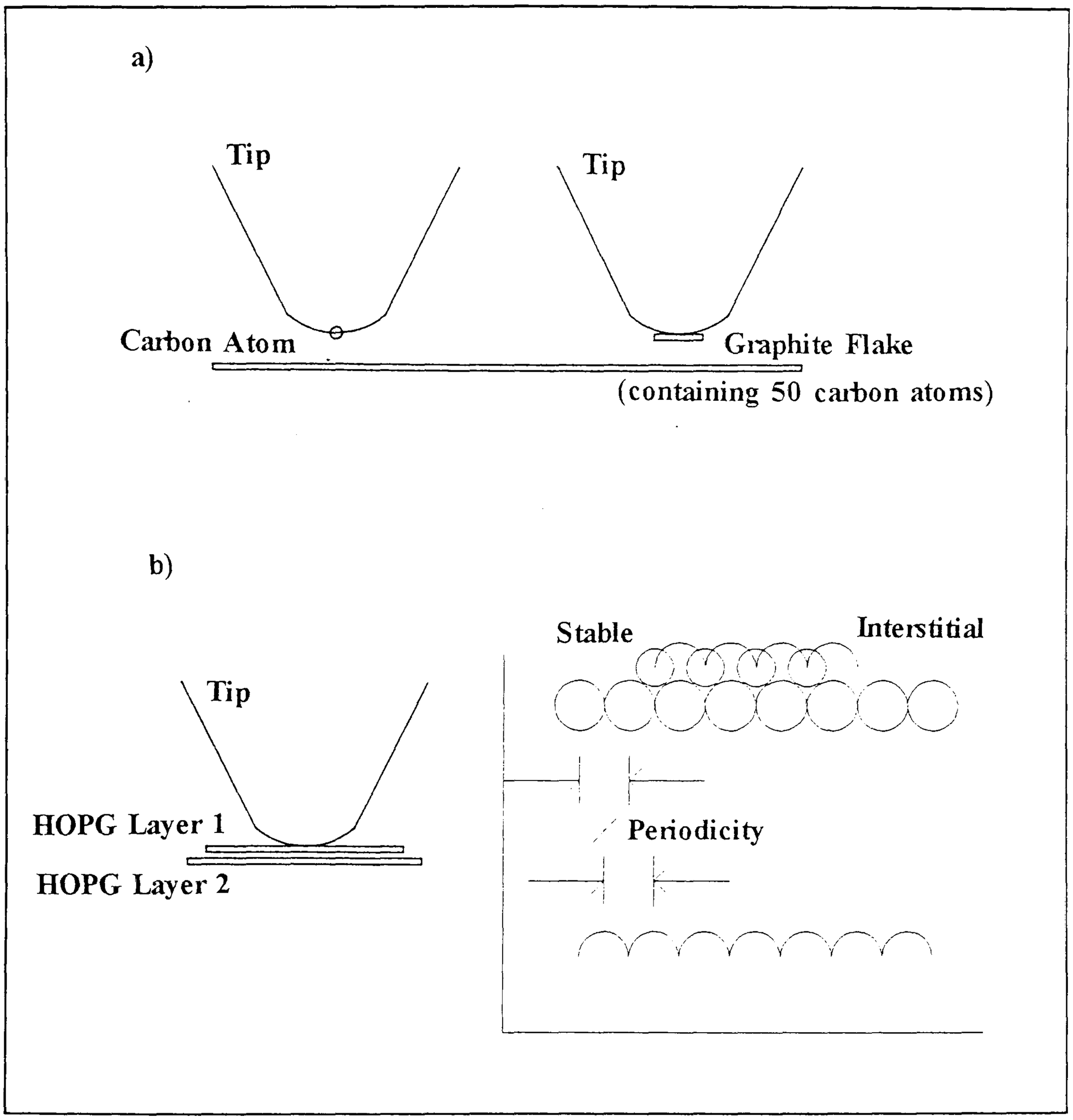

Figure 3.9: The effect of the tip imaging with a) a graphite flake was calculated by Abraham & Batra[1989]. b) A similar approach by Pethica [1986] suggests that atomic resolution on layered materials results from the matching and mismatching of adjacent layers. The periodicity of the matching is the same as the lattice parameter and can be confused with it. This approach also explains why very high 'atomic' corrugation images are obtained with almost no sample defects.

stable single atom apex to the tip, but flakes of HOPG are highly abundant, making imaging possible. The model also explains that a simple rotation in one layer with respect to the other gives the observed trigonal and hexagonal symmetry.

Slip-Stick Model

Landman at al[1989] modelled the tip interacting with a Si(111) lattice using the molecular dynamics simulation discussed above. The results indicated that as the tip was scanned laterally across the sample surface, the actual motion of the tip comprised of a series of jumps or slip-stick movements.

Landman et al suggested that the atoms within the contact area adhere to the surface (as described above) and under the action of a critical lateral force, disengage allowing movement of the tip. During the slipping stage, the tip measurably rises in the 'interstitial' position and then falls. The tip then adheres to the sample again and the process repeats itself (see figure 3.10). The slip-stick motion of the tip occurs at a periodicity determined by the characteristics of the surface and in some cases is the same as the periodicity of the lattice. In this case it is very easy to confuse the data obtained with that of the true topography.

3.4 POLYMER IMAGING

The treatments introduced so far are concerned with explaining the atomic resolution on metallic or other more ideal surfaces. There have been very few simulation studies of the interaction between an AFM tip and a polymer sample. However an excellent study by Sumpter, Getino and Noid[1992] calculate the interaction between a silicon tip and a crystalline polymer sample, as a function of tip radius and force applied. Another group (Meyers, DeKoven and Seitz[1992]) examine the tip interactions on a glassy amorphous polymer. The results of both are outlined below and suggest that the significant interactions discussed with respect to the metallic surfaces above

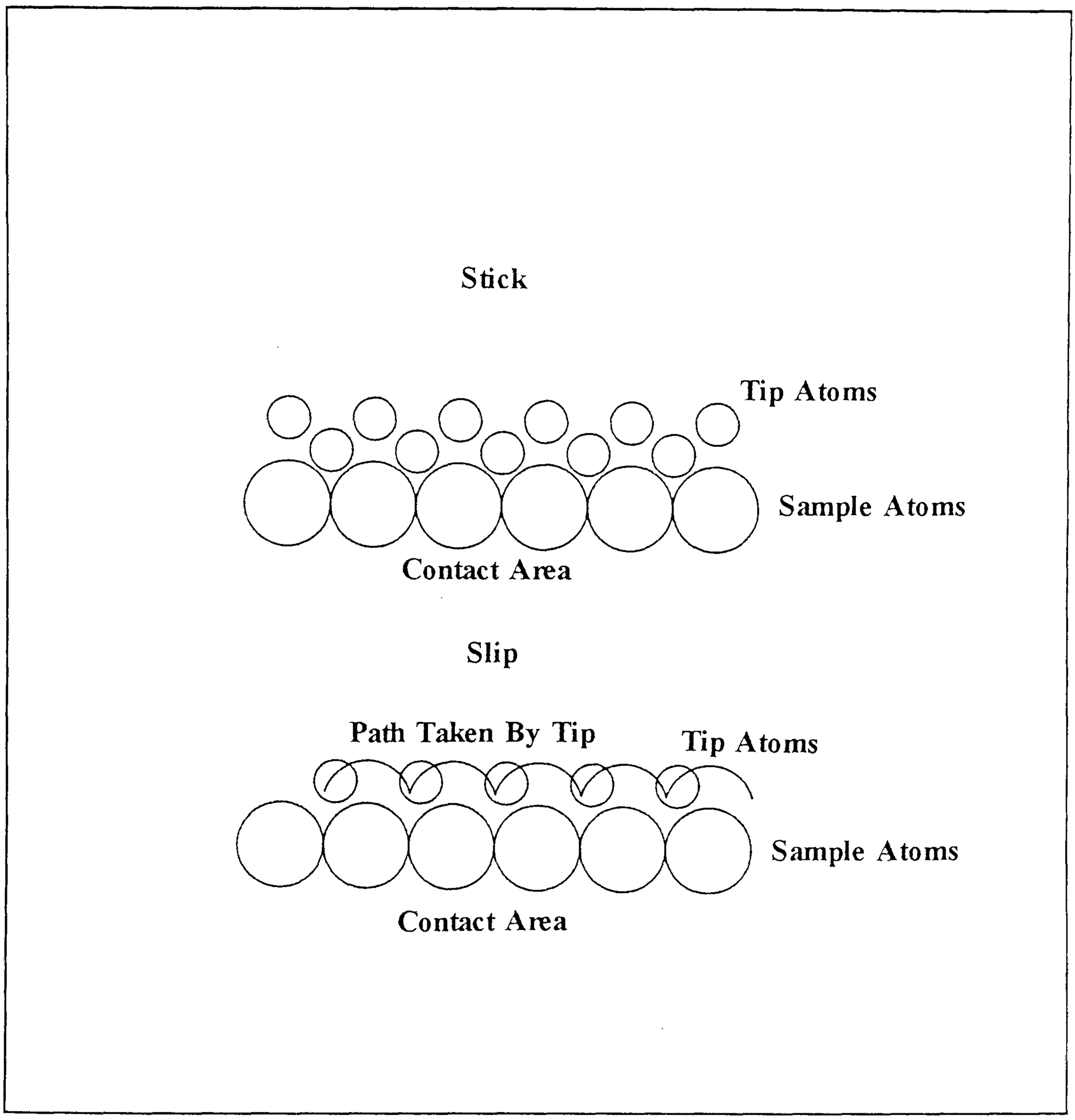

Figure 3.10: Landman [1990] calculated that the AFM tip progress as it is scanned across the sample surface would be punctuated by a 'stick-slip' movement. The tip sticks in one position and then slips suddenly to a new sticking position. The contact area is large and the sticking periodicity can again be confused with the lattice parameter.

are, also valid for polymeric samples in general. This means that there is a limit to the resolution obtainable by AFM on these materials.

AFM Tip/ Crystalline Polymer

Sumpter, Getino and Noid[1992] calculated the tip polymer interactions by the molecular-dynamics method, based on a silicon tip and a crystalline polymer. The tip used in the model contained 1650 silicon atoms. The sample used in the model was an orthorhombic polyethylene-like polymer crystal. A total of 58 polymer chains were ordered perpendicularly to the substrate and comprised of 100 CH_2 units (see figure 3.11). The interaction was calculated for applied forces in the range of $1x10^{-4}$ N to $1x10^{-13}$ N and for a range of tip radii (1nm-10nm).

The results obtained indicate that the polymer is resistant to damage at the non-contact end of the force range ($F<1x10^{-11}$ N) and even at forces more associated with the contact regime($F\approx1x10^{-8}$ N). The calculations show that the resolution suffers considerably with increasing tip radius. Sumpter et al suggest that the ideal operating conditions that result in little or no sample damage and good quality (high resolution) images are achieved when the force used is in the range 10^{-8} - 10^{-11} N.

The study also revealed that a pseudo-atomic resolution of the polymer chains was possible in samples where the chains were orientated in a direction parallel with the substrate. The AFM image reveals one in every four CH_2 (0.5nm resolution) groups along the carbon-carbon backbone. The authors speculate that to achieve greater resolution would require forces in excess of those required to damage the sample.

It should be noted that the study does not recommend the use of higher force regimes, most notably the contact mode of operation. All the calculations in this paper involve tip-sample separations greater than 0.4nm. Sumpter et al point out that it is reasonable to assume that in the contact mode of operation the sample would be subject to large deforming forces and resolution would be limited to a value much greater than the 0.5nm indicated above.

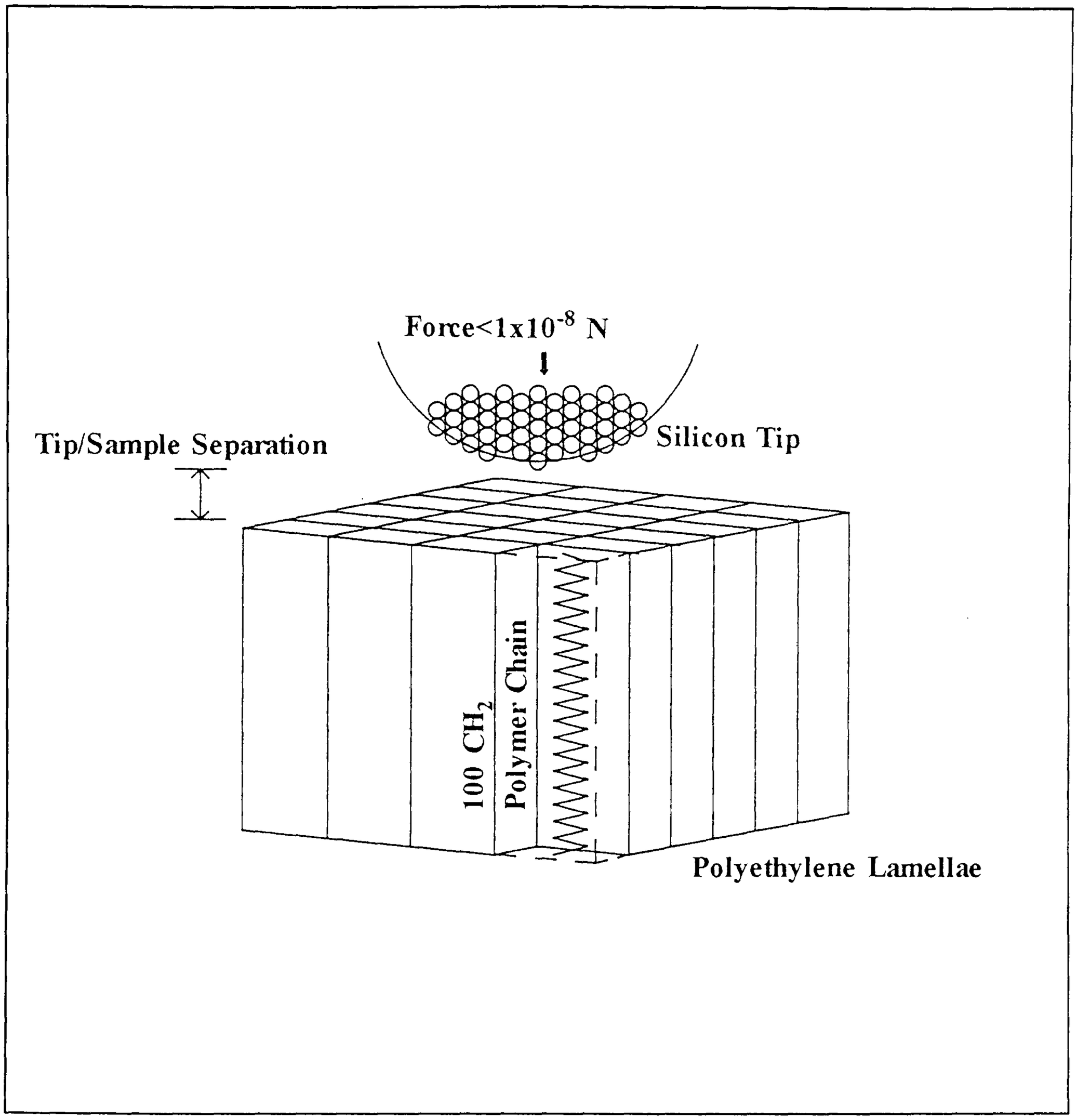

Figure 3.11: Sumpter, Getino & Noid[1992] calculated the interaction between a silicon tip and a polyethylene-like crystal by the molecular dynamics method. The tip contained 1650 silicon atoms and the polymer sample was composed of molecular chains containing 100 CH_2 sites. The calculations suggest that although the polymer is deformed, reliable images can be obtained if the force used is less than $1x10^{-8}$ N.

AFM Tip/ Amorphous Polymer

Meyers, DeKoven and Seitz[1992] examine the effect of the AFM tip scanning on a glassy polystyrene(PS) polymer. The images obtained in their study were for a scanning time of only fifteen minutes over a variety of different molecular weights. The study reveals a variety of orientation patterns produced as a direct result of tip-sample interaction, speculated by Schallamach[1971].

Meyers et al[1992] used a force of $1.5x10^{-8}$ N, in the contact mode and calculated that the tip penetrated the PS sample by as much as 1nm. The patterns produced (which are orientated perpendicularly to the tip scanning direction) are as a direct result of the large contact area and interaction between the tip and sample. As the tip passes across the polymer sample, the adhesion between the two results in a pulling of material behind the tip and a pushing of material in front of the tip. The authors suggest that taken to this limit (and if the polymer is soft enough), the polymer film could be combed into the individual polymer chains i.e. disentangled into its constituent parts.

The results of this study suggest that the surface of this polymer is not one of a hard, glassy material, but that of a rubbery surface susceptible to tip interactions. The 'combing' effect of the tip is a direct result of significant tip-sample interactions and severely effects the resolution of the AFM on this material. Further more, there is no possibility of achieving atomic resolution on this film. For the study of amorphous films in general, it should be noted that true morphological details may be obtainable for only the hardest of films (polycarbonate being one of them).

3.5 SUMMARY

The AFM is operated in two different regimes which are distinct from one another. The non-contact operation or mode, applies when the tip is several nanometres from the sample surface and attractive Lifshitz-van der Waals

forces are dominant. In this mode the tip-sample contact in minimal but the resolution is limited. The contact mode applies when the tip is moved so close to the sample surface that the electronic orbitals interact and a repulsive force is experienced. The tip-sample contact area is very much larger than was previously thought and atomic resolution is not thought to be reliably achieved on many samples. However in this mode fine surface detail can be obtained especially if the sample is relatively hard. The prospect of imaging successfully polymeric materials is good particularly if the sample is hard and glassy. Calculation by Sumpter et al suggest that better images are achieved if the tip is reasonably sharp; the force used is less then 10^{-8}N and horizontal resolution at levels less than the contact diameter (≈2nm) are not sought.

CHAPTER 4

POLYMERS

4.0 POLYMERS

Polymers are long chains of organic material composed of many repeat units. In general the chain consists of many carbon atoms or groups forming a backbone with pendant side groups. The variety of different chemical groups available is such that a wide range of polymers can be manufactured with an equally wide spectrum of mechanical, electrical and chemical properties. In general one associates polymers with plastics, moulded to perform a number of different tasks. However polymers are being increasingly used in situations diverse as medicinal drug transport agents and in sensor technology.

The suitability of a polymer to a particular task can depend on the morphology of the material. A riot shield must be very strong and transparent, a requirement fulfilled by partially amorphous polycarbonate(PC). However the same polymer in an advanced stage of crystallinity (as a result of contact with petrol or other solvents) becomes significantly weaker and unsuitable for the task in hand.

This chapter discusses the different morphological conformations adopted by polymer chains with a view to further assessment by scanning probe microscopy. For example, the solvent induced crystallization of polycarbonate (see riot shield example above) involves the gradual and precise ordering of PC chains, from an amorphous to a crystalline structure. This process is discussed below.

4.1 POLYMER TACTICITY

Depending on the polymer chain tacticity (see figure 4.1), the solid polymer may have a variety of structures ranging from purely amorphous to almost totally crystalline. The former solid contains chains which lie randomly throughout its volume and is the typical conformation found with polymers containing atactic or randomly positioned side groups where there is little or no chance of neat, side by side packing. The crystalline polymeric material forms from polymers with chains which are either syndiotactic i.e regularly

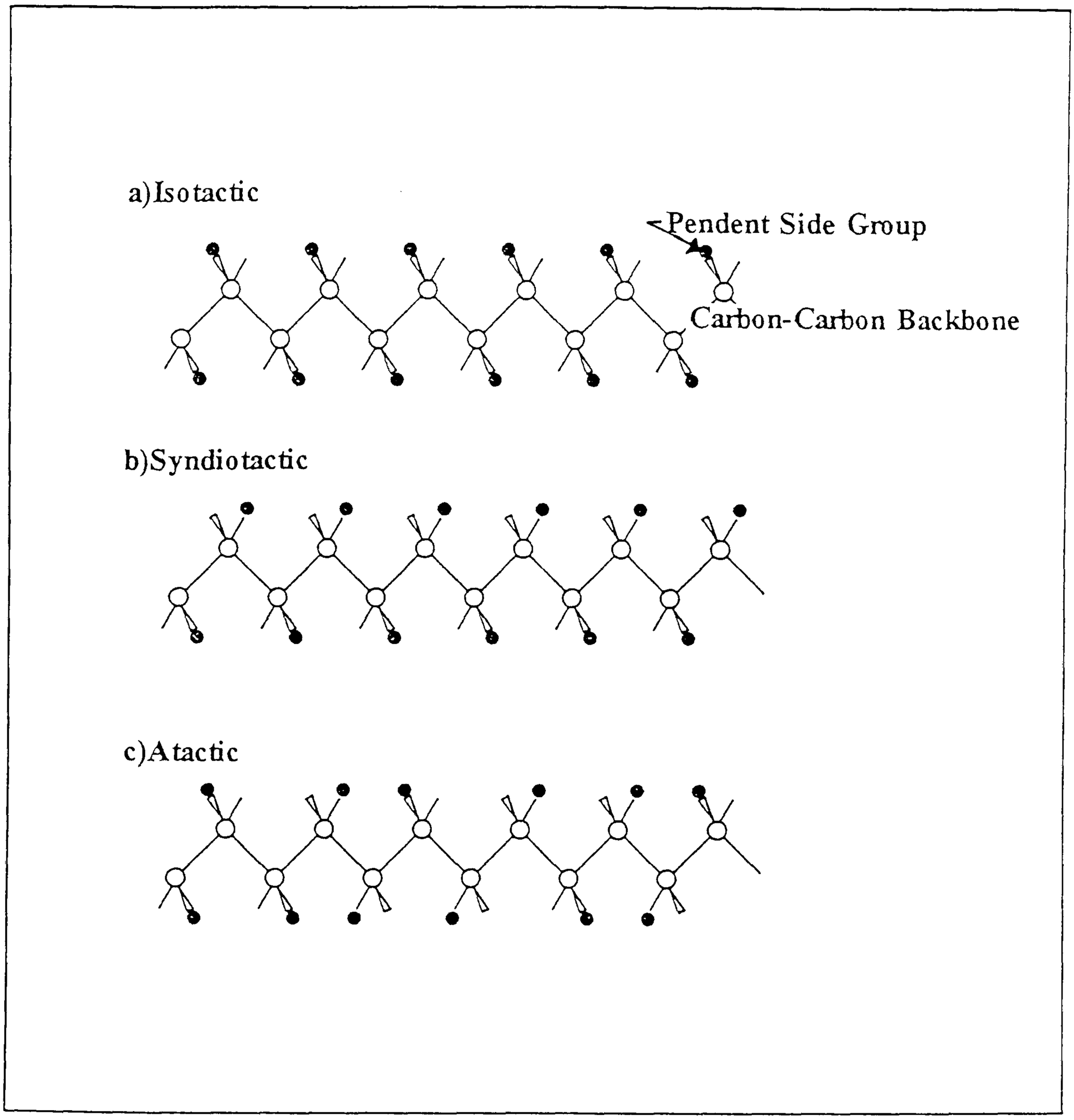

Figure 4.1: Polymer notation as regards the position of pendant side groups. a)Isotactic chains have pendent groups on one side of the chain only. b) Syndiotactic chains have pendent groups distributed in a regular pattern along their length. c) Atactic chains have pendent groups randomly distributed along their length.

positioned side groups or isotactic i.e. side group with only one spatial position. The crystalline polymer contains chains which can align in neat tightly packed regions which are highly ordered.

The primary aim of this thesis is to determine the morphology of three thin polymer films. Although the polymers under investigation in this study exhibit a large range of morphological features, it is possible to categorise them in terms of their state of order. The films of PMMA and PVP are expected to be amorphous whereas, with suitable treatment, the films of PC may be crystallized.

4.2 AMORPHOUS POLYMER STRUCTURE

Amorphous polymer films contain polymer chains that lie randomly in the film. If the temperature of the film is increased the rotation and bending of the lowest energy polymer chain components e.g. pendent side groups begins. At this stage there is no appreciable change in structure or physical properties.

With a further increase in energy supplied to the film (i.e. increase in temperature), other larger components of the polymer and eventually those bonds that hold the backbone together start to move. The molecular stiffness of the film components decreases and this results in the film becoming progressively more rubbery. The temperature at which the polymer experiences a transition from the glassy state to a rubbery one, is termed the glass transition temperature (T_g).

Eventually if the polymer chains acquire enough energy to start moving away from their neighbours, the film becomes molten. The transition temperature at which the rubbery phase becomes liquid is termed the melting temperature (T_m).

The transitions mark important physical and structural changes within the film and an example of the physical change can be observed in figure 4.2 which demonstrates the changes in tensile modulus of a polymer film as a function of temperature.

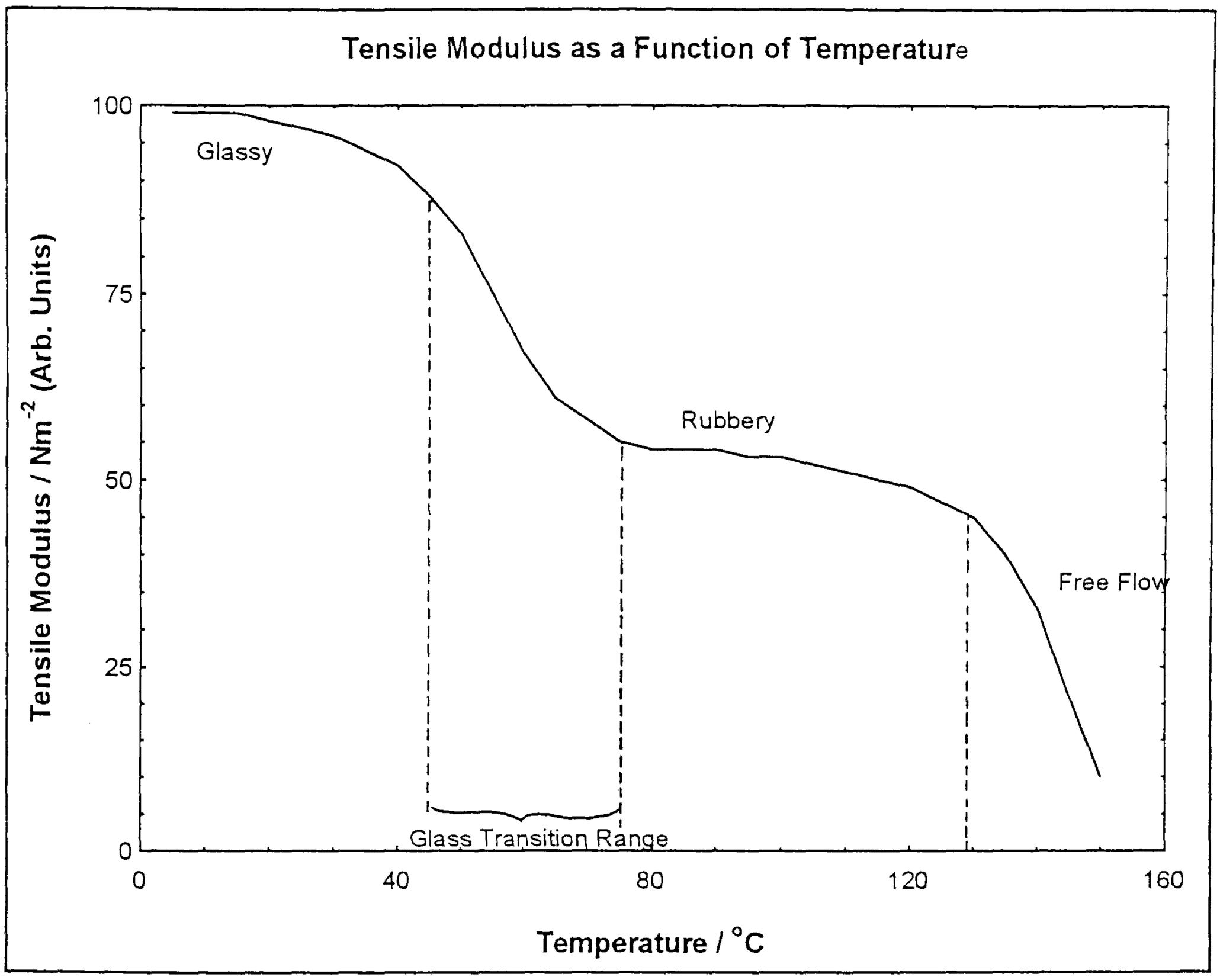

Figure 4.2: The amorphous polymer film consists of randomly entangled chains. As the temperature of the polymer increases the film goes through stages of physical change, demonstrated here by changes in tensile modulus. Starting with molecular rotations and going through a stage of main chain movement (although not free motion)at the glass transition temperature Tg. Eventually at Tm, the chains have enough energy to move freely.

The energy required to mobilize the polymer components depends on the composition, size and spatial distribution of the components. Because every polymer is compositionally unique, it is not surprising to find that each polymer has its own values of T_g and T_m. The wide range of values of transition temperatures accounts for the very diverse uses for polymer films. For example a polymer used as a rubber seal must exist in the rubbery phase at the operating temperature. If the value of T_g is too high, the plastic becomes glassy and is liable to shatter. This example was unfortunately demonstrated in the 1986 Challenger Space Shuttle disaster. In this case, a seal used in the booster rockets although rubbery at room temperature fell below T_g in the presence of the liquid fuel propellant. The seal subsequently shattered, the fuel ignited and the shuttle was destroyed.

4.2.1 Amorphous Polymer Films at Room Temperature

Amorphous polymers such as PMMA and PVP used in this study are atactic (see figure 4.1). The absence of regularity prevents the ordering of the polymer chains under almost any condition. Films formed from these polymers are never expected to crystallize and the physics of these materials is similar to that of glasses and rubbers.

The evaporation of the solvent from the polymer solution (in which the polymer chains may be extended and considered floating freely in the solvent) will leave the polymer chains confined to the plane of the substrate. The polymer is expected to form a glass (if room temperature is less than T_g)consisting of a random mass of interwoven, intermingled, tangled chains. Although there may be glide planes along which the chains may move under stress, there remains an absence of boundaries and discontinuities that characterize most other non-liquids.

Indeed the strength of organic polymer glasses (including the non-crystalline form of bisphenol-A-polycarbonate) is of industrial importance particularly because it can exceed that found in inorganic glasses. An example of this is in the commercially available 'unbreakable glass' which is made

from polycarbonate and is as strong as glass. The 'unbreakable' property has been attributed to slight plastic deformation within the polymer film, achieved by relaxation of the chains (Lee[1989]).

There is a remote possibility that even the amorphous polymer may form small approximately nanometre sized, ordered regions in which the chains are approximately parallel[Mills, 1986]. The occurrence of these aligned regions is more likely and easily measured in polymers where the packing of chains is energetically very favourable for example in PC. However the formation of similar regions in PMMA and PVP, perhaps due to stresses in the film or some unknown nucleating process cannot be ruled out.

However to date there has been no reliable optical or electron microscope evidence for the existence of ordered material in films composed of atactic polymer chains. The predicament may be due in part to the failure of the measuring device for example from sample degradation under electron microscopy operating conditions and sample preparation. However, if ordering is achieved, it may be possible to resolve these entities using Scanning Probe Microscopy (SPM)

4.3 POLYMER CRYSTALLIZATION

Polymers may crystallize if an energetically favourable conformation of tightly packed, neatly aligned chains can be achieved (see figure 4.3). This situation is only likely to arise with those polymers with a regular structural conformation such as isotactic polymers, linear polymers with little in the way of side groups or syndiotactic polymers (which may twist to form helices, before inclusion into the crystalline form).

The temperature range between T_g and T_m of crystallisable polymer represents an important and exploitable window in which crystallization experiments may be initiated. It is within this temperature range that the polymer chains may overcome the potential energy barrier for crystalline development and reorganize in a more orderly semi-crystalline state over a time scale dependent on factors such as viscosity.

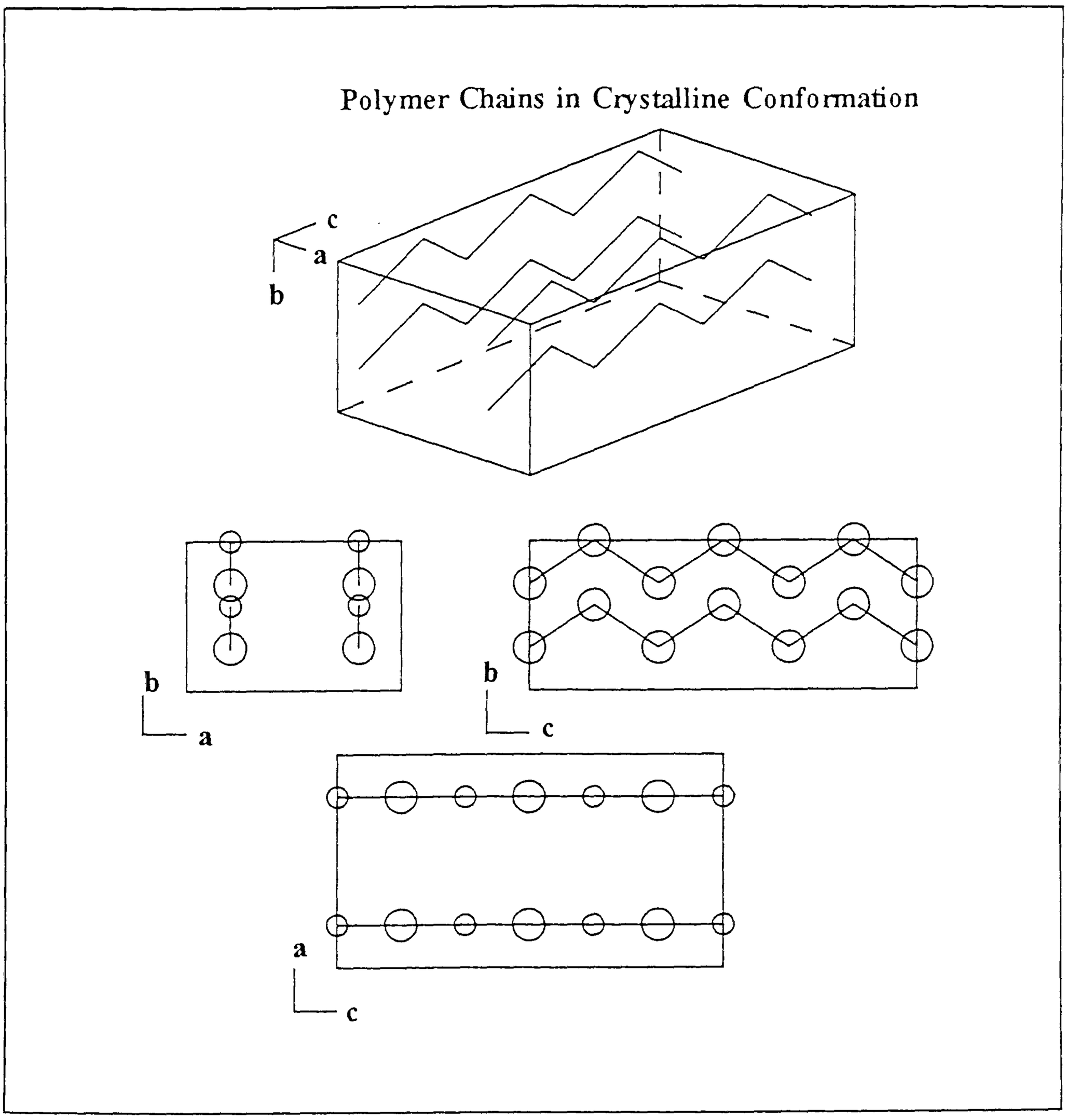

Figure 4.3: Some polymers (which are usually symmetrical) have a morphology that enables the constituent chains to fit together in a close packed ordered, crystalline way complete with a unit cell. The unit cell may be repeated throughout the crystalline material and has dimensions denoted by a,b, and c.

4.4 TYPICAL CRYSTALLINE STRUCTURES

If a polymer has an energetically favourable crystalline conformation that it can adopt it is not apparent from microscopic techniques how this process is actually achieved. A particular polymer in a crystalline state (as determined by x-ray diffraction techniques) does not reveal the single crystal development associated with low molecular weight materials (for example $CuSO_4$) when observed by optical or electron microscopy. Instead a wealth of complicated, hierarchial structures, seemingly unrelated to the expected unit cell reproduction is observed.

The range of structures found is large and current research has yet fully to explain their origin or composition in terms of more primitive structures, including the unit cell. One of the most simple of polymer crystalline structure is found in materials such as polyethylene(PE) and polyetheleneoxide(PEO). For these polymers, crystallization from a very dilute solution (in the same way as low molecular weight inorganic materials), results in the formation of a single crystal (see figure 4.4). The crystal formed for example from PE, is lozenge shaped and contains molecules orientated perpendicularly to the plane of the substrate (i.e. across the thickness of the crystal). The crystal (which is known as a lamellae sheet) has a uniform thickness which is considerably less than the PE chain length and the formation of which can only occur if there is folding of the constituent chains [Keller, 1957].

The mechanism for chain folding is not well understood but it is thought that the chains are incorporated into the growing crystal and may fold into adjacent sites (see figure 4.5) or into distant sites as envisaged in the 'switchboard' mechanism. A recent review by Buckley and Kovaks[1984] suggests that the growth mechanism for PEO proceeds by a kinetic approach concerning the growth of the crystal from a secondary nucleation process at the 'active' surface. Here the growth occurs in the plane of the crystal where its thickness is always an integer fraction of the chain length (see figure 4.4).

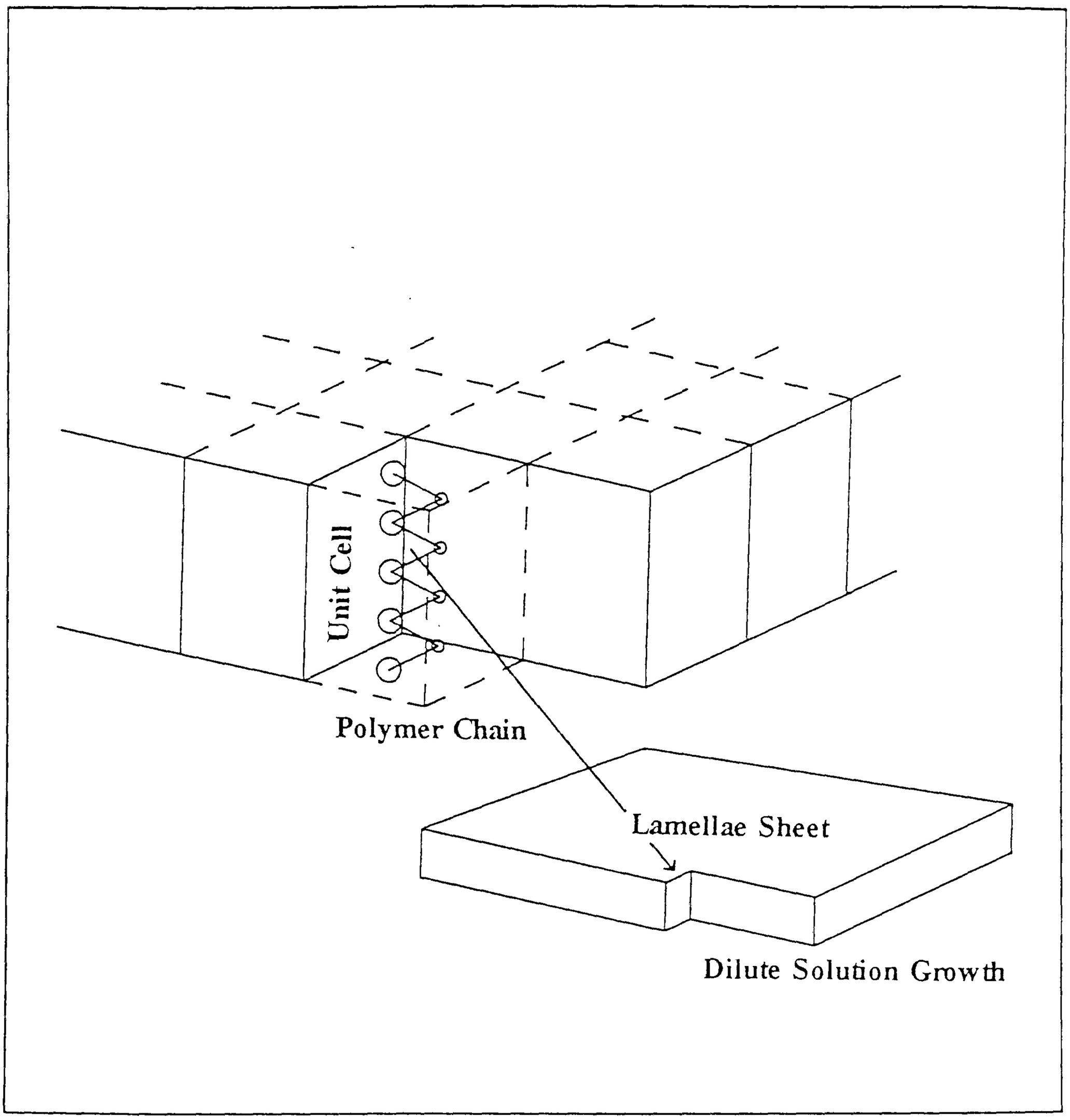

Figure 4.4: Some polymers, for example polyethene are crystallized from a dilute solution. The resultant crystalline formation is extensive and comprising of crystal unit cells. A single crystal microns in size may be produced by this method and is known as a lamellae sheet.

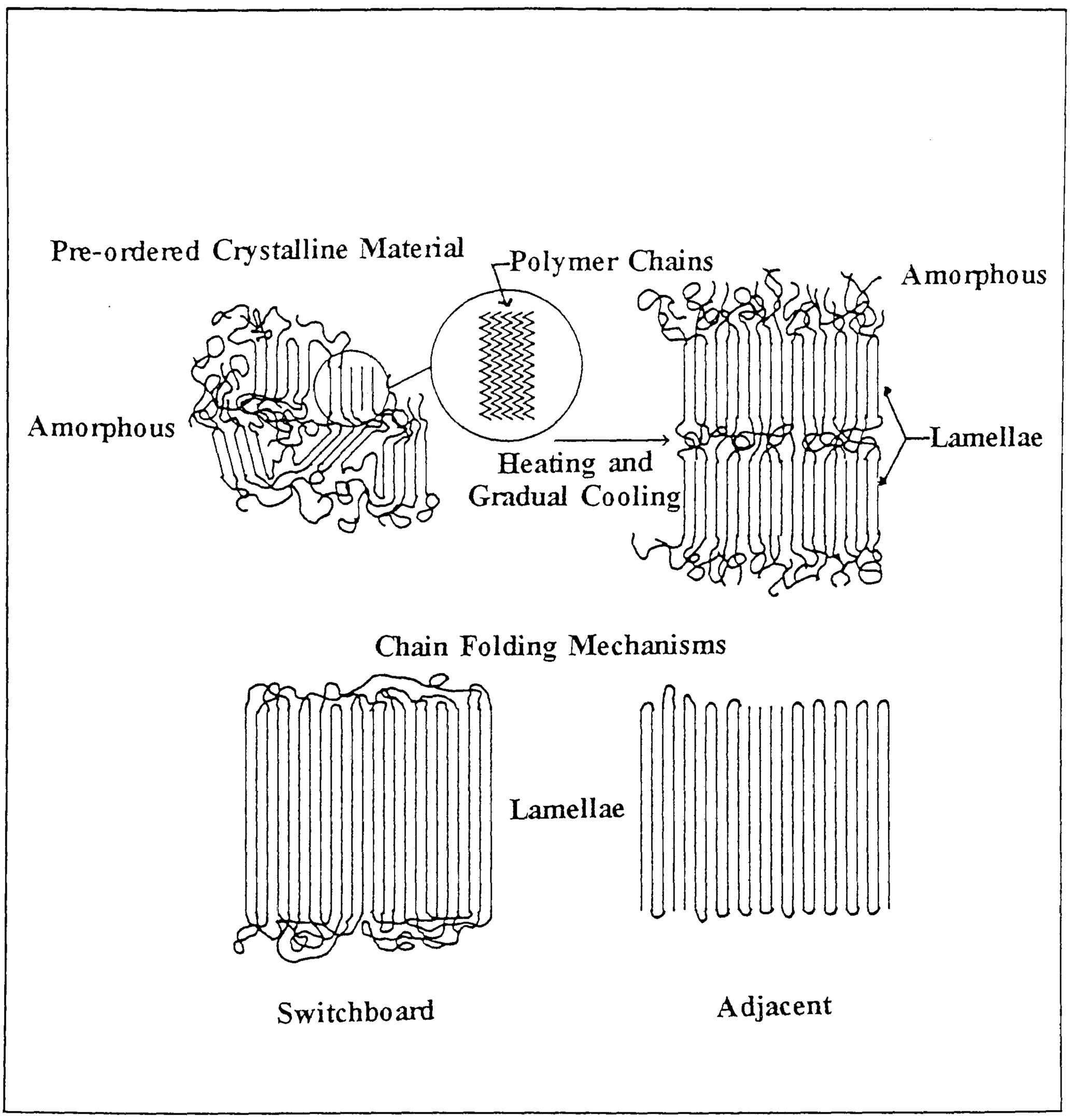

Figure 4.5: Many polymers if supercooled, may form crystalline features from the melt. The polymer may crystallize and the film as a whole can be over 80% crystalline. However the crystalline development is not of 'single crystal' in appearence (i.e. the structure of the unit cell is not manifest on the macroscopic level) The chains may fold and bend in either a a switchboard fashion or in a regular adjacent folding. These folded areas form the basis of fibrils and spherulites.

4.4.1 Initial Fibril and Rod Formation

As the concentration of the solution is increased, the single crystal formation is disrupted by the formation of multiple single crystal layers. The formation of multiple layers of lamellae sheets (crystal planes) separated by the non-growing crystal surface which contains the loops and ends of the polymer chains (or amorphous material) results in the formation of three dimensional rods and plates. The growth of the sheets especially in one particular direction results in the formation of primitive fibrils.

Until this point, only materials crystallized from solution have been considered. This represents a special case as the predominant mode of crystallization in polymers is achieved from the solidifying of the mobile phase or melt crystallization. Indeed most polymers including polycarbonate can only be crystallized in this way. The 'melt' crystallization method is used in almost all industrial applications where crystalline polymer films are required.

The morphological differences between the solution grown single crystals and those grown from the melt are large. In the latter no neatly ordered regions are observed even though x-ray data suggests the majority of the film should be crystallized. The films contain spheres of branching and twisting fibrils. The link between the ideal single crystals and the melt crystallized entities has become more clear as further research into the structure of the fibrils is completed. The fibrils formed in general from any crystallization technique have common features which include polymer chain folding into lamellae sheets i.e. folding in a plane perpendicular to the growth direction and with a precise thickness.

4.4.2 Fibrils

In both methods i.e. crystallization from dilute solutions and from the melt, the lamellae sheets are packed together to form fibrils but in the melt crystallization case their growth is frequently interrupted by impurities and tangled amorphous regions. At each interruption the lamellae growth either

branches or is inhibited, giving the fibril a filamentous appearance (see figure 4.6). If the growth of the fibril is very rapid and in the absence of impurities, the lamellae sheets may extend over hundreds of nanometres without branching and appear as a radial spoke from the original central nucleating point.

4.4.3 Spherulites

The polymer fibrils which are formed from the lamellae sheets, grow from the initial nucleation site by absorbing amorphous material at the 'active' face of the sheet. At each imperfection or non-crystallizable amorphous clump, the fibre branches. The ultimate structural result of the branching, twisting growth of many fibrils growing from a single nucleation site is, given a three dimensional amorphous phase, a sphere of semicrystalline material which is called a spherulite. An accepted model of the spherulite structure is shown in figure 4.7.

Separated nucleation sites in the polymer result in spherulites growing until they impinge on each other forming polyhedral semicrystalline entities. The larger the number of nucleation sites the greater the abundance of spherulites and the smaller their ultimate size.

The usual method for observing the structure of spherulites is to grow them in two dimensions in the form of a thin film, sandwiched between glass cover slips or to take a cross section through a thick layer of crystallized polymer. Optical and electron microscopy images reveal the fibrillar structure of the spherulite. The polymer chains are orientated perpendicular to the fibril axis or spherulite radius and this results in a refractive index slightly different to that found in the direction of the fibril growth. This birefringence may be observed (under optical conditions and under polarized light) as a maltese cross pattern.

The structure and growth of the spherulites in particular the conformation of the fibrils is of great importance to polymer physics and under the appropriate growth conditions these entities may be observed using SPM.

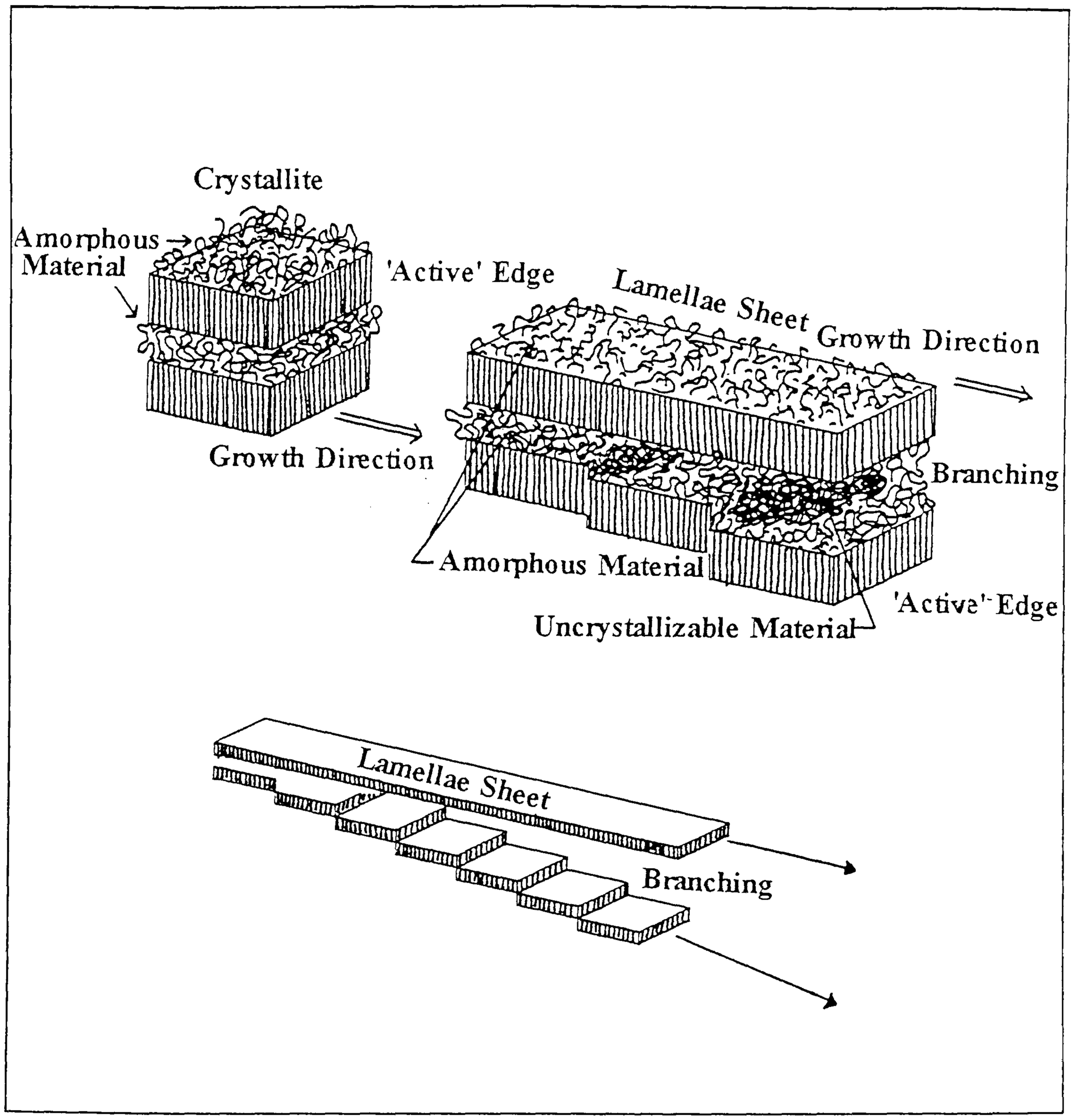

Figure 4.6: The folded, lamellae sheets contiue to grow from the 'active' edges (where amorphous material can align with folded crystalline chains. Where impurities or highly tangled regions, or even obscurely orientated crystallites are absorbed during the growing process, the lamellae sheet branches and twists.

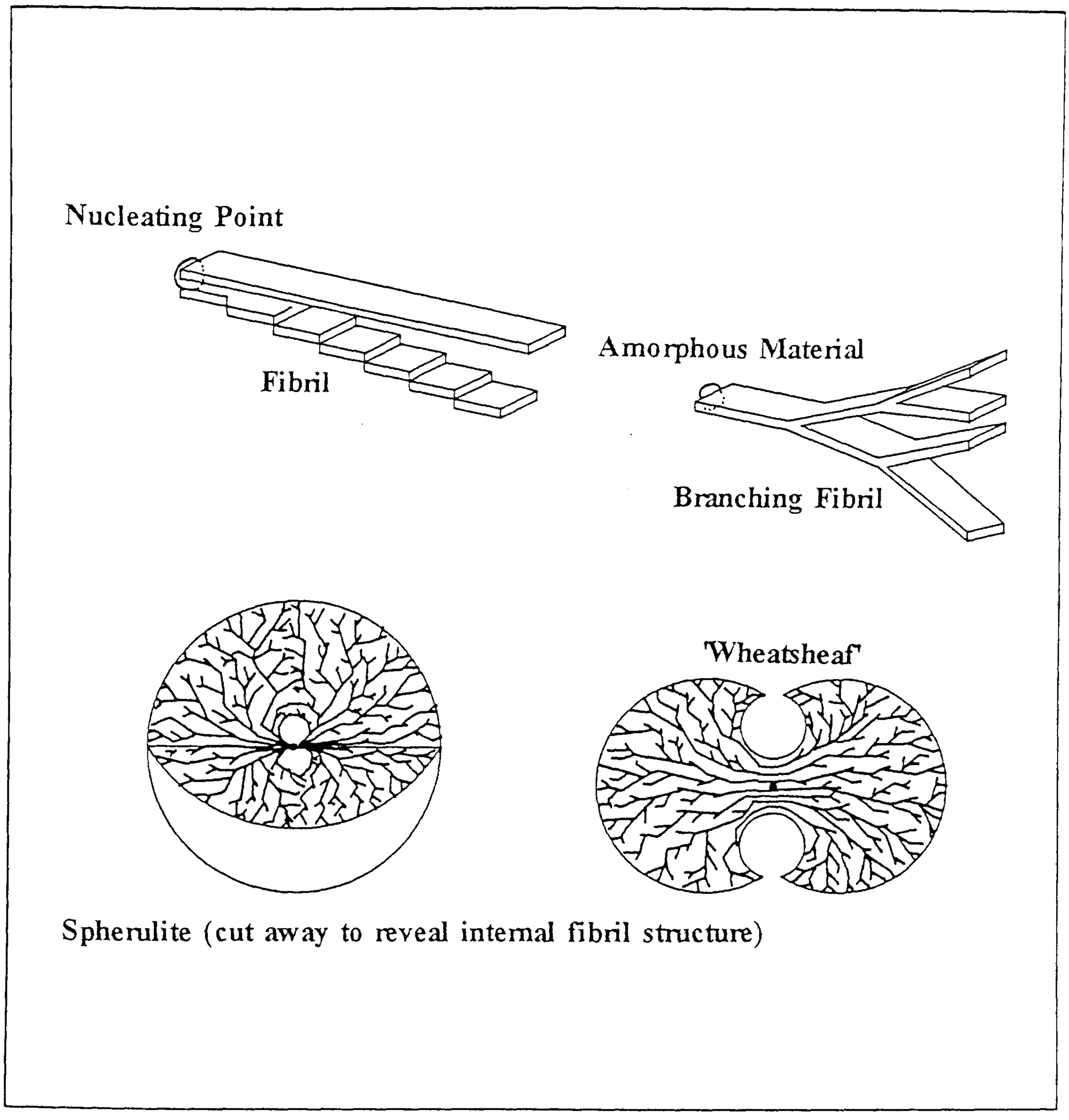

Figure 4.7: As a result of the fibrils growing and branching from a central nucleating point, a 'wheatsheaf' and finally a spherical entity known as a spherulite is formed.

4.5 KINETICS OF SPHERULITIC GROWTH

In a variety of previous works [Okada et al, 1992; Heberer et al, 1991 and Lee et al, 1993] a relationship between the overall crystallization kinetics and the crystal morphology has been established through the Avrami exponent 'n'. Exact mathematical solutions have been produced for one dimensional crystallization (linear growth features), two dimensional growth (forming a disc) and three dimensional spherulitic growth. It is usual and prudent to use the analysis in the early stages of growth, where the spherulites may be sufficiently separated to avoid impingement. In this domain the kinetics of growth are relatively simple.

It is reasonable to assume that the radius (r) of the spherulite is proportional to the time (t) since growth was initiated and the two are related by a growth constant G. If the appearance of nucleation sites (number η) is related to time (t) in a similar way, by nucleation constant N, then two equations may be given as:

$$r = Gt$$

$$\eta = Nt$$

Given a three dimensional amorphous polymer matrix (weight W_o)at time t=0, and that after time t=t there is weight W_s of converted crystalline polymer, then the Avrami model relates the fraction of crystalline material to film weight to the density of the amorphous phase and crystalline phases (ρ_a and ρ_c respectively - although ρ_c may not necessarily remain constant) and the time, t by :

$$\frac{W_s}{W_0} = \frac{\pi N G^3 \rho_c t^4}{3\rho_a}$$

The morphology of the film and the nucleation processes involved influence the power of t in the Avrami model above which describes the rate of crystallization within the film. If the crystallization process is carried out in a very thin film with nucleation sites becoming available as a linear function

of time (i.e. sporadic nucleation), it is found that $W_s/W_o \alpha t^3$. The spherulites produced in this case are found to be disk like. However if there are instantaneous nucleation sites instead of sporadic ones, W_s/W_o is found to be proportional to t^2 .

It is convenient to use the Avrami exponent, n where $W_s/W_o \alpha t^n$. 'n' can be split into two components c and d (where n=c+d) and represent the nucleating process and dimension respectively. The dimensional component, d is the number of dimensions in which the spherulite is allowed to grow and the nucleating component, c is either 1 or 0, depending on whether the nucleation process varies as a function of time. As an example, in the case above where the film is confined to two dimensions (d=2) and where sporadic nucleation sites are utilized (c=1), thus n=3 if sporadic nucleation sites exist and n=2 if only instantaneous sites exist. Table 4.1 (figure 4.8) below gives the Avrami exponent and the equivalent morphological development.

In the past, dilatometric measurements of the density of polymer as a function of time during crystallization were the best way of determining data on the polymer crystallization; however SPM which may measure volumes, changes of volumes and rates of growth may accomplish the same task, in situ, whilst imaging the morphology of the polymer.

4.6 NUCLEATION IN POLYMERS.

Nucleation in crystallizing polymer films is considered to occur by either homogeneous or heterogeneous nucleation (see figure 4.9). Although the two processes may, given the right conditions happen simultaneously, it is thought [Sharples, 1966] that for a given polymer system, one process dominates.

4.6.1 Homogeneous Nucleation

During the casting of polymer films, there may be clumps of chains or semi-crystalline regions located within the randomly distributed polymer chains

Avrami Exponent n = (d+c)	d	c	Morphological Equivalent
4	3	1	Spherulitic growth from sporadic nuclei.
3	3	0	Spherulitic growth from instantaneous nuclei.
3	2	1	Disc-like growth from sporadic nuclei.
2	2	0	Disc-like growth from instantaneous nuclei.
2	1	1	Rod-like growth from sporadic nuclei.
1	1	0	Rod like growth from instantaneous nuclei.

Table 4.1: A table to show the morphological observation of polymer structure for given values of the Avrami exponent.
After Sharples [1968].

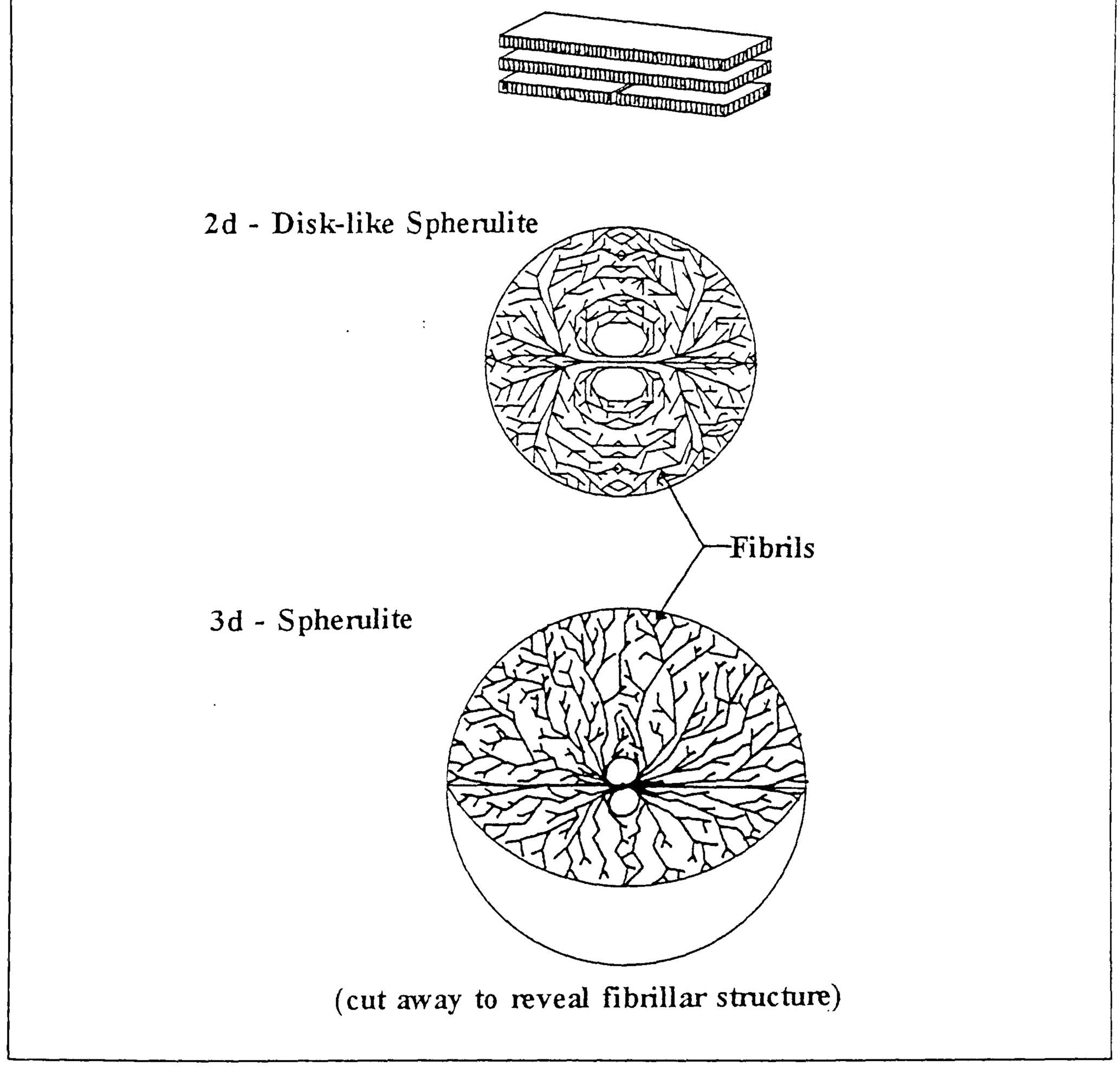

Figure 4.8: The hierachy associated with spherulitic growth as identified by Avrami. a)In one dimension, rod-like growth occurs. b)In two dimensions disk-like growth emerges. c)In three dimensions spherulitic growth is encountered.

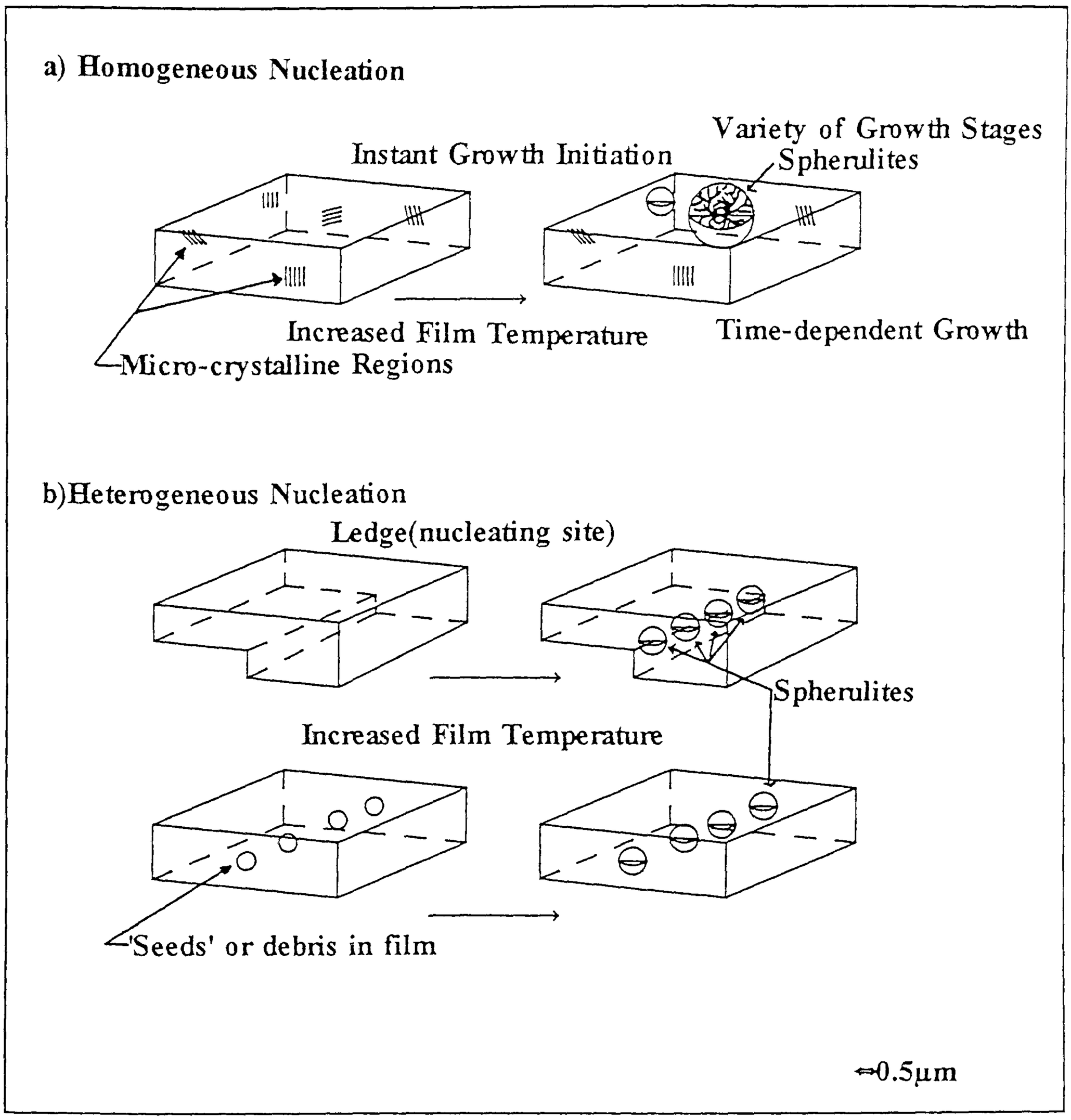

Figure 4.9: There are two methods of nucleation, and these are based on homogeneous and heterogeneous processes. The former (a), relies on nucleation relies on pre-ordered material within the polymer. The latter (b) relies on surface roughness and asperities, and also on debris and other species within the polymer matrix.

of the amorphous glassy phase. These entities may not have gained the structural significance of the spherulites or even polymer fibrils, but may still act as nucleation sites when the surrounding chains have sufficient mobility to adopt the crystalline structure. The location of the homogeneous nucleation sites is expected to be random and to increase linearly as a function of time at a constant temperature.

4.6.2 Heterogeneous Nucleation

Nucleation which does not involve the random aggregation of polymer chains is known as heterogeneous nucleation and covers a very wide range of nucleating sources. The possible entities responsible for this type of nucleation may include impurities randomly distributed within the amorphous phase or impurities on any surface in direct contact with the polymer. There may be no need for impurities if the surface/polymer interface contains ledges, crevices or other features capable of trapping the polymer. This latter case has important implications for any SPM study: In such a study the substrate used for sample deposition may possess grains and ledges suitable as sites for heterogeneous nucleation.

Once the crystallization process is under way, in general, it is assumed that all the heterogeneous nucleation sites are utilized instantly. Pursuing this logic results in the situation where crystalline structures formed at these sites will be approximately the same size. However it is possible that not all heterogeneous sites become available instantly and only a study of nucleation as a function of time at a given set temperature will enable heterogeneous and homogeneous nucleation to be differentiated.

4.6.3 The Cormia, Price and Turnbull Experiment.

In order to gauge which of the aforementioned processes dominates in a given polymer system, it is necessary to eliminate or minmize one of the processes. For example if all of the heterogeneities within a system are

removed and yet the final spherulite size and crystalline weight is similar to that found in the bulk, then it can be assumed that homogeneous nucleation is dominant. This type of approach was adopted by Cormia, Price and Turnbull [1962] (see figure 4.10).

This group allowed tiny droplets of molten polymer (PE) to be suspended in a heated medium at a temperature normally associated with extensive crystallization in the bulk polymer. On close inspection only a few had crystallized. On lowering the temperature to a point where the polymer was super-cooled (where homogeneous nucleation is dominant), a rapid increase in crystallization was observed. Thus those droplets containing heterogeneities, crystallized almost immediately without homogeneous nucleation.

It was inferred that for the bulk polymer system, heterogeneous nucleation was the dominant process.

4.7 POLYCARBONATES

Bis-phenol-A-polycarbonate [Makrolon 3000, molecular weight 30k approximately.] is a polymer which will crystallize when cooled slowly from the melt or cast from solution in a slowly evaporating solvent and will adopt the crystal structure shown in figure 4.11 as determined by X-ray diffraction techniques [Schnell, 1968].

When solidified quickly or cast from a solution of a quickly evaporating solvent an 'amorphous' film is observed. However on closer inspection and using X-ray techniques, as much as 40% of the amorphous PC film was found to be in a crystalline state [Schnell, 1968]. The data suggests that the film was likely to contain many regions of ordered material each so small (i.e. with dimensions less than the wavelength of visible light) that the film appeared amorphous [Schnell, 1964; Prietzschk, 1958]. However, the X-ray technique used was only able to achieve an average characterization of the surface, no micro-crystalline regions were found when these films were imaged by TEM or SEM.

The use of the SPM for micro-crystalline identification in PC films is

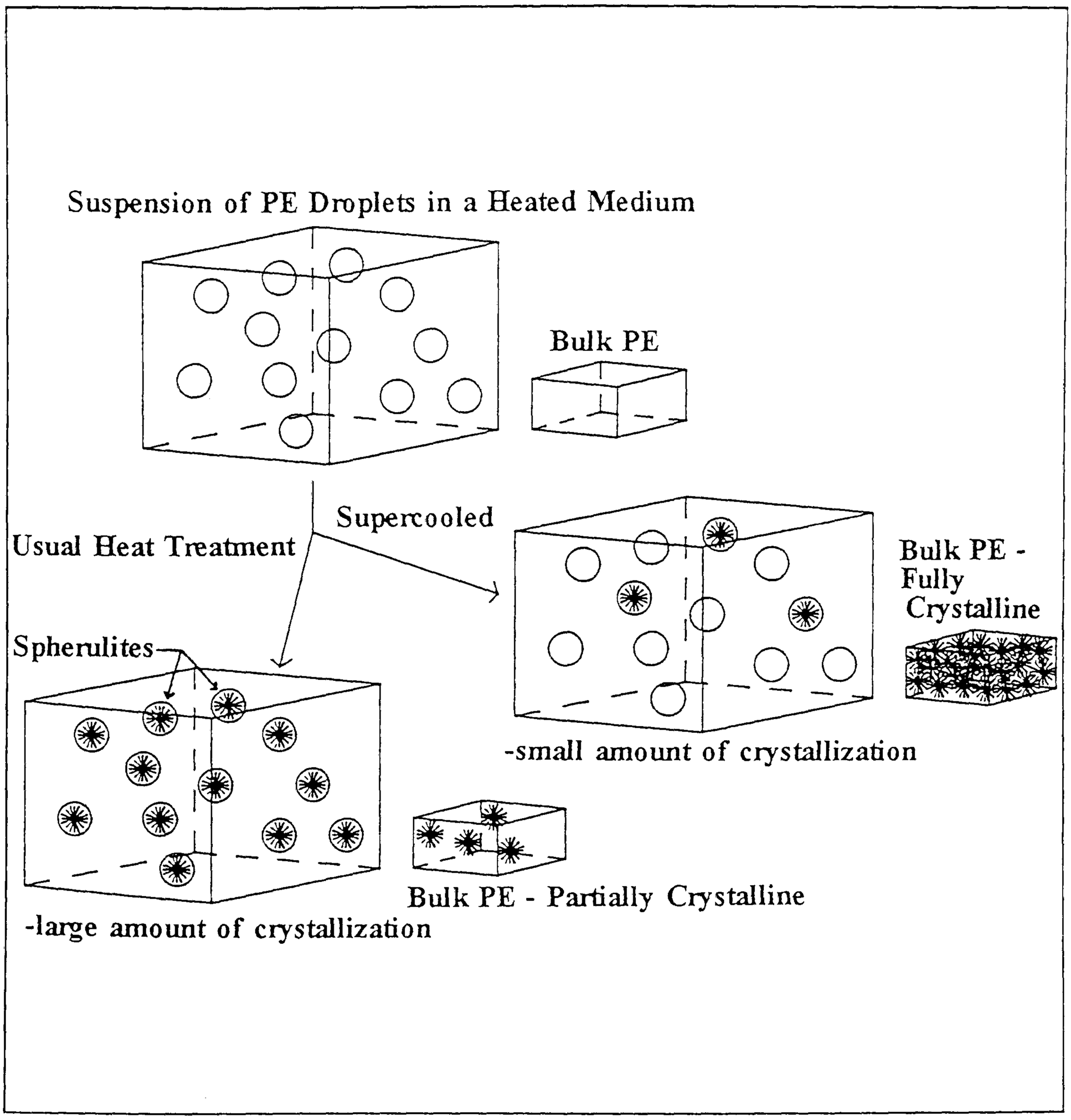

Figure 4.10: The Cormia, Price & Turnbull Experiment involves changing the temperature of a suspension of tiny PE droplets. At the ideal crystallization temperature (for the bulk polymer) only a small number of droplets developed any ordering. However when the polymer was supercooled, to a level associated with homogeneous nucleation, many of the droplets did crystallize.

attempted in this study. The SPM family offers the one of the best methods available for the detailed topographical study of material surfaces.

4.7.1 Melt Crystallization

Amorphous PC films may be heat treated in the same way as many other crystallisable polymers, to a point somewhere above the glass transition temperature of 151°C. The polymer is then observed to crystallize [Magonov and Cantow 1991 and 1992] albeit slowly to form the typical crystalline features including spherulites. However, there are a number of problems associated with the melt crystallization of PC which renders the SPM study of such a system very difficult and industrially unproductive. These problems are outlined below.

Firstly in the presence of atmospheric oxygen, and when when the temperature is held between T_g and T_m, the PC films readily degrade. Secondly, given ideal experimental conditions, the process is very slow. One study found only 18%-28% crystallinity in the PC film even after 10 days [Turska et al, 1968].

The reason why PC is so difficult to crystallize in the traditional way is because of the awkward position of the side groups. The polymer back bone is kinked and the resulting viscosity is very high. Even at a temperature above T_m, the viscosity prevents rapid movement of the chains.

4.7.2 Solvent Induced Crystallinity in Polycarbonates

For crystallization to occur, the viscosity must be reduced and the mobility and rotation of key parts of the polymer chain must be increased (effectively lowering the glass transition temperature). Williams, Landel and Ferry[1955] considered the glass transition in terms of fractional free volume (or viscosity). They showed that at T_g , all polymers have the same fractional free volume which increased linearly as a function of temperature above T_g. Later workers such as Cohen and Turnbull [1959, 1961] noted that adding a solvent (or plasticizer) increased the free volume of the polymer/solvent

system. The free volume in this context permitted the polymer chains a freedom of movement more associated with the molten polymer. In this situation, the T_g has been effectively reduced.

Studies specifically on Polycarbonate by Conix and Jeurissen[1965] and Onu, Legras and Mercier[1976] use the following equation to describe the suppression effect of the plasticizer on the T_g as:

$$T_{gps} \alpha k \frac{w_p T_{gp} + w_s T_{gs}}{w_p + w_s}$$

Where T_{gps} is the glass transition temperature of the polymer-solvent system (T_{gp} and T_{gs} are the transition temperatures for the polymer and solvent respectively), w_p is the weight fraction of polymer and w_s is the weight fraction of solvent. The value k is related to the difference in expansion coefficients(in a glassy and molten state) of both the polymer and solvent. Using this method, Kambour, Karasz and Deane[1966] calculated that acetone could depress T_{gp} for polycarbonate from 151°C to ambient.

With such an increase in fractional free volume, the chains are sufficiently apart that interlocking groups are able to slide across each other and free rotation of the key main chain components is possible. The increased mobility and freedom from steric hinderance results in rapid and extensive crystallization [Cope, 1977].

In general, molecules found to suppress the T_g of PC and promote (solvent induced) crystallization are small, low molecular weight and liquid. Many studies [e.g. Conic and Jeurissen, 1965; Miller, Visser and Morecroft, 1971; Cope, 1977; Daniewska, Kocinska and Dobkowski, 1986] have shown PC crystallization in the presence of for example ketones, esters, toluene and one or two organic acids. In chapter 7, the solvent induced crystallization of PC under the influence of butyl acetate is discussed. Further work on this theme is introduced in chapter 8 where the effects, solvents other than butyl acetate, have on the PC film.

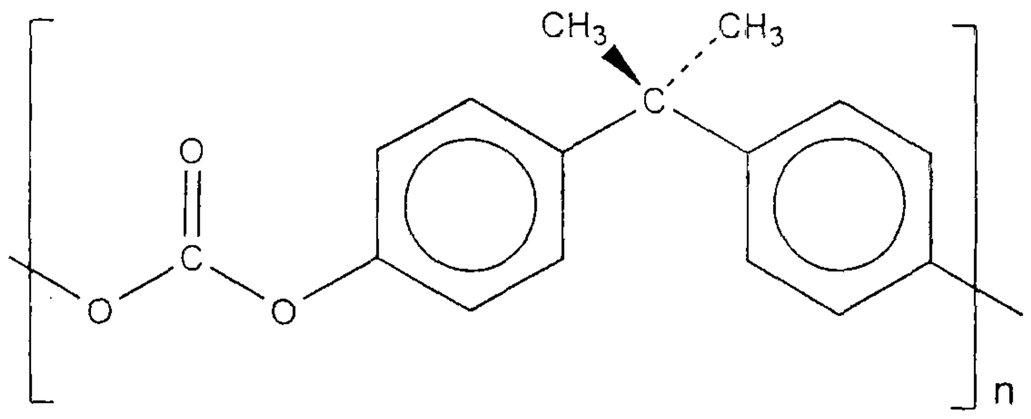

Bisphenol-A-polycarbonate

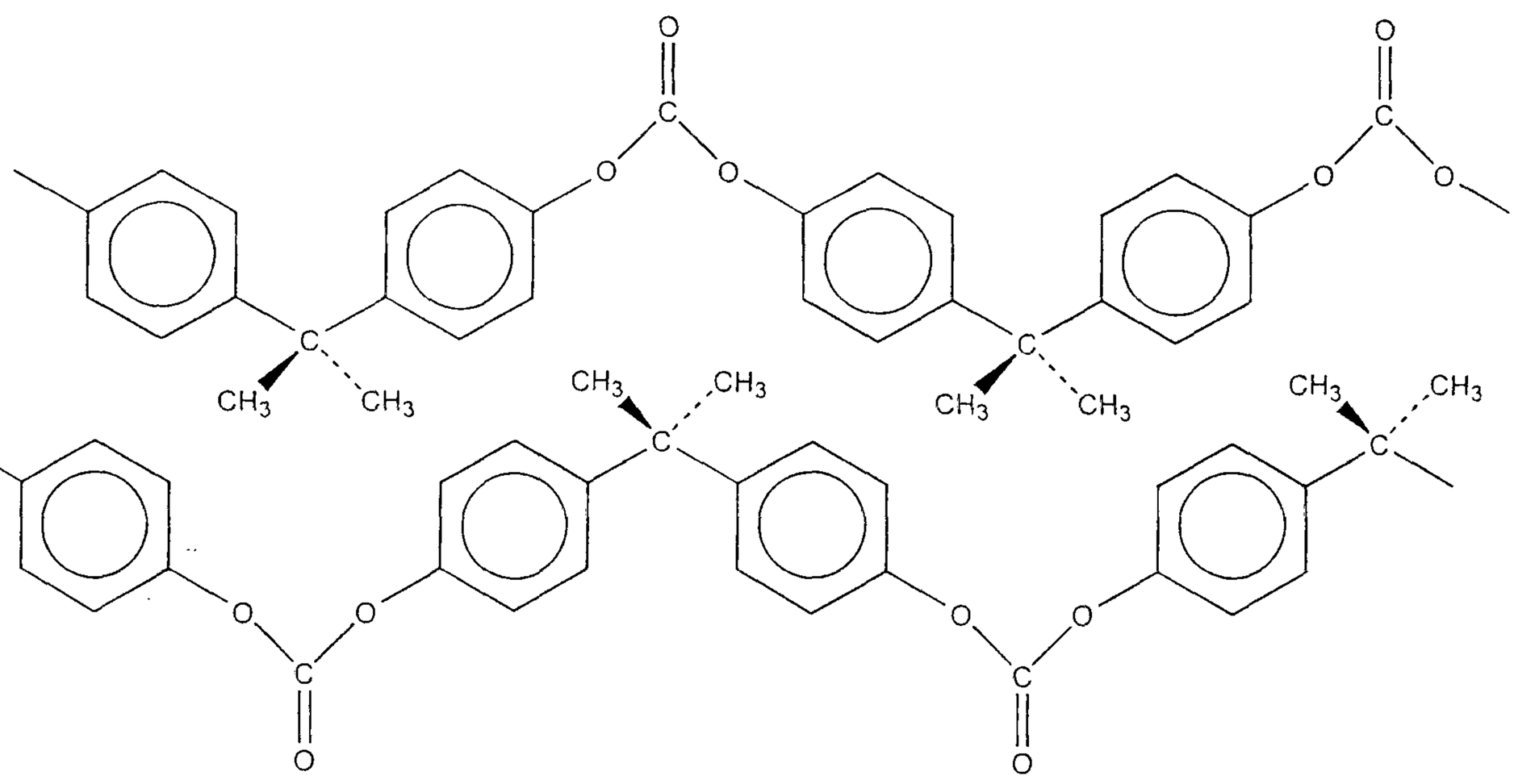

Crystalline Structure of Polycarbonate

Figure 4.11: The chemical structure of bis-phenol-A-polycarbonate. The chains of this polymer are able to form a lower energy, stable, crystalline state.

4.7.3 Morphological Features

Polycarbonate is able to crystallize below normal temperature because the plasticizer ingression effectively reduces the T_g to that of ambient temperature allowing the chains to rotate and move freely. For subsequent crystalline developments the rate of plasticizer evaporation becomes more important, the faster the rate, the more limited the growth and the sooner the PC returns to the 'glass' phase. Once more plasticizer is added, the process resumes.

This continual solid-rubber-growth-solid cycle is used to the advantage of the current work. It enables thin films of PC to develop firstly the smallest crystalline regions, then the larger crystallites, then the development proceeds through fibrils and eventually into spherulites. At all times the process is controlled allowing any crystalline features to be assessed at key stages of development.

The time resolved study of the polymer crystalline development may allow growth rates and nucleation experiments to be carried out. A wealth of data may be extracted in an comparatively straight forward manner, where in the past many instruments and much time was used for the same job.

4.8 POLYMER SOLUTIONS

4.8.1 Introduction to solubility in polymers.

The solubility of polymers in solvents poses many problems, mainly of compatibility. Some polymers will dissolve in a wide range of solvents, others may not dissolve at all. It is also possible that a polymer may partially or wholly dissolve in a range of solvents giving a solution, but from which cast films may display a variety of film characteristics.

It is important to an SPM study of polymer film morphology that the polymer is dissolved in the most compatible solvent possible and that on casting from solution the film must be consistently uniform. This then allows the reproduction of similar films (with similar morphology) and a good

estimate of film thickness to be achieved.

To ascertain whether the dissolution of a polymer in a given solvent is possible and to what extent, requires an intimate knowledge of the interaction between the molecules of the solvent and polymer in terms of their structure, of any hydrogen bonding or dipole moments etc. This interaction may be simplified and quantified by comparing polymer and solvent solubility parameters [Hildebrand, 1962]. With certain concessions, the most compatible solvent for a given polymer is that with the solubility parameter most similar to the solubility parameter of the polymer. A description of the solubility parameter is given below.

4.8.2 A simple picture of dissolution.

The dissolution process may be as follows: The solvent, incident on the polymer surface may diffuse into the polymer. The chains are separated by the solvent molecules and the polymer appears jelly like. The polymer chains once subjected to additional solvent may simply relinquish any contact with each other and become totally separated forming the solution.

On film casting, the situation is reversed, the thin layer of solution with rapid solvent evaporation, results in the gel being formed where the polymer chains lie randomly orientated to each other and often entwined. The evaporation of the last solvent molecules from between the polymer chains results in an amorphous and uniform film.

This state is idealised and two basic assumptions have been made:

1) Solvent - Polymer compatibility.

The polymer solution is such that each polymer chain exists in a state where it is entirely separated and extended and is surrounded by solvent molecules. Any deviation from this state introduces the possibility that the polymer may only partially dissolve, where bundles

of chains may exist in solution as large clumps. On solvent evaporation, these bundles may be deposited and a very non-uniform film will be cast.

2) The polymer must be amorphous and without crosslinks.

As the solvent encounters the polymer film it will diffuse between the polymer chains, hence any crystalline region with a highly ordered, compact arrangement of chains will present a barrier to further solvent ingression. Similarly if the film is significantly cross-linked then the chains cannot become separated by the solvent molecules and although the film may swell in the presence of the solvent it will not dissolve.

4.8.3 Solubility

The thermodynamics of solubility may be aptly described by the change in the Gibbs free energy ΔG:

$$\Delta G = \Delta H - T\Delta S$$

where:

i) Solubility occurs when ΔG is zero or negative.

ii) ΔS is the entropy of mixing at temperature T and is usually negative.

iii) ΔH is the enthalpy of mixing and must be small for ΔG to be negative.

Thus ΔH is of critical importance when considering polymer solutions and Hildebrand to account for solubility, related the enthalpy of mixing to the cohesive energy density (E/V) where E is the molar energy of vaporization and V is the molar volume. From this treatment the solubility parameter was defined by Hildebrand as $\delta=\sqrt{(E/V)}$. It can be shown [Cowie, 1992] that the

enthalpy of mixing is given by:

$$\Delta H_{mix} = (\delta_s - \delta_p)^2 V\phi_1\phi_2$$

where 'ϕ' represents the volume fraction, V is the volume of the mixture and subscript 's' and 'p' refer to the solvent and polymer respectively. δ is the solubility parameter and has units $(J\ cm^{-3})^{½}$.

4.8.4 Solubility Parameter

ΔH must be as small as possible for dissolution to occur and this may happen if δ_s and δ_p are very similar, i.e within about $2(J/cm^3)^{½}$.

To calculate the value of δ_p it is necessary to sum all the molar attraction coefficients that when combined, make up the repeat unit of the polymer. It should be noted that the value for the solubility parameter may be over simplified and may not truly reflect the interaction between polymer and solvent. For example although PMMA and PVC have very similar values for solubility parameter, PMMA will dissolve easily in chloroform but PVC will not.

It is therefore important to modify the solubility parameter to take into account the effects of some secondary forces such as hydrogen bonding (δH), dipole-dipole interaction (δD) and van der Waals forces (δW). This model forms the basis of the three compoment Hansen Solubility Parameter (Hansen, 1967; Brandrup and Immergut, 1989). The modified solubility parameter takes on the form:

$$\delta = (\delta H^2 + \delta D^2 + \delta W^2)^{½}$$

The modified solubility parameter described above is particularly useful when describing the effects of various plasticizers on a polycarbonate film (see Chapter 8). It this case plasticizers of very similar δ_s have quite different effects on the growth of PC crystalline entities and workers such as Daniewska et al [1986] suggest that the δD component becomes highly

significant.

4.9 CONCLUSION

This section has described how and why polymers crystallize and what is meant by an amorphous polymer film. If the temperature of the polymer film is raised to that between the melting and the glass transition point, some polymers (if it is energetically favourable for them to do so) undergo crystallization.

For polycarbonate, the process of melt crystallization is not very successful due to the very high viscosity of the polymer even at temperatures well above T_g. To enable studies of PC to be achieved, solvent induced crystallization must be used.

The crystallization process, which for PC, may be observed step, by step, results in the formation of a wide variety of features from fibrils to spherulites and is initiated by polymer chains becoming ordered at a nucleation site. The polymer spherulites grow through the amorphous phase until they impinge on one another and boundaries are then created.

This chapter also considered the effect of the solvent used for casting purposes on amorphous film morphology. It was noted that the polymer dissolution could be described in terms of the solubility parameter. The most compatible solute/solvent mixtures occurred when the respective solubility parameters were most similar. In the case of 'good compatibility' then the cast film was expected to be uniform; given poor compatibility the cast film was expected to be non-uniform and not suitable for SPM observations.

CHAPTER 5

EXPERIMENTAL

5 EXPERIMENTAL

5.1 INTRODUCTION

The aim of the study was to image successfully the surfaces of a variety of insulating polymer films with both the STM and AFM. This chapter is divided into two parts. The first focuses on the main equipment and procedural details required to image polymer films by both AFM and STM. The second part outlines the details of the experimental work.

5.2 APPARATUS

5.2.1 The STM at De Montfort University

A Nanoscope II combined STM/AFM has recently been acquired. However the bulk of the STM work completed in this project was achieved using a home built machine. It was designed by Shen [1991] to operate at liquid helium temperatures and to achieve atomic resolution. An example of the work achieved from the microscope is given in Shen et al[1992].

A schematic diagram of the STM system used is given in figure 5.1. The tip is mounted on a piezoelectric ceramic tube with a maximum scan range of $(600nm)^2$. The tube is fixed to a metal diaphragm which in turn is supported by a spring loaded ball bearing. The spring is compressed by an 80 pitch screw, a small rotation of which, compresses the system and results in a hundreds-of-nanometre movement of the tip in the direction (z) of the sample. Further nanometre and sub-nanometre movement of the tip is achieved by appropriate voltage control of the piezo-tube.

The sample is mounted on a tripod of bolts and resides a millimetre or so away from the tip during non-operation. Before operation commences, the nuts are tightened in such a way as to move the sample towards the tip until a micron gap is achieved. Subsequent fine movement is made until appreciable tunnelling can be measured. This translation requires three stages

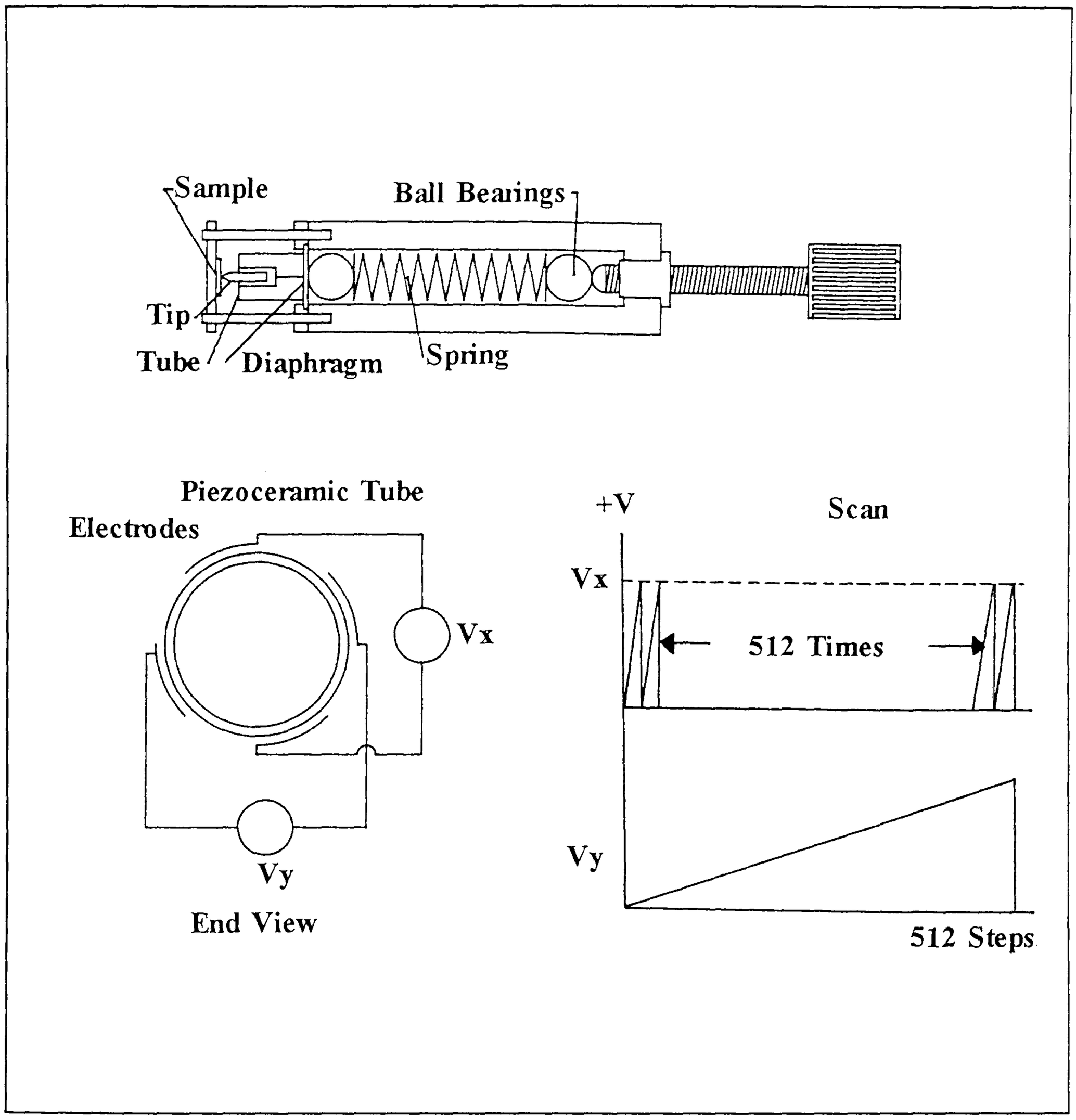

Figure 5.1: The mechanical and piezoceramic components of the STM used in this study. It was designed to be operated at liquid helium temperature and has achieved atomic resolution on a number of materials [Shen, 1991, 1992].

and these are explained below (see figure 5.2):

a) The sample is moved manually towards the tip under a travelling microscope by tightening screws on the sample holder. The separation at this stage is typically 50μm.

b) The STM is connected to the feedback loop. The tip is moved towards the sample by an 80 pitch screw pushing a spring which deforms a stiff steel membrane until a detectable tunnel current is produced. A two degree screw turn results in a 20nm forward movement.

c) The feedback loop increases the bias on the z-electrode on the piezoceramic tube until the pre-set tunnel current is reached.

The feedback loop characteristics and the piezoceramic control is achieved by an Archimedes 440 computer. Appropriate control signals are administered to the piezoceramic tube via TET(DL40-2A) 40V supplies (which are sufficiently stable to allow atomic resolution to be achieved).

STM Data Acquisition

The image data is stored on the Archimedes in a format comprising of two scans each of 512x256 (x,y) pixels each with a 'z' component formed from a 12bit ADC response of the feedback loop. The two images represent a positive and negative 'x' tip travel i.e. a single image contains data from the tip travelling in one direction only, the other contains data from the return trip (see figure 5.3).

The highest magnification images take approximately thirty seconds to achieve and the lowest magnification images can take up to twenty minutes. The long period of time to achieve a single large scale image is due to the limited scanning speed. Significant image distortion can result if the sample is not stable over the longest scan time (instability can be due to temperature

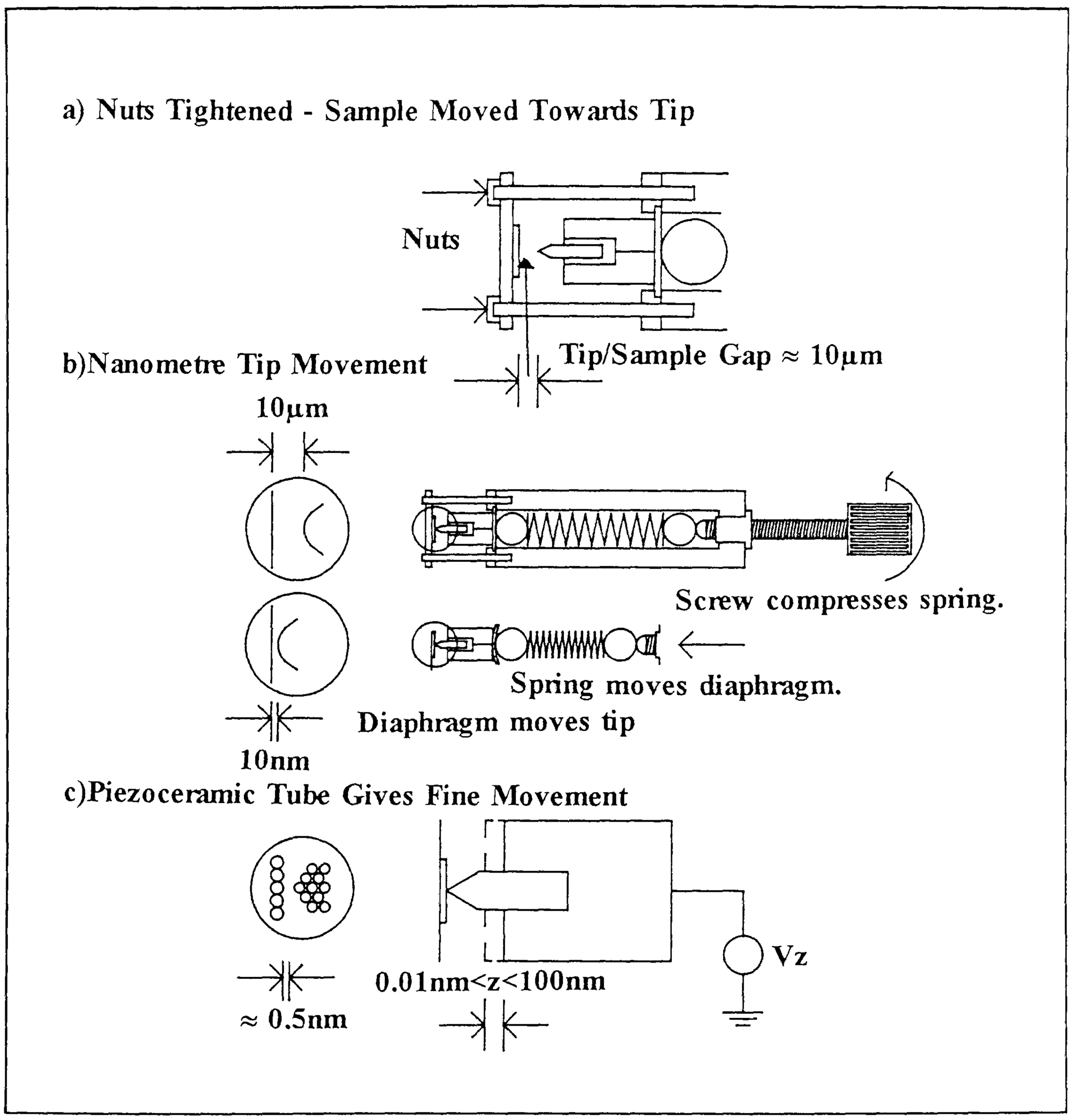

Figure 5.2: The translation of the sample towards the tip, to within tunnelling range is accomplished in three stages. a) The sample is moved manually towards the tip by tightening appropriate nuts. b) The tip is then advanced to close the gap by an 80pitch screw, the movement of which is geared down by a factor of 10^6. c) The final movement is achieved by direct control of the piezoceramic tube.

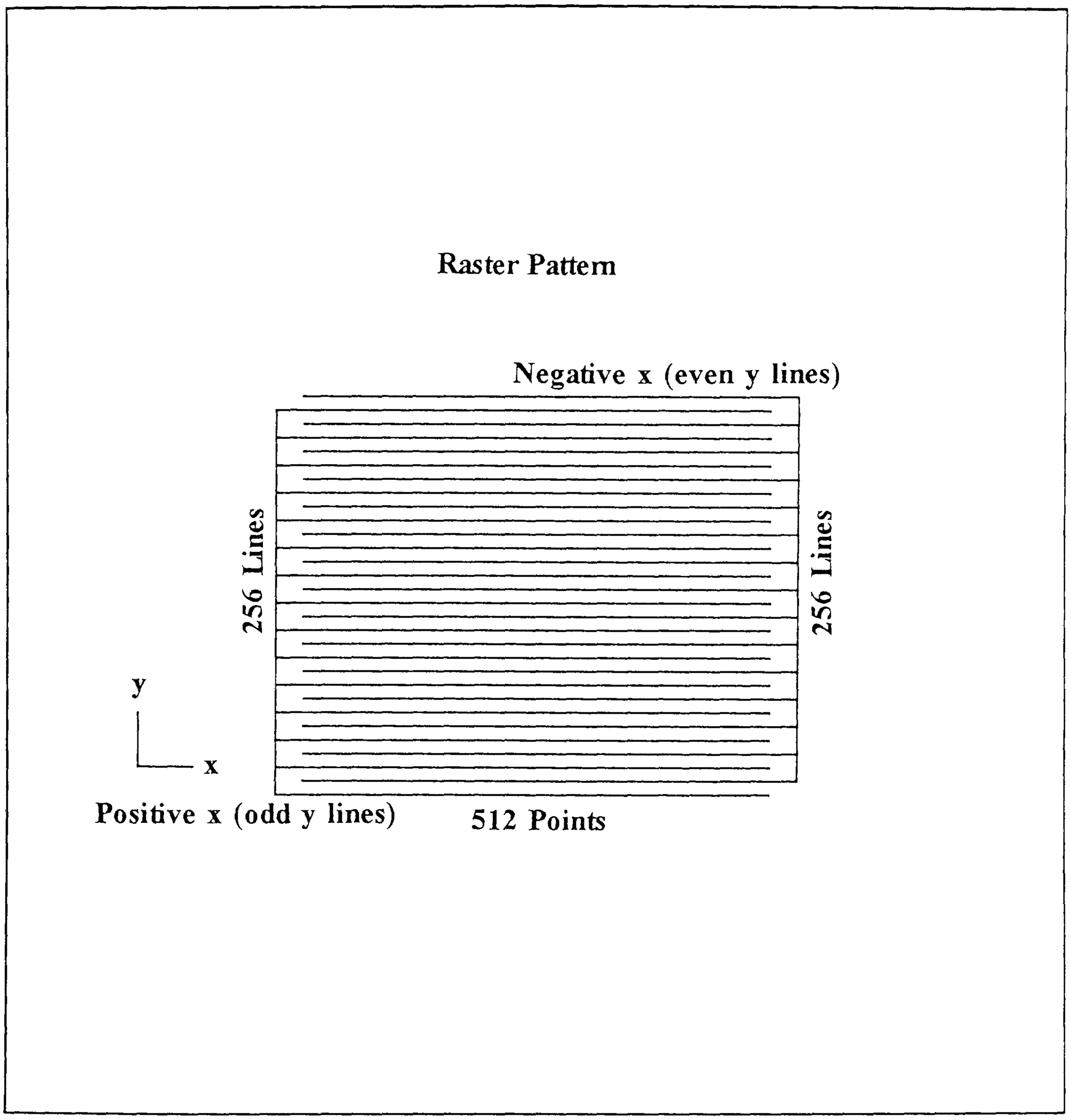

Figure 5.3: The image construction for the STM contains two halves. One half represent the data obtained from the positive scan direction, the other contains data from the negative scan direction.

variations within the laboratory).

Great care was taken to ensure very stable samples for example, a thermal polystyrene cover was used and the sample was allowed to 'settle down' for a number of hours before imaging was commenced.

The images were stored on hard disk and with appropriate data compression (where no image resolution is lost) each occupied on average 125k of disc space. In addition to user defined tunnel bias and current, scan size and feedback loop parameters, the software for the Archimedes 440 (4MB RAM) contained the following image enhancing facilities:

1) Plane Subtraction.
2) Histogram Correction.
3) Spatial Filtering.
4) Profile Measurement.
5) 3D Hidden Line Projection.
6) Colour Coded Contour Projection.

Further details are found in Shen[1991].

5.2.2 Vibrational Isolation

For atomic resolution to be achieved the STM must be highly isolated from vibration. The vibrations within the lab are too large for the STM, and if left unfiltered, the tunnel gap would be impossible to maintain. A detailed analysis of the successful damping of the SPM system to common vibrations found in the laboratory can be found in Pohl[1986].

The STM is rested on a 100kg slate bed which is suspended on elastic chords. The platform has a low resonant frequency (1 or 2 Hz). The amplitude of the high frequency environmental vibrations are then reduced by a factor of 1000 (from micron to nanometres) at the STM platform. Thus the platform acts as a high frequency filter. The STM head itself has a high resonant frequency because of the high rigidity and compact construction. The low frequency vibrations at the STM platform are then further reduced.

Thus the STM head itself acts as a low frequency filter.

The net result of combining the two filters is to attenuate the vibration amplitude from microns to a sub-nanometre level in the tunnel gap. The system is well damped, resulting in good stable imaging conditions (see figure 5.4).

5.2.3 Tip Production

The method of tip production employed in the present work was designed by Fotino[1992] and involved the electrochemical etching (5M NaOH etch at 10V a.c.) of a short piece of tungsten wire. The wire was inverted and etched at 0.5V a.c. for 10 minutes, washed in ethanol and dried. Fotino suggests that the inversion causes the bubbles to rise up and away from the forming tip. The electrolyte is forced onto the tungsten surface by the rising bubbles and increases the local etching effect (see figure 5.5). An SEM was used to image a tip formed by this method of production and such an image is given in figure 5.6.

5.3 MODIFIED STM FOR ENVIRONMENTAL STUDIES

The STM built at De Montfort University by Shen[1991] was modified for the purposes of this project to allow various environmental changes during operation. The main alterations involved mounting the STM head vertically through a base plate and establishing a gas inlet and outlet flow system. A bell jar is then placed over the entire assembly after stage 1 of tip-sample approach (as discussed above) had been completed. Once the covering bell jar was in place, the STM was moved to the vibration isolation platform and stages 2 and 3 of tip-sample approach completed. The apparatus is shown in figure 5.7.

The new system was designed to be capable of supporting a low vacuum and this was readily achieved. The gas effect on the STM images under study varied between the effect of butyl acetate on polycarbonate films,

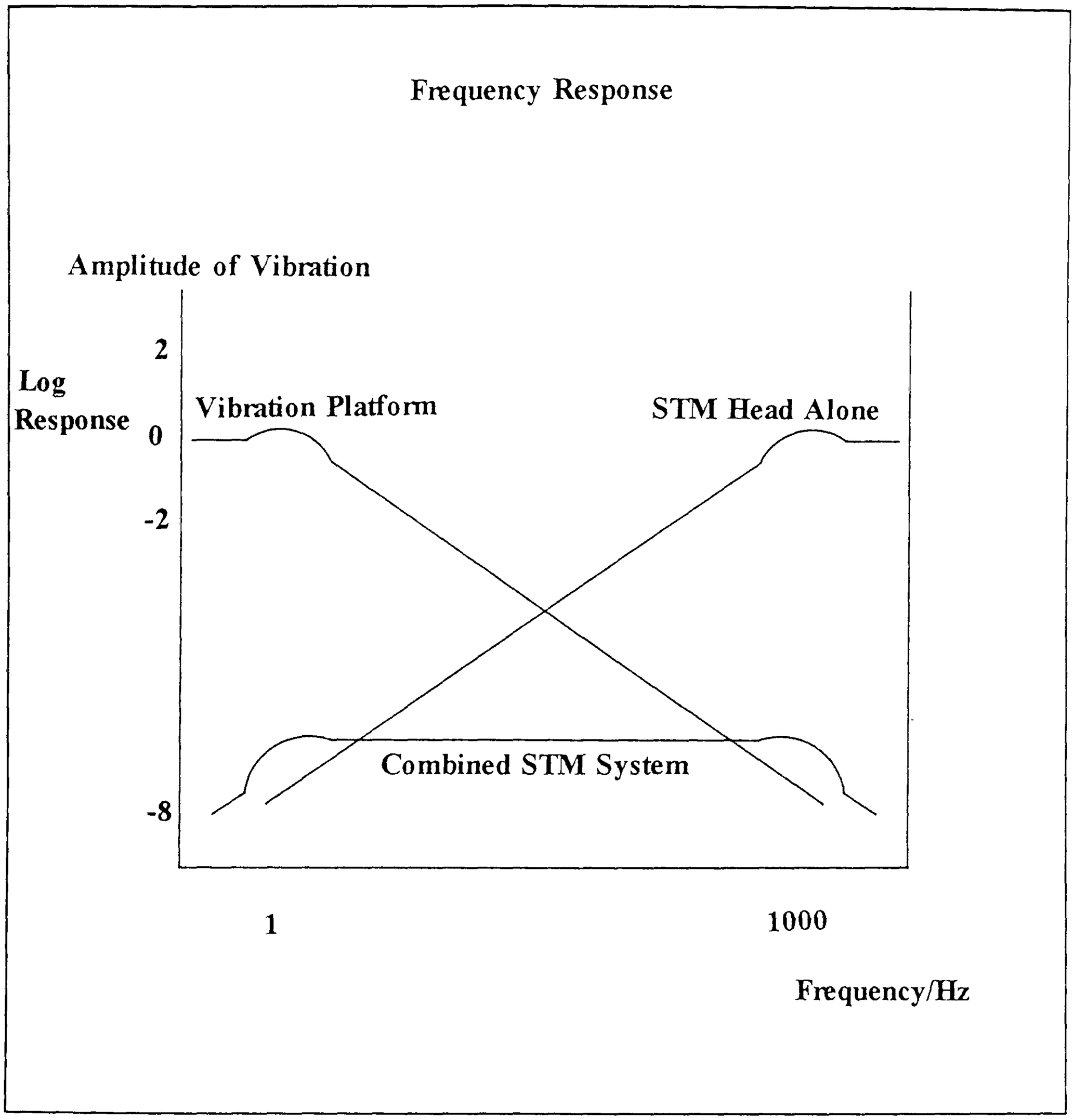

Figure 5.4: The vibrational isolation system for the STM relies on the combination of a rigid compact and small STM head (with a high resonant frequency) and a high mass, low resonant frequency platform. The system attenuates the vibration amplitude to an acceptably small level.

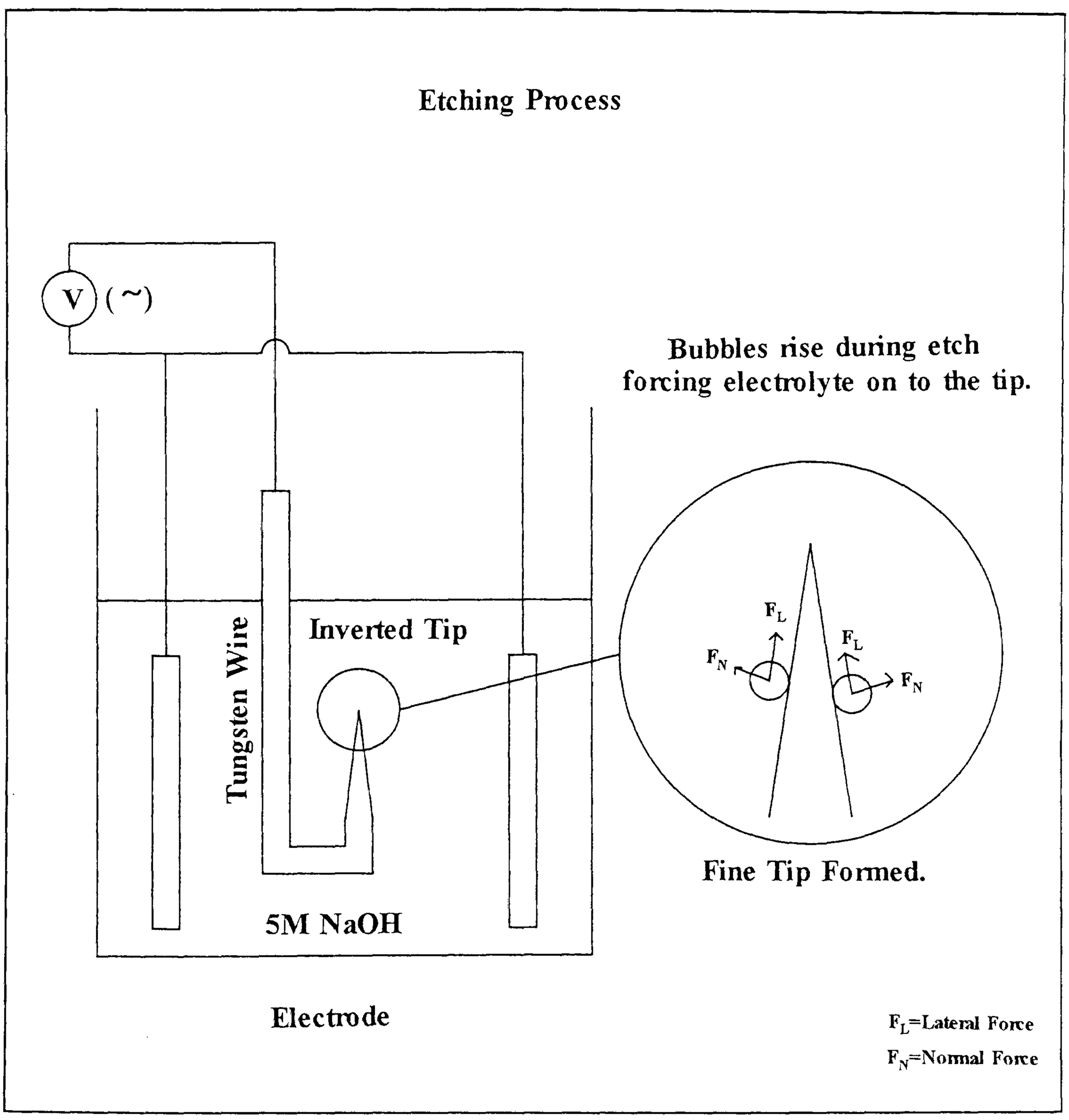

Figure 5.5: The tip production method [after Fotino, 1992] involves the etching by electrochemical means of a thin tungsten wire. The tip is etched into a fine point as the electrolyte is forced onto the metal surface by the rising bubbles.

Figure 5.6: An SEM image of the STM tip, etched using an electrochemical process.

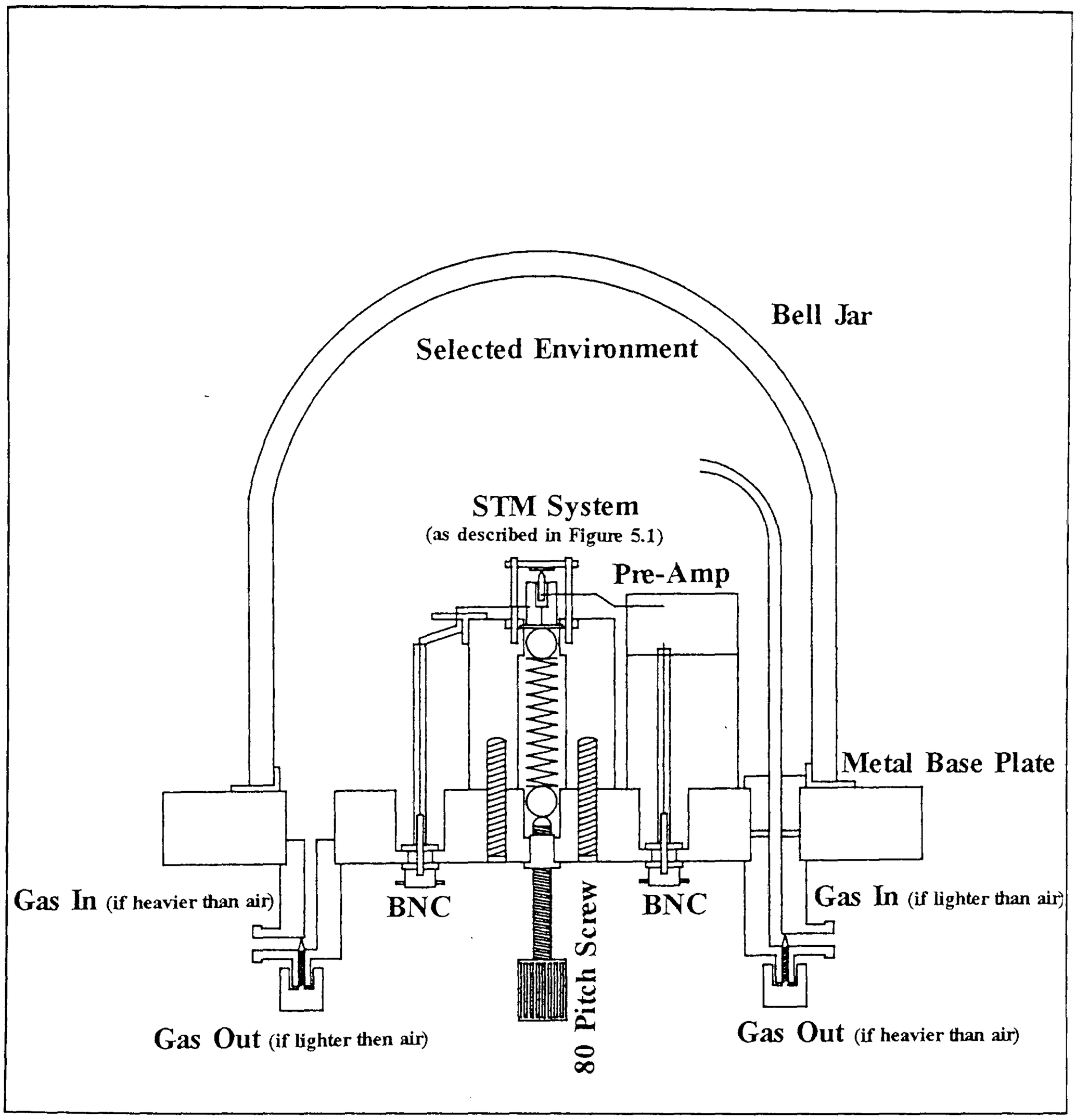

Figure 5.7: The environmental modifications to the existing STM system include a vacuum chamber with gas inlet and outlet valves. Either the relative humidity or the vapour concentration of the plasticizer can be varied and controlled for monitoring purposes.

to that of humidity levels within the bell jar, on various films. The required dry environment was achieved by flowing dry nitrogen or argon (via a drying agent) through the system.

5.4 NANOSCOPE II

5.4.1 NSII: STM

The Nanoscope II is a combined STM/AFM and was used successfully in this study. For the first time, those results obtained by the home built machine could be verified and repeated using a different STM. There are little in the way of Nanoscope STM images in the results sections, this is because the images from the home built STM were found to convey the same detail. Where Nanoscope STM images are shown, this is because this microscope offers the added advantage of a very large scan area $(86\mu m)^2$.

The operating procedure for sample loading and tip-sample approach is very different from the home built STM. The basic differences are that the sample is placed beneath the tip on the piezoceramic scanner. The tip is fixed in a cradle and lowered onto the sample by a levering method. The coarse approach is controlled by a stepper motor and the fine approach is controlled by the scanning tube.

The technical specifications for this STM that are important for this study are:

	Scan Head A	Scan Head J
Maximum Scan Size	$(792nm)^2$	$(86000nm)^2$
Bias Voltage Range	+/-10000mV	+/-10000mV
Effective Tunnel Current Range	(10-10000)pA	(10-10000)pA

5.4.2 NSII: ATOMIC FORCE MICROSCOPE

The second probe microscope available to this study was the Atomic Force Microscope (AFM). The instrument used was a Nanoscope II, and became available for use in October 1993. There was also limited access to the Nanoscope III and its tapping mode AFM from March 1994 [Goddard, 1994].

The advantage of using an AFM over an STM is that insulating materials can be imaged directly and with less problems when it comes to issues of image interpretation [Blackford, 1991; Haggerty, 1992; Smithson, 1992] compared to the STM study of similar materials. The initial stage of this work was mainly concerned with imaging polymers with the STM, discerning structure and investigating aspects of the associated imaging mechanism. The AFM at this stage was used purely as an aid to interpreting STM images.

The second stage of the work involved extensive use of the AFM with particular reference to the study of the crystallization of polycarbonate thin films (PC). Where the PC films were sufficiently thin, STM was used as this resulted in less damage to the films than AFM use. However for the thick PC films, the AFM was used exclusively.

Sample Loading

Details of the apparatus may be found in the handbook issued by Digital Instruments, Santa Barbara, California, USA. However a brief discussion in the sample loading and tip-sample approach is given here.

The Nanoscope II AFM head consisted of a scanning tube on which the sample was mounted and a cradle which housed the AFM tip and deflection detection system as shown in figure 5.8. After the sample (which may be up to 7mm x 7mm in size) was loaded, the tip assembly was placed on the three screws, two of which were operated manually and the third is controlled by a stepper motor. The tip is lowered automatically as shown in figure 5.9, until a deflection in the laser beam is recorded by the feedback loop. The sample may now be imaged.

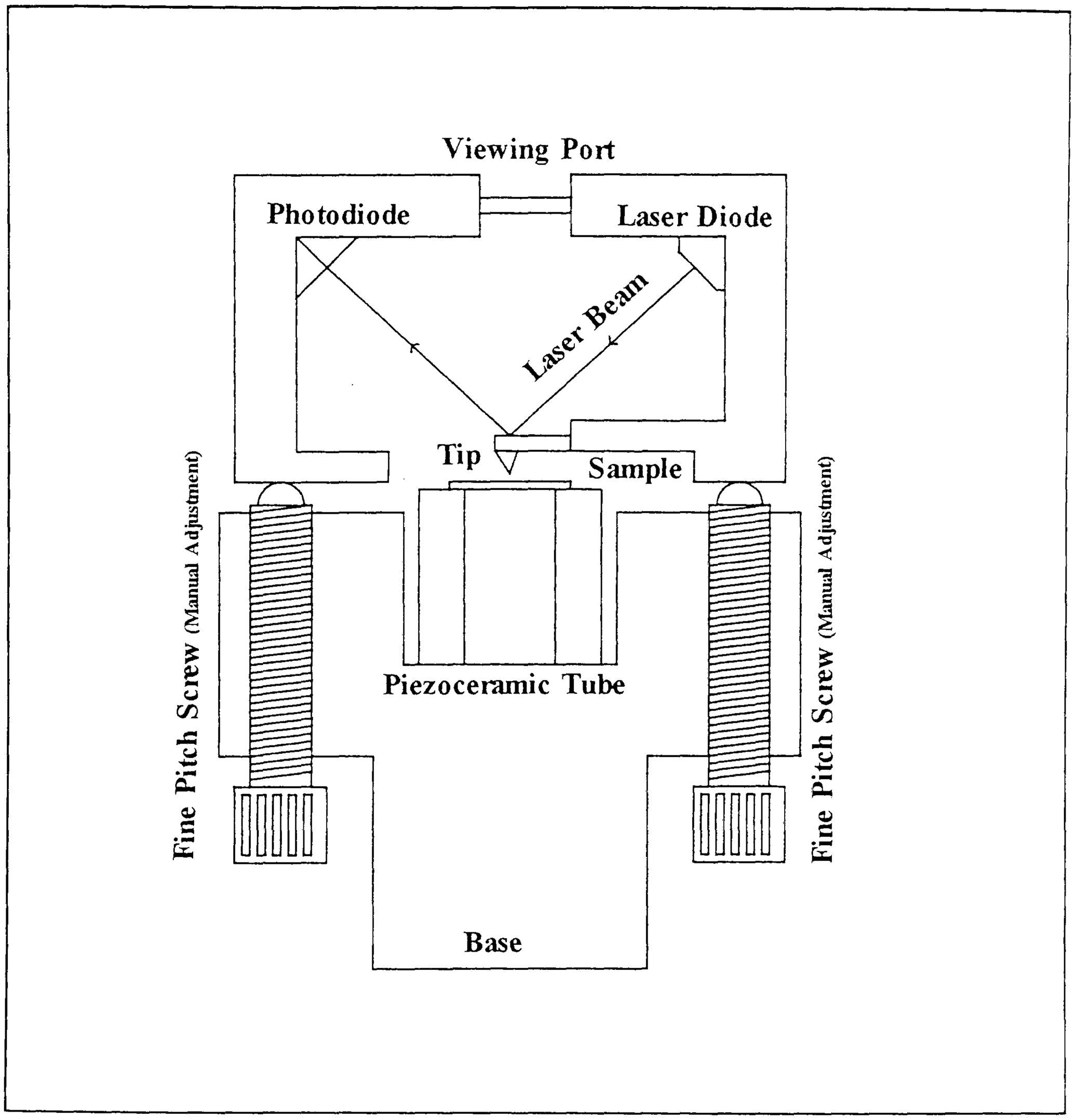

Figure 5.8: The Nanoscope II AFM system. A laser beam is reflected from the back of the cantilever and into the split photodiode. The sample is scanned relative to the tip.

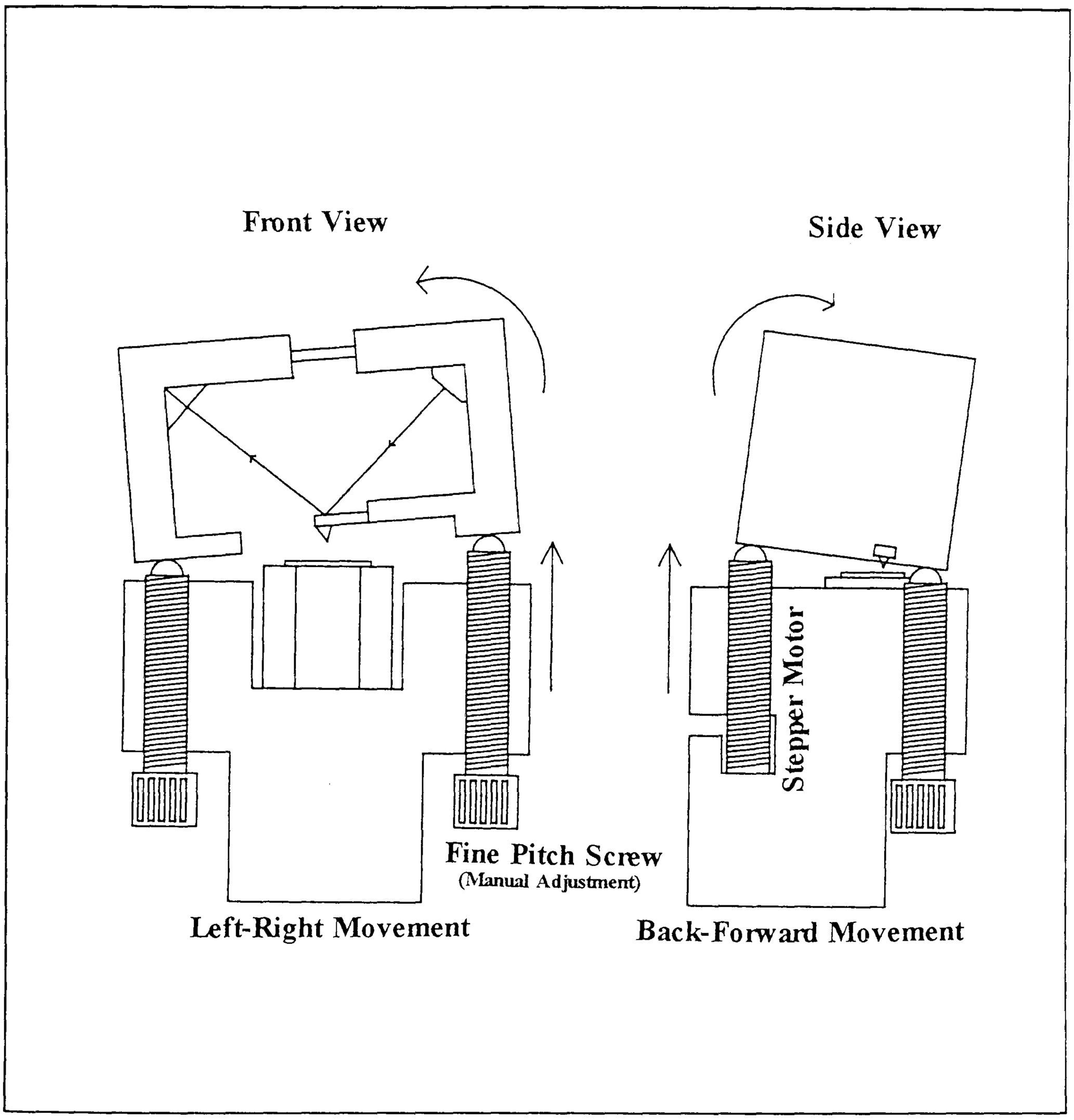

Figure 5.9: The method used for the tip towards the sample in the AFM, employs three finely pitched screws. Two are manually adjusted to close the gap from millimetres to micrometres. The third screw is turned by a stepper motor and the gap is closed until an appropriate deflection in the laser beam indicates tip-sample contact. All subsequent movement is achieved by the piezoceramic tube.

Force Calibration

Facilities on the AFM allow a spectroscopic determination of the force-vs-separation curve. This curve is vital to the correct set up of the microscope and contains data on the tip-sample interaction. The software available allowed the user to reduce the forces between the tip and sample, thus reducing the possibility of sample damage. The software also allowed the user to operate the AFM in other force regimes as discussed in chapter 3.

The specifications for the Nanoscope II, which are important to this study are included below:

	Scan Head A	Scan Head J
Maximum Scan Size	$(792nm)^2$	$(163000nm)^2$

AFM Software and Data Acquisition

The AFM images were obtained as a 400x400 or 200x200 pixel (x,y) format. Each pixel was assigned a 'z' value obtained from the 16bit ADC. The images took approximately thirty seconds to achieve, regardless of the scan size. With the largest scan size (J head), and whilst observing on a large (>100µm) scale, the scanning speed was lowered to reduce the chances of damaging the sample.

Aside from the force calibration, there are many important software additions included in the Nanoscope which allow for increased information extraction from the raw data. Most details may be found in the handbook issued by Digital Instruments but below are listed some of the image processing facilities available:

1) Plane Subtraction
2) Filtering:
    -Spatial filtering
    -Fast Fourier Transform
3) Image Presentation:
    -Hidden line projection
    -False colour contour
    -Solid 3d projection with variable light source
    -Line scan, angular and height measurements

Tip Production

The AFM tips used were not constructed in our laboratory. The tips were purchased from a micromachining company and imaged by an SEM (see figure 5.10). There were four tips in each block, two tips directly accessible during and after sample loading. Each of the four tips were mounted on cantilevers with varying spring constant, allowing more control over the tip-sample interaction, which is especially important for imaging samples of greatly differing strength and hardness.

5.5 THE LOW VOLTAGE SCANNING ELECTRON MICROSCOPE

To enable the most complete study of the polymer films, as well as imaging by AFM and STM, a low voltage scanning electron microscope (SEM) was used. This form of microscope allows the polymer films to be observed in a truly non-contact way and the images are subtly different from those achieved by SPM.

The imaging mechanism for the SEM requires a vacuum to increase the path length of the beam of electrons used. The electrons are accelerated to several tens of kilovolts (typically 20kV) for image production and it is because of these harsh imaging conditions that the SEM is unsuited for imaging bare, ultra-thin organic samples.

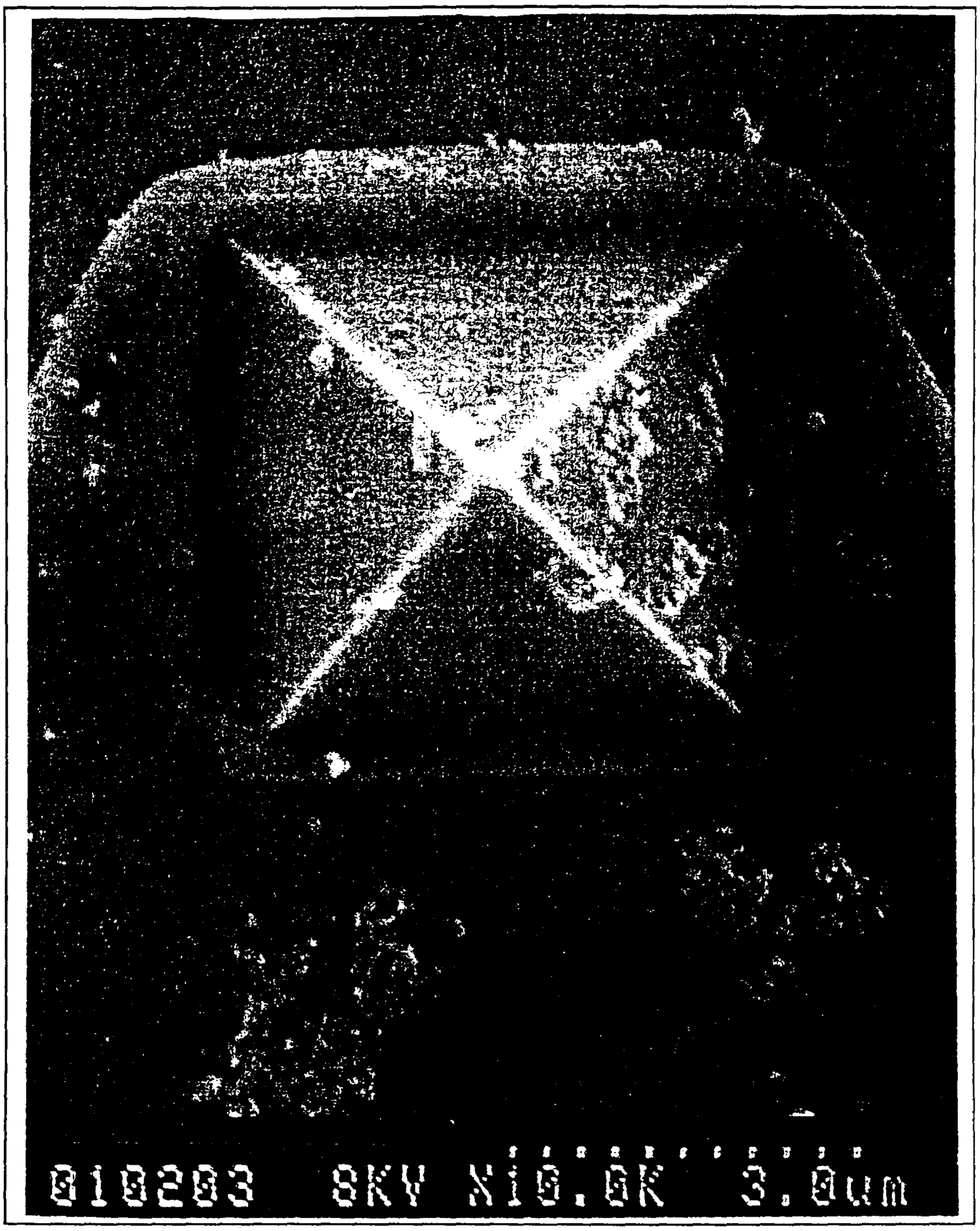

Figure 5.10: An SEM image of the pyramidal AFM tip. The tip is approximately a micron wide at the base and tens of nanometres at the tip. Debris may be observed clinging to the tip, the occurrence of which limits the resolution of the AFM image and results in sample damage.

The technique has been modified substantially and there are two options for improving the imaging of such films.

1) To coat the sample with a fine metallic layer and to image under a less energetic beam, i.e, the low voltage SEM.

2) To use the transmission mode electron microscope (TEM), where a thin metal coat or replica, over the original sample is removed and imaged with very high resolution.

However, the TEM samples take a long time to prepare and are only replicas of the original sample. The samples were viewed using the low voltage SEM at AEA Risely. The typical operating voltage was approximately 1kV. Images of the polycarbonate films and of the imaging tips were recorded.

EXPERIMENTAL DETAILS

5.6 POLYMERS

5.6.1 Introduction

The three main polymers selected were Polymethylmethacrylate(PMMA), PolyVinylpyrrolidone(PVP) and Polycarbonate(PC) in the form of Makrolon 3200, 3000 & 2800. The polymers were obtained from the Polymer Standard Calibration Kit, Polymer Labs Ltd. Shropshire(U.K) with the exception of the polycarbonate which was supplied by ALBIS U.K. The relative molar mass was approximately 32k, 30k & 28k for PC, 280k for PMMA and 700k for PVP. The molecular weight (which for the polymer grades selected may be considered high) in general is not considered crucial* in SPM investigations [Reneker,1990].

*The low molecular weight grades of polycarbonate do not crystallize well [Sweeting, 1967] but in this context a molecular weight of 30k was suitable for crystallization purposes.

5.6.2 THE CHOICE OF POLYMER

The polymers employed in this study were all similar in that they were all typical examples of insulating, high purity, high molecular weight, easily soluble polymers. However each of the polymers chosen had a particular important physical property or behaviour that would enable the image interpretation and structural determination from the STM and AFM to be assessed from the sub-nanometre to the micron level.

Poly(methyl methacrylate)

PMMA was chosen because of its low water absorption (the effect of water on the sample is known to be important when imaging by STM) and also its totally amorphous film forming properties. The films are expected to be stable under the operating conditions and environmental changes and show little morphology.

Poly(vinyl pyrrolidone)

PVP was chosen because like PMMA it is an amorphous film forming polymer. However unlike PMMA, PVP is very hygroscopic and will absorb up to 30% of its weight as water, depending on the environmental humidity. Consequently the water will act as a semi-permanent plasticizer, altering the internal structure of the polymer. Thus PVP is expected to be unstable during any environmental water content changes.

Polycarbonate

PC was chosen as the main polymer for SPM investigations. It may be cast in a variety of ways to vary the extent of crystalline growth in the film. For an amorphous film containing no microscopically resolved (as observed by optical or Electron Microscopic techniques) crystalline regions, rapid film

formation using a fast evaporating solvent is required. The polycarbonate film may be crystallized by the addition of a plasticizing agent. The effect is to alter the morphology considerably; thus the PC film is reasonably stable to moisture changes but very unstable in the presence of a suitable low molecular weight organic plasticizer.

The polymer solvents used in this study:

Table 5.1, gives the polymers and the solvents used. To ensure a complete uniform coverage the polymer must be completely dissolved in the solution. This only happens if the solution is very dilute and/or the solubility parameter of the solvent is similar to that of the polymer as discussed above.

Solution Characteristics For SPM Study

The concentration of each of the polymer solutions was varied until the film showed evidence of sub-monolayer coverage (revealing the underlying substrate).

PVP, PMMA and PC were cast from the solutions by the spin or drop methods discussed below as a film on the substrates. After deposition, the samples were placed in a desiccator and/or oven at 40°C for several hours to remove all traces of water and/or solvent.

The PC/Dichloromethane solution was spin coated at 2400 rpm on a gold substrate. The films were dried for several hours in an oven at 40°C.

5.7 SUBSTRATES

The ideal substrate characteristics for polymer deposition are:

i) Atomically flat planes over distances of hundreds of nanometres.

ii) Inert as a function of time.

iii) Conducting (for STM studies).

iv) Mechanically stable.

v) Allows reasonable adhesion of the polymer*.

[Dietz & Herrmann, 1990]

Technique	Polymer	Solvent†	Concentration
STM	PMMA	Chloroform	70mg/10ml
	PVP	Chloroform	10mg/10ml
	PC	Di-chloromethane	5mg/10ml
AFM	PC	Di-chloromethane	20mg/10ml
TM AFM	PC	Di-chloromethane	20mg/10ml

†The very small amount of polymer in the solution demands that the solvent be of high quality and leave an insignificant amount of dry residue to avoid confusion with the polymer film. Spectroscopy grade chloroform and di-chloromethane with volatile impurities and 18MΩ water were used.

Table 5.1

The table shows the polymer solutions used in this study. The polymer and the solvent solubility parameters are also given.

*The adhesion between the polymer and substrate is discussed below.

The availability of substrates that fit this description is very limited. The most common substrates for STM work are Highly Orientated Pyrolytic Graphite(HOPG) and gold. For AFM work polished silicon wafers and mica are both used.

5.7.1 HOPG

The HOPG (from Union Carbide, Switzerland, bought as 10x10x2 mm slabs) possessed large atomically flat planes. The atomic lattice was imaged regularly and used to calibrate the STM x,y motion.

HOPG satisfies many of the requirements for substrate suitability stipulated by Dietz & Herrmann and is the cheapest STM substrate used. Although there are some problems with artifacts associated with this substrate (see results chapter 8) almost every group involved in STM work has observed and at one time used the HOPG as a substrate. Any of the good reviews (see reference chapter) will discuss this substrate further.

5.7.2 Gold

Because there are several anomalies associated with imaging samples on HOPG, a trend has been set amongst users away from this substrate towards other more stable and easily imaged samples including gold.

Gold is expensive but a good substrate may be formed by the following methods:

i) Evaporated under vacuum on freshly cleaved mica.

ii) Grown as a single crystal.

iii) Heated as a wire to form a tiny ball with atomically flat ledges.

[Clemmer & Beebe, 1992]

The gold used in this study (Johnson Matthey, UK, as wire) was evaporated

onto freshly cleaved mica or highly polished silicon (in the form of a wafer) at $1x10^{-7}$ torr in a home built liquid nitrogen cooled evaporation plant. The gold films formed grains which on closer examination displayed very flat tops.

5.7.3 Mica

Mica is a silicate based planar material similar to graphite. It may be cleaved parallel to the planes to form a large, flat and clean substrate. The mica used in this study was purchased from Agar Scientific, U.K and needed no special treatment prior to cleavage.

5.7.4 Silicon Wafers

The silicon wafers used in this study were bought cut from a single silicon crystal and with one side remaining highly polished. The wafers were suitable for device microfabrication purposes. In general silicon wafers are doped and sold as n or p type material. The doping was of no significance in this context as the substrate was used only for AFM work. Prior to use as a substrate the wafers were cut in to 5mmx5mm squares.

5.8 POLYMER/ SUBSTRATE ADHESION.

For a material to be acceptable for polymer deposition and study, the polymer/substrate interaction was found to be critical. The nature of the interaction and the adhesion of the polymer (preferentially to the substrate rather than to the tip) is not easy to estimate let alone calculate.

At first, the assumption is made that the surfaces are clean, i.e. free from contaminants and most importantly free from water or hydroxyl ions (this is never the case in air). Given that the polymer chain conformation on the surface is assumed to be fairly random and that there is an absence of attractive surface sites, the relevant mechanisms for polymer-metal adhesion become:

1) Physisorption based on Lifshitz-vdW forces,
2) Molecular interactions e.g. Hydrogen bonding,
3) Chemical interaction and electrostatic attraction.

[Lee, L-H; 1991]

The Lifshitz-vdW forces result from dipole and dispersion attractions which result in physisorption of the polymer onto the substrate. It has been noted by Stachurski [1986] that dispersion forces may account for all of the internal strength of the polymer and may play an important role in bonding with the surface. However even though the physisorbed polymer is not fixed to the surface by a bond of any real strength (in comparison to a chemical bond), wetting of the surface by the polymer is commonly observed.

Hydrogen bonding is also possible between the polymers and substrates mainly in the presence of a contaminating water layer and this is discussed under the next heading.

Finally chemical interaction and electrostatic attraction is the least likely method of adhesion in this context. A chemical covalent or otherwise bond is unlikely to form between the polymer and substrate as the substrates were specifically chosen for their inertness. Some groups notably Leggett et al[1991] have attempted to chemically modify the gold substrate thereby enabling the polymer to chemically bond with the substrate. This method has met with some success [see Leggett et al, 1991 etc].

If the surface is covered by a contamination layer (which is almost inevitable) polymer adhesion can be affected severely. In this context, the most likely contaminant is water or hydroxyl ions. The presence of this species on the substrate may actually increase polymer adhesion, but in general a decrease is observed for example using freshly cleaved mica in a humid environment results order of magnitude drop in polymer/substrate adhesion [Good, 1986].

In principle the polymer and substrate are attracted by interatomic and short range forces. However the presence of the contamination layer may serve to increase the separation until the interatomic forces diminish and the intermolecular forces become much more significant.

If the separation(r) is very large i.e. several tens of nanometres, the retarded dispersion forces (where the potential U, is proportional to r^{-7}) will replace the non-retarded dispersion force (U is proportional to r^{-6}). The adhesion forces are likely to be very small and the polymer/substrate affinity consequently low.

The deposition of the polymer film from a solvent may result in competition between the solvent and polymer to adsorb onto the surface. In this case, the intensity of the competition is likely to depend on the electron donating and accepting behaviour of all three materials involved i.e. the substrate, the polymer and its solvent.

Given that there may be only a few ideal solvents for the polymer, the choice of substrate becomes important. Where the wrong choice is made, the film may end up not adhering to the substrate at all. An example of this problem is given by Schreiber et al[1983] and Ponce et al[1987], who noted that casting basic PMMA from an acidic solvent (Chloroform) on an acidic substrate of silica, resulted in poor adhesion because the solvent affinity for the polymer was high. Casting the same polymer onto the same substrate but using a very basic solvent (THF) resulted in poor adhesion because the solvent molecules were displacing the polymer from bonding with the substrates. The best adhesion results were to cast the polymer from a neutral solvent (tetrachloromethane) - see figure 5.11.

It may be assumed that the most suitable substrates may be those where the bonds with the polymer are strongest or where the surface has a neutral affinity for water or are even hydrophobic. In the present study gold and HOPG substrates conformed to the poor affinity for water, wheras mica and silicon did not. The best substrates used in this study were formed from gold, vacuum deposited on mica or silicon wafer.

5.9 FILM PREPARATION

Film Deposition Techniques

The film must be as uniform as possible and adhere to the substrate. Once the

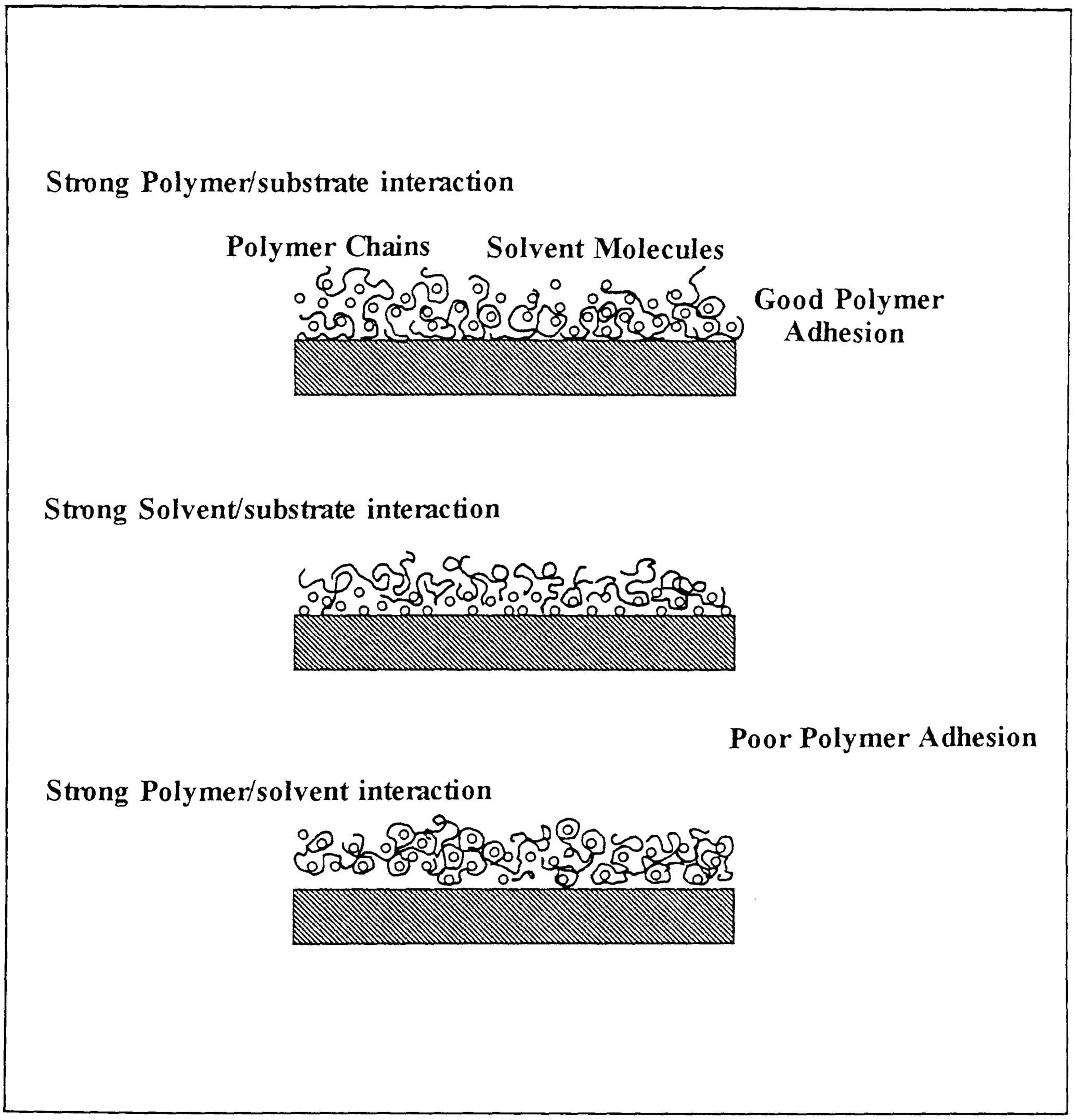

Figure 5.11: The ideal solvent for film casting will not compete with the polymer for active or bonding sites on the substrate surface. Schreiber et al[1983] and Ponce et al[1987] found that when casting PMMA from THF on to silica, adhesion was poor because the THF displaced the PMMA from the surface.

best choice in polymer/solvent/substrate combination is made the film formation technique becomes the crucial element in the film morphology. If the best film deposition technique is employed it is possible to form a film with as few defects as possible. Unfortunately the film formed is never completely even and some areas are thicker than others [Caple et al, 1990] and if the solvent/polymer/substrate combination is inappropriate, or the concentration of the solution is sufficiently weak, the morphology of the film may result in polymer clumping and substrate exposure [Yang et al, 1989]. If the solution is sufficiently weak, the substrate exposure reveals the characteristic underlying morphology which may act as an excellent calibration reference to aid measurements of polymer features.

The film deposition methods described below, have been used successfully elsewhere [for example: Shen,1991; Reneker,1987; Smithson et al, 1992; Stange et al, 1992], and fall into three main categories:

i) Spin Coating.

Deposition of the polymer solution on the substrate is followed by rapid spinning at 2400rpm for ten minutes. The spinning helps to remove excess solution and form an even film. This method was used for work with PMMA and PVP in chloroform and PC in dichloromethane. This technique employs the standard techniques available in the department via its Inelastic Electron Tunnelling Spectroscopy (IETS) research area [see for example Malik, 1983; Line, 1994].

ii) Drop Method.

This technique involves the deposition of the polymer solution on the substrate without spinning. The solvent evaporates leaving a cast film usually of variable thickness. This method was used for work with PVP because it was found that spinning the water soluble polymer on the hydrophobic substrate formed little or no measurable film.

iii) Langmuir Blodgett or LB Trough method.

This method relies on the transfer of the polymer molecules from the surface of a liquid to the substrate by dipping or drawing the latter through the polymer layer. By appropriate polarity treatment, this method may successfully allow layers of precise thickness (corresponding to chain length) to be deposited. Some good examples of this technique applied to SPM work may be observed in Schaper et al[1993], Niemi et al[1993], Kishi et al[1992] etc.

Unfortunately where this latter method tends to produces films with the carbon backbone orientated perpendicular to the substrate, the samples are unsuited for STM (which requires a thin sample only attained if the molecules are deposited parallel to the substrate). This method although available from the IETS work was not used because of the unsuitable orientation of the polymer molecules in the film. It was also considered that most technologically important polymer films are either cast from solution or cooled from the melt with the chains parallel to the surface and data from similarly formed films would be more appropriate.

5.10 STAGE 1: STM OF POLYMER FILMS

Films Cast

A variety of polymer/solvent/substrate combinations were used. The polymers PMMA, PVP and PC were deposited as either thick (t>2nm) or thin (t<1nm) films. In the case of PVP, both water and chloroform were used as solvents. Each film was imaged on both substrates by both the STM and the AFM. Table 5.2 gives the polymer, its solvent and the concentration of solution prepared.

SPM Technique	Polymer	Solvent and Solution Concentration	Deposition Method	Volume Deposited / µl
STM	PMMA	Chloroform 20mg/10ml	Spin	50 +/- 5
	PVP	Chloroform 10mg/10ml	Spin	50 +/- 5
	PVP	Water 10mg/10ml	Drop	50 +/- 5
	PC	Dichloromethane 5mg/10ml	Spin	50 +/- 5
AFM	PC	Dichloromethane 20mg/10ml	Spin	50 +/- 5
TM AFM	PC	Dichloromethane 20mg/10ml	Spin	50 +/- 5

Table 5.2

This table shows the solutions used and the methods of deposition used for the formation of thin polymer films.

STM Operating Conditions.

Whilst imaging thick layers of polymer, if the polymer is contributing towards the conduction process, then it is important to take the value of the bias into account [Garcia, 1990]. The bias is not so crucial when imaging thin polymer layers but this parameter is still chosen carefully. In some studies a very small picoAmpere (12pA) pre-set tunnel current was used to enable the tip to ride above any organic material [Salmeron et al, 1991] although in general higher tunnel currents are used.

The parameters (tunnel current It and the tunnel bias Vt) used in this study were typically: Vt=400mV, It=1nA. Major STM studies on polymers and the typical parameters used are shown in Table 5.3:

Environmental Changes

The films of PMMA, PVP and PC were then introduced to the environmental STM. The humidity was varied by the gradual flushing with a dry gas (in this case argon) of the relatively high humidity chamber. Humidity levels above R.H 60% were achieved by placing a damp tissue within the chamber and after a maximum humidity was reached, the flushing begun. Table 5.4 describes the conditions each of the polymers was subjected to, but in general the conditions may be described as high, medium and low humidity.The films were then all imaged with the STM in the modified microscope.

The polycarbonate film was then placed in the environmental chamber and the plasticizing fluid was included around the sample. Evaporation of the plasticizing agent resulted in an interaction with the film and polymer crystallization resulted. After a specific period of plasticizer doping time, the chamber was flushed through with an inert gas (argon) and the plasticizer vapour source removed. The sample was then imaged under the ideal humidity levels discussed above.

AUTHOR ,Year	SAMPLE	It/ nA	Vt/ mV
Brown et al, 1990	Carbon Fibres	1.0	250 - 600
Dietz et al, 1990	n-Alkanes	10.0	50
Dovek et al, 1988	PODA, PMMA	0.5	600
Leung, 1992	Polydiacetylene	0.1 - 0.3	100 - 500
Reneker et al, 1990	Polythene	3.0	500
Jericho et al,1990	Biological material	0.15	1300
Jungblut et al,1992	HIV-1	0.2	-700
Kim et al, 1993	n-Octadecanethiol	1.0	1000
Lee et al, 1992	Algal Polysaccarides	0.1 - 1.0	600 - 1536
Mou & Wang, 1992	Phenylalanine	1.0	+/-20
This Study	PMMA, PVP, PC	0.3 - 1.8	100 - 600

Table 5.3

This table shows a survey of STM operating conditions which give the best STM images.

PMMA and PVP Relative humidity RH%	PCRange of doping times / Minutes
<10	0
10<RH<60	2
>60	20

Table 5.4

The environmental changes made to the chamber containing the PVP, PMMA and PC samples.

5.11 STAGE 2: FILMS USED FOR THE AFM STUDY OF SOLVENT INDUCED CRYSTALLIZATION OF PC

The concept of the solvent induced crystallization process has been discussed in chapter 4. Polycarbonate thin films which are cast in a high energy amorphous configuration are lowered in energy by adopting a crystalline morphology. The path from the amorphous to the crystalline state is impeded by an energy barrier associated with the rigidity and steric hinderance of the PC molecules leading to a very high viscosity. Under the influence of a suitable plasticizer, the energy barrier is lowered and rapid and extensive crystallization is achieved.

This process is ideal for study by the AFM because different stages of the crystallization may be achieved by appropriate control of the plasticizer. The growing polymer entities are observed in a way not possible by conventional microscopic techniques.

The Plasticizer

The plasticizer must be a low molecular mass organic liquid and the choice of suitable molecules is large and includes examples such as acetone, ethyl acetate and some phenolic compounds. The latter molecules may be associated with slow evaporating liquids and as such are used industrially as permanent plasticizers. PC films exposed to this class of molecule may totally crystallize. For the successful control of the crystallization process, the aliphatic liquids are favoured as these are fast evaporators and diffusers[Cope, 1977]. The process of converting the amorphous material may be completed in a step-wise manner by short plasticizer exposure times, achieving the aims of the work. Unless otherwise stated the plasticizer used was spectroscopy grade butyl acetate.

Crystallization

The thin films of polycarbonate formed as described above, were placed in a simple chamber (see figure 5.12) and exposed to butyl acetate in either vapour or liquid form. The vapour doping of the film was considered to be

Film Number	Casting Method	Doping Method	Doping Time/ mins	Drying Time
1	Spin	None		
2a	Spin	Vapour	10	60
2b		Vapour	10	
3	Spin	Liquid	5	60
4	Spin	Liquid	30	60

Table 5.5

The coating method and plasticizer doping methods used in the study of the solvent induced crystallization of thin polycarbonate films.

Film Number	Deposition Method	Doping Method	Doping Time / mins	Drying Time / mins
5a	Spin	Vapour	20	120
5b	Spin	Vapour	60	120
5c	Spin	Vapour	120	120
5d	Spin	Vapour	240	120
5e	Spin	Vapour	480	120

Table 5.6

Plasticizer methods and exposure times for a variety of polycarbonate thin films.

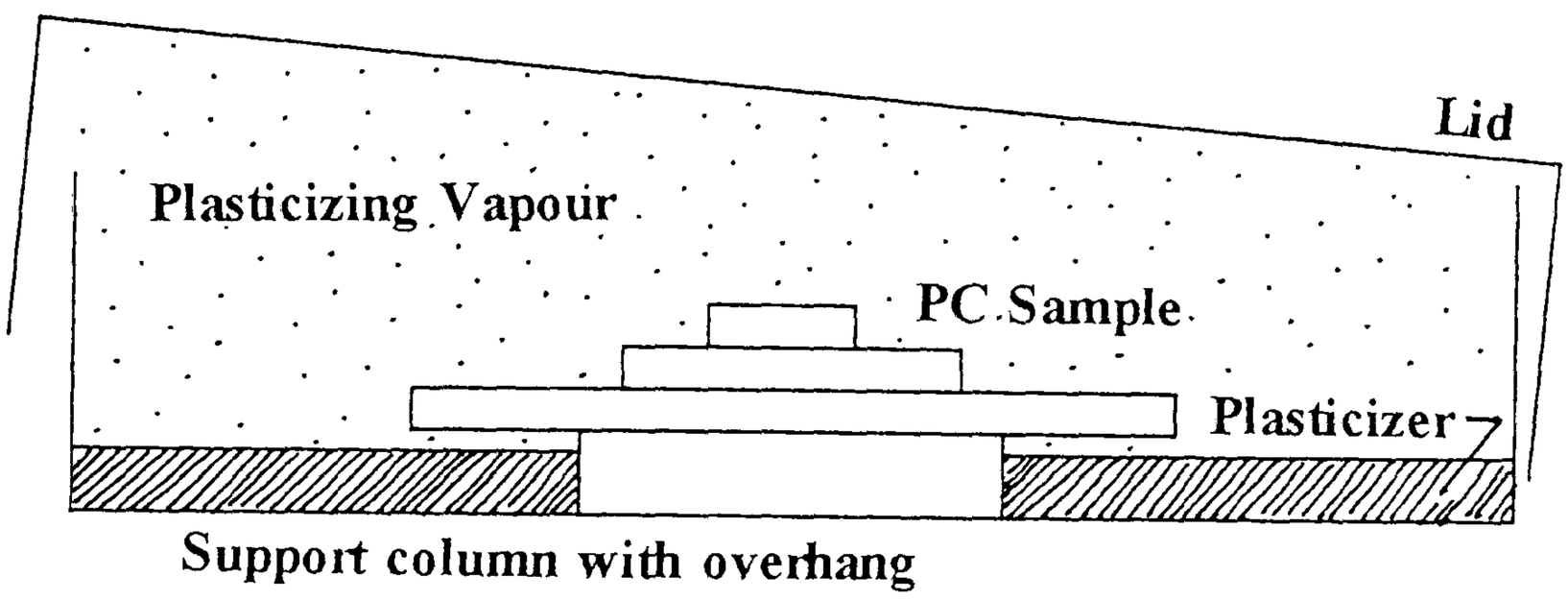

Figure 5.12: A simple chamber was used during the vapour doping of the PC film by an appropriate plasticizer. The vapours rise and fill the chamber until all the plasticizer evaporates. A slight angle on the chamber lid prevents condensation of the plasticizer and accidental liquid doping.

the most consistent and accurate form of doping and unless stated otherwise was the method employed.

Liquid Doping

A single drop of butyl acetate was placed on the PC film. After several minutes, excess solvent was removed and the film was dried.

Vapour Doping

The PC film was exposed to a saturated vapour of butyl acetate. The time of exposure was limited to several hours, when the sample was removed and dried.

Following casting and crystallization, the films were dried at 40°C in a clean environment for several hours. The drying allowed the plasticizer to fully evaporate from the film, allowing the mobile polymer chains to return to the glassy phase. Table 5.5 gives the butyl acetate exposure, doping method and drying times.

Measurement of Approximate Growth Rates

The process of continual stopping and starting of the crystallization can enable (provided the crystallization time is accurate) a 'time resolved' picture of the spherulitic growth. To assess the validity of the time resolved AFM imaging, a brief kinetic study was undertaken, the aim of which was to show that the area of a disc-like spherulite from an instantaneous nucleation site increases as a function of time (see chapter 4).

5.11.1 TREATMENT BY OTHER PLASTICIZERS

The general effect of a suitable plasticizer on the polycarbonate film is to enhance crystalline development in the form of spherulites. Although a number of plasticizing agents will crystallize PC films, the structure and size of the resultant spherulites produced is far from similar. A study by Daniewska, Kocinska and Dobkowski [1986] used eight plasticizers with

varying solubility parameter components. They measured the spherulite size by x-ray diffraction, optical microscopy and small angle light scattering (SALS) techniques. The results obtained show that different plasticizers give different sized spherulites that the size of the spherulites is inversely proportional to the polarity of the plasticizer.

In addition to the polarity/size relationship, the study also revealed that the structure of the spherulites also varied with plasticizer type although in what way could not be determined.

In a brief study here a number of different plasticizers were used to crystallize the PC film. The approximate size of the spherulites was estimated from the AFM images and compared to the results obtained by Daniewska. In addition the internal structure of the spherulites was assessed from the resultant AFM images.

5.11.2 NUCLEATION

The polycarbonate crystallization process relies on the presence of nucleating sites. These are formed either naturally from ordered regions in the polymer film (homogeneous nucleation) or from small impurities, particles or rough edges (heterogeneous nucleation). To investigate the nucleation processes, two simple experiments were performed on the crystallizing PC film. The first was aimed at the deliberate 'seeding' or addition of nucleation sites to the amorphous film, prior to solvent treatment. The second after Cormia, Price & Turnbull[1962] examined the crystallization of small islands of PC.

Addition of Nucleation Sites

A suspension of latex spheres with an average diameter of 86nm (Agar Scientific, U.K) was diluted by a factor of one hundred (to give solution X), spin coated on to the gold substrate and imaged by AFM. The frequency of 'seeds' on the substrate were varied by successive dilution of the latex sphere suspension (X). The adhesion of the spheres to the substrate was tested by washing with the polycarbonate solvent. The polycarbonate film was spun

Latex Sphere Concentration
0
X/8
X/4
X/2
X

Table 5.7

Latex sphere concentration with respect to the original suspension which was diluted by a factor of 100 to give solution X

Sample	Head Size*	Scan Rate Hz	Gain 1	Gain 2	Filters
PMMA	LSH	2.48	0.91	0.91	PF
	SSH	8.00	5.00	3.00	PF
PVP	LSH	2.48	0.91	0.91	PF
	SSH	8.00	5.00	3.00	PF
PC	LSH	2.48	0.91	0.91	PF
	SSH	8.00	5.00	3.00	PF

Table 5.8:

The ideal AFM operating conditions used for the studies of thin polymer films (* SSH is the Small Scan Head and LSH is the Large Scan Head).

over the sphere contaminated substrate and allowed to dry before crystallization and imaging. Table 5.7 gives the latex sphere concentrations used.

The Crystallization of Small PC Islands

The polycarbonate film was spin coated on a substrate of bare silicon wafer and allowed to crystallize under the liquid doping regime. The interaction between polymer and substrate resulted in extensive film disruption and the formation of isolated PC islands. These were examined over a period of half an hour for crystalline entities.

5.12 THE AFM OPERATING CONDITIONS

The conditions necessary to achieve an AFM image are not as critical as the corresponding STM images in this context. The AFM will achieve a reasonably coherent image with a wide range of scan frequencies, tip dimensions and spring constants. However, the following guidelines (given in table 5.8) were established and found to result in the best images whilst scanning in the contact mode.

CHAPTER 6

RESULTS : STAGE 1
THE SPM STUDY OF PMMA, PVP AND PC FILMS

6.0 RESULTS

6.1 INTRODUCTION

This chapter is divided into three main sections and broadly covers the STM study of the chosen polymers systems (see chapter 7 for the main AFM results). Firstly, the materials used as substrates for polymer deposition were imaged in the absence of a sample coating. The suitability of each of the surfaces for stabilizing the polymer whilst remaining both electronically and structurally unaltered during imaging was assessed. The first part of the study also addressed the defects, artifacts and anomalies which were deemed significant enough to impair image interpretation of any covering polymer layer.

The second section involved the characterization of the thin polymer films deposited on the substrates by both STM and AFM. The results in this section show how very thin layers of PMMA and PVP were deposited successfully on to the substrates and imaged by the STM. A technique utilizing line scans was developed to cross section the image and to reveal the tip path at constant current over the substrate and polymer regions. Variations observed in the line scan trace were found to increase in both amplitude and frequency over the suspected polymer regions of the sample. The polymer regions were then identified with additional data from appropriate AFM images (the force microscope was used as a complimentary technique in this context). The polymer film morphology and any subtle variations therein were imaged by STM. The surface coverage and thickness as a function of solution concentration was assessed. In addition, the uniformity of the films was estimated from the STM images and any differences observed between the PMMA and PVP uniformity, were related to the nature of the solvents used.

The third and final section introduces the effect of a plasticizing vapour on an amorphous PC film. The appropriate plasticizer treatment results in a significant change in the structure of the PC film, a change which is observed by both STM and AFM. Previous results [Cope, 1977] suggest that extensive

crystallization occurs during the plasticizer treatment. The previous studies achieved measurements on the sample by averaging techniques like Xray diffraction. This section shows how the STM can be used to ascertain the dimensions of the basic PC crystalline entities, a study that is developed much further in chapter 7.

Additionally the effect of varying the environment around the sample and the tip and the presence of the scanning tip so close to the sample is discussed. It was found that in many images a tip-sample interaction occurred. The damaging effect of both the STM and AFM tips are compared. The concequence of tip-induced damage of the sample in the context of further polymer imaging is discussed as is the effect of an environmental change in the system. The presence of water in the tip-sample gap is known to have an effect on imaging, this is also shown. The presence of other gases especially those which act as plasticizers are also discussed.

The main thrust of the chapter is to ascertain whether the STM is a viable technique for imaging polymer films. A simple test as outlined above could be if the STM images show a definite increase in structure between amorphous (PMMA and PVP) and semi-crystalline (PC) polymers. In addition, morphological measurements obtained from STM images were assessed as a change in film structure was observed between PC films exhibiting a low and high degree of crystallinity. The features observed in the latter sample can be compared and in some cases are superior to the images of the same material obtained by AFM. It should be noted that the crystalline entities observed by STM in this chapter are comparable with those achieved by the tapping mode AFM which is a technique developed especially to image soft materials.

6.2 THE SUBSTRATE

The materials used as substrates were Highly Orientated Pyrolitic Graphite (or HOPG), gold (evaporated onto freshly cleaved mica or onto a polished silicon wafer), and highly polished silicon wafers (although the latter substrate was only used for AFM studies on account of its insufficient

conductivity). The following is an account of the materials used as substrates for the deposition of polymers and initially imaged without sample coating by both STM and AFM.

6.2.1 HOPG

HOPG has been widely used as a substrate in STM work since the mid 1980's. The substrate is probably the most frequently examined surface to date, and a large amount of useful data has emerged from experiments in which it has been used. The images obtained in this study were found to be consistent with the accepted appearance of HOPG as imaged by many other groups [see for example Clemmer & Beebe, 1992; Albrecht et al, 1988; etc].

The STM and AFM images of HOPG on a large scale (low magnification) reveal flat terraces and the occasional large scale defect characteristic of the grade of HOPG used (figures 6.1). Intermediate scan sizes of several hundred nanometres in dimensions show clearly the extensive and flat terraces (figure 6.2). The smallest useful scan areas of about $(5nm)^2$ reveal the typical and frequently observed HOPG lattice. The periodic lattice structure contains features in the xy plane that are 0.246nm apart (see figures 6.3). The six-membered hexagonal rings that form the graphite lattice are shown in figure 6.4. Although the ring contains six carbon atoms, electronically and structurally these are not equivalent. The top graphite layer is displaced from the layer below and this results in three types of atom centre, labelled A, B & C and these sites are shown in figure 6.5.

Giant Corrugations in HOPG

The amplitude of the 'atomic' corrugations observed (i.e. measured in along the z axis) were sometimes more pronounced than the 0.2-0.4nm[Lawunmi & Payne, 1990] expected (see figure 6.6). The corrugations observed frequently in this study are not easy to explain as the expected corrugations from crystallographic data are less than an Angstrom. The generally accepted view [Coombes & Pethica, 1986; Soler, 1986 etc.] is that the graphite is very

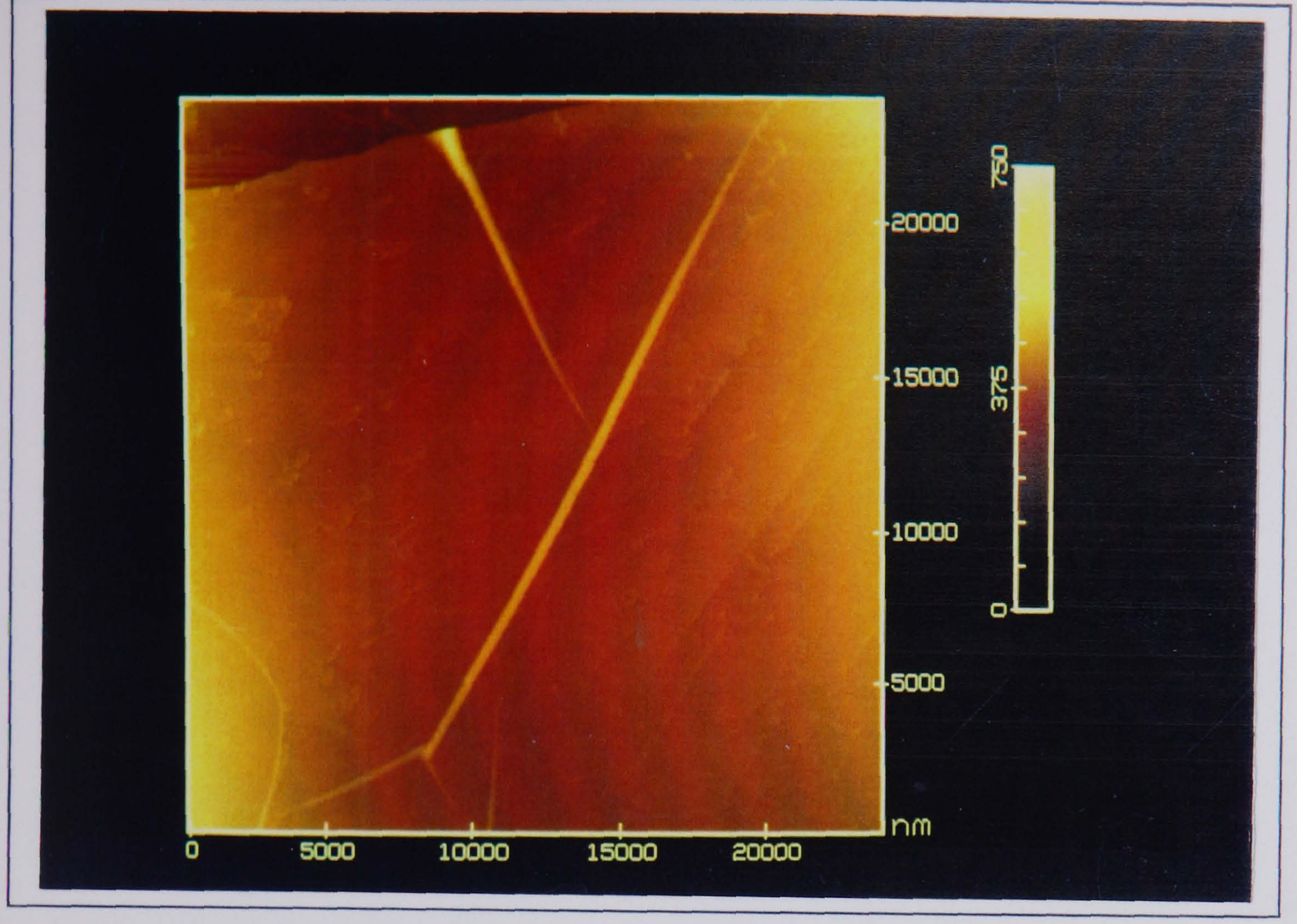

Figure 6.1: The graphite surface exhibits extensive terracing bordered by ledges a few graphite layers thick.

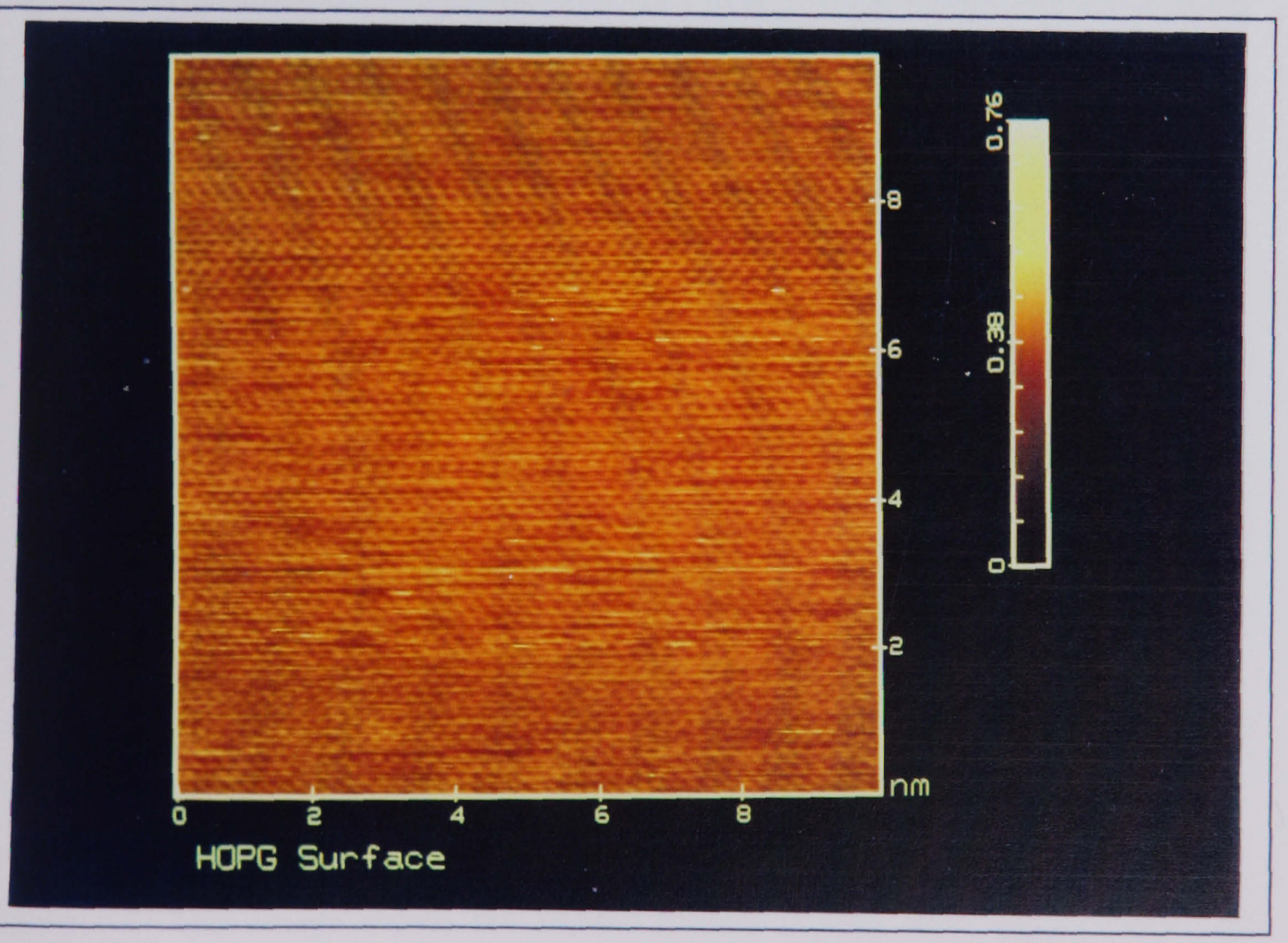

Figure 6.2: The graphite lattice is observed in this image of the HOPG surface at a higher magnification.

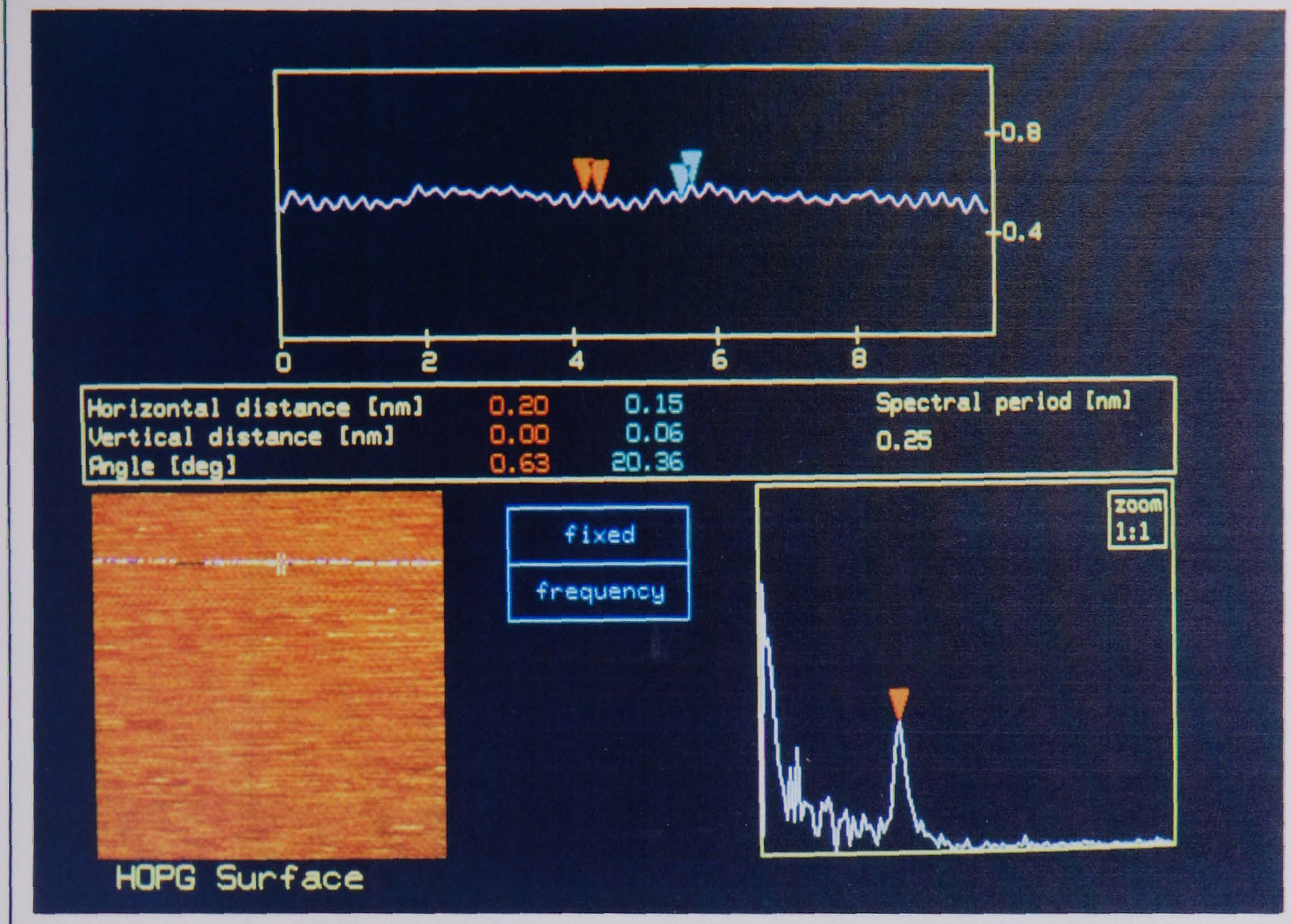

Figure 6.3: The line scan reveals the atomic corrugations and the frequency spectrum shows a peak at 0.25nm indicating the lattice parameter.

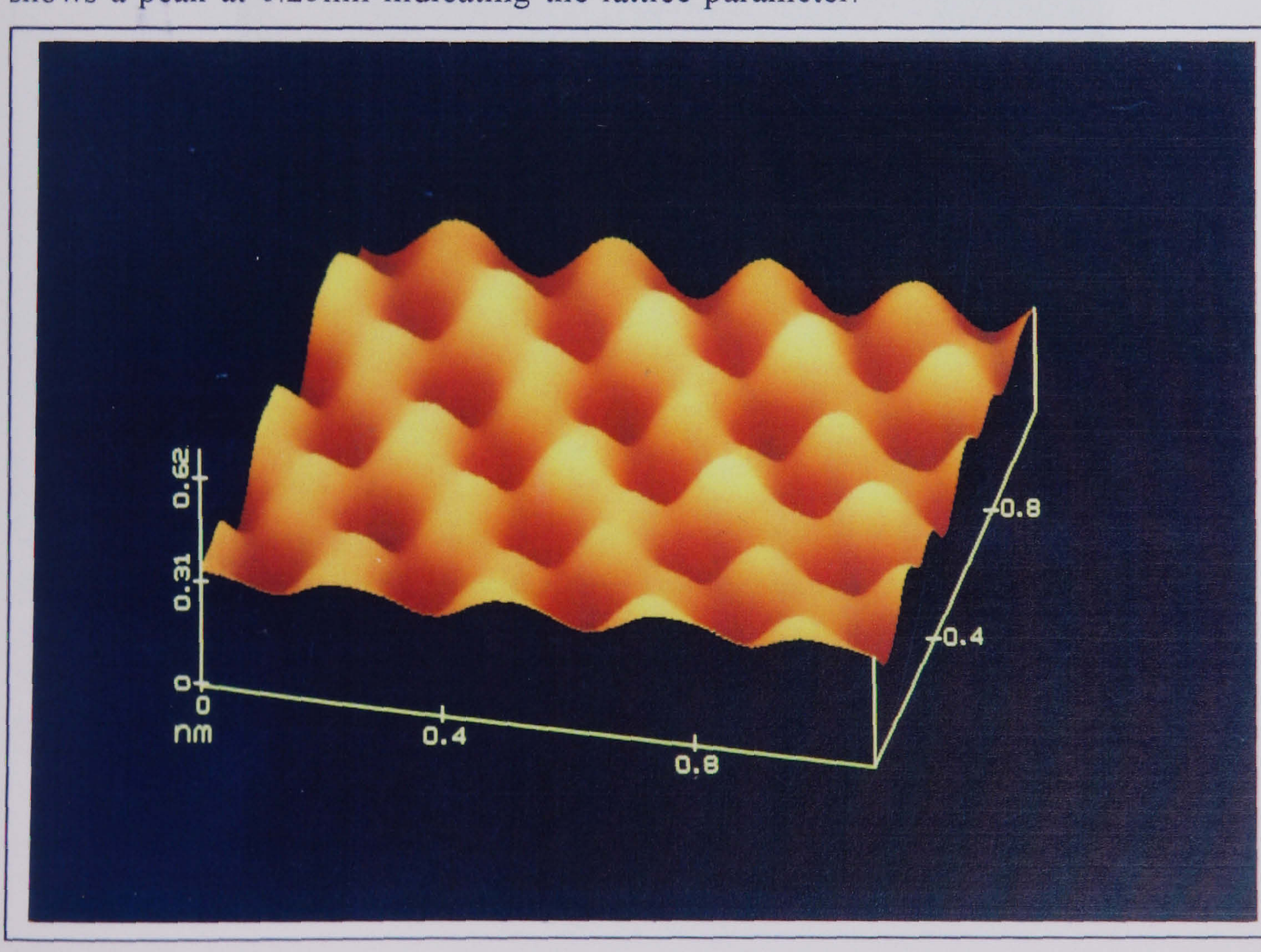

Figure 6.4: This image shows the HOPG surface at very high magnification. The atomic corrugations are easily observed and have a 0.246nm periodicity.

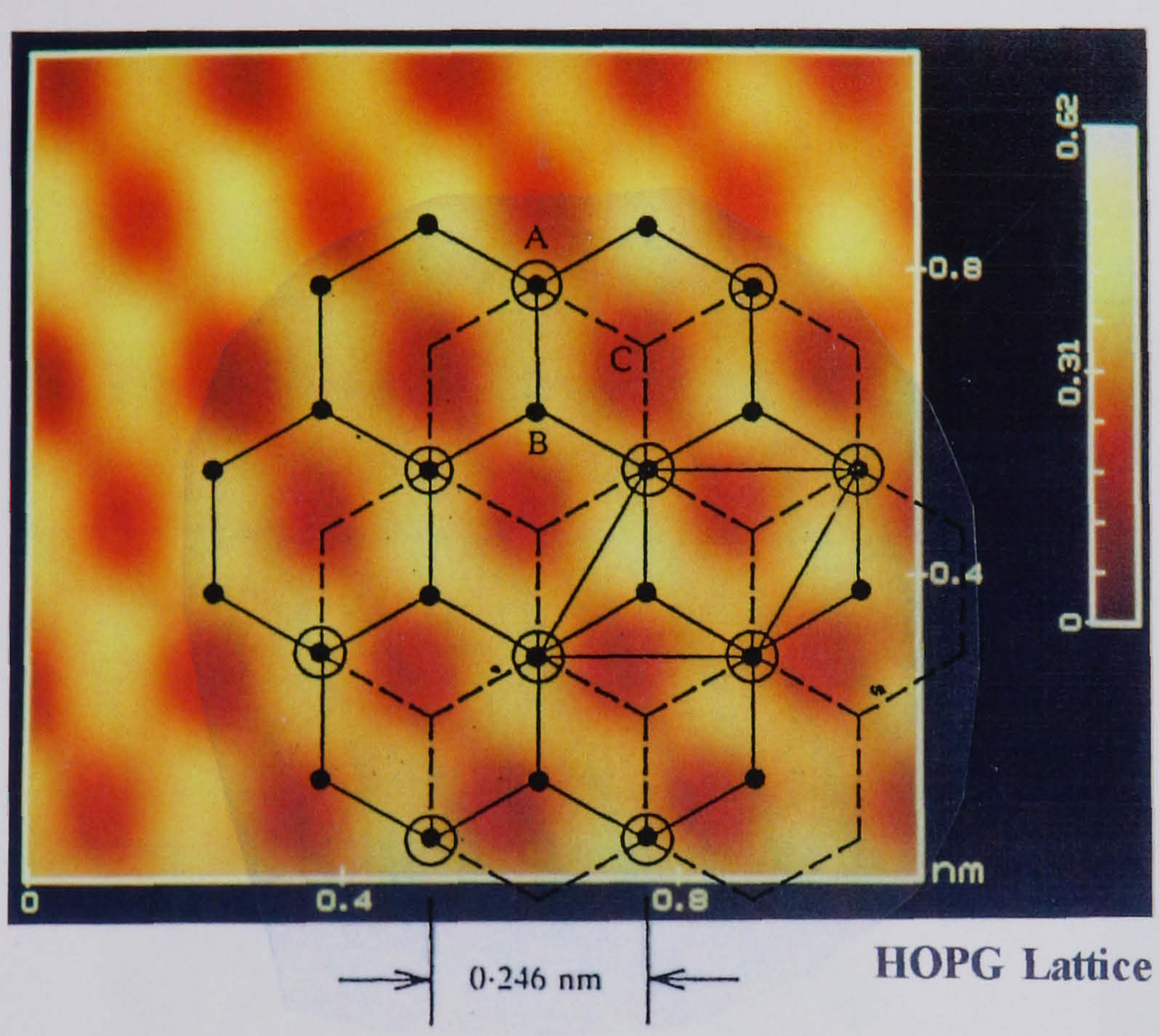

Figure 6.5: a) The HOPG lattice parameter corresponding to the position of the carbon atoms is well known (0.246nm) and can be used to calibrate the x,y movement of the STM tip. b)The theoretical and the measured lattice of HOPGare combined to identify sites A,B & C.

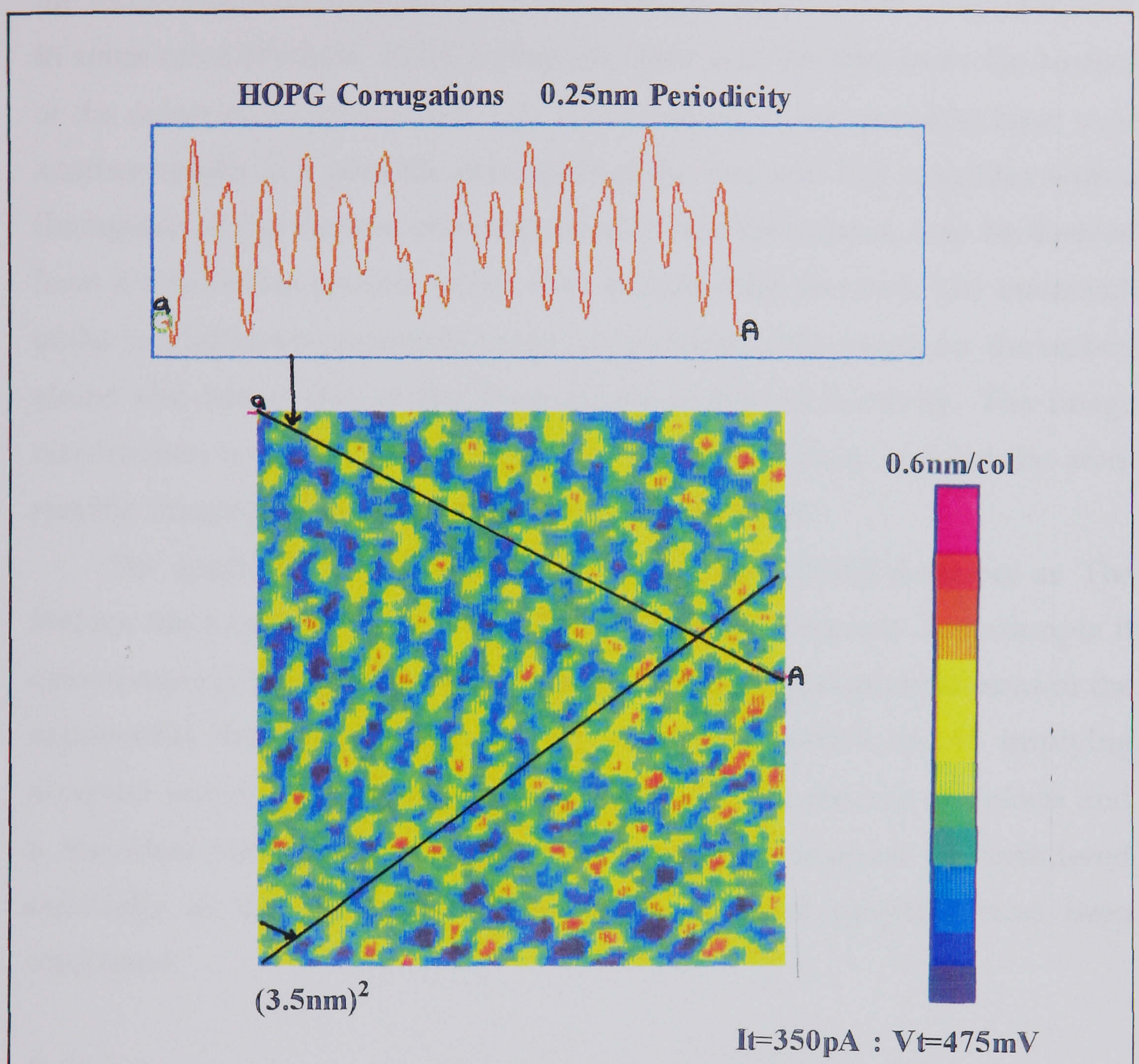

Figure 6.6: This figure shows the mismatch of one HOPG layer with another. This type of defect can also be confused with the image contribution from an adsorbed layer (sample).

soft, the tip comes into contact with the surface repulsive forces deform the latter. The contact lowers the barrier to the tunnelling electrons, giving an increased conductance. The resulting image shows artificially high peaks over the most compliant sites and very low troughs over the less compliant sites. In some cases [Pethica, 1986] a graphite flake may be torn from the surface of the substrate to form a new tip. The scanning of one graphite layer over another results in a periodic mismatch of the two and this coincides with a fluctuation in the current observed (in this case the current may be derived from a conduction process rather than a tunnelling process). The mismatch of the two lattices corresponds to the components of the lattice i.e. the carbon atoms and hence also to the fluctuations in the conductivity. The image construction contains data on the inter-flake conductivity and not the atom specific imaging more often associated with the STM.

The applicability of this phenonema that Chen[1993] describes as 'The Pethica Mechanism' depends on the sort of image obtained. For example it cannot explain the appearance of linear defects and dislocation patterns or the exponential decrease in current with separation (which would implying accepted tunnelling characteristics). However in the absence of defects and a non-ideal current-separation curve this mechanism must be considered especially as the presence of flakes and pieces of graphite have been confirmed.

Calibration

The HOPG lattice was used for calibration of the x and y pizeo movement. Numerous measurements of the HOPG surface were compared with the accepted value of the same surface. If a difference exists between measured and accepted values, caused perhaps by small differences in characteristics of the piezoceramic material, the software controlling Vx and Vy can be modified. The newly calibrated movement was checked by imaging and measuring the graphite lattice once again.

It should be noted that the dimensions of graphite in the z-plane, i.e. the corrugations of the atomic surface, are not accurate enough for calibration

purposes. The corrugations were found to fluctuate in amplitude depending on a variety of factors that include variability in tip shape, environment and on any tip-sample contact made inadvertently.

Graphite Defects

The results obtained, of the graphite surface by SPM, indicate that graphite complies with almost all of the specifications envisaged by Dietz & Hermann [1990] that describe the ideal substrate. HOPG was found to be inert, flat and conducting, however mechanical stability under the scanning tip and some polymer adhesion problems were encountered.

The unusual defects found on the graphite substrate are one of the main disadvantages of using this material for polymer deposition mainly because confusion between the substrate and polymer features may arise.

1) Flakes of Graphite (various shapes and sizes)
2) Linear defects including:
   - i) Ledges
   - ii) Helices
   - iii) 'Carbon Chains'
3) Fish-Net Defect.

The first type of defect noted is formed from flakes of HOPG. This defect was encountered by Everson & Helms [1992] and a similar defect discovered in this study is shown in figure 6.7. It is envisaged that a loose piece of graphite is perhaps lifted or scourged from the surface during sample preparation or by tip-substrate interaction. The hole from which it was torn may be evident (as in fig. 6.7) or else the flake may be carried some distance by the tip only to be deposited as a flake elsewhere and confused for example, with a small array of organic molecules. The transport of flakes of material by the tip and deposition on a non-conducting sample for example a polymer clump or a DNA molecule, is a suggested mechanism for image formation and was forwarded by Blackford et al in 1991. The movement of material is very

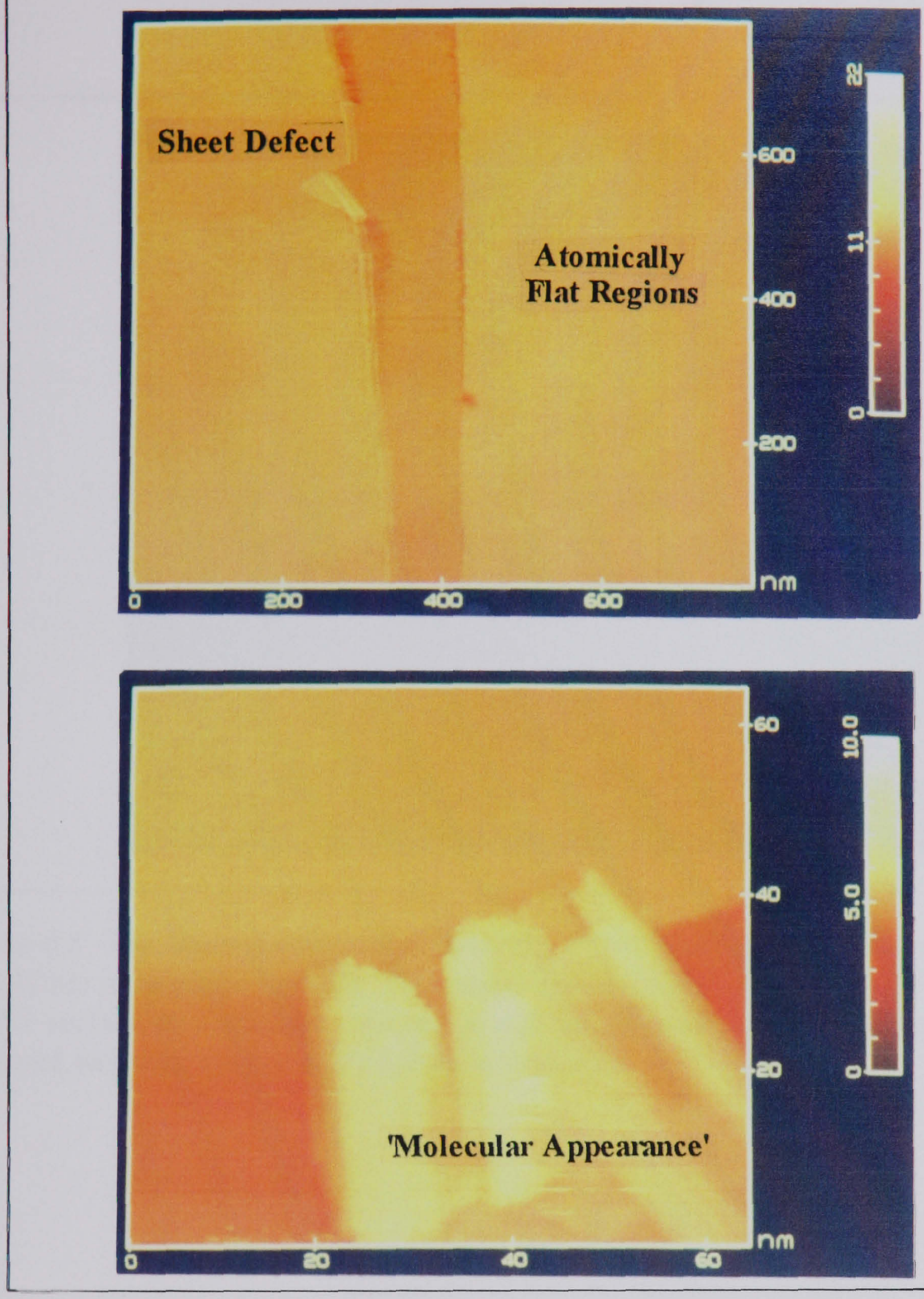

Figure 6.7: The STM tip can snag the ledges of HOPG as it scans. In this case flakes can be created which can be confused with islands of adsorbed sample.

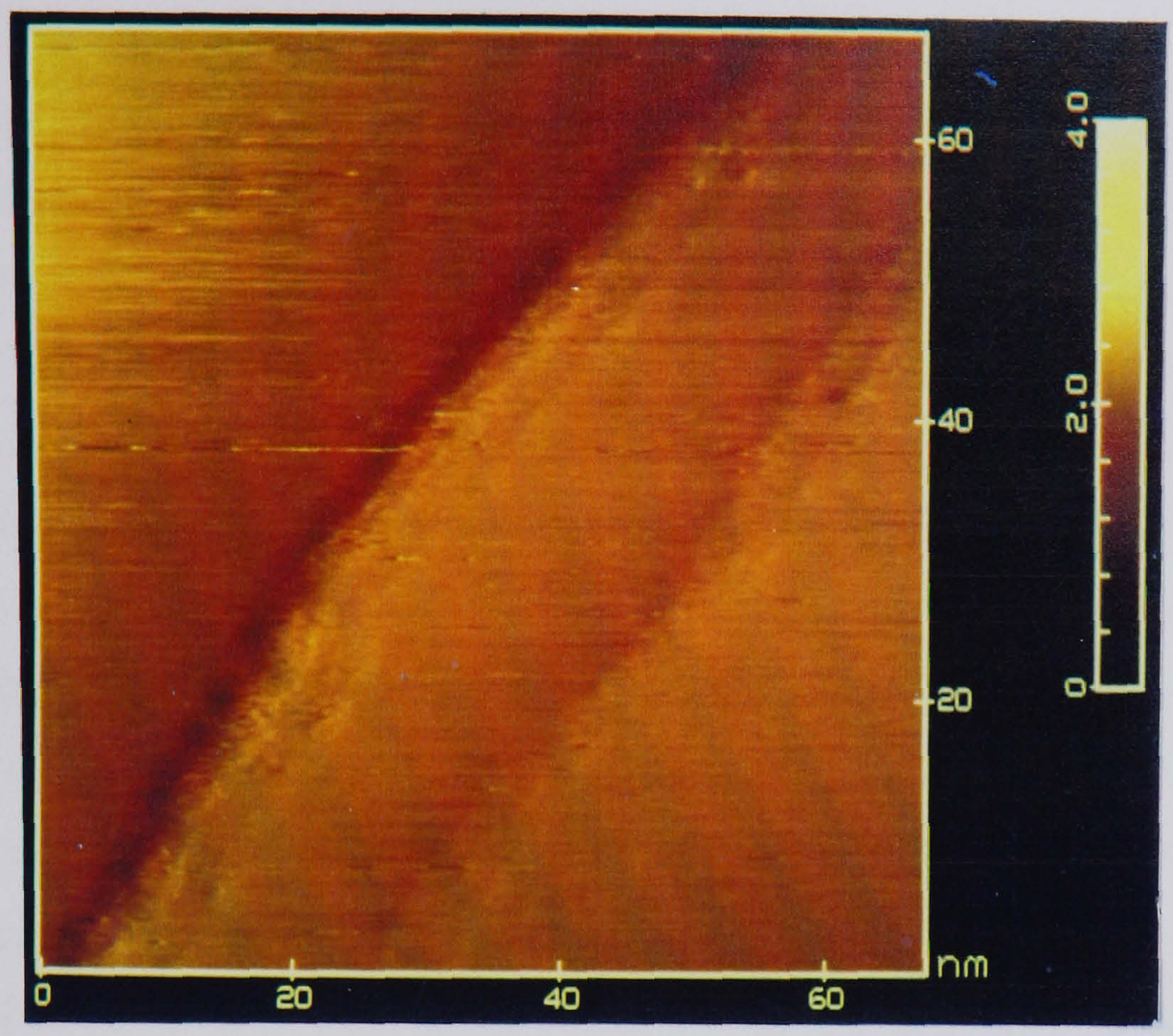

Figure 6.8: The linear features that cross the HOPG surface are easily misinterpreted as polymer or organic features. The image above was formed from a freshly cleaved HOPG surface and was not exposed to polymeric material. The feature can also be observed twisting, giving a DNA-like appearance

difficult to assess and the coating of the tip by a graphite flake may also result in exaggerated or impressive atomic resolution [Pethica & Coombs, 1986].

The next type of defect encountered was the linear defect on the graphite surface. There were three manifestations of this defect noted in this study and these were, ledges, helices and 'carbon-chains'. The first of these arise at the edge of the large flat regions on graphite. The absence of these defects in an image may indicate an artificially high quality surface and lend weight to the argument by Pethica[1986] outlined above. The problem with linear defects becomes apparent when in some cases, fibrillar like structures appear orientated at large angles to the ledges described above. For example figure 6.8 shows a feature which does not resemble the ledges but instead appears very similar to a twisting helix across the HOPG surface. Many groups have noted the similarity between these features and DNA molecules [Fuchs, 1994]. A state of confusion is relatively easily achieved as pitch angles and dimensions of such defects in HOPG match closely those found in other, non STM studies of DNA. This defect may be responsible for other claimed atomically resolved images of biological and organic matter including polymers.

The fish-net defect identified in this study has not been well documented elsewhere and an example is given in figure 6.9. The pattern may be a result of the cleaving process as discussed by Yang et al[1992] who suggests that the large forces exerted on the upper few layers of the graphite slab during the peeling process (by adhesive tape) results in the dislocation of the upper graphite layers. Other groups [Leggett, 1993] who have also observed this feature, demonstrates that this is a rare but important phenonema the formation of which remains unknown at this stage.

In general, the defects found in HOPG provided very confusing and easily misinterpreted images. However, by charting the defects accurately (as above), when a new image is first taken it is relatively straight forward to distinguish between the defect and the polymer regions.

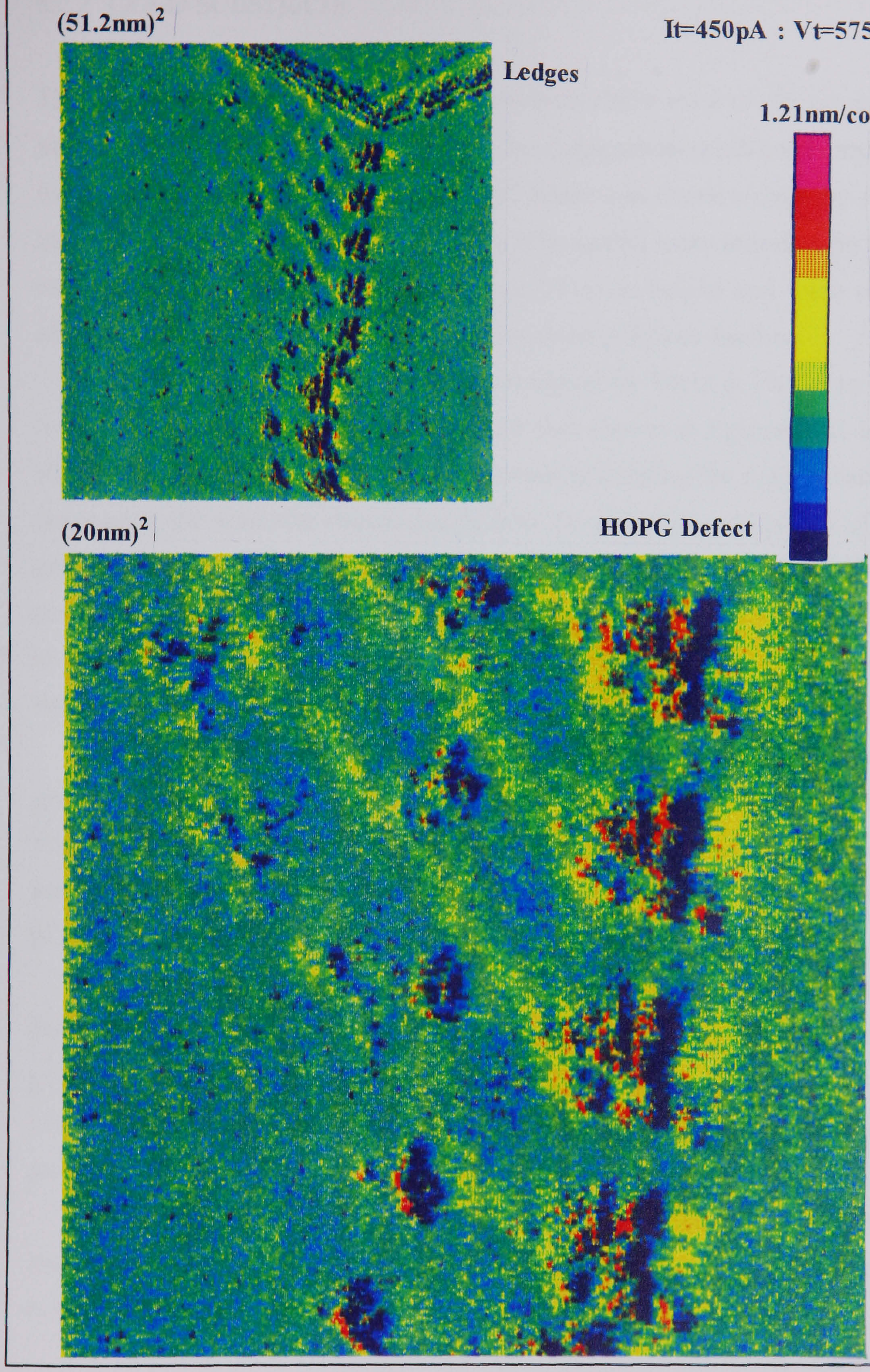

Figure 6.9: This image shows the 'fish-net' type defect on the surface of graphite. The cause of this type of defect is not known at present but may be misinterpreted as a regular array of organic molecules. Image size $(51.2nm)^2$.

6.2.2 GOLD SUBSTRATE

The gold was evaporated, under vacuum onto either mica or silicon and was imaged by both STM and AFM. Under the evaporation conditions employed, the morphology of the 100nm thick gold films was characterized by a grain like structure (on both mica and silicon). The grains were found to be tens of nanometres in diameter and a maximum 20nm in height and were used to allow direct comparison with nanometre sized polymer feature.

The substrate characteristics as stipulated by Dietz & Hamman [1992] include flatness. On a large scale, such as that shown in figures 6.10, images show an apparently 'flat' substrate. However increasing the magnification by decreasing the scan size shows clearly how the surface is comprised of small grains see figures 6.11. The images of gold were then cross-sectioned by line scans and the characteristic grain-structure measured in this way was used to asses the surface features of the grains. At high magnification, a general study of the gold grains revealed the topographical data given in table 6.1

The atomic resolution of gold is much more difficult to achieve than graphite because there is an absence of lattice enhancing mechanisms [e.g. Pethica, 1986]. On several occasions the gold was imaged with atomic resolution figure 6.12 and a lattice parameter similar to that found elsewhere [Green, et al, 1988] was observed.

The size and shape of the gold grains were as expected. Clemmer & Beebe [1992], in their study of evaporated gold as a substrate found a similar gold morphology. They also found that the size of the gold grains varied considerably under different evaporation conditions (i.e. temperature of the mica and vacuum pressure used).

Other methods of gold substrate production are detailed in other studies and involve heating the gold until reconstruction occurs or else growing extended flat areas of single crystal under stringent conditions.

There have been few accounts of defects on gold which may hamper the interpretation of deposited organic (polymeric) material but studies including one by Wilkins et al [1992] show that annealed gold substrates can occasionally exhibit super-periodicities which can be confused with organic

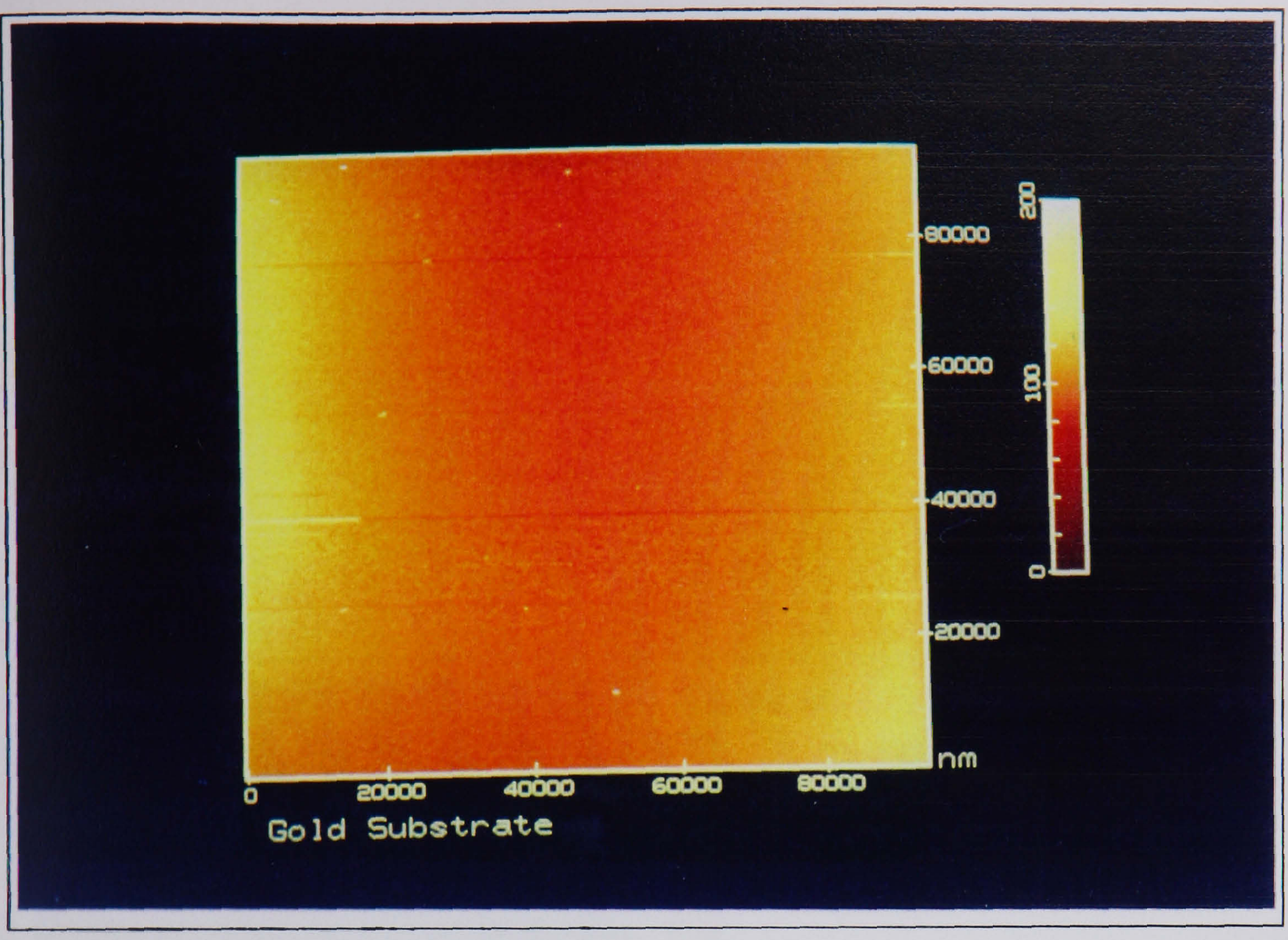

Figure 6.10: Extensive use of gold as a substrate for observation at low magnification is preferred over HOPG because of the superior uniformity of the surface. In this image the gold grains are not visible.

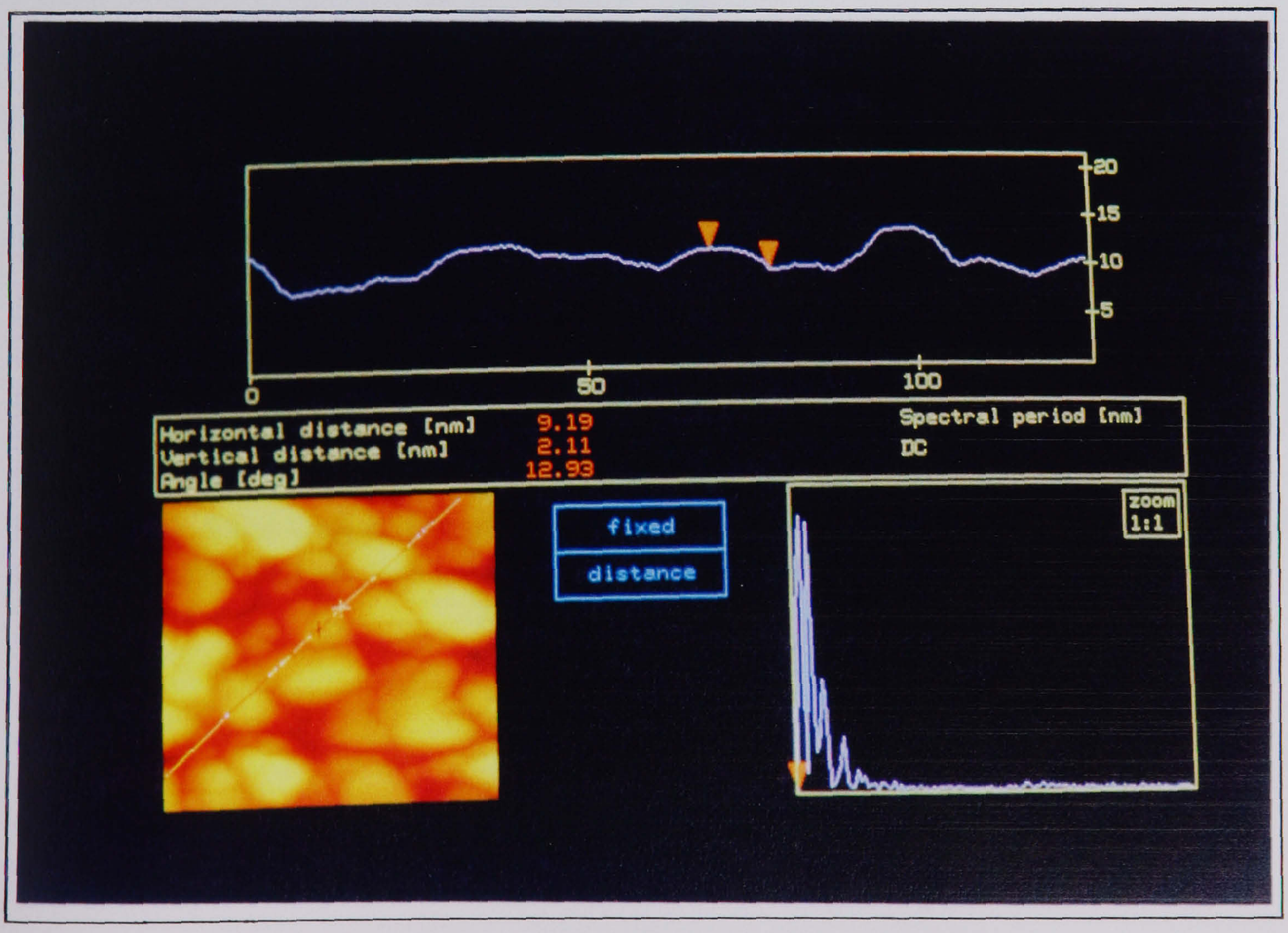

Figure 6.11: At high magnification, the gently undulating gold grains provide a useful substrate for polymer observations mainly because of the absence of features of the same size as those of the polymer entities.

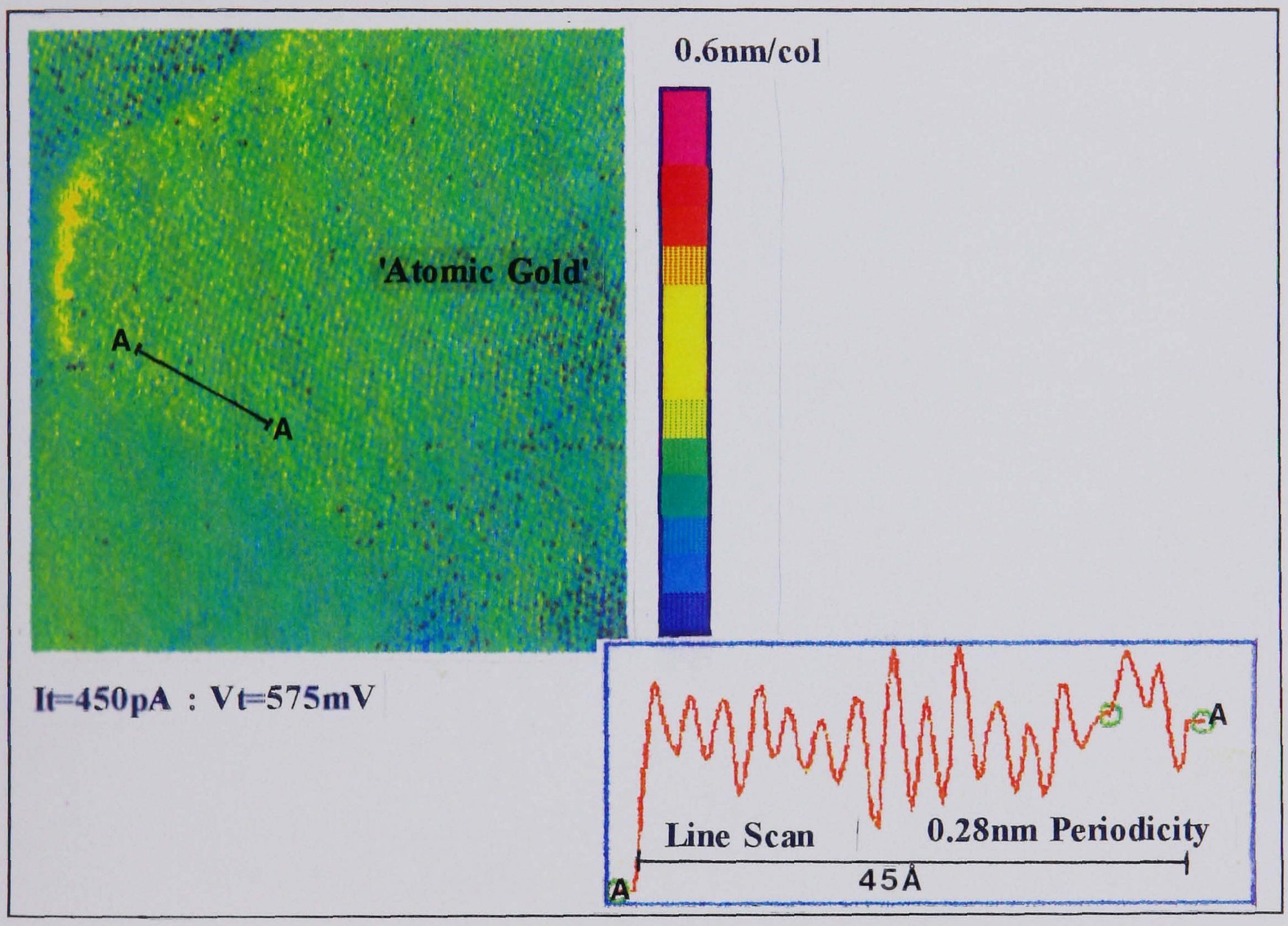

Figure 6.12: STM images of the gold grain tops revealing a periodicity commensurate with similar studies on this substrate [Green et al, 1988]. Image size $(18nm)^2$.

Grain Diameter	Grain Height	Grain Top Size	Grain Top Flatness*
(20-75)nm	(10-20)nm	(15-45)nm	(0.1-2.5)nm

Table 6.1

*This figure is a measure of the average z displacement within a given box area.

monolayers.

Tip Shape Assessment

The imaging of gold grains also provided a way of assessing the tip shape. Many SPM tips contain imperfections such as lop-sidedness or tip multiplicity. Studies by SEM and other techniques show the grains to be pebble-like and some SPM images clearly reproduce this (see figure 6.13a).

The presence of tip malformation results in unusual grain morphology including duplication. The image shown in figure 6.13b shows the result of a multiple tip imaging the grains. The tip was rotated by 90° and the duplication was also found to rotate. The tip shape can additionally influence the image, for example triangular or elongated grains are seen in images obtained from lop-sided tips. Under these circumstances tip replacement is the only method deemed satisfactory in restoring the quality of the image.

Polymer contamination of the tip can also change the image formed by the tip. Although for the STM tip, the polymer is unlikely to directly change the tip shape (instead acting to connect the tip to the substrate), the AFM tip is directly affected.

There has been some progress towards deconvoluting the SPM image to obtain a more realistic surface representation. Any SPM image contains a combination of data from both the tip and the surface especially if the surface feature is commensurate in size with the tip. For example where the sample contains a thin rigid protrusion which is smaller than the tip, the resulting image scan reveals that the surface protrusion images the tip. It should be possible to image the tip by using an ideal surface protrusion and to thus characterize the spatial configuration of the tip. The data would then be subtracted from any image formed by the tip in a deconvolution process. The final image would then more truly represent the surface. Some work on this matter has been done by Hu et al [1992] who deconvoluted images of DNA. Work by Snyder, Eklund and Stanley-Williams [1990] show the effect of the tip shape on atomic resolution on HOPG.

a)Usual Tip

b)Multiple Tip

Tip Induced 'Blurring'

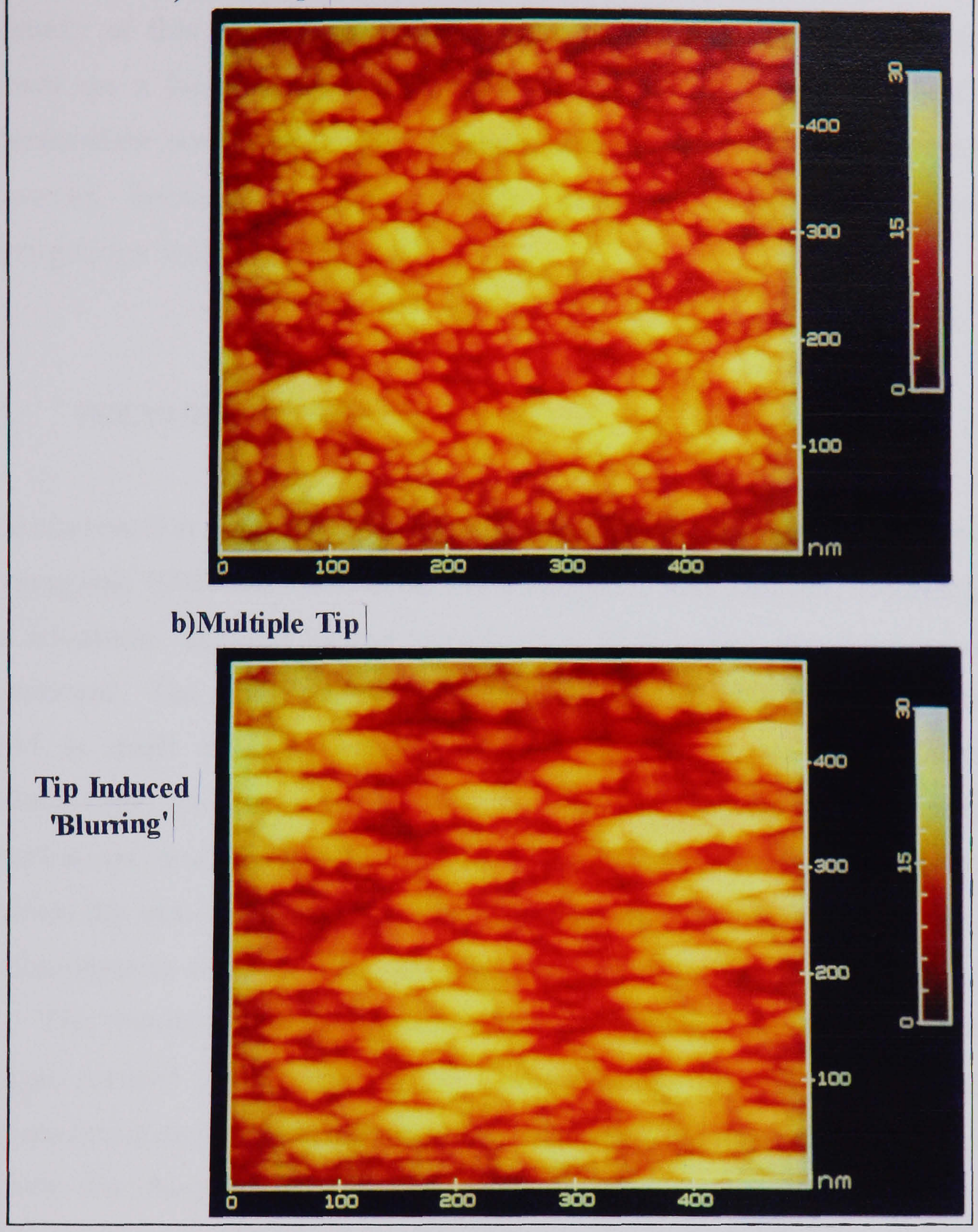

Figure 6.13: The effect of the tip shape on the image is readily observed by imaging the gold surface. a) The grains are normally hemispherical or pebble-like in shape but with an unusual shaped tip, b) the image changes subtly.

6.2.3 SILICON WAFER

A study of this surface for use as a substrate in force microscopy (AFM) shows on a large scale, extended flat regions (see figure 6.14). On an intermediate scale the surface flatness was maintained (see figure 6.15), however, because of surface oxide formation, atomic sized surface corrugations were not observed.

6.3 POLYMERS BY SPM

The observation of thin polymer films by SPM has been reviewed elsewhere [Travaglini, 1990, Blackford et al, 1991, Haggerty and Lenhoff, 1992 etc], and the advances allowed by the introduction of this class of microscopes are significant. The main problems with imaging and interpretation with the AFM is dealt with in other studies for example Burham, Colton & Pollock[1991]. However the imaging problems encountered where polymer samples are imaged by STM are concerned are far more serious notably because the samples do not conduct significantly in the bulk and conduction mechanisms in the thin films are not clear at this point (see chapter 2).

The results of the SPM study of the polymers presented here address images formed mainly from STM. Careful image analysis and the use of surface line scan profiling enhances the STM imaging of polymers. The results include the images obtained from several different polymers deposited on gold and graphite substrates and under a variety of sample preparation and imaging conditions. The film characteristics for PMMA, PVP and PC (in a crystalline and non-crystalline form) were assessed i.e. the polymer uniformity, coverage and structure. The AFM was used at this point to give a complementary analysis of the same film characteristics. The STM and AFM images were compared and a general film description forwarded.

Ultimately the results aim to confirm that polymers may be imaged by STM under certain conditions and that the complex film morphology, in addition to the general structure of thin polymer films may be obtained.

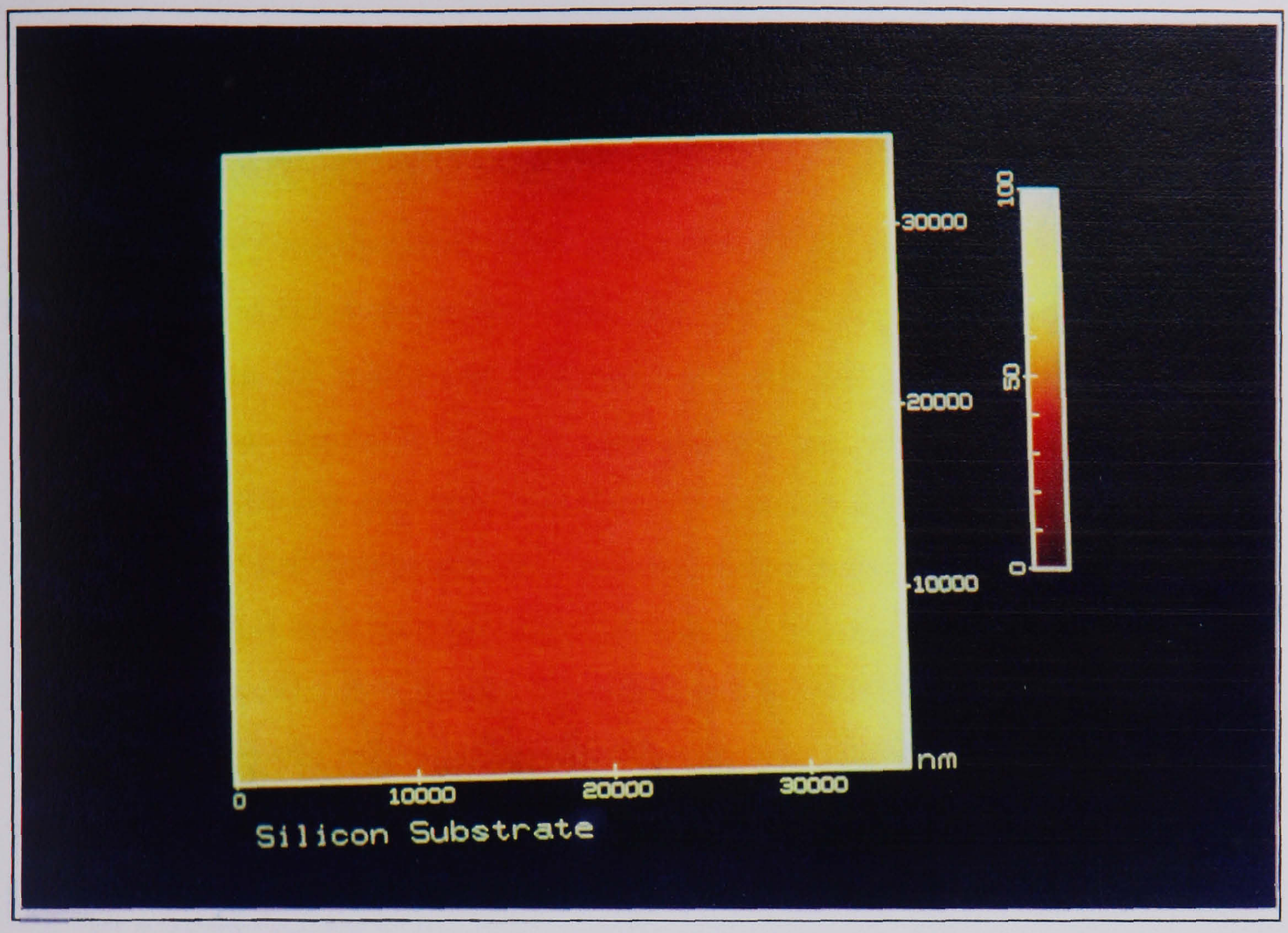

Figure 6.14: This image shows the highly polished silicon wafer on a large scale. The silicon surface associated with AFM imaging and not STM imaging (due to poor conductivity).

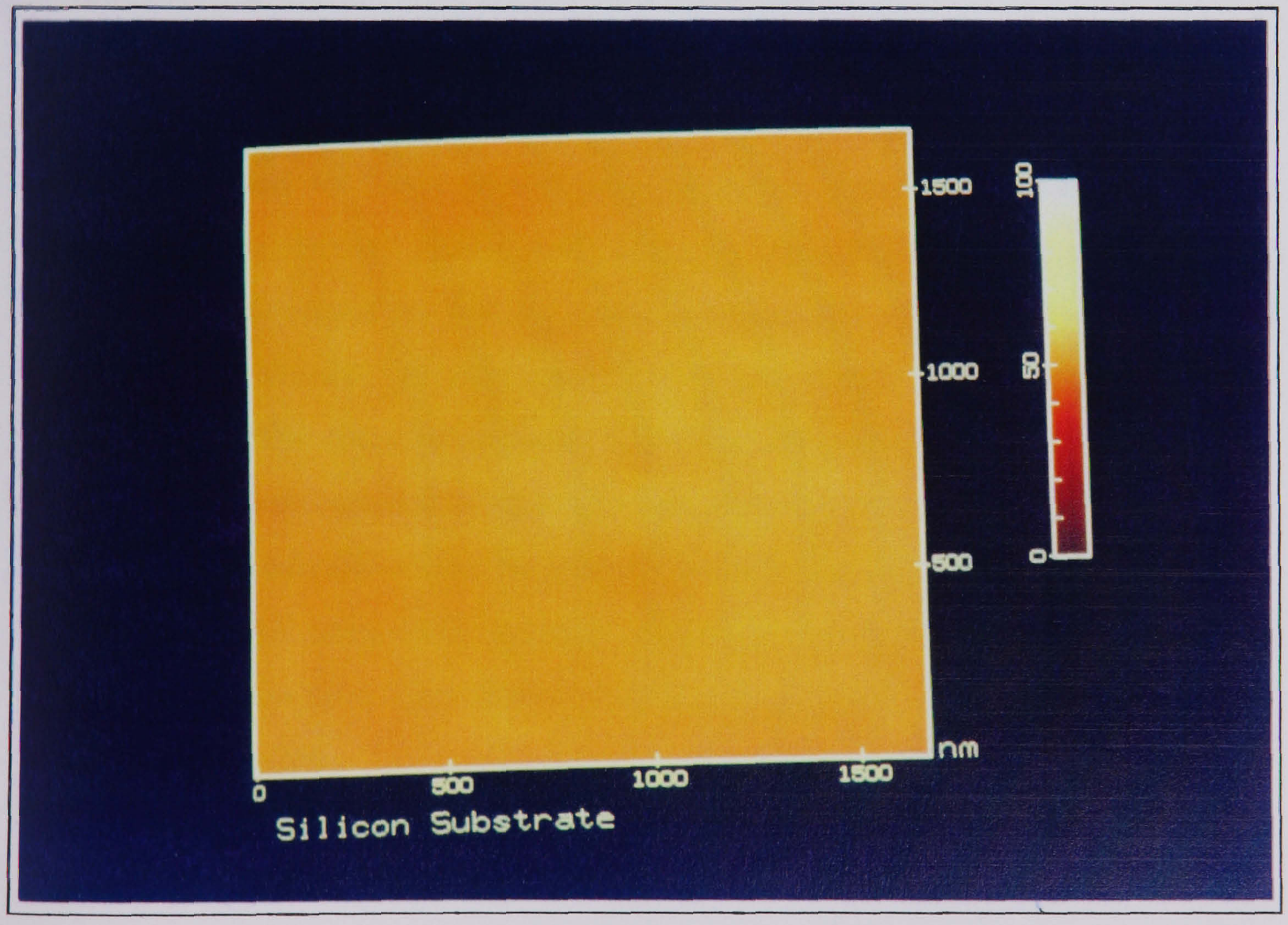

Figure 6.15: This image shows the silicon surface (as measured by the AFM) on a high magnification setting. The surface is very flat.

6.3.1 LINE SCANS

The imaging mechanisms that allow the STM to function at such high magnification are reasonably well understood for metals and semiconductors. The situation for insulating polymers is however more problematic at the present time. Infact no single mechanism has emerged as adequate in explaining existing experimental data. As a result image interpretation can be difficult. To aid interpretation, the use of line scan profiling of the surface was employed and its advantages discussed below.

If the conduction mechanism between the STM tip and sample changes during an individual scan, then a change in the nature of the image across the scan could be expected. To illustrate this, as a tip moves from an area of bare gold substrate to an area of polymer, the conventional barrier tunnelling is replaced by a complex, possibly varying conduction mechanism. The current-separation characteristics over the polymer may not exhibit an exponential relationship and may be considerably more linear.

To maintain a constant current, the tip may be forced much further away from or toward the sample, resulting in a large fluctuation in the voltage applied to the z piezo element. In an image this process will be manifest as a 'noisy' patch and may be enhanced by various filtering techniques. However by taking a line scan across the surface, the areas of polymer are shown (in this study) to exist where the fluctuation in the amplitude of the trace is greatest. The fluctuations in the line scan or FLS, may exhibit low spatial frequency components that are seen to map the underlying substrate of true large scale morphological features. On the other hand, the high frequency spatial frequency components arise from the variable conduction processes encountered over polymeric or other contaminant areas.

The images presented below, where the image interpretation is difficult especially given the false colour presentation of the images, show relevant line scans, cross-sectioning the image and traversing possible polymer regions.

6.3.2 SPM STUDY OF POLY(METHYL METHACRYLATE) or PMMA

Under a standard laboratory optical microscope (x200), PMMA formed an even film that appeared to coat all of the substrates, giving a faint colour change. The thinnest films were undetectable by optical methods.

STM OBSERVATIONS OF PMMA

Graphite Substrate

The PMMA film was imaged and a typical image obtained is given in the example shown in figure 6.16. There is a boundary between the amorphous polymer region and the very flat substrate. The flat substrate in the lower half of the image was confirmed by imaging of the typical atomic carbon in the HOPG lattice. The amorphous region of the polymer which dominates the image has some degree of ordering in the middle left of the image. It is not clear why the PMMA should order in this way although previous studies [Shen, 1991; Albrecht; 1988] have imaged 'ordered' regions of PMMA.

The thinnest films of PMMA on HOPG cast and imaged at high magnification show the atomic lattice convoluted with a twisting shape. The image shown in figure 6.17, is dominated by the HOPG corrugations. Spanning the image is a feature 0.8-1.1nm wide which is similar in width to a PMMA fibril [0.9nm - Dovek,1988]. The twisted region could be that of the polymer.

Explanations forwarded for the image mechanism in this case include Blackford et al [1992] who considered a flake of graphite torn from the substrate could cover the polymer fibrils and act as a conductive coat. In this case the image would be that of the graphite lattice with undulation consistent with the dimensions of the PMMA. Another explanation of the imaging of the polymer in this way could be from the modified electronic substrate approach outlined in chapter 2. Workers such as Miles et al [1991], McGonigal et al [1992], Rabe et al [1992] and Eng et al [1992] suggest that the STM images the interaction of the polymer with the substrate (provided it is sufficiently thin to fit inside the tip-substrate gap). The interaction modifies

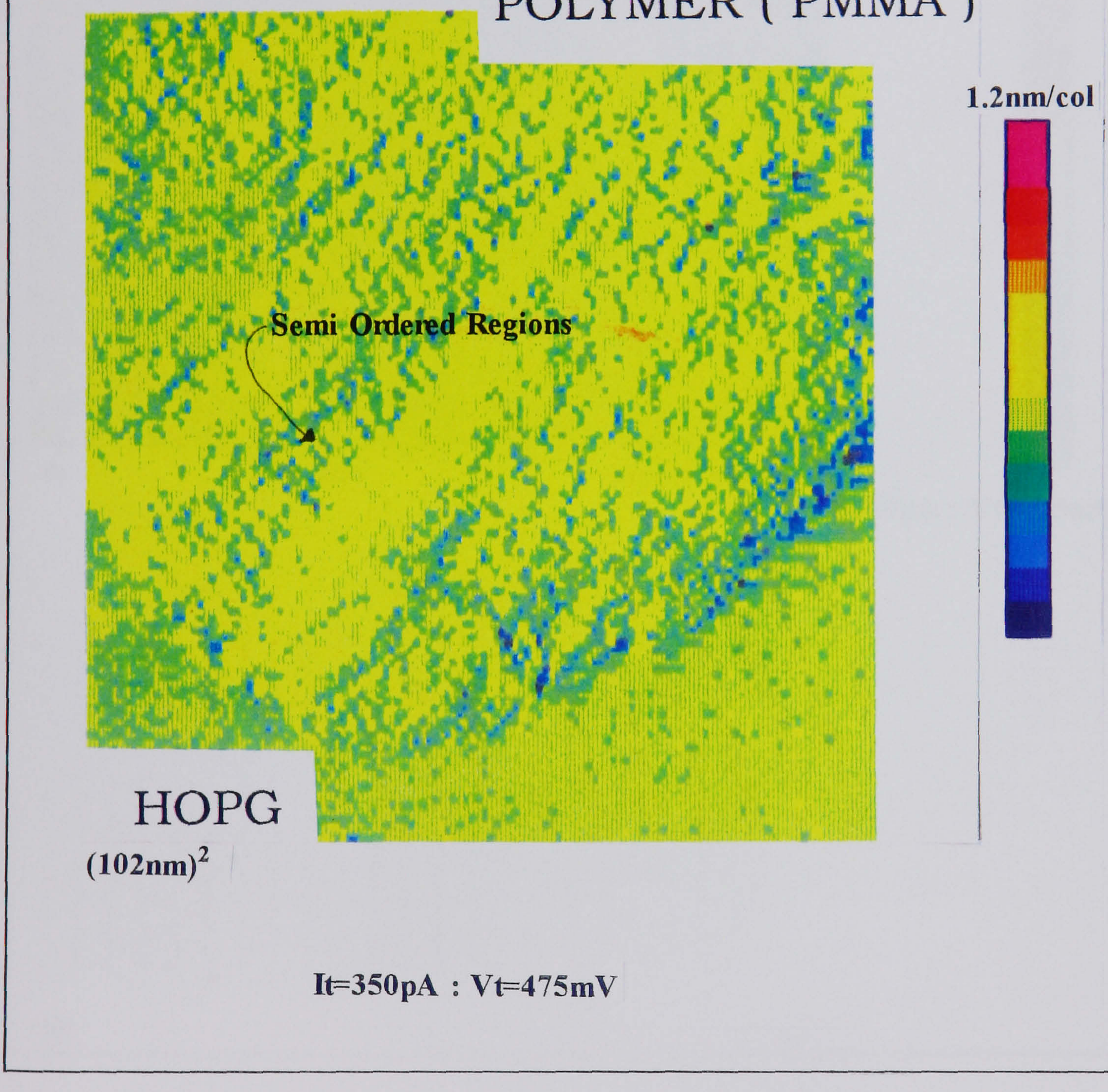

Figure 6.16: This STM image shows a typical image associated with the polymer coated HOPG substrate. The polymer region is much rougher than the smooth HOPG. There are some quasi-ordered regions on the polymer which may indicate a degree of tip-sample interaction. However in general, polymer film morphology, coverage and uniformity may be obtained from such images. Image size $(102.4nm)^2$.

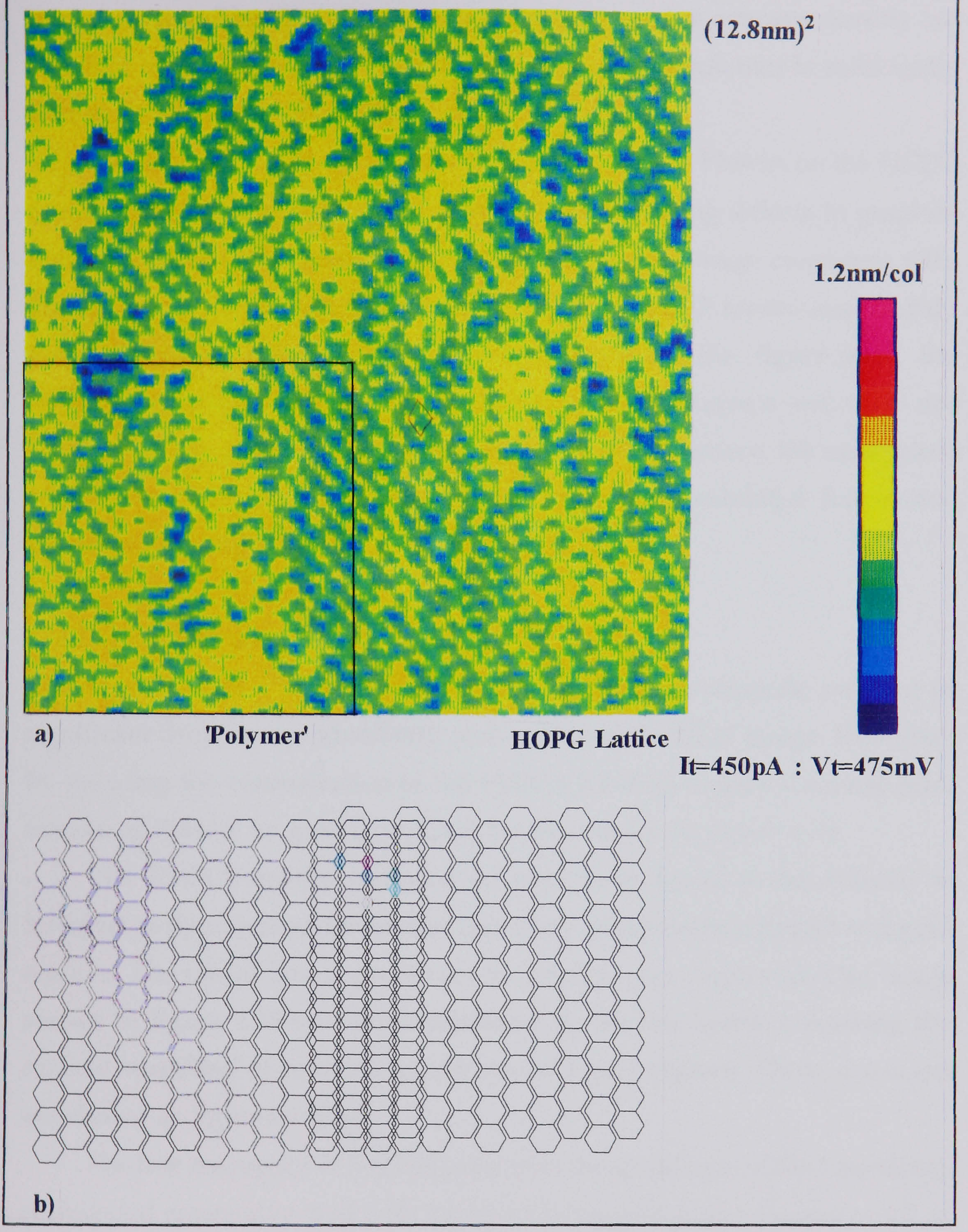

Figure 6.17: a)This STM image of a thinner PMMA film coated on an HOPG substrate reveals complex surface features. The film is likely to be thinner than the tunnel gap and the image is expected to comprise of both polymer and substrate features. This image is clearly dominated by the HOPG lattice (indicated), however the boxed region highlights a linear portion of slightly raised substrate. b)The appearance of such a region may be due to the polymer modifying the electronic surface. However it is equally likely that the feature is due to a dislocation in the HOPG lattice. Confusion of this nature hampers image interpretation and as a result, gold substrates are increasingly being used. Image size $(12.8nm)^2$.

the electronic surface of the HOPG to an extent dependent on the strength of the interaction. The STM does not necessarily image the polymer directly but its effect on the substrate. This situation arises if the polymer is sufficiently thin to fit inside the tip-substrate gap.

On the other hand, the presence of any amount of PMMA on the HOPG can be questioned in view of the multitude of confusing defects in graphite discussed above. The most likely defect to cause an image consistent with that in figure 6.17 would be a mismatch in two HOPG layers, one slightly above the other. However in this particular sample (i.e. figure 6.17), the twisting formations extended over the entire HOPG surface and were not confined to any particular area (like figure 6.8). Furthermore, the same piece of graphite, imaged before the polymer deposition exhibited flat atomic planes at this magnification.

Gold as a Substrate.

The deposition of a thick film of PMMA on the gold substrate resulted in significant drop in reproducibility and quality of the STM image. However, by reducing the concentration of the PMMA solution to give a thinner film, images of PMMA on gold is typified by that shown in figure 6.18.

The PMMA images obtained on gold were found to be difficult to interpret as there was an ill-defined boundary between the polymer and gold regions. The use of line scans across the surface was employed. The image shown in figure 6.18 was cross-sectioned by six line scans, traversing the regions suspected of containing polymer and gold regions. These line scans are shown as figures 6.19a-f.

The low frequency FLS (Fluctuations in the amplitude of the Line Scan), correspond reasonably well with the underlying gold grains (as measured on bare gold) although there is an increased high frequency FLS component in general across the whole surface.

The regions in which the polymer film may be thickest include the middle left of the image. This region is cross-sectioned by many of the line scans (e.g. figures 6.19b, c & f) and in all of these cases, the FLS are rapid with a high spatial frequency. The amplitude is also increased in this region.

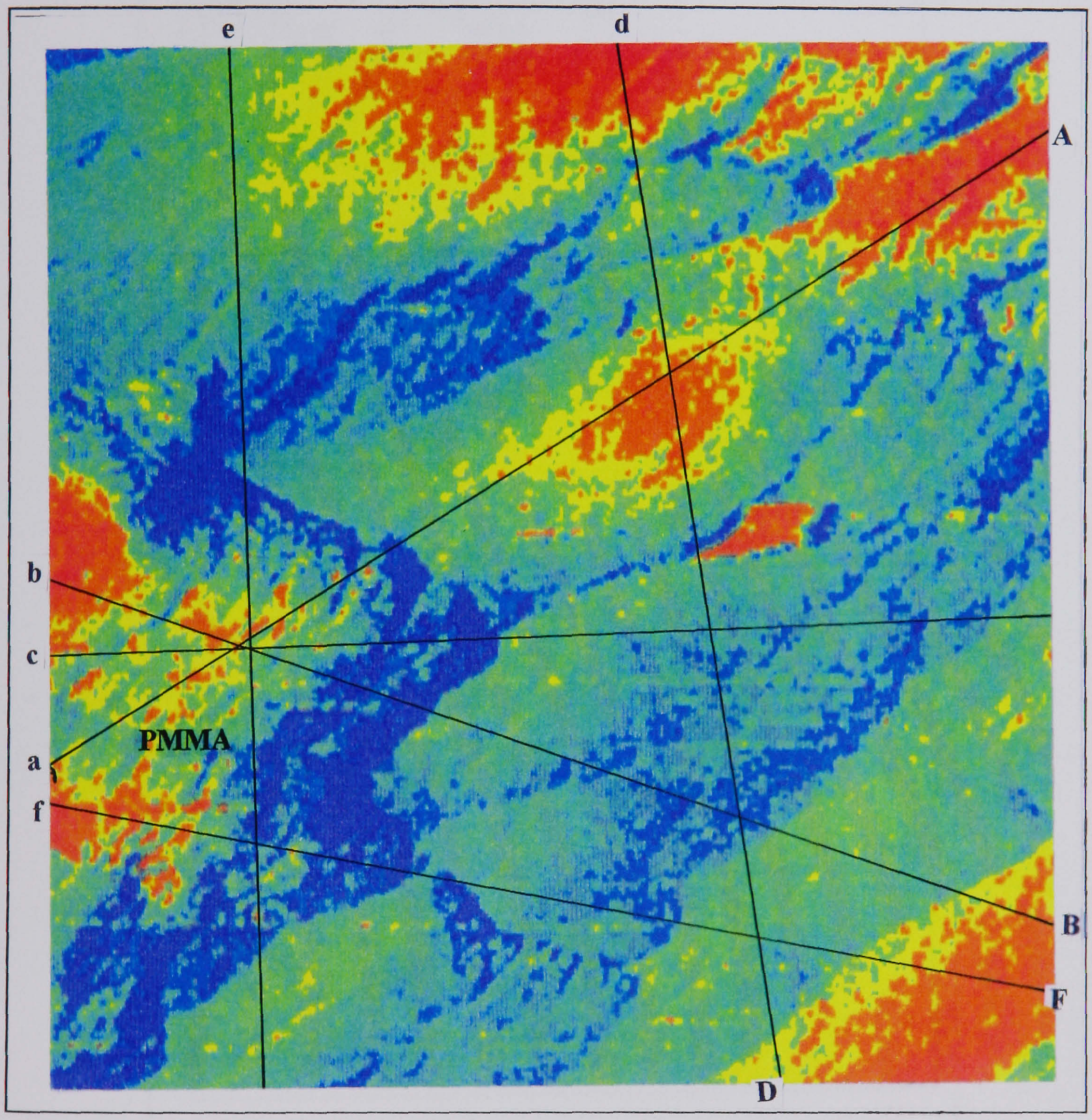

Figure 6.18: The casting of a five nanometre (approximately) thick PMMA film on to the gold substrate gives an STM image that contains both gold grain and polymer-like features. The interpretation of this image is hampered because of the lack of a clear boundary between the polymer and gold regions (although this fact suggests that the film forms a very even coating across the substrate). To aid interpretation, a series of line scans were made that cross-sectioned the image. Image size $(200nm)^2$.

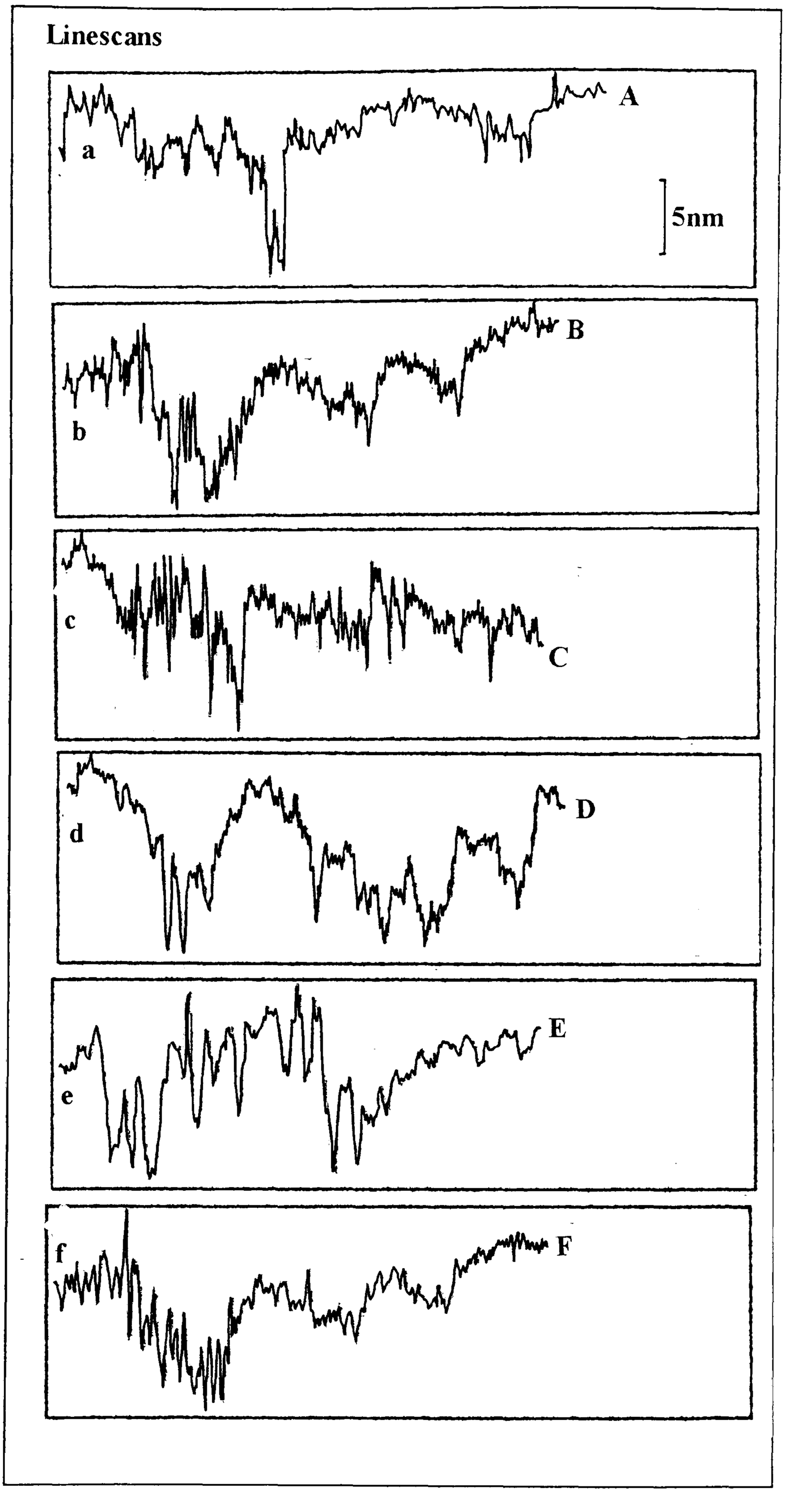

Figure 6.19a-f: A series of line scans (indicated in figure 6.18) were used to aid image interpretation of the polymer coated gold sample. The fluctuation in the line scans (FLS) are observed and low frequency components attributed to the underlying gold substrate. High frequency FLS were attributed to the presence of the polymer on the sample.

Line scan 6.19b for example starts in a region dominated by large amplitude, high frequency FLS and then traverses approximately three gold grains (see the schematic representation given in figure 6.20). The line scan clearly reveals four grains in total; the FLS over the first grain are greater in amplitude compared with the others and the grain is probably covered in a thick amount of polymer. The remaining three grains although consistent in size with the results obtained on bare gold, have FLS levels increased by only a small amount. This increased FLS could be attributed to a thin layer of PMMA.

The rough area that resemble furrows and ridges in the thick polymer, can be located at approximately eight different locations within this one image and these positions are confirmed by further line scans.

The thin and even coating is expected from the film forming properties of PMMA on gold investigated in the present study by the AFM (Nanoscope III). Observations of the PMMA film deposited on the gold substrate show a film of varying thickness, completely covering the gold. A typical example is seen in figure 6.21. The morphology of the underlying grain structure is clearly visible through the diffuse and shroud-like PMMA coating. The polymer layer itself although evenly coating the gold, is in places too thick for the substrate to show through.

It is clear that both the STM images and the AFM images of the PMMA layer show a film that is evenly coated across the substrate, with the occasional thicker area. Both the STM and AFM images reveal the gold grain morphology modified by the presence of the polymer. The modification of the grains is observed by the AFM as a covering layer of diffuse material and in the STM as an increase in the amplitude of the fluctuations in the line scan. The AFM did not reveal any structure of the polymer film although this situation was different with the STM which revealed some ridged and furrowed regions

The typical 'ridged and furrowed' polymer region seen by other users and discussed above were identified in various parts of the film. The film

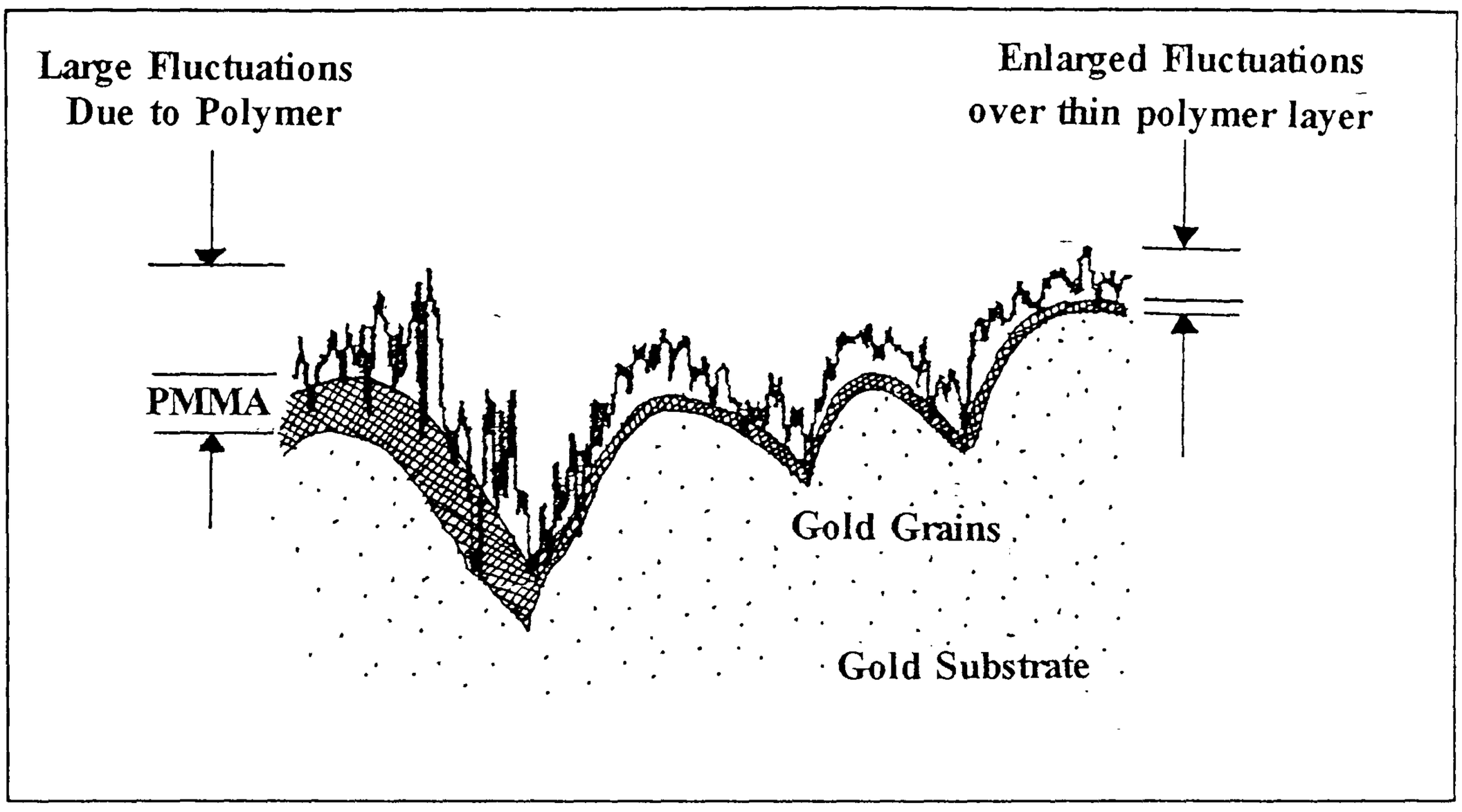

Figure 6.20: This line scan given here, shows the probable location of the regions of PMMA on the sample. The increased fluctuations-generally across the sample, in the line scan are associated with an unusual and possibly variable conduction mechanism within the polymer. Thus the position of the polymer can be deduced.

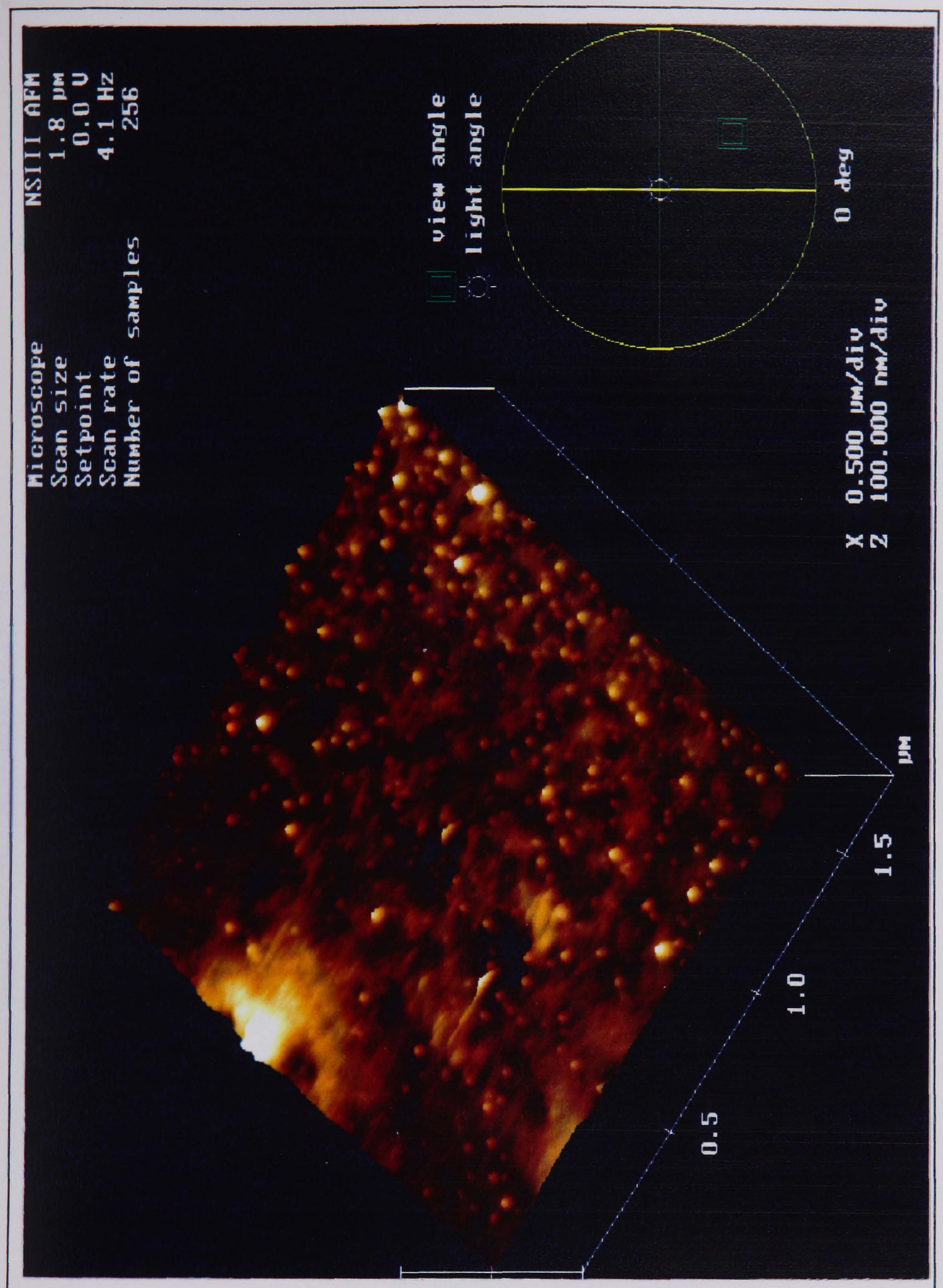

Figure 6.21. This AFM image of the PMMA coated cold sample, clearly shows both the gold grain and diffuse polymer morphology. The polymer can be observed covering some grains and obscuring them completely, but in places the film is thin enough for the grains to show through. This image is consistent with the STM image of the same film given above (figure 6.18).

morphology in these regions is similar to that imaged by Albrecht et al[1988] etc and were characterized by highly exaggerated fluctuations in the line scans that cross-sectioned them. It is proposed that these regions occur in areas where the PMMA layer is thickest. Away from the 'thick' polymer, the presence of the film was only detected by a slight increase in the usual line scan fluctuations.

6.3.3 SPM STUDY OF POLY(VINYL PYRROLIDONE)

PVP was not easily cast from the water solution to the various substrates, particularly HOPG and gold, due to the hydrophobic nature of the surface [Blackford, 1992]. The droplet only evaporated after several hours in a desiccator. On observation by the optical microscope, a multitude of tiny globular particles was seen.

STM OBSERVATIONS

HOPG as a Substrate

The PVP clumps as observed under STM were not easily locatable. However figures 6.22&6.23 both show small, round edged clumps. The underlying graphite defects are clearly observed in figure 6.22a and typified by long straight lines and rectangular pieces. In contrast the rounded clumps (not apparent on bare HOPG) cannot be mistaken for any HOPG defect yet studied [Blackford, 1991; Clemmer & Beebe, 1992; Everson & Helms, 1992]. The clumps also exhibited an increased amplitude and frequency in the FLS. From the PMMA study this indicates the presence of polymeric material. The clumps were assumed to be composed of PVP and cover approximately 5-15% of the surface. The coverage was only weakly dependent on the concentration of the solution from which the films were cast.

No PVP fibrils were observed emanating from the bulk clump as although HOPG atomic resolution was achieved around the clumps, the lattice did not appear to contain fibrils.

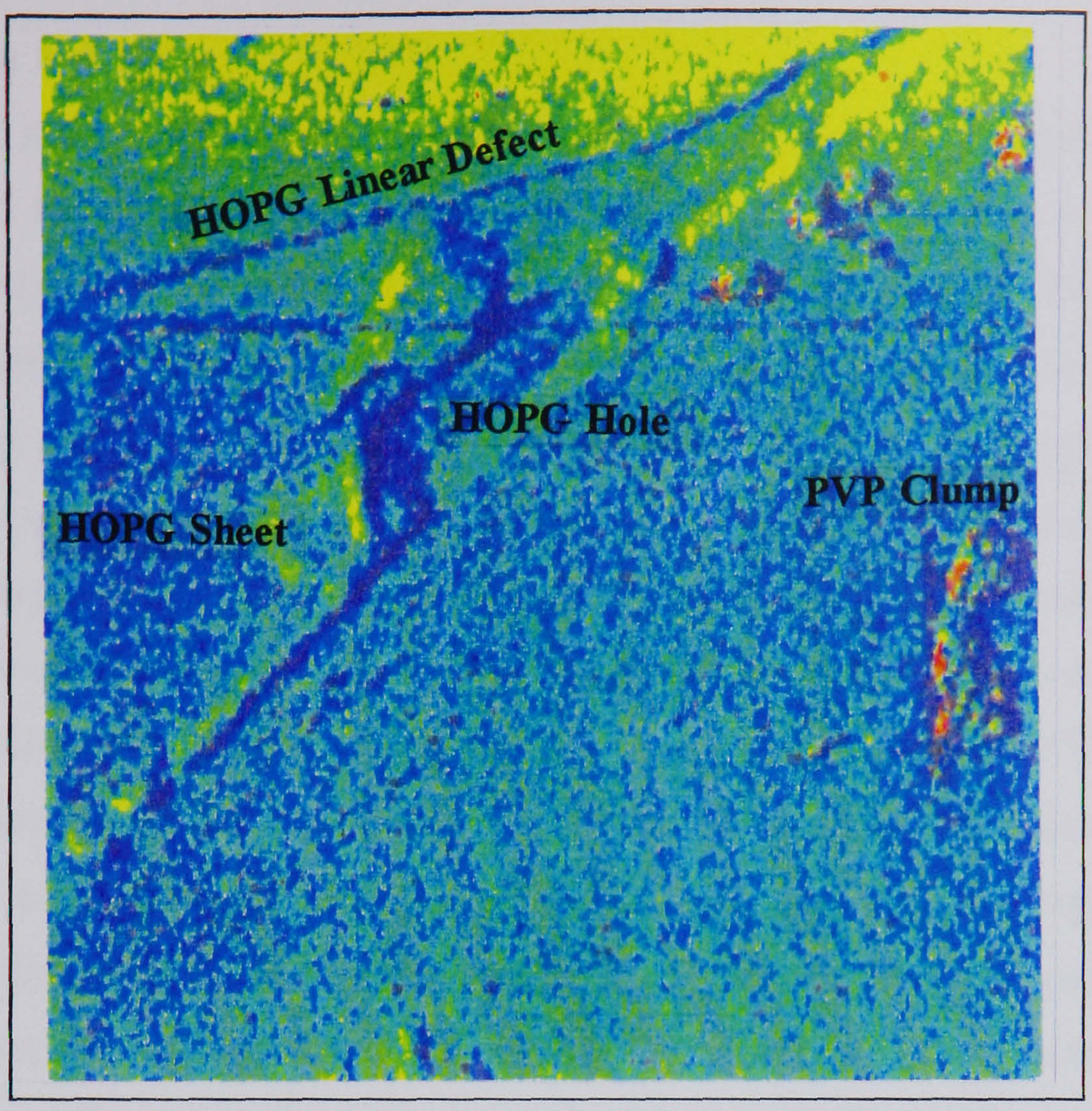

Figure 6.22: An STM of PVP deposited on HOPG. The image shows an isolated area of PVP and an extensive area of disrupted HOPG surface. The defects are both linear and sheet-like. A hole from which the material has been torn can also be observed. The PVP clump is very rough in comparison to the HOPG and has curved boundary with the HOPG, indicating poor sample adhesion. Image size $(102nm)^2$.

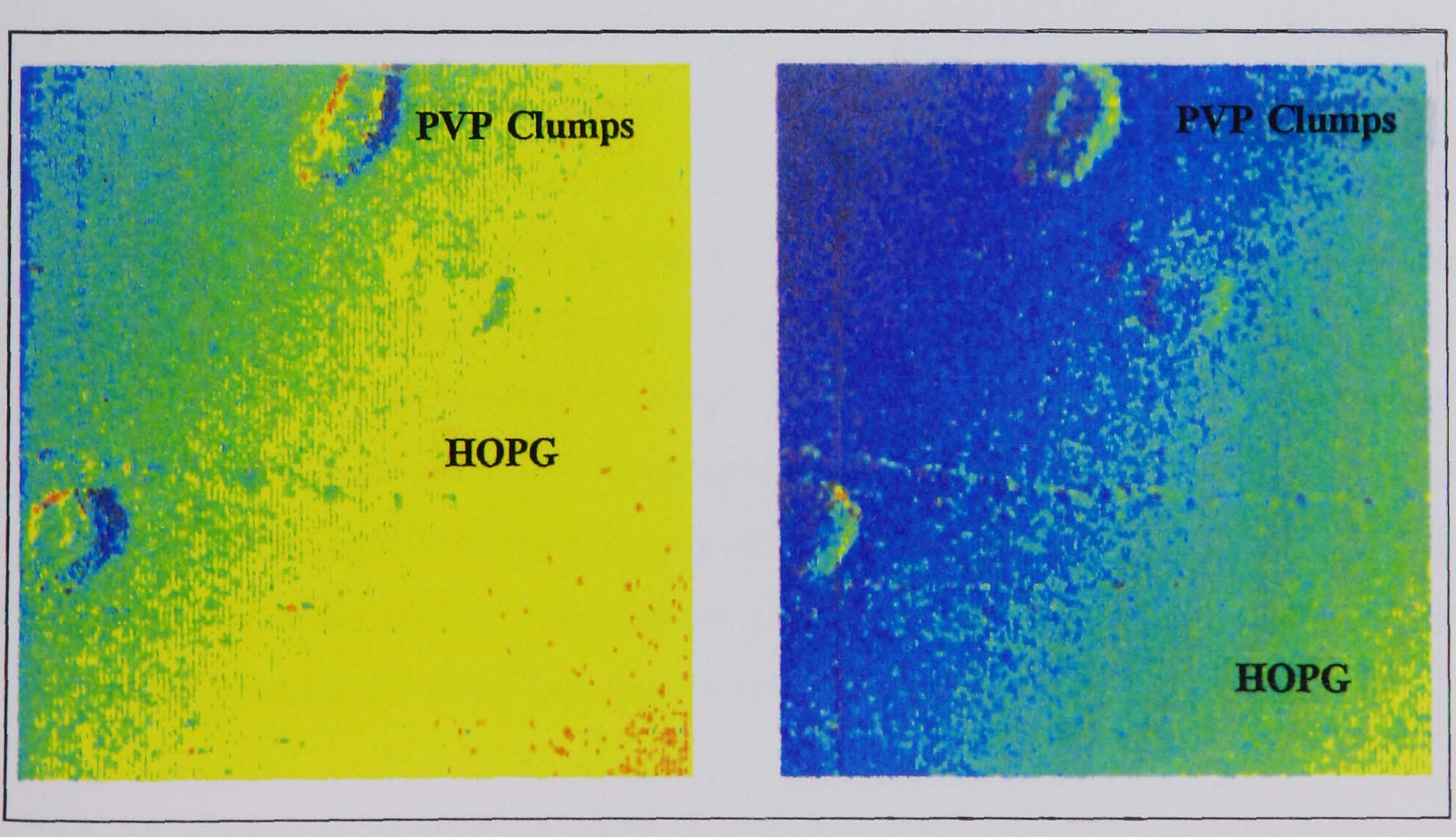

Figure 6.23: This image shows the odd and even scan directions obtained by the STM used [Shen, 1991]. The images show rounded clumps of PVP on the surface of HOPG. The HOPG lattice was observed between and around the large clumps, indicating that the polymer adhered poorly to the substrate. Image size $(500nm)^2$.

Gold as a Substrate

The STM study of PVP on gold utilized the high resolution small scan range head and the frequency of polymer findings was low due to a low surface coverage (see the AFM study). In the absence of recognizable PVP areas, the gold grains were found to be very smooth and the amplitude of the high frequency component of the FLS across the grains were amongst the lowest of any measured even including the bare gold. This indicated that away from the PVP regions, the gold was remarkably contaminant free, clean and stable.

The sample was searched systematically and PVP regions were observed in approximately 10% of the images. The appearance of the PVP area was reminiscent of a 'glacier' amongst hills or of jelly amongst pebbles on a beach and such an area is given in figure 6.24. The area contained a high degree of reproducible ordered material consisting of parallel furrows and striations, several such areas impinging on each other. The line scan treatment of the area given in figures 6.25a-g, revealed that an increased amplitude and spatial frequency of FLS were observed. The transition between the upper polymer region and the lower gold region is very obvious, for example typical line scans show a 'several-orders-of-magnitude' increase in amplitude of the FLS when traversed across the polymer/gold boundary and into the polymer.

Further line scans taken from this and successive images of the same sample not confirm that increased FLS exist over the polymer but also reveal more subtle variations in the film. An example of this is a low frequency component of the FLS that traverse the polymer regions. These features correspond to the morphology of the underlying gold grains. For example line scan 6.25b is represented schematically in figure 6.26, and clearly shows that a third grain exists under the polymer. The amplitude of the fluctuations in the line scan increase over the area of polymer although it should be noted that the frequency of the fluctuations is not as pronounced as similar trace characteristics found over the thick PMMA regions.

The AFM images of PVP on gold (see figure 6.27) confirm the observations made by the STM in that PVP does not form an even coating but instead exists as clumps on the surface of the gold. In this image the clumps are

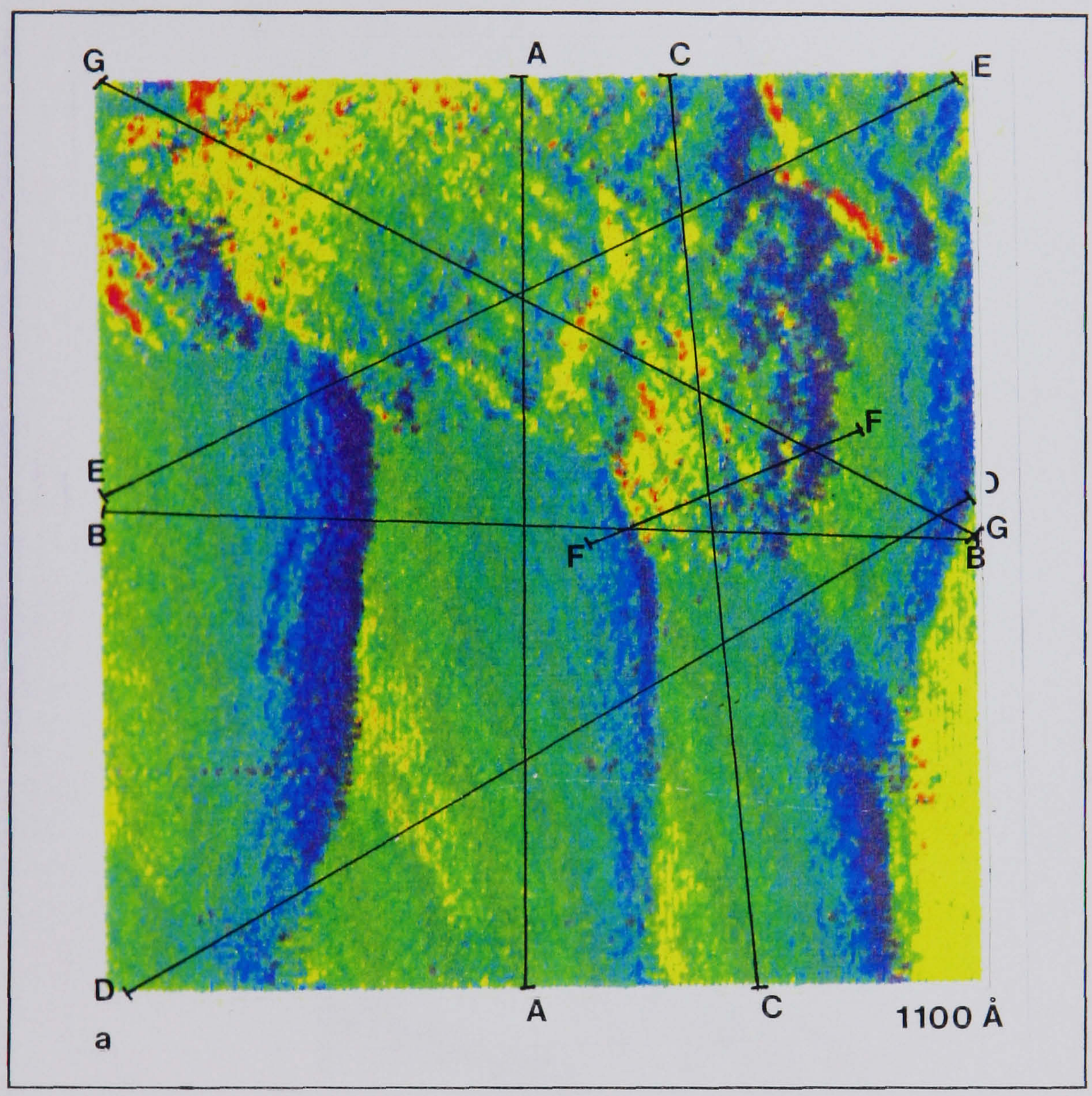

Figure 6.24: This STM image shows the PVP region lying between several gold grains. The grains were found to be very smooth and free from polymer coating. The PVP region however exhibited a variety of structures giving a 'glacier' like appearance. The PVP film does not cover the gold grains like the PMMA film was observed to, instead forms clumps or islands of thicker material. Line scans were again used to cross-section the image and the fluctuations therein are shown in figure 6.28. Image size $(200nm)^2$.

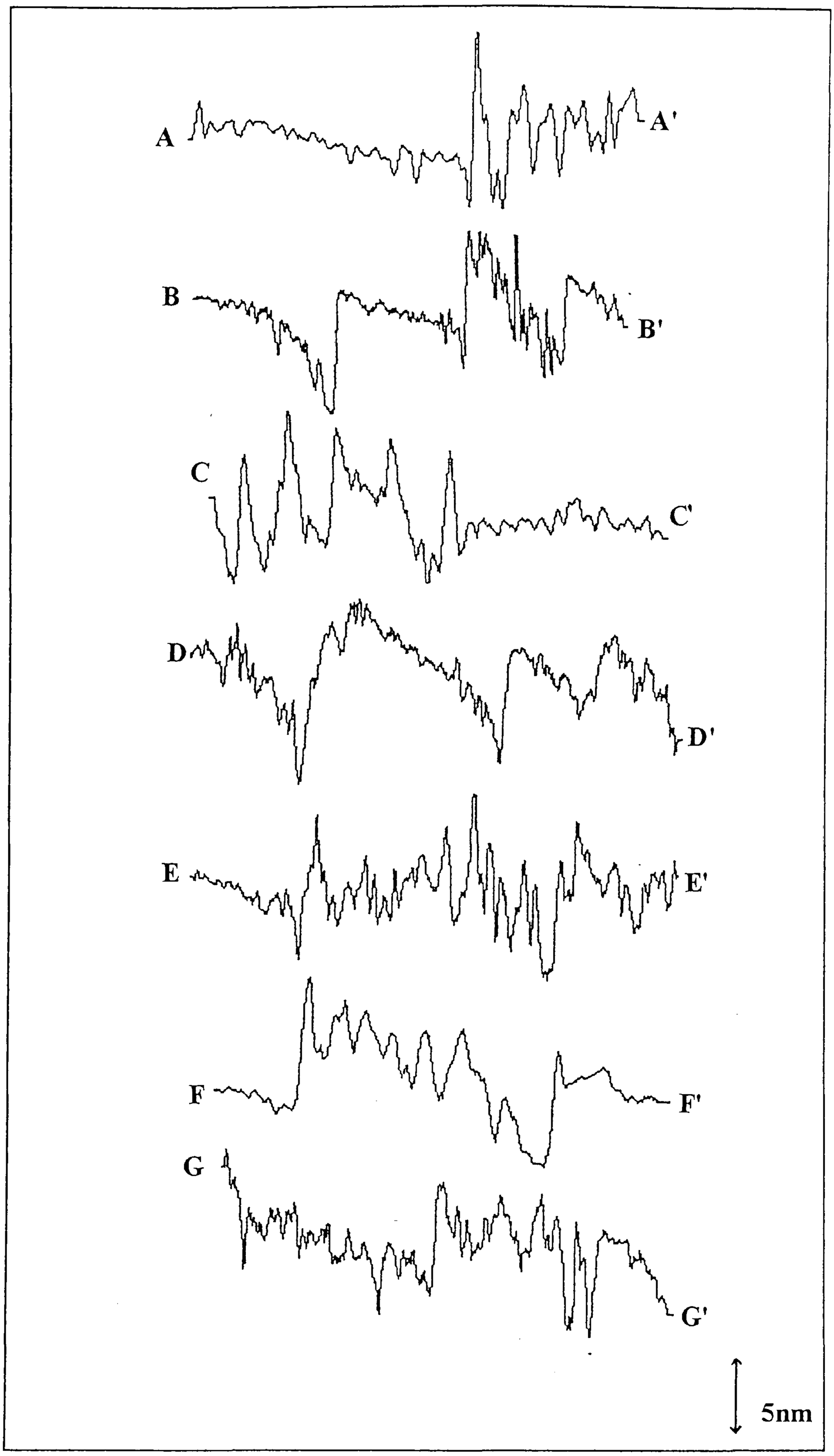

Figure 6.25a-g: The line scans(a-g) were used to cross-section the image. Although it is clear from figure 6.24, which area of the image is dominated by the polymer, the fluctuations in the line scans confirm this. The high frequency FLS occur in the presence of the polymer. Low frequency components occur over the gold grains.

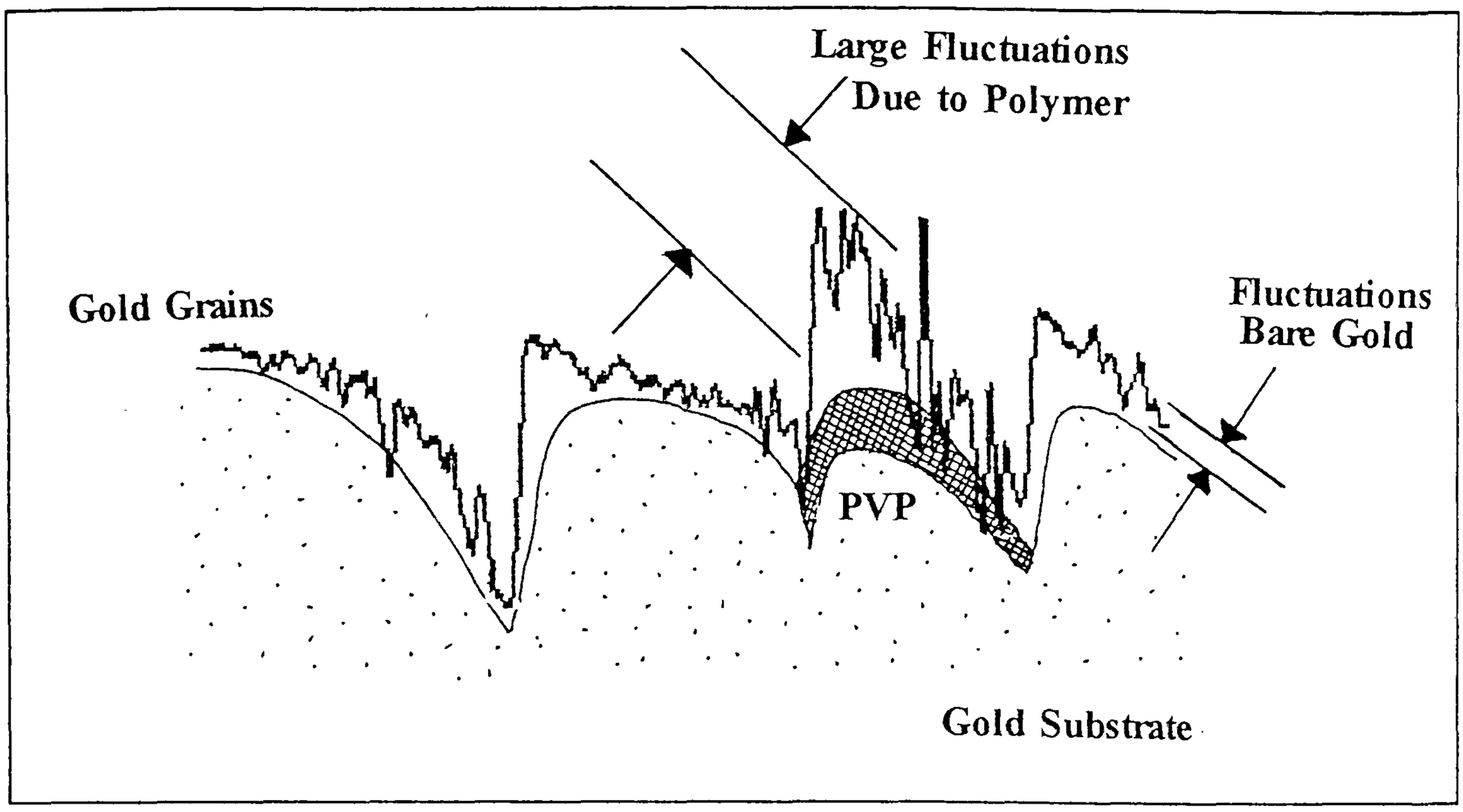

Figure 6.26: This line scan given here shows the probable location of the regions of polymer on the sample. The increased fluctuations in the line scan are associated with an unusual and possibly variable conduction mechanism within the polymer. Thus the position of the polymer can be deduced.

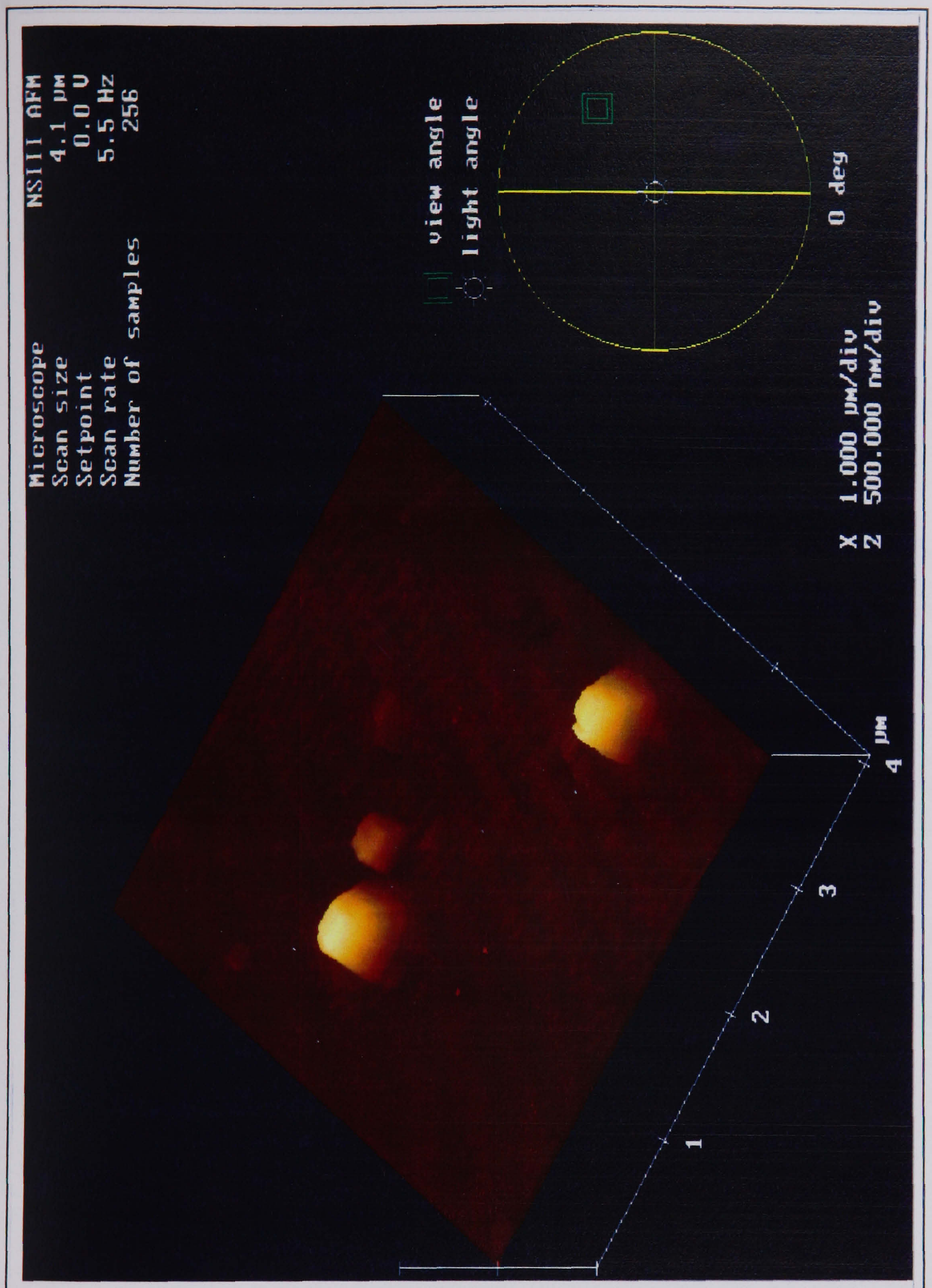

Figure 6.27: The AFM reveals the PVP clumps on the gold surface. The film is not uniform with the majority of the PVP material existing in a few isolated clumps of material.

variable in size but all are quite distinct from the surrounding plane (the gold grains at this scan size are too small to resolve, thus the substrate appears totally flat). A thick film was also cast and the incompatibility between the polymer and substrate is demonstrated by the 'peeling' of the film away from the surface after several hours in a moist environment (see figure 6.28).

Increasing the magnification of the image to the same level as the STM images, resulted in the granular gold structure in evidence but without a thin PVP covering. In addition the AFM images did not reveal any detailed structure on the PVP clump and continual imaging resulted in a non-stable image and subsequent tip degradation.

It is clear that the STM images of PVP show a very different film in comparison with the film of PMMA, on the same substrate. The PVP film although containing similar amounts of polymeric material as the PMMA, is in no way similar in structure. The PVP film shows definite clumping and non-coating of the surface.

In addition, the AFM results of the thickness of the PVP film suggest they are very thick although this fact is not apparent from the STM images where the polymer region does not protrude (on average) vertically much more than the gold grains. The results suggest that the tip must enter the polymer to achieve sufficient conduction. The tip-polymer contact may then obscure any actual surface detail and the ridges observed are artificial (see Discussion below.)

6.3.4 THE STM STUDY OF POLYCARBONATE

Optical observations of the Polycarbonate (PC) film revealed very little. The film was too thin and uniform to be observed although a slight colour change on the surface was noted. The PC film was deposited on HOPG and subsequent images achieved are shown here. Images of the film deposited on the gold substrate form the majority of the next chapter of the thesis

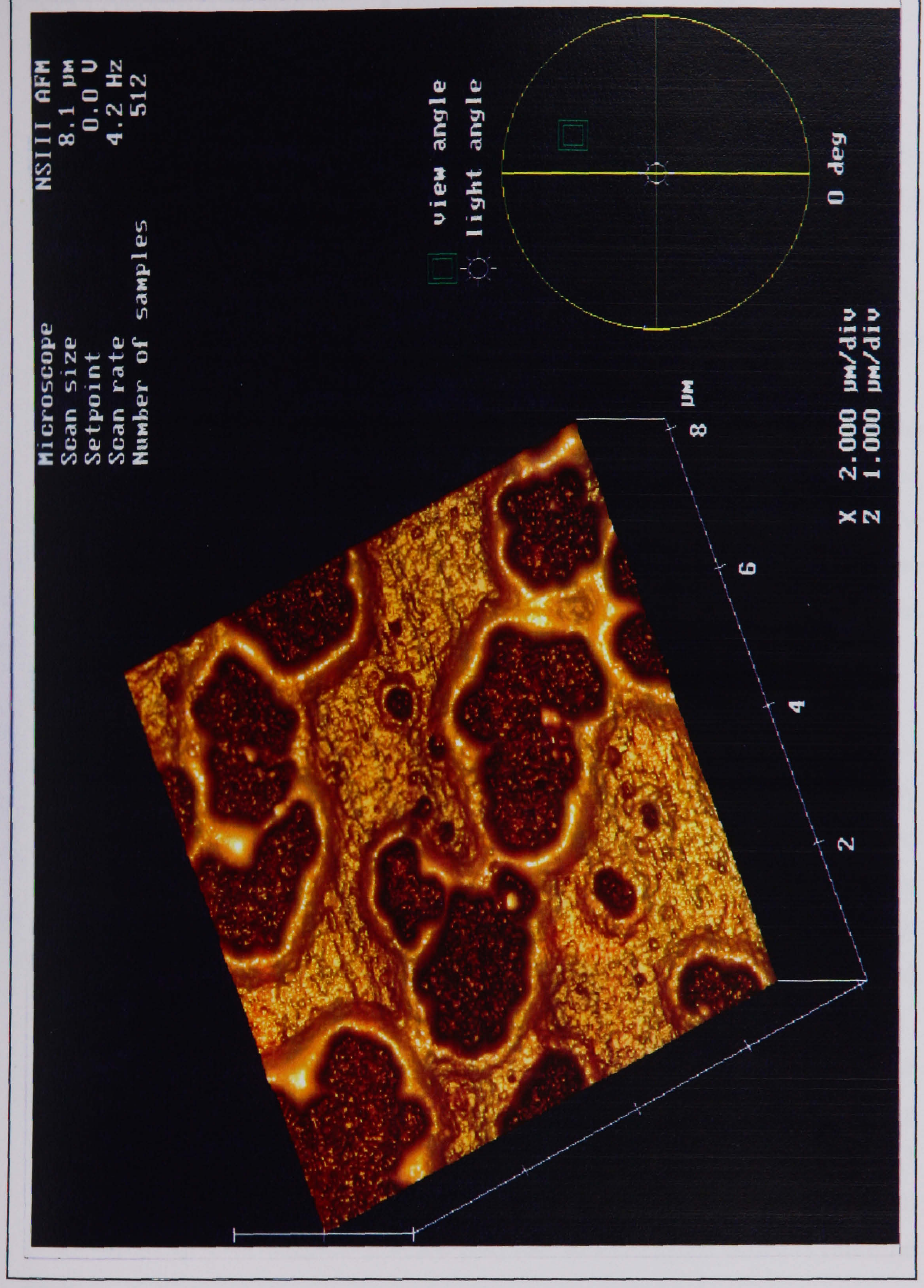

Figure 6.28: This AFM image of a very much thicker PVP film shows how, with poor substrate-polymer adhesion, and under the action of the scanning tip, the PVP film slowly peels away from the surface. The material that once filled the holes (in which the bare gold grains are visible) now occupies the sausage-like rim around the holes.

STM OBSERVATIONS

Graphite Substrate

The polycarbonate film was spun on to the HOPG and imaged. In general the images revealed a polymer film very similar in appearance to the PMMA film. The coating was found to be very even and not characterised by clumping. Figure 6.29 shows the upper and right part of the image consisting of PC, with a clear transition to the HOPG which dominates the lower and left part of the image.

The line scan technique was once again employed to indicate the polymer regions. Two line scans cross-sectioning figure 6.29 and labelled 6.29a & b show an order of magnitude rise in the amplitude of the fluctuations over the region dominated by the polymer compared to the fluctuations across the flat HOPG. This latter region was further examined to show the characteristic HOPG lattice structure.

Higher magnification images of the PC regions were taken and a typical example is given in figure 6.30. The PC film is observed and incompletely covers the substrate leaving an upper and lower middle region of uncovered HOPG. The appearance of the PC film is of an amorphous film with regions of highly ordered material. The best example of the amorphous region is given in the middle and right of figure 6.30. The best example of the ordered material is found in the upper right of the image.

Highly ordered regions were also found in almost all of the PC films (see figure 6.31). The ordered components are typically (25 +/- 5)nm long with a periodicity (perpendicular to their direction or length) measured at (1 +/-0.2)nm, which fits the description of the b-dimension of the PC unit cell (see chapter 4). This suggests that the polymer in this region is in a crystalline form.

Studies by Schnell[1964] and Prietzschk[1958] suggested that in deposited PC films, considered to be amorphous by optical and other microscopic (excluding SPM) examinations, actually contain as much as 40% crystalline material. This upper limit figure was deduced by Xray techniques

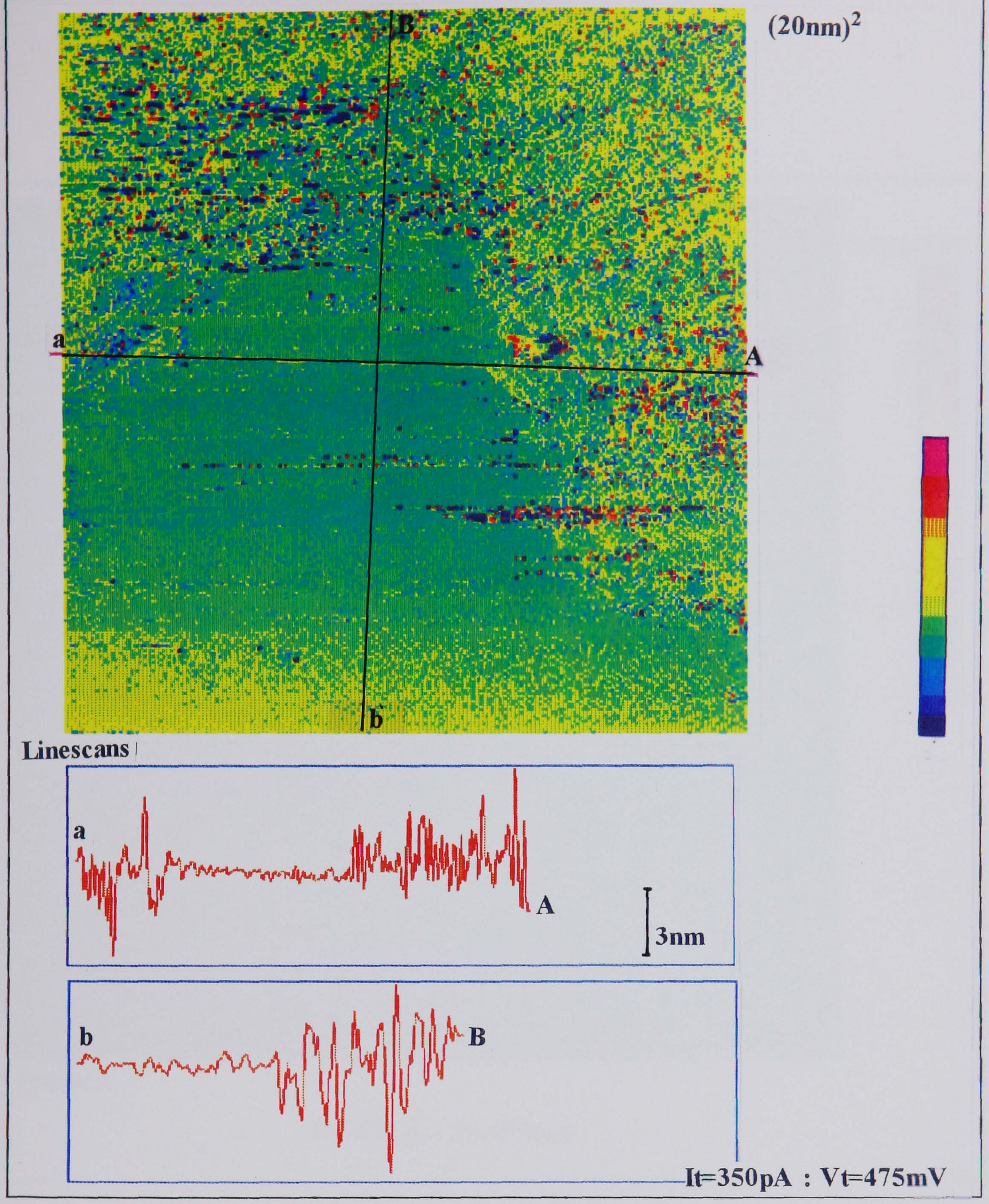

Figure 6.29: This image shows the polycarbonate (PC) film deposited on an HOPG substrate. The HOPG region is characteristically flat and the PC film is shown as an amorphous patch in the upper right of the image. The two line scans show an increase in the amplitude of the trace fluctuations.

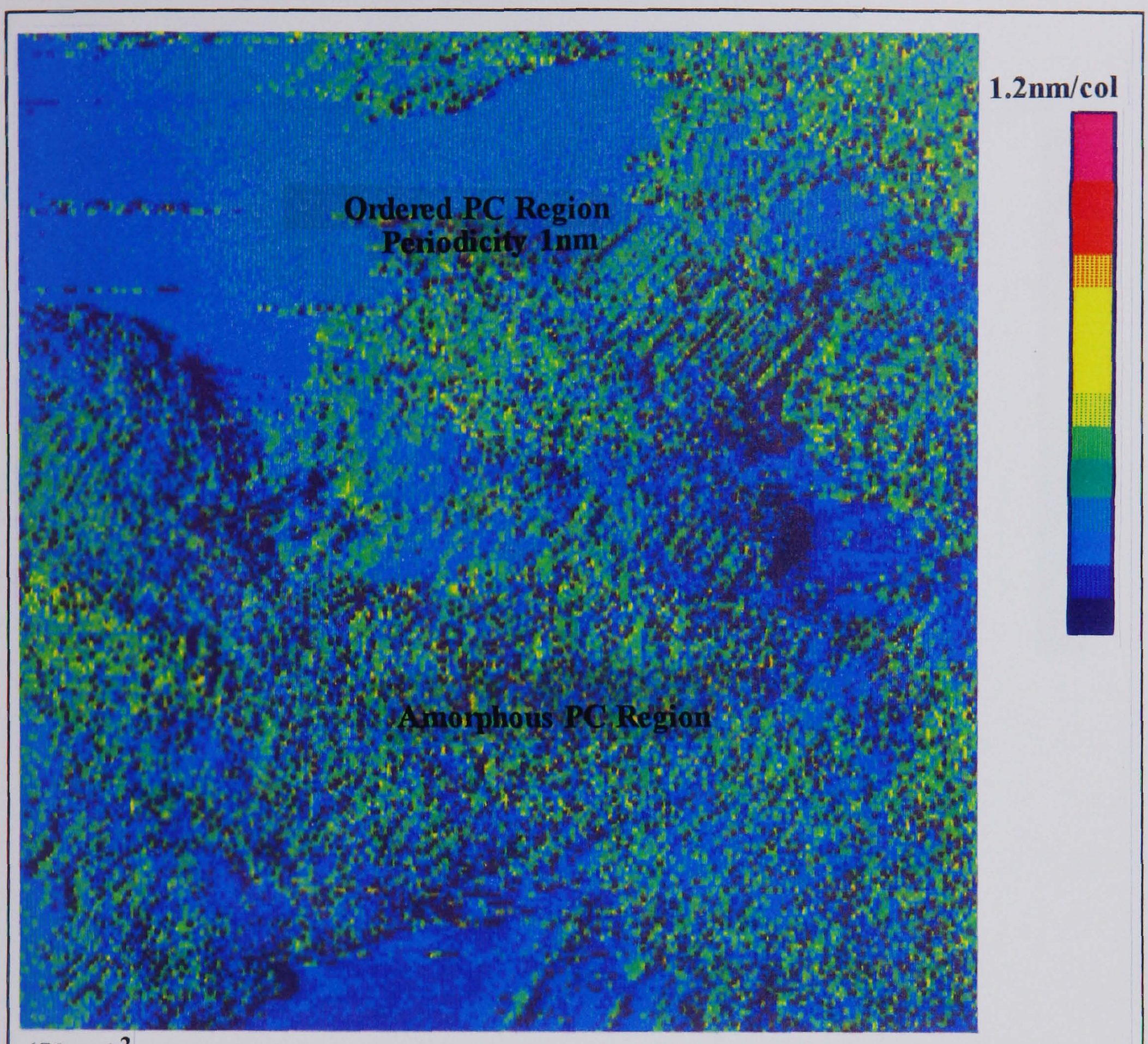

Figure 6.30: This STM image of the PC film shows the amorphous regions but also some areas with a degree of crystalline ordering. The ordered region has features that are about 20nm long and with a periodicity of approximately 1nm. The image given here, on closer inspection contains 20-40% ordered material. This is to be expected from polycarbonate - studies indicate that ordered regions exist within the amorphous matrix of polycarbonate although this has never been proved by microscopy.

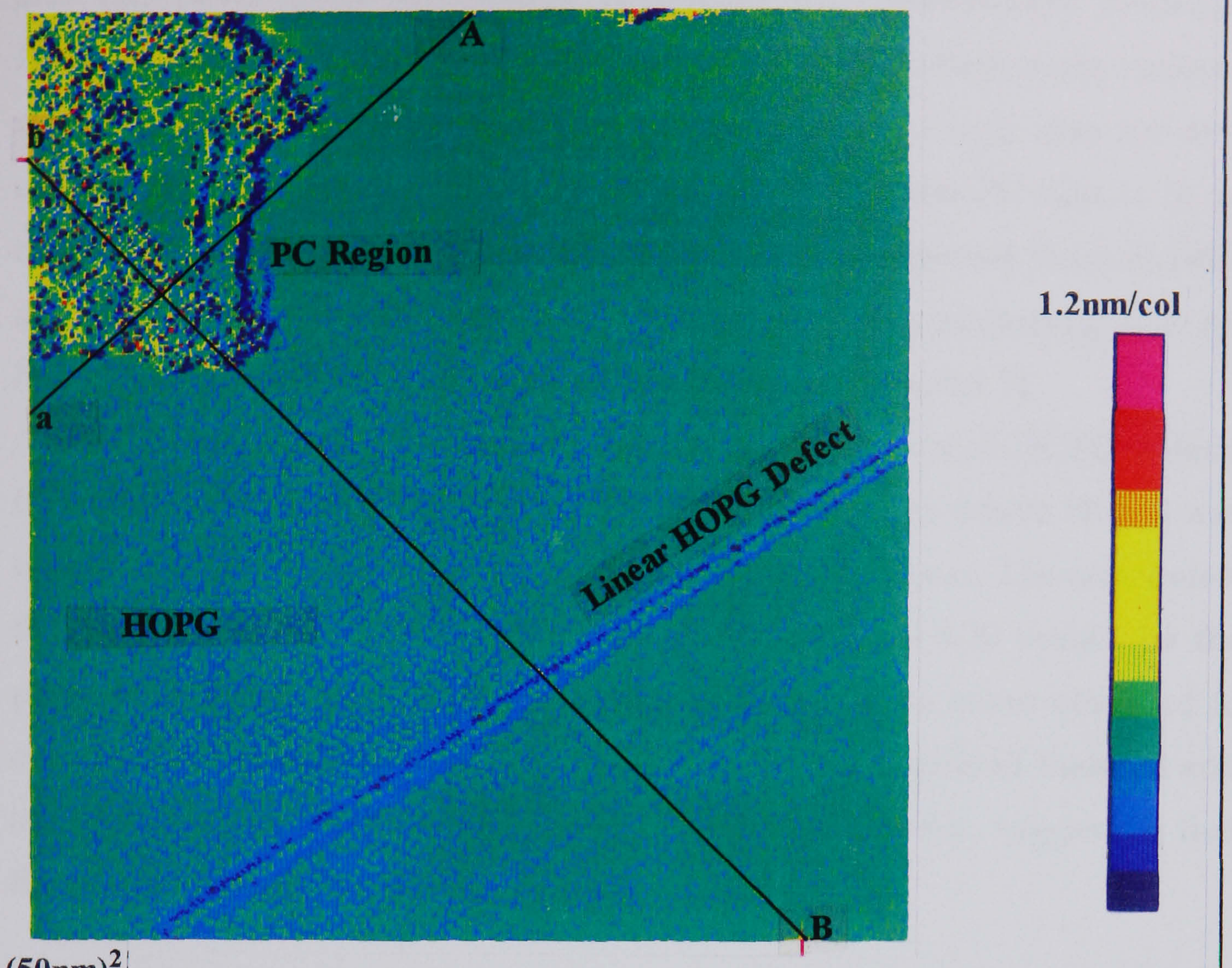

Figure 6.31: Other images of PC films (at high magnification) show ordered regions and this image is one of them. The same periodicity emerges (approximately 1nm) within the polymer region. Note there is an HOPG defect in the lower half of the image.

and has never been successfully correlated with microscopic evidence. However it is clear that the films observed here do contain some ordered material with PC existing in the crystalline form. A rough area for area calculation from figure 6.30 indicates that 20-40% of the PC film is in an ordered state. The appearance of such regions is to be expected [Schnell,1964] and it is the presence of these small regions that act as nucleating sites for homogeneous nucleation in much thicker films (see chapter 7).

It is important, once again to discount the presence of HOPG defects from this study. It should be noted that on all the images where HOPG was used as a substrate, the defects were characteristically linear. The only defect that could account for the features observed in figure 6.30 would be the presence of flakes of graphite. However, the flakes were never observed to contain features consistent with both ordered and non-ordered material and in addition were never found to have a complex perimeter, suggesting that the image is truly that of PC.

In general, the PC film exhibited a fairly even covering of the substrate with no incidence of clumping. The appearance of the very thin film was that of a combination of amorphous material with some degree of crystallinity being achieved.

The Effect of the Plasticizer on the Images of PC

The PC film described above was then subjected to a plasticizing vapour. A considerable change in the image was observed. A typical example of the re-ordering of the PC film is given in figure 3.32.

In figure 3.32, there are two distinct regions, the upper HOPG region and the lower PC film region. The HOPG region is very flat and higher magnification studies revealed the HOPG lattice. The PC region however is very different from that observed in 6.30 by virtue of the elongated regions that extend for several tens to hundreds of nanometres. The elongated features are equivalent to the lamellae or basic polymer crystalline elements observed in spherulites and introduced in chapter 4. They consist of folded PC chains and are approximately 25+/-5nm wide. Two line scans cross-

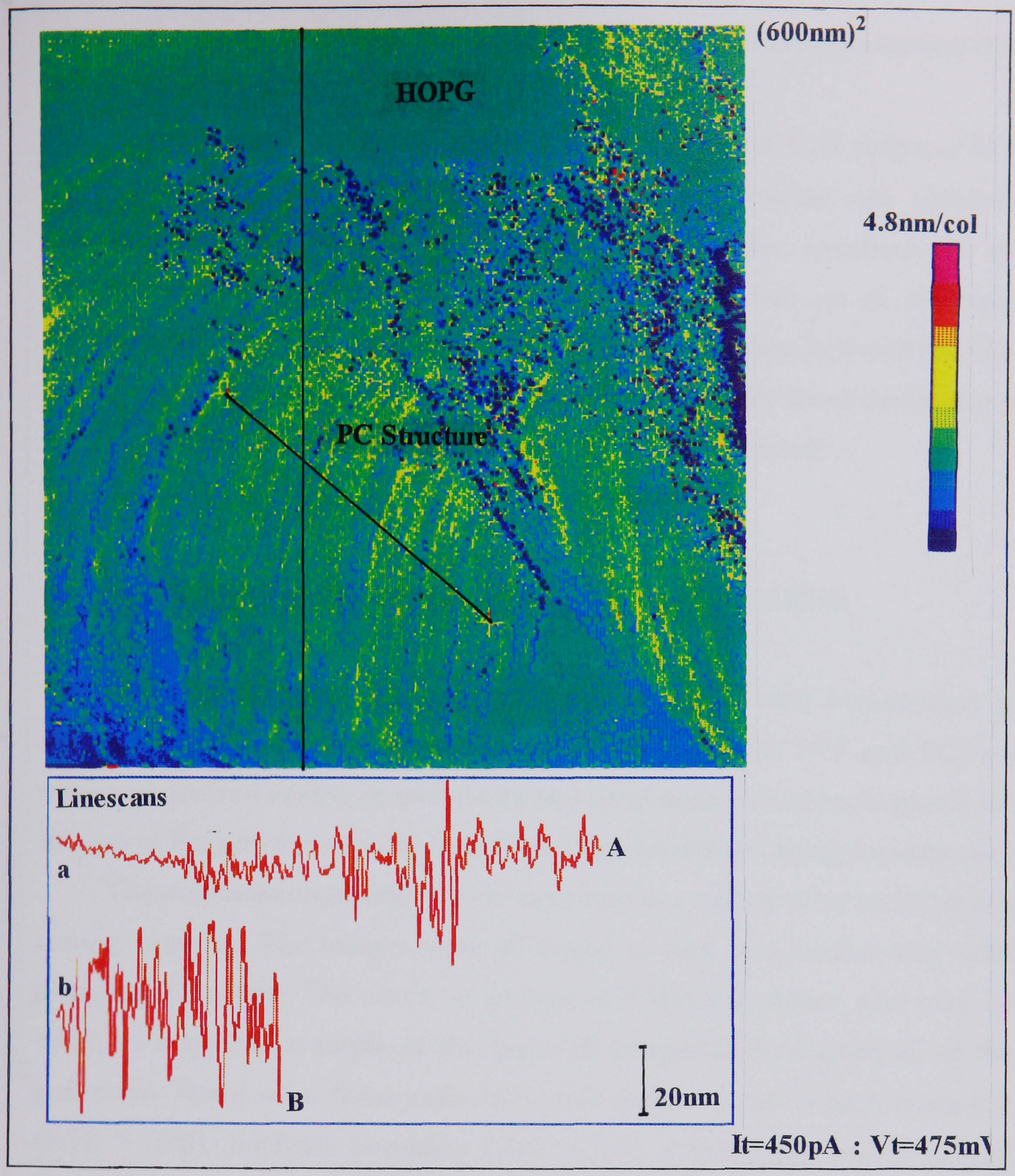

Figure 6.32: This STM image shows the PC film after exposure to the plasticizing vapour. The features that are visible in this image are much larger than the ordered regions observed in figures 6.30 and 6.31 and are rod-like in appearance. It is these rods that are the extended lamellae of the polymer crystal and form the basic building block of all of the PC crystalline entities (see chapter 4).

section the image and demonstrate again how the fluctuations increase over the polymeric regions.

These features are very important in the context of both polymer STM observations and of polymer crystallinity. The lamellae are observed extensively in the next chapter (where the entities involved in the crystallization of PC films are observed by AFM) but are of the same dimensions as those observed in figure 6.32. The correlation between the STM and the AFM images indicated that the features are truly those belonging to the PC film and arise as a result of the plasticizer treatment.

6.4 THE ENVIRONMENTAL EFFECT ON STM IMAGING

The effect of water on the imaging mechanism has been well documented. In this chapter, the specific polymers under study (PMMA, PVP and PC) are observed under a variety of environmental conditions set out in chapter 5, the images of the polymers under humid and dry conditions being investigated.

The polymers under study were subjected to a variety of humidity levels during imaging. The images were all found to vary in a similar way with changing humidity. The effect on images of PMMA is shown and may be taken as a typical example of the types of images formed from all of the polymers. There were three main humidity regimes, that of high humidity (R.H. > 60%), medium humidity (10% < R.H. < 60%) and low humidity (R.H.<10%)

The Wet or High Humidity Regime (R.H. > 60 %)

The image shown in figure 6.33a is of a PMMA film in a high humidity environment. The polymer film structure and the level of detail therein is very similar to those shown in above. This is to be expected as most of the SPM images are taken in the laboratory where the average humidity recorded over one year was R.H.= (65+/-10)%. The gold grains are detectable using the line scan technique.

Other images, including that of the gold grain morphology were

observed under very high humidities (R.H. > 80%). The images of all the materials were relatively easy to achieve. Even the some thick (t>2nm) polymer films were imaged although there was some degree of furrowing within the image, indicating a significant tip-sample interaction.

Medium Humidity Regime (10% < R.H. < 60%)

The polymer films observed in this regime and typically PMMA (figure 6.33b), show the polymer features in much the same way as the those in figure 6.33a. However theimaging was not as stable and several scans had to be recorded before a reasonable image was produced. The image was easily achieved at the high humidity end of the range investigated, but under drier conditions (R.H. < 30%) the number of unsuccessful attempts were made before a good image was formed increased considerably. In those images that were not fully achieved, there were many lines and blank regions where no morphological data was recorded.

Images of the bare gold grains, under these conditions was also studied and they showed more rapid variations in the fluctuations of the line scans, than when observed in the 'wet' regime.

The Dry or Low Humidity Regime (R.H. < 10%)

The dry regime was found, in this experiment to be unsuitable for image acquisition. There were no successful images recorded of polymers under this humidity range. There were very few partial images (where less than three-quarters of the image showed morphological data), and these contained many poor regions, unsuitable for further examination. The image shown in figure 6.33c was a typical image produced under these conditions.

The dry regime was also found to be unsuited for imaging the bare gold grains. Figure 6.33c shows the grains under this regime and there are not many data of any significant use for this project.

6.5 DISCUSSION

6.5.1 Morphology and Conduction Mechanisms.

The hydrophobic nature of both substrates made PVP film formation with

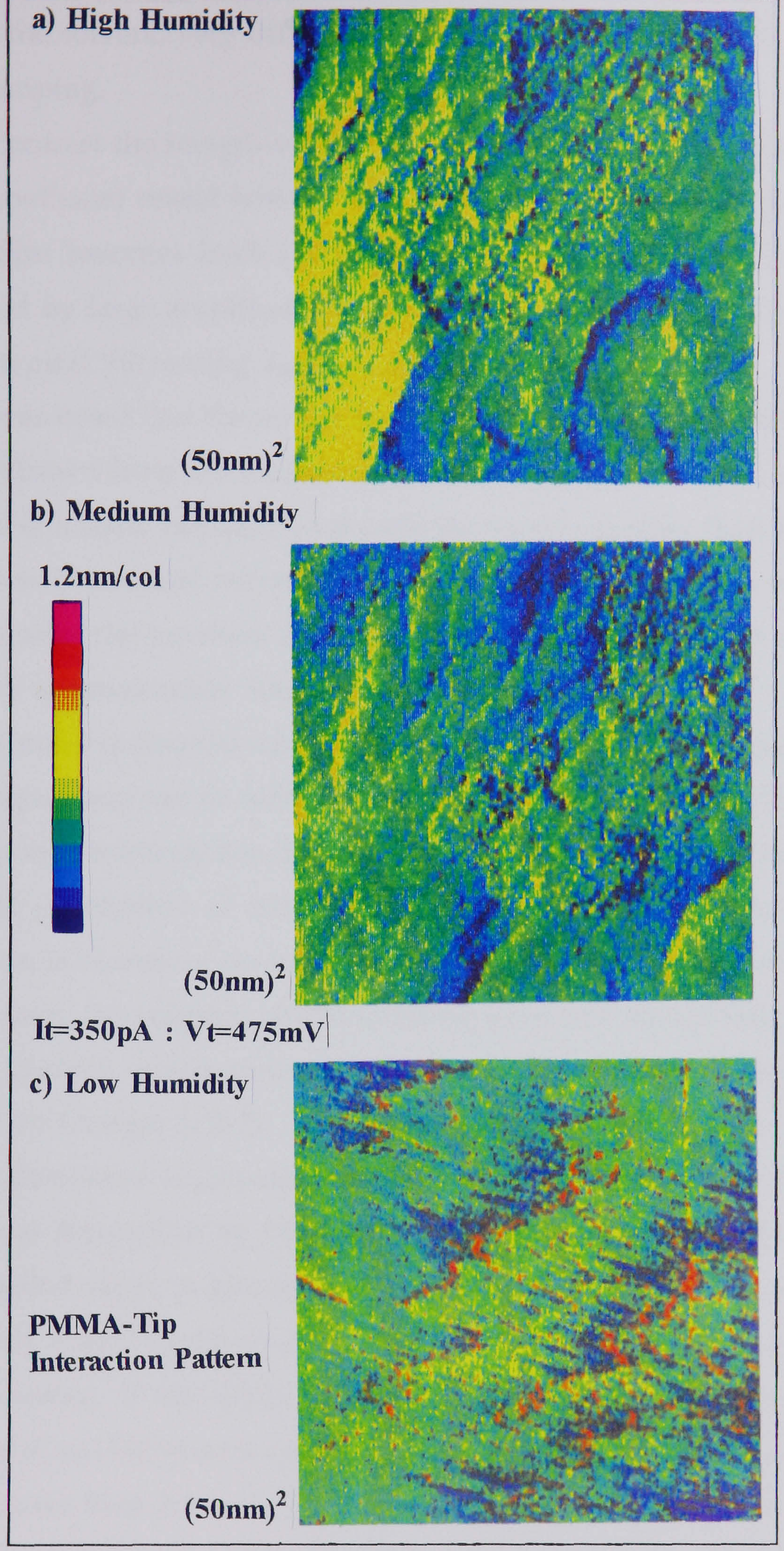

Figure 6.33: The effect of a change in humidity on the STM images of PMMA coated gold grains was investigated. a) Imaging whilst in the moist regime gave the best STM images. b) Imaging under medium humidity levels gave unstable STM images. c)Imaging under dry conditions gave very poor results. The polymer films from the latter experiment were found to be 'swept' away by the tip with no topographical data being extracted.

water as the solvent, very difficult. All the images of PVP by STM and AFM show clumping.

In contrast the images of PMMA and PC (dissolved in chloroform and dichloromethane) reveal how a smooth film is always formed. In places the PMMA film becomes thick (as observed by AFM) and the STM image is dominated by large amplitude high frequency fluctuations in the line scans and the typical 'furrowing' appearance is observed.

It was noted that the tunnel current did not drop appreciably as the tip was withdrawn from the thickest polymer covered area. The tunnel current remained at a fairly constant level until the tip was further than 100nm from the surface. The tunnel current then dropped significantly to a value below the response of the feedback loop. The tip then had to be moved towards the sample by approximately 100nm to resume imaging.

The non-exponential decay of the tunnel current with increasing tip / sample separation can be tentatively explained by Lindsay & Sankey[1992] as a tip/polymer interaction. In this case the tip/polymer interaction involves the actual penetration of the polymer, enabling conduction to occur. The penetration is necessary to cause polymer adhesion to the tip. When the tip is withdrawn, the polymer acts as chewing gum and strings link the surface and tip. Limited conduction may occur through these polymer 'wires' as observed by Creager [1992].

An alternative explanation for the non-exponential decay of the tunnel current was forwarded by Woodford et al [1991] who suggested that as a contamination layer is almost inevitable when scanning in air. Any layer (most likely water) could act as a charge transport medium, the conductivity thus increasing. If the layer (assumed to be water) as is described by Woodford et al[1992] forms a bridge between the surface and tip, large forces (much greater than AFM forces) may be applied to the polymer. The thick polymer layer is quite likely to be distorted and may even appear furrowed. The bridge may still exist at larger sample/tip separations and disrupt the exponential decrease of this relationship.

The non-exponential decay of the tunnel current indicates that to achieve

sufficient conductivity, the STM tip must in some circumstances interact with the polymer. The amount of 'scarring' on the polymer surface that is associated with the interaction is related to the conduction mechanism and is manifest in the form of furrowing. The series of images obtained at varying humidities (figures 6.33a-c) show an increasing furrowing as the humidity drops.

If the furrowing is the scarring of the surface by the tip in pursuit of a suitable level of conductivity then a drop in humidity could lead to a drop in the number of conduction pathways across the surface of the material (see chapter 2). The conduction mechanism is then modified from a surface dominated process suggested by Woodford et al[1991] and Hu et al[1992] to a bulk process suggested by for example Lindsay & Sankey[1992] and Joachim & Sautet[1990]. The obvious experimental example of this is shown by comparing similar sized samples of PMMA and PVP, the latter showing less high frequency 'furrowing' than the former, because the surface conduction process is dominant (in this water saturated polymer) - see figure 6.34.

At this point it should be noted that some of the AFM tip-sample interaction processes (that are assumed to be less significant in STM work) may go a long way to describing the furrowing appearance in many images. Leung [1991], Burnham et al[1991 & 1993] and others also indicate that as the AFM tip interacts with the sample the image contains linear features. In general however, a hallmark of this type of sample feature is a single direction within a given image. In the AFM studies given above, the features were generally of a single orientation and perpendicular to the scan direction. Some of the 'furrowed' regions observed in the PMMA sample were slightly offset from the direction perpendicular to the scan direction but all such features within a given region had a particular orientation.

There is however little doubt that the presence of water in the environment immediate to the STM system, i.e. the sample and tip plays an important role in both the sample morphology (especially for the hygroscopic materials like PVP) and the conduction mechanism. Insufficient water concentration on or around the sample during imaging may result in a

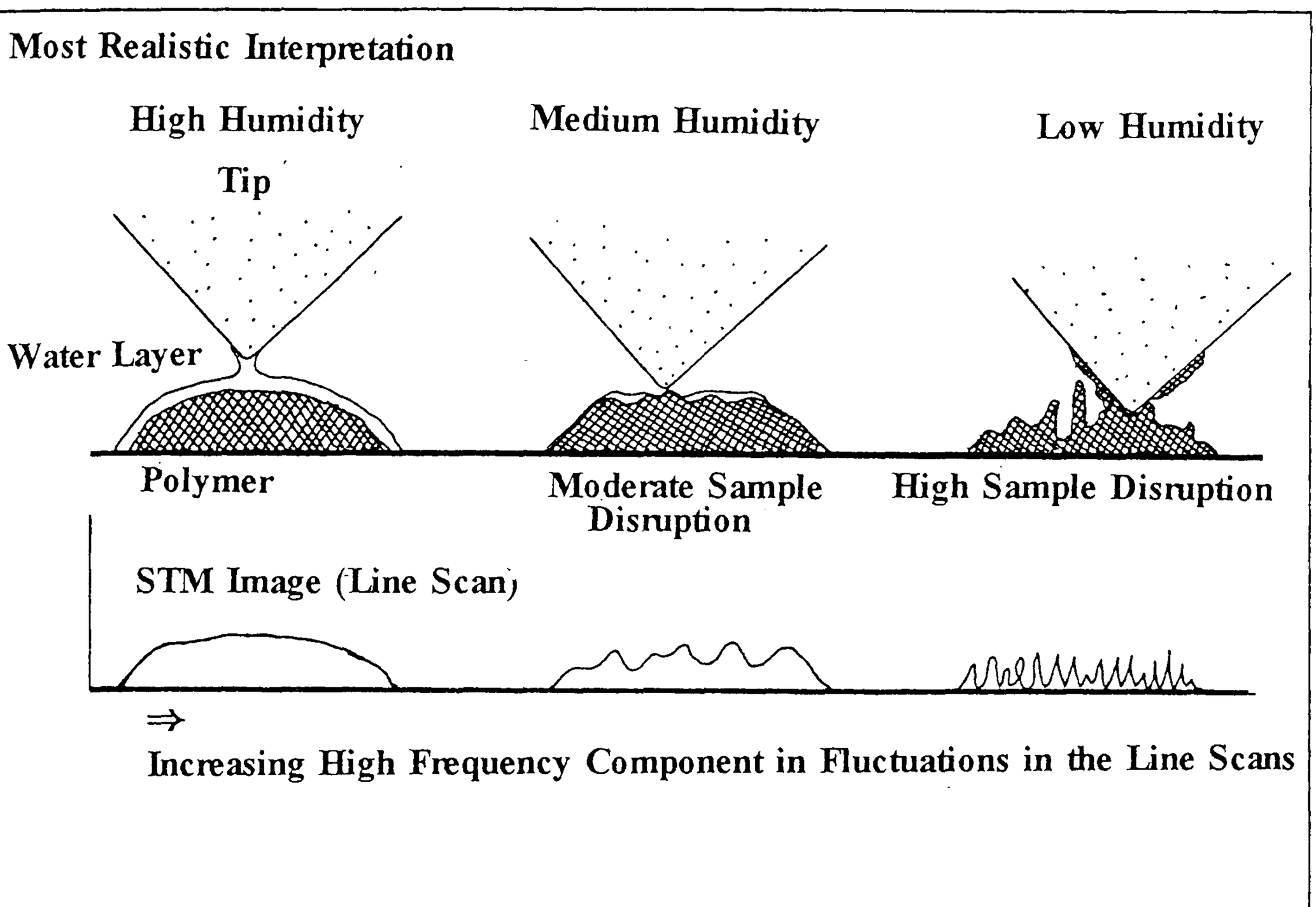

Figure 6.34: This figure demonstrates how with a decrease in conductivity, the STM tip enters the polymer and damage to the film results. The decrease conductivity can be attributed in part to a decreases in available water. This can happen if there is a drop in humidity or if the water-retaining property of the sample changes i.e. if the sample is more hydrophobic than hydrophilic (or hygroscopic).

considerable decrease in image contrast and stability.

6.5.2 Adhesion of Polymers to The Substrate

The adhesion of polymers to the substrate is of key importance to the understanding of any morphology observed. This study used PMMA, PC and PVP, the former two polymers tending to form a different film from the latter. The adhesion of polymers to surfaces has been discussed in Chapter 5 and it was argued that the solvent choice was critical in determining the success of a polymer-substrate bond.

The wettability of the polymers used [Good et al, 1987], suggests that PVP and PMMA are medium wettability polymers and PC is a characteristically high wettability polymer. All the polymers should coat the sample in a predictable and similar way. However the situation is not as simple as this as the polarity or acid-base(electron donating and accepting) characteristics of the solvent, the substrate and the polymer must be considered as one system (see chapter 4). Although the wetabilities are similar, the solvent polarities are very dissimilar. Water is highly polar compared to chloroform and dichloromethane. In addition the polymer PVP, is highly hygroscopic. The incompatibility between the surface and the water rich PVP (i.e. the hydrophobic nature of the gold or HOPG) make for very poor adhesion and the polar aspect of the system far out-weighs the conventional wettability approach.

In general the polymers were not found to adhere well to the graphite or the gold substrate and in the example of PVP, the film formation was severely impaired. The choice of water as the solvent for PVP, where HOPG is known to be hydrophobic, is likely to have severely hampered the film forming ability of PVP.

The adhesion between the polymers and the substrate is enhanced by the presence of surface defects. This point was noted as the transition from the higher grade HOPG (containing fewer defects) to the lower grade HOPG (containing more defects) was made. The transition resulted in an increase in tackiness of the substrate i.e. the substrate was more likely to retain the polymer film after casting if the lower grade HOPG was used.

With the increase in the number of defects affecting the adhesion of the polymer film, a subsequent increase in difficulty in differentiating between the defects and the polymer film occurred. The use of gold as a substrate in preference to HOPG enabled more complete assessment of the film.

6.5.3 The Resolution of PC Structural Data

The increase in apparently ordered material within the PC surface that is observed in the STM images is consistent with other studies on this material [Cope, 1977] as the exposure times to the plasticizing agent are increased. In addition, the partially crystallized PC film allows the observation of both crystalline and amorphous material. It is important to note that the image crystalline regions are subtley yet crucially different from the 'furrowed' or scarred material formed as a result of the tip sample interaction in PMMA. The crystalline regions were observed to lie at many different orientations on the surface and these were observed within the same image. Tip-polymer interactions are unlikely to have resulted in features exhibiting such an array of different angles. This is an important point as the image could be interpreted as containing a) thick polymer where the crystalline area exist and b) thin polymer where the amorphous regions exist.

The STM is able to distinguish between ordered and non-ordered PC material and shows thus that STM can be used reliably on polymers where not only the coverage and uniformity of the film is required but also details on the structure of the polymer are required.

CHAPTER 7

RESULTS : STAGE 2
AFM OF THE SOLVENT INDUCEDCRYSTALLIZATION OF POLYCARBONATE THIN FILMS

CHAPTER 7

THE AFM STUDY OF THE SOLVENT INDUCED CRYSTALLIZATION OF THIN POLYCARBONATE FILMS

7.1 INTRODUCTION

This chapter gives the results of the experiment proposed in chapter 5. In brief, a polycarbonate film, spun at high speed during casting from a dilute solution forms a film generally thought to be amorphous in appearance (see chapter 4). The film was then treated with a plasticizing liquid or vapour (in this case butyl acetate) for the specific periods detailed in chapter 5.

The PC molecules are hindered from adopting a low energy crystalline conformation by steric interactions even at elevated temperatures. However plasticizer molecules diffuse into the film and allow the polymer molecular chains to separate to a point where crystallization is achieved rapidly.

This chapter shows how the morphology of a variety of polycarbonate films changed with specific and controlled exposure to the plasticizing vapour. Some films were exposed more than once and remained uncoated during imaging by SPM. This process has not been attempted before and the results are given below.

7.2 AMORPHOUS POLYCARBONATE: Film 1

The amorphous PC films imaged by the AFM were obtained by the spin coating method detailed in chapter 5. This technique allows a film to be cast with sufficient speed to inhibit the formation of significant amounts of ordered material comprising of those structures associated with the crystalline polymer phase. A typical example of such a film imaged before any plasticizer treatment is given in figure 7.1.

This AFM scan shows pimples and pock-marks around a micron or so

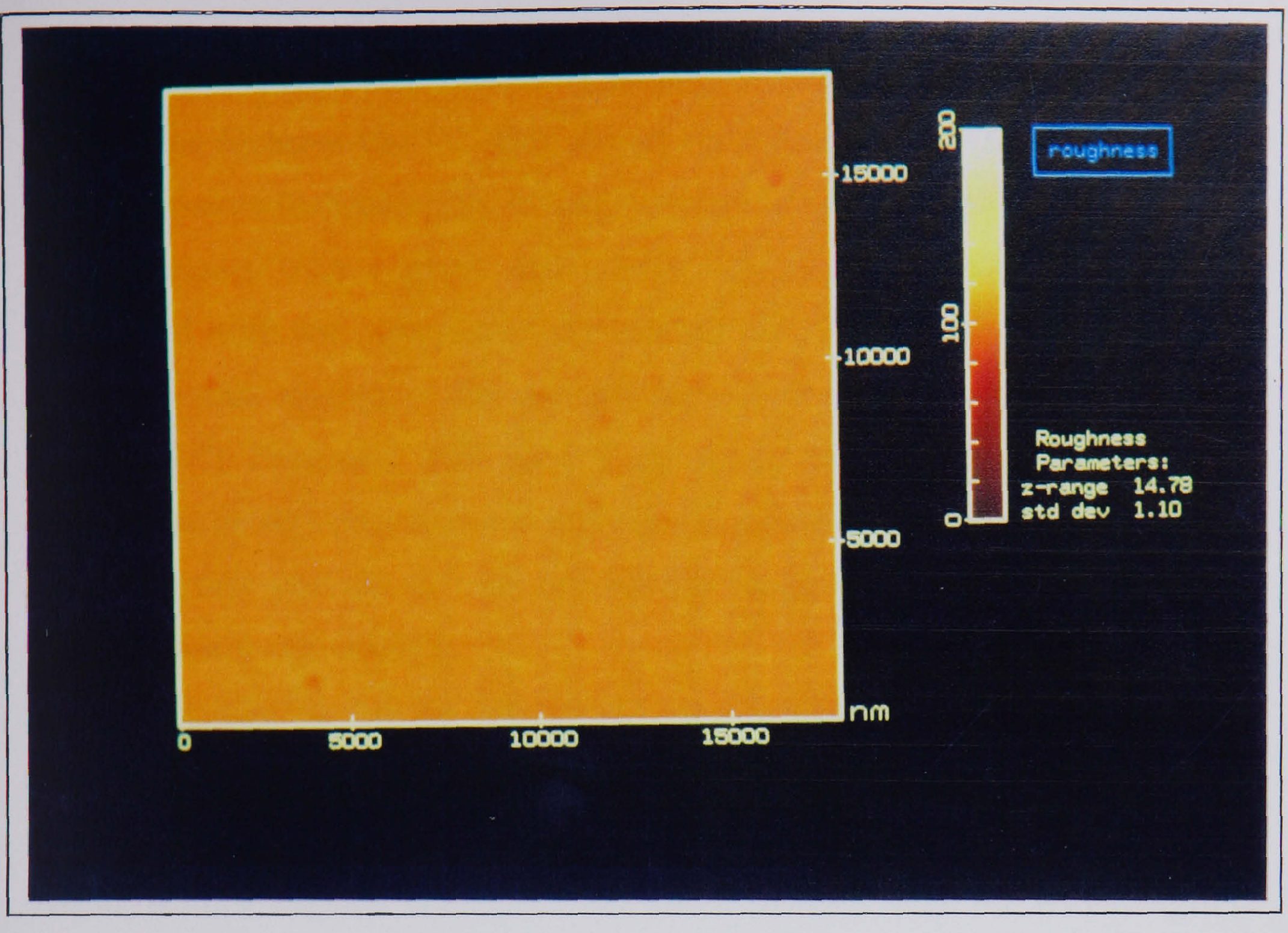

Figure 7.1: This AFM image is of the amorphous polycarbonate film. There is little in the way of surface structure and roughness measurement (right most figure) gives an indication of the smoothness of the surface.

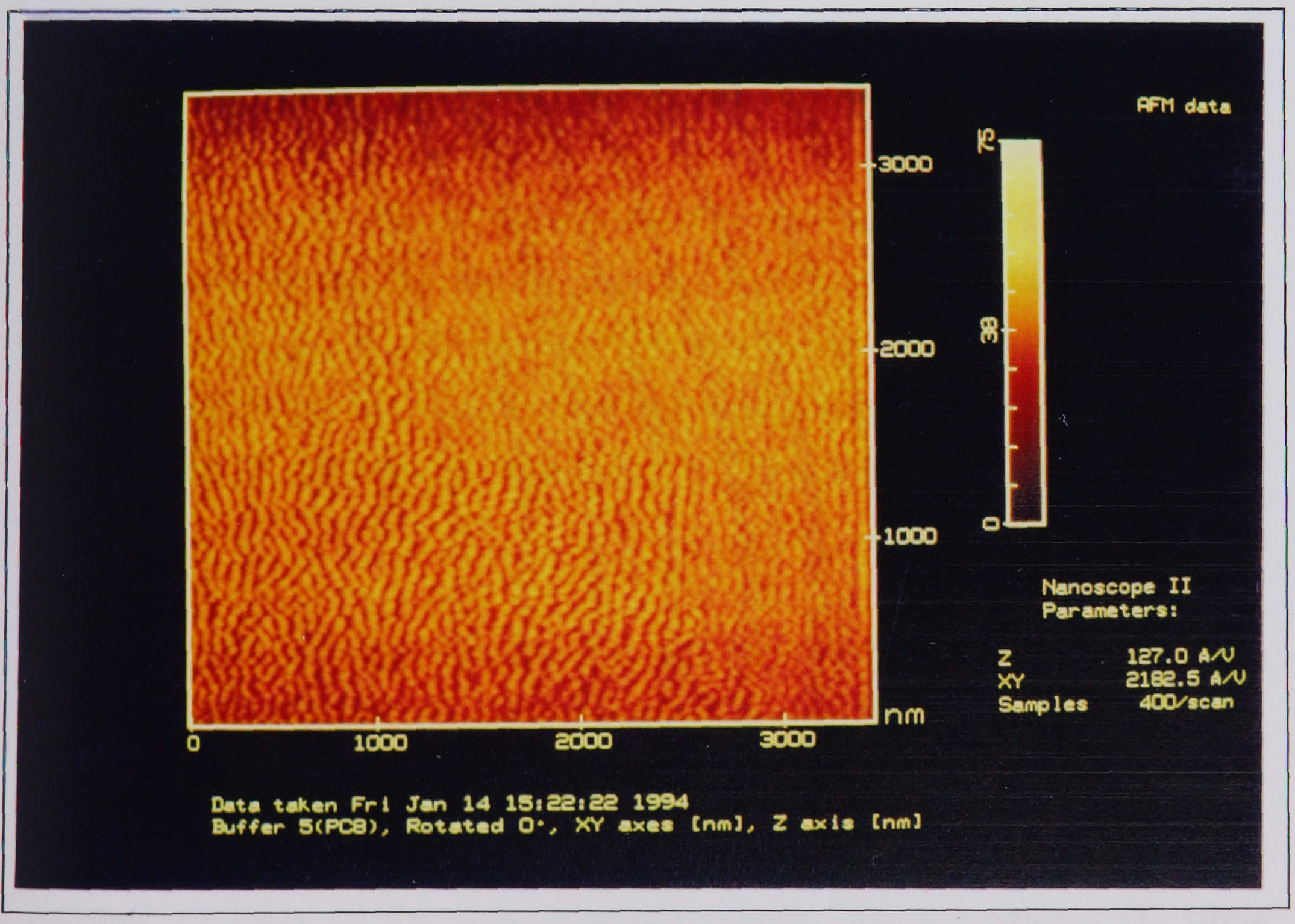

Figure 7.2: The effect of the plasticizing vapour on the amorphous polymer film is to induce mobility in the polymer chains. Under the influence of the scanning tip, the polymer rucks and forms the typical ridge-like pattern observed here.

in diameter, distributed randomly across the surface of the PC film. Other than these features the PC film shows no other details. Surface roughness measurements (estimated by taking average height variations of the surface from a mean, over a given area) were obtained (see table 7.1) and later compared with the post-plasticizer treated film values.

Previous studies of the morphology of the polycarbonate films [e.g. Cope, 1977; Prietzcsk, 1958 and Carr et al, 1968] have indicated that a correlation exists between the 'orange-peel' pock-marks and pimples observed of the surface and small 'micro-crystalline' regions, the evidence for which comes from x-ray studies.

If a crystalline phase does exist in the film imaged in figure 7.1 then it is very different from the phase envisaged by Sharples[1966], in which rods, fibrils and spherulites are present. It has been suggested [Carr et al 1968] that the crystalline regions are numerous, small (smaller than the wavelength of visible light) and immature; that the film in general has not reached the stage of rods and fibrils.

The STM study in Chapter 6 identified these regions of ordered material and placed a size limit of tens of nanometres. This figure is commensurate with the estimates obtained by other workers [Frank et al, 1967].

Thus a combination of STM and AFM results confirm the existence of small regions of material that are different from the surrounding amorphous film. This indicates that PC spin-cast from solution forms a film that cannot be described either as amorphous or crystalline but of one that displays pre-ordering in an amorphous matrix i.e. the film exists in a 'sub-crystalline' phase.

7.3 BRIEF EXPOSURE TO BUTYL ACETATE VAPOUR

Film 2

The effect of the butyl acetate vapour (plasticizer) on thin PC films is to increase mobility of the polycarbonate chains. The amorphous PC films produced by the spin-casting method were examined after a brief plasticizer exposure and suitable drying period (i.e. the polymer was allowed to dry

Trial	R /nm
1	14.78
2	15.62
3	15.04
4	14.46
5	14.68
Ave	14.92

Table 7.1: The roughness measurements R, of the surface of the amorphous film.

Trial	Fibril size/nm
1	48
2	65
3	53
Ave:	55

Table 7.2:

This table shows the fibril dimensions as measured from figure 7.2

fully). The resulting film (film 2) shows a change in surface morphology which is typified by the appearance of elongated fibres of PC 50nm-100nm in diameter (see figure 7.2). There are domains within the surface for example, within the lower left and upper right of the image, which contain a fibrillar morphology.

The size of the fibrils may be measured from this image and compared to the approximate dimensions of the polymer chain. The folding of the molecular chains within larger scale crystalline features like fibrils is of fundamental importance to polymer physics (see chapter 4). Line scans were taken in a direction perpendicular to the fibril direction. Table 7.2 gives the approximate width of the fibrils.

Tip-Polymer Interaction

The orientation of the fibrils is predominantly perpendicular to the tip scan direction which suggests a certain amount of tip to polymer contact occurring as a consequence of image acquisition. Thus the next stage in the experiment was to observe the action of the scanning tip on the surface whilst the films were 'wet' or still saturated with plasticizer (i.e. the polymer chains were mobile). The scanning process was allowed to proceed whilst the plasticizer was present.

The effect of scanning the 'wet' film was pronounced and highly significant in the context of direct imaging. The results suggest that the area scanned repeatedly for a fixed period of time (1 minute) showed an increased fibril formation. Scanning for a further period (5 minutes) showed even more heightened fibril formation (surface roughness values are approximately 20nm, compared to 15nm for the pre-treated film in figure 7.1).

On decreasing the magnification of the image, the region altered by repeated scanning (and described above) contrasts with the smoother surrounding polymer (see figure 7.3). The effect of the repeated scanning can be mimicked by operating in a destructive mode. This mode is associated with a high frequency scanning coupled with a poor feedback-loop response, parameters typically used only on very hard and flat materials. However

when employed for polymer studies where the sample is likely to be soft and mobile, significant tip interaction may be expected. The image shows the central 'disturbed' region surrounded by a smoother border.

Further measurements were made from the rough region with pronounced fibril formation. Figure 7.4 shows the rough region (bottom left of the image) cross-sectioned by line scans, or surface profiles (shown at the top and centre of the image). The line scans were then transformed into frequency space and the Fourier spectrum displayed in the lower right of the image. Key spectral periodicities or peaks in the spectrum were measured. Six such spectra are given in figure 7.5 where the white arrow gives the position of the specific peak in the spectrum recorded in table 7.3.

The scan size was increased in stages and the effect of the continual scanning was aptly demonstrated in figure 7.6. Here five scan areas can be seen within each other. A region falling within successive scans appears more pronounced.

To demonstrate the artificial nature of the process, the next image shown in figure 7.7 shows seven individual scan areas constructed in an 'H' pattern. The time taken to construct each square was approximately five minutes and the internal structure of each was similar to that shown in other disturbed areas on this film. The fibril dimensions were also found to be similar between each of the 'H' components and the order in which each was formed cannot be discerned from the image indicating a degree of permanency of the features. On returning to this sample after 24 hours, the pattern could still be observed and with approximately the same ridge amplitude.

Implications for Further Imaging

If the polycarbonate film is imaged in the contact mode whilst retaining a proportion of plasticizer, then significant polymer reorganisation can be expected. Other workers, most notably Leung & Goh [1992], Meyers, DeKoven and Seitz[1992] present very good examples of the manipulation of a polymer surface by the AFM tip. In both cases, operating in a moderately

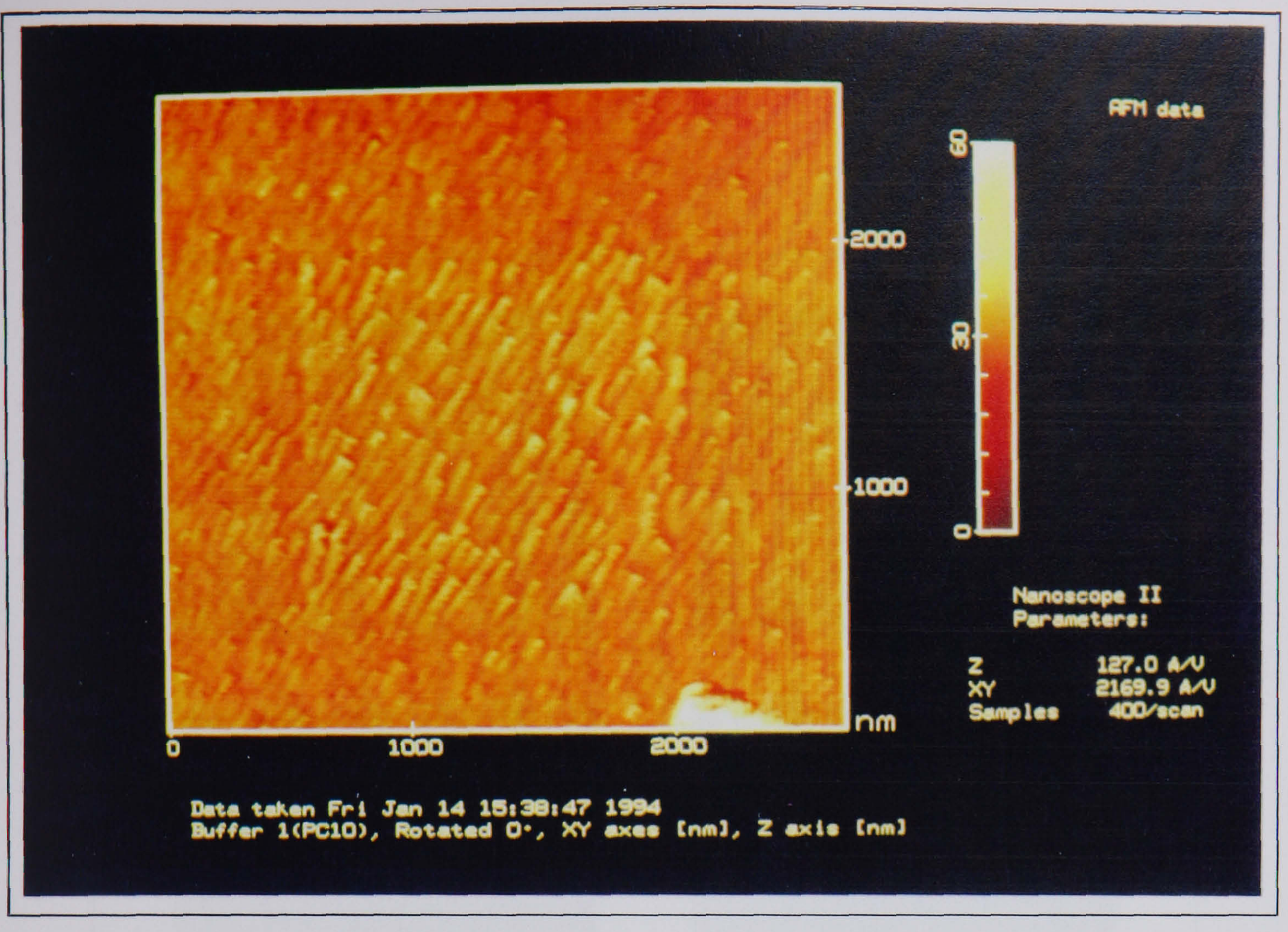

Figure 7.3: This image clearly shows the effect of scanning in the presence of the plasticizing vapour. The central region shows just such an area of polymer (having previously been scanned whilst saturated by plasticizer). The film was allowed to dry before this image was taken.

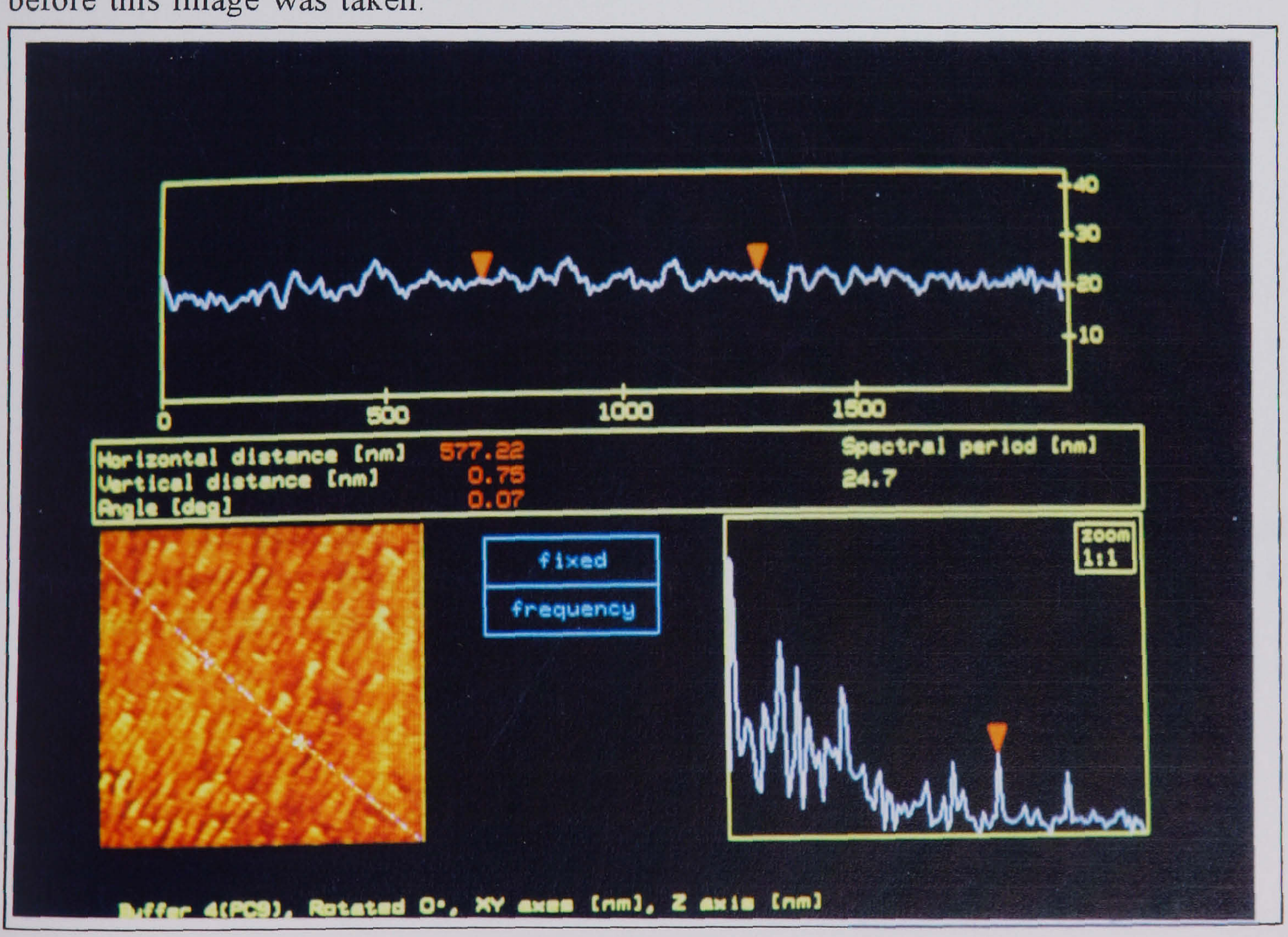

Figure 7.4: The rough area in the centre of figure 7.3 was investigated by cross-sectioning by line-scans. The line scans reveal the surface profile and other subtle measurements can be made (see figure 7.5).

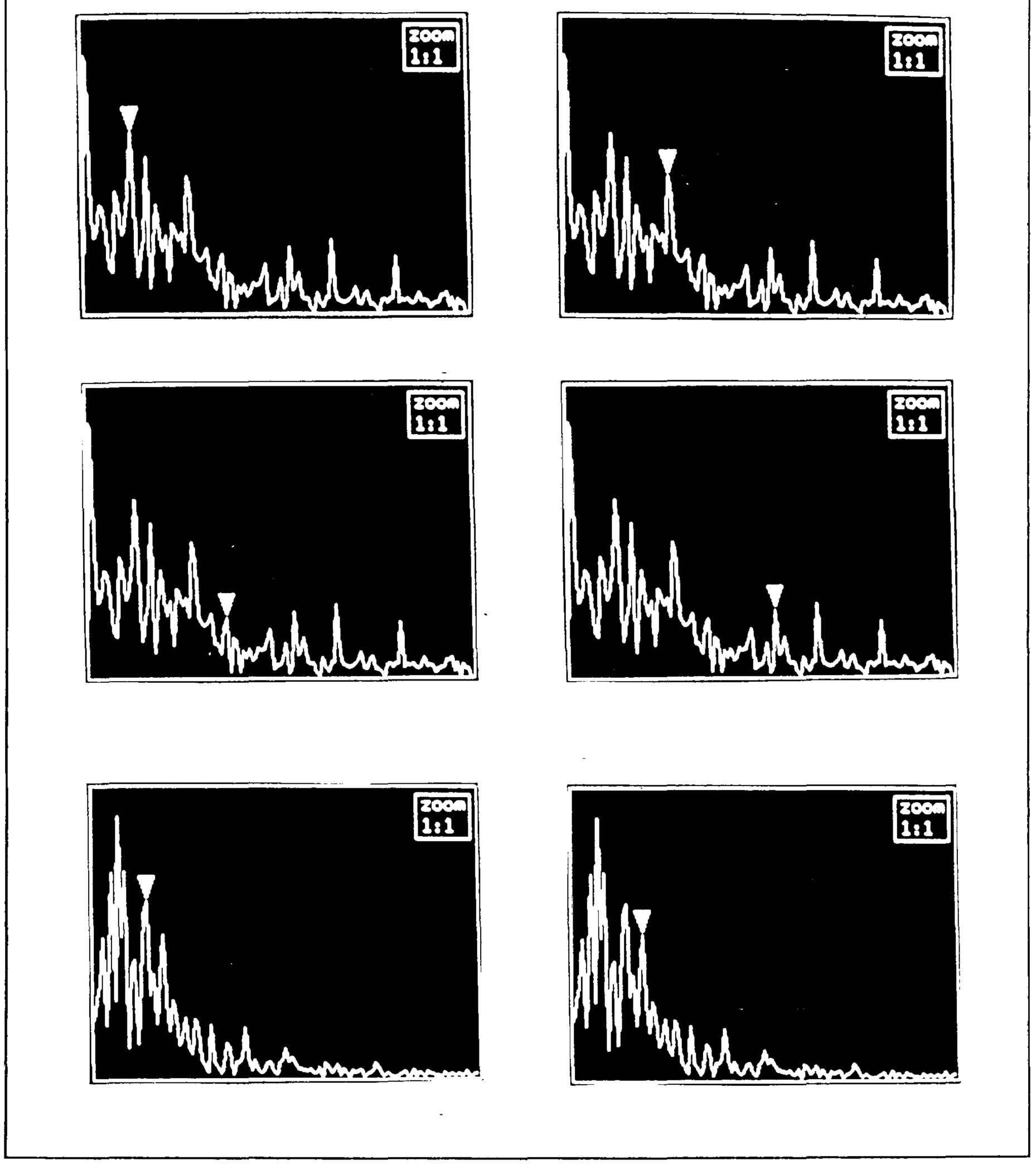

Figure 7.5: The line scans taken across the image shown in figure 7.3, were converted in to frequency space and the key spectral periodicities of the line scans measured. It was found that the spectral periodicity was related to the polymer chain dimensions.

Figure 7.4		Figure 7.5	
Peak Designation	Spec. Period /nm	Peak Designation	Spec. Period /nm
a	139.0	a	131
b	65.6	b	59.8
c	50.7	c	44.9
		d	29.9
		e	24.7

Table 7.3:

This table gives the spectral periodicities of the key peaks in the frequency spectrums of the line scans of figures 7.4 and 7.5. The peaks relate to the dominant fibril dimensions.

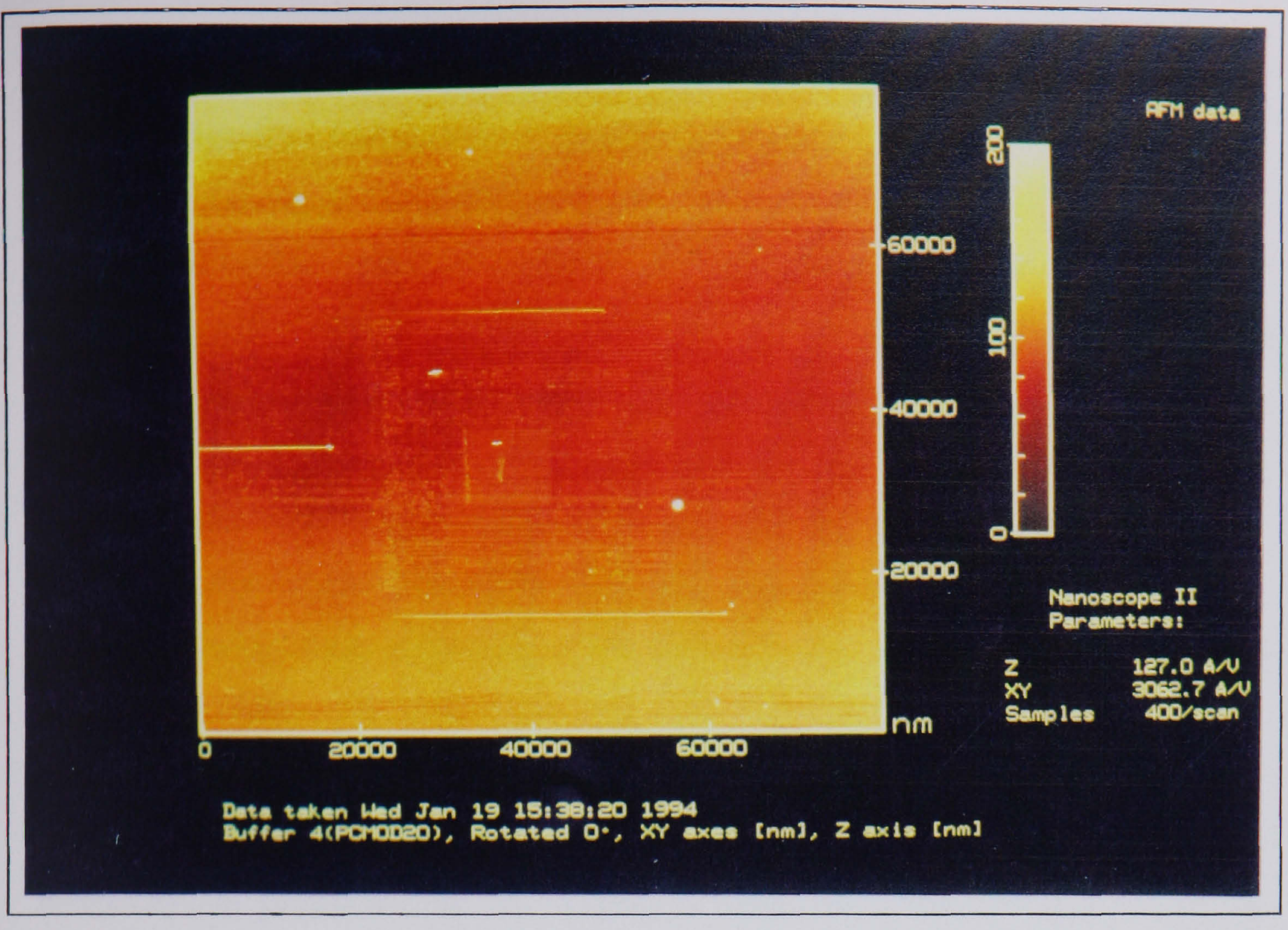

Figure 7.6: As the image scan size was increased in stages, the effect of the tip on the polymer (and plasticizer) was to produce a series of nested squares corresponding to the previous image area.

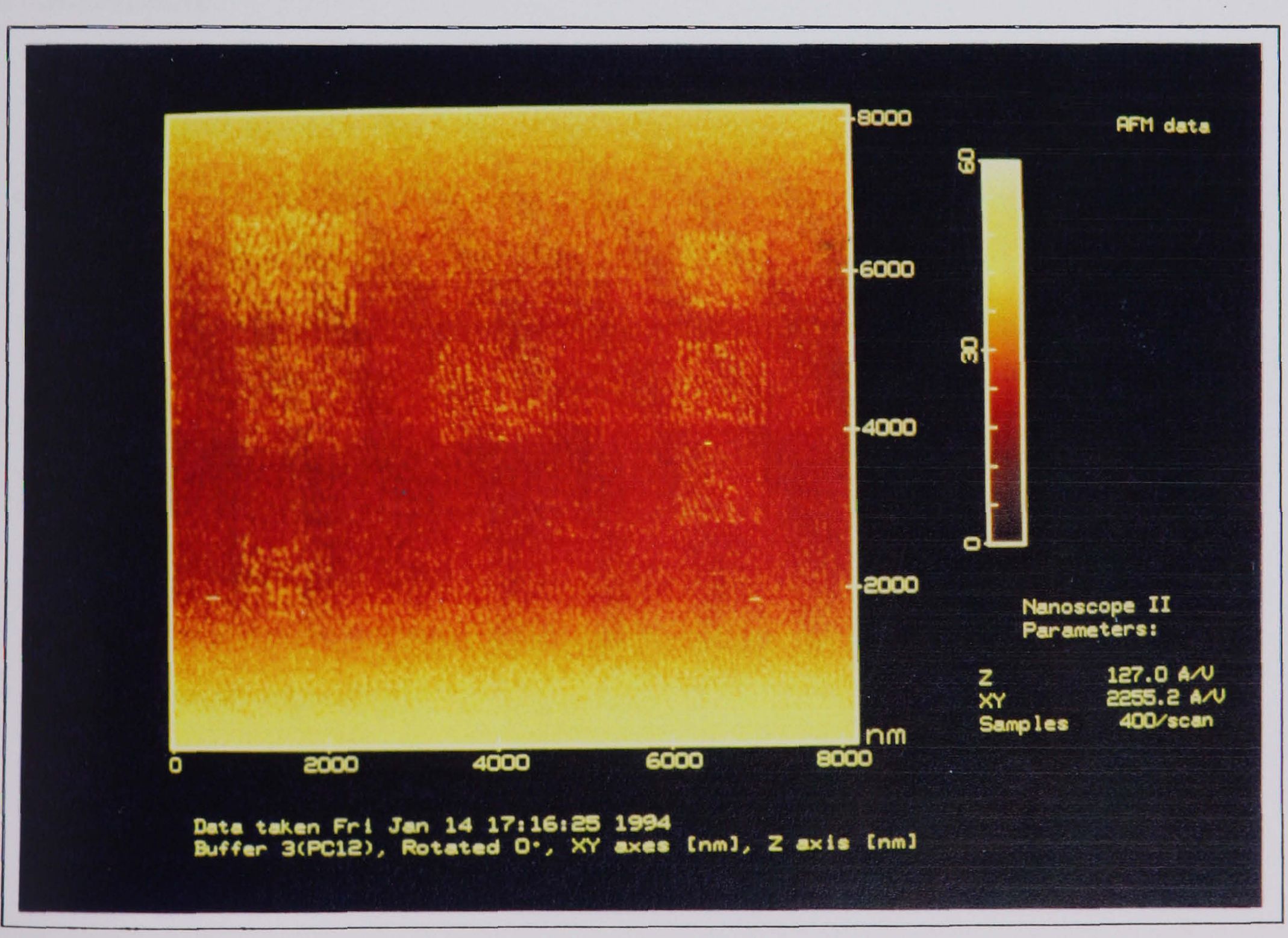

Figure 7.7: This image shows the effect of scanning in small areas in a regulated pattern. In this case each of the squares was produced by scanning a one micron area in the presence of the plasticizer. The tip was moved away to the next site and the procedure repeated. The modified area remained visible for over 24 hours.

high force mode (10^{-8}N) over a polystyrene film resulted in the formation of linear, ridge-like features in a direction perpendicular to the tip scanning direction. Leung & Goh[1992] refer to the molecular dynamics calculations performed by Landeman et al[1990] on the interaction between a nickel AFM tip and a gold substrate (see chapter 3) to explain the strong adhesive forces involved. The former describe the polymer chains wetting the tip in the same way that Landeman et al[1990] describe the Au atoms wetting the Ni tip. However the very long molecular chains of the polymer prevent permanent wetting of the tip and instead the tangles formed in films of polymers of high molecular weight aid clumping or the formation of polymer chain aggregates within the film.

The results presented here show the same linear patterns as described above and the formation of the 'square' region of altered polymer and its longevity, is predicted by the Leung & Goh[1992] results and by Jin & Unertl[1992]. The pattern observed in figures 7.5-7.7, was accentuated by the presence of the plasticizer and drying out the films sufficiently minimized the interaction.

By drying out the PC films, immobilization of the polymer chains resulted and little in the way of subsequent crystalline growth ensued. Thus it should be noted that it was not possible to directly observe the crystallization process whilst the plasticizer was present. In a different study [Schwindlein, 1995], the AFM was used to image PEO doped with nickel bromide. Under certain experimental conditions, the salt was observed to prevent or inhibit the crystallization process, to the extent that the spherulitic development was only partial throughout the film. However on imaging with a relatively high force and over successive scans, the tip acted as a 'nucleating' source and new spherulitic development occurred only in those areas scanned repeatedly.

The direct observation of any crystallization process even under other AFM modes (for example, one of lower force or non-contact) is not sanctioned as even a minimal tip-sample contact could influence the crystallization.

7.4 FILM 3: Initial Spherulitic Growth

The existence of pre-spherulitic polycarbonate material was observed in the form of linear bundles of fibres or rods (see figure 7.8) and were formed from the liquid doping of a relatively thick polycarbonate film. In figure 7.8 there are over twenty bundles, some lying over each other and all randomly distributed on the gold substrate. A higher magnification image of the bundles is shown in figure 7.9 and some detailed surface structure may be deduced. For example, the bundles are seemingly comprised of parallel fibres. The bundles are all very similar in both width and in the length of their linear portion (see table 7.4).

The occurrence of these rods is very important as a comparison can be made with these and some of the STM images taken after plasticizer treatment. The STM images show rods and large linear species (20-30)nm wide and several hundred nanometres long (figure 6.35). The same basic component of the polymer crystalline entity can be observed in the much larger AFM image (e.g. figure 7.9). The AFM does not rely on a conduction mechanism to achieve images and hence although the STM can observe the most basic PC units, (rods and micro-crystalline regions), it is suggested that for bare samples of this thickness, the AFM alone is used.

As the length of the rods reaches a micron or so, branching is observed. It should be noted that where the length of the rods is much less than a micron, no branching is observed. Figure 7.10 shows a different region of the substrate from figure 7.8, but in both cases, fibrils are observed fanning out from the ends of the rods. A particularly good example of the branching may be seen just right of centre in figure 7.10. Here a 'critical length' of just over a micron is reached and the constituent fibrils no longer lie parallel to each other. Instead the fibrils show low angle branching and the 'wheatsheaf' formation which is well understood to be a primitive two dimensional spherulite is formed.

Also visible in figure 7.10 is a star shaped feature. Situated in the top left of the image, this highly symmetrical feature is most unusual and unexpected. A higher magnification image is given in figure 7.11. This

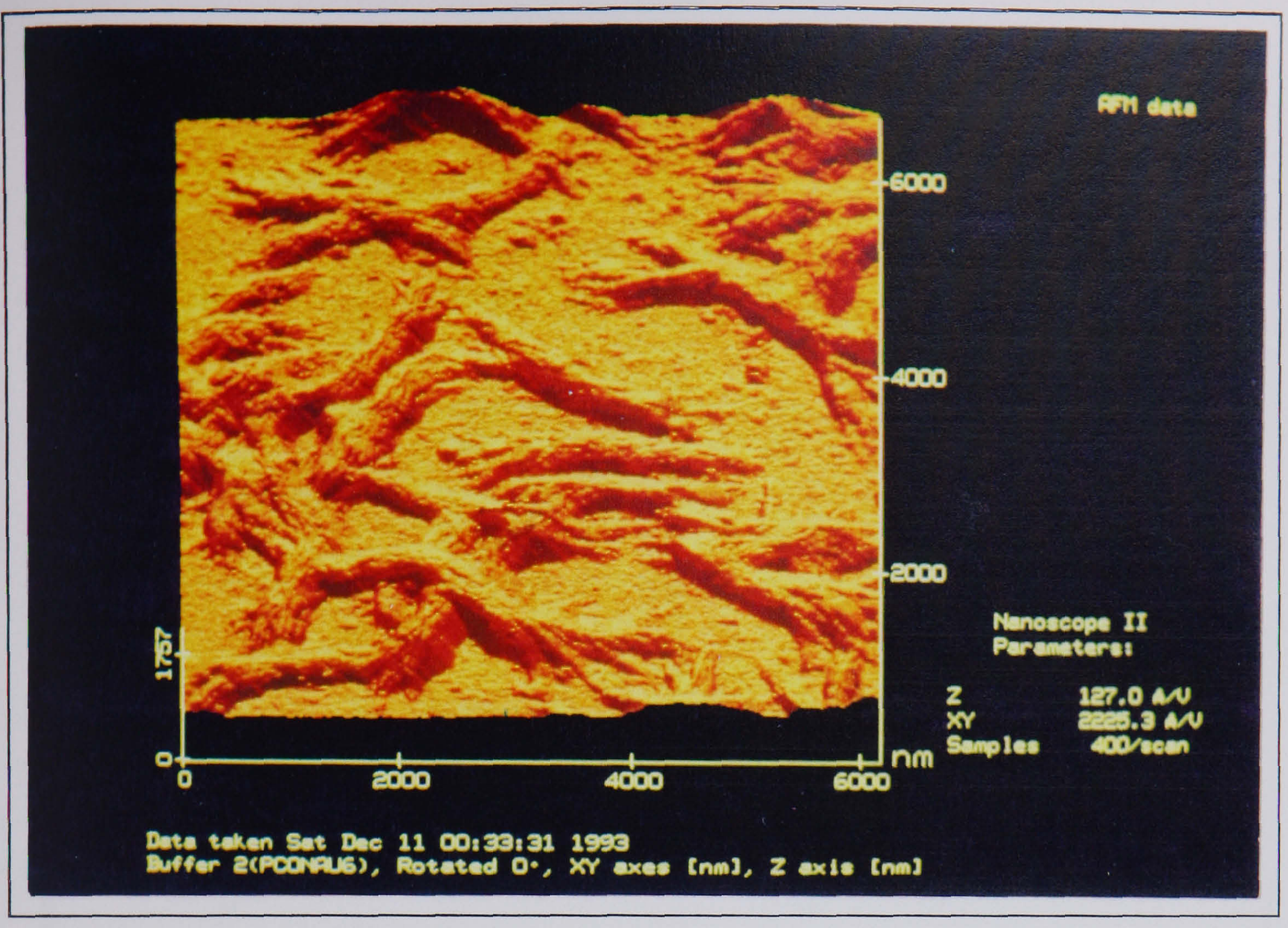

Figure 7.8: This image shows bundles or rods of PC crystalline material in the form of fibres distributed across the gold substrate. The rods are one to two microns in length and (up to) half a micron in width.

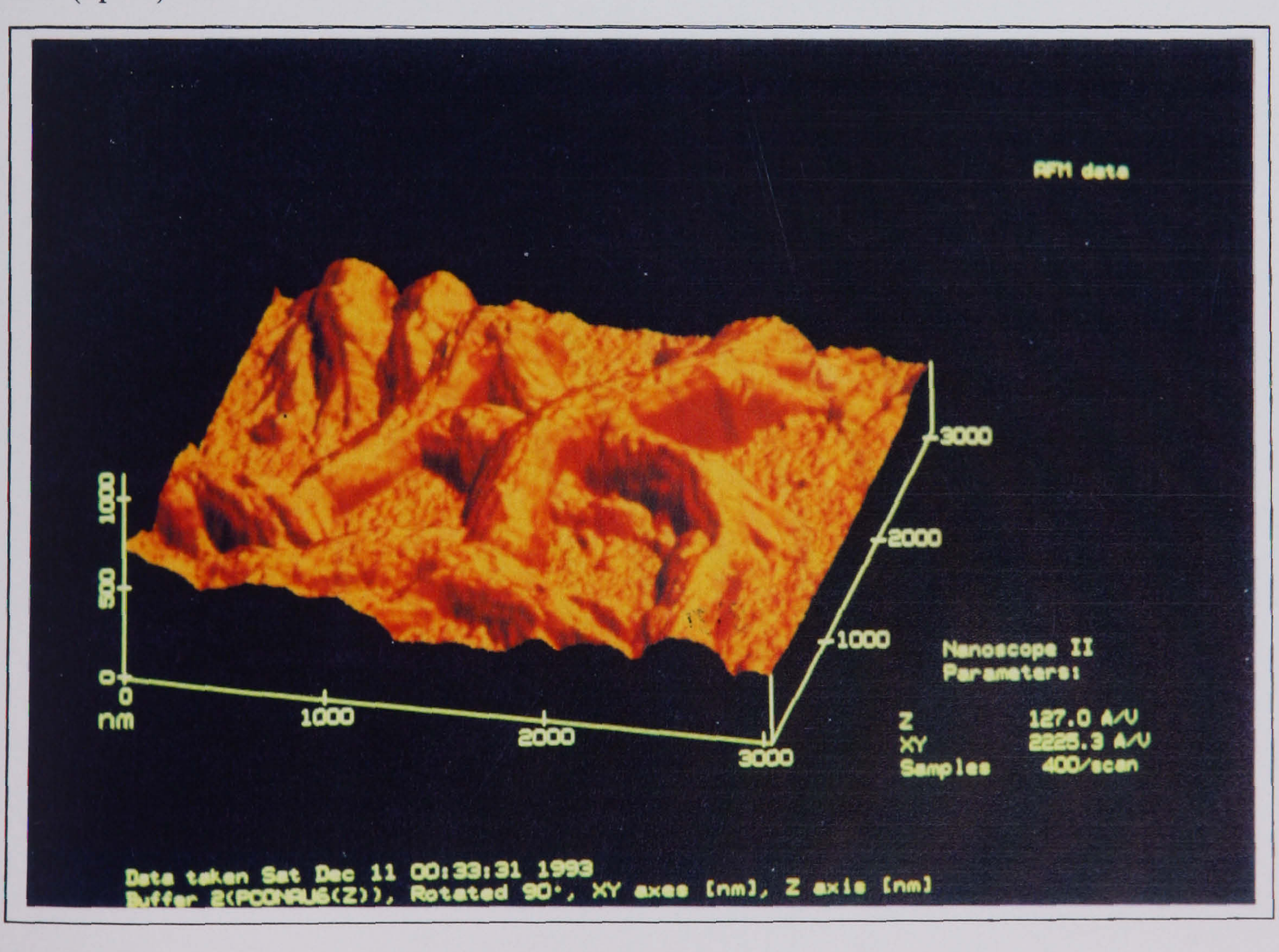

Figure 7.9: This Image shows the PC rods at a higher magnification. On this image the rods appear to contain parallel (and axially orientated) fibres 20nm-30nm in width.

Bundle or Rod	Width /nm	Height /nm	Length* /nm
a	545	241	2000
b	550	173	1450
c	516	192	1600
d	525	180	1700
e	540	218	1850
Average	540 +/- 11	200 +/- 20	1750 +/- 180

Table 7.4:

This table shows the dimensions of five rod-like bundles taken from figure 7.8. *The length of the rod in this instance is defined as the length of the portion before the onset of branching.

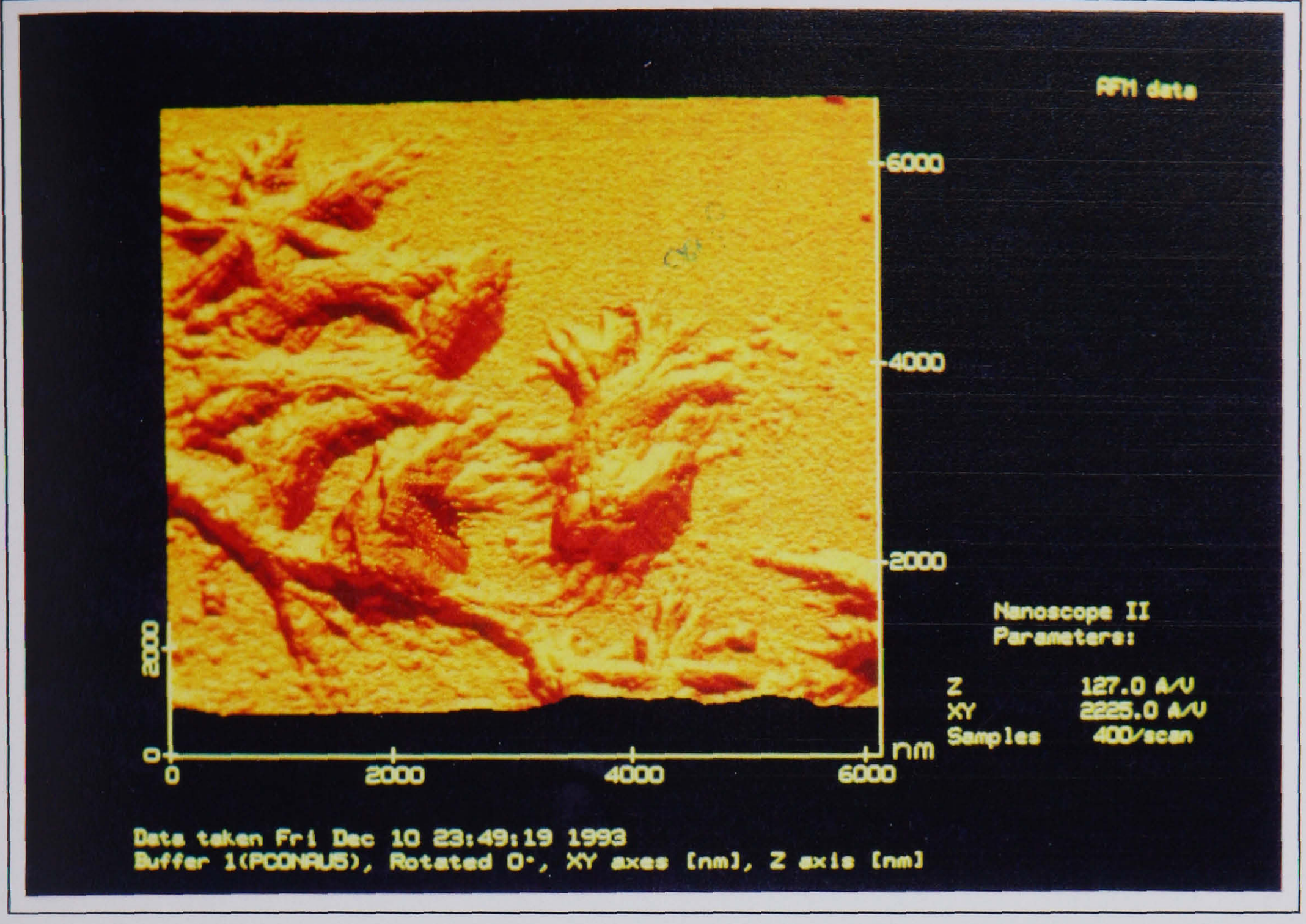

Figure 7.10: This AFM image of the PC rods shows the initial branching of the rods. The branching occurs as the fibres (at the end of the rod) branch to initiate spherulitic development. Note the 'star' formation in the upper right of the image.

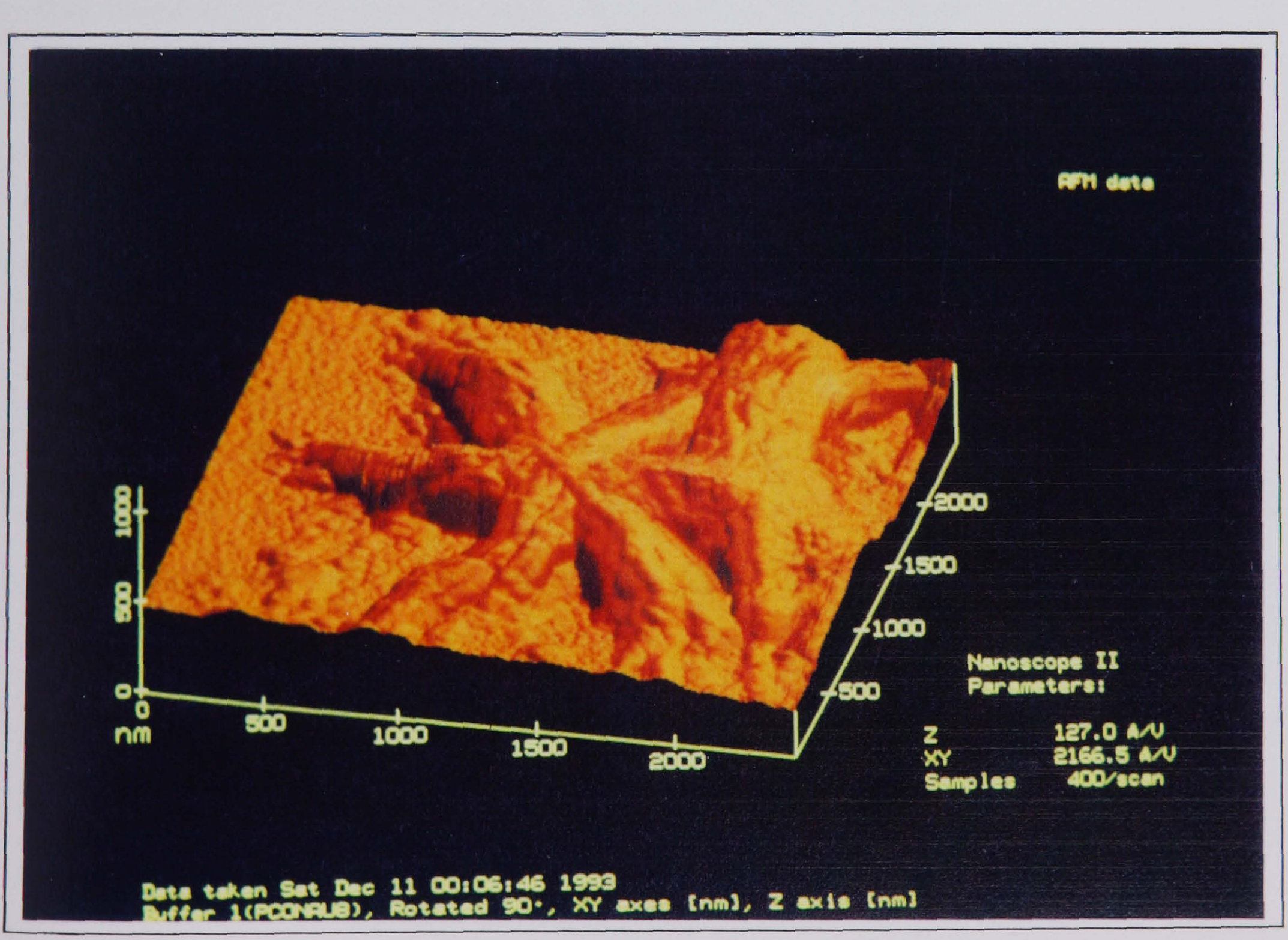

Figure 7.11: A magnified image of the star shaped feature from figure 7.10. The arms of the star are clearly composed of parallel fibres. The formation was found to be very rare, the usual pre-spherulite feature being the simple rod.

particular formation shows the striation associated with parallel fibrillar alignment with a rod width of approximately 500nm. It appears that perhaps six rods may have nucleated at the same point. The angle between adjacent rods is measured from the heavy black lines along the rod from the centre of the star (as depicted in figure 7.12) and recorded in table 7.5.

There are other star shaped entities amongst the rods and fibrils. Figure 7.13 shows two more, again both highly symmetrical although some of the legs are obscured by overlying material. The formation of the 'star' is believed to occur from a central nucleating entity initiating growth on all directions[Okada, Saito & Inoue, 1992]. Similar features are common in other polymers for example PE. However in most of the polycarbonate samples imaged, the growth seems to have started with a single crystal (rod) through unidirectional growth. Further development by growth, branching and fanning out of the fibrils results in a 'sheaf' formation (see chapter 4). The 'star' shaped growth and the sheaf-like growth result in two dimensional spherulitic growth in the form of discs. It should be noted that nucleation in this manner for PC has not been reported in the literature.

7.5 PRIMITIVE SPHERULITIC GROWTH FILM 4

A relatively thick (750nm) polycarbonate film was exposed to the liquid dopant for a period specified in chapter 5. An attempt was made to advance the growth of the fibrils from the rod like stage into the 'wheatsheaf' formation associated with spherulitic growth. Figure 7.14 shows three distinct regions on the surface, i.e. the substrate, the amorphous and the crystallized PC film.

The substrate is identified by the mottled gold grain structure typically formed as a result of the evaporation process (see figures 6.10 & 6.11). The gold grains are small on the scale of the image shown here and are only just resolved.

The amorphous material appears smooth and its surface structure is

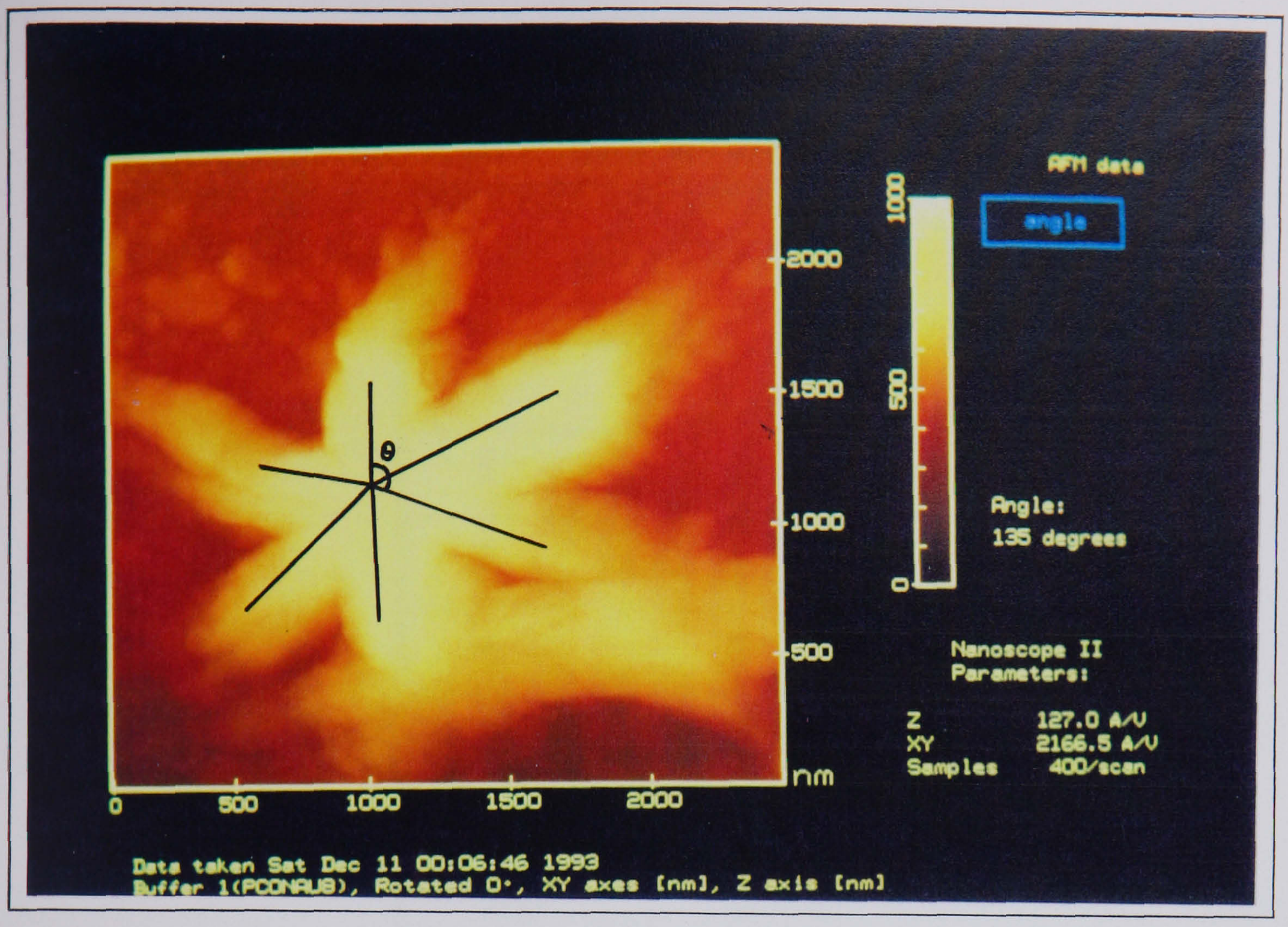

Figure 7.12: The angle between the arms of the star shaped feature were measured and were found to be approximately 60°.

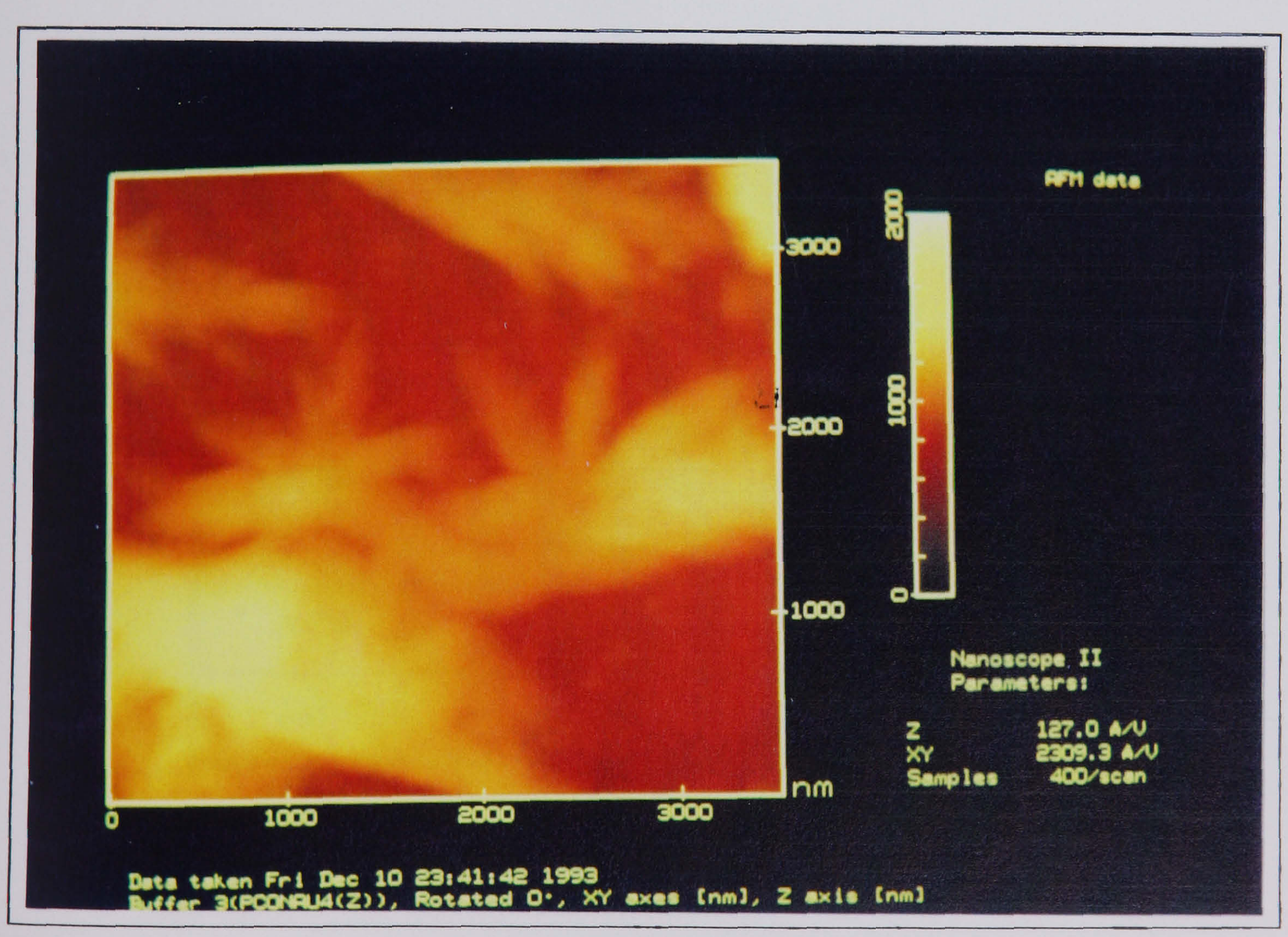

Figure 7.13: Other star shaped formations were observed along with the usual linear rod shaped development. This image shows two of the former features.

Rod Number	Angle / °
1	60
2	50
3	65
4	60
5	56
6	69
Ave	60 +/-5

Table 7.5:

This table shows the angle between the points of the star formation. The evidence is of a highly regular and symmetrical formation totally unexpected in this study.

SPM Trial	Ave. Width /nm	Ave. Length /nm
AFM	25 +/- 5	175 +/- 50
TMAFM	24 +/- 4	150 +/- 50

Table 7.6:

This table gives the approximate dimensions of the sub-fibrillar components.

very similar to the film examined in figure 7.1. There are no detectable fibrillar entities in the film, unlike the 'wet' films described in figure 7.2 and this is because drying the film reduces its softness and constituent chain mobility.

Emanating from the amorphous film, the crystalline polycarbonate is clearly at a more advanced state than the rod-like structures observed in figure 7.4. The linear rod structures containing bundles of polymer fibrils may still be discerned in the centre of the development and are about a micron or so long. The low angle branching and extensive growth of the fibrils from both ends of the rod result in the characteristic 'wheatsheaf' formation (discussed in chapter 4). There are two such sheafs in figure 7.14 and part of a third, lies just to the upper left of the image. The size of the sheafs at this stage is approximately four microns in length.

A thicker PC film as imaged by the low voltage SEM, at the same stage of development is shown in figure 7.15. The film has been coated in gold to prevent charging and enhance the image and the extra film thickness has allowed appreciable three dimensional, hemispherical growth. Despite the fact that the sample is no longer bare and cannot be crystallized further, the 'wheatsheaf' of crystalline development is shown emanating from the dark amorphous polymer.

More plasticizing liquid was added to the polycarbonate film and this resulted in the assimilation of the surrounding amorphous polymer into the crystalline entity as shown in figure 7.16. The increase in size of the two dimensional 'sheaf' is achieved by lengthening and branching of the fibrils. The entity in this image still presents the rod-like bundle of parallel fibrils at the nucleation point but the branching from this region has extended to five or even six microns at the greatest extent and this is slightly larger than the entities observed in figure 7.14. An SEM image of the primitive 'wheatsheaf' like entity is given in figure 7.17. The fibril structure in this image shows branching and some evidence of sub-fibrillar - lamellae construction.

The continual low angle branching of the outer-most fibrils of the rod

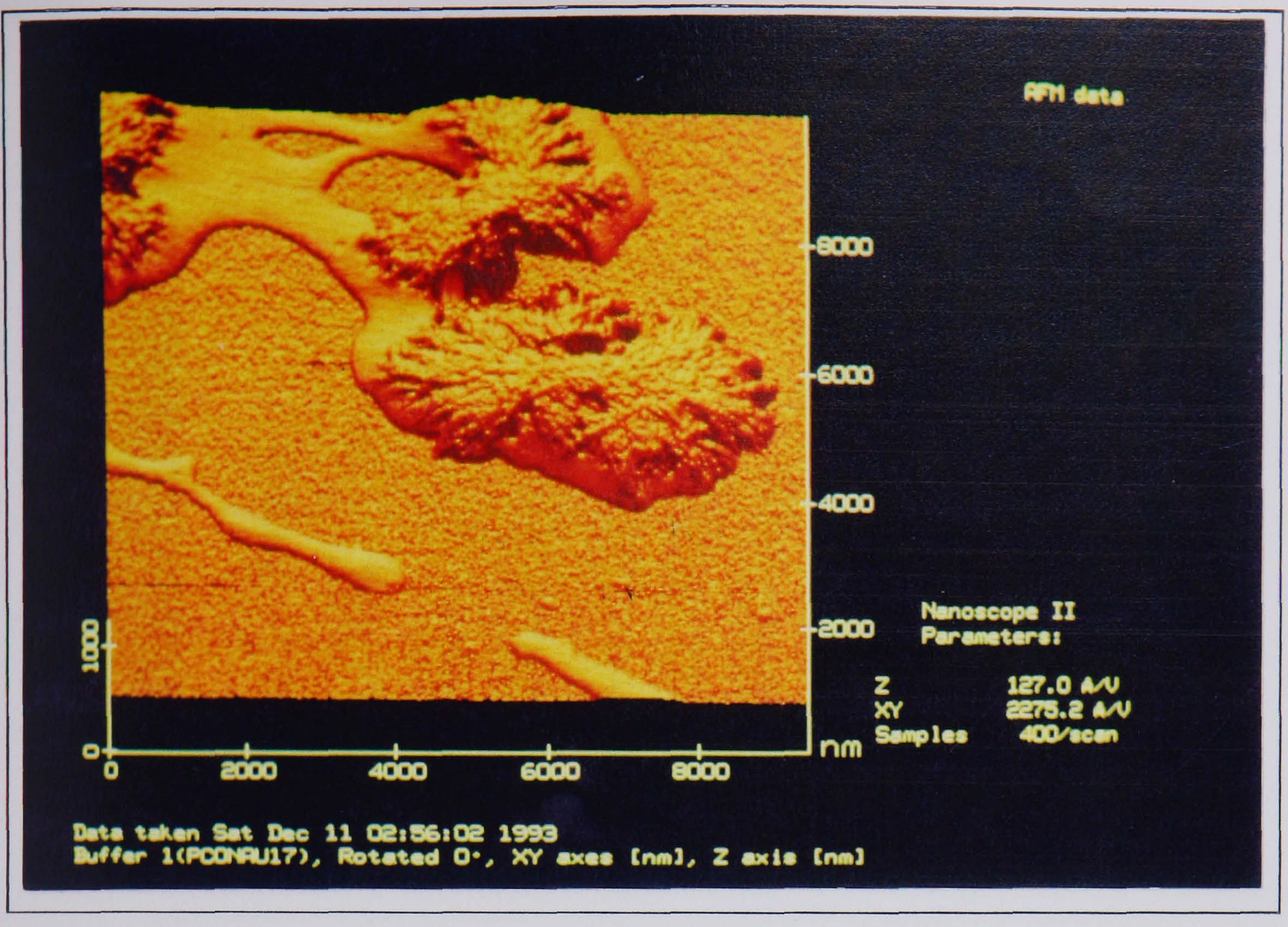

Figure 7.14: This figure shows the next stage in the development of the polymer spherulite. In this image the linear rod components have branched sufficiently to create the 'wheatsheaf' formation. The amorphous PC film and the gold substrate are also visible.

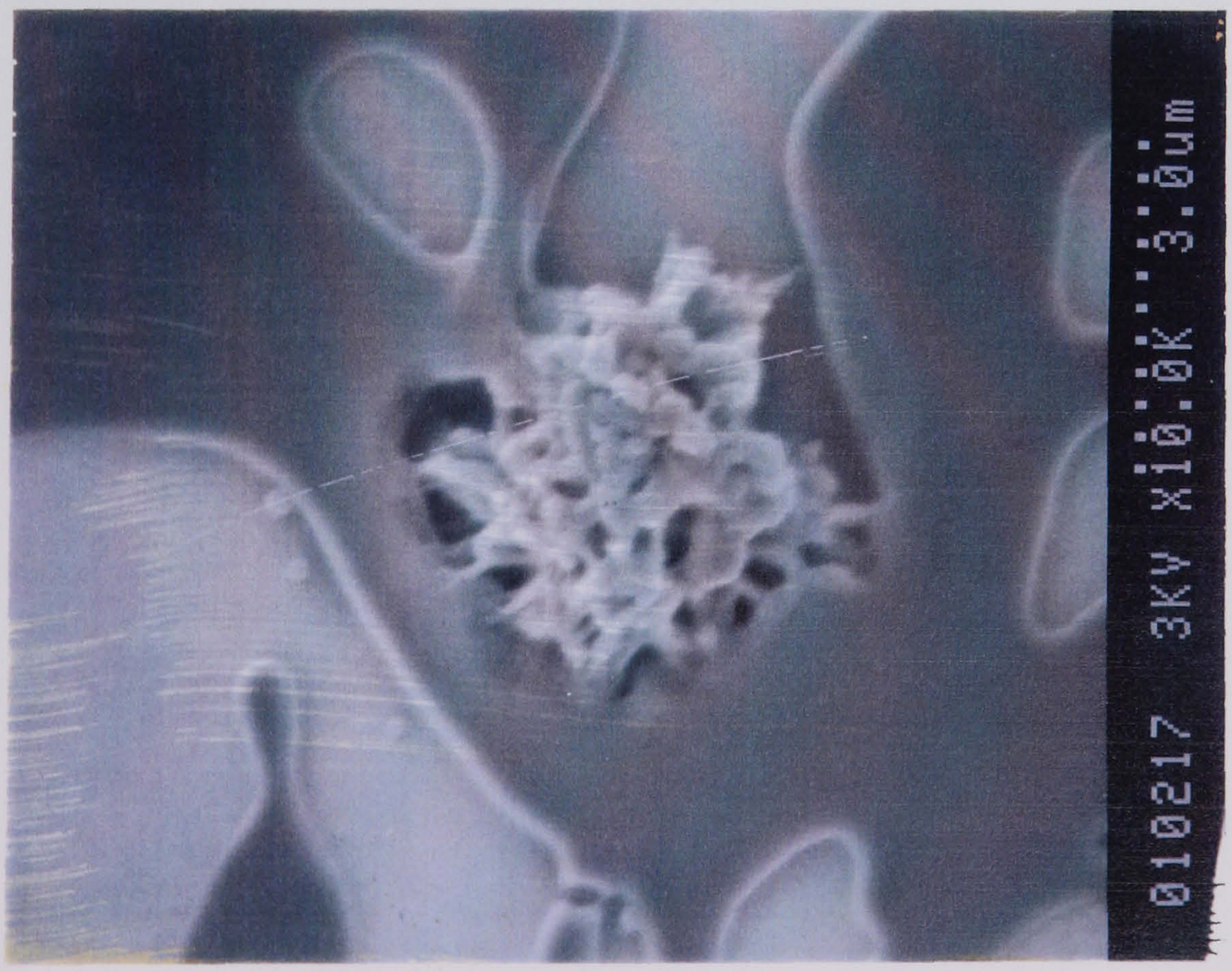

Figure 7.15: An SEM image of a partially crystallized PC film at the same stage as the film in 7.14. The amorphous PC film and the gold substrate are also visible.

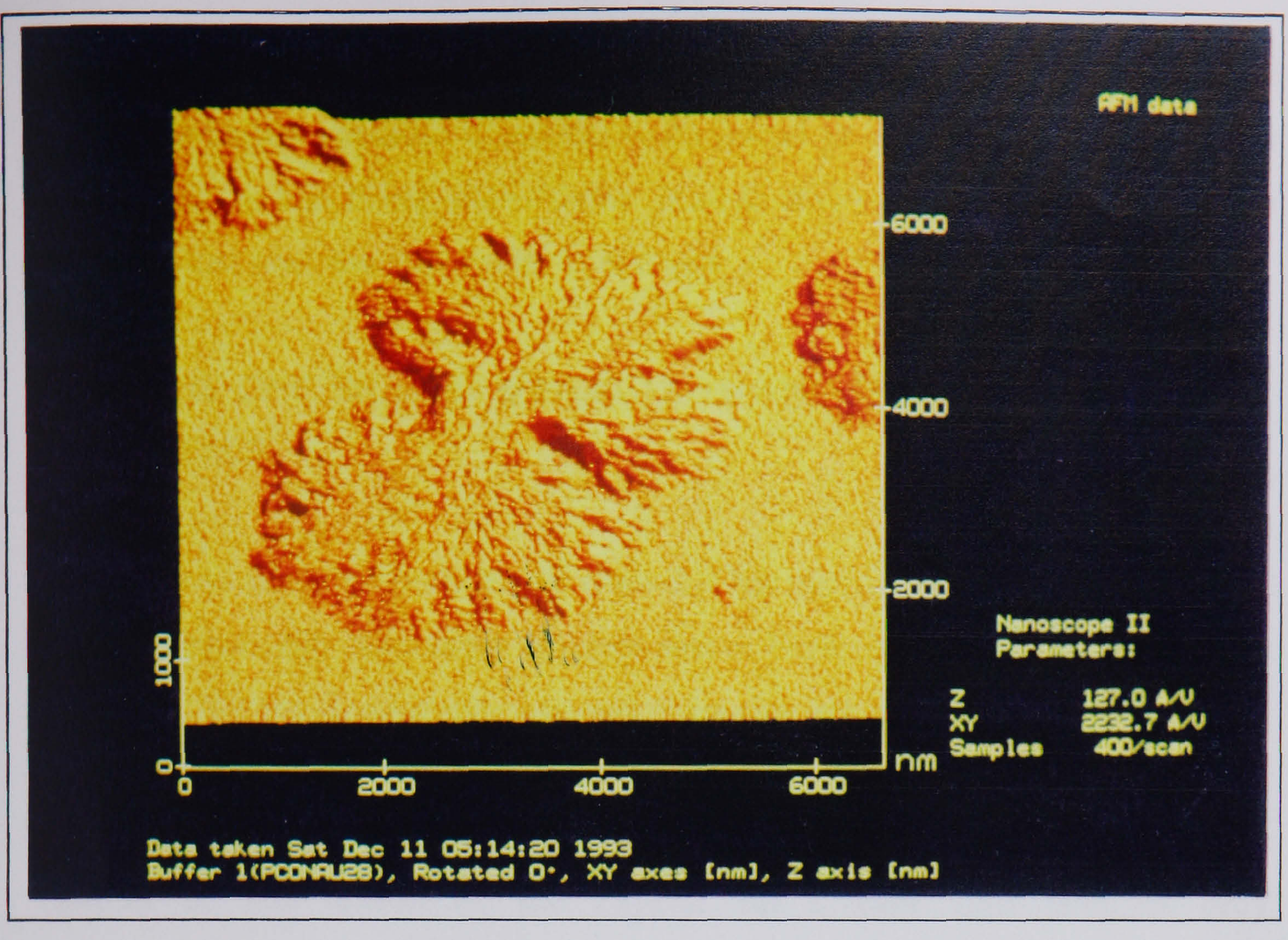

Figure 7.16: An AFM image of the film given in figure 7.14 but after further plasticizer treatment. The assimilation of the surrounding amorphous PC material has resulted in a larger 'wheatsheaf' formation.

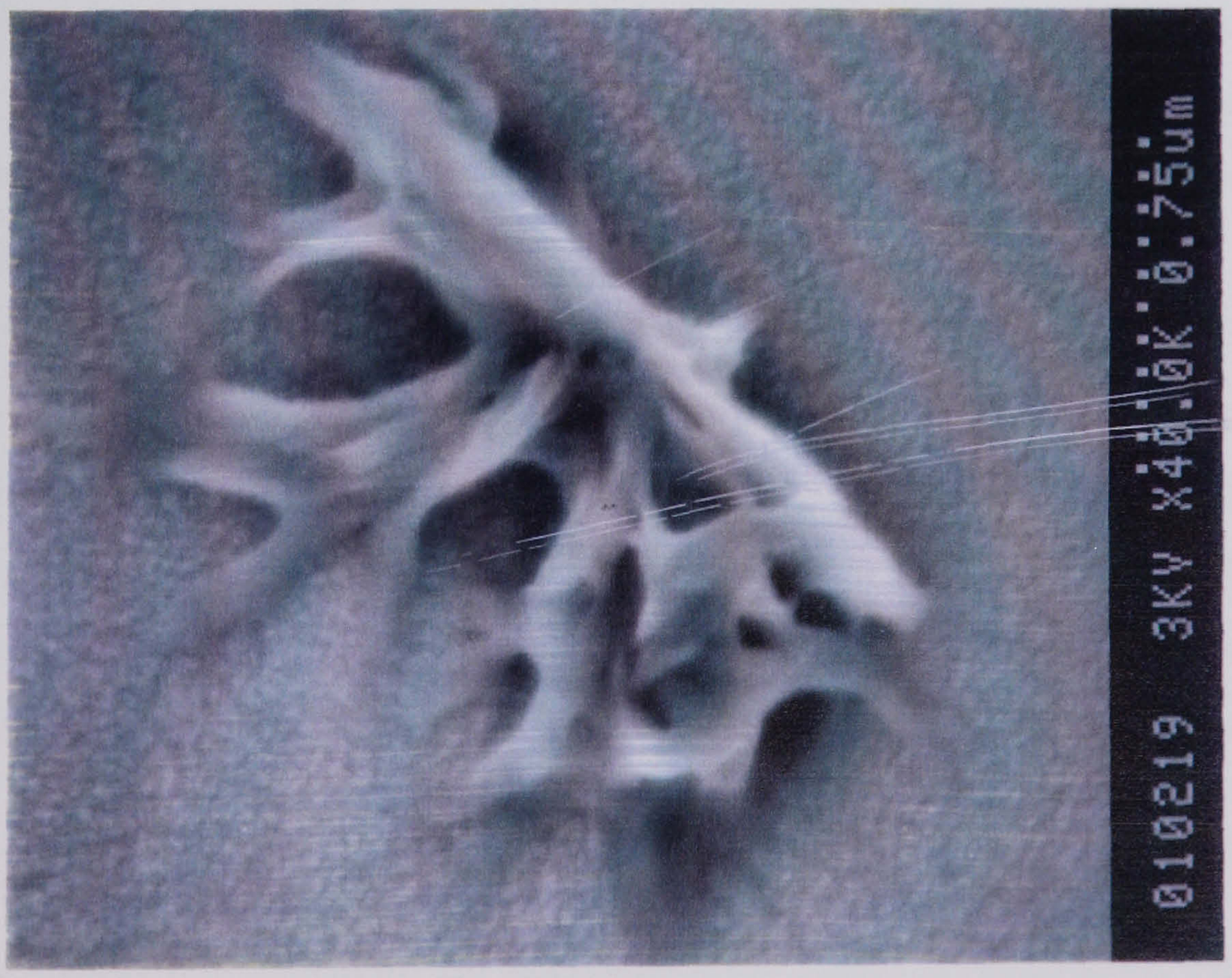

Figure 7.17: An SEM image of the film given in figure 7.16. The amorphous material is no longer visible.

soon results in growth perpendicular to the rod direction. Eventually the fibril growth is in the opposite direction to its initial growth and the space either side of the rod is filled with fibrils. It is at this stage that the wheatsheaf shape is lost and the spherulite is formed.

7.6 THE DISC SHAPED SPHERULITES AND THEIR GROWTH FILM 5

The films so far have been liquid doped. This method was found to produce the pre-spherulitic structures in abundance. However the film is somewhat disrupted by the doping process and extensive spherulitic growth over long periods was not achieved in this way. A more controlled method of spherulite production was achieved by vapour doping and is described in chapter 5. The action of the vapour on a very thin film of only (approximately) 10nm thick polycarbonate, caused an 'instant' mobilization of the polymer as described in 7.2. However the plasticizer may be left in the film for any length of time by saturating the vapour above the film. At equilibrium, the number of plasticizer molecules evaporating from the film is matched by those diffusing into it. After a period of several minutes, the vapour was removed and the film dried quickly. During the doping period the film changed morphology and whilst drying hardened enough to halt crystalline development.

The first image shown here (figure 7.18) is of the amorphous film once again, with only brief plasticizer treatment there are a few pock-marks and holes but no typical crystalline development observable within $(25\mu m)^2$. The next doping period resulted in a 'wheatsheaf' crystallite of largest diameter 1μm (see figure 7.19) associated with limited growth. It should be noted that the only gold substrate visible at this stage, was observed within the holes.

The next few periods of plasticizer treatment resulted in the formation of a disc-like spherulite followed by successive increases in diameter. The series of images given here (7.20 to 7.22) show this development.

The image shown in figure 7.23 is a large spherulite about nine microns

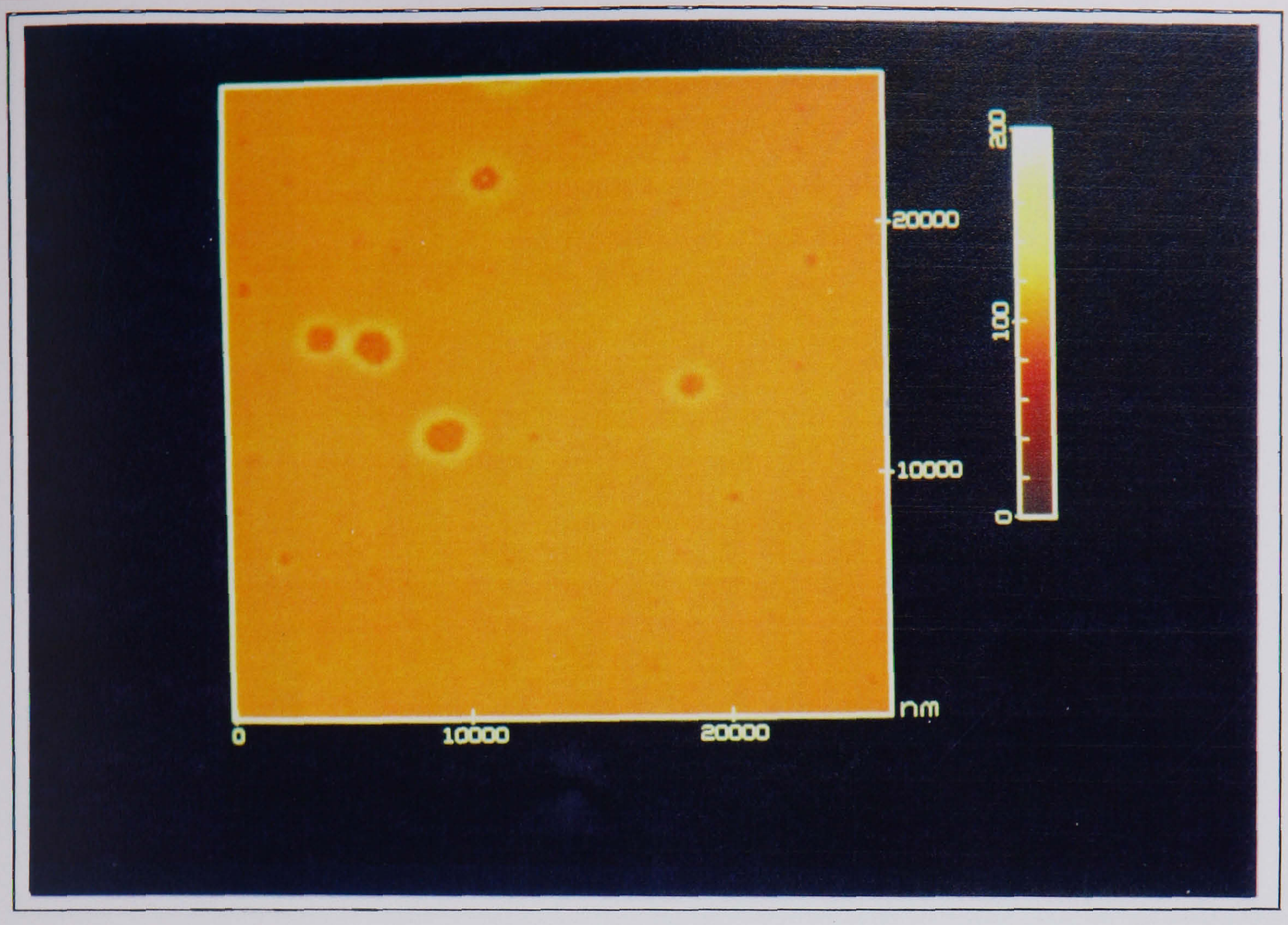

Figure 7.18: The amorphous material after a very brief period of plasticizer doping. The film is occasionally punctuated by holes. However at this stage no spherulitic development has occurred.

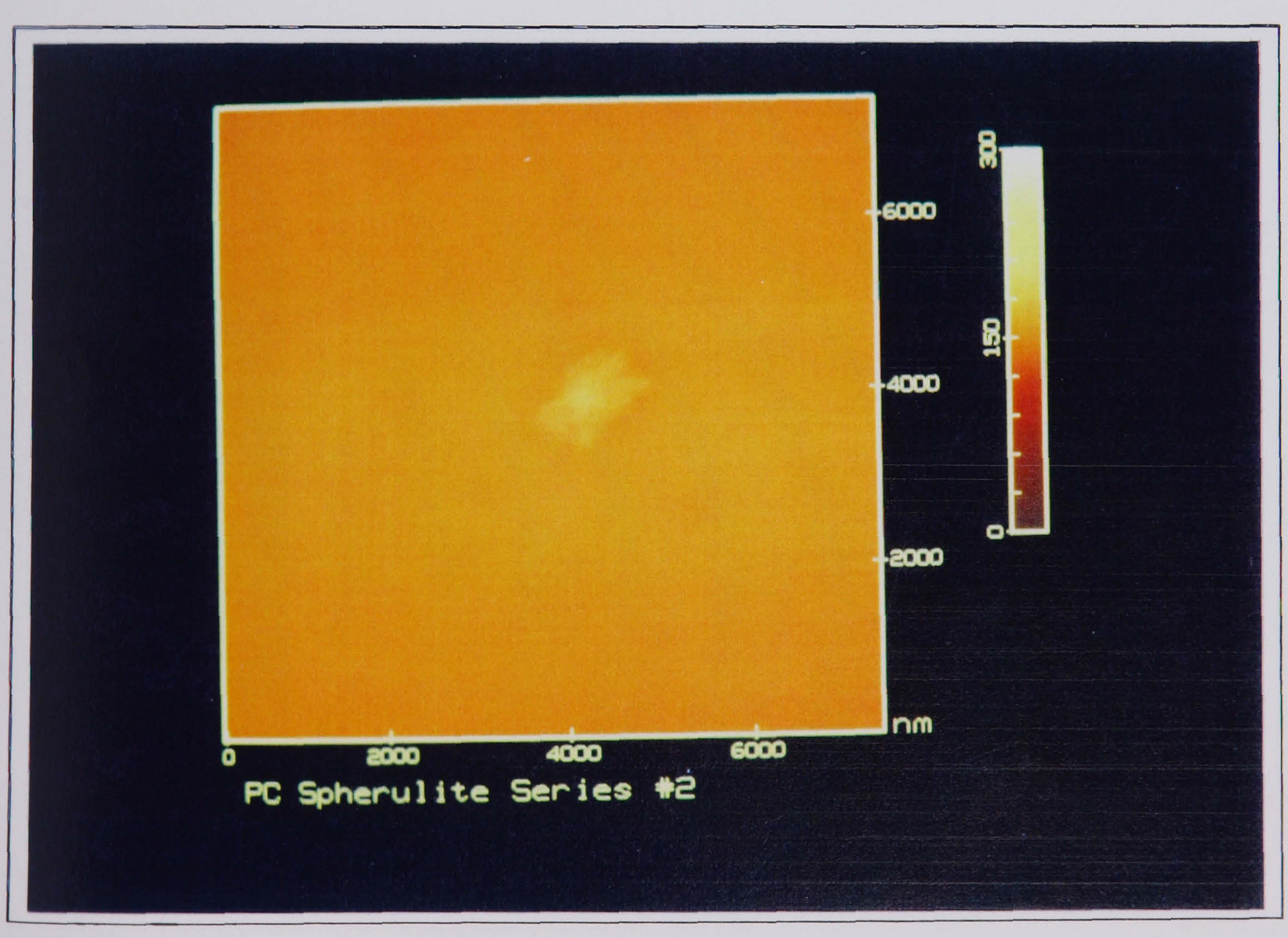

Figure 7.19: The first indication of spherulitic development emerged as a small 'wheatsheaf' formation. This feature is similar to those observed earlier (see figure 7.14 etc.)

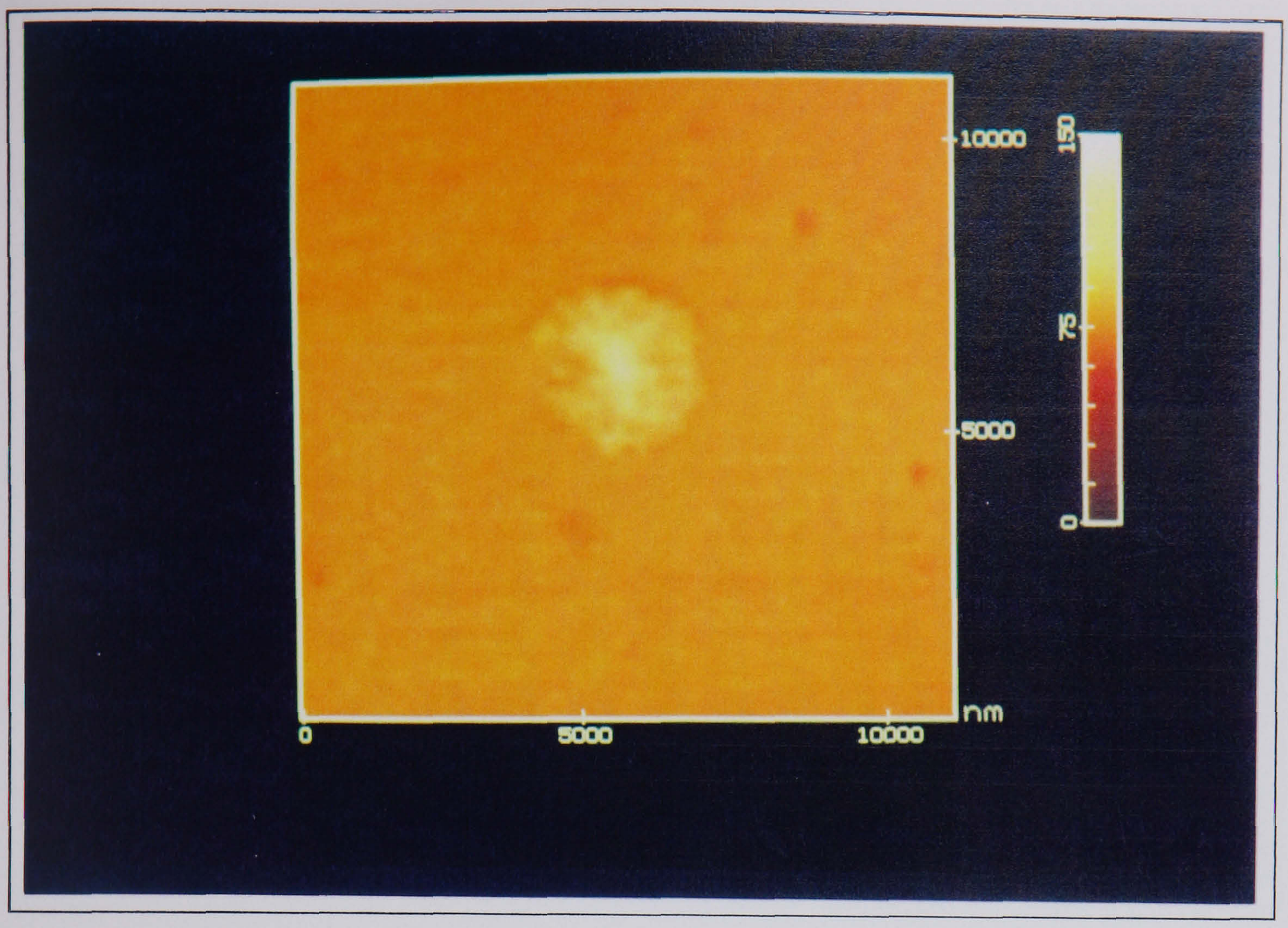

Figure 7.20: The first of three images charting the growth of the small spherulite. The 'wheatsheaf' formation has given way to a disc-like morphology'

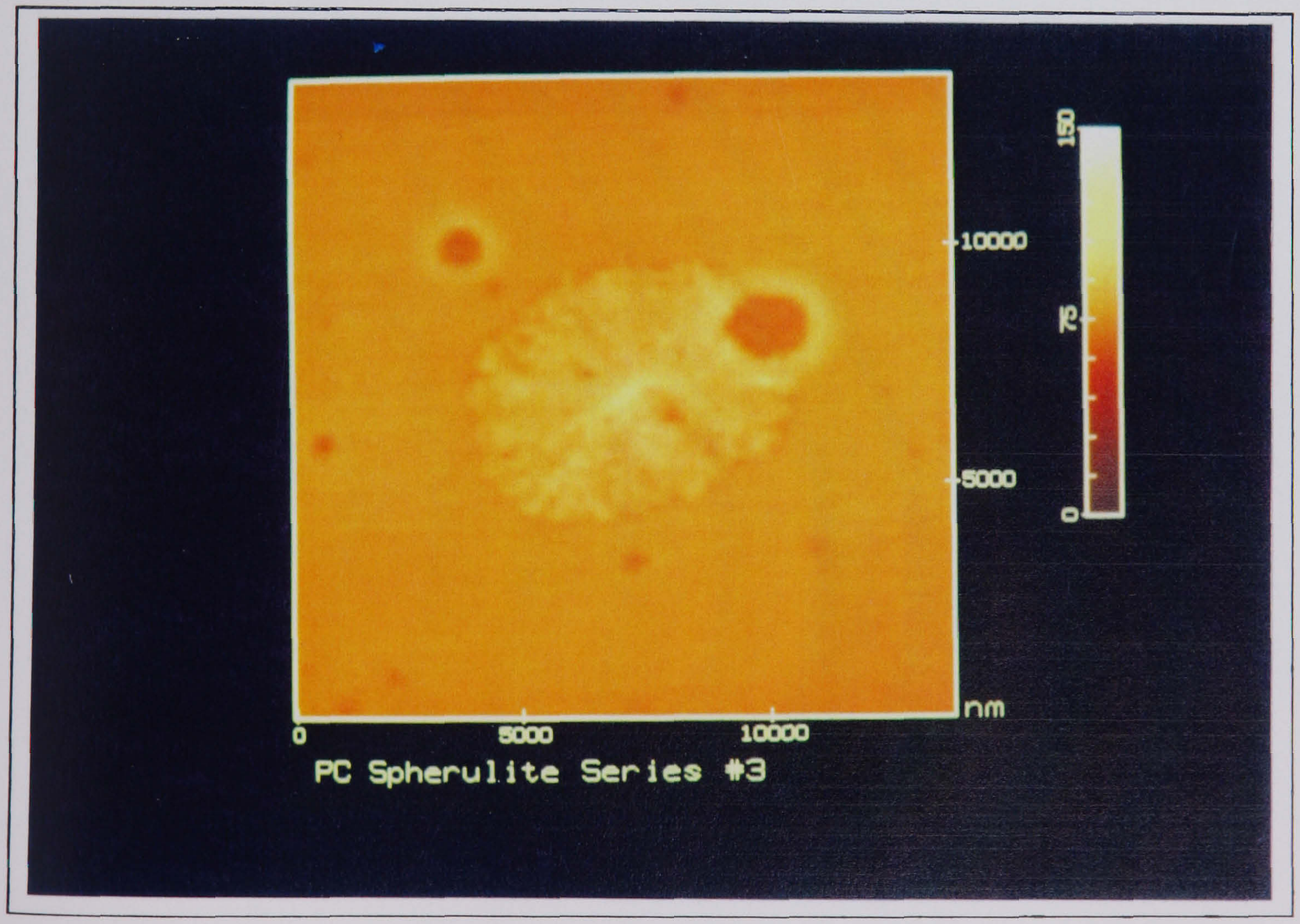

Figure 7.21: The second in a series of images charting the growth of the spherulite. The diameter of the disc-like spherulite has increased.

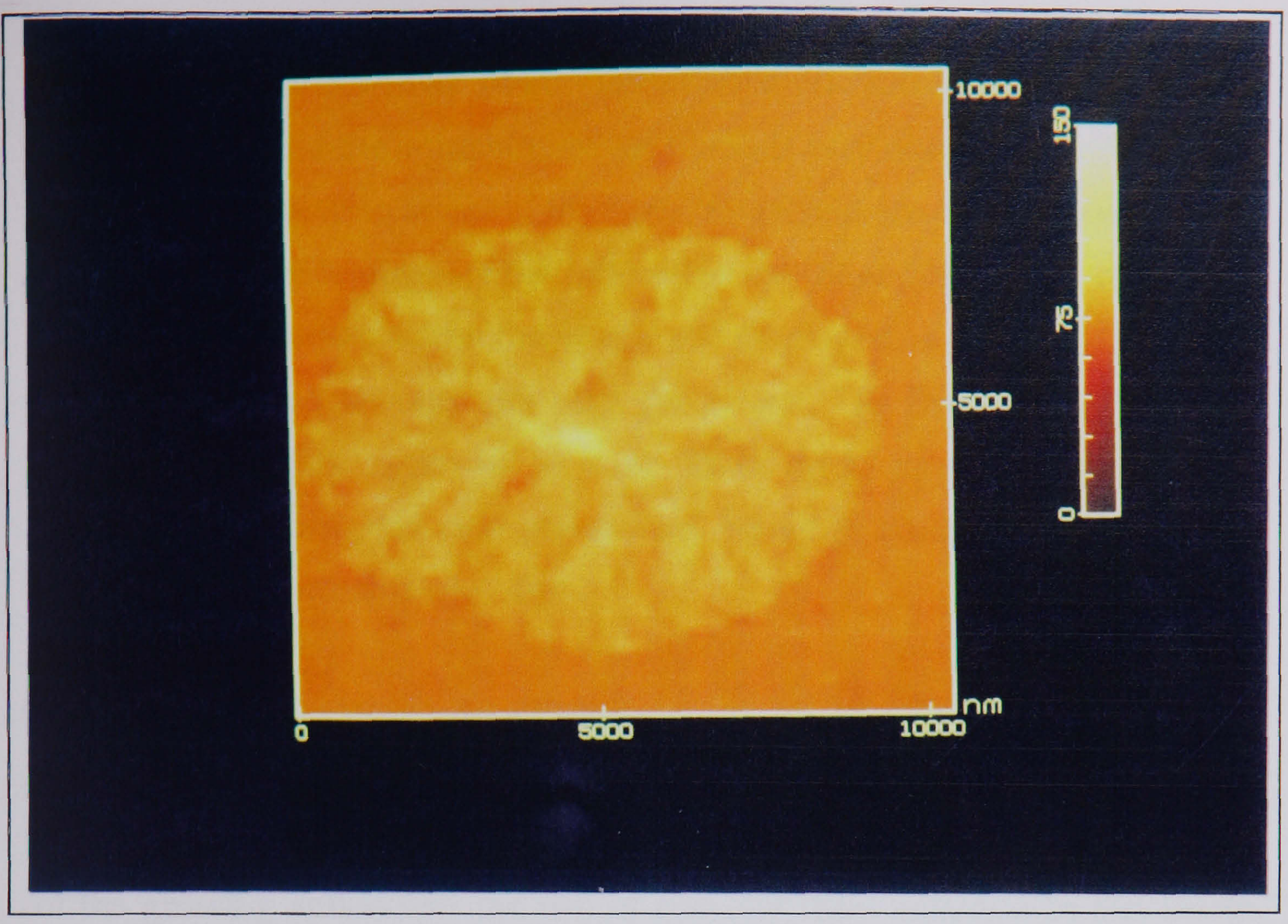

Figure 7.22: The third image in a series charting the growth of the PC spherulite. The entity has now grown much larger as a result of the plasticizer treatment.

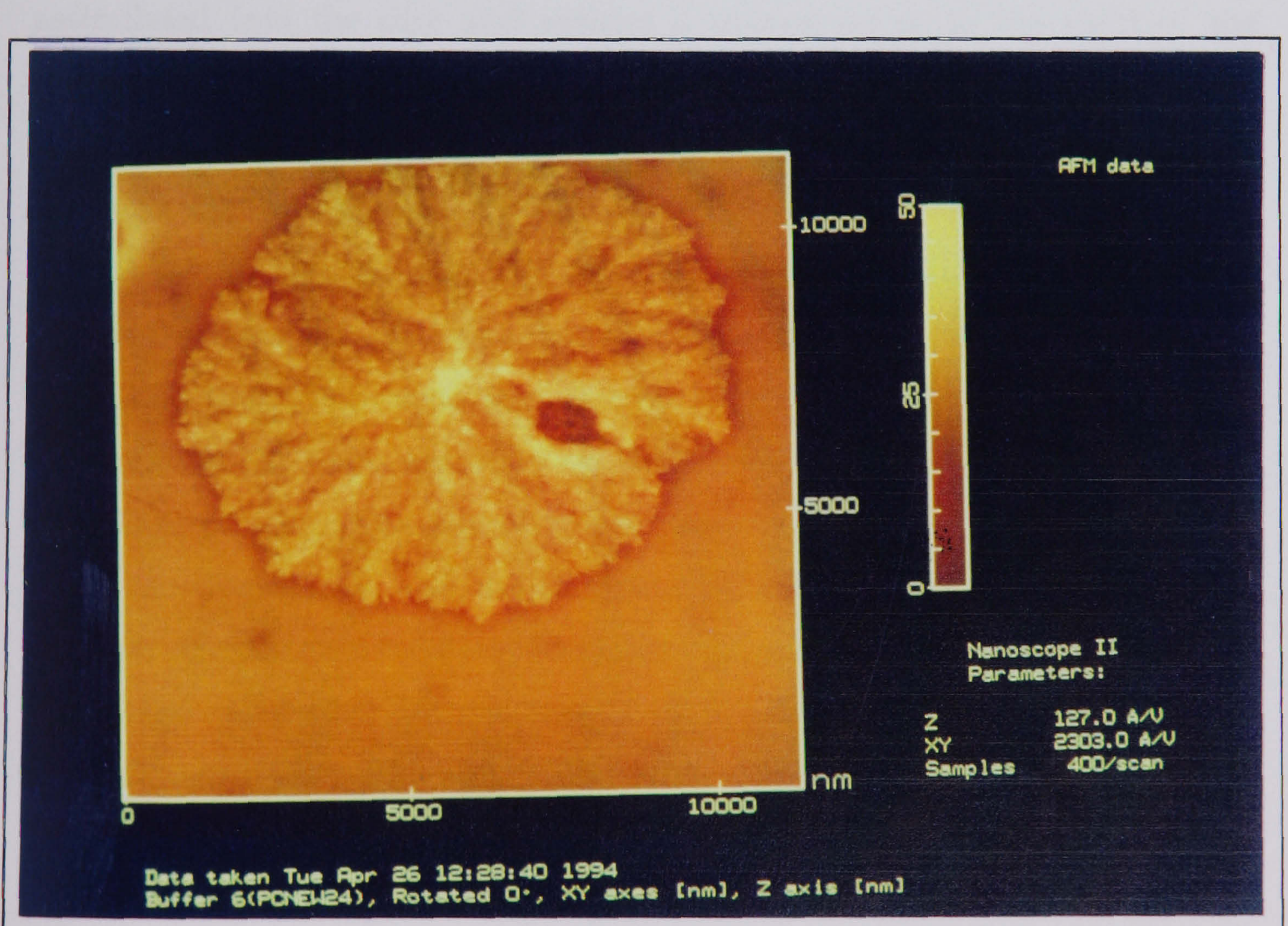

Figure 7.23: An AFM image of a large PC spherulite (maximum diameter approximately 9 microns). The nucleating region is visible as are the constituent fibrils that fan out from the nucleation point.

in diameter at the widest point. The central nucleating region is about a micron in size and the branching of the fibrils is very clear. Figure 7.24 shows a higher magnification image of the branching fibrils the dimensions of which are not very easy to measure but fall within the range 200-600nm. A series of line scans were taken across the image and displayed as images 7.25a-b. The central nucleation site appears very prominent. The line scan 7.25a (green figure) shows this region to be over 30nm thick, more than double the thickness of the original amorphous film. Note the average thickness of the spherulite is approximately 10nm.

The Existence of a Pre-Ordered Phase

Within figure 7.23, the amorphous film (surrounding the spherulite) shows evidence of pock-marks and holes. Two large holes were found in the vicinity of the growing spherulite; the rim of one, not fully included in this image may be found in the upper left side of figure 7.23 and the other (although in the earlier stages of growth, separate from the spherulite) has become assimilated into the disc and resides a micron or so to the right of the nucleating site. The holes are useful in that the underlying gold grains are uncovered and the periodicity of the underlying substrate may be determined for calibration purposes.

A more revealing aspect of the holes is that the volume of the material within the rim of the holes cannot account for the material lost from them, indicating that the process may not be one of film reorganisation (energy minimisation) to form a droplet on the surface (as was the case for PVP in chapter 6) although this cannot be dismissed. As the holes appear only after plasticizer ingression, and the thickness of the film remains constant, one possible explanation for their formation is an increase in film density. Of course the spherulitic entities have a higher density than the surrounding amorphous polymer film and the holes may exist because of the amorphous film shrinkage. However the holes were found to exist before the onset of extensive spherulitic growth indicating that the amorphous film had shrunk appreciably at a very early stage. This would be the case if a pre-ordered phase in the 'amorphous' PC film was present.

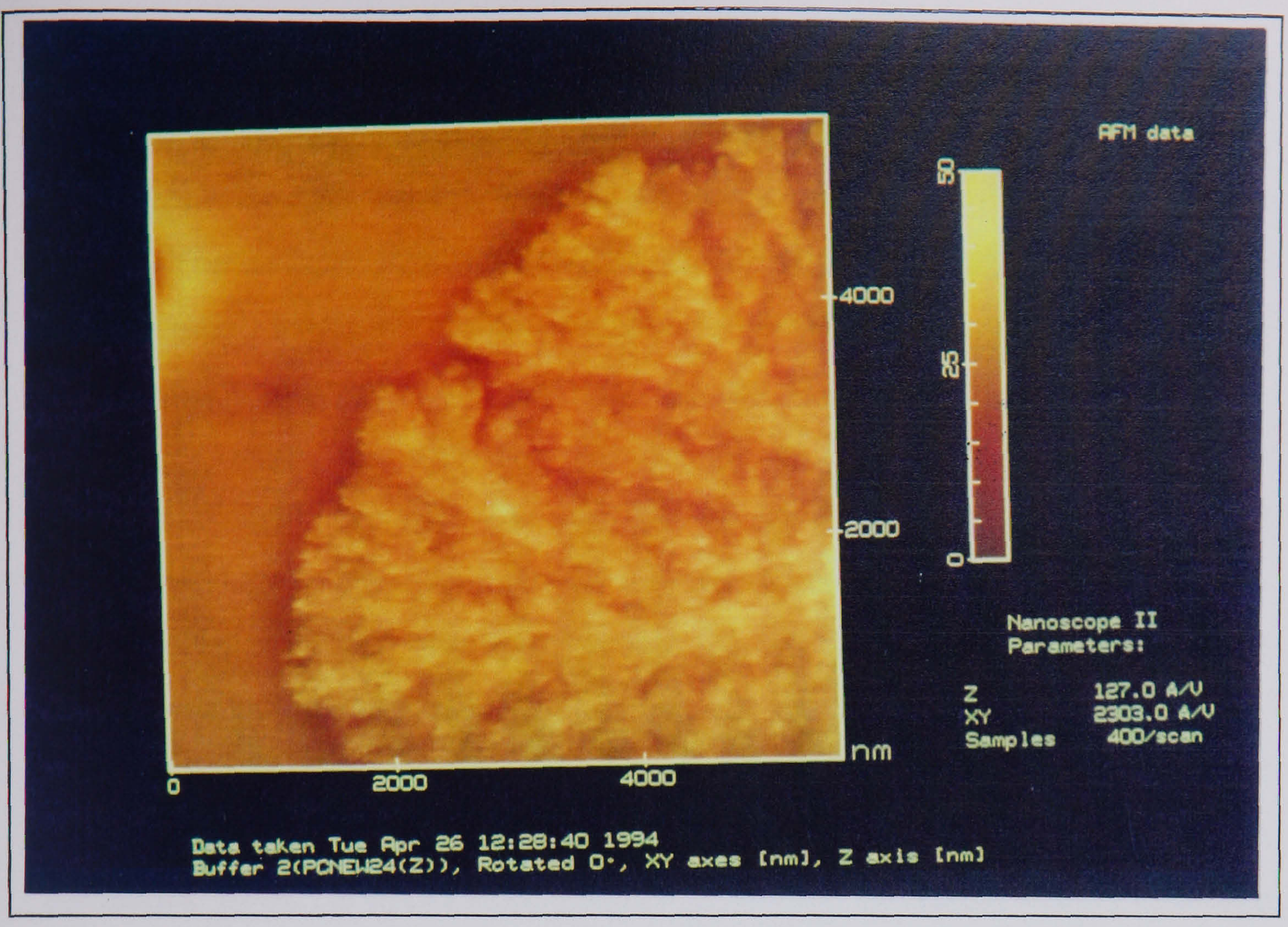

Figure 7.24: A higher magnification image of the fibril structure from the spherulite in fig 7.23. The fibril dimensions are difficult to assess but are about 200nm-600nm wide.

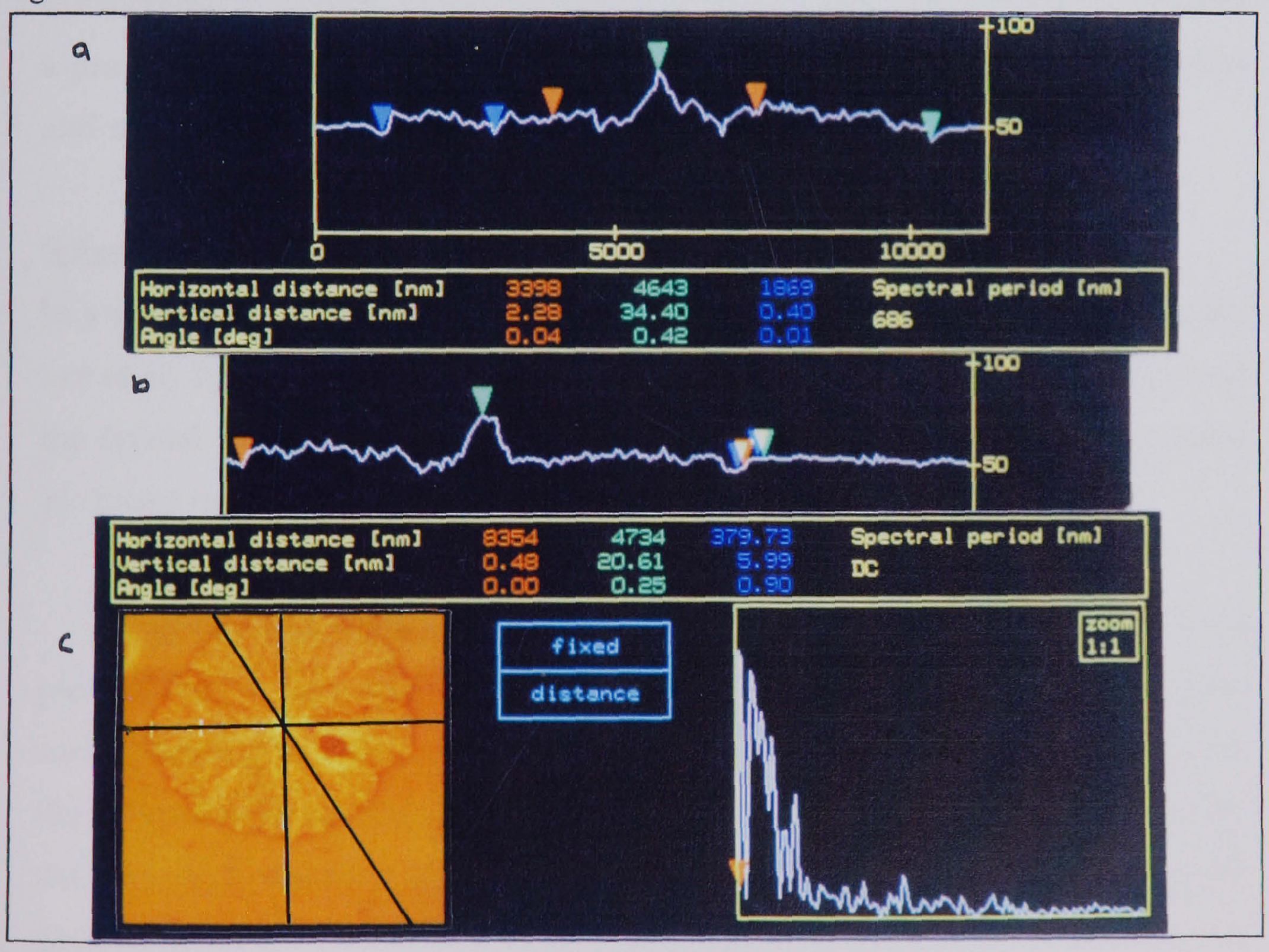

Figure 7.25: Line scans taken across the spherulite to reveal structure. The prominent nucleation region is very much thicker than the surrounding PC film.

The existence of a pre-ordered phase within the 'amorphous' PC film is expected from previous studies by Prietzschk[1958] and Schnell[1964], who suggest that even in rapidly cast PC films the crystallinity content is as high as 40%. The authors also indicate that the crystalline material is expected to exist in small micro-crystalline regions, undetectable to optical microscopy and partially observed in some SEM studies. The STM results given in the last chapter give further evidence to the existence of these regions (see figure 6.30). It should be stressed that the micro-crystalline regions are not analogous to the rods and fibrils discussed above, instead are randomly orientated and spaced nanometre sized aggregates that exist throughout the amorphous polymer matrix.

As the plasticizer is introduced, these micro-crystalline regions either grow independently or join together and have the potential to become the nucleation point for spherulitic growth. However the initial situation, which is one of global growth at the expense of amorphous material, can result in the increase in density of the polymer film as a whole. The film soon reaches a maximum density (indicated by the cessation in the growth of the holes) and spherulitic growth ensues.

Spherulite Growth Rate

In a wide variety of previous works [Okada et al, 1992; Herberer et al, 1991; Lee et al, 1993] a relationship between the overall crystallization kinetics and the crystal morphology has been established through the Avrami exponent 'n'. Exact mathematical solutions have been produced (see chapter 4).

Figure 7.26a shows a growth curve in which spherulite dimension is plotted as a function of time and clearly shows a plateau region corresponding to the impingement of neighbouring spherulites. The data for the spherulite dimension at a given time are obtained from a mean value for the size of all observed spherulites. Investigation of the error in obtaining the dimension of an individual spherulite shows clearly that any variation in spherulite size at a given time between members of the sample are too small to be detected. Error bars are shown in figure 7.26 for the individual points

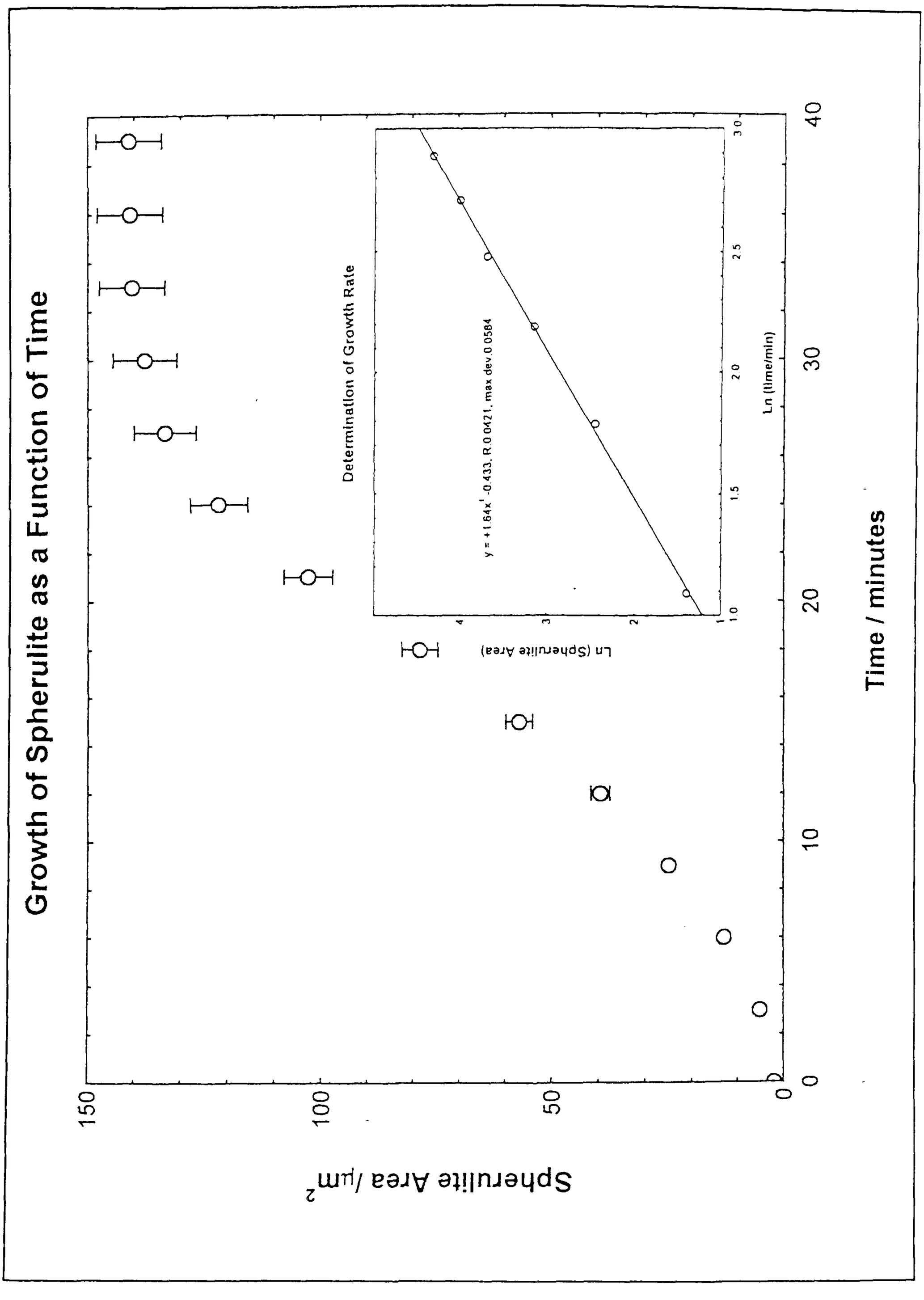

Figure 7.26: This graph shows the change in spherulite area as a function of time. The spherulite impingement occurs after 20 minutes of doping and eventually there is no observed increase in spherulite diameter. The early period of growth (t<20 minutes) is plotted as a ln-ln plot and the gradient is equivalent to the Avrami exponent 'n'. In this case n has a value of approximately 1.6 although the Avrami model predicts a value of n=2. Non-integer values have been reported in the literature.

on a graph of spherulite area against time. A log-log plot of the initial portion of the graph indicates a t^n dependence where n=1.64+/-0.05. This is not in very good agreement with the value of n=2 predicted in Chapter 4 by the Avrami analysis for disc-like growth from instantaneous nucleation.

Similar situations have been reported in the literature for other polymers where non-integer values of n occur, which are significantly different from neighbouring integral values predicted by the model. These differences can be understood in terms of known deficiencies of the model [Sharples, 1968] and are not associated with the simultaneous occurrence of two processes, each with a different value of n; these can be ruled out as a result of the direct observation of the growing disc-like entities by the AFM.

7.7 THE CRYSTALLINE PHASE

FILM 6

The vapour doping method allowed prolonged exposure and subsequent extensive crystalline growth within the very thin polymer film. The expansion of the spherulites continued until those closest to each other touched. At the impingement boundary, the spherulitic growth ceased with the transformation of the remaining amorphous material. This state is shown in figure 7.27. Here the two spherulites have met and the boundary between them is sharp and straight.

The continual doping of the film by the appropriate plasticizer (butyl acetate) vapour for a further 18hrs, resulted in continued growth of the spherulite entities until the whole surface was covered by polycarbonate in the semi-crystalline state. Figure 7.28 shows the surface covered by spherulitic entities. The disc-like morphology has been lost and replaced by one dominated by polygons with sides typically numbering five or six.

The next series of images (7.29 to 7.33) show an increase in magnification of the boundary between three spherulites. In the first of these images, the spherulite centres are quite obvious. As the magnification increases the low angle branching of the fibrils becomes even more apparent until in figure 7.33 the resolution is sufficient for the structure of the fibrils

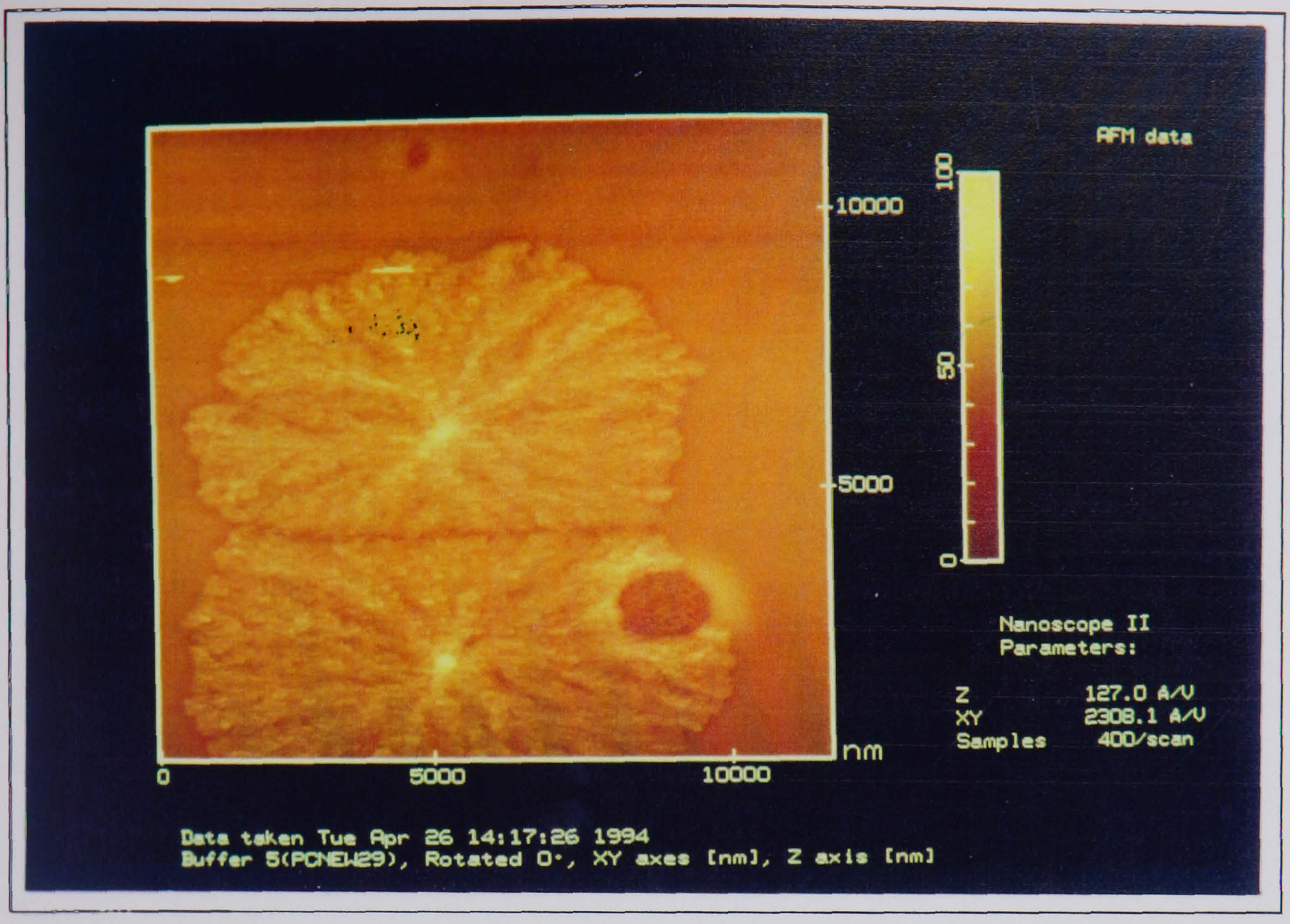

Figure 7.27: An AFM image of the impingement of two polymer spherulites as the growth of the crystalline material spreads throughout the amorphous matrix. The boundary between the two is straight and perpendicular to the direction of the two nucleating centres, indicating uniform growth.

Figure 7.28: The continual doping of the polymer film with the plasticizing vapour, eventually leads to the impingement of all the spherulites.

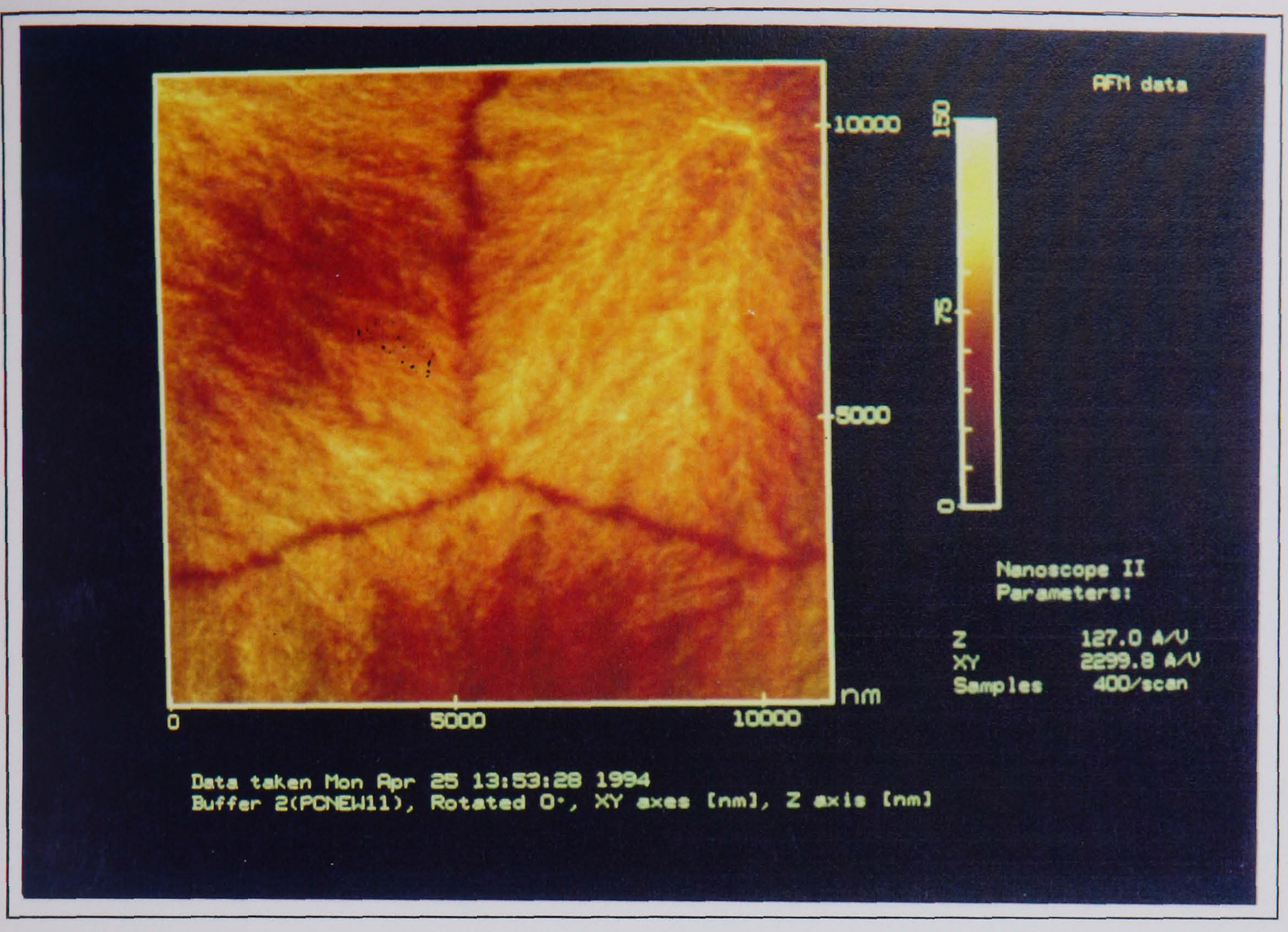

Figure 7.29: The boundary between the three spherulites indicated in figure 7.28, was magnified in stages. This first image reveals the complex fibril structure emanating from the central nucleating point.

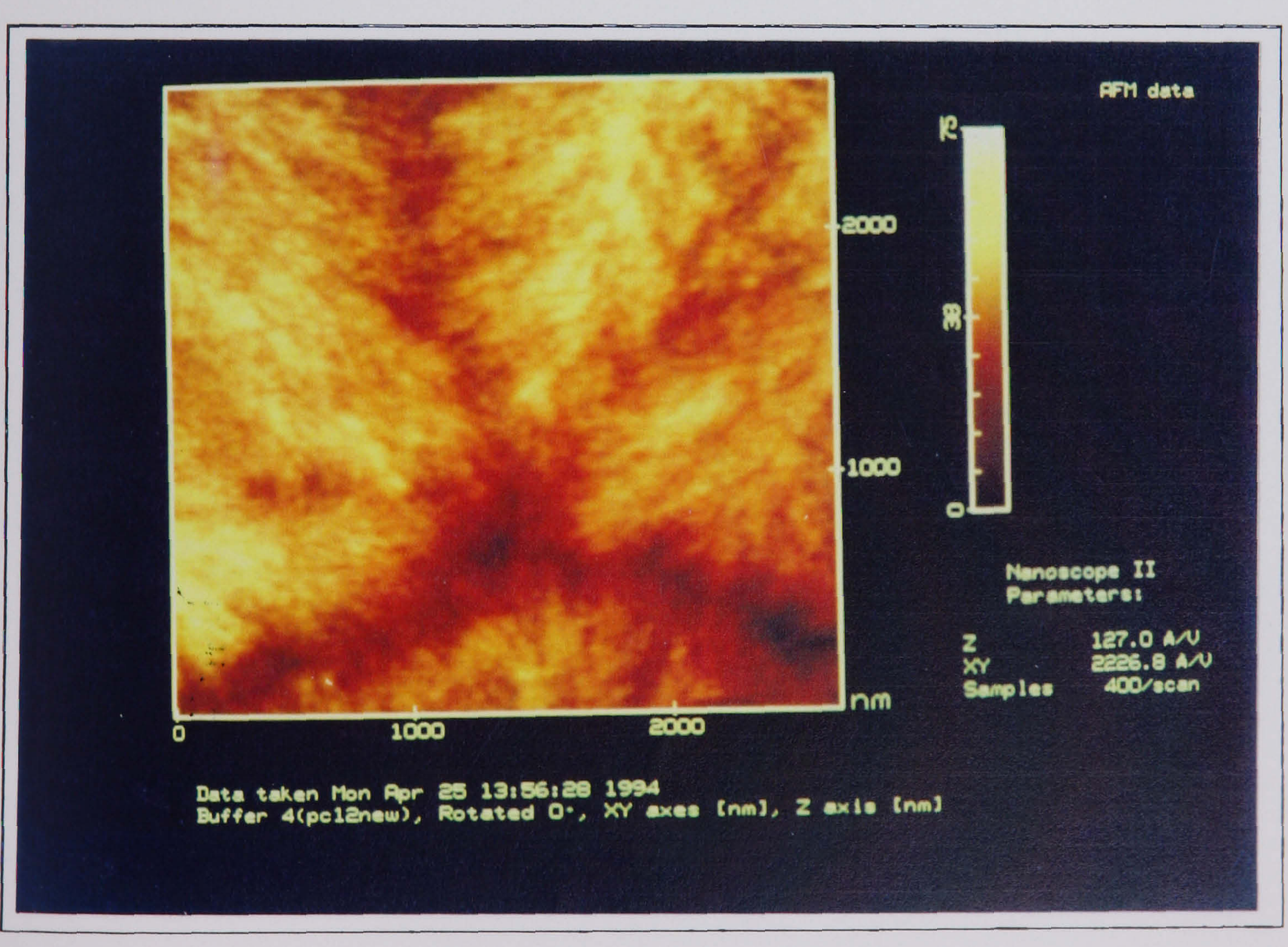

Figure 7.30: The second in a series of magnified images of the boundary between three spherulites. In this image the fibrils are observed to contain many branches and sub-divisions.

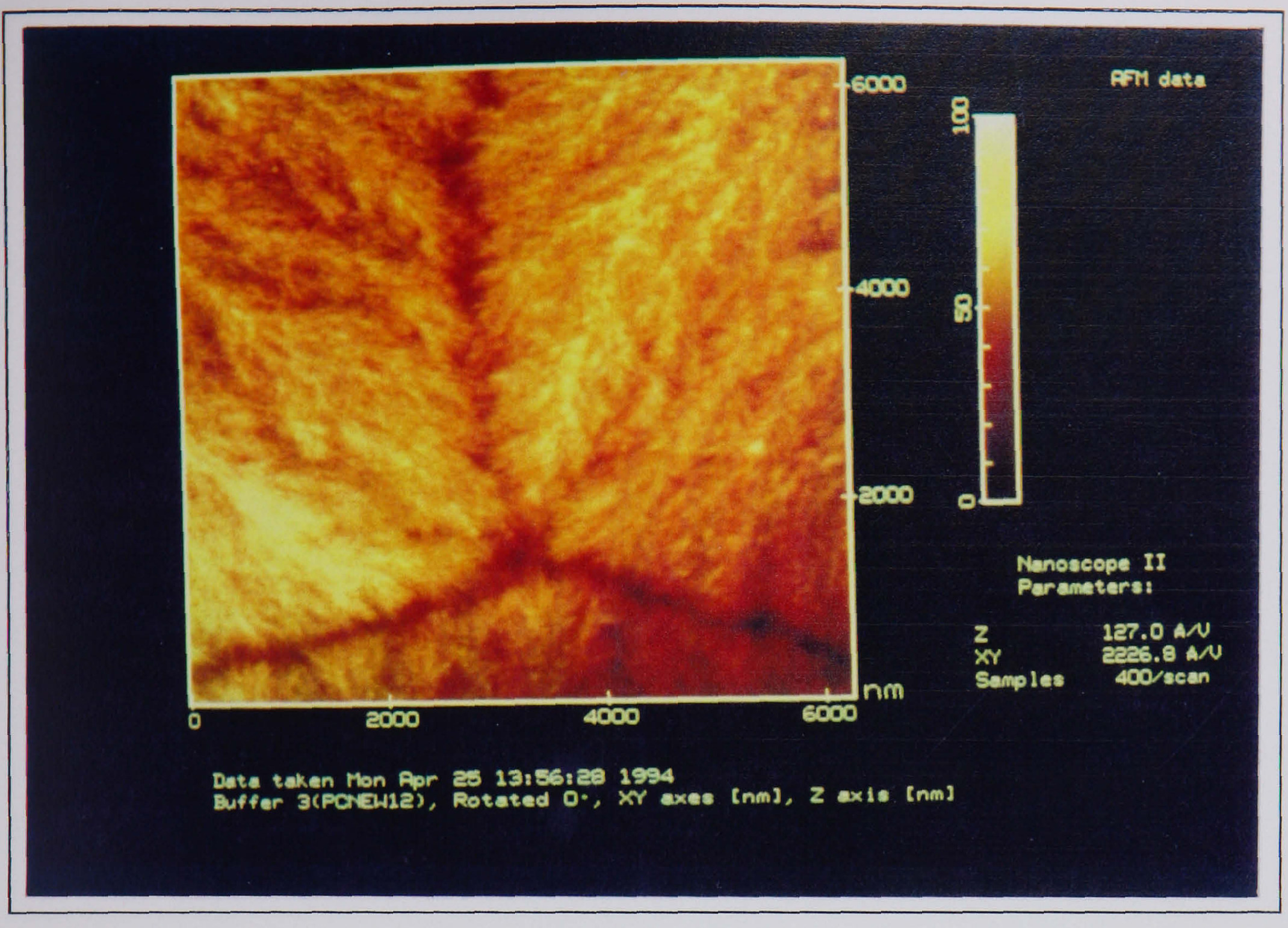

Figure 7.31. The third image in a series of magnifications of the inter-spherulitic boundary. For the first time, the elongated features which are the smallest components resolvable by the AFM are encountered.

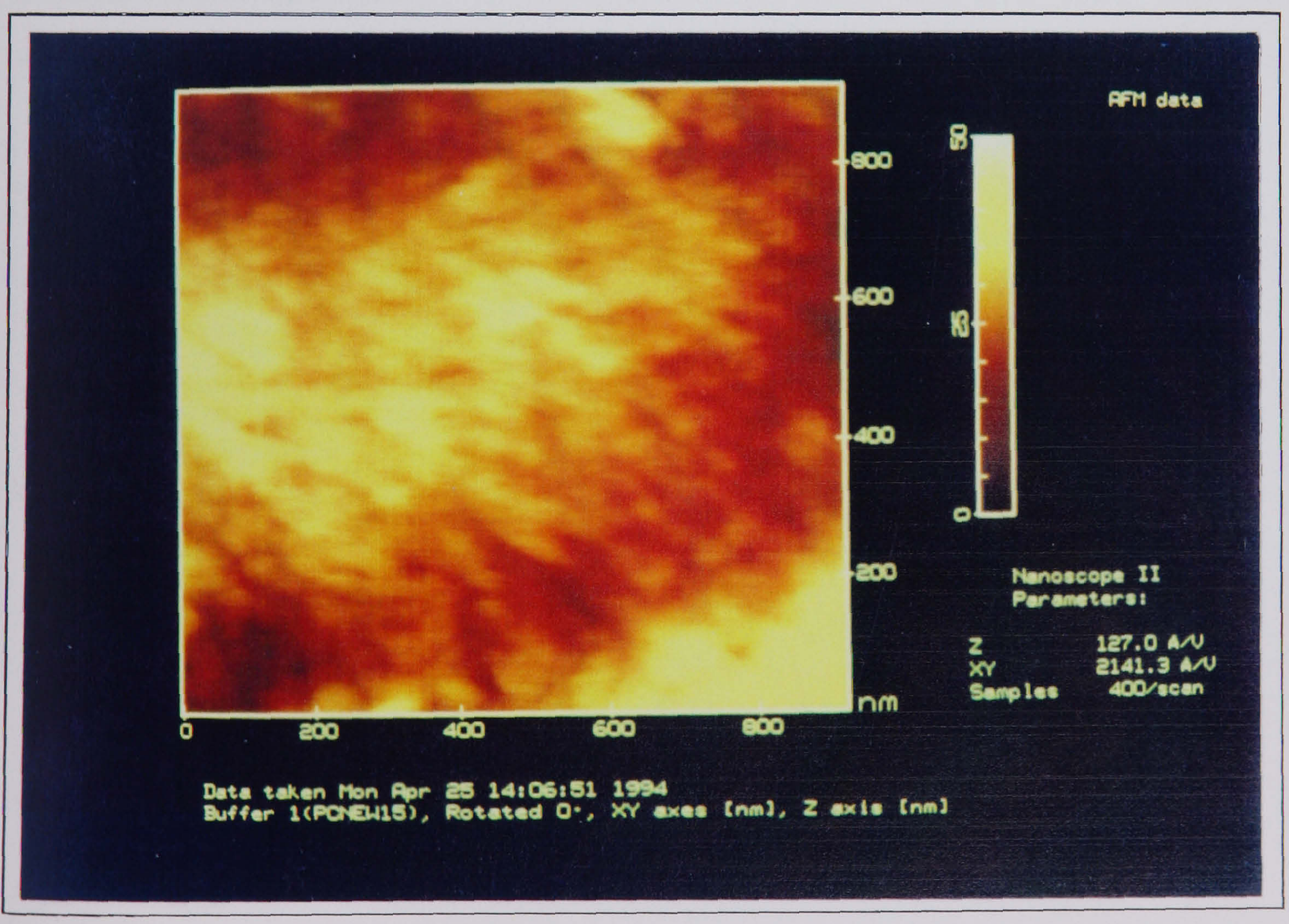

Figure 7.32: A magnified image of the fibril in the lower left of figure 7.31. This image is important because not only are the elongated sub-fibrillar components visible (20nm-60nm wide), but so is the boundary (lower third of the image) between neighbouring spherulites. The boundary shows signs of material sharing.

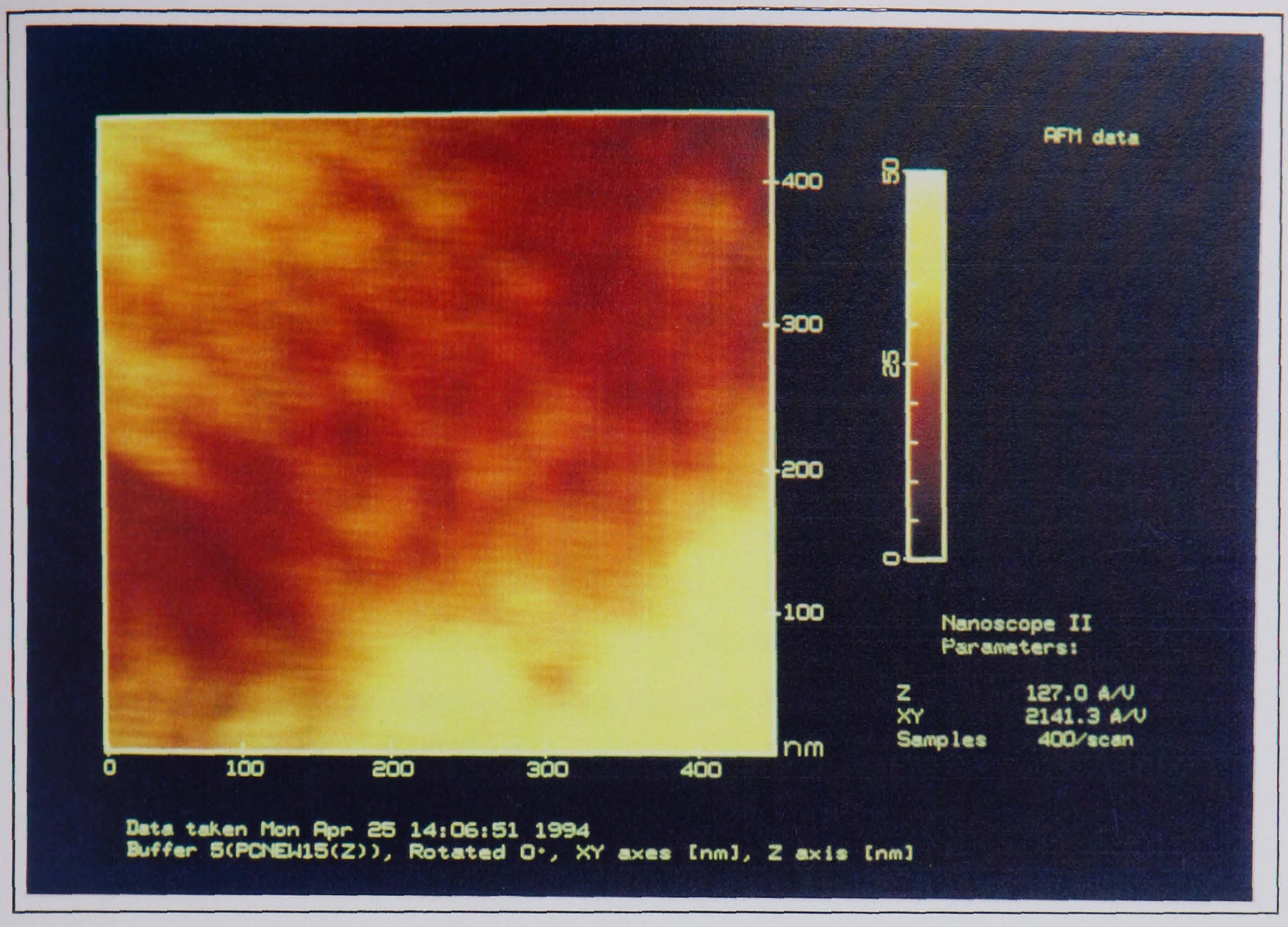

Figure 7.33: This is the final image in the sequence of increased magnification scans over the interspherulitic boundary. The limit of useful resolution has been approached and elongated strands crossing the boundary can be observed thus forming a connective material between spherulites.

Figure 7.34: An SEM image of a the surface of a very thick PC film. The three dimensional spherulites are quite clear.

to be assessed.

In figure 7.33, the fibrils show some degree of granular composition. The film is too thick for such a complexion to be as a result of the gold grain substrate. With closer inspection, elongated single fibrils were observed. Further studies including those carried out using the on the Nanoscope III TMAFM of the detailed surface structure of the spherulites are detailed below.

Thick PC FILM: AFM and SEM Images.

A very thick (in this context 'very thick' is about 50μm) polycarbonate film was exposed to ethyl acetate vapour for several days. Given that the size of initial 'wheatsheaf' and the branching there from, was very much smaller than the thickness of the film, the spherulites were expected to adopt a spherical morphology (from the Avrami equation in chapter 4). This growth results in a three dimensional version of the film observed in figure 7.28.

As expected the film contains spherulites with diameters of around tens of microns. The best example of this film may be seen in the SEM image figure 7.34. An AFM image was not possible at this scale as the growth of the spherulites, out of the plane of the substrate (in this case the bulk PC film) limit the use of the AFM in this context (which has a maximum z-range of 5800nm).

A more detailed image of the spherulite surface was taken by both SEM (figure 7.35) and AFM (figure 7.36). The area of the image is somewhat larger in the SEM image but the structure of the spherulite is observed to contain flecks or thin long strips, branching and twisting across the surface. Figure 7.37 shows an AFM image (at higher magnification) where these flecks and strips are quite clearly observed and their approximate dimensions given are table 7.7.

Lamellae: The Basic Polymer Components

The advantage of using the AFM over the SEM for some polymer samples is that very thin polymer films can be imaged bare i.e. with no conductive coating to limit the resolution of the instrument. It is with this in mind that

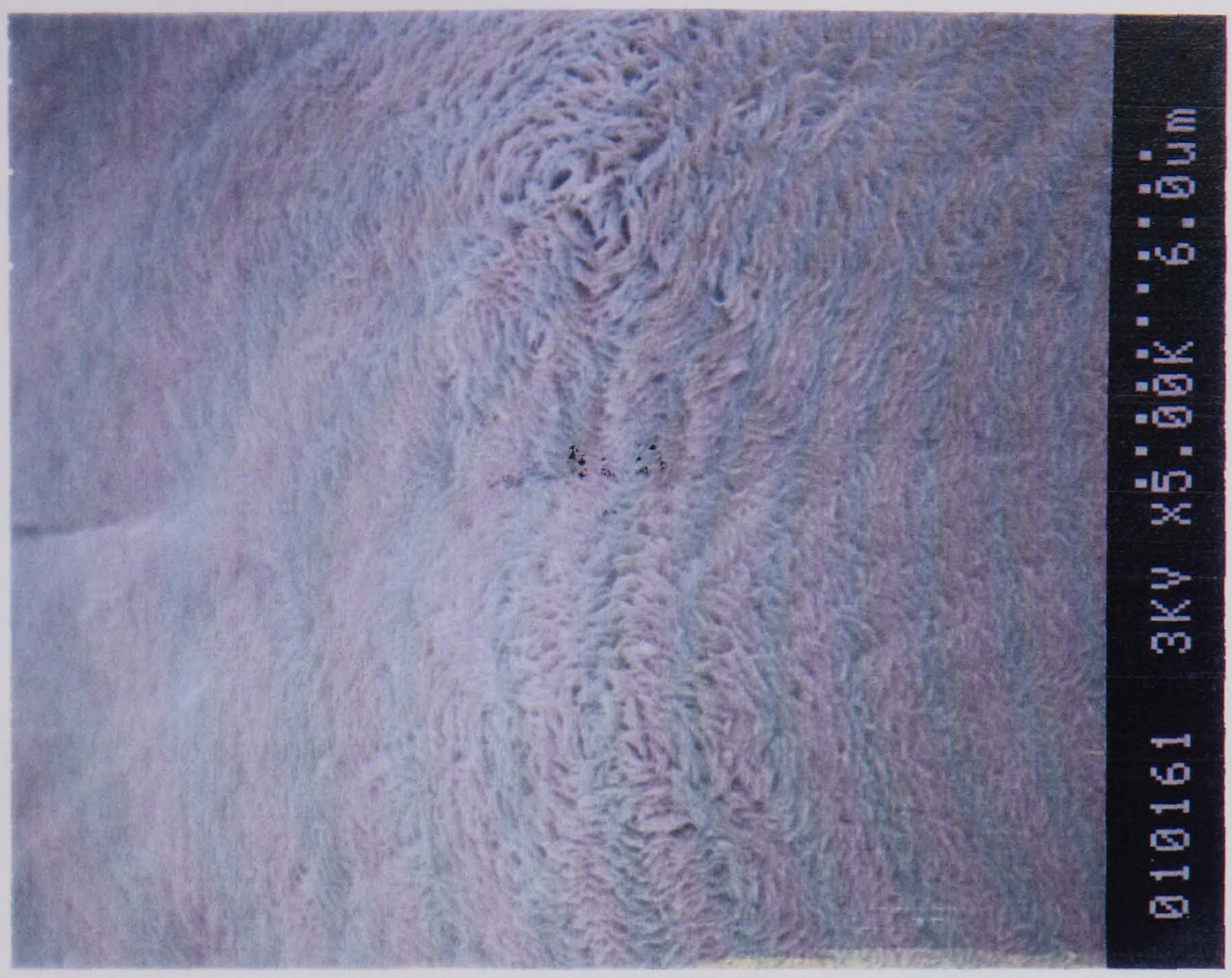

Figure 7.35: An SEM image of the same film imaged in figure 7.34 but at a higher resolution. The complex fibril structure can be observed.

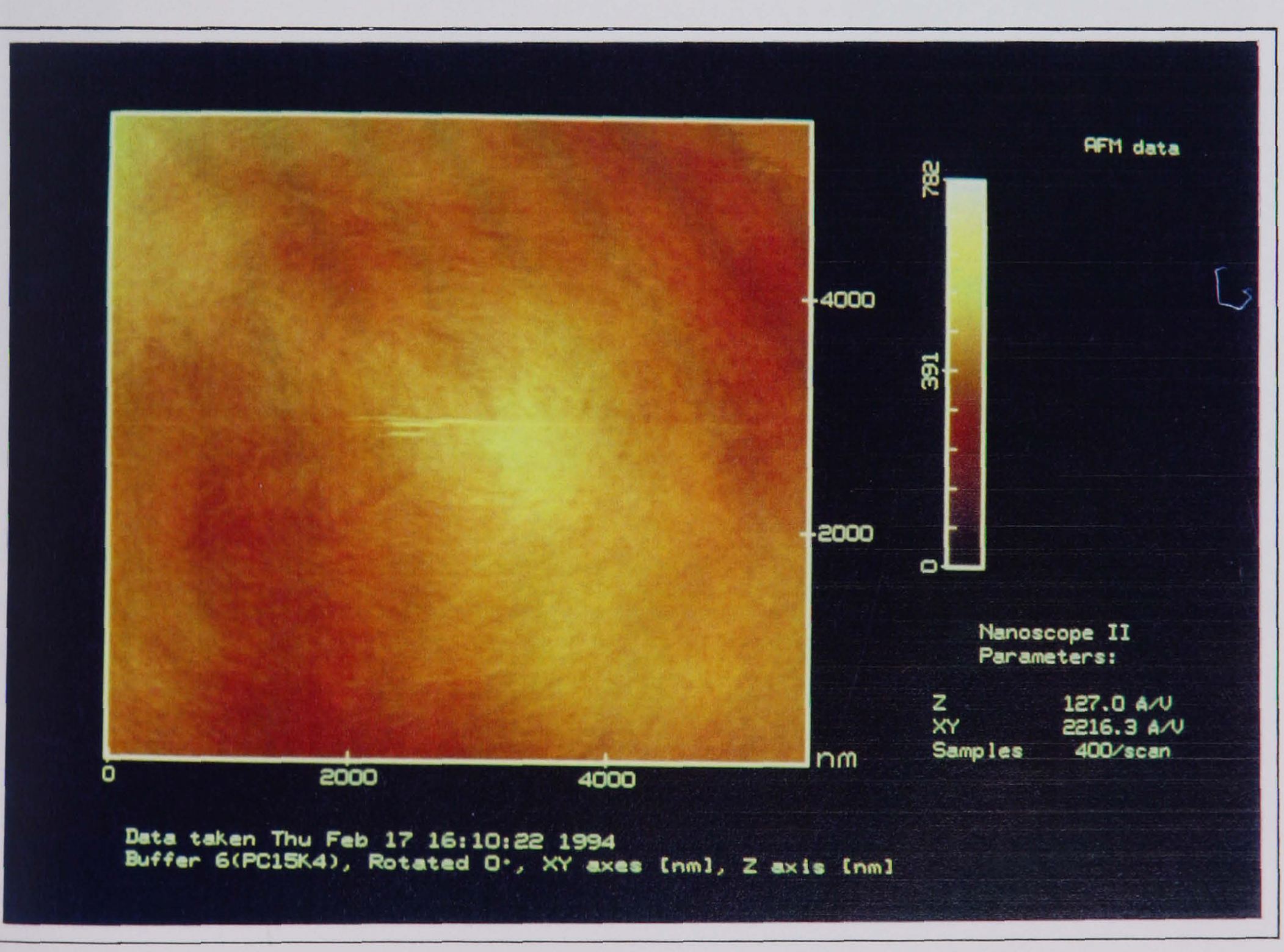

Figure 7.36: The AFM can obtain images comparable with those of the SEM. The detailed surface structure is resolvable and the general shape of the spherulites from the AFM image is consistent with that from the SEM.

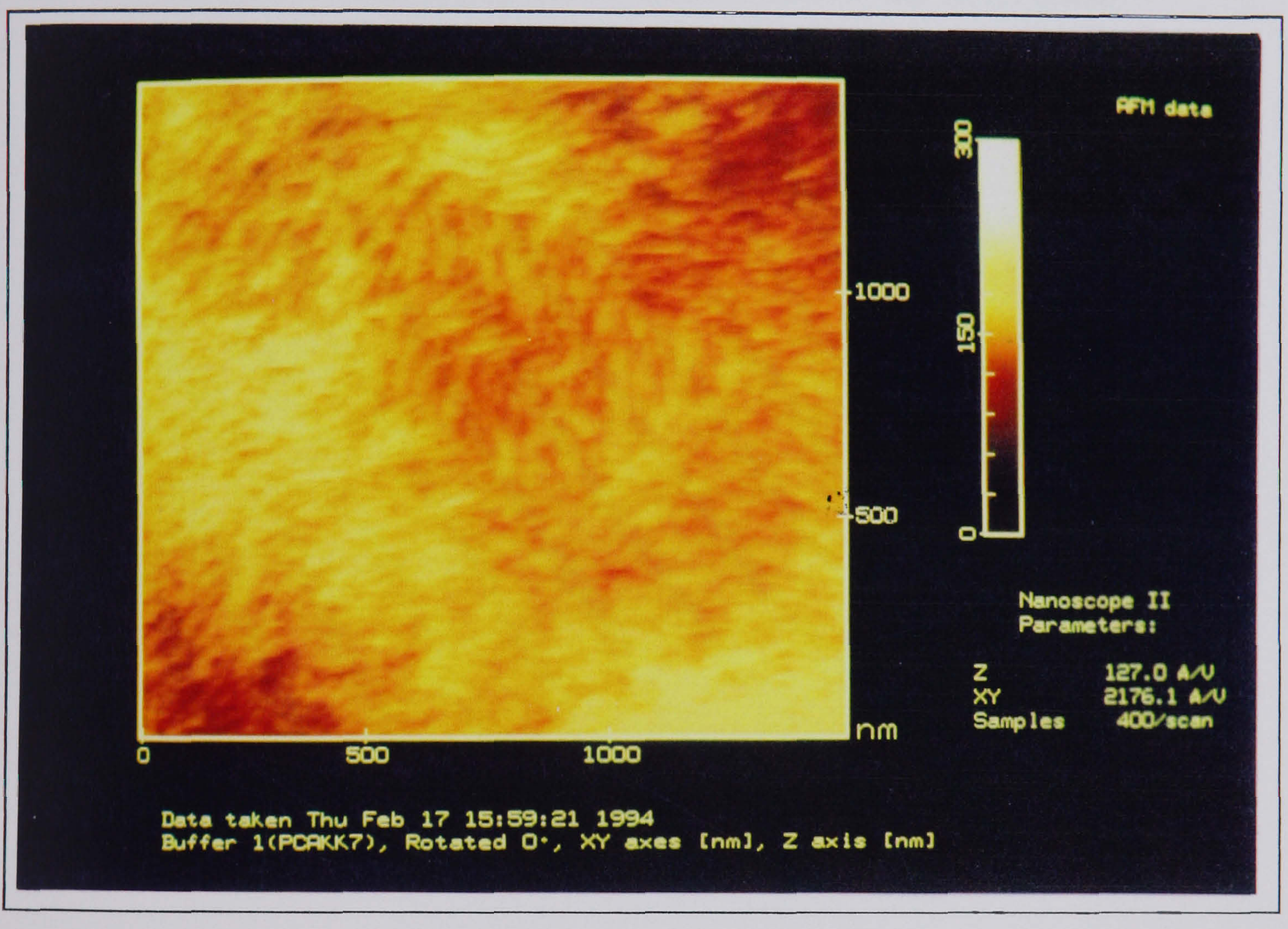

Figure 7.37: The AFM was used to obtain detailed measurements from the thick PC spherulitic film. The flecks and strips observable in the figures above are again visible here.

SPM Trial	Ave. Width /nm	Ave. Length /nm
AFM	50+/- 10	200 +/- 75

Table 7.7: The approximate dimensions of the fibril ends.

the samples mentioned above were imaged with as high a resolution as possible whilst still retaining valuable data. It should be noted that as the tip can interact with the sample quite considerably (see chapter 3) and the final image is always a convolution of the tip shape and the sample surface detail; thus it is not possible to resolve detail which is smaller than the smallest imaging part of the tip.

A common feature obtained from the high resolution images of the PC spherulites achieved by the Nanoscope II AFM (NSII) is the granular, elongated components that constitute the sub-fibrillar structure. In an attempt to verify the images achieved in figures 7.32 and 7.33, the Nanoscope III Tapping Mode AFM was used. This instrument which was made available at the Company Research Labs, BNFL, Preston, utilizes a very sharp AFM tip (cone angle of tip was smaller than the cone angle used on the AFM contact mode tips) and scans in a less destructive manner than in the case for the contact mode (see Chapter 3). The resolution on a standard gold substrate was found to be similar but the images of the PC spherulites were subtly different from those achieved on the NSII.

Figure 7.38 shows the transition from independent PC spherulite growth to impingement. There are four distinct regions in this image, the crystalline and amorphous PC film, the holes and the gold grains (within the holes - see figure 7.39). Figure 7.39 shows a line scan that cross-sections a higher magnification image of the lower middle of figure 7.38. The line scan reveals the gold grains, the subsequent thickness of the amorphous film (approximately 12nm) and the ridges around the holes. Note that the region within the rim of the hole is not large enough to account for all the material missing from the hole.

Two very much higher resolution images of PC spherulites is given in figure 7.40 and 7.41. The elongated fibrillar and sub-fibrillar structures, identified in the NSII images (figures 7.32 and 7.33) are now resolved by the NSIII. The dimensions of the features are slightly smaller than the NSII images at (23+/-4)nm in width and up to 100nm long (the decrease in size of the feature is consistent with the use of a sharper AFM tip).

It is very likely that the elongated features observed in figures

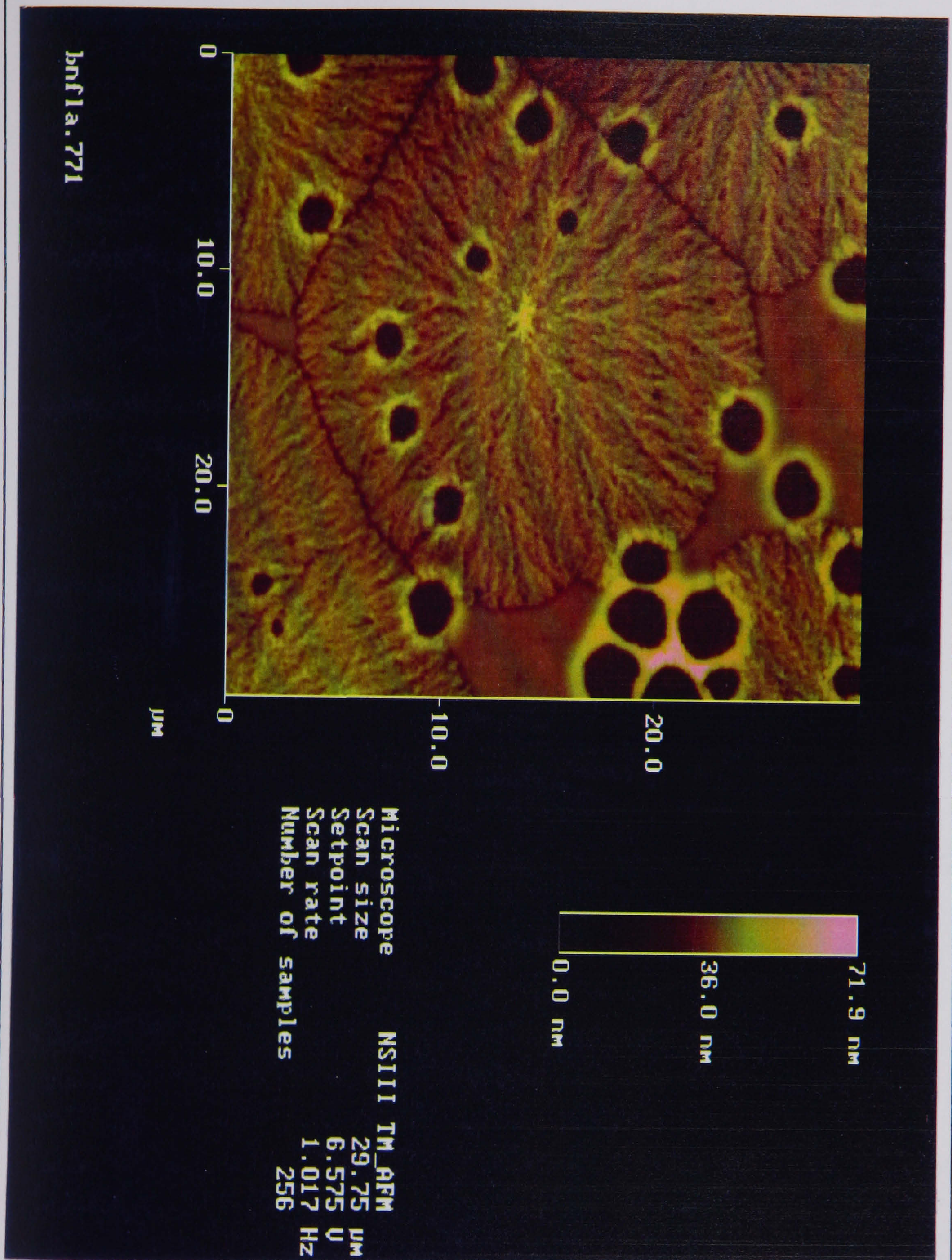

Figure 7.38. A Tapping Mode AFM image (achieved on the NSIII instrument) of the spherulite growth within a PC film. The branching of the fibrils and the amorphous material can all be observed. The holes reveal the gold grains of the substrate and may be used to gauge the thickness of the polymer film.

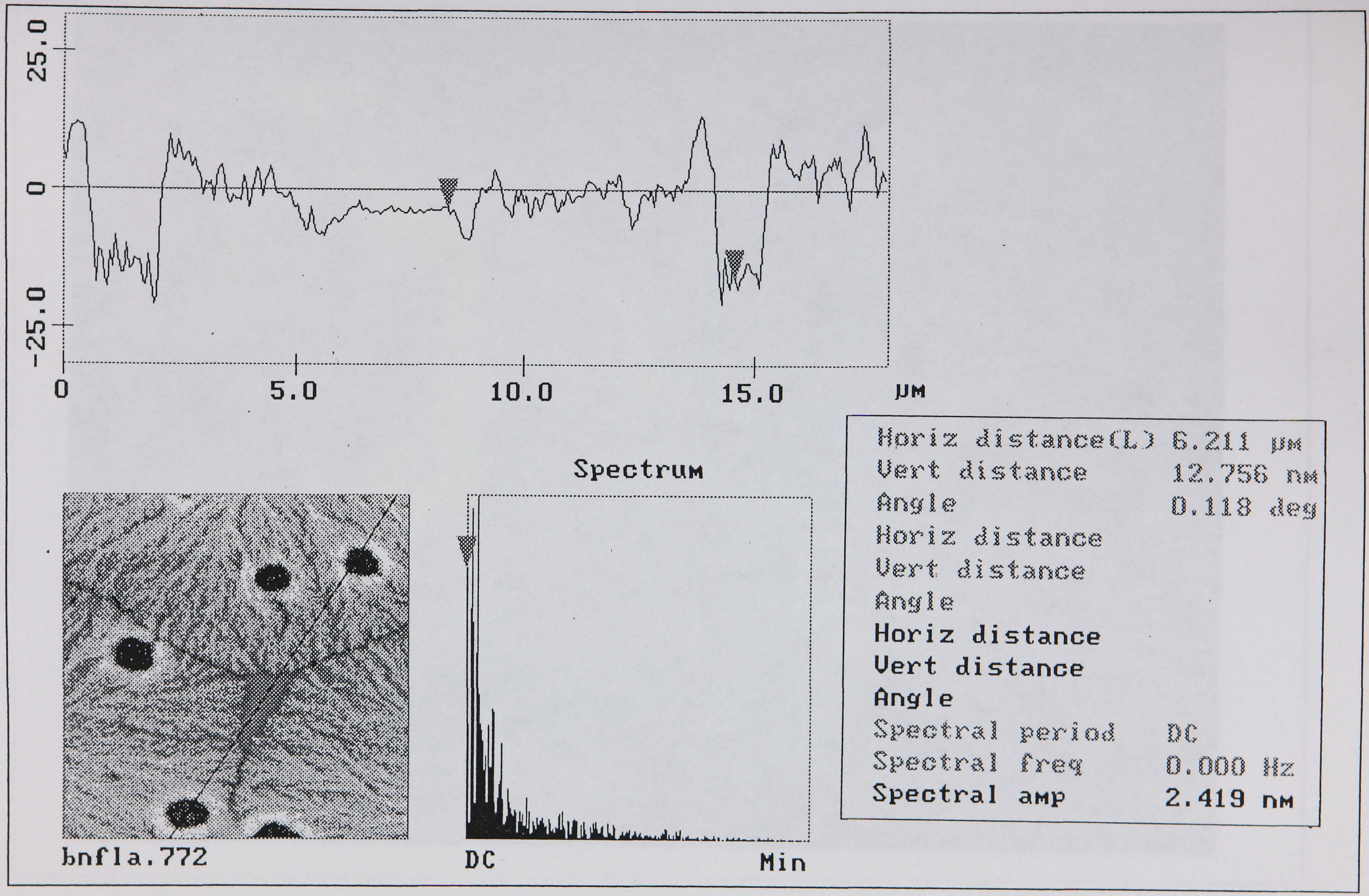

Figure 7.39. The line scan taken across the NSIII image shown in figure 7.38 gives an indication of the thickness of the amorphous film (approximately 12nm) and also of the volume of the material in the rim of the holes. The material within the rim cannot fill the hole alone, which suggests that the film must have experienced a stage of shrinkage.

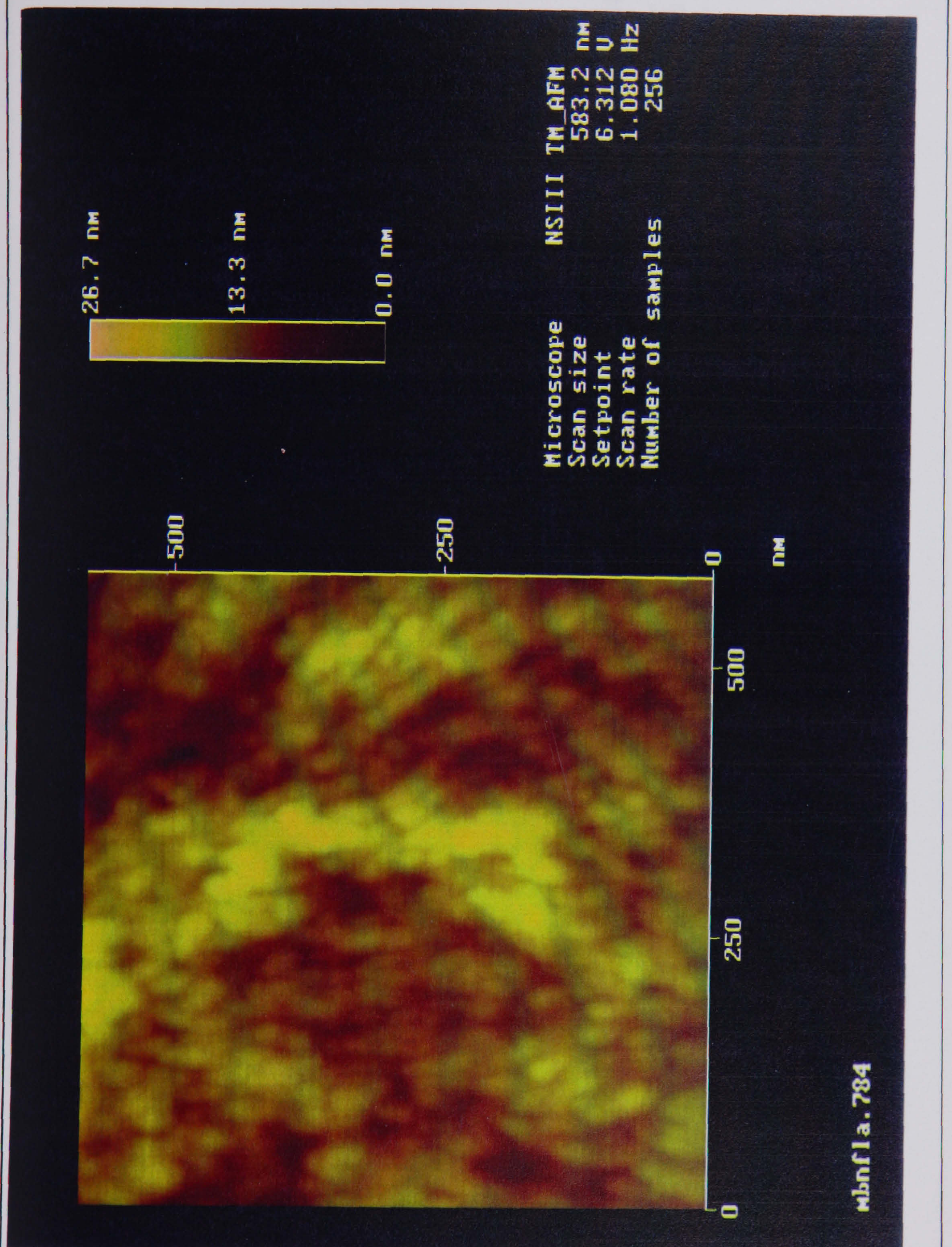

Figure 7.40: A NSIII image of the surface of a spherulite. The elongated regions or lamellae units, that were only just resolvable by the conventional contact mode AFM are quite clearly shown here. The axial direction of the lamellae units is in towards the central nucleation point.

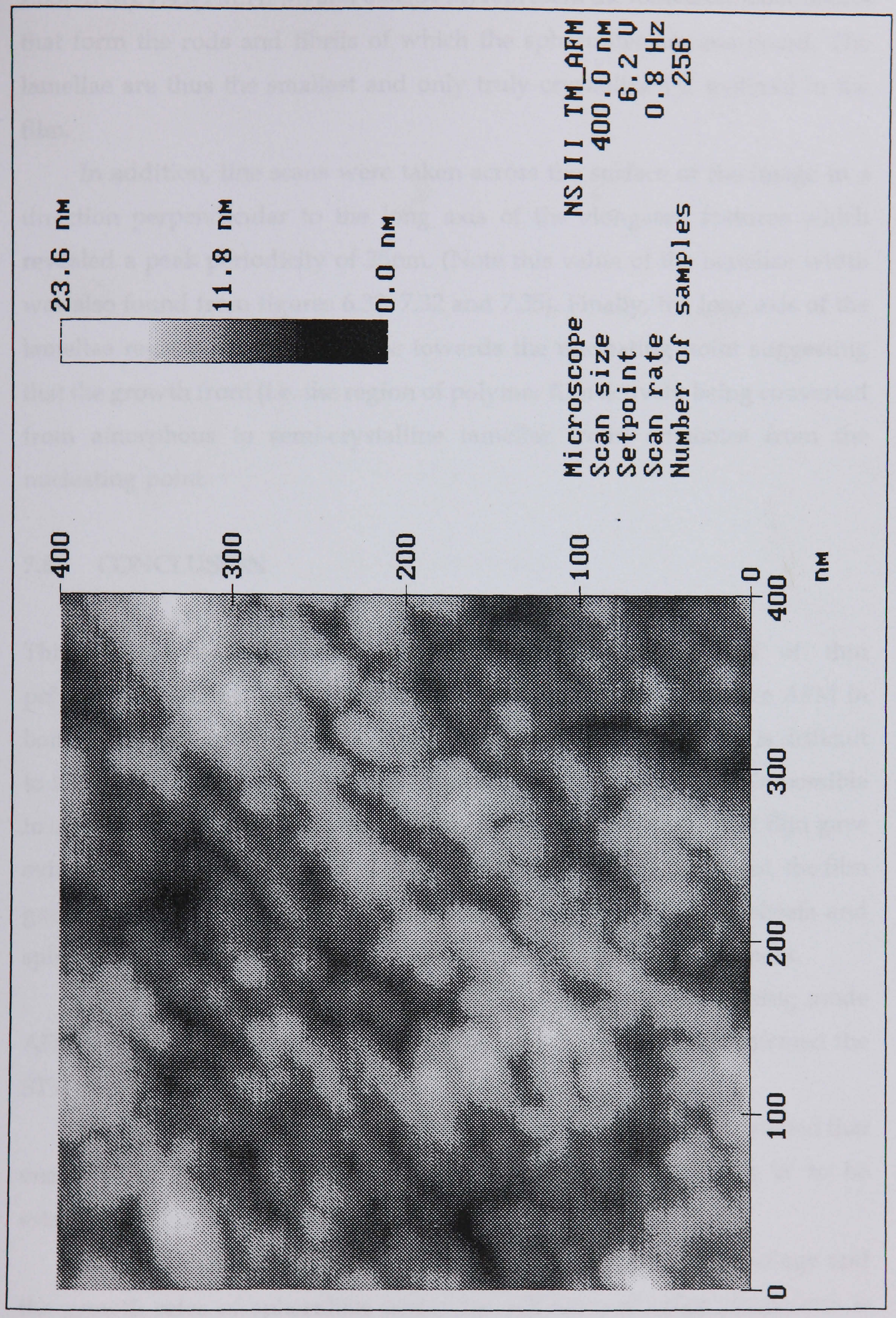

Figure 7.41: The lamellae units that comprise the basic building components of the polymer spherulites are clearly visible here. The tapping mode AFM produced higher definition images than the contact mode because of the more gentle action of a sharper tip. This image can be directly compared to figure 7.32 and 7.33.

7.33(AFM), 7.41(TM.AFM) and 6.32(STM) represent the folded lamellae sheets that form the rods and fibrils of which the spherulites are composed. The lamellae are thus the smallest and only truly crystalline PC material in the film.

In addition, line scans were taken across the surface of the image in a direction perpendicular to the long axis of the elongated features which revealed a peak periodicity of 25nm. (Note this value of the lamellae width was also found from figures 6.32, 7.32 and 7.35). Finally, the long axis of the lamellae regions was found to be towards the nucleating point suggesting that the growth front (i.e. the region of polymer film actively being converted from amorphous to semi-crystalline lamellae from) emanates from the nucleating point.

7.8 CONCLUSION

This chapter addressed the solvent induced crystallization of thin polycarbonate films. Imaged were obtained using an SEM and the AFM in both the contact and tapping modes. Results suggest that whilst it is difficult to image spherulitic growth ion the presence of the plasticizer, it is possible to observe the key stages of growth at the near nm level. The initial film gave evidence for a 'pre-crystalline' phase and after appropriate treatment, the film gave rise to rods and fibrils. These in turn grew to form wheatsheafs and spherulites, the development of which was curtailed at impingement.

The high resolution morphology study, notably by the tapping mode AFM, revealed the basic polymer lamellae and data obtained confirmed the STM results outlined in chapter 6.

During the spherulitic development a growth curve was constructed that enabled the growth rate and a value of the Avrami exponent 'n' to be established (for the PC/butyl acetate system).

In the next chapter a further study by the AFM, of the morphology and the growth rates of spherulites under the influence of other plasticizers is presented.

CHAPTER 8

FURTHER WORK
THE STUDY OF A THE EFFECT OF A VARIETY OF PLASTICIZERS ON THE CRYSTALLIZATION OF POLYCARBONATE
NUCLEATION IN POLYCARBONATE FILMS

8.0 FURTHER AND FUTURE WORK

It is generally unclear whether nucleation in polycarbonate films proceeds via an homogeneous or an heterogeneous process. In this final section of the work, results achieved in identifying the nucleation process for the polycarbonate spherulites are discussed.

In addition the effects of plasticizers other than butyl acetate are discussed. Daniewska, Kocinska and Dobkowski [1986] studied the effect on morphology of several chemically different plasticizers on the polycarbonate thin film. Their study measured the size of the spherulites formed as a function of solvent polarity, and proposed that a relationship between the two exists; in addition it was proposed that the spherulites would show different compositional structures. Daniewska et al[1986], however, were unable to view the crystalline entities with the resolution they required and although other studies [e.g. Cope, 1977] have observed the plasticizer effect using the SEM, this study is the first to use the AFM. The results described in this chapter clearly show that the spherulites not only have different sizes but also have different fibrillar arrangements.

The AFM study revealed that the use of different plasticizers resulted in a wide range of spherulite growth rates within a given film. It is proposed that for future work in this field, data regarding growth rates and not just the ultimate spherulite size could provide rewarding insight into the crystallization process in polycarbonates.

8.1 NUCLEATION (FILM 7)

The aspects of nucleation have been discussed in chapter 4 and there is little doubt that this process becomes very important when seeking an understanding of the spherulite growth. In this section the result of 'seeding' the substrate with small latex spheres is observed. In general it was found that the number of spherulites in any given area increased in proportion to

the concentration of the latex sphere solution deposited on the substrate.

The Avrami model in section 4.5, describes in a mathematical way, the rate of growth of the spherulites as a function of time. The model predicts that the growth rate of the crystalline polymeric material (as a fraction of the total amount of polymer in the film) depends on whether the nucleation sites appear instantaneously (heterogeneous) or as a function of time (homogeneous). This section describes the results of several experiments outlined in chapter 5 which enable the nucleation processes to be assessed.

Homogeneous Versus Heterogeneous Nucleation

Firstly the polycarbonate film was deposited on bare gold and crystallized in the manner described in chapter 7. The film morphology was similar to that observed earlier (see chapter 7) and it was noted that the average density of spherulites formed was 14 +/- 2 - see figure 8.1; (it was convenient to define the density of spherulites as the number of spherulites per $(40\mu m)^2$ image area).

The gold substrate was then covered with the latex spheres (86nm in diameter) and imaged with the AFM. Images (not shown here) show the spheres scattered somewhat randomly on the surface.

The polycarbonate was then deposited on top of the latex spheres, dried and then imaged. The film did not show any crystalline development. However after doping with butyl acetate, the spherulite formation was once again observed (figure 8.2). The density of spherulites had increased to 960 +/- 20.

The process was repeated on a different gold substrate with the number of latex spheres doubled. After plasticizer treatment spherulitic development was again observed and shown in figure 8.3. The density of spherulite formation was found to be approximately double that observed in figure 8.2. Additional substrates with a further doubling of the number of latex particles and consequently higher density of spherulites were imaged (see figure 8.4).

Table 8.1 gives an indication of the increase in number of spherulites in a given area, as a function of latex sphere concentration.

Latex Sphere Concentration*	Incidence Of Spherulites†
0	14+/-2
X/8	960+/-20
X/4	1856+/-39
X/2	3840+/-78
X	8192+/-160

Table 8.1.

This table shows how the number of spherulites grown in a polycarbonate film may be influenced by adding a nucleating agent. In this case tiny latex spheres only 86nm in diameter were used.

*The original solution purchased from Agar Scientific, UK, was diluted by a factor of 100 to give solution X. This solution was diluted by a factor of 2,4 & 8 and a drop of each was spin coated on the substrate.

†The incidence of spherulite formation was achieved by counting the number of spherulites in a $(40\mu m)^2$ box.

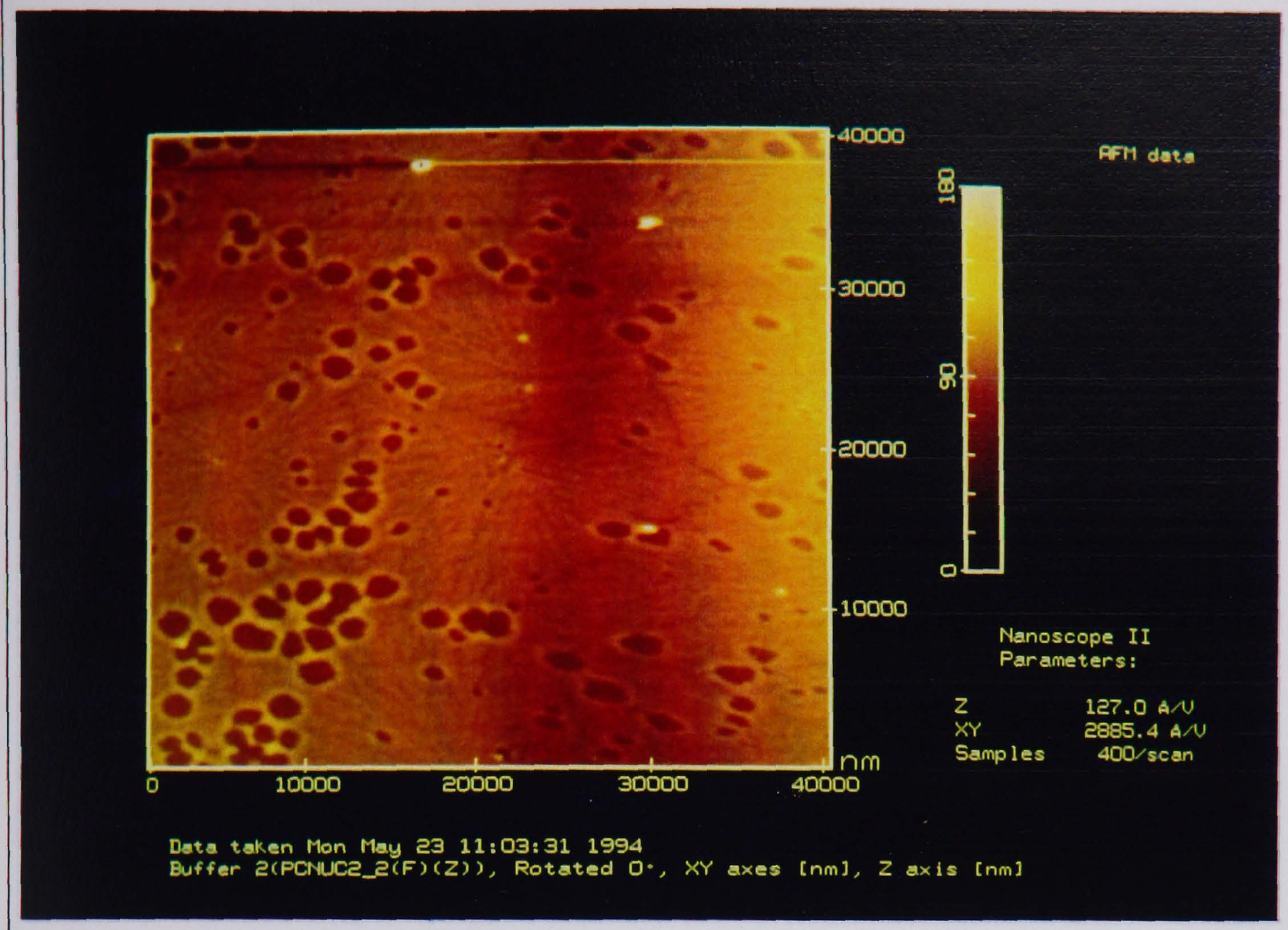

Figure 8.1: The substrate naturally harbours nucleation sites. When the PC is exposed to the plasticizer, some of these sites are utilized and spherulites are formed. In this figure there are approximately 14 spherulites.

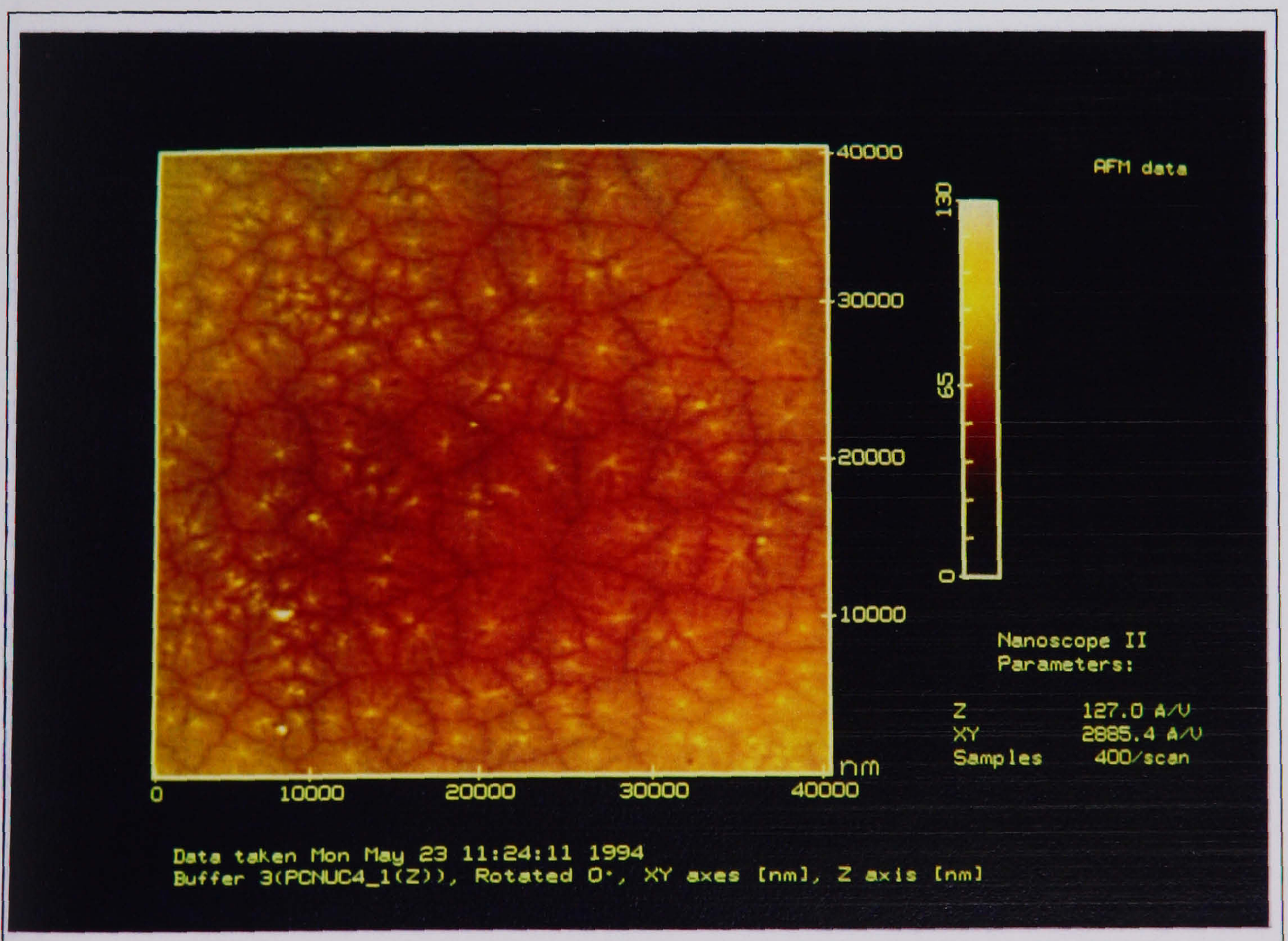

Figure 8.2: Introducing latex spheres, increases the number of nucleation sites available for PC crystallization.

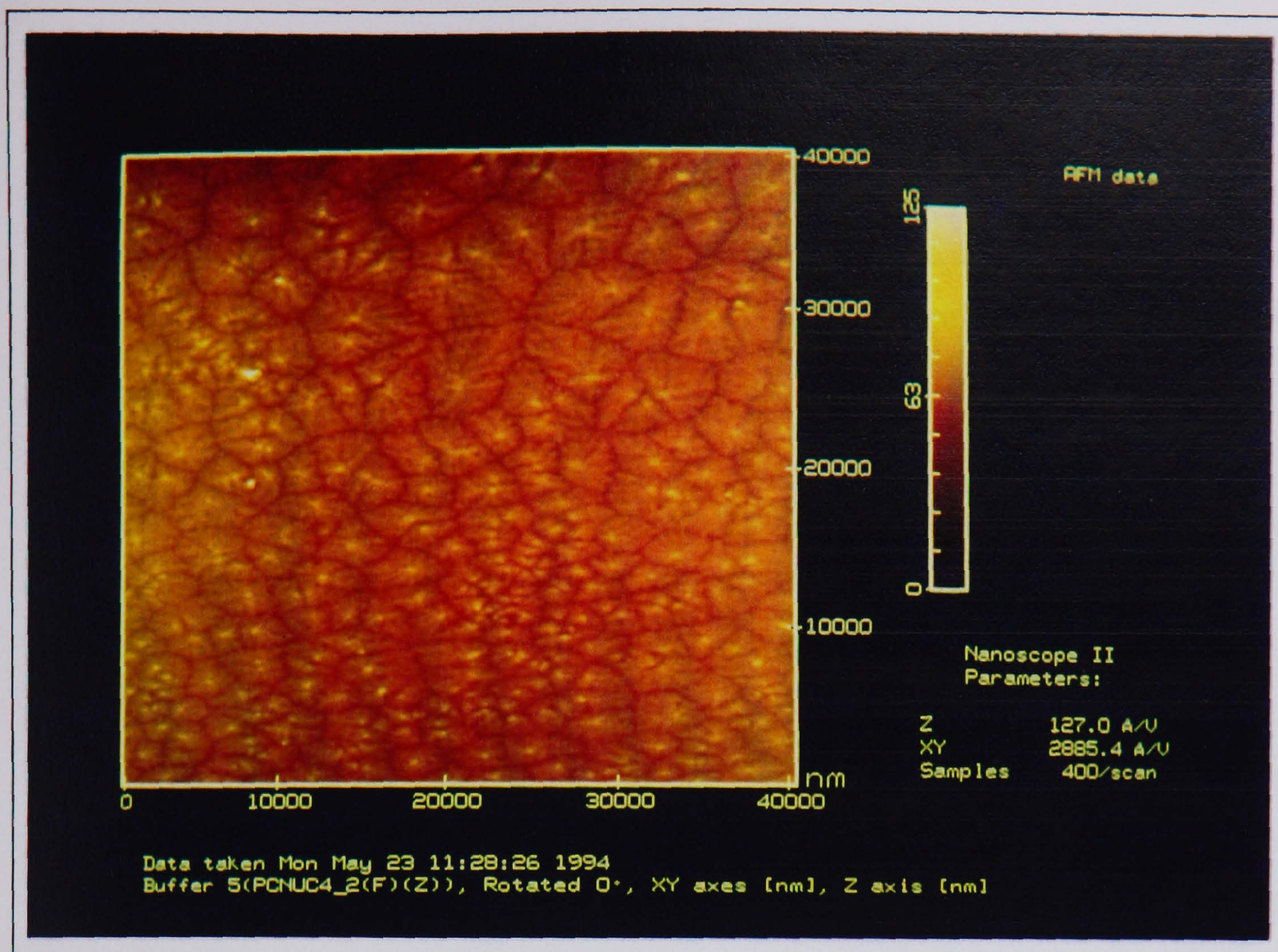

Figure 8.3: Increasing the concentration of latex spheres on the surface, results in the formation of even more PC spherulites.

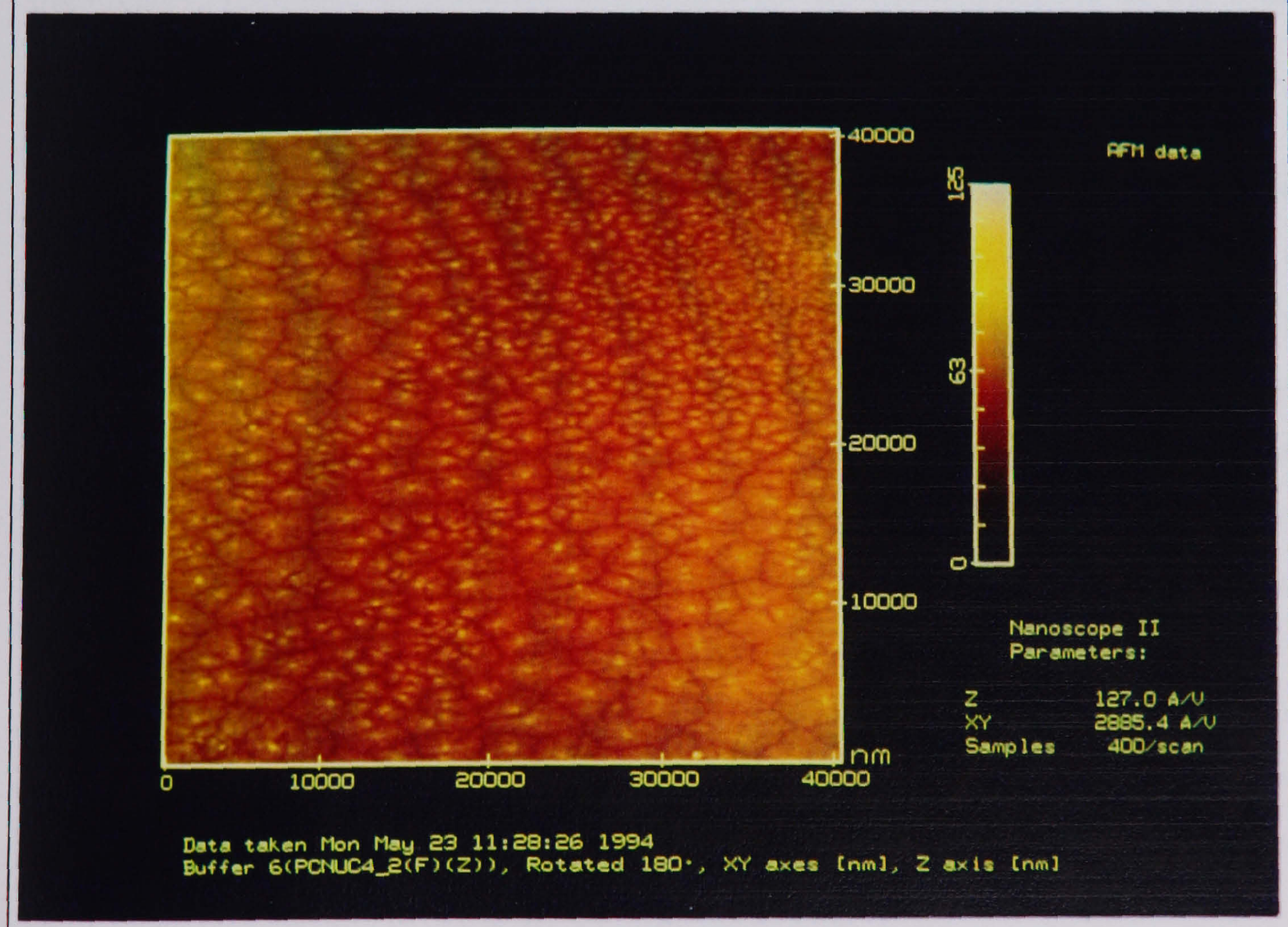

Figure 8.4: In this figure, the latex sphere concentration was very high and consequently, the size of the spherulites was reduced significantly from those observed in figure 8.1.

Returning to the film with zero latex sphere concentration, the spherulite growth was imaged as a function of time; this enabled the time dependence of the nucleation process to be established. It was deemed necessary to stop the growth of the spherulites after only a few minutes and before the onset of interspherulitic contact. It was found that approximately 95% of the spherulites (the total of which was determined by counting before impingement occurred) were initiated immediately. The growth rate was constant and consequently at any given time the spherulites were all about the same size (for the early stages of growth). However approximately 5% of the total number of spherulites were observed to 'appear' or nucleate before the onset of general impingement yet after the initial development period.

After appearing, the rate of growth was the same as for the other spherulites. A sketch of the distribution of spherulite size at a given time for the crystallization process (initiated by butyl acetate) is shown in figure 8.5. It should be noted that for long duration experiments, when considering the total number of spherulites in the film, the fraction of spherulites formed sporadically would increase as a function of time. In the case of this plasticizer, sporadic spherulites accounted for no more than 5% of the total crystalline phase.

A further experiment was conducted to ascertain the nucleation process and it was similar to Cormia et al (see chapter 4). In the work by Cormia et al, a fine suspension of PE was allowed to crystallize. It was found that only those droplets of PE that contained a nucleation site crystallized under the conditions that normally yielded the most rapid crystallization. Cormia et al deduced that if the nucleation process was predominantly homogeneous (which was not the case) then the separation of accidental heterogeneous nucleation sites from regions making up some 90% of the polymer would not prevent those regions from crystallizing. The majority of the droplets did not crystallize because they contained no heterogeneities, thus Cormia et al eliminated homogeneous in favour of heterogeneous nucleation as the dominant nucleation process in the PE bulk.

In this study, polycarbonate droplets were formed by depositing the film

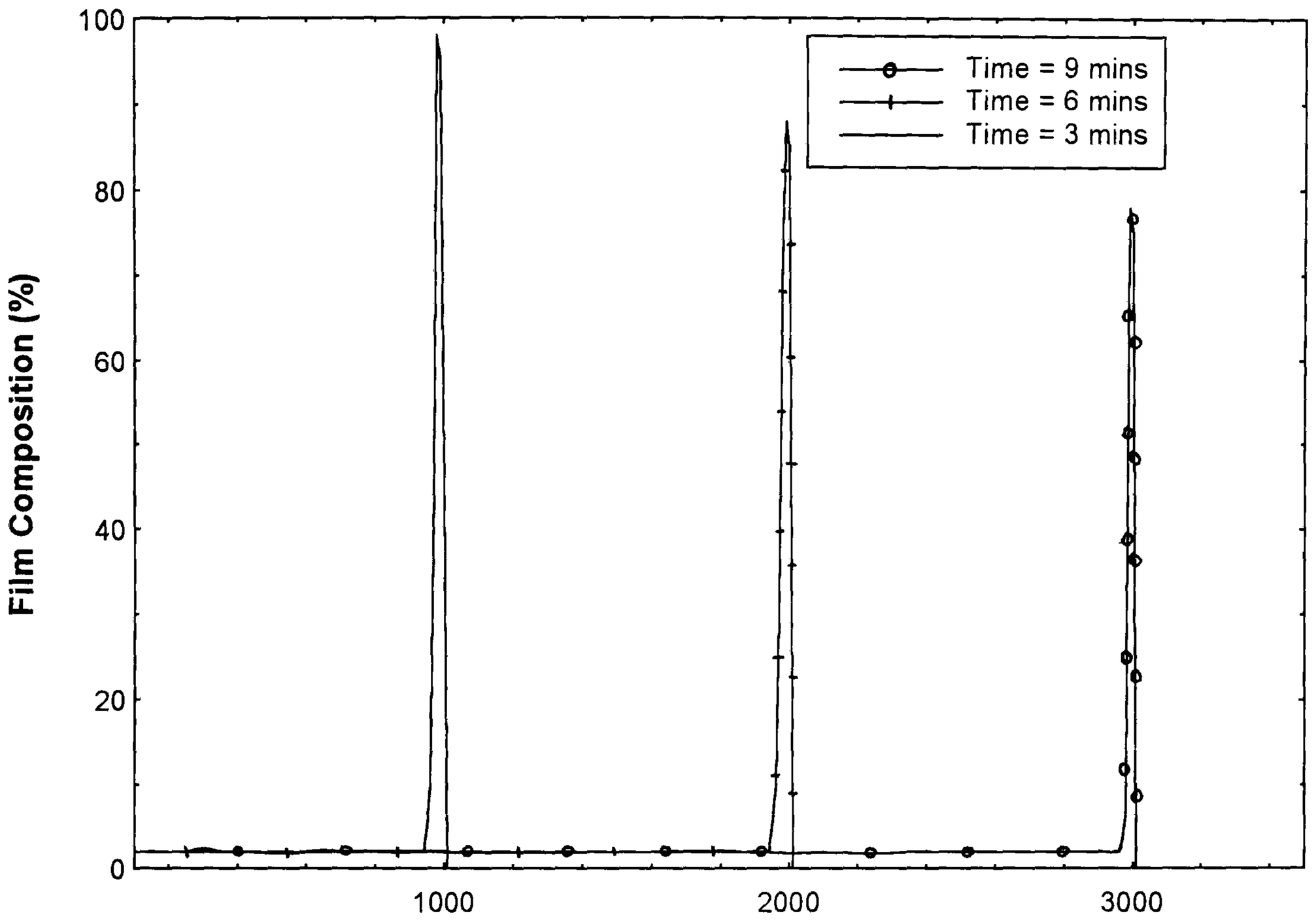

Figure 8.5: This schematic demonstrates the increase in fraction (of total number of spherulites in the film) resulting from homogeneities. However it is assumed that over the time-scale of the experiment, the majority of the spherulites are formed from heterogeneities.

on an unsuitable substrate (in this case SiO_2). The images of droplets subsequently treated with the plasticizer are given in figures 8.6 and 8.7. The substrate in figure 8.6 is covered in small globules of polycarbonate. The average size is about a micron in diameter. The polycarbonate islands are different shapes, and although most of the islands are disc-like, flat and smooth, there are others that are composed of rods and structures associated with the crystalline polycarbonate.

In this experiment, approximately 10% of the polymer was found to be in a crystalline state. After a relatively long period of time (several tens of minutes), treatment with the plasticizing vapour resulted in only a few more flat areas developing some internal structure (doping for this length of time would be sufficient to induce significant spherulitic structure in the continuous PC film). The island to the left of the crystalline region in figure 8.7, shows some evidence of internal structure.

Using a similar argument as Cormia, Price and Turnbull, it was noted that the PC islands containing the heterogeneous nucleation sites have crystallized in the same way as the usual continuous film. However the growth is curtailed by the exhaustion of amorphous material in the drop and adjacent drops devoid of both heterogeneities and contact from the crystallite, remain amorphous (for a longer period of time than is predicted from the kinetic growth curve below) until such time that the polymer crystallizes as a result of random motion (i.e. nucleation from an homogeneity).

8.2 TREATMENT BY OTHER PLASTICIZERS

8.2.1 Introduction

The aim of this section was to use the combined 'morphology and kinetic' study introduced in chapter 7 to monitor the effects of chemically different plasticizers on the PC film. The AFM in both the tapping and contact modes was used and the growth of the spherulites formed charted as a function of time. Specific attention was made to any differences in morphology or growth

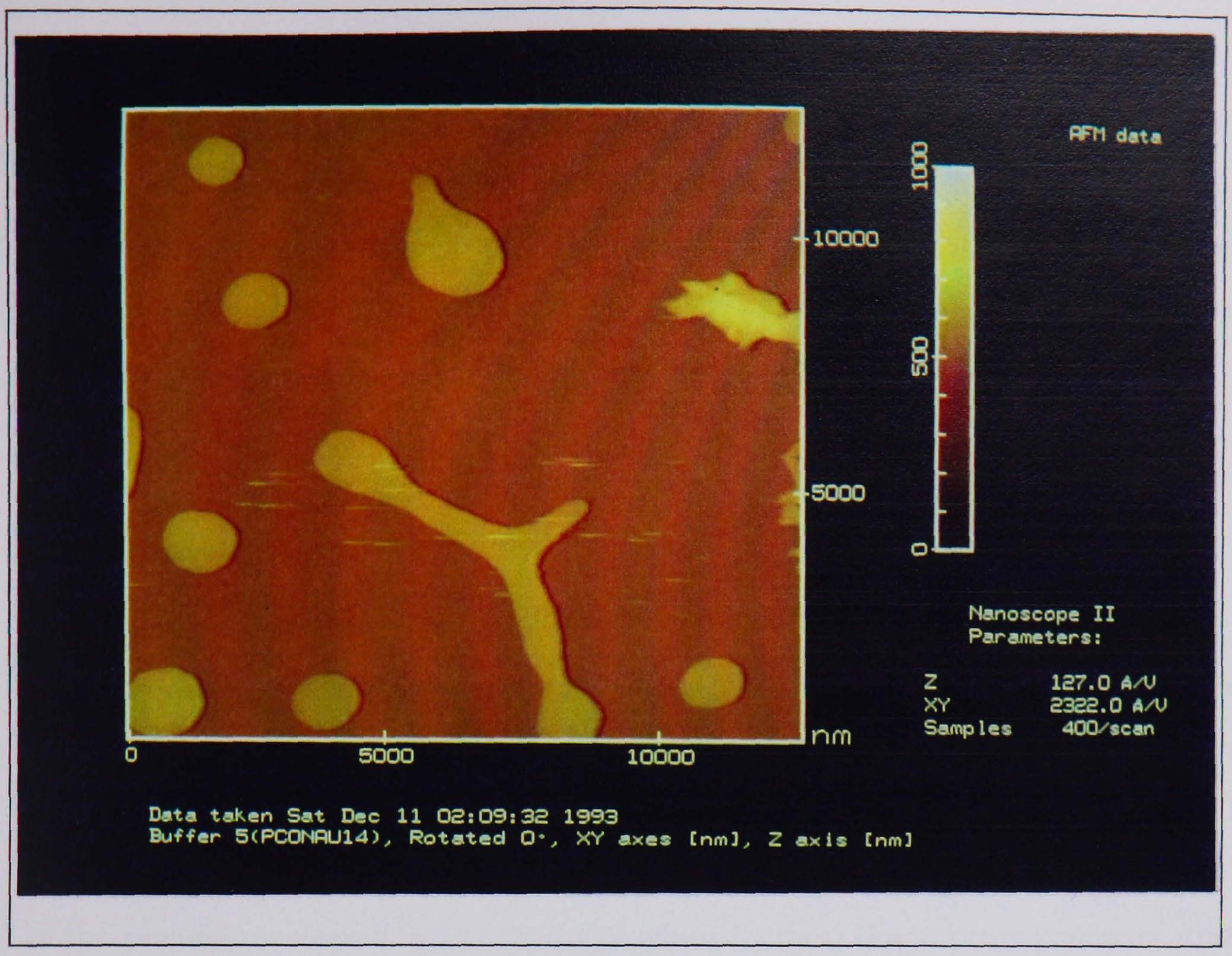

Figure 8.6: An image of the PC droplets, here only 5-10% of the PC regions crystallized after a substantial doping period (that would normally be long enough to induce crystallinity over the whole film).

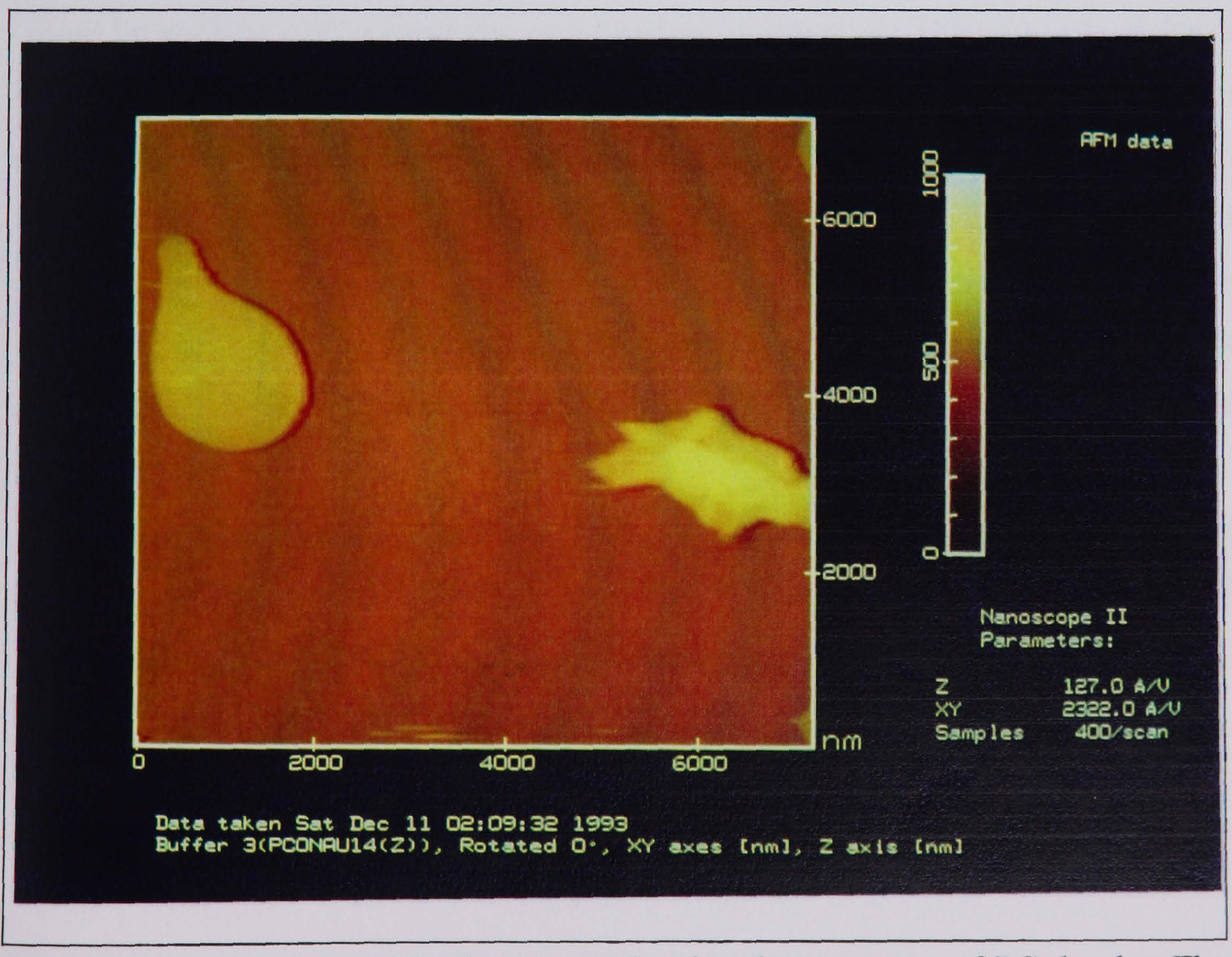

Figure 8.7: A higher magnification image showing the two types of PC droplet. The left-most region has almost no significant morphology, whereas the droplet on the right contains linear features associated with the crystalline polymer.

rate within the PC films as a function of plasticizer. The growth curves were then manipulated in such a way that the Avrami exponent could be derived. For one dimensional growth from instantaneous nucleation sites, the exponent is expected to be 1. Results were then compared to previous studies notably by Cope [1977] and Daniewska et al[1986], where the plasticizer type was identified as significant in the crystallization process.

8.2.2 Experimental

The experimental procedure outlined in chapter 5 was repeated in this study, the only change being the chemical nature of the plasticizer (the plasticizers used in this study are listed in Table 8.2). To achieve a successful comparison of the plasticizer effects on the crystallization process, careful experimental conditions were observed. It was understood [Cope, 1977], that the 'activity' of the plasticizer depends on (amongst other factors) the vapour pressure and hence temperature, thus it was important to conduct the experiment at constant temperature [(24.5 +/-0.2)°C]. In addition, the thickness of the film must be such as not to limit the penetration of any slow diffusing plasticizers over the time scale of the experiment. The results indicated that a film thickness of 20nm was sufficiently thin such that significant film penetration delay by the plasticizers involved could be ignored. Spherulitic development was observed in almost all films. Additionally, the temperature of the crystallization process was deemed sufficiently high such that each plasticizer used could be described as reducing the Tg of the polymer to ambient (see chapter 4).

Each film was imaged after treatment by the AFM in both the tapping and contact modes. The procedure was repeated for a further period of crystalline growth. The diameter of the spherulites (formed under the action of each plasticizer) was recorded as a function of time.

8.2.3 Results

The film morphology was observed for each of the plasticizers given in table

	Plasticizer	δ_D	δ_P	δ_H	SP	ΔSP	Vm
1	Dichloromethane	18.2	6.3	6.1	20.3	0.0	63.8
2	Trichloromethane	17.8	3.1	5.7	19.0	1.3	80.7
3	Tetrachloromethane	17.8	0.0	0.6	17.8	2.5	97.1
4	Ethyl formate	15.5	8.4	8.4	19.6	0.7	80.2
5	Ethyl acetate	15.8	5.3	7.2	18.2	2.1	98.5
6	Ethyl n-butyrate	-	-	-	-	-	-
7	Butyl Acetate	15.8	3.7	6.3	17.4	2.9	132.5
8	Acetone	15.5	10.4	7.0	20.1	0.2	74.0
9	Toluene	18.0	1.4	2.0	18.2	2.1	106.8
10	n-Hexane	14.8	0.0	0.0	14.8	5.5	-
	Polycarbonate	19.4*	0.8**	5.7**	20.3*	n/a	-

Table 8.2.

The Hansen Solubility Parameters (units $(J\ cm^{-3})^{1/2}$) for Polycarbonate and some of the plasticizers used in this study.

Key:

δ values are the individual Hansen solubility parameters relating to the Dispersion, Polar and Hydrogen bonding. SP is the general solubility parameter and ΔSP is the difference between PC and the solvent general solubility parameter. Vm is the molar volume and is an indication of the size of the solvent (an arbitrary units).

Solvent Source: Polymer Handbook ed. Brandrup and Immergup; Wiley Interscience; 3rd Edition; 1967
Polycarbonate Sources: * Daniewska et al [1986] **Shaw, M.T.; Journal of Applied Polymer Science; Vol. 18; pp449; 1974

8.2. Growth rates were also obtained from each plasticizer and a ln-ln plot of diameter as a function of time calculated (the gradient of such a curve is the Avrami exponent, derived in chapter 4). The AFM images of the effect of a number of plasticizers are given in this section and they include acetone, toluene, dichloromethane, chloroform and n-hexane. Results were compared with those obtained by Daniewska et al[1986], one of the few papers on this topic.

Acetone

Figure 8.8 shows the AFM image $(30\mu m)^2$ of the PC film exposed to acetone for only a few minutes (see rate curves below). The spherulites are clearly defined and have reached a maximum diameter of (13+/-3)μm where growth is uninhibited by impingement. Further treatment of the film resulted in full impingement and a mean spherulite diameter of (10+/-3)μm (Daniewska et al give mean diameter as 7.8μm).

One of the spherulites in the middle left of figure 8.8 was imaged at higher magnification to give figure 8.9, size $(6.2\mu m)^2$. At this level of resolution the spherulite fibrils can be observed and it should be noted that the fibrillar morphology is dominated by a high degree of branching giving a dense, packed spherulite. The tapping mode AFM (TMAFM) was also used to observe this film and images are given in figure 8.10a. The film details were found to be consistent with contact mode images of the film. High resolution TMAFM images (not shown here) allowed fibrillar dimensions to be assessed at 75-100nm long and 25-35nm wide.

Toluene

The film exposed to Toluene vapour was imaged and a typical example of the morphology is given in figure 8.11, size $(100\mu m)^2$. The spherulites in this image, measured before impingement have attained a maximum diameter of (20+/-4)μm. After impingement the mean spherulite diameter was calculated as (15+/-4)μm (Daniewska et al give mean spherulite diameter as 12.6μm).

A magnified image of one of the spherulites is given in figure 8.12, size $(30\mu m)^2$. One of the most obvious features in this image is the 'banding' or

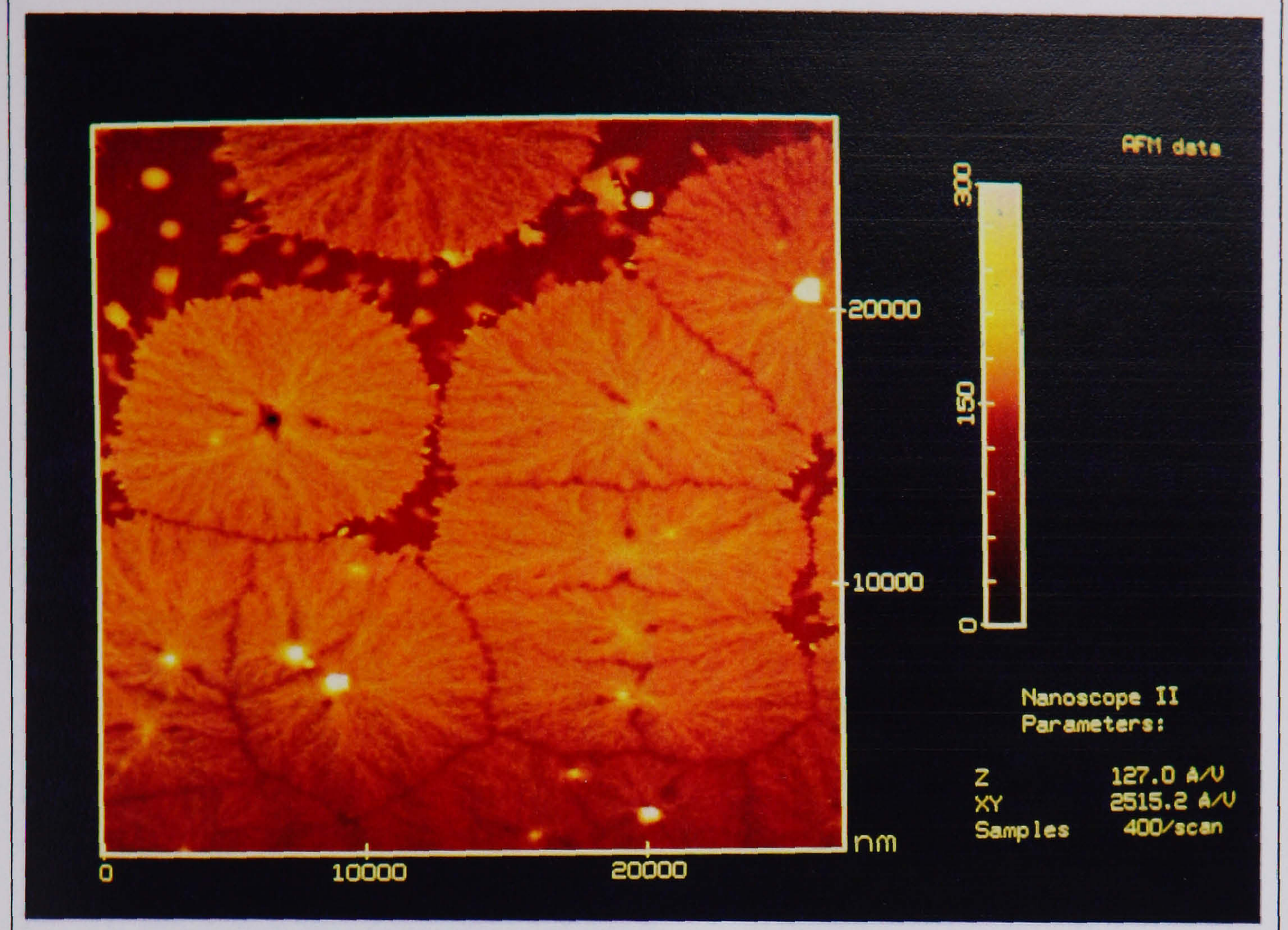

Figure 8.8: This figure shows the exposure of the PC film to acetone. The spherulites formed are disc-like and densely packed with fibrils.

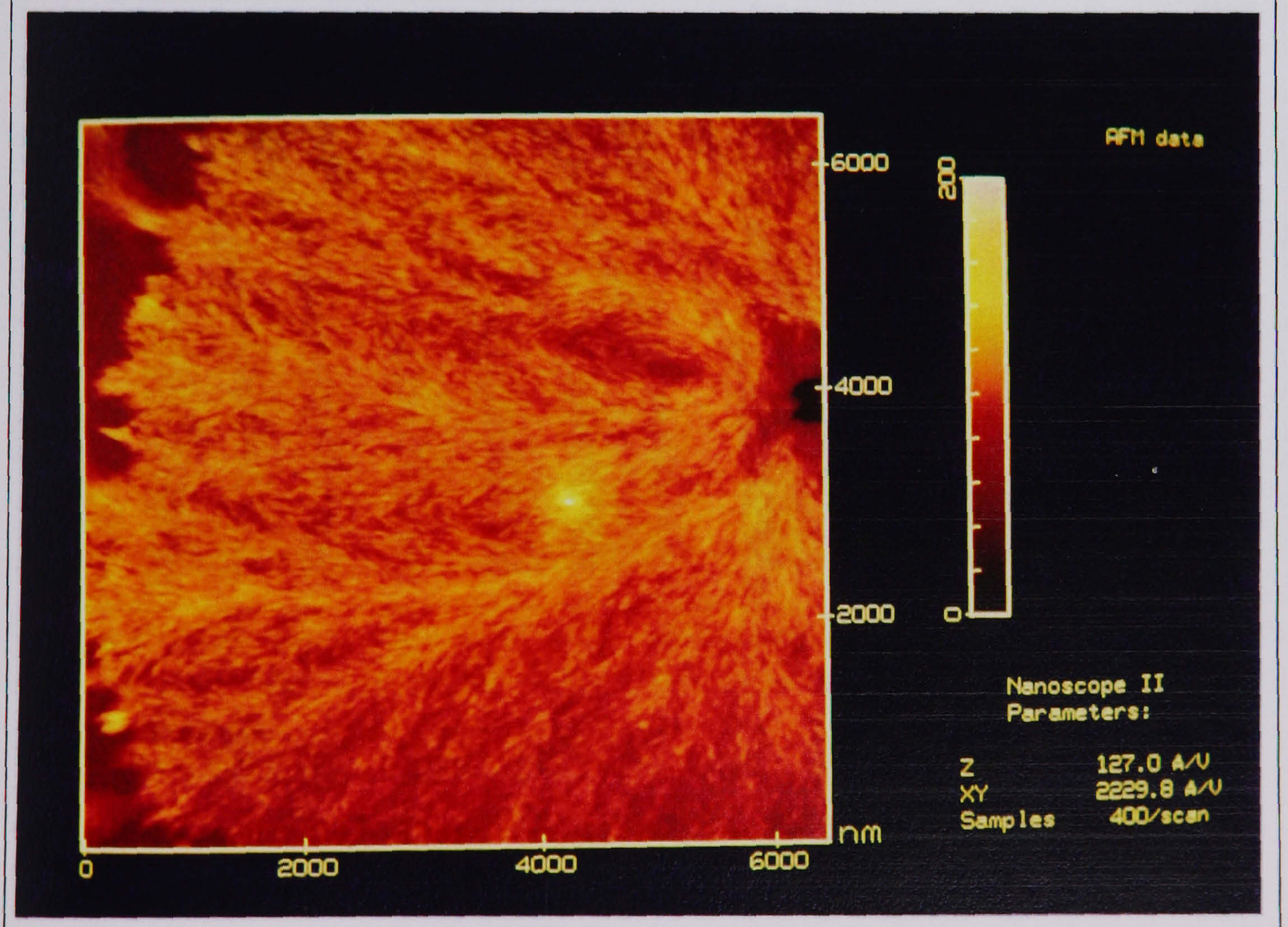

Figure 8.9: Higher magnification images of the fibrillar structure of the acetone induced spherulites, reveal high incidence of branching.

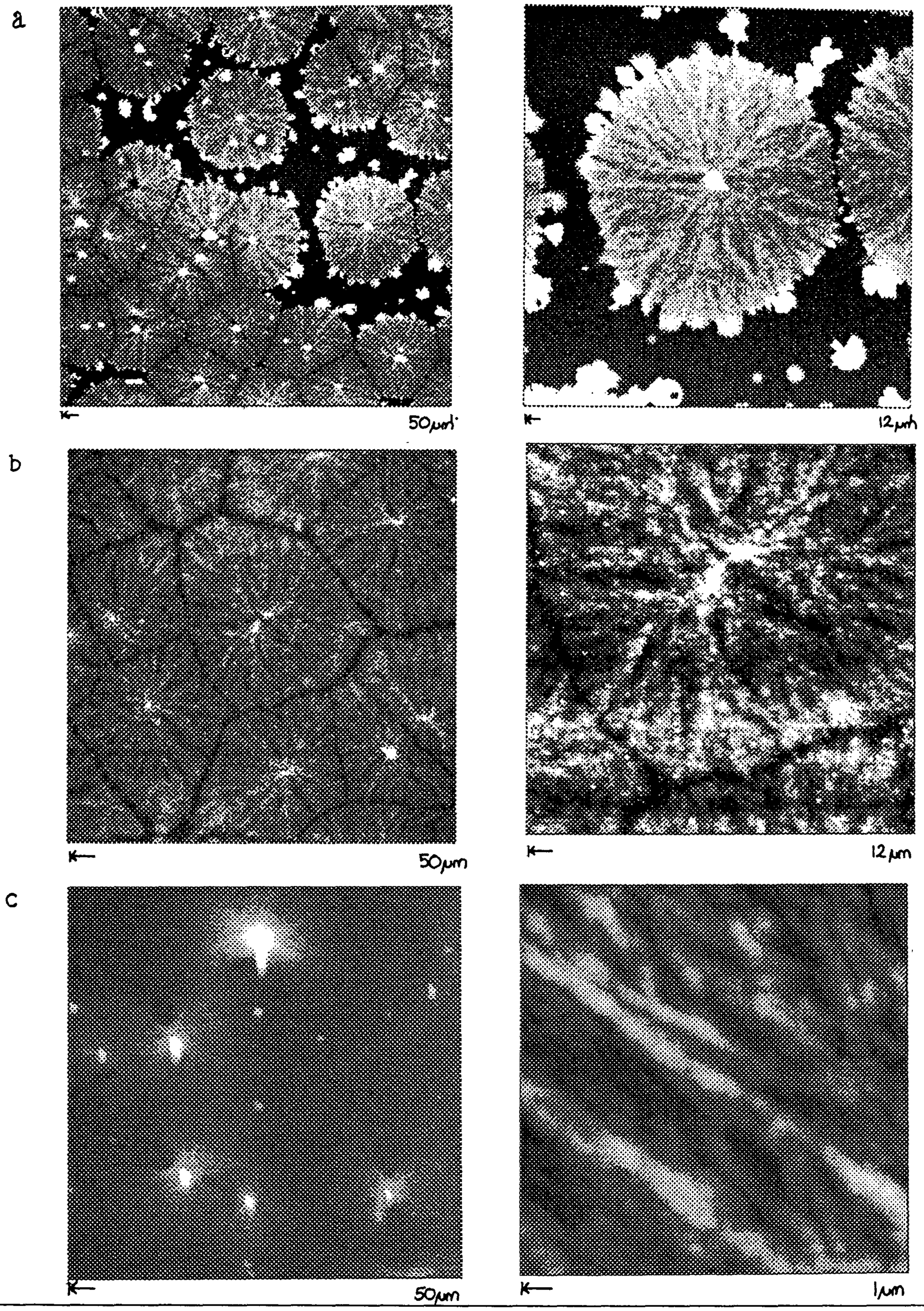

Figure 8.10: The tapping mode AFM was used to confirm the contact mode images. In this series of images three different plasticizers are used. a) Acetone, b) Toluene and c) Dichloromethane.

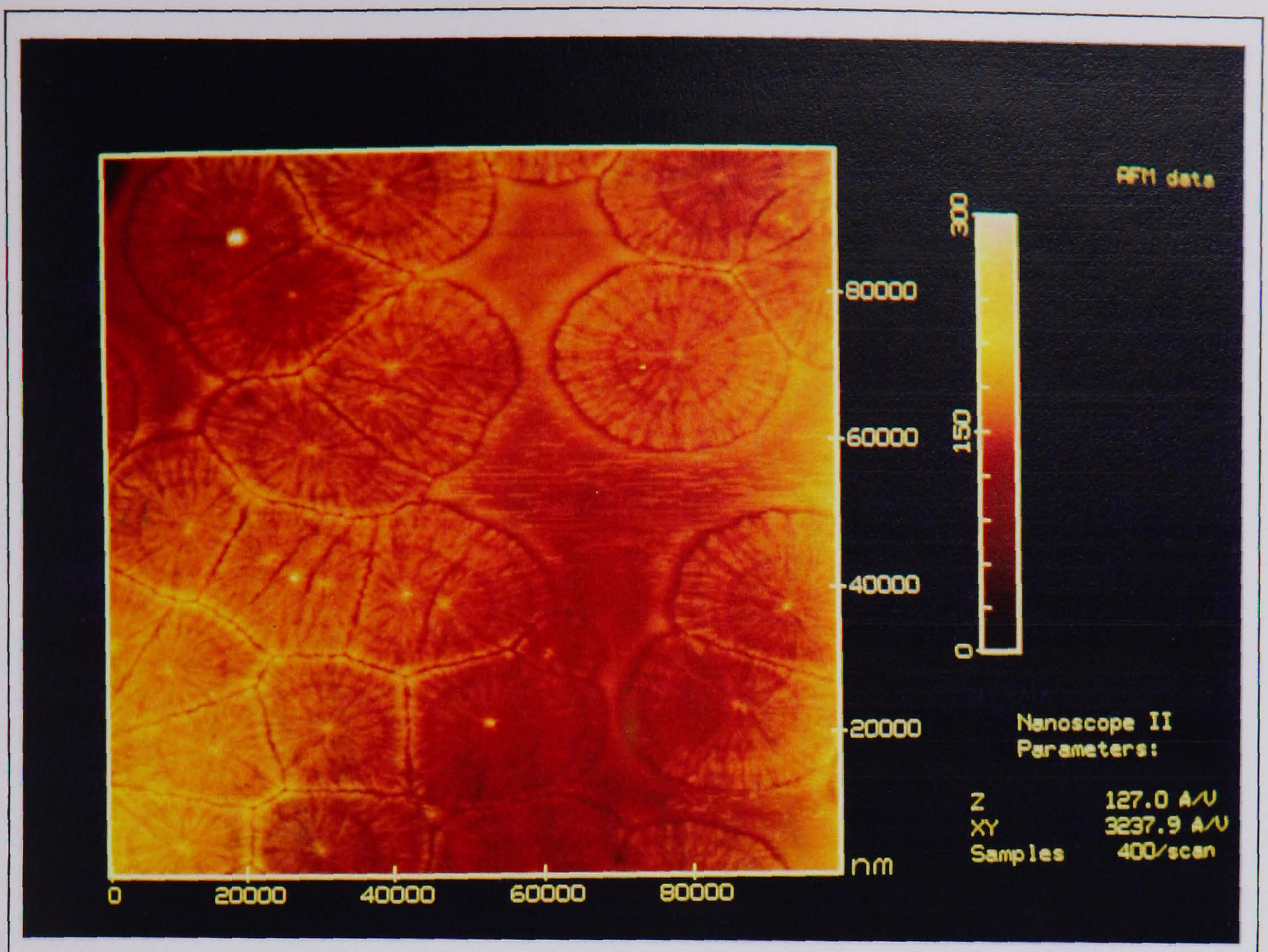

Figure 8.11: This image shows the result of toluene vapour on the PC film. The spherulites are disc like.

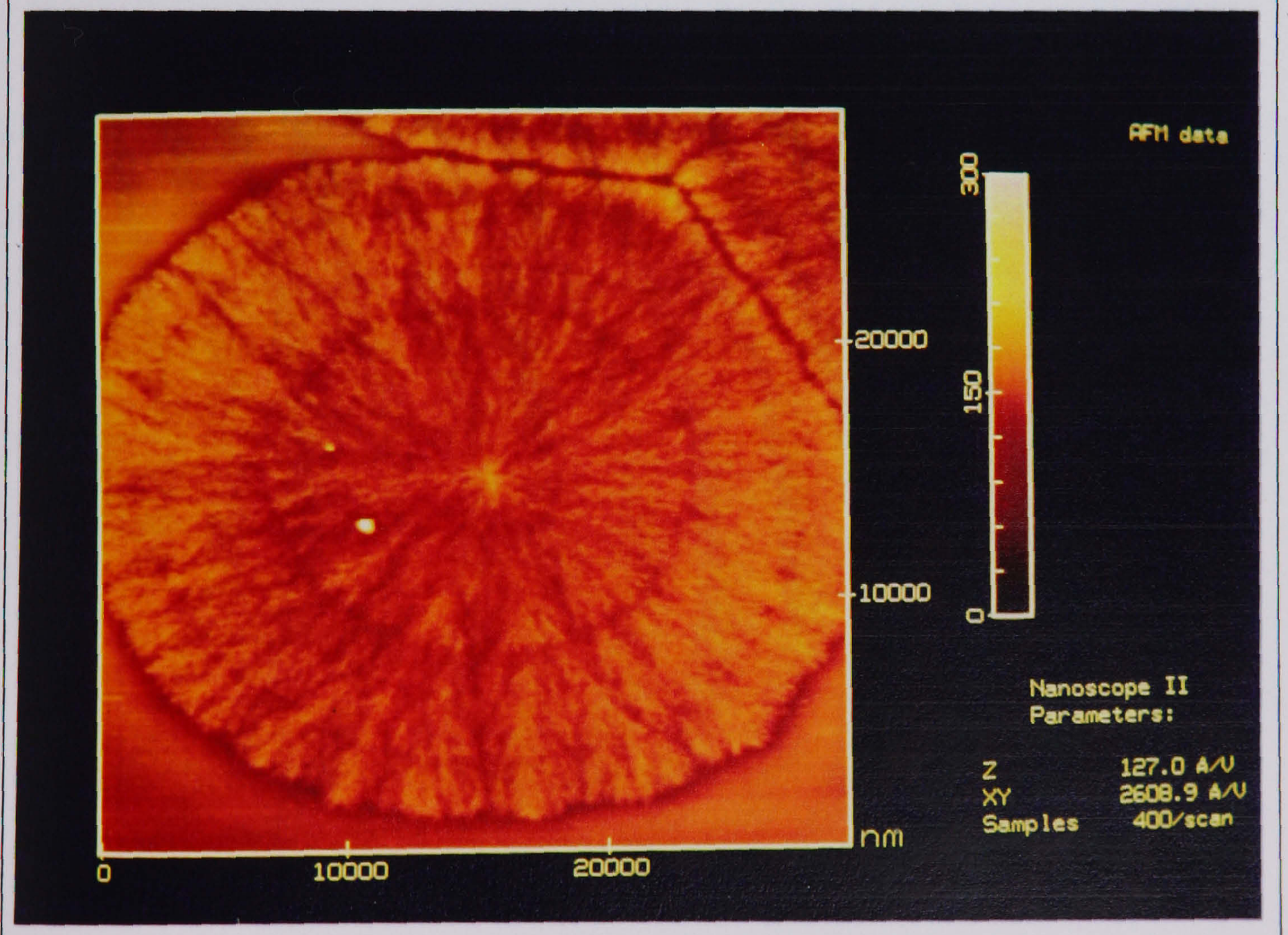

Figure 8.12: The toluene doped film produces spherulites with a banded structure. The diameter of the bands is related to the growth process used to determine the growth rate curves.

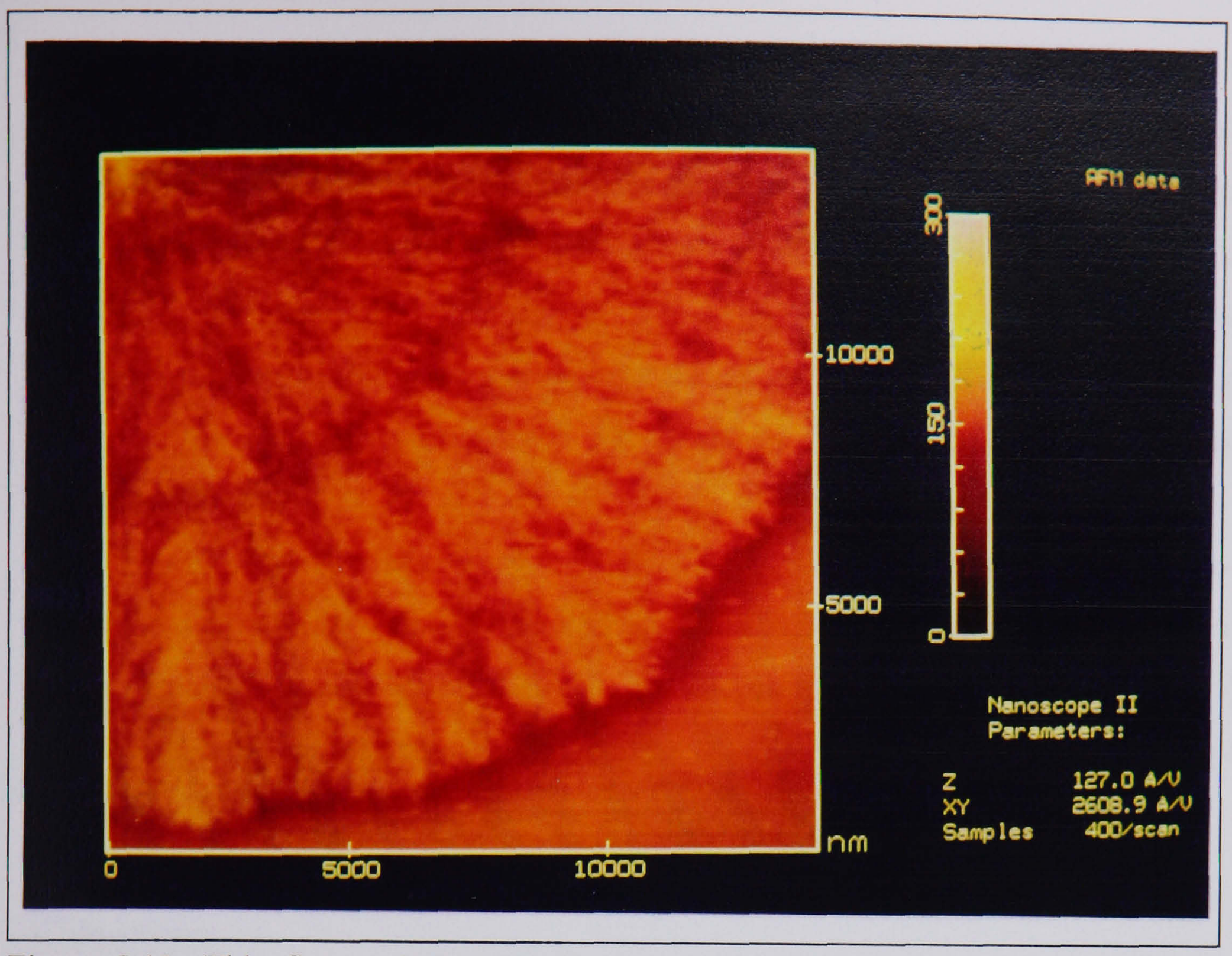

Figure 8.13: This figure shows the fibril structure to be dominated by extensive branching and densely packed lamellae regions. The banding is well defined.

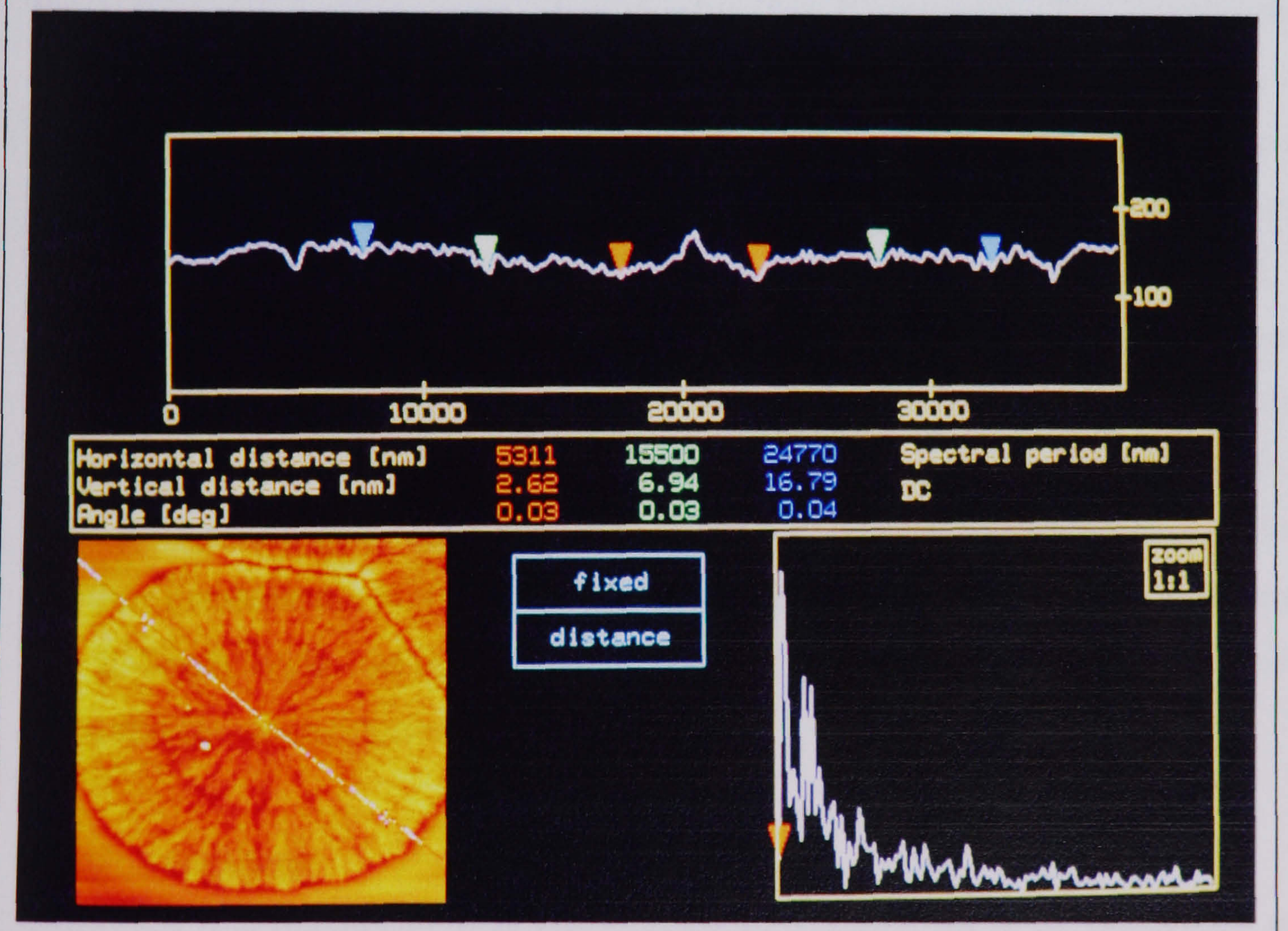

Figure 8.14: This surface profile of the toluene induced spherulite, enables the band diameters to be measured (see the green, red and blue markers on the top-most display).

appearance of dark concentric rings, centred on the nucleation point. A higher magnification image - figure 8.13, size $(15\mu m)^2$ reveals that there are four bands in all and that their diameter is proportional to the doping time for each stage in the growth curve (see also figure 8.14 which gives a surface profile of the spherulite). The origin of the rings is unexpected but could be related to a slightly different film crystallization process during the drying stage of the cycle (see chapter 5 for details on the cycle). The rings are discussed below.

The fibril structure is very similar to that of acetone, with a high degree of branching, giving a dense, packed spherulite. TMAFM images of this film were obtained (see figure 8.10b) and further images (not shown here) permitted detailed analysis of the fibrils and confirmed that toluene treatment resulted in fibrils of similar size to those of acetone.

Chloroform

The next film to be analyzed had been doped with chloroform. Figure 8.15, size $(15\mu m)^2$ shows that the spherulitic material has advanced little more than the wheat-sheaf stage, even after doping for 10 minutes. The maximum spherulite diameter was very hard to measure although in this image, a radius figure greater than 7μm can be estimated. Further treatment followed by re-imaging revealed the mean spherulite diameter to be (21+/-5)μm compared with a mean diameter of 26.7μm measured by Daniewska et al.

The fibril structure of the spherulites was considerable different from those already mentioned i.e. acetone, toluene (see above) and butyl acetate (see chapter 7). The branching is less frequent, allowing the formation of a void (1.5+/-0.5)μm in diameter, either side of the central nucleating bundle. Further measurements (from the TMAFM) indicate that the fibril dimensions are 25-35nm wide but up to 200-300nm long (this latter figure is consistent with the lower incidence of branching).

Dichloromethane

Although this plasticizer was not studied by Daniewska et al, the effects of the chlorinated plasticizer - with a tendency to produce long straight fibrils,

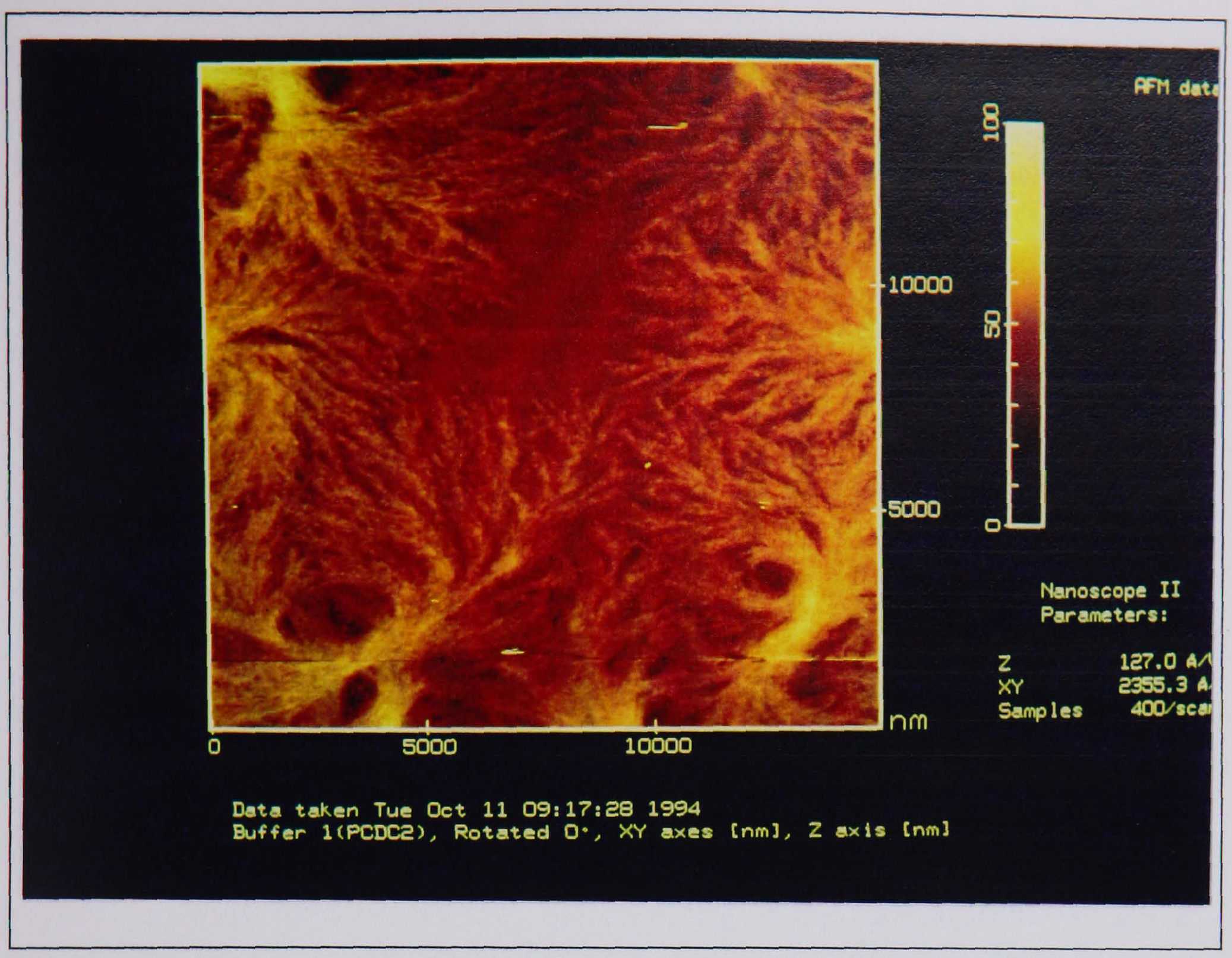

Figure 8.15: This figure shows the Chloroform induced spherulites. The structure of the spherulite is pre-disc or wheat-sheaf. The fibril arrangement is less densely packed and the branching less frequent compared to acetone or toluene.

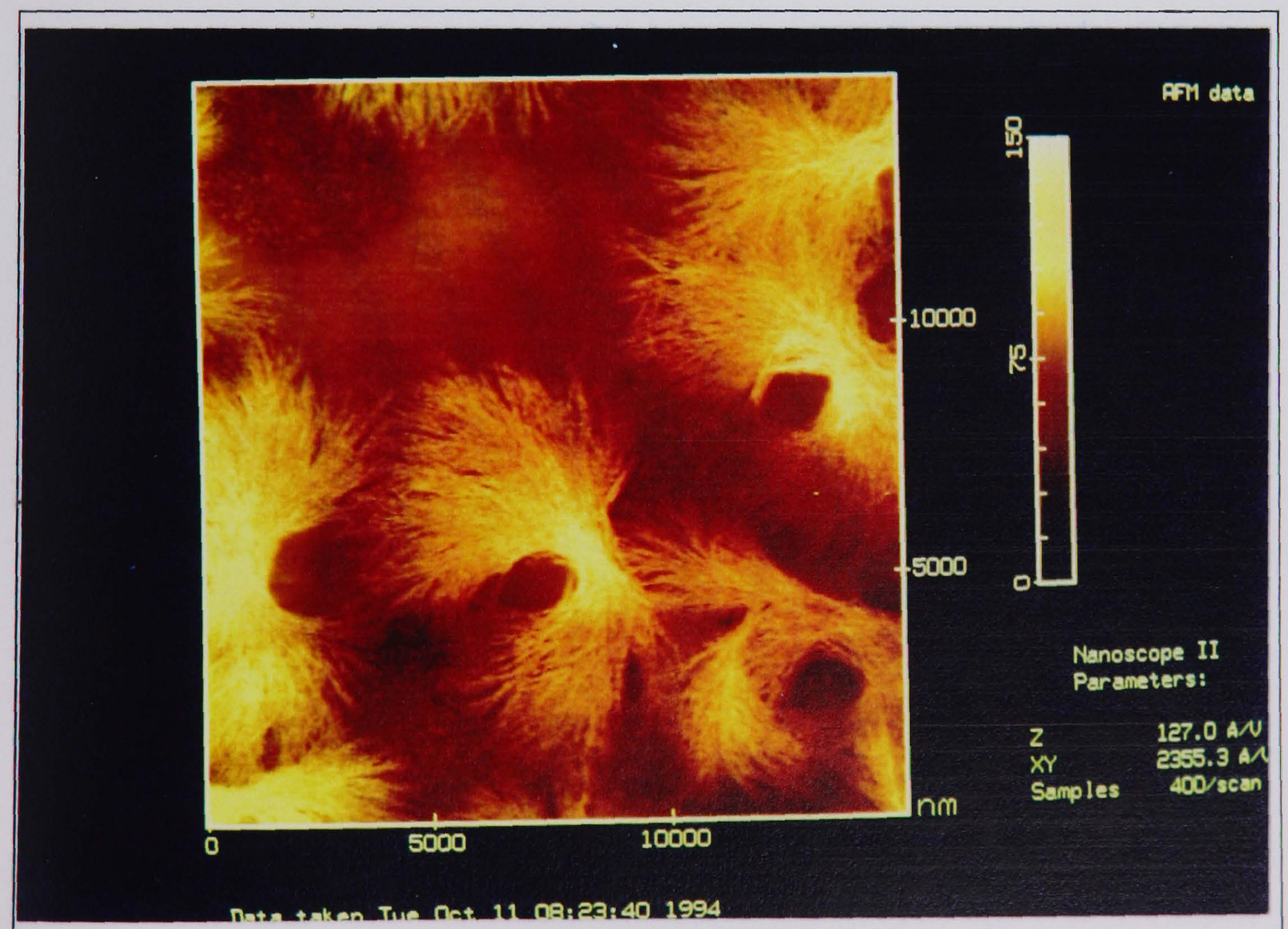

Figure 8.16: The dichloromethane doped PC film resulted in 'wheat-sheaf' formations with large voids either side of the central nucleating bundle. The voids are characteristic of low angle and low frequency branching.

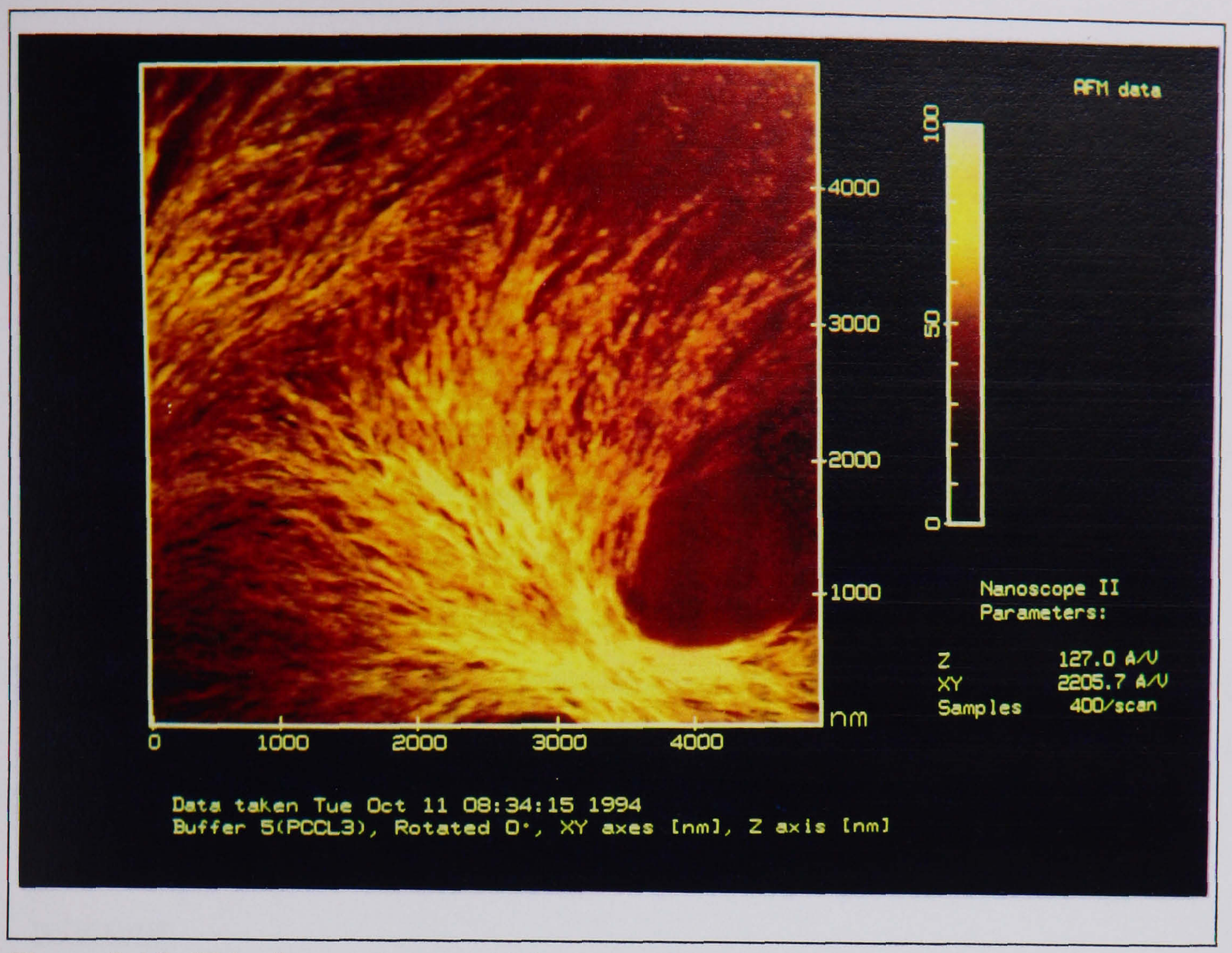

Figure 8.17: This figure shows a higher magnification image of the dichloromethane doped PC film. The incidence of branching in the lamellae bundles or rods is lower than every other plasticizer tested.

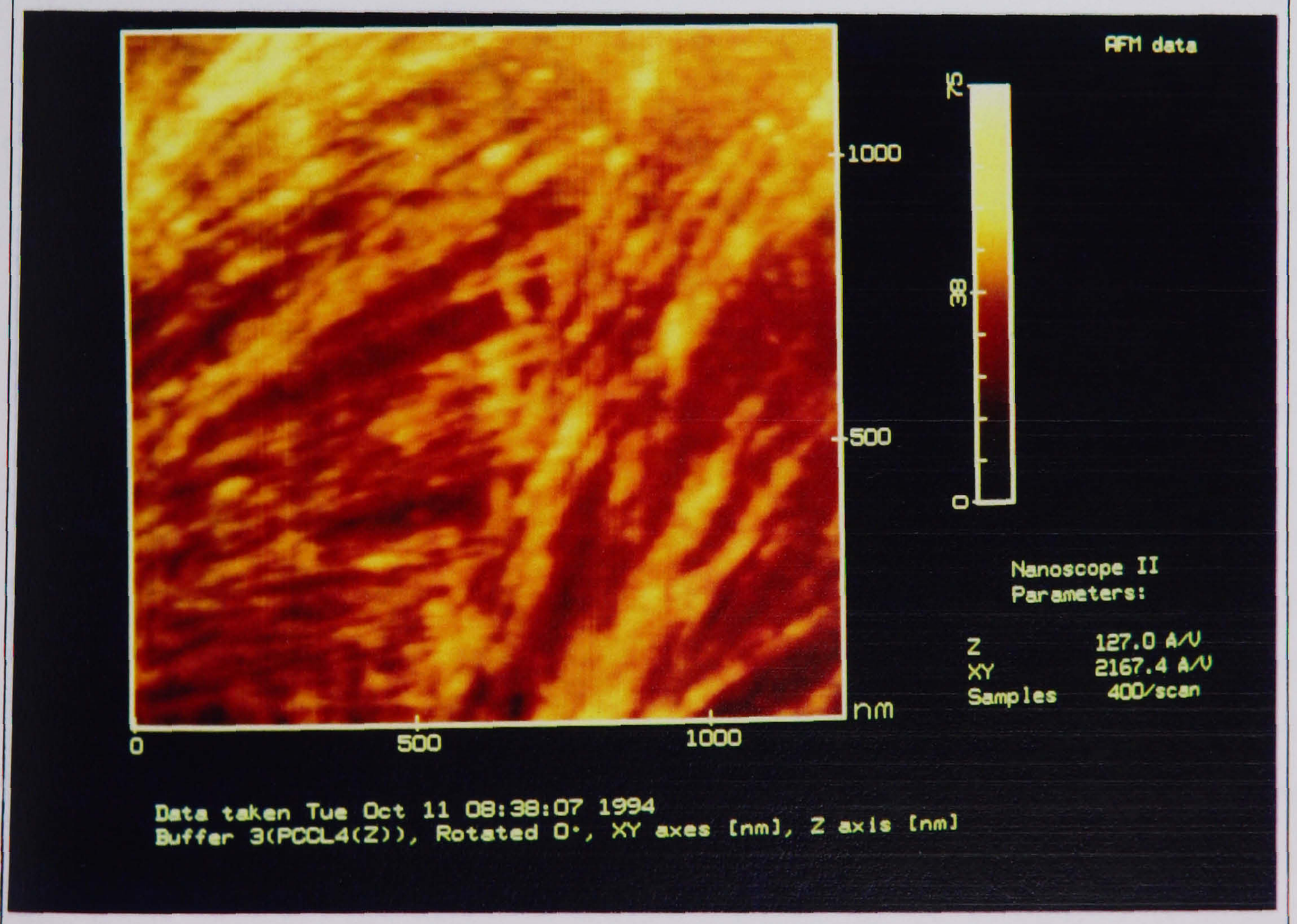

Figure 8.18: This image is a further, higher magnification image of the dichloromethane doped PC film. The fibril structure is dominated by long, straight parallel lamellae, with dimensions consistent with previous measurements made.

is clearly demonstrated. In figure 8.16, size $(15\mu m)^2$ the pre-spherulitic wheat-sheaf can be observed. The maximum diameter of the formation can be estimated at (10+/-3)μm with a mean spherulite diameter measured after total impingement at (14+/-3)μm.

The fibril structure consists of long straight lamellae regions, imaged in figure 8.17, size $(5\mu m)^2$ and figure 8.18, size $(1250nm)^2$. The fibrils have a very low angle of branching and the void, formed either side of the nucleating bundle is larger, at (3+/-0.5)μm than that formed by chloroform. The length of the individual rods or lamellae regions, observed in figure 8.18 was measured at 500-1000nm, before the onset of branching.

The TMAFM images (for example figure 8.10c) again confirm the contact mode images and other detailed studies give a rod width of (30+/-5)nm and length of 750-1000nm.

n-hexane

This solvent had no discernable effect on the PC film. Several different temperatures were used but on each occasion, no crystalline features of any description were observed.

Other Solvents

The PC films were imaged after treatment by all the solvents listed in Table 8.2 and their morphology studied. The internal structure of the spherulites was assessed and in general the chlorinated plasticizers e.g. chloroform, dichloromethane and tetrachloromethane produced low angle branching of low incidence, resulting in a void either side of the nucleating bundle. However, the non-chlorinated plasticizers produced spherulites with a densely packed structure and fibrils with a high-incidence of branching and no voids. The reasons for this observation remain unclear, although the most linear fibrils were observed on dichloromethane, a solvent with exactly the same solubility parameter as PC (the chlorinated hydrocarbon solvents are generally considered the best solvents for PC). Further studies could observe the fibril morphology under a variety of different chlorinated compounds, relating the size of the void to the incidence and angle of branching.

Growth Rates and Avrami Plots

In addition to the detailed morphological study given above, which compared the mean spherulite diameter readings to those obtained by Daniewska et al[1986], a study of the growth rates and function (described by the Avrami exponent) for a wide range of plasticizers was made.

Figure 8.19 shows the raw data for the spherulite size as a function of time, for each plasticizer. There is a wide range of spherulite growth rates and also a noticeable 'tail-off' in the rate of increase of the spherulite size as impingement is reached (see the curve for acetone).

Figure 8.20 gives the growth rates for toluene and acetone and figure 8.21 gives the ln-ln plots of the same data (the data points used for these curves were derived from the early stages of growth). The values for the growth rate and Avrami exponent are given in Table 8.3.

Figure 8.22 and 8.23 give the growth rates and Avrami exponent plots for the esters used. The values are recorded in Table 8.3. Finally the growth rates and ln-ln plots for the chlorinated plasticizers used are given in Figures 8.24 and 8.25 and appropriate values recorded in Table 8.3.

Estimation of Errors

The main source of error associated with obtaining measurements from the system under study arise from the irregular shape of the spherulites. It was found that the diameter, within a single spherulite typically varied by 4%-8% and this figure is indicated on the graphs by error bars. When deriving the ln-ln plot, a higher and lower value for the diameter was used when ln-diameter was calculated; in every case the new error bars were smaller than the point markers on the graph and so were not used. The error values noted in Table 8.3 were the most pessimistic error estimations for both the growth rate and the Avrami exponent using variations in diameter (typically +/-4%)

It was assumed that the error in calculating the plasticizer vapour exposure time was insignificant. This assumption is based on the relatively short time required for the vapour and polymer film to reach equilibrium during the initial doping phase and a similarly short period of time taken for

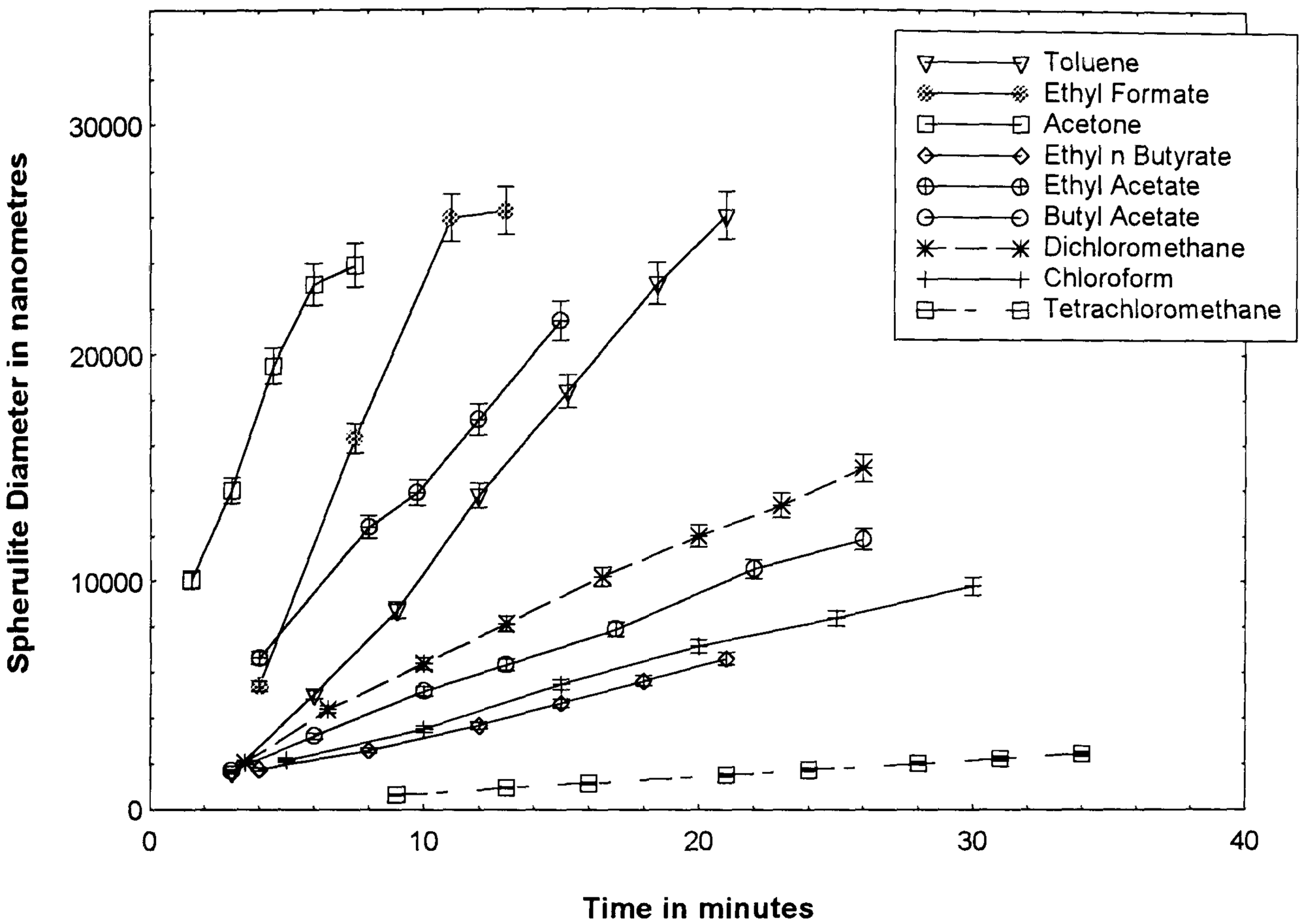

Figure 8.19: This graph shows the increase in diameter of induced spherulites as a function of time for all the plasticizers tested.

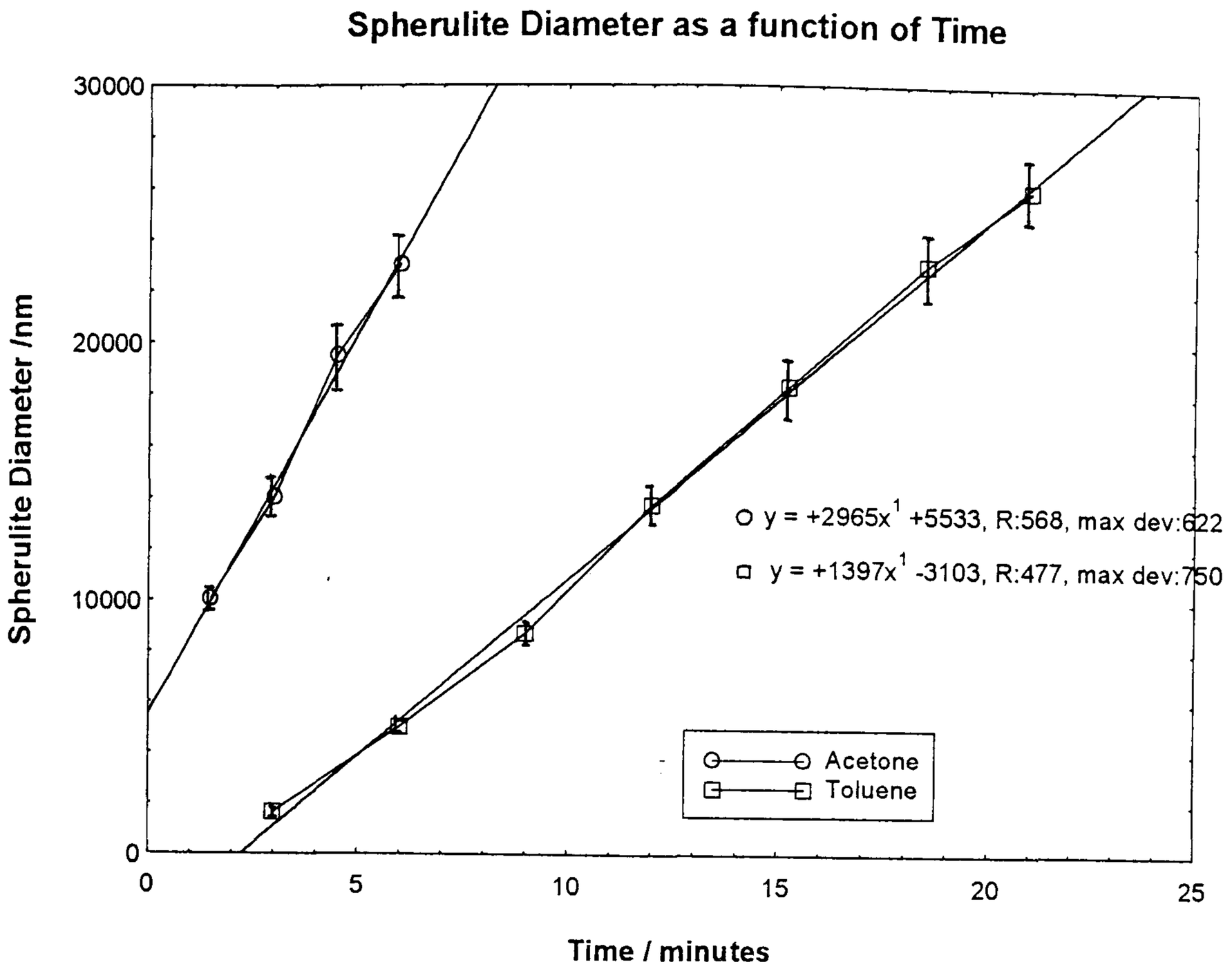

Figure 8.20: This graph gives the growth rates for acetone and toluene induced PC spherulites.

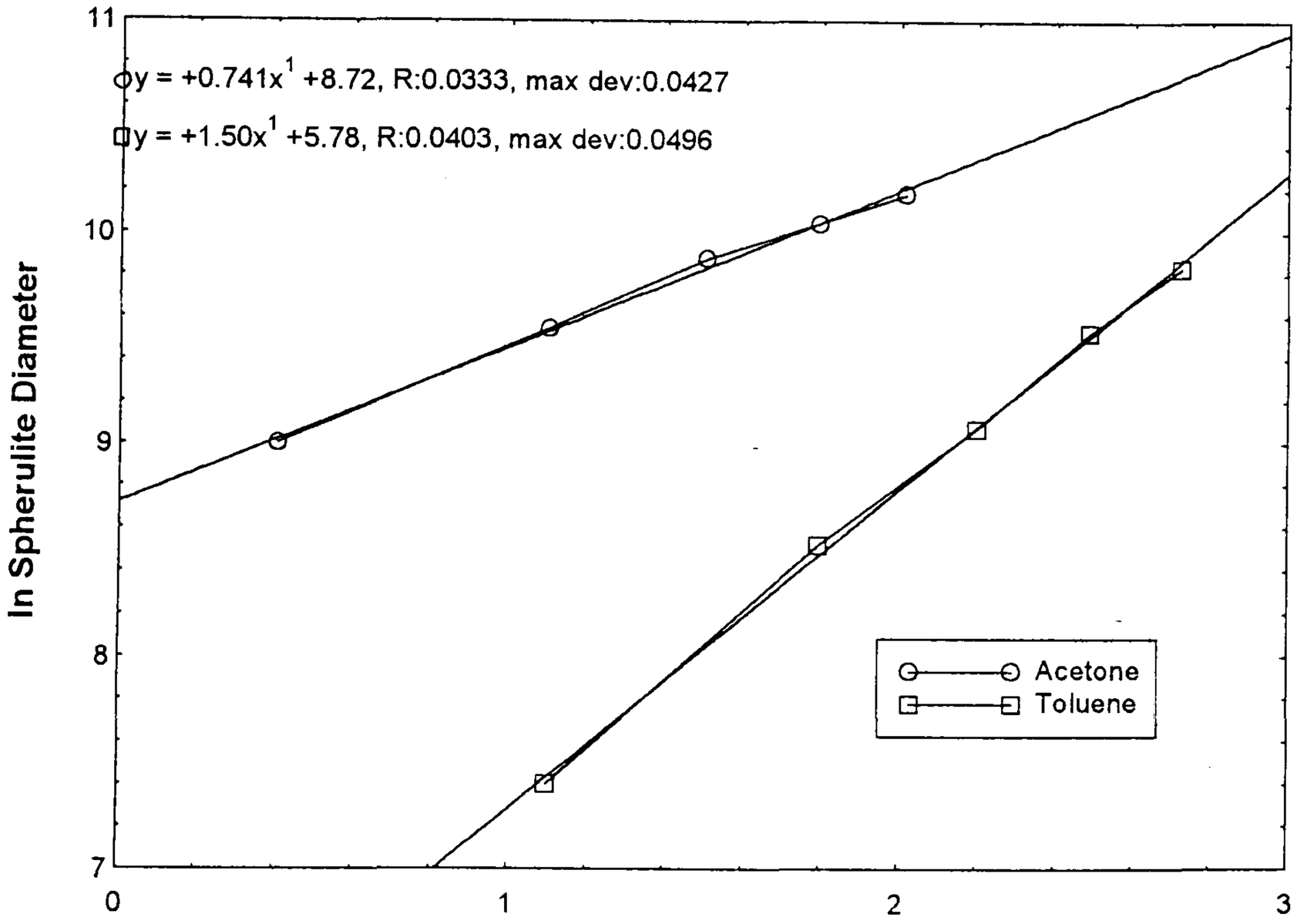

Figure 8.21: This figure shows the ln-ln plot of the growth curves for acetone and toluene given in figure 8.20. The gradient for this curve is the Avrami constant or exponent - 'n'.

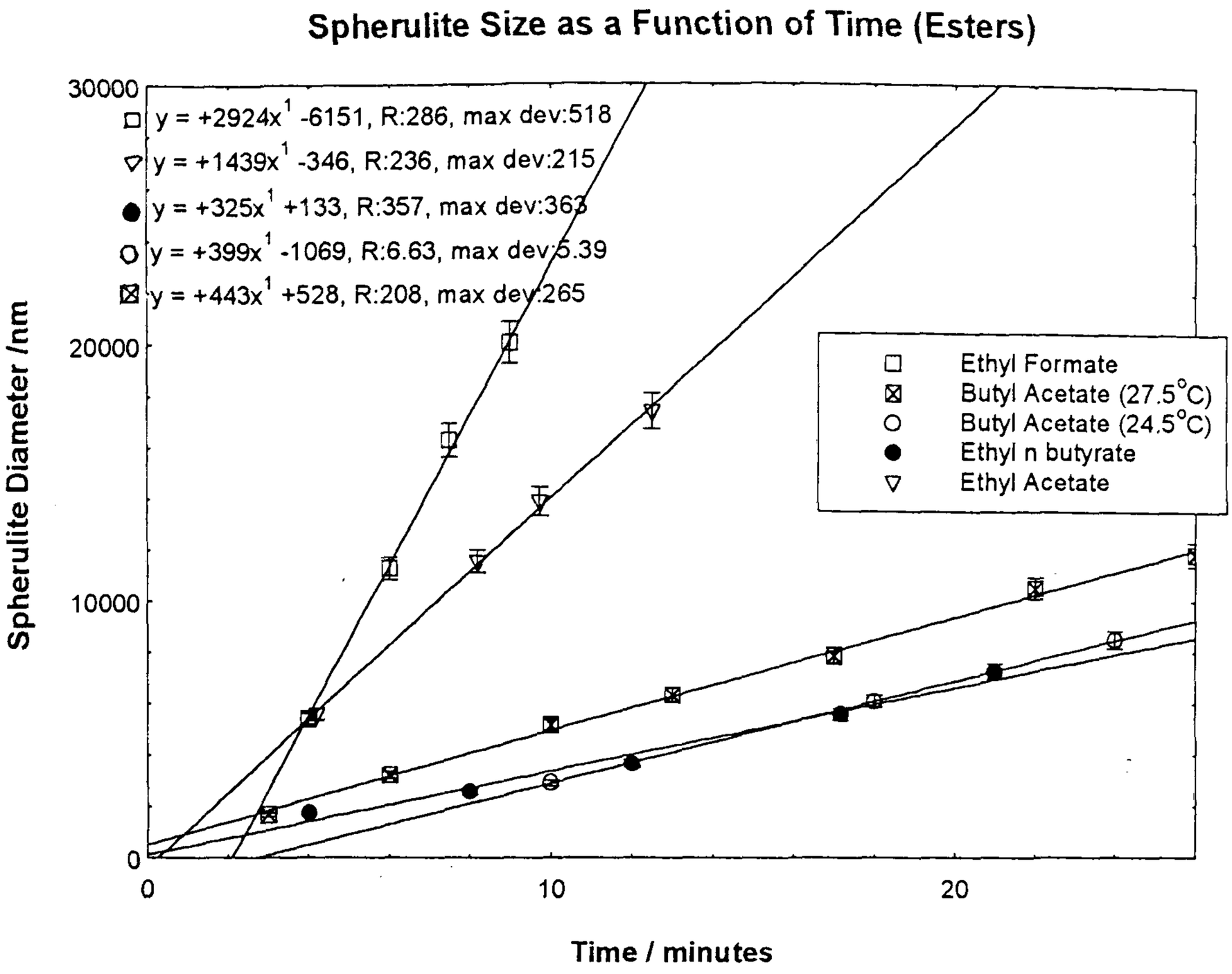

Figure 8.22: This graph shows the growth curves for the esters used to induce spherulitic growth. Note that the growth rates for butyl acetate and ethyl-n-butyrate are very similar.

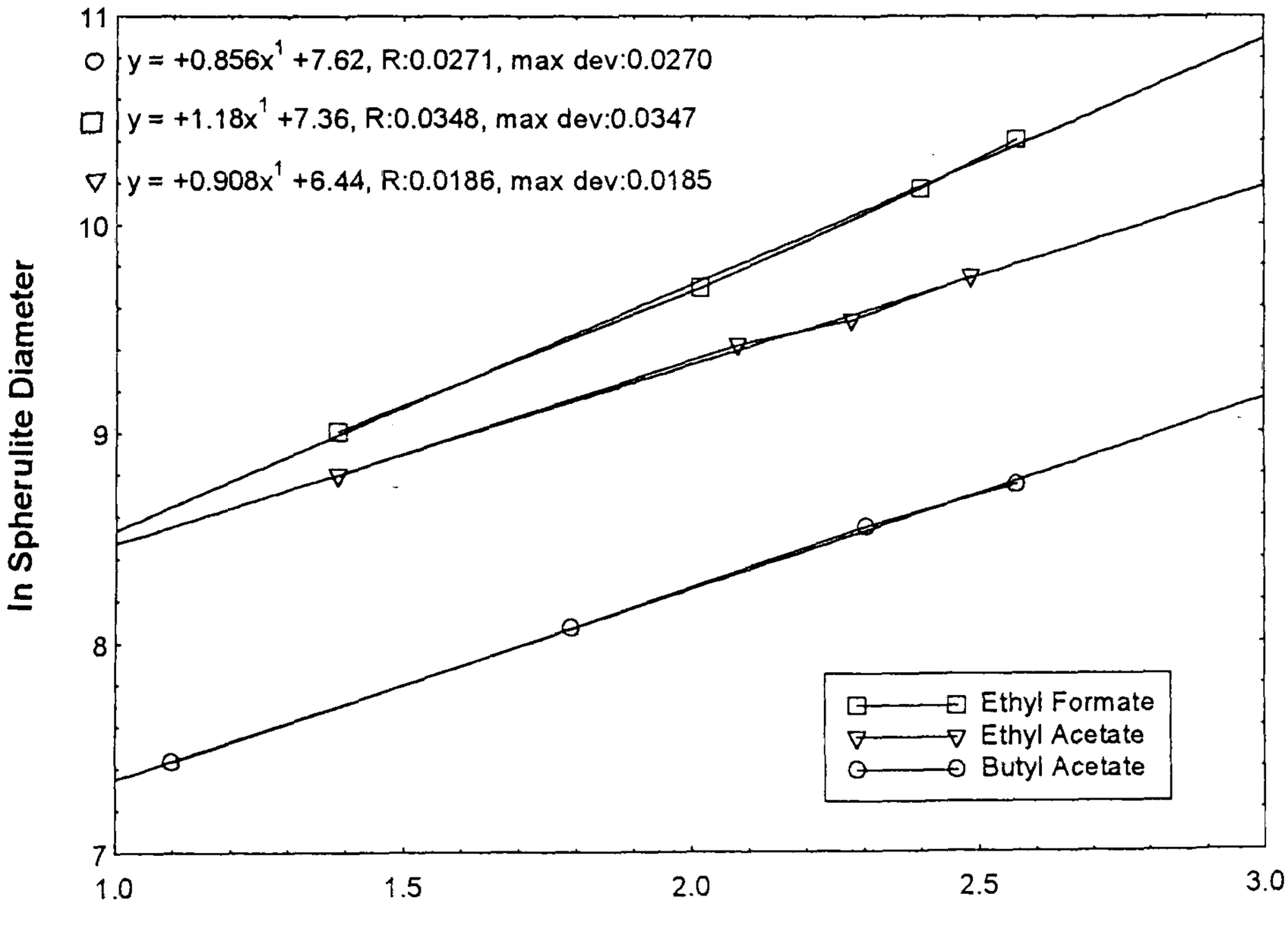

Figure 8.23: The Avrami exponent can be derived from the ln-ln plot of the growth as a function of time. The values quoted are for ethyl formate, ethyl and butyl acetate.

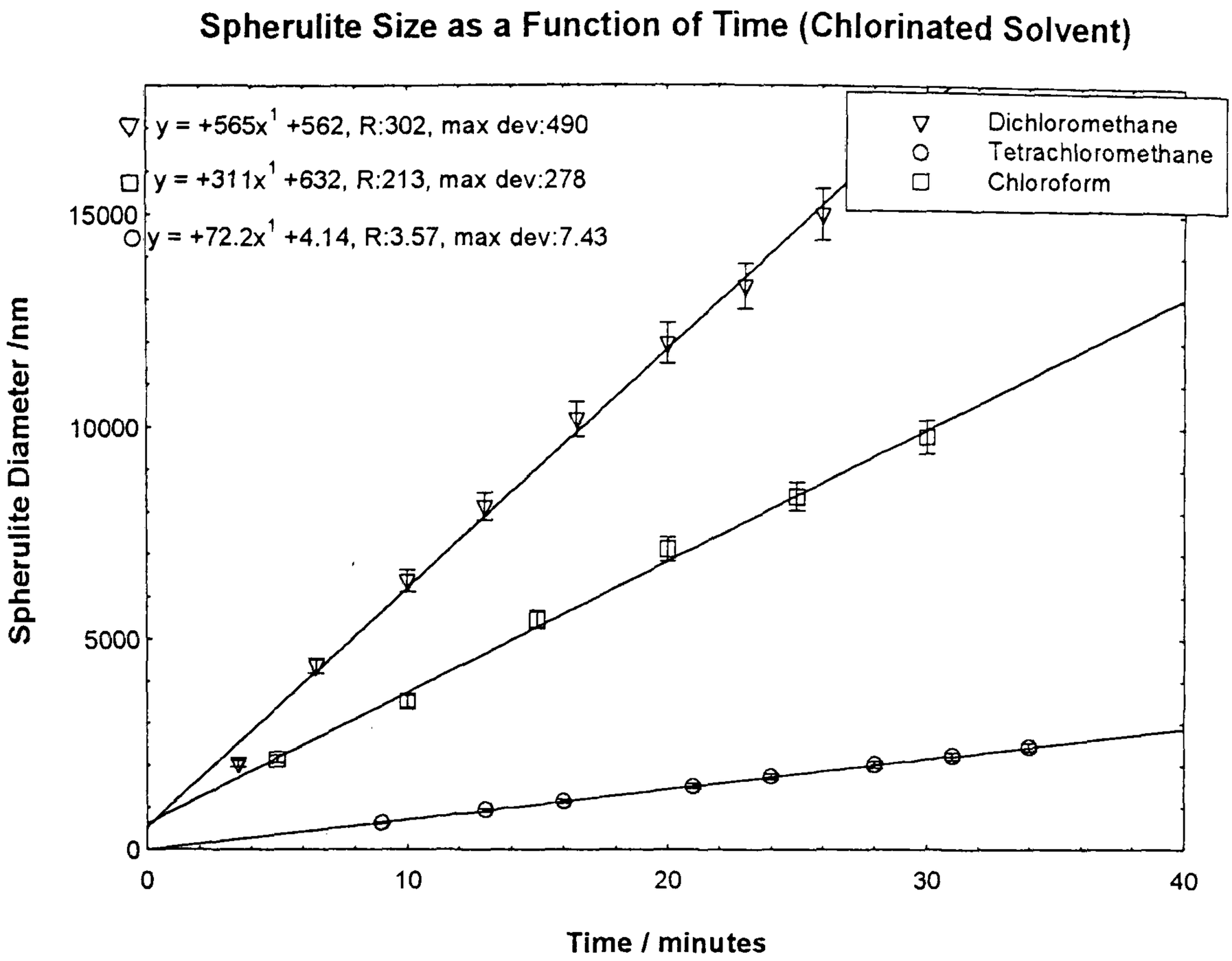

Figure 8.24: The growth rates for the spherulites induced by the chlorinated solvents are given in this graph.

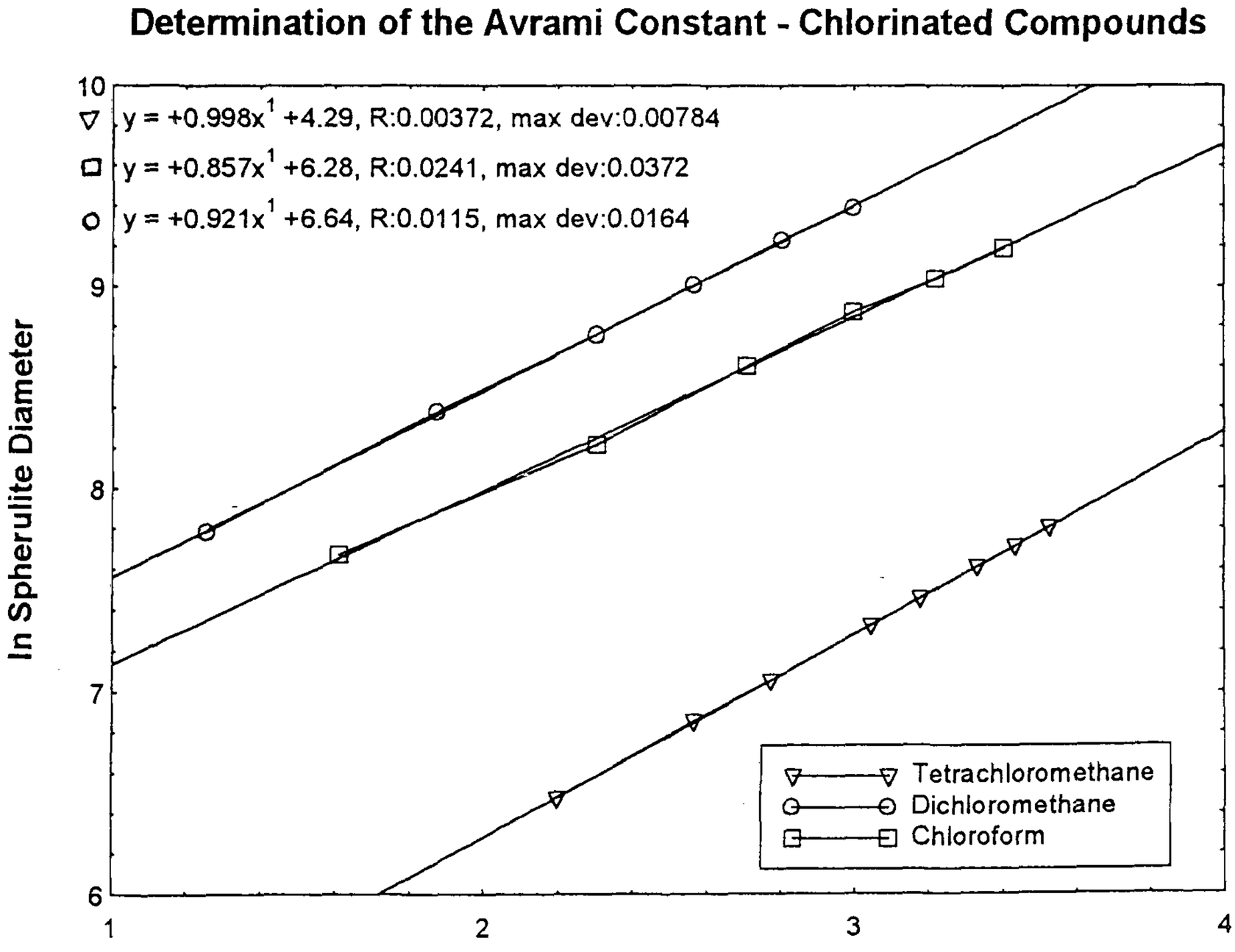

Figure 8.25: The Avrami exponent was calculated for the PC spherulite formation, induced by chlorinated plasticizers.

the plasticizer to evaporate during the drying phase. A possible source of error emerges if there is a significant delay or 'lead-in/lead-out' time at the start and finish of each doping period. Evidence for such a delay is found in the spherulite 'banding' clearly visible in the toluene induced spherulites.

The occurrence of the banding (only found in toluene) is related to the doping process; each time the sample is dried and then re-doped a ring appears. It is possible that the spherulite growth continues during the drying phase until all the solvent has evaporated. The rate or process involved during the 'extra' growth could be significantly different from the usual case (where the solvent in the film is in equilibrium with the solvent vapour) resulting in a scar on the spherulite. This effect could be used to the advantage of a future study. The banding, like rings found in trees, gives the growth history of a single spherulite. It should be possible to assess any variations in local growth rate (caused for example by variations in polymer molecular weight) by observing the asymmetry in the band structure

However the banding (in toluene) may not be significant when determining timing errors and, in general the timing was assumed to be sufficiently accurrate to ignore the need for error bars. This assumption, especially in the light of the banding in toluene was tested by measuring the growth rate using 3 individual doping periods (spanning a specific time period) and comparing with the rate derived from a similar film subjected to 6 doping periods (for the same total time period). For each of the plasticizers, the rates were found not to differ. This latter observation would mean that the doping edge-effects were insignificant in the determination of the growth rate.

Errors associated with the nucleation process were minimal. It was found that the significant majority of spherulites formed were nucleated instantaneously from heterogeneities (described above).

8.2.4 Discussion

General Observations

Before discussing the results obtained it is necessary to reconsider the

crystallization system as a whole. In general the solvent induced crystallization of PC was achieved by those solvents capable of increasing the fractional free volume of the PC film. This allowed free rotation of the PC backbone and rapid and extensive spherulitic growth ensued [Cope, 1977].

The system requires the solvent vapour incident on the PC to interact with the chains and by diffusing into the film create the free volume necessary to induce crystallization. In an attempt to describe the 'affinity' between the polymer and the solvent, other workers (e.g. Daniewska et al[1986]) have resorted to the Hansen solubility parameter described in Chapter 4. It was assumed that the closer the values of the solubility parameter for polymer and solvent are to each other, the higher the affinity and the more productive the spherulitic growth process. In general, this study shows that those solvents with a total solubility parameter within a small range of that of the polymer, could initiate spherulitic development.

It should be noted that when comparing spherulites induced by different plasticizers, it would be incorrect to assume that spherulites of similar sizes always contain equal amounts of crystalline polymer (where the chain conformation can be defined by the unit cell). The assumption is based on the idea that the structure of the spherulites is similar. However when comparing the toluene and dichloromethane spherulites this was found not to be the case. It is possible that spherulites with a dense-packed, highly branching structure (toluene) contain more imperfections than the spherulites of dichloromethane, where the structure is dominated by linear (truely crystalline) lamellae regions.

Thus references to a 'crystallization rate' refer to 'spherulitic growth rate', which may be different.

The wide range in spherulite growth rates measured was not wholly unexpected because the solvents used covered a broad spectrum of functionality, polarity, h-bonding, vapour pressure, size and other factors. The exact relationship between the growth rate and the nature of the solvent remains unknown and no definite trends have been established from this study. Some factors that were deemed significant and may influence further

studies are discussed below.

Avrami Analysis

The results from the ln-ln plots used to determine the Avrami exponent (see table 8.3) were important to the understanding of the fundamental growth process involved. The general trend is that regardless of the solvent (perhaps with the exception of acetone), the PC crystallizes in a way predicted by the Avrami model. The model describes growth in one dimension in the form of rods and fibrils with ln-ln plots resulting in a gradient or Avrami exponent (n) of 1. There is a cluster of values around the n=1 mark and a value of n=1.50+/-0.06 for acetone. This later non-integer value cannot be ignored and where similar non-integer values have been reported in the literature, the non-conformity with the Avrami Analysis has been attributed to deficiencies in the Avrami model [Sharples, 1966; Heberer et al, 1991; Lee et al, 1993]. However, the average value was calculated at 0.99+/-0.14, indicating that for most of the plasticizers, there is close agreement with the Avrami Model.

Polarity-vs-Spherulite Size

The results compare the spherulite size obtained as a function of plasticizer to those values reported by Daniewska et al[1986]. Within experimental error, there is general agreement and initially there would seem to be a relationship between the solvent polarity and the spherulite size. Daniewska et al[1986], to explain their results claim that there is an inverse relationship between the mean size of spherulite and the magnitude of δ_P(the polar interaction component of the Hansen solubility parameter).

The results from this study indicate that, when experimental errors in determining the mean diameter are considered, there is not a strong relationship between spherulite size and solvent polarity. For example toluene has a lower δ_P value (of 1.4 $(J\ cm^{-3})^{1/2}$) than chloroform (3.1 $(J\ cm^{-3})^{1/2}$) and yet the spherulites for chloroform are marginally larger (although, taking into account the errors involved, the two are almost the same size).

It should be noted that the ultimate size of the spherulite depends solely on the number of nucleation sites utilized. The use of solvents resulting in

Plasticizer	Growth Rate /nm min^{-1}	Avrami Exponent
Acetone	2965+/-120	0.74+/-0.03
Toluene	1397+/-56	1.50+/-0.06
Ethyl Formate	2924+/-117	1.18+/-0.05
Ethyl Acetate	1439+/-60	0.91+/-0.04
Butyl Acetate	399+/-16	0.86+/-0.03
Dichloromethane	565+/-23	0.92+/-0.04
Chloroform	311+/-12	0.86+/-0.03
Tetrachloromethane	72+/-3	1.00+/-0.04

Table 8.3

This table contains the growth rates and Avrami exponent derived from the early stages of growth of induced spherulites.

large spherulites may merely inhibit the utilization of available heterogeneities, rather than influence the spherulitic development. To gain further insight into the polymer-plasticizer interaction a more productive approach was to study the spherulitic growth rate as a function of plasticizer (before impingement). However, in such a study here, no convincing, direct relationship between the plasticizer polarity and the spherulite growth rate was obtained.

H-Bonding and Crystallization

Daniewska et al also claim that spherulitic development in general, is not induced by solvents with extreme values of δ_H (the H-bond component), and forward evidence that tetrachloromethane, n-hexane and acetic acid do not induce crystallization. The results presented in this study show that although n-hexane does not induce crystallinity (probably because the overall solubility parameter is significantly different from that of PC), tetrachloromethane does. In addition, other studies [for example Cope, 1977; Kashmiri, 1968 and Moore, 1961] all indicate that acetic acid is a good plasticizer.

One explanation for the apparent discrepancy for tetrachloromethane is that at low temperatures (considerably less than 24°C) the rate of spherulitic development is very slow. Other workers [Cope, 1977] note a minimum temperature below which this solvent is not associated with crystallization.

In general however there was no trend observed between the spherulite growth rate and δ_H. Table 8.2 reveals that even solvents with a comparatively low value of δ_H like toluene, exhibits a growth rate greater than for butyl acetate, dichloromethane and chloroform all of which have higher δ_H values.

Other Factors to influence Crystallization

The exact relationship between growth rate and solvent characteristic requires further investigation. This study noted that in general the solvents able to facilitate spherulite growth were those whose solubility parameter was within $3(J\ cm^{-3})^{½}$ of polycarbonate. Those solvents to fall outside this limit like n-hexane were unable to crystallize PC even though other factors like vapour pressure and molecular size are comparable with those of the other solvents

(which were able to induce crystallization). It is assumed that once the solvent has penetrated the film, the most important factor in determining the future spherulite growth is the solubility parameter.

A factors that must be considered when comparing the effects of various platicizers is the vapour pressure. The vapour pressure is a guide to the number of solvent molecules incident on the PC film surface. Cope[1977] noted that by diluting the plasticizer with hexane or other PC non-solvent, the 'activity' of the plasticizer (with respect to spherulite formation) is diminished. As from Roalts law, the partial pressure (or vapour pressure) is proportional to the mole fraction, it follows (from Cope[1977]) that the vapour pressure of the plasticizer is related to its 'activity'.

A comparison of growth rate with vapour pressure figures is given in table 8.4. In this case there is a correlation between the two - as expected from Cope[1977]. In addition an attempt was made at varying the vapour pressure of butyl acetate by raising the solvent temperature by 3°C (see figure 8.20). There was a slight increase in the rate of spherulitic development, indicating that a possible relationship exists. However there are some inconsistencies for example dichloromethane, with the highest vapour pressure has a fairly low growth rate. It is suggested for further work that measurements for the spherulite growth rate are made under a variety of vapour pressures for a range of solvents.

A future study following this work, may start with the concept that a number of competing factors influence the spherulitic growth. Some of these factors are physical, for example vapour pressure and temperature; others are chemical and related to the interaction between polymer and solvent (aptly described by the solubility parameter). A future study involved with elucidating the polymer-solvent interaction would need to address the physical and chemical causes of spherulitic growth. An experiment could eliminate the contribution of the vapour pressure by, for example raising the temperature of the solvent bath (and not the PC sample) to a suitable temperature (for each solvent) such that the vapour pressure for a range of solvents is identical. In this case, comparable numbers of solvent molecules

Plasticizer	Growth Rate /nm min^{-1}	Vapour Pressure /torr
Acetone	2965+/-120	191.0
Toluene	1397+/-56	42.0
Ethyl Formate	2924+/-117	222.0
Ethyl Acetate	1439+/-60	80.0
Butyl Acetate (27.5°C)	443+/-18	21.5
Butyl Acetate (24.5°C)	399+/-16	18.4
Ethyl-n-butyrate	325+/-13	16.0
Dichloromethane	565+/-23	409.0
Chloroform	311+/-12	165.0
Tetrachloromethane	72+/-3	94.0

Table 8.4

This table contains the growth rates and the vapour pressure.

The vapour pressure is derived from the formula $Log_{10} P = (-0.2185A/K) + B$ where the pressure is in torr, the temperature K is in Kelvin and the constants A and B are obtained from the CRC Handbook of Chemistry and Physics.

are incident on the PC surface and a relationship between the growth rate and the nature of the solvent becomes easier to obtain.

8.3 SUMMARY

Nucleation

In general it is assumed that heterogeneous nucleation has a zeroth order dependence on time i.e. all the sites become immediately available for crystallization initiation. It is also assumed that homogeneous nucleation proceeds as a first order function of time, i.e. homogeneous sites become available throughout the amorphous film whilst spherulitic growth continues. Thus from the results detailed above, it can be assumed that there are two competing processes at work.

It is suggested that the nucleation process which dominates in the context of this study is heterogeneous because a) the majority of nucleation sites appear instantly and b) the incidence of spherulitic nucleation is proportional to the number of the artificial sites added.

Plasticizer Effect

It was found that the spherulite size and structure, observed as a function of different plasticizers varied according to the type of solvent used. It was also found that solvents with a solubility parameter over $3(J\ cm^{-3})^{½}$ from that of Polycarbonate did not produce any crystalline features. The spherulite internal structure, including the angle and frequency of branching was highly solvent dependent. The lowest incidence of branching was observed with the chlorinated plasticizers (chloroform and dichloromethane) whereas larger angle and more frequent branching was observed with acetone and toluene.

It was also found that the spherulite growth rates were also dependent on the type of plasticizer used and some factors relating to the growth rate such as the vapour pressure and the three component Hansen Solubility Parameter were discussed. Initial results suggest that small increases in vapour pressure can result in a measurable increase in the growth rate and

future work may be able to establish a significant relationship.

The Avrami exponent was derived for each of the growth curves obtained and found to be n=0.99+/-0.14. It was found that, within experimental error, the spherulitic growth, in each case (except acetone), conformed to the Avrami model for the formation of rods and fibrils (i.e. n=1).

CHAPTER 9

CONCLUSIONS

9.0 SUMMARY & CONCLUSIONS

9.1 THESIS AIMS

The study aimed systematically to investigate the morphology, uniformity, coverage and structure of the thin films of insulating polymers by STM and AFM. The interpretation of the STM images was investigated and resulting structural features discussed. The study continued using both STM and AFM as complementary techniques firstly to resolve details in the polymer film. The study advanced to a stage where it was possible to elucidate and confirm complex structural entities within PMMA and PVP films.

The initial study (stage 1) culminated with the observation by STM alone of the solvent induced crystalline features in a PC thin film sample. The dimensions and characteristics of the ordered phase were found to be distinctly different from both the amorphous PC film and the other amorphous polymers studied.

The study continued (stage 2) with the imaging by AFM of the growth of crystalline entities in a PC film, without the need for harsh sample treatment or metal coating. A method of casting and crystallizing the films was developed such that the growth was predominantly in two dimensions and consequently ideal for observation by AFM. Different stages of crystalline growth were observed, starting with pre-spherulitic material and finishing with fully developed spherulites.

The shape, size and structure of the spherulites was assessed and additionally the constituent lamellae units were imaged. The latter were found to be structurally very similar to the features observed in the study using STM.

In addition a further and future work section enabled the nucleation of the PC spherulites to be assessed in terms of homogeneous and heterogeneous nucleation processes. The study finished with the kinetic and morphological study of the effect on the PC film of a variety of chemically different plasticizers (including butyl acetate). The structure, size and shape of the spherulites as a function of plasticizer was assessed.

9.2 STAGE 1

Substrate

The STM was used to image substrates formed under a variety of different conditions. The pre-requisite salient features of a substrate were defined by Dietz & Herrmann[1990]. They are that the substrate must be flat on the scale of the sample, chemically inert, mechanically stable and able to form reasonable adhesion to the polymer. In addition, for STM studies the substrate needs to be conducting. The substrates investigated by STM were HOPG (graphite) and gold (evaporated onto a very flat surface).

It was found that HOPG fulfilled the criteria for the ideal substrate given by Dietz & Herrmann[1990] (although some mechanical instability and sample adhesion problems were encountered). However this substrate displayed a variety of defects that may lead to confusion between the polymer and substrate features. The type of defects identified in this study were flakes of graphite, linear features, fish-net features and tip induced effects.

It was found that the substrate formed from the vacuum evaporation of gold on to a highly polished silicon wafer or freshly cleaved mica also fulfilled the criteria given by Dietz & Herrmann. It was noted that although the surface included large undulating gold grains, these could aid image interpretation by forming a characteristic underlayer clearly visible in subsequent line scans. The sample adhesion was found to be sufficient for the requirements of this study.

For the purposes of this study, the gold substrate was used most often because confusing defects were never encountered. HOPG was only used as a substrate where no confusion existed between the polymer and graphite surface detail.

The Presence of the Polymer Film

Polymer material was deposited on the substrates in a well defined way. It was found that by changing the concentration of the polymer solution, films of varying thickness were achieved. The next stage of the study was to

identify characteristics of possible regions of polymer film by the STM. A film was deposited such that the substrate was exposed through the film. A line scan taken through the film and including both polymer and bare substrate regions revealed that highly increased amplitude in the scan fluctuations occurred over the polymer region. The fluctuations were not necessarily due to noise and were more likely caused by a varying conduction mechanism [Garcia & Garcia, 1990].

Film Uniformity and Structure

Two polymers PMMA and PVP were imaged by STM on both HOPG and gold substrates. Line scans were used to cross-section the image and the increased fluctuation in the amplitude of the scans observed over those areas of the image associated with the polymer. AFM images of the films were also achieved and compared with the STM images.

It was found that PMMA formed an even film across the gold surface, with the gold grains being covered by polymer material. The AFM and the STM images are consistent in estimations of the film thickness (both techniques show that gold grains are visible in the presence of the polymer). The line scans taken by the STM contain components of the substrate (slowly undulating grains) and fluctuations due to the polymer. The even coating of the substrate by the polymer was expected because of the polarity of the solvent.

The PVP film was found to be very different from that formed by PMMA, in that large areas of the STM image were dominated by the underlying substrate. Line scans were taken that show an increase in amplitude of the fluctuations in the trace over the PVP area. AFM images confirmed the STM results with respect to the coverage of the film, the uneven film coating was attributed to the incompatibility of the hygroscopic sample with the hydrophobic substrate.

Environmental Influences

The PMMA sample was imaged in a specially developed 'environmental' chamber containing the STM. The humidity level were varied and it was

found that the best images were achieved when the humidity of the chamber was high (R.H. >50%). Images of the polymer under low humidity regimes were very difficult to interpret and marred by significant tip-polymer contact. It was deduced that water played an important part in the conduction mechanism responsible for image construction. This is a view supported by the literature[Leggett, 1992].

Polycarbonate (PC) films were also subjected to a change in environment. The film was imaged by the STM in a moist atmosphere and then subjected to the vapours of a suitable plasticizing agent. The initial film was found to be 60%-80% amorphous. However the remainder of the film contained small ordered regions only several tens of nanometres in size. The ordered regions in the 'amorphous' PC film have never been imaged microscopically before but are well documented [Schnell, 1964] in the light of diffraction experiments [Prietzschk, 1958].

After exposure to the plasticizing vapour, the film was imaged by STM and a significant morphological change in the image was noted. The image was dominated by elongated regions, parallel to each other that were approximately 25nm wide and several hundred nanometres long. The rods or lamellae units observed contain the folded PC chains and form the building blocks of all further crystalline development.

The success of the imaging of polymer films by STM is very important. This study shows that the STM can reveal subtle changes in the polymer morphology. The crystallization of PC results in the ordering of the polymeric material and most probably of conduction sites and pathways utilized by the STM conduction mechanism. Thus the STM can image samples such as PC lamellae that are too thin and unstable to image directly (or bare) with electron microscopy. This study demonstrates the feasibility of the STM as a viable method for further experimental study on this type of material, despite the poorly electrical conducting nature of the sample.

9.3 STAGE 2

The crystallization of polycarbonates is a technologically important process as it can cause sudden and catastrophic failure of this class of materials in industrial applications. The growth of the crystalline regions is still not well understood but this study shows how the AFM was used in conjunction with the solvent induced crystallization process to chart the development of crystalline entities.

The Crystallization Process

To crystallize polymers in general it is necessary to supply the relevant initial 'activation' energy by heating the film. This process is unsatisfactory for PC because of the high viscosity of the sample and of degradation processes associated with this polymer at elevated temperatures. However working with methods developed by Cope[1977], appropriate solvent (plasticizer doping) treatment of the PC film resulted in rapid and extensive crystallization. Unlike Cope[1977] (who utilized the SEM of thick and metal coated samples), this study used bare samples (imaged by AFM) thus enabling an individual sample to be treated and imaged many times. At each stage of the stringently controlled growth process, the film was imaged and its morphology assessed.

Growth Observed

The PC film was exposed to the plasticizing agent and a variety of morphological features were observed. The initial plasticizer treatment resulted in an increase in density of the PC film (although no crystalline entities were observed). The increase in density was attributed to the formation of an initial crystalline phase containing many small crystalline regions dispersed in an amorphous matrix.

Continued plasticizer exposure (doping) resulted in a successive hierarchy of pre-spherulitic entities including rods and 'wheatsheaf' formations. The rods contained parallel bundles of elongated material of the same dimensions as the lamellae units observed by the STM.

Spherulitic development was observed and the branching of the constituent fibrils to form two dimensional disks noted. The area of a crystalline region was assessed as a function of doping time (t). It was found that the area of the disk increased as a function of t^2, which is in agreement with the kinetic studies of polymer crystallization forwarded by Avrami (see Sharples[1966]). Because the polymer is observed to behave in a way that is predicted from first principles calculations, the AFM can be used as reliable tool for comparative kinetic studies in polymer crystallization.

As the growth continued, the area-vs-time curve was found to move through a turning point and eventually reach a maximum area value. This was observed, *in-situ* as the point of impingement of the spherulites (turning point on the graph). The spherulite continued to assimilate the amorphous material until total impingement occurred (giving a maximum spherulite area).

High magnification studies of the spherulite-dominated film by the AFM show that the fibrils contained smaller constituent parts and a sharing of polymer material between neighbouring spherulites). However the AFM operating in the contact mode results in significant tip-sample interaction on this small scale, limiting the resolution. The poor resolution is improved however by the use of the tapping mode AFM (TMAFM) which is less damaging to the sample. The TMAFM images show the lamellae units, lying approximately parallel to each other and longitudinally orientated in the direction of the nucleation site. The lamellae units were of the same approximate size as those observed by the STM.

9.4 FURTHER AND FUTURE WORK

Nucleation

The nucleation process that initiates the spherulite growth was still unknown. However, work completed in this study shows that the process is likely to be influenced by heterogeneous nucleation. A substrate was deliberately covered in small spherical particles or 'seeds' (86nm in diameter). The incidence of

nucleation was found to be directly proportional to the number of particles present. In addition small islands of PC were formed and exposed to the plasticizing vapour. It was found that the incidence of nucleation was very low and even after a time period associated with a high degree of spherulitic development, some islands remained uncrystallized. The evidence suggests that heterogeneous nucleation and not homogeneous nucleation is the dominant nucleation process.

The effect of other plasticizers.

A wide range of chemically different plasticizers was then used to induce crystallization in the PC film. Detailed high resolution images by the AFM in both the contact and tapping modes revealed that the spherulite size, shape and structure was highly plasticizer dependent. It was noted that the ultimate spherulite size is related to the number of nucleation sites utilized in the presence of the plasticizer. The shape, fibril structure and growth rate of the spherulite was dependent on the chemical nature of the plasticizer. Although no clear relationship between any individual solvent parameter and the growth rate was found, a discussion on the topic revealed some important factors involved.

The Avrami analysis of the growth rates confirmed that the Avrami exponent was approximately 1 (0.99 +/- 0.14), regardless of the plasticizer used (with the exception of acetone). This exponent value corresponded to linear growth of the fibrils as a function of time.

The further results confirmed, using a novel experimental method, that the AFM was a viable tool for obtaining both high resolution morphological data and kinetic data.

Future Work

The effect of the various plasticizers on the PC film was noted. However it was not possible to explain, unambiguously, why the spherulite growth rate for one plasticizer was significantly different from another. It was noted that both the vapour pressure and the three component Hansen solubility

parameter were important and future work could assess these separately.

9.5 CONCLUSION

This study shows how polymer films can be imaged by both STM and AFM. Despite the poorly conducting nature of the polymer sample, detailed and convincing images of this class of materials were achieved by STM. The initial study involved the successful imaging and characterization of the difference in morphology before and after the crystallization of polycarbonate. The 'amorphous' PC film was observed to contain small ordered regions in roughly the same proportion as that predicted by diffraction studies[Prietschk, 1959 & Schnell, 1964], this has never been observed by a microscopy technique. Furthermore, images of the crystalline film contained elongated lamellae units that form the basic building blocks of polymer spherulites.

Thus the STM can be used to study thin polymer films and to deduce the morphology therein. Possible studies include the assessment of film uniformity, coverage and structure.

The AFM was used to observe the morphology of the spherulites formed as a result of the solvent induced crystallization of polycarbonate. The spherulites were grown and imaged successfully in many stages, giving a broad insight into the crystallization process at a resolution unobtainable by most other microscopy techniques. The process developed in this study allowed the rate of growth, in addition to the size and structure of the spherulites within the two dimensional film to be assessed for a range of chemically different plasticizers.

The lamellae units were found to be the smallest resolvable feature in the film and at all times the AFM, TMAFM and STM images were in agreement with each other.

REFERENCES AND BIBLIOGRAPHY

REFERENCES AND BIBLIOGRAPHY

A

Abraham, F.F; Batra, I.P; 'A theoretical interpretation of AFM images of graphite; Surface Science; Vol. 209; L125; 1989.

Adzic, R.R; Hsiao, M.W; Yeager, E.B; 'STM of stepped single crystal surfaces of gold'; Surface Science Letts; 273; L425-L429; 1992.

Agrait, N; Rodrigo, J.G; Vieria, S; 'On the transition from point-contact: graphite'; Ultramicroscopy; 42-44(A); pp177-183; 1992.

Agrawal, C.M; Hunter, K; Pearsall, G.W; Henkens, R.W; 'Application of STM to the study of fracture morphology of polycarbonate'; J.Mater. Sci; Vol 27; pp2606-2612; 1992.

Albrecht, T.R; Dovek, M.M; Lang C.A; Grutter, P; Quate, C.F; Kuan, S.W.J; Frank, C.W; Pease, R.F.W; 'Imaging and modification of polymers by scanning tunnelling and atomic force microscopy'; Journal of Applied Physics; 64(3); pp1178-1184; 1988.

Albrecht, T.R; Quate, C.F; 'Atomic resolution imaging of a non-conductor by atomic force microscopy'; Journal of Applied Physics; Vol. 62; pp2599; 1987.

Allen, M.J; Balooch, M; Subbiah, S; Tench, R.J; Siekhaus, W; Balhorn, R; 'Scanning tunnelling microscopy images of adenine and thymine at atomic resolution'; Scanning Microscopy; Vol. 5; No. 3; pp625-630; 1991.

Allen, M.J; Balhorn, R; Balooch, M; Siekhaus, W.J; Tench, R.J; Subbiah, S; 'Progress in DNA-imaging: Double-stranded multimers and bases of DNA deposited on the basel plane of graphite'; AIP Conf. Proc. #241; pp176-189; 1992.

Allen, M.J; Hud, N.V; Balooch, M; Tench, R.J; Siekhaus, W.J; Balhorn, R; 'Tip-radius-induced artifacts in AFM images of protamine-complexed DNA fibres'; Ultramicroscopy (B); Vol. 42-44; pp1095-1100; 1992.

Allen, M.J; Balooch, M; Subbiah, S; Tench, R.J; Balhorn, R; Siekhaus, W; 'Analysis of adenine and thymine adsorbed on graphite by scanning tunnelling and atomic force microscopy'; Ultramicroscopy (B); Vol. 42-44; pp1049-1053; 1992.

Allenspach, R.; Salemink, H; Bischof, A; Weibsel, E; 'Tunnelling experiments involving magnetic tip and magnetic sample'; Z. Phys. B; Vol.67; pp587; 1989.

Alves, C.A; Smith E.L; Porter M.D;`Atomic Scale Imaging of Alkanethiolate Monolayers at Gold Surfaces with Atomic Force Microscopy'; J.Am.Chem.Soc; 114; pp1222-1227; 1992.

Arscott, P.G; Bloomfield, V.A; 'STM of DNA and RNA'; Chapter 6 in 'STM & SFM in Biology; Acad. Press Inc.; pp259-272; 1993.

Avouris, Ph; Lyo, I.W; 'Probing the chemistry and manipulating surfaces at the atomic scale with the STM'; Applied Surf. Scvi.; Vol.60/61; pp426-436; 1992.

B

Bai, C; Wang, D; Gu, J; Dai, C; Jia, Y; Gong, L; Lu, C; 'STM barrier height images and topographic images of denaturted DNA'; Nanobiology; 2; pp55-63; 1993.

Bai, C; Zhu, C; Huang, G; Yang, J; Wan, M; Chen, R; 'Scanning microscopic imaging of doped polyaniline'; Ultramicroscopy (B); Vol. 42-44; pp1079-1082; 1992.

Bardeen, J.; Physics Review Letters; 6; p57; 1961.

Bashkin, M.O; Bespalour, V.A; Emelyanov, A.V; Inkin; Portnov, S.M; Zimin, A.V; Kharkevich, S.I; Menshikov, O.D; 'Surface modification of organic films deposited on graphite by the scanning tunnelling microscope'; Ultramicroscopy (B); Vol.42-44; pp977-982; 1992.

Best, M.E; Prime, R.B; 'Characterization and control of cure of polymer coatings on optical disks'; SPIE vol.1774; pp169; 1992.

Bianco, B; Bonfiglio, A; Cambiaso, A; Vavelleri, O; 'Molecular monolayer structure investigations by STM'; Mol.Cryst.Liq.Cryst.; Vol.235; pp109-114; 1993.

Binh, V.T; Garcia, N; 'On the electron and mettalic ion emission from nanotips fabricated by field-surface-melting technique: experiments on W and Au-tips'; Ultramicroscopy (A); vol.42-44; pp80-90; 1992.

Binnig, G; 'Force Microscopy'; Ultramicroscopy (A); Vol. 42-44; pp7-15; 1992.

Binnig, G; Rohrer, H; Gerber, Ch; Weibel, E; Physics Review Letters; 49; p57; 1982.

Binnig, G; Quate, C.F and Gerber, Ch, 'Atomic Force Microscope'; Phys. Rev. Lett. Vol. 56; p930; 1986.

Binnig, G; Gerber, Ch.; Stoll, E; Albrecht, T.R and Quate, C.F; 'Atomic Resolution with atomic force microscopy'; Europhys. Lett; Vol. 3; p1281; 1987

Blackford, B.L; Jericho, M.H; Mulhern P.J; `A Review of Sanning Tunnelling Microscope and Atomic Force Microscope Imaging of Large Biological Structures: Problems and Prospects'; Scanning Microscopy; Vol.5 No.4; pp907-918; 1991.

Bloomfield, V.A; Arscott, P.G; 'Scanning tunnelling microscopy of nucleic acids'; Nucleic Acids and Molecular Biology; Vol.5; (Ed. Eckstein, F & Lilley, D.M.J); Springer-Verlag; Berlin; pp39-53; 1991.

Bonnell, D.A; Angelopoulos, M; 'Spatially localized electronic structure in polyaniline by STM'; Synthetic Metals; Vol.33; pp301-310; 1989.

Bosbach, D; Rammensee, W; 'Surface manipulation on layered organic crystals by scanning force microscopy'; Ultramicroscopy (B); pp976; 1992.

Bottomley, L.A; Jones, J.A; Ding, Y; Allison, D.P; Thundat, T; Warmack, R.J; 'STM imaging of electrostatically immobilized nucleic acids. The influence of self-assembled monolayer structure on the binding of plasmid DNA to gold surfaces'; SPIE Vol.1891; 'Advances in DNA Sequencing Technology'; pp48-55; 1993.

Brandrup, J and Immergut, E.H (Eds.); Solubility Parameter Values; Chapter VII/519-559, in Polymer Handbook; Wiley Interscience; New York; 1989 (ISBN 0-471-81244-7).

Brown, N.M.D; You, H-X;`A scanning tunnelling microscopy study of PAN-based carbon fibre in air.'; Surface Science; 237; pp273-279; 1990.

Bu, H; Chen, E; Yao, J; Xu, S; Kuang, Y; 'Scanning tunnelling microscopy studies of single-molecule single-crystals'; Polymer Engineering & Science; Vol.32; no.17; pp1202-1212; 1992.

Buckley, C.P; Kovacs, A.J; 'Chain-folding in polymer crystals: evidence from microscopy and calorimetry of poly(ethylene oxide)' in Structure of Crystalline Polymers; Ed. Hall, I.H; Elsevier Applied Science Publishers; London & New York; ISBN 0-85334-236-9; Chapter 7; pp261-301; 1984.

Burkinshaw, L.D; Caird, D.W; 'Polycarbonates' in The Science and Technology of Polymer Films; Ed. Sweeting, O.J; Wiley-Interscience; J.Wiley & Sons, Inc. ISBN 0-471-83894-2; Chapter 11; pp459-486; 1971.

Burnham, N. A.; Colton, R.J.; Pollock, H.M; 'Interpretation issues in force microscopy.'; J.V.S.T: A; Vol. 9; No. 4; pp2548-2555.

Burnham, N.A; Colton, R.J; Pollock, H.M; 'Interpretation of force curves in force microscopy'; Nanotechnology; Vol. 4; pp64-80; 1993.

Caple, G; Wheeler, B.L; Swift, R; Porter, T.L; Jeffers, S; 'Scanning Tunnelling Microscopy of Polythiophene, Poly(3-Methylthiophene), and Poly(3-Bromothiophene)'; J.Phys.Chem; Vol. 94; pp5639-5641; 1990.

Casero, R; Serena, P.A; Garcia, N; 'Large enhancement of transmission probability in non-equilibrium time evolution quatum mechanics'; Ultramicroscopy (A); Vol.42-44; pp134-139; 1992.

Chen, C.J; '*In-situ* characterization of tip electronic structure in scanning tunnelling microscopy'; Ultramicroscopy (A); Vol. 42-44; pp147-153; 1992.

Chen, C.J; 'Introduction to Scanning Tunnelling Microscopy'; Oxford Series in Optical and Imaging Sciences; Eds. Lapp, M. et al; Oxford Univerity Press; New York and Oxford; ISBN 0-19-507150-6; 412 pages; 1993.

Chen, Y; Xu, W; Huang, J; 'A simple new technique for preparing STM tips'; J. Phys. E: Sci. Instrum.; Vol.22; pp455-457; 1989.

Chiang, S;' Molecular imaging by STM'; Springer Series in Surface Sciences; Vol. 20; Scanning Tunnelling Microscopy I (Ed. Guntherodt); pp181-205; 1992.

Cho, K; Joannopoulos, J.D; 'Tip-surface interactions in STM'; Phys. Rev. Letts; Vol.71; No.9; pp1387-1390; 1993.

Ciraci, S; Tekmann, E; Gokcedag, M; Batra, I; Baratoff; 'Adhesive energy: force & barrier height between simple metal surfaces'; Ultramicroscopy (A); Vol.42-44; pp163-168; 1992.

Ciraci, S; 'Atomic-scale tip-sample interactions and contact phenomena'; Ultramicroscopy (A); pp16-21; 1992.

Clemmer, C.R; Beebe, T.P.Jr; 'A Review of Graphite and Gold Surfaces Studies for use as Substrates in Biological Scanning Tunnelling Microscopy Studies.; Scanning Microscopy; Vol.6; No.2; pp319-333; 1992.

Cohen, M.H and Turnbull, D; Journal of Chemistry Physics; Vol. 31; pp1164; 1959.

Cohen, M.H and Turnabull, D; Journal of Chemistry Physics; Vol. 34; pp120; 1961.

Cohen, S.R; 'An evaluation of the use of the AFM for studies in nanomechanics'; Ultramicroscopy (A); pp66-72; 1992.

Conix, A.J and Jeurissen, L.G; Adv. Chem Ser; No. 48; pp172; 1965

Cormia, Price and Turnbull as cited in Sharples [1966]

Cope, B.C; 'Crystallization and crazing in Polycarbonates'; Ph.D thesis CNAA; Leicester Polytechnic; 1977.

Cotterill, G.F; Fergusson, J.A.E; Gani, J.S; Burns, G.F; 'STM of callogen I reveals filament bundles to be arranged in a left-handed helix'; Biochem. & Biophys. Res. Comm.; Vol. 194; No.2; pp973-977; 1993.

Cowie, J;'Chemistry and Physics of Modern Materials'; 2nd Edition; John Wiley & Sons; New York; 1992.

Creager, S.E; 'STM Imaging and Electronic Conductivity Mechanisms in Oxidatively Doped Poly(N-Methylpyrrole) Thin Films'; J.Phys.Chem; Vol. 96; pp2371-2375; 1992.

Cricenti, A; Selci, S; Chiarotti, G; Amaldi, F; 'Imaging of Single-Stranded DNA'; AIP Conf. Proc. #241; AIP Publishers; New York; 1992.

D

Dahn, D.C; Cake, K; Hale, L.R; 'STM of unbroken chloroplasts'; Ultramicroscopy (B); Vol.42-44; pp1222-1227; 1992.

Daniewska, I; Kocinska, E; Dobkowski, Z; 'Morphology of polycarbonate crystallized under the influence of solvent vapours'; Morphology of Polymers; pp449-456; 1986.

Daw, M.S and Baskes, M.I; 'Embedded-Atom method: Derivation and application to impurities, surfaces, and other defects in metals'; Phys. Rev. B; Vol.29; p6443; 1984.

Debye, P.J.W; Phys. Z; Vol.21; pp178; 1920.

Delaine, E; Fourcade, A; Poulin, J.C; Barbin, A; Couloud, D; Cam, E.L; Paris, E; 'Comparitive observations of biological specimens, especially DNA and filamentous actin molecules in atomic force, tunnelling & electron microscopes'; Microsc. Microanal. Microstruct.; Vol.3 pp457-470; 1992.

Demuth, J.E; Hamers, R.J; Tromp, R.M.; 'Spectroscoping imaging of surfaces with atomic resolution'; Solvay (Pringer Series on Surface Science); Vol.14, pp236-243; 1988.

Derjaguin, B.V; Muller, V.M and Toporov, Yu.P; 'Effect of contact deformations on the adhesion of particles'; J. Coll. Interface. Sci.; Vol. 53; p314; 1975.

Diemann, E; Brandig, A; Muller, A; 'Towards the localization of metal clusters in proteins via molecular conductivity'; Naturwissenschaften; Vol. 79; pp267; 1992.

Dietz, P; Herrmann, K.H; 'Scanning Tunnelling Microscopy of Thin Organic Films on Conducting Substrates'; Surface Science; Vol.232; pp339-345; 1990.

Duke, C.B; 'Tunnelling in Solids'; New York; Academic Press; 1969

Dzyaloshinskii, I.E; Lifshitz, E.M; Pitaevskii; ' The general theory of van der Waals forces'; Adv. Phys; Vol. 10; pp165; 1961.

E

Ehara, S; Takagi, T; Yoshida, Y; Inabe, H; Naito, H; Okuda, M;' Negative resistance in an organic thin film'; Modern Physics Letters; B; Vol.6; No.19; pp1205-1207; 1992.

Emch, R; Zenhausen, F; Jobin, M; Taborelli, M; Descoutes, P; 'Morphological differences between fibronecti sprayed on mica and on PMMA'; Ultramicroscopy (B); Vol.42-44; pp1155-1160; 1992.

Emch, R; Nogami, J; Dovek, M.M; Lang, C.A; Quate, C.F; 'Characterization of Gold Surfaces for use as Substrates in Scanning Tunnelling Microscopy Studies'; J.Appl.Phys; Vol.65; No.1; pp79-84, 1989.

Eng, L.M; Fuchs, H; Bucholtz, S; Rabe, J.P; 'Ordering of didodecylbenzene on graphite: a combined SFM/STM study'; Ultramicroscopy (B); Vol.42-44; pp1059-1066; 1992.

Eng, L.M; Fuchs, H; Jandt, K.D; Petermann, J; 'Investigating poly(1-butene) films by STM/SFM'; Ultramicroscopy (B); Vol.42-44; pp989-997; 1992.

Everson, M.P; Helms, J.H; 'A Scanning Tunnelling Microscope Study of the Electrochemical Polymerization of Perchlorate-Doped Polypyrrole on Highly Orientated Pyrolytic Graphite'; Synthetic Metals; Vol. 40; pp97-109; 1991.

F

Feenstra, R.M; 'Scanning Tunnelling Microscopy: Semiconductor Surfaces, Adsorption, and Epitaxy'; Scanning Tunnelling Microscopy and Related Methods; Ed. Behm,R.J et al; Kluwer Academic Publishers; Netherlands; pp211-240; 1990.

Fischer, U.Ch; Durig, U.T; Pohl, D.W; Applied Physics Letters; Vol. 52; pp249.

Fisher, A.J; Blochl, P.E; 'Adsorption and scanning tunnelling microscope imaging of benzene on graphite and MoS_2'; Phys. Rev. Letts.; Vol.70; No.21; pp3263-3266; 1993.

Fotino, M; 'Nanotips by Reverse Electrochemical Etching'; Appl. Phys. Lett; Vol.60; No.23; pp2935-2937; 1992.

Forbes, R.G; 'What do we mean by "workfunction"; Scanning Tunnelling Microscopy and Related Methods; Ed. Behm,R.J et al; Kluwer Academic Publishers; Netherlands; pp163-172; 1990.

Fowler, R.H and Nordheim, L W; Proceedings of the Royal Society; Vol. A119; pp173; 1928

Frank, W; Goddar, H; Stuart, H.A.; Journal of Polymer Science (B); Vol. 5; pp711; 1967.

Franke, F; Keller, D; 'Towards high resolution imaging of DNA'; SPIE Vol.1891 - Advances in DNA Sequencing Technology; pp78-84; 1993.

Frenkl, J; Physics Review; Vol. 54; pp647; 1938.

Fuchs, H; Schimmel, Th; Lux-steiner, M; Bucher, E; 'Investigating atomic-scale structures generated with the STM'; Ultramicroscopy (B); Vol.42-44; pp 1295-1302; 1992.

Fuchs, H; Schimmel, Th.; 'Time-stable modifications of bare surfaces on an atomic scale'; Conf. Proc. #241; pp480-489; 1991.

G

Garbarz, J; Lacaze, E; 'Dislocation networks in graphite: Am STM study'; Philosophical Magazine (A): Vol.65; No.4; pp853-861; 1992.

Garcia, R; Yuqui, R; Schabtach, E; Bustamante, C; 'Deposition and imaging of metalcoated biomolecules with the STM'; Ultramicroscopy (B); Vol.42-44; pp1250-1254; 1992.

Garcia, R; Garcia, N; 'Electron Transport in Disordered Organic Chains'; Scanning Tunnelling Microscopy and Related Methods; Ed. Behm,R.J et al; Kluwer Academic Publishers; Netherlands; pp391-398; 1990

Garcia, R; Jiang, Y; Dunlap, D; Bustamante, C; 'Scanning Tunnelling Microscopy of Metal-Coated Biomolecules'; SPIE vol 1639 (Scanning Probe Microscopies); Vol.1639; pp119-126, 1992

Garcia, R; 'Atomic-scale manipulation in air with the STM'; Appl.Phys.Letts; Vol.60; No.12; pp1960-1962; 1992.

Gata, M.A; Antoniewicz, P.R; 'Resonant tunnelling through adsorbates in scanning tunnelling microscopy'; Phys.Rev.B; Vol.47; No.20; pp797-807; 1992.

Gautier, F; Ness, H; Stoeffler, D; 'Electronic structure of transition metal tips and tip-surface interactions'; Ultramicroscopy (A); Vol.42-44; pp91-96; 1992.

Gimzewski, J.K; Stoll, E; Schlitter, R.R; Surface Science; Vol. 181; pp267; 1987.

Gobel, H.D; Horber, J.K.H; Gerber, Ch.; Leitner, A; Hansch, T.W; Molecular structures of lipid monolayers on ITO glass and on graphite imaged by an STM'; Ultramicroscopy (B); Vol. 42-44; pp1260-1268; 1992.

Goddard, D.T; Weaver, W; Harron, H.R; Steele, A; 'Imaging soft and delicate materials'; Microscopy and Analysis; Materials World; Vol. 96; pp616-618; 1993.

Golubok, A.O; Vinogradura, S.A; Tipisev, S.Y; Bonisev, A.Y; Taisova, A.S; 'STM/STS study of photosynthetic bascterial membrane'; Ultramicroscopy (B); Vol. 42-44; pp1228-1235; 1992.

Gomez-Rodriguez, J.M; Aserjo, A; Salvarezza, R.C; Baro, A.M; 'Measuring the fractal dimension with STM: application to vacuum-evaporated gold'; Ultramicroscopy (B); Vol.42-44; pp1321-1328; 1992.

Grafstrom, S; Pobst, O; Dey, S; 'STM studies on dye molecules embedded in ordered liquid crystal structures and an approach for LASER assisted STM'; SPIE Vol.1891 - Advances in DNA Sequencing Techology; pp56-65; 1993.

Gutowski, W; 'Thermodynamics of Adhesion' in 'Fundamentals of Adhesion' Ed. Lee, L-H; pp87-136; Plenum Press; New York; 1991.

H

Haberle, W; Horber, J.K.H; Ohnesorge, F; Smith, D.P.E; Binnig, G; '*In-situ* investigations of single living cells infected by viruses'; Ultramicroscopy (B); Vol. 42-44; pp1161-1167; 1992.

Haggerty, L; Lenhoff, A.M; 'STM and AFM in Biotechnology'; Biotechnol. Prog; Vol.9; pp1-11; 1993.

Hallmark, V.M; Chiang, S; Meinhardt, K.P; Hafner, K; 'Observation & Calculation of internal structure in STM images of related molecules'; Phys. Rev. Letts; Vol.70; No.24; pp3740-3734; 1993.

Hallmark, V.M; Chiang, S; Brown, J.K; Woll, Ch.; 'How well can the STM distinguish between two very similar molecules'; Synthetic Microstructures in Biological Research; Eds. Schnur, J.M & Peckeror, M; Plenum Press; NY; pp79-90; 1992.

Hamada, E; Kaneko, R; 'Micro-tribological evaluations of a polymer surface by atomic force mocroscopies'; Ultramicroscopy (A); Vol. 42-44; pp184-190; 1992.

Hamaker, H.C; Physica 4; pp1058; 1937.

Hamers, R.J; 'Fundamentals and applications of Scanning Tunnelling Microscopy: a short course'; Materials Research Society; New York; 1990.

Hanrieder, W; Mock, R; Meixner, H; 'The whip-motion of ultra-thin tunnelling tips'; Ultramicroscopy (A); Vol.42-44; pp169-176; 1992.

Hansen, C.M.; J. Paint Technology.; Vol. 39; No. 505; pp104; 1967 (as cited in Brandrup and Immurgut, 1989)

Hansma, H.G; Sinsheimer, R.L; Gould, S.A.C; Weisenhorn, A.L; Gaub, H.E; Hansma, P.K; 'Towards sequencing DNA with an AFM'; AIP Conf. Proc. #241; pp136-143; 1992.

Hara, M; Sasabe, H; 'Organic MBE and organic STM "Nanoscopic' molecular systems'; Mol. Cryst. Liq. Cryst.; Vol.217; pp207-209; 1992.

Harron, H.R; Pritchard, R.G; Cope, B.C.; Goddard, D.T; 'An atomic force microscopy study of the solvent induced crystallization of polycarbonate thin films'; Journal of Polymer Science; Part B - to be published.

Hartmann, U; 'Intermolecular and surface forces in noncontact scanning force microscopy'; Ultramicroscopy (A); pp59-69; 1992.

Hawley, M.E; Benicemicz, B.C; 'Structural study of a wholly aromatic polyamide with a rigid pendent group by scanning tunnelling microscopy'; J.V.S.T (B); Vol. 9; No. 2; pp1141-1147; 1991.

Heckl, W.M; Binnig, G; 'Domain walls on graphite mimic DNA'; Ultramicroscopy (B); Vol.42-44; pp1073-1078; 1992.

Heinzelmann, H.; Meyer, E; Rudin, H.; Guntherodt, H.J; 'Force Microscopy'; Scanning Tunnelling Microscopy and Related Methods; Ed. Behm,R.J et al; Kluwer Academic Publishers; Netherlands; pp163-172; 1990.

Hentschke, R; Schurmann, B.L; Rabe, J.P; 'Molecular Dynamics Simulations of Ordered Alkane Chains Physisorbed on Graphite'; J.Phys.Chem; Vol.96; No.8; pp6213-6221; 1992.

Hiesgen, R; Meissner, D; 'Problems of roughness measurements using STM'; Ultramicroscopy (B); Vol. 42-44; pp1403-1411; 1992.

Hietschold, M; Sbosny, H; 'Simple model for the topographic imaging process in a scanning tunnelling microscope'; Ultramicroscopy (A); Vol.42-44; pp200-205; 1992.

Horber, J.K.H; Schuler, F.M; Witzemann, V; Muller, H; Ruppersberg, J.P; 'Imaging Biological Membrane Structures with a Scanning Tunnelling Microscope'; AIP Conf. Proc #241; New York; pp209-218; 1992

Hu, J; Gu, M; Zhang, L; Xu, Y; 'STM studies of uncovered SiO_2 nanometre-particles'; Ultramicroscopy (B); Vol.42-44; pp1394-1397; 1992.

Hu, J; Gu, M; Wang, Z; Yao, X; Xu, Y; Zhang, L; Huang, Z; Zhu, J; Li, M; 'Multiple tip effects on STM images of DNA'; Jpn. J. Appl. Physics; Vol. 31; Part 1; No.1; 1992.

I & J

Israelachvilli, J.N; Intermolecular and Surface Forces; Academic Press, New York; 1985.

Jahanmir, J; Haggar, B.G; Hayes, J.B; 'The scanning probe microscope'; Scanning Microscopy; Vol. 6; No. 3; pp625-660; 1992.

Jandt, K.D; Eng, L.M; Petermann, J; Fuchs, H; 'Scanning force microscopy of nanostructured uniaxially orientated ultra thin film surfaces of isotactic polystyrene'; Polymer; Vol.33; No.24; pp5331-5333; 1992.

Jin, X; Unertl, W.N; 'Submicrometre modification of polymer surfaces with a surface force microscope'; Appl. Phys. Lett; Vol.61; No.6; pp657-659; 1992.

Joachim, C; Sautet, P; 'Electron Tunnelling Through a Molecule'; Scanning Tunnelling Microscopy and Related Methods; Ed. Behm,R.J et al; Kluwer Academic Publishers; Netherlands; pp377-389; 1990

Jungblut, H; Campbell, S.A; Giersig, M; Muller, D.J; Lewerenze, H.J; 'STM observations of biomolecules on layered materials'; Faraday Discussions; Vol. 94; pp183-197; 1992.

K

Kaelble, D.H; Physical Chemistry of Adhesion'; Wiley-Interscience; John Wiley & Sons; New York; 1971.

Kambour, R.P.; Karasz, F.E.; Deane, J.H.; Journal of Polymer Science - A; Vol. 4; pp327; 1966.

Kamrava, S.J; Zagorska, M; Krische, B; Soderholm, S; 'Evidence for Microlamella Structure in Polythiophene; A Morphological Study of Conducting Polymers by Scanning Tunnelling Microscopy'; Physica Scripta; 44, pp112-115; 1991.

Kashmiri, M.I and Sheldon, R.P; Journal of Polymer Science, Pt B; Vol. 6; pp45; 1968.

Kasper, K; Hermann, K-H; Dietz, P; Hansma, P.K; Inacker, O; Lehmann, H-D; Rintlen, Th; 'Investigation of dialysis membranes with atomic force microscopy'; Ultramicroscopy (B); Vol.42-44; pp1181-1188; 1992.

Kawazu, A; Ara, N; Yoshimura, M; 'STM of organic conductors'; Springer Series in Surface Science; Vol. 24; (Eds. Tong et al); pp214-226; 1991.

Kell. D.B; 'Are the current carriers tunnelling electrons or hydrated protons'; Bioelectrochemistry & Bioenergetics : J.Electroanalytical Chem.; Vol.342; pp235-237; 1992.

Keller, R.W; Keller, D.J; Bear, D; Vasenka, J; Bustamante, C; 'Electrodeposition procedure of E.Coli RNA polymerase on to gold and deposition of E.coli RNA polymerase on to mica for observation with SFM'; Ultramicroscopy (B) pp1173-1180; 1992.

Keller, R.W; Bustamante, C; Bear, D.G; 'STM of E,coli RNA polymerase electrochemically deposited on a gold substrate'; AIP Conf. Proc #241; pp166-175; 1992.

Kenkre, V.M; Biscanni, F; Bustamante, C;' Theoretical framework for the interpretation of STM images of adsorbates'; Ultramicroscopy (A); Vol.42-44; pp122-127; 1992.

Kim, Y-T; McCorley, R.L; Bard, A.J; 'Observation of n-Octadecanethiol multilayer formation from solution on to gold.'; Langmuir; Vol. 9; No. 8; pp1941-1944; 1993.

Kim, Y-T; Bard, A; 'Imaging and etching of self assembled n-octadecanoethiopl layers on gold with the STM'; Langmuir; Vol. 8; pp1096-1102; 1992.

Kimura, M; Sakurachi, K; Okumura, A; Miyamura, K; Gohshi, Y; 'Scanning tunnelling microscope characterization of organic molecules'; Analytical Sciences; Vol. 7 (Supplement); pp389-390; 1991.

Kishi, E; Matsuda, H; Kuroda, R; Takimoto, K; Yamano, A; Eguchi, K; Htanka, K; Nakagari, T; 'Barrier-height imaging of fatty acid LB films'; Ultramicroscopy (B); Vol. 42-44; pp1067-1072; 1992.

Kolbe, W.F; Ogletree, D.F; Salmeron, M.B; 'Atomic force microscopy imaging of T4 bacteriophages on silicon substrates'; Ultramicroscopy (B); Vol. 42-44; pp1113-1117; 1992.

Koopal, C.G.J; Feiters, M.C; Nolte, R.J.M; deRuiter, B; Schorfoort, R.B.M; Czajka, R; van Kempen, H; 'Polypyrrole micro-tubules and their use in the construction of a third generation bio-sensor'; Synthetic Metals; Vol. 51; pp397-405; 1992.

Kulawansa, D.M; Langford, S.C; Dickinson, J.T; `Scanning Tunnelling Microscope Observations of Polymer Fracture Surfaces'; J.Mater.Res; Vol.7; No.5, pp1292-1302; 1992.

Kwak, J; Bard, A.J; Analytical Chemistry; Vol. 61; pp1221; 1989.

L

Lacaze, E; Garbarz, J; Quillet, V; Schott, M; Pham, M.C; Moslih, J; Lacaze, P.C; 'STM of conducting polymer thin films formed by electropolymerization on graphite and gold'; Ultramicroscopy (B); Vol. 42-44; pp1037-1043; 1992.

Landman, U; Luedtke, W.D; Nitzan, A; 'Dynamics of tip-substrate interactions in atomic force microscopy; Surface Science; Vol. 210; L177; 1989.

Landman, U; Luedtke, W.D;' Atomistic mechanisms and dynamics of the tip-substrate interactions; Proc. of STM'90/NANO I Conference, Baltimore, MD; July 23-27, 1990.

Lang, N.D; 'Theory of single atom imaging in the STM'; Solvay Conference on surface science - Springer Series in Surface Science; Vol. 14; 1988.

Lawunmi, D; Payne, M.C; 'A Theoretical Study of Scanning Tunnelling Microscope Images of Graphite'; Adv.Mater.Proc, Eur. Conf. #1; Ed. Exner, H.E; Vol.2; pp1397-1402; 1990.

Lee, L.H; 'The Chemistry and Physics of Solid Adhesion' in Fundamentals of Adhesion; Ed. Lee, L.H; Plenum Press; New York; ISBN 0-306-43470-9; Chapter 1; pp1-75; 1990.

Lee, I; Atkins, E.D.T; Miles, M.J; 'Visualization of the algal polysaccharide carageenan by scanning tunnelling microscopy'; Ultramicroscopy (B); Vol. 42-44; pp1107-1112; 1992.

Leggett, G.J; Davies, M.C; Jackson, D.E; 'Studies of covalently immobilized protein molecules by STM; the role of water in image contrast formation'; J. Phys. Chem; Vol. 97; pp8852-8854; 1993.

Leggett, G.J; Davies, M.C; Jackson, D.E; Roberts, C.J; Tendler, S.J.B; 'Recent advances in the application of scanning probe microscopy in polymer science'; TRIP; Vol. 1; No. 4; pp115-121; 1993.

Leung. M.S; Ives, N.A; Stupian, G.W; 'Imaging of polydiacetylene on graphite by STM'; J. Appl. Phys.; Vol. 69; No. 4; pp2044-2047; 1991.

Leung, M.S; Ives, N.A; Stupian, G.W; 'Investigation of Polymer Crystallites on Graphite by Scanning Tunnelling Microsopy'; AIP Conf. Proc. #241; pp298-301; 1992.

Leung, O.M; Goh, M.C; 'Orientational Ordering of Polymers by Atomic Force Microscope Tip-Surface Interaction'; Science; Vol. 255; pp64-66, 1992.

Li, S; Hanley, S; Han, I; Varshney, S.K; 'Surface micelle formation at the air/water interface from nonionic diblock copolymers'; Langmuir; Vol. 9; No. 8; pp2243-2246; 1993.

Li, Y.Q.; Tao, N.J; Pan, J.; Garcia, A.A.; Lindsay, S.M.; 'Direct measurement of interaction forces between colloidal particles using the scanning force microscope.'; Langmuir; Vol. 9; pp637-641; 1993.

Lindsay, S.M; Sankey, O.F; 'Contrast and Conduction in STM Images of Biomolecules'; AIP Conf.Proc. #241; pp125-135, 1992

Lindsay, S.M; Pan, L.J; Thundat, T; Nagahara, L.A; Oden, P; DeRose, J.A; Knipping, V; White, J.W; 'Studies of the electrical properties of large molecular adsorbates'; JVST: B; Vol. 9; No. 2; pp1096-1101; 1991.

Lindsay, S.M; 'Potentiostatic deposition of DNA for scanning probe microscopy'; Biophys. J.; Vol.61; pp1570-1584; 1992.

Littke, W; Haber, M; Guntherodt, H.J; 'Investigatio of crystal surfaces on organic layer lattice structures using scanning tunnelling and atomic force microscopies'; J.Cryst.Growth; Vol. 122; pp80-86; 1992.

Loo, B.H; Liu, Z.F; Fujishima, A; 'STM images of an azobenzene derivative differently deposited on HOPG'; Surf. Sci.; Vol. 227; pp1-6; 1990.

Lucas, A.A; Vigneron, J.P; Lambin, Ph.; Laloyaux, Th.; Derycke, I; 'Theroetical aspects of STM'; Surf. Sci.; Vol. 269/270; pp74-80; 1992.

McCrea, C; 'Ultra thin metal films for imaging low-conductivity surfaces by STM'; Ultramicroscopy (B); Vol. 42-44; pp1337-1339; 1992.

McMaster, T.J; Morris, V.J; 'Scanning Microscopy of Biopolymers'; In Methods in Molecular Biology; Vol. 14; Glycoprotein Analysis in Biomedicine; Ed. Hounsell, E.F; Chapter 22; pp277-297; 1993.

Magonov, S.N; Bar, G; Keller, E; Yagubskii, E.B; Loakhina, E.E; Cantow, H-J; 'Surface analysis of organic superconductors by scanning probe techniques: STM and AFM'; Ultramicroscopy (B); pp1009-1018; 1992.

Magonov, S.N; Kempf, S; Kimmig, M; Cantow, H-J; 'Atomic force microscopy on polymers and polymer related compounds'; Polymer Bulletin; Vol.26; pp715-722; 1991.

Magonov, S.N; Cantow, H.J; 'Surface analysis of polymeric materials by AFM'; L'actualite Chemique; pp196-199; 1992.

Magonov, S.N; Cantow, H.J; 'Applications Of Scanning Tunnelling Microscopy to Layered Materials, Organic Charge Transfer Complexes and Conductive Polymers'; Scanning Tunnelling Microscopy and Related Methods; Ed. Behm,R.J et al; Kluwer Academic Publishers; Netherlands; pp367-376; 1990

Mamin, H.J; Ruger, D; 'Fast atomic emission from a gold STM tip'; AIP Conf. Proc #241; pp462-466; 1991.

Manivannan, A; Nagahara, L.A; Yanagi, H; 'Scanning tunnelling Microscopy observation of zincphthalocyanine'; Thin Solid Films; Vol.226; pp6-8; 1993.

Marrian, C.R.K; Colton, R.J; 'Low-Voltage Electron Beam Lithography with A Scanning Tunnelling Microscope'; Appl. Phys. Lett; Vol.56; No.8; pp755-757; 1990

Marshall, P; Price, J; 'Topography of carbon fibre surfaces'; Composites; Vol. 22; No. 5; pp388-393; 1991.

Masaki, N; Machida, K; Kado, H; Yokayama, K; Tohda, T; 'Molecular-resolution images of asprin crystals with atomic force microscopy'; Ultramicroscopy (B); Vol. 42-44; pp1148-1154; 1992.

Matsuda, H; Kishi, E; Kurada, R; 'Parallel arrangement of fatty acid molecules in films deposited at a lower surface pressure'; Thin Solid Films; Vol. 224; pp248-252; 1993.

Mayne, A.J; Cataldi, T.R.I; Knall, J; 'Chemisorption of organic adsorbates on Si and Au studied by STM'; Faraday Discussions; Vol. 94; pp199-212; 1992.

McCord, M.A; Pease, R.F.W; 'Lift-off Metallization using poly(methylmethacrylate) Exposed with a Scanning Tunnelling Microscope'; J.Vac.Sci.Technol.B; Vol.6. No.1; pp293-297; 1988

McGonigal, G.C; Bernhardt, R.H; Yeo, Y.H; Thomson, D.J; 'STM Imaging of Physisorbed Molecules at the Liquid/Graphite Interface'; AIP Conf.Proc. #241; New York; 1992

McMaster, T.J; 'STM of poly(γ-benzyl, L-glutamate)'; Macromolecules; Vol. 24; pp1428-1430; 1991.

Mendez, J; Luna, M; Baro, A.M; 'Preparation of STM W Tips and Characterization by FEM, TEM and SEM'; Surface Science; Vol. 266; pp294-298; 1992

Mercier, J.P. and Legras, R; Journal of Polymer Science - A; Vol. 2; pp4159; 1964.

Meshkov, S.V; Molotkov, S.N; 'New approach to numerical simulations of STM'; J.E.T.P; Vol.73.; No. 5.; 1991.

Meyers, G.F; DeKoven, B.M; Seitz, J.T; 'Is the molecular surface of polystyrene really glassy?'; Langmuir; Vol. 8; pp2330-2335; 1992.

Michel, B; Travaglini, G; Rohrer, H; Joachim, C; Amrein, M; Z. Phys B; Vol. 76; pp99; 1989.

Miles, M.J; Carr, H.J; McMaster, T.C; I'Anson, K.J; Belton, P.S.; Morris, V.J.; Field, J.M; Shewry, P.R; Tatham, A.S; Proceedings of the National Academy of Science -USA; Vol. 88; pp 68; 1991.

Mizes, H.A; Loh, K.G; Miller R.J.D; 'Scanning tunnelling microscopy and atomic force microscopy of thin polymer films; Mol. Cryst. Liq. Cryst.; Vol. 194; pp305-310; 1991.

Moore, W. R and Sheldon, R.P; Polymer; Vol. 2; pp315; 1961.

Moriarty, O; Hughes, G; 'Atomic resolved material displacement on graphite surfaces by scanning tunnelling microscopy'; Appl. Phys. Letts.; Vol. 60; No. 19; 2338-2340; 1992.

Morishige, K; Takami, Y; Yokota, Y; 'Structures of alkanes and alkanols adsorbed on graphite in solution: comparison with scanning tunnelling microscope images'; Phys. Rev. B; Vol. 48; No. 11; pp8277-8281; 1991.

Mou, J; Yang, W.S; 'Scanning tunnelling microscopy studies of alanine and phenylalanine molecules adsorbed on graphite'; Ultramicroscopy (B); Vol. 42-44; pp1025-1030; 1992.

Mulliken, R.S; Electronic Structure of Molecules'; Journal of Chemistry and Physics; Vol. 2; pp782; 1934

Musselman, I.H; Russell, P.E; 'STM & AFM of fibrillar structures in liquid crystal polymers'; Microbeam Analysis (1991) - Eds. Howitt, D.G; San Fransisco Press; U.S.A; pp377-381; 1991.

N

Nejoh, H; Smith, D.P.E; Aono, M; 'Cyanobophenyl-group alignment by an STM'; Nanotechnology; Vol. 2; pp214-220; 1991.

Niemi, H.E.M; Ikonen, M; Levlin, J.M; Lemmetyinen, H; 'Bacteriorhodopsin in LB films imaged with an STM'; Langmuir; Vol. 9; pp2436-2447; 1993.

Nishikawa, O; Tomotori, M; Iwawaki, F; 'Effect of Tip Apex on STM and STS'; Springer Series in Materials Science, Eds Yoshimori et al; Vol. 17; pp39-46; 1992.

Niu, L; Shiau, W.L; Vesenka, J; Larson, D.D; Handerson, E; 'AFM of DNA-colloidal gold and DNA protein complexes'; SPIE vol. 1891, Advances in DNA Sequencing Technology; pp71-77; 1993.

Nogues, J; Costa, J.L; Roa, K.V; 'Fractal dimension of thin film surfaces of gold sputter deposited on mica: an STM study'; Physica Acta; Vol. 182; pp532-541; 1992.

O

Obcemea, Ch; Vidic, B; 'Bilipid layer molecular organization in P_β phase studied by scanning tunnelling microscopy'; Ultramicroscopy (B); Vol. 42-44; pp1019-1024; 1992.

Ohmi, T; Shibata, T; 'Scientific VLSI manufacturing in the 21st century'; Interface; Winter; pp32-37; 1992.

Onu, A; Legras, R; Mercier, J.P; Journal of Polymer Science - B; Vol. 14; pp1187; 1976.

Oshio, T; Nakatani, N; Sakai, Y; Suzuki, N; Kataoka, T; 'Atomic force micrsocope detection system using an optical fibre heterodyne interferrometer free from external disturbances'; Ultramicroscopy (A); Vol. 42-44; pp310-314; 1992.

Overny, R.M; Howald, L; Frommer, J; Meyer, E; Brodbeck, D; Guntherodt, H-J; 'Molecular surface structure of organic crystals observed by atomic force microscopy'; Ultramicroscopy (B); pp983-988; 1992.

Patrick, D.L; Cee, V.J; Beebe, T.P.Jr.; 'Molecular corrals: for studies of monolayer organic films'; Science; Vol.265; pp231-234; 1994.

Pauling, L; 'The Nature of the Chemical Bond'; Cornell University Press; Ithaca; New York; 1966.

Peltonen, J.P.K; He, P; Rosenholm, J.B; 'Order and defects of LB films detected with the AFM'; J. Am. Chem. Soc. ; Vol. 114; pp7637-7642; 1992.

Pendry, J.B; 'Electronic processes at disordered surfaces'; Solvay Series on Surface Sciences; Springer Series in Surface Science; Vol. 14; pp222-226; 1988.

Pethica, J.B; ' Interatomic forces in scanning tunnelling microscopy: Giant corrugations of the graphite surface'; Phys.Rev.Letts; Vol. 57; p3235; 1986

Pethica, J.B and Sutton, A.P; 'On the stability of a tip and flat surface at small separations'; JVST-A; Vol. 6; p2490; 1988.

Piner, R; Reifenberger, R; Martin, D.C; Thomas, E.L; Apkarin, R.P; 'A STM study of single crystal polyethylene'; J. Polymer. Science; Part C; Vol. 28; pp399-410; 1990.

Pitarke, J.M; Flores, F; Echenique, P.M; 'Tunnelling Spectroscopy: surface geometry and interface potential effects'; Surface Science; Vol. 234; pp1-16; 1990.

Ponce, S et al; 'Component Interaction and Properties of Pigmented Epoxy Systems'; International Meeting of the Adhesive Society'; Williamsberg; 1987.

Porter, T.L; Jeffers, S; Caple, G; Wheeler, B.L; Swift, R; 'Scanning Tunnelling Microscopy Studies of Polythiophene and Poly-3-Bromothiophene Films'; Surface Science Letters; Vol. 238; pp L433-L438; 1990

Porter, T.L; Caple, K; Vaple, G; 'Surface structure of free-standing polyaniline films'; Synthetic Metals; Vol. 60; pp211-214; 1993.

Prietzschk, A; Kolloid-Z; Vol. 156; p8; 1958.

Pritchard, R.G; 'Scanning Tunnelling Microscopy: a short course'; Czech Republic Summer School; 1990.

Quate, C.F; 'Scanned Probe Microscopes'; AIP Conf. Proc #241; p1-8; 1992

Qun, D; Jianwu, D; Yaxian, S; 'STM of glycophorin A, F-actin and plasmid DNA in H_2O'; Journal of Beijing Medical University; Vol. 25; No. 1; pp77-79; 1993.

Rabe, J.P; 'Molecules at interfaces: STM in materials and life sciences'; Ultramicroscopy (A); Vol. 42-44; pp41-54; 1992.

Rabke-Clemmer, C.E; Wenzler, L.A; Beebe, T.P; 'STM, AFM and surface analysis methods for the investigation of biomolecular structure at a solid surface'; SPIE vol. 1891; Advances in DNA Sequencing Technology; pp38-47; 1993.

Reiss, G; Bruckl, H; 'The influence of surface roughness on electronic transport in thin films'; Surface Science; Vol. 269/270; pp772-776; 1992.

Reneker, D.H; Howell, B.F; 'Summary Abstract: Preparation of Polymer Molecules for Examination by Scanning Tunnelling Microscopy'; J.Vac.Sci.Technol.A; Vol.6. No.2; pp553-554; 1988.

Reneker, D.H; Schneir, J; Howell, B; Harary, H; 'Polyethylene Crystallized from an Entangled Solution Observed by Scanning Tunnelling Microscopy'; Polymer Communications; Vol.31; pp167-169; 1990.

Ricci, D; Bonfiglio, A; Cincotti; diZitti, E; Elementi, L; 'High resolution imaging of physisorbed organic monolayers by STM'; Mol. Cryst. Liq. Cryst. ; Vol. 229; pp235-240; 1993.

Roberts, C.J; Hoffmann-Millack, B; Steer, W.S; 'The Observation of Adsorbates on a Gold Surface in air: Their Deposition and Removal using Scanning Tunnelling Microscopy'; Surface Science; Vol. 224; pp1-12; 1989

Roberts, C.J; Davies, M.C; Jackson, D.E; Tendler, S.J.B; 'Towards the low-force imaging of biological and biomedical materials by AF<'; Nanobiology; 2; pp73-79; 1993.

Roberts, C.J; Sekowski, M; Davies, M.C; 'Topographical investigations of human ovarian carcinoma polymorphic epithelial micin by STM'; Biochem. J.; Vol. 181-185; 1992.

Rohrer, H; 'STM: 10 years after'; Ultramicroscopy (A); pp1-6; 1992.

S

Sacks, W; Noguera, C; 'Investigation of the tunnelling current for adsorbates on a surface'; Ultramicroscopy (A); Vol. 42-44; pp140-146; 1992.

Salmeron, M; Ogletree, D.F; Neubauer, G; Murray; M.N; Wilson, T.E; Bednarski, M.D; Kolbe, W; Folch, A; 'Imaging of Biological Material with STM/AFM'; SPIE Scanning Microscopy Instrumentation; 1556; pp40-54; 1991.

Sano, M; Sasaki, D.Y; Kunitaki, T; 'Structural study of polyethers on graphite by scanning tunnelling microscopy polymerization-induced epitaxy'; Macromolecules; Vol. 25; pp6961-6969; 1992.

Sarid, D; 'Scanning Force Microscopy: with applications to electric, magnetic and atomic forces'; Oxford Series in Optical and Imaging Sciences; Eds. Lapp, M. and Stark, H; Oxford University Press; New York and Oxford; 249pages; ISBN 0-19-506270-1; 1991.

Sasano, K; Nakamura, K; Kaneto, K; '*In-situ* observation and selective electrochemical deposition of polypyrrole by STM'; Jpn. J. Appl. Phys.; Vol. 32; Part 2; No. 6B; ppL863-L865; 1993.

Sautet, P; Joachim, C; 'Are electronic interference effects more important for STM imaging of substrates and adsorbates? A theoretical analysis'; Ultramicroscopy (B); Vol. 42-44; pp115-121; 1992.

Sautet, P; Joachim, C; 'Interpretation of STM images: copper phthalocyanine on copper'; Surface Science; Vol. 271; pp387-394; 1992.

Sautiere, L; Day, S; Miles, M.J; 'Smetic structures in a two-components liquid crystal mixture'; Ultramicroscopy (B); Vol. 42-44; pp1054-1058; 1992.

Schabert, F; Hefti, A; Goldie, K; Stemmer, A; Engel, A; Meyer, E; Overney, R; Guntherodt, H-J; 'Ambient pressure scanning probe microscopy of 2D regular protein arrays'; Ultramicroscopy (B); Vol. 42-44; pp1118-1124; 1992.

Schallamach, A; A.Wear; Vol. 17; pp301; 1971

Schmid, M; Varga, P; 'Analysis of vibration-isolating systems for STMs'; Ultramicroscopy (B); Vol. 42-44; pp1610-1615; 1992.

Schnell, H; 'Chemistry and Physics of Polycarbonates'; Interscience; John Wiley and Sons; New York; 1964.

Schnupp, P; Phys. Stat. Solid.; Vol. 21; pp567; 1967

Schonherr, H; Snetivy, D; Vanesco, G.J; 'A nanoscopic view at the spherulitic morphology of isotactic polypropylene by AFM'; Polymer Bulletin; Vol. 30; pp567-574; 1993.

Schreiber, H.P et al; Acid-base considerations of surface interactions in polymer system control by microwave plasma treatment: phyico-chemical aspects of polymer surfaces volume 2; Ed.Mittal, K.L; Plenum Press, New York; 1983.

Schwindlein, W; 'Crystallization of PEO doped with $NiBr_2$ '; Personal Communication; 1994 and 1995.

Seanor, D.A; 'Electrical Conduction in Polymers' in Electrical Properties of Polymers: Ed. Seanor, D.A; Academic Press; New York & London; ISBN 0-12-633680-6; Chapter 1; pp1-58; 1982

Sharples, A; 'Introduction to polymer crystallization'; Edward Arnold (publishers) ltd.; London; 1966.

Shen, J; `Construction and Evaluation of A Scanning Tunnelling Microscope'; Ph.D Thesis CNAA; Leicester Polytechnic; 1991

Simic-Krstic, J; Voelker, M; Andjelkovic, M; Trifunovic, M; 'Imaging of tubulin in microtubules and zinc-induced sheets by STM'; Nanobiology; Vol. 2; pp65-72; 1993.

Siperko, L.M; Hurbam, S.S.; Spalik, J.M.; Katani, A.D.; 'Complementary STM and SEM studies of electroplated gold surfaces'; J.V.S.T: A; Vol. 10; No. 4; pp2400-2402; 1992.

Siqueiros, J.M.; Macherro, R; Valenzuela, J; Morales, L; Regarlardo, L.E; 'A study of the dispersive behavoir of an anisotropic gold film on mica'; Springer Proceedings in Physics; Vol. 62; pp295-300; 1992.

Smithson, R.L.W; Stange, T.G; Evans, D.F; Edstrom, R.D; Hendrickson, W.A;'AFM and STM of Organic Macromolecules'; AIP Conf. Proc. #241; New York; pp219-231; 1992.

Snetivy, D; Vanesco, G.J; Rutledge, G.C; 'Atomic force microscopy of polymer crystals: Molecular imaging and study of polymorphism in poly(p-phenyleneterepphthalamide) fibres'; Macromolecules; Vol. 25; pp7037-7042; 1992.

Snyder, E.J; Eklund, E.A; Williams, R.S; 'Effects of Tip Size and asymmetry on Scanning Tunnelling Microscopy Topographs'; Surface Science Letters; Vol. 239; L487-L492; 1990.

Snyder, S.R; Foecke, T; White, H.S; 'Imaging of stacking faults in HOPG using the STM'; J. Mater. Res.; Vol. 7; No. 2; pp341-345; 1992.

Soto, M.R.; 'The effect of point defects on the STM image of graphite'; Surface Science; Vol. 225; pp190-194; 1990.

Stange, T.G; Mathew, R; Evans, D.F; 'Scanning Tunnelling Microscopy and Atomic Force Microscopy Characterization of Polystyrene Spin-Coated onto Silicon Surfaces'; Langmuir; Vol.8; pp920-926, 1992.

Stocker, W; Bickermann, B; Magonov, S.N; Cantow, H.J; 'Surface structure of polymers and their model compounds observed by atomic force microscopy'; Ultramicroscopy (B); Vol. 42-44; pp1141-1146; 1992.

Stachurski, Z.H; Journal of Material Science; Vol. 21; pp3231; 1986.

Sumpter, B.G; Getino, C; Norid, D,W; 'Computational studies of submicron probing of polymer surfaces'; J. Chem. Phys.; Vol. 96; No. 9; pp7072-7085; 1992.

Stillinger, F.H; Weber, T.A; 'Computer simulation of local order in condensed phases of silicon' Phys. Rev. B; Vol. 31; pp5262; 1985.

Sweeting, O.J; 'The Science and Technology of Polymer Films'; Vol. 2; Wiley Interscience; Wiley & Sons; New York; 1971.

T

Tabor, D;' Surface Forces and Surface Interactions'; J. Colloid Interface Sci; Vol. 3; pp137; 1977.

Taki, S; Ishida, K; Okabe, H; Matsushige, K; 'Direct observation of the growth process of organic crystals by STM'; J. Cryst. Growth; Vol. 131; pp13-16; 1993.

Tarasov, N.A; 'On the dynamics of statistical fluctuations in the electron tunnelling process and the problems of the STM resolution'; Ultramicroscopy (A); Vol. 42-44; pp223-230; 1992.

Taylor, M.E; 'Inelastic processes in tunnelling electrodes'; Ultramicroscopy (A); Vol. 42-44; pp215-222; 1992.

Tersoff, J; 'Theory of Scanning Tunnelling Microscopy and Spectroscopy'; Scanning Tunnelling Microscopy and Related Methods; Ed. Behm,R.J et al; Kluwer Academic Publishers; Netherlands; pp77-95; 1990

Tersoff, J; Hamman, D.R; 'Theory and application for the scanning tunnelling microscope'; Phys. Rev. Letts; Vol. 50; No. 25; pp1998-2001; 1983

Thomson, N.H; Miles, M.J; Tatham, A.S; Shewry, P.R; 'Molecular images of cereal proteins by STM'; Ultramicroscopy (B); Vol. 42-44; pp 1204-1213; 1992.

Thompson, G; Shen, J; Connolly, P; Cooper, J; 'Gold as a substrate to image-immobilized biomolecules by STM : Part 1'; Nanobiology; Vol. 2; pp43-53; 1993.

Thundat, T; Allison, D.P; Warnock, R,J; Ferrel, T.L; 'Imaging isolated strands of DNA molecules by atomic force microscopy'; Ultramicroscopy (B); Vol. 42-44; pp1101-1106; 1992.

Thundat, T, Warnock, R.J; Allison, D.P; Ferrell, T.L; 'Electrostatic spraying of DNA molecules for investigation by scanning tunnelling microscopy'; Ultramicroscopy (B); Vol. 42-44; pp1083-1087; 1992.

Timoshenko, S and Goodier, J; Theory of Elasticity; 3rd Edition; McGraw Hill; New York.

Travaglini, G; Amrein, M; Michel, B; Gross, H; 'Imaging and Conductivity of Biological and Organic Material'; Scanning Tunnelling Microscopy and Related Methods; Ed. Behm,R.J et al; Kluwer Academic Publishers; Netherlands; pp335-347; 1990.

Tsukada, M; Kobayashi, K; Isshiki, N; Kageshima. H; 'First principles theory of STM'; Surface Science Reports; Vol. 13; pp265-304; 1991.

Tsukruk, V.V; Reneker, D.H; Bengs, H; Ringsdorf, H; 'AFM of ordered monolayer films from discotic liquid crystals'; Langmuir; Vol. 9; No.8; pp2141-2144; 1993.

Turska, E; Przygocki, W,; Maslowski, M; J. Polymer Science : C; Vol. 16; p3821; 1968

U & V

Umemoto, T; Ishikawa, K; Takezoe 'Photoisomerization observed by means of STM'; Jpn. J. Appl. Phys.; Vol. 32; ppL936-L939; 1993.

Vernetti, L.A; Sarid, D; Gandolfi, A.J; Cress, A.E; Nagle, R.B; McCuskey, R; Hameroff, S.R; 'STM images of cytokeratin and binding IgG antibody'; AIP Conf. Proc. #241; pp232-234; 1991.

Vasenka, J; Guthold, M; Tang, C.L; Keller, D; Delaine, E; Bustamante, C; 'Sunstrate preparation for reliable imaging of DNA molecules with the scanning force microscope'; Ultramicroscopy (B); Vol. 42-44; pp1243-1249; 1992.

W

Wan, M; Yang, J; Zhu, C; Bai, C; 'Scanning Tunnelling Microscopy images of Polyaniline'; Thin Solid Films; Vol.208; pp153-155; 1992

Wang, Y; Xu, Q; Xie, Y; Gui, L; Tang Y; 'Characterization of Polymer-Protective Transition Metal Colloids by Scanning Tunnelling Microscopy'; J. Colloidal and Interfacial Science; Vol.151; No.2; pp392-395; 1992

Wang, J; Angnes, L; Martinez, T; 'Scanning tunnelling microscopic probing of surface fouling during the oxidation of nicotinamide coenzymes'; Bioelectrochemistry and bioenergetics; Vol. 29; pp215-221; 1992.

Weisenhorn A.L; Schmitt, F.J; Knoll, W; Hansma, P.K; 'Streptavadin binding observed with an atomic force microscope'; Ultramicroscopy (B); Vol. 42-44; pp1125-1132; 1992.

Wells, T.N.C; Steadman, M; Leatherbarrow, R.J; 'Imaging of proteins by STM'; Ultramicroscopy (B); Vol. 42-44; pp1200-1203; 1992.

Wessling, B; Hiesgen, R; Meissner, D; 'STM investigations on primary particle morphology of polyaniline'; Acta Polymer; Vol. 44; pp132-134; 1993.

West, P.E; 'The AFM: Extending microscopy to the sub-nanometre range'; International Microscopy Loboratory; Vol. 1; p3; 1992.

Wetsel, G.C; McBride, S.E; 'Stable nanometre-sized patterns produced by high electric fields'; AIP Conf. Proc. #241; pp467-479; 1991.

Wickramasinghe, H.K; 'Scanned probes, old & new'; AIP Conf. Proc. #241; pp9-25; 1992.

Wiesendanger, R; 'Fabrication of nanometre structures using the STM'; Appl. Surf. Sci.; Vol. 54; pp271-277; 1992.

Wilkins, M.J; Davies, M.C; Jackson, D.E; Roberts, C.J; Tendler, S.J.B; Williams, P.M.; 'Observation of super periodic features on gold with an STM'; Appl. Phys. Letts; Vol. 60; No. 12; pp1436-1437; 1992.

Williams, M.L; Landel, R.F; Ferry, J.D; American Chemical Society; Vol. 77; pp3701; 1955

Woodward, T; Zasadzinski, J.A; Yoan, J.Y; Zhifeng, S; Gao, C; - 'Correspondance on alternative method of imaging surface topologies of non-conducting bulk specimens by STM'; Phys. Rev. Letts; Vol. 68; No. 16; pp2563-2564.

X, Y & Z

Xue, Z.Q; Lui, W.M; Zhao, X.Y; Gao, H.J; Zhu, C; Ma, Z; Pang, S; 'Observed Lattice Structures of Polyethylene with TEM and STM'; Vacuum; Vol.43; No.11; pp1119-1121; 1992

Xue, Z.Q; Gao, H.J; Lui, W.M; Zhu, C; Ma, Z; Pang, S; 'Investigation of periodic structures of polyethylene crystal lamellae with STM'; Appl. Surf. Sci.; Vol. 60.61; pp346-349; 1992.

Yackoboski, K; Yeo, Y.H; McGonigal, G.C; Thomson, D.J; 'Molecular position at the liquid/solid interface measured by voltage-dependent imaging with the STM'; Ultramicroscopy (B); Vol. 42-44; pp963-967; 1992.

Yamada, H; Akamine, S; Quate, C.F; 'Imaging of organic molecular films with atomic force microscope'; Ultramicroscopy (B); pp1044-1048; 1992.

Yang, R; Smyrl, W.H; Evans, D.F; Hendrickson, W.A; 'Evolution of polypyrrole band structure: A STS study'; J.Phys.Chem. ; Vol. 96; pp1428-1430; 1992.

Yang, R; Evans, D.F; 'STM evidence of semicrystalline and helical conducting polymer structures'; J.Phys. Chem; Vol. 94; pp6117-6122; pp6117-6122

Yang, R; Evans, D.F; Christensen, L; Hendrickson, W.A; 'Scanning Tunnelling Microscopy Evidence of Semicrystalline and Helical Conducting Polymer Structures'; J.Phys.Chem; Vol.94; pp6117-6122; 1990.

Yang, R; Yang, X.R; Evans, D.F; Hendrickson, W.A; Baker, J; 'Scanning Tunnelling Microscopy Images of Poly(ethylene oxide) Polymers: Evidence for Helical and Superhelical Structures'; J.Phys.Chem; Vol.94; pp6123-6125; 1990.

Yang, R; Smyrl, W.H; Evans, D.F; Hendrickson, W.A; 'Evolution of Polyprrole Band Structure: A Scanning Tunnelling Spectroscopy Study'; J.Phys.Chem, Vol. 96, pp1428-1430; 1992.

Yang, W.S.; Yanfang, Li; Mu, J.; Yan, J; Atomic charge superposition calculations of STM images of glycine and alanine adsorbed on graphite'; Ultramicroscopy (B); Vol. 42-44; pp1031-1036; 1992.

Yang, X; Bromm, Ch. Geyer, U; von Minnigerode, G; 'Several large scale superperiodicities on HOPG observed by STM.'; Annalen der Physik; Vol. 1; pp3-10; 1992.

Yaniv, D.R.; McCormick, L.D; 'Polypyrrole nanoplating on HOPG utilizing an STM tip'; Nanotechnology; Vol. 3; pp44-47; 1992.

Youngquist, M.G; Driscoll, R.J; Coley, T.R; Goddard, W.A; Baldeschwieler, J.D; 'STM of DNA in UHV'; AIP Conf. Proc. #241; pp154-158; 1992.

Zajac, G.W; Patterson, M.Q.; Burrell, P.M.; Metaxas, C; 'Scanning probe microscopy studies of isotactic polypropylene'; Ultramicroscopy (B); Vol. 42-44; pp998-1003; 1992.

Zenhausern, F; Adrian, M; Emch, R; Tabenelli, M; Jobin, M; Descoute, P; 'Scanning force microscopy and cryo-electron microscopy of tobacco mosaic virus as a test specimen'; Ultramicroscopy (B); Vol. 42-44; pp1168-1172; 1992.

Zeppenfeld, P; Lutz, C.P.;Eigler, D.M.; 'Manipulating atoms and molecules with a scanning tunnelling microscope'; Ultramicroscopy (A); Vol. 42-44; pp128-133; 1992.

Zhang, H; Horden, L.S; Kuan, S.W.J; Maccagno, P; 'Exposure of Ultrathin Polymer Resists with the Scanning Tunnelling Microscope'; J.Vac.Sci.Technol.B; Vol.7; No.6; pp1717-1722; 1989

Zhu, C; Shen, J; Ma, Z.; Pang, S.; 'Morphology of monolayer LB film by STM'; Vacuum; Vol. 43; No. 11; pp1111-1113; 1992.